

UNCLASSIFIED REPORT DOCUMENTATION PAGE			
1a. REPORT SECURITY CLASSIFICATION Unclassified		1b. RESTRICTIVE MARKINGS None	
2a. SECURITY CLASSIFICATION AUTHORITY DTIC ELECTE APR 30 1990 IBER(S)		3. DISTRIBUTION/AVAILABILITY OF REPORT Approved for public release; Distribution unlimited.	
AD-A221 215		5. MONITORING ORGANIZATION REPORT NUMBER(S) AFOSR-TR-90-0502	
6a. ADDRESS (City, State, and ZIP Code) CeramPhysics, Inc. 921 Eastwind Drive, Suite 110 Westerville, OH 43081		7a. NAME OF MONITORING ORGANIZATION Air Force Office of Scientific Research	
6b. ADDRESS (City, State, and ZIP Code) Building 410 Bolling AFB, DC 20332-6448		7b. ADDRESS (City, State, and ZIP Code) Building 410 Bolling AFB, DC 20332-6448	
8a. NAME OF FUNDING/SPONSORING ORGANIZATION AFOSR		8b. OFFICE SYMBOL (if applicable)	
9. PROCUREMENT INSTRUMENT IDENTIFICATION NUMBER F49620-86-C-0049		10. SOURCE OF FUNDING NUMBERS	
8c. ADDRESS (City, State, and ZIP Code) Building 410 Bolling AFB, DC 20332-6448		PROGRAM ELEMENT NO. 61102F	
		PROJECT NO. 2301	
		TASK NO. B2	
		WORK UNIT ACCESSION NO.	
11. TITLE (Include Security Classification) Research on High-Specific-Heat Dielectrics (2)			
12. PERSONAL AUTHOR(S) W.N. Lawless			
13a. TYPE OF REPORT Final		13b. TIME COVERED FROM APR 80-31 Aug 85	
14. DATE OF REPORT (Year, Month, Day) 1990, January 31		15. PAGE COUNT 386	
16. SUPPLEMENTARY NOTATION			
17. COSATI CODES		18. SUBJECT TERMS (Continue on reverse if necessary and identify by block number)	
FIELD	GROUP	SUB-GROUP	
19. ABSTRACT (Continue on reverse if necessary and identify by block number) A large amount of experimentation has been performed on ceramic samples of zinc chromite and cadmium chromite prepared under new conditions of doping, stress, purity, and particle size. No structures in the specific heats of these spinels are induced above 15 K by wide variations in one or all of these conditions. Under various doping conditions, the specific heat peak in cadmium chromite can be sharpened, broadened, or eliminated, but not split. In contrast, the specific heat peak in zinc chromite is easily split into two components by all dopants studied. Calorimetric, magnetic susceptibility, and EPR measurements are in basic agreement in characterizing these effects. (25)K			
20. DISTRIBUTION/AVAILABILITY OF ABSTRACT <input type="checkbox"/> UNCLASSIFIED/UNLIMITED <input type="checkbox"/> SAME AS RPT. <input type="checkbox"/> DTIC USERS		21. ABSTRACT SECURITY CLASSIFICATION OF PUBLIC RELEASE	
22a. NAME OF RESPONSIBLE INDIVIDUAL MAJ John PRINCE		22b. TELEPHONE (Include Area Code) 202/767-4208	
		22c. OFFICE SYMBOL N4	

Block 19. ABSTRACT, Con't.

Monte Carlo calculations have shown how the perfect frustration of the cubic lattice can be partially or fully removed by tetragonal distortions, and the theoretical suggestions are that zinc chromite is characterized by a partially frustrated, a less than c , second-order, antiferromagnetic transition, whereas cadmium chromite may remain essentially cubic and highly frustrated. Incorporation of spin-clustering successfully explains the double specific heat peaks observed in zinc chromite. The Monte Carlo calculations show the sensitivity of the thermal properties of the chromite spinel lattice to tetragonal distortions. In contrast, however, the specific heat peaks in zinc chromite and cadmium chromite are experimentally unaffected by stress types (tensile or compressive) or stress magnitudes. Here also, the thermal, magnetic susceptibility, and EPR measurements are in basic agreement. In addition, low temperature thermal contraction measurements show that both materials are distorted at the transition temperatures.

In very fine-grain powders (approximately 100 angstrom) broad specific heat maxima are found in these spinels and correspond to antiferromagnetic transitions. Surprisingly, a 5% Gd doping restores a sharp specific heat peak in zinc chromite but not in cadmium chromite. Calorimetric data show that powders have the highest density of free spins below the transition, especially so in the case of Gd doping. The EPR measurements, however, are not in agreement with this finding.

Monte Carlo calculations show that for the a less than c tetragonal distortion, the transition is second order; however, for the a greater than c distortion, the transition can be either first or second order. The slow temperature drifts used in the specific heat measurements are extremely sensitive to first-order latent heats at transitions, and no evidence of a latent heat is observed in all of the samples. Either all transitions are second order, or, if first order, have very small latent heats.

Dielectric anomalies are observed at the transitions in zinc chromite and cadmium chromite and these findings have been explained theoretically by incorporating a coupling between the polarization and the magnetization in the spin-frustration model.



CeramPhysics, Inc.

921 Eastwind Drive, Suite #110, Westerville, Ohio 43081
Telephone (614) 882-2231 FAX (614) 882-1437

✓

AFOSR Contract # F49620-86-C-0049
NTIS GRA&I
DTIC TAB
Unannounced
Justification
This report is available
to the public
CATHEN, J. K. 1990
Chief, Technical Information Division

FINAL REPORT

Approved for public release;
distribution unlimited.

for

AFOSR Contract # F49620-86-C-0049

RESEARCH ON HIGH-SPECIFIC-HEAT DIELECTRICS

Prepared by

CeramPhysics, Inc.
921 Eastwind Drive, Suite 110
Westerville, Ohio 43081

January 31, 1990

Accession For	
NTIS GRA&I	<input checked="" type="checkbox"/>
DTIC TAB	<input type="checkbox"/>
Unannounced	<input type="checkbox"/>
Justification	
By	
Distribution/	
Availability Codes	
Dist	Avail and/or Special
A-1	

RECEIVED
AFOSR
JAN 31 1990

INDEX

Topic	Page
I. SUMMARY.....	1
II. INTRODUCTION AND BACKGROUND.....	4
III. SAMPLE PREPARATION METHODS AND RESULTS.....	7
A. SAMPLE PREPARATIONS AT PENN STATE UNIV.....	8
B. SAMPLE PREPARATIONS AT WEST VIRGINIA UNIV.....	56
IV. SPECIFIC HEAT STUDIES.....	69
A. BROAD RANGE SPECIFIC HEAT METROLOGY.....	70
B. BROAD RANGE SPECIFIC HEAT MEASUREMENTS.....	105
C. SUMMARY OF SPECIFIC HEAT STUDIES.....	184
V. THERMAL EXPANSION, DIELECTRIC CONSTANT, AND AC CONDUCTIVITY STUDIES.....	186
A. THERMAL EXPANSION AND DIELECTRIC STUDIES OF CERAMICS.....	186
B. THERMAL CONTRACTION OF COMPOSITE SAMPLES.....	193
C. DIELECTRIC CONSTANT MEASUREMENTS ON DOPED AND HUP'D SAMPLES.....	202
D. AC CONDUCTIVITY MEASUREMENTS.....	207
E. SUMMARY AND CONCLUSIONS OF MEASUREMENTS.....	207
VI. MAGNETIC SUSCEPTIBILITY AND EPR MEASUREMENTS.....	210
A. INTRODUCTION.....	210
B. EXPERIMENTAL METHODOLOGY AND SAMPLE DETAILS.....	212
C. EXPERIMENTAL RESULTS.....	214
D. EFFECT OF PROCESS VARIABLES.....	228
E. CONCLUSIONS.....	239
VII. THEORETICAL STUDIES.....	243
A. IMPURITY SPIN DOPING ON UNDISTORTED SPINEL LATTICE.....	244
B. IMPURITY SPIN DOPING ON DISTORTED SPINEL LATTICE, $a > c$	263

C. IMPURITY SPIN DOPING ON DISTORTED SPINEL LATTICE, $a < c$	281
D. GINZBURG-LANDAU ANALYSIS OF PHASE TRANSITIONS.....	301
E. MONTE CARLO CALCULATIONS OF MAGNETIC PHASE DIAGRAM.....	322
F. IMPURITY SPLITTING OF SPECIFIC HEAT PEAKS.....	364
G. SUMMARY OF THEORETICAL STUDIES.....	381
VIII. CONCLUSIONS AND DISCUSSION.....	384
A. STATUS OF EXPERIMENTS AND THEORY.....	384
B. FUTURE RESEARCH DIRECTIONS.....	385

I. SUMMARY

This research program was originally based on the preparation of the spinels ZnCr_2O_4 and CdCr_2O_4 by sophisticated ceramic methods and by single-crystal-growth methods. With the one exception of an isostatically pressed sample, no further samples were produced by these methods. Fortunately, however, a large variety of samples of these spinels unexpectedly became available from a separate Air Force program, and these latter samples incorporated both multiple dopings, multiple stress configurations, and combined doping + stress conditions. Also, very fine grain powder samples became available, including Gd-doped powders; consequently, the experimental efforts in this program became directed toward these alternate samples, and this in turn steered the theoretical efforts in this direction also.

A novel drift method for measuring specific heats was developed in order to extend the measurement capability to 100 K and to take advantage of computer-interfacing. The method was calibrated using ETP copper samples and the NBS tables.

Broad range specific-heat measurements were performed on the spinels under a variety of conditions: (1) Undoped samples, including high-purity samples; (2) Samples doped with Mo, V, Al, and Gd, including sulfur-exchanged samples; (3) Glass/ceramic composites which put the ceramic grains in tension; (4) Epoxy/ceramic composites which put the ceramic grains in compression; (5) Combined doping + stress conditions in glass/ceramic composites involving Al and Gd dopants; and (6) Very fine grain ceramic powders, both undoped and Gd-doped. Thermal expansion measurements were performed on some of the composite samples to confirm that the thermal-expansion differences were such as to put the ceramic grains in tension or compression.

No structure in the specific heats of either of these spinels is induced above 15 K by any or all of the above preparation conditions. Nor are the dominant specific heat peaks in either of the spinels affected by stress effects, whether compressive or tensile.

Magnetic susceptibility and EPR measurements were performed on eighteen samples chosen from the above and based on the results of the specific heat measurements. The samples chosen for these measurements were the doped ceramic samples and the high-purity samples (composites were not investigated).

Under a variety of doping conditions, the specific heat peak in CdCr_2O_4 can be sharpened, broadened, or eliminated, and some impurities must be present for the peak to appear. No conditions in CdCr_2O_4 lead to a splitting of the peak, but, in contrast, in ZnCr_2O_4 the specific heat peak is easily split into two components by all dopants studied, regardless of the dopant spin. The calorimetric, magnetic susceptibility, and EPR measurements are in basic agreement in characterizing these effects.

Monte Carlo calculations show how the perfect frustration in the cubic spinel lattice can be partially or fully removed by tetragonal distortions. The theoretical conclusions are that ZnCr_2O_4 is characterized by a partially frustrated, $a < c$, second-order, antiferromagnetic transition, whereas CdCr_2O_4 may remain essentially cubic and therefore highly frustrated. The incorporation of spin-clustering successfully explains theoretically the splitting of the specific heat peak in doped ZnCr_2O_4 , regardless of the spin of the dopant (including zero spin).

The Monte Carlo calculations show the sensitivity of the specific-heat properties to tetragonal distortions in the spinel lattice. It is puzzling, then, that the specific heats are not affected by tensile or compressive stresses.

In very fine grain powders ($\sim 100 \text{ \AA}$) of the spinels, broad specific heat maxima are found which correspond to antiferromagnetic transitions. Surprisingly, a 5% Gd doping induces a very sharp specific heat in ZnCr_2O_4 but not in CdCr_2O_4 . Calorimetric measurements show that powders have the highest density of free spins below the transition temperature, especially so in the case of Gd-doping. The EPR findings, however, are not in agreement with this finding.

Monte Carlo calculations show that for the $a < c$ tetragonal distortion, the transition is second order; for the $a > c$ distor-

tion, however, the transition can be either first or second order. Experimentally, the slow temperature drifts involved in the multitude of specific heat measurements provide an extremely sensitive method for resolving latent heats at first order transitions. In no case was any evidence seen for a latent heat in all the specific-heat experiments in this program. Either all transitions in all samples are second order, or what first-order transitions may exist have very small latent heats.

Low temperature thermal contraction measurements on ZCN(9/1) and CCN(9/1) ceramic samples show that there is a distortion in the lattice constants of each material at the respective antiferromagnetic transition temperature.

Anomalies in the dielectric constant are observed in the neighborhood of the transitions in ZnCr_2O_4 and CdCr_2O_4 samples prepared under a variety of conditions. These findings have been explained theoretically by incorporating a coupling between the polarization and the magnetization in the spin-frustration model.

Measurements of the ac conductivity of the spinel samples have been performed in the neighborhood of the transition temperatures. No new information was found as the samples act as perfect dielectrics.

Directions for future research areas are discussed.

II. INTRODUCTION AND BACKGROUND

In the late 70's, Dr. W. N. Lawless, President of CeramPhysics, Inc., discovered two remarkable properties of the spinels ZnCr_2O_4 and CdCr_2O_4 : (1) These spinels sinter into hard, dense ceramic bodies if, and only if, a columbite mineralizer is present; and (2) These ceramics exhibit enormous specific-heat maxima at 10.5 and 8 K, respectively (The specific heat values achieved approach that of water at room temperature). These discoveries spurred several applied programs aimed at utilizing these effects for the enthalpy-stabilization of superconductors; programs funded from Wright-Patterson AFB were directed toward Nb_3Sn and, more recently, the YBCO ceramic superconductor, and a NASA-funded program was aimed at NbTi. In the case of the Al5 intermetallic superconductors, long lengths of both Nb_3Sn and NbTi have now been coated with dielectric insulations which incorporate these enthalpy-stabilizing spinels or variations of these spinels.

The applied programs based on these spinels have led to basic research programs funded by AFOSR to understand the physics of these unusual materials. The first AFOSR program (#F49620-82-C-0129) involved CeramPhysics, Westinghouse, and Ohio State Univ., and in this program very precise specific heat data were measured and analyzed on the spinel/columbite ceramics. It was found that antiferromagnetic transitions were involved, but a large density of free spins was present below the transition temperatures. Anomalies in the thermal conductivity at the transition temperatures were also found, and the theoretical studies began to lay the groundwork for a spin-frustration model for these spinels.

In the second AFOSR-sponsored research program (#F49620-86-C-0049) the resources of CeramPhysics, Ohio State Univ., Penn State Univ., and the Univ. of W. Virginia were marshalled to further the research. The specific heat measurements were extended to pure samples of the spinels, and magnetocaloric measurements in intense magnetic fields above and below the transi-

tion temperatures yielded a more complete picture of the free spins and a phase diagram of magnetocaloric effects. Unusual dielectric properties were discovered at CeramPhysics in that the dielectric constant of both spinels displayed anomalies at the antiferromagnetic transition temperatures. Magnetic susceptibility and EPR measurements at WVU provided needed data and information on the nature of the transitions and the density of free spins below the transitions. Theoretical progress at Ohio State Univ. succeeded in explaining the salient features of the specific heat and dielectric constant characteristics at the transition temperatures. Unfortunately, the question of why the columbite mineralizer leads to hard, dense ceramics of these spinels was not adequately addressed at Penn State Univ.

In this the third AFOSR-sponsored research program, the same institutions were involved as in the second program above, and the experimental research was based upon the fabrication of samples using sophisticated ceramic methods and single-crystal growth methods proposed by Penn State. However, after the program started, most of the ceramic methods were unilaterally discarded by Penn State, and the single-crystal-growth attempts were fruitless, leaving the present program devoid of the proposed samples for experimentation. Consequently, on the advice of AFOSR, the subcontract with Penn State was canceled in the 16th month of this 18-month program, the crystal-growth research was transferred to W. Va. Univ., and a no-cost program extension was granted by AFOSR. As will be seen below, however, this program rearrangement did not allow WVU sufficient time or funds to complete the crystal-growth research.

However, approximately mid-way through this originally proposed 2-year AFOSR program, a large variety of new samples based on the ZnCr_2O_4 and CdCr_2O_4 spinels unexpectedly but fortunately became available from an applied, parallel program funded by Wright-Patterson AFB. In these samples, the spinels were subjected to doping and stress conditions that had not hitherto been investigated but which were suspected to contain rich information on the physics of these materials. This indeed proved

to be the case, and the present program diverted to extensive experimental and theoretical studies of the new phenomena discovered in these alternate samples. Consequently, this Final Report deals primarily with the discoveries and physics related to these alternate samples, and it might be argued by hindsight that the findings reported here may be more important for the physics of these spinels than what might have been learned from the originally proposed Penn State samples.

This Final Report is organized along the following lines: In Section III are documented the sample-fabrication efforts at Penn State Univ. and the Univ. of W. Va., and in Section IV are documented the extensive specific-heat measurements performed at CeramPhysics, together with the development of a novel broad-range specific heat measurement technique. In Section V, the thermal expansion, dielectric constant, and ac conductivity measurements at CeramPhysics are documented, and in Section VI the magnetic susceptibility and EPR measurements at the Univ. of W. Va. are documented. In Section VII the theoretical studies at Ohio State Univ. are documented, and Section VIII contains a discussion of the results of the program and outlines future research directions. Each Section contains a summary of the findings for that section.

This Final Report is a large document, and no attempt has been made to number the figures, tables, and equations sequentially throughout the report. Rather, a decision was made to write each section as a stand-alone section with the figures, tables, and equations numbered sequentially within that section. Thus, where necessary, for example, the figures are referenced by the section in which they appear in the text.

III. SAMPLE PREPARATION METHODS AND RESULTS

Three types of CdCr_2O_4 and ZnCr_2O_4 samples were prepared for this program: Ceramics, fine-grained powders, and single crystals. The emphasis for the ceramic samples was placed on preparation methods (e.g., hot pressing), and the fine-grained powders were prepared as starting materials for ceramic processing.

In addition to the above, samples of these spinels became available from a separate research program funded by Wright Patterson AFB. These samples comprised doped ceramics, ceramic/glass composites, and doped-ceramic/glass composites. Going further, samples of ceramic/epoxy composites from an earlier NASA-funded program were also available.

In this Section, the preparation methods and results specific to this AFOSR program are described. In Section III.A. below, the efforts at Penn State Univ. are described, and in Section II.B., the efforts at West Virginia Univ. (note that Section I.A. also contains a description of the samples prepared separately under the WPAFB program).

EXPERIMENTAL METHODS

Polycrystalline Spinel

Fundamentally, fabrication technologies for all ceramic materials have the same basic process steps which are: powder preparation, powder processing, green forming, densification and final characterization.

Powder preparation techniques explored in this program to fabricate spinels and the fluxes used in crystal growth, included 1) mixing/calcination; 2) coprecipitation; and 3) hydrothermal methods.

These methods are reviewed in Table I. The mixing of components followed by calcination to the desired phase(s) and milling is the most widely used powder preparation method and thus was used to prepare the various crystal growth fluxes and much of the spinels and spinel/glass composites. However, the high temperature calcination generally produces an agglomerated powder which requires milling, in which powders in the range of $\sim 1\text{-}2\ \mu$ are easily achieved, but, contamination may occur.

Table I
Some of the methods used to prepare powders.⁽¹⁾

Method	Particle Size	Comments
Mixing/Calcination	Submicron to hundreds of microns	- Impurities from starting materials and milling
Coprecipitation	If calcined, near size of $< 0.5\ \mu$	- Possible Cl^- due to poor wash - Milling usually required - Low impurity level
Hydrothermal	Nanosized-- $50\ \mu\text{m}$	- Low amount of crystalline defects

Coprecipitation is a chemical technique in which compounds are precipitated from solution by the addition of, for example, a hydroxide. The metal salt is then calcined to the desired phase. The advantage of this technique over mixing/calcination techniques is that more intimate mixing

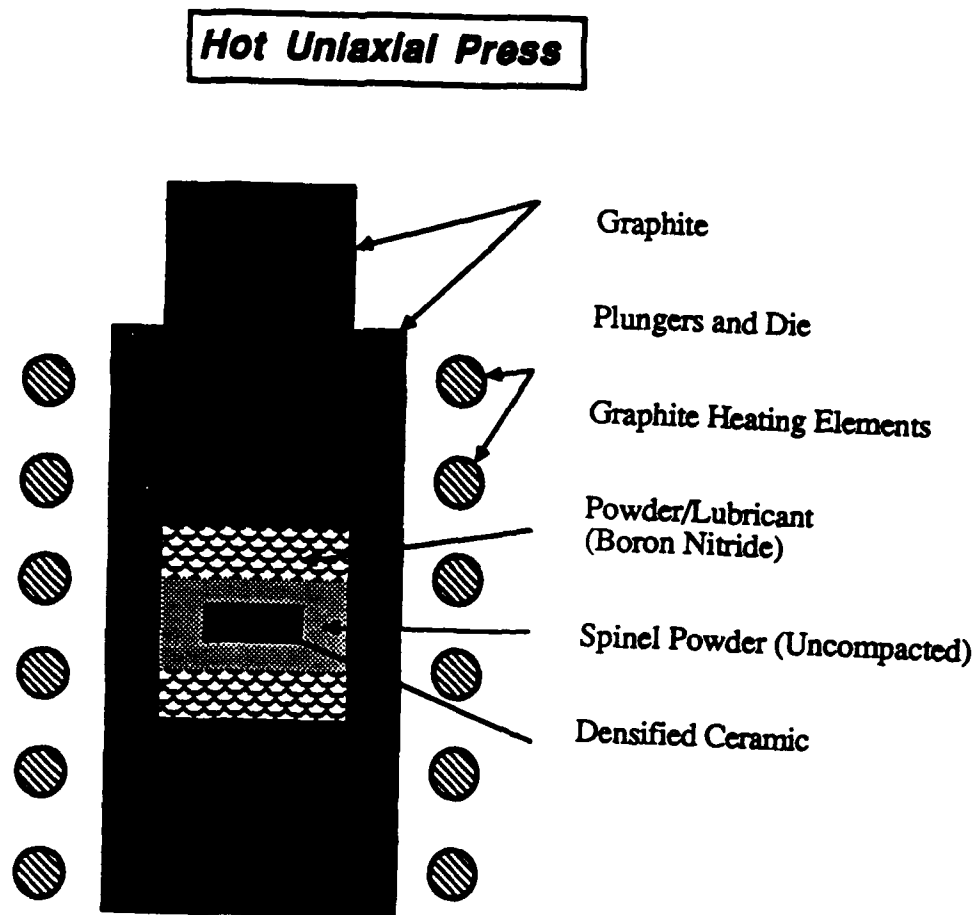


Figure 1. Schematic of hot uniaxial press.

generally occurs. Consequently, lower calcination temperatures can be used, typically resulting in finer particles.

Hydrothermal processing uses hot water above 100°C under pressure to produce crystalline oxides. The advantage of this technique is the powders can be produced at temperatures significantly lower than those required for calcination. Again, very fine well crystalline powders can be produced.

Initially, both hydrothermal or co-precipitation preparation techniques were proposed to prepare powders that were (1) high purity and (2) reactive, being submicron in size. Hydrothermal processing was thought to be an ideal powder preparation technique, but preliminary analysis of the spinel systems proposed indicated that very high pHs (> 12) would be required,⁽²⁾ resulting in compromised/purity due to severe reaction with the material construction, e.g., the nickel liner in the autoclave, etc. In addition to the problem of Ni contamination successful hydrothermal processing requires much trial and error and thus coprecipitation was chosen and found to be a much simpler process capable of producing fine powders, however, the question of purity levels is still uncertain. Henceforth, to look at purity, 99.999% pure oxide components, ZnO⁺, Cr₂O₃⁺, and CdO⁺ were obtained and the associated spinels fabricated using carefully controlled mixing/calcination technique. Spinel prepared using conventional reagent grade powders⁺ (~ 99%) were made in parallel for comparison.

Green Forming and Densification

As in powder fabrication there are many different ways to form green ceramics, but in this work only uniaxial pressing was used. In this method powders and binders added to provide green strength, were simply placed into a die (typically cylindrical in shape) and pressure applied through rams.

Densification techniques generally require high temperatures to eliminate porosity in the green ceramics. In addition to pressureless sintering, hot pressing techniques are used. As previously stated, dense polycrystalline ceramic spinels could not be made readily without the addition of columbite mineralizers, thus hot pressing techniques were suggested. However, in the course of the study it was found that highly dense samples of ZnCr₂O₄ could be readily achieved using high temperature pressureless sintering (≥ 1600°C) if one controlled ZnO volatility. In addition, dense ceramics could be obtained using just conventionally prepared ZnCr₂O₄ powders. This discovery was made after the work statement of the new proposal was made and as such had not been included.

Utilizing hot pressing, highly dense samples of ZnCr₂O₄ could be achieved by hot uniaxial

⁺Alfa Products, Morton Thiokol, Danvers, MA 02927

pressing (in vacuum) at temperatures as low as 1400°C, again using only conventionally prepared mixed oxide powders. However, as shown in the schematic of the hot press⁺⁺ in Fig. 1, the sample must be in contact with the pressure vessel, being graphite with boron nitride powder for lubrication which may lead to contamination. The question of cation reduction in a vacuum at high temperatures was also a concern.

For the case of the Cd spinel, densification could not be achieved by conventional sintering due to the very high volatile nature of CdO. Hot uniaxial pressing was not feasible again due to the CdO volatility and CdO → Cd metal reduction problem which would severely contaminate the hot press. Hot isostatic pressing of ZnCr₂O₄ was deemed to be unsuccessful based on the HUP results with the temperature limitation of the HIP being only 1200°C.⁺⁺⁺

Though ultrafine powders of the spinels were successfully prepared, and were found to be more reactive in terms of phase formation, as with most fine powders they did not pack efficiently, resulting in low green densities and corresponding low fired densities. The latter may have been attributed to a volatility problem associated with the very high surface area of the powders.

Further details of the experimental methods will be presented in the next section.

CHARACTERIZATION

Characterization of the powders and sintered ceramics were performed to insure reliable results in terms of phase purity, particle size, etc. Component powders were characterized for Loss on Ignition (LOI) to insure stoichiometry. X-ray powder diffraction was used to examine phase purity of the raw materials and to determine phase(s) present in calcined samples. X-ray diffraction was also performed on sintered samples to again insure phase purity of the spinels. Particle size of the coprecipitated powders as well as other powders was determined through the use of specific surface area.⁺ The average particle size was determined based on the following equation:

$$S. A. = \frac{6}{pD_{SAV}}$$

where S.A. is the surface area in m²/g, p the theoretical density in kg/m³ and D_{SAV} the average

⁺Quantachrome Inc., Model MS-12, Syosset, NY 11791

⁺⁺Advance Vacuum Systems, Inc., Ayer, MA 01432 (Model 4VGF-4-4-2200-3 (HP) Vertical Hot Press)

⁺⁺⁺HIP Model 3000, LECO Corp./Tem-Press Div., Bellefonte, PA 16823

diameter assuming spherical particles. For extremely fine powders. e.g., $< 1 \mu\text{m}$, which are out of the realm for sedigraph and light scattering techniques,⁽³⁾ the BET surface area technique used was felt to be the simplest and most reliable, in particular, as compared to x-ray diffraction line broadening.

The density of green formed and sintered samples were determined by geometric means. Weight loss of samples before and after sintering was used to determine the level of ZnO or CdO volatility.

Microstructural characterization of densified samples was performed using Scanning Electron Microscopy or SEM to determine relative grain size(s), porosity, etc.

SINGLE CRYSTAL GROWTH

The usual method of obtaining crystals from melts cannot be applied to the ZnCr_2O_4 and CdCr_2O_4 spinels owing to their high vapor pressure of ZnO and CdO near the melting points. Thus, it was suggested the crystals be obtained using the flux growth technique. Basically, the flux growth technique involves a mixture of the material and a flux(s) heated until molten, thereafter controlling the nucleation and growth to yield single crystals.

A literature search on crystal growth resulted in three potential flux growth systems. In the search, literature on various properties associated with the spinels was also found and the information was sent to CeramPhysics.⁽⁴⁻⁸⁾ Little information on CdCr_2O_4 spinel single crystal growth was obtained, data being mostly on the ZnO analogue. This was probably due to the problem of CdO volatility, reactivity, and its carcinogenic toxicity. Thus, only growth of the ZnCr_2O_4 spinel was felt possible. It is important to remember that crystal growth using the flux technique is a relatively slow process and as such, growth runs generally took at least one week to perform.

Various fluxes reported and associated references are presented in Table II. Details of the crystal growth processes are presented in the next section.

Table II
Flux growth components of ZnCr_2O_4 crystals.

Flux(s)	Reference
$\text{Na}_2\text{W}_2\text{O}_7 + \text{Na}_2\text{WO}_4$	(4)
$\text{PbO}, \text{PbF}_2 + \text{MoO}_3$	(5)
Bi_2O_3	(6)

EXPERIMENTAL PROCEDURE AND RESULTS

In this section we will fully describe the experimental methods used to fabricate and characterize the various spinels as proposed. The results reported and methods selected were based on best effort and our scientific judgement as the work progressed.

It is important to mention that during the course of this program the toxicity of CdO and Cd based compounds were upgraded to a carcinogen and thus more work was performed with the ZnCr_2O_4 spinel analogue.

The following section will be organized into three parts (1) polycrystalline spinels, (2) single crystals, and (3) doped-spinels and glass composites.

POLYCRYSTALLINE SPINELS

High Purity Spinel

To prepare high purity polycrystalline spinels, 99.999% purity component powders of ZnO, CdO, and Cr_2O_3 were obtained. The component powders were characterized for loss on ignition to insure chemical stoichiometry.

The powders were weighed out according to the appropriate spinel formula and placed in a nalgene bottle with alcohol and ZrO_2 media. Mixing was performed using a vibratory mill.⁺ The media used was of a particular hard and wear resistant type to avoid possible contamination. Following drying the powder was placed in a 99% dense alumina crucible and calcined at 1150°C for 4 hrs. for the ZnCr_2O_4 mixture and 950°C for the CdCr_2O_4 mixture. To insure completion of spinel formation the mixtures were doubly calcined. X-ray powder diffraction was used to insure that the powders were fully reacted. X-ray powder diffraction patterns are presented in Appendix A. SEM photomicrographs of the calcined powders are shown in Fig. 2. As evident in the figures the particle sizes were in the range of 1-2 μ .

The calcined powders were then pressed into cylinders (approx. 1/2" diam. by 1/4" thick) using a small hydraulic press. The green densities of the pellets were calculated geometrically from the weight and dimensions determined using a micrometer. Note: After green pressing the surface of the disks were polished to remove any contamination as a result of the die.

Sintering of the disks were done in closed high purity alumina crucibles. The pellets were placed on platinum foil to avoid any reaction between the spinel and the Al_2O_3 . Closed crucibles were used to help prevent ZnO and CdO volatility.

⁺Sweco, Inc., Model-18-5, Florence, KY

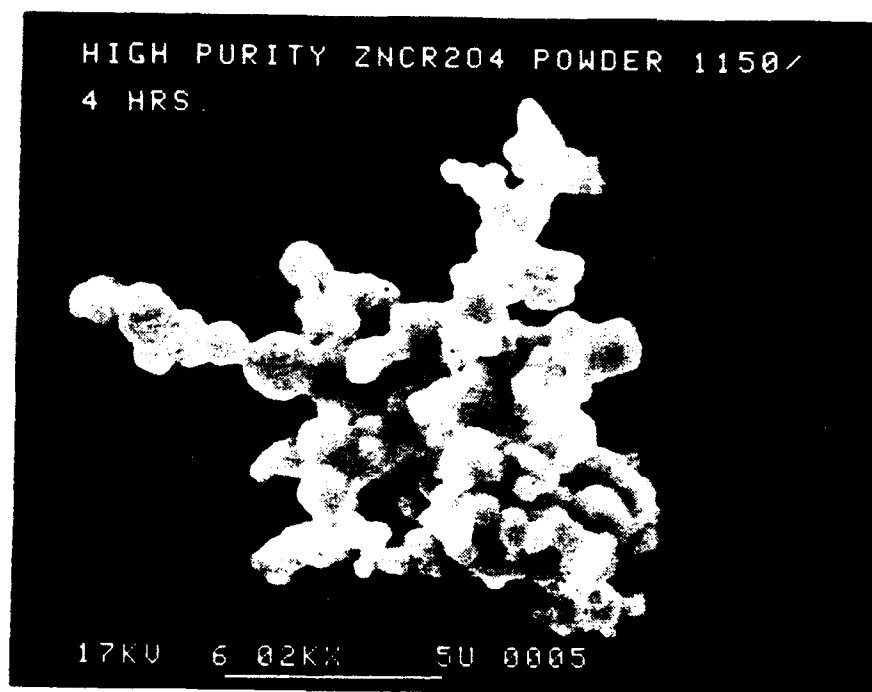


Figure 2. SEM photomicrographs of calcined high purity spinel powders.

A molybdenum disilicide resistance furnace (or SiC type) with a programmable controller was used for the firings. The ZnCr_2O_4 samples were fired at 1600°C for 4 hrs. with the CdCr_2O_4 being fired at 1250°C also for 4 hrs. It had been previously observed that higher firing temperatures resulted in excess weight loss through volatilization.

The fired disks were then characterized for weight loss, geometric density, phase purity, and grain size as determined by SEM analysis. The fired samples were found to have < 1 wt% loss and were phase pure. See Appendix A for x-ray powder patterns. The grain size as determined by SEM of fractured surfaces were found to be ~ 5 - $10\ \mu$ for ZnCr_2O_4 and 1 - $3\ \mu$ for the CdCr_2O_4 , spinels, respectively. SEM photomicrographs of the sintered ZnCr_2O_4 spinel is shown in Fig. 3. The various physical characteristics are reported in Table III.

To be able to compare the effect of purity on the low temperature properties, conventional reagent grade powders (~ 98 - 99% pure) were obtained and processed in parallel as the high purity samples. The physical characteristics are presented in Table III for comparison. Also, SEM photomicrographs are shown in Fig. 4. As presented in Table III, the density of all the samples were quite low as compared to the theoretical values of $5.47\ \text{g/cc}$ and $5.86\ \text{g/cc}$ for ZnCr_2O_4 and CdCr_2O_4 , respectively. Note that the high purity ZnCr_2O_4 samples had a significantly lower density than that for the conventional sample. This was probably attributed to impurities enhancing the sintering kinetics.

Table III
Physical Characteristics of High Purity and Reagent Grade Spinel.

Material	Firing Condition	Density g/cc	Phase	Grain Size (μm)
ZnCr_2O_4 (Reagent Grade)	$1600^\circ\text{C}/4\ \text{hrs}$	3.6	Spinel	4-5
99.999%	$1600^\circ\text{C}/4\ \text{hrs}$	2.5	Spinel	5-10 (Bimodal)
CdCr_2O_4 (Reagent Grade)	$1250^\circ\text{C}/4\ \text{hrs}$	2.6	Spinel	1-3
99.999%	$1250^\circ\text{C}/4\ \text{hrs}$	~ 2.6	Spinel	1-3

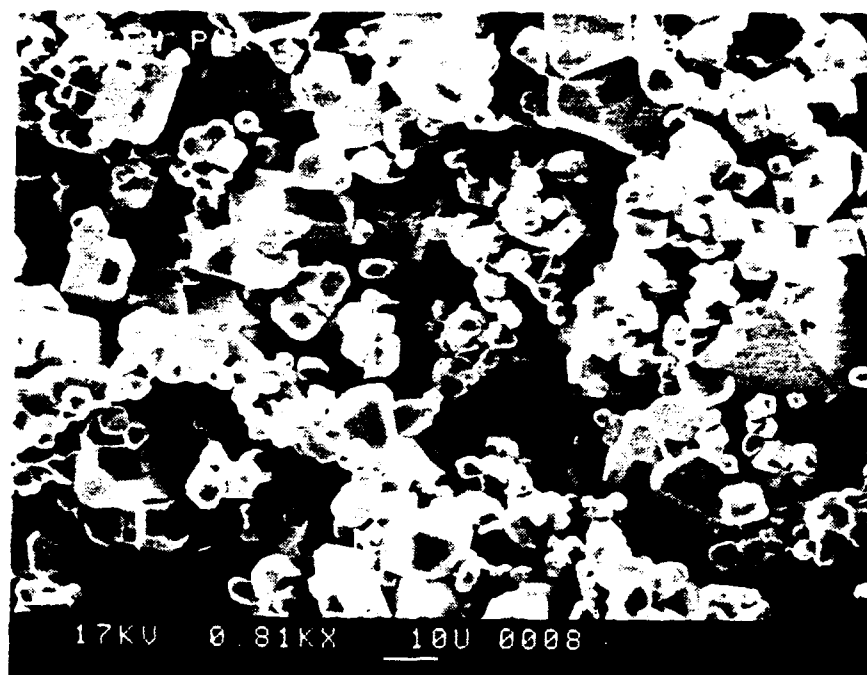


Figure 3. SEM photomicrographs of sintered high purity ZnCr₂O₄ spinel (fractured surface).

Conventional Pressureless Sintering

As previously stated, highly dense ($> 90\%$ theoretical) polycrystalline disks of ZnCr_2O_4 could be achieved by controlling the ZnO volatility. This discovery was found near the end of the previous program. Using this approach permits us to fabricate samples, that would otherwise be possibly contaminated in hot pressing and is overall a simpler process.

The samples were prepared similar to that described for the high purity samples. A double calcination step was again used to insure phase purity. See Appendix A for x-ray powder diffraction patterns. To enhance the reactivity of the powders, the calcined slug was ground using a mortar and pestle and subsequent comminution was performed using a vibratory mill. The powders were milled to $\sim 1\text{-}2\ \mu$ in size.

To be able to control the ZnO volatility, a ZnCr_2O_4 firing sand was prepared. A firing sand is a powder of similar composition, but somewhat coarser than that being sintered. Firing sands are commonly used in controlling PbO volatility in such compositions as $\text{Pb}(\text{Mg}_{1/3}\text{Nb}_{2/3})\text{O}_3$ and $\text{Pb}(\text{ZrTi})\text{O}_3$ electronic ceramics. Firing sands are also used in firing multilayer capacitors to aid in temperature uniformity.

The firing sand was prepared similarly to that of conventional ZnCr_2O_4 powder, except that multiple calcinations were used ($950^\circ\text{C} \rightarrow 1150^\circ\text{C} \rightarrow 1300^\circ\text{C}$) to coarsen the powder while preventing ZnO volatility. The resultant calcine slug was broken down using a mortar and pestle followed by hammer milling.⁺ The pressed disks were buried in the sand and placed in a closed alumina crucible.

Samples were fired at various times and temperatures ranging from 0.5 hrs to 8 hrs and from 1400°C to 1700°C . The wide range of sintering conditions were used to determine the lowest temperature at which densification would occur and to vary the grain size. The temperature of 1700°C was found to be the maximum allowable, based on weight loss due to ZnO volatility.

The fired samples were characterized for density, phase purity, and grain size with the results reported in Table IV. See Appendix A for x-ray diffraction analyses. SEM photomicrographs are shown in Fig. 5.

As shown in Fig. 5 and reported in Table IV, highly dense samples ($> 90\%$ theoretical) could be achieved at temperatures as low as 1600°C . It is interesting to point out that samples fired at 1600°C , as reported earlier in Table III, being fired without the ZnCr_2O_4 sand, were significantly lower in density ($\sim 65\%$ theoretical), thus showing the importance of ZnO partial pressure control.

Sintering at temperatures greater than 1600°C was found not to further enhance densification, probably due to increased ZnO volatility. Little grain size variation was achieved for

⁺Spex Industries, Mill Model 5200, Metuchen, NY 08840

the dense samples with all the grain sizes in the range of 5 to 10 μ . Grain sizes for samples fired below 1600°C were smaller, but the samples were poorly densified.

As with the ZnCr_2O_4 spinels, a CdCr_2O_4 firing sand was prepared and disks were fired. However, no significant increase in densification was observed. Severe CdO weight loss was found to occur at temperatures above 1300°C.

No further attempts to control the CdO volatility were made due to the fact that CdO is carcinogenic and as such we did not want excessive amounts of free CdO contamination.

Hot Pressing

Using reagent grade powders, prepared in the previous section, one inch diameter disks of ZnCr_2O_4 were hot uniaxially pressed at 3000 psi in vacuum at various temperatures including 1250°C, 1400°C, and 1450°C. Temperatures greater than 1450°C were not tried due to excessive ZnO loss as evident by ZnO or Zn deposits in the hot press. The pressed disks were found to be much darker than conventionally fired samples which may have indicated partial reduction of the Zn^{+2} or Cr^{+3} cations.

Characterization of the disks, by x-ray diffraction (see Appendix A), however revealed that the samples were phase pure spinels. The samples were characterized for geometric density and grain size with the results reported in Table V. SEM photomicrographs are shown in Fig. 6.

Densities > 90% theoretical were obtained for hot pressing at $\geq 1400^\circ\text{C}$, temperatures significantly lower than those needed for the conventionally sintered samples. However, a question of volatility as well as reduction remains. Being fired at lower temperatures, the grain sizes were lower only 1-2 μ .

Table IV
Physical Characteristics of *Sintered ZnCr_2O_4 Spinel.

Material	Firing Condition	Density (g/cc)	Phase	Grain Size (μm)
ZnCr_2O_4 (Reagent Grade)	1500°C/4 hrs	3.18	Spinel	1-3
	1550°C/8 hrs	2.73	Spinel	1-3
	1600°C/4 hrs	4.9	Spinel	5-10
	1650°C/4 hrs	4.8	Spinel	5-10
	1700°C/0.5 hrs	4.8	Spinel	5-10

*Firing sand of ZnCr_2O_4 was used.

From Tables IV and V, it is shown that grain sizes ranging from 1 to 10 μ were achieved for ZnCr_2O_4 while maintaining good densification. The fact that densification of ZnCr_2O_4 through

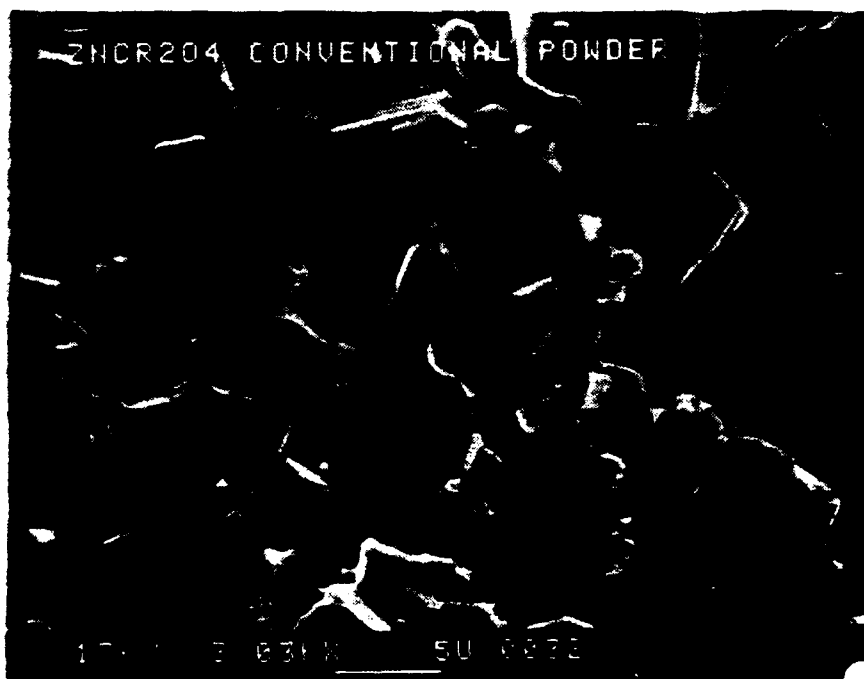
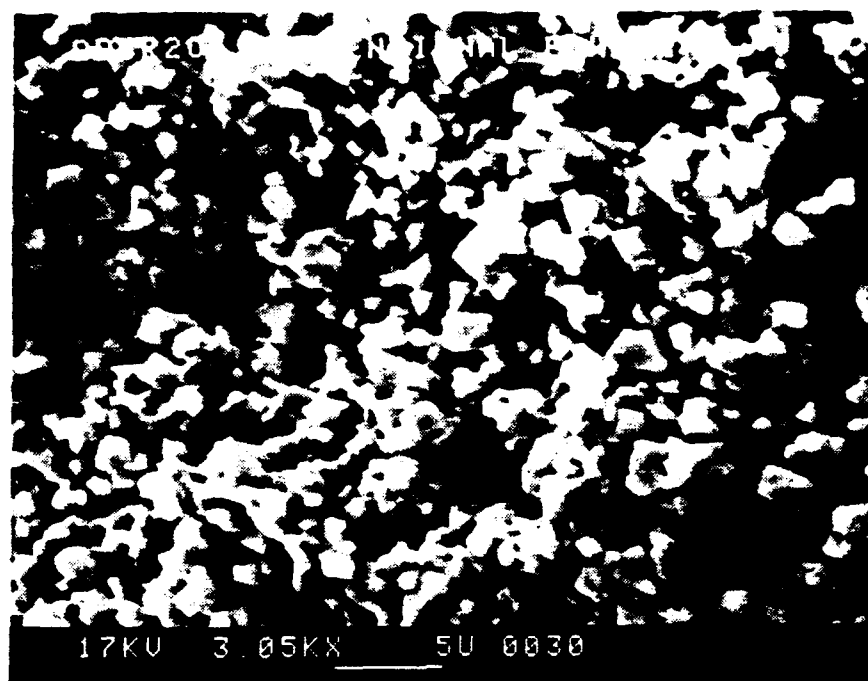


Figure 4. SEM photomicrographs (fractured surface) of conventionally prepared sintered spinels. Top: CdCr₂O₄ sintered at 1250°C/4 hrs. Bottom: ZnCr₂O₄ sintered at 1600°C/4 hrs.

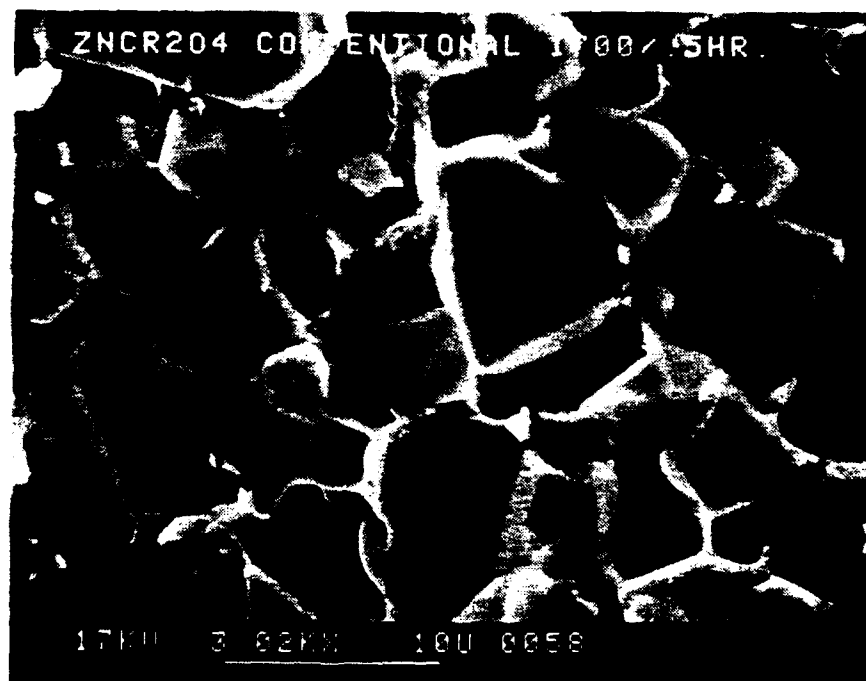


Figure 5. SEM photomicrographs (fractured surface) of ZnCr₂O₄ spinels. Top: sintered 1600°C/4 hrs (firing sand). Bottom: sintered 1700°C/0.5 hrs (firing sand).

hot uniaxially pressing could only be achieved around 1400°C, clearly indicated that hot isostatic pressing (HIP), which is limited to ~ 1200°C, would not result in dense samples and thus was not tried.

As stated, the high volatility associated with spinel CdCr_2O_4 and its potentially hazardous reduction capability (CdO - Cd metal.), made it impossible to attempt hot pressing. In addition the reactive nature of the CdO would result in high degree of contamination.

Table V
Physical Characteristics of Hot Pressed ZnCr_2O_4 Spinel.

Material	Hot Press Conditions (3000 psi)	Density g/cc	Phase	Grain Size
ZnCr_2O_4 (Reagent Grade)	1250°C	3.7	Spinel	1-2
	1400°C	5.1	Spinel	1-2
	1450°C	5.0	Spinel	1-2 (a few large grains)

Chemically Prepared Spinel

A chemical method for the preparation of fine powders of ZnCr_2O_4 and CdCr_2O_4 spinels was developed. Using ZnCr_2O_4 as the example, the method consisted of the following steps:

- (1) Dissolve 24.72 grams (0.1 moles) of $\text{Cr}(\text{C}_2\text{H}_3\text{O}_2)_3 \cdot \text{H}_2\text{O}$ and 10.98 grams (0.05 moles) of $\text{Zn}(\text{C}_2\text{H}_3\text{O}_2)_2 \cdot 2\text{H}_2\text{O}$ in 500 ml distilled H_2O at 65-80°C.
- (2) Dark green solution resulting from step (1) is added slowly to a stirring solution of 20 wt% tetraethyl ammonium hydroxide (TEAOH).
- (3) The resulting solution from step (2) is pan dried at 120 to 140°C for 24 hours to form a black powder.
- (4) The black powder is then calcined to form the desired spinel ZnCr_2O_4 powder.

The key to the above process for the preparation of a fine and highly reactive spinel ZnCr_2O_4 powder is the atomic-scale mixing in the liquid state, so that calcination at low

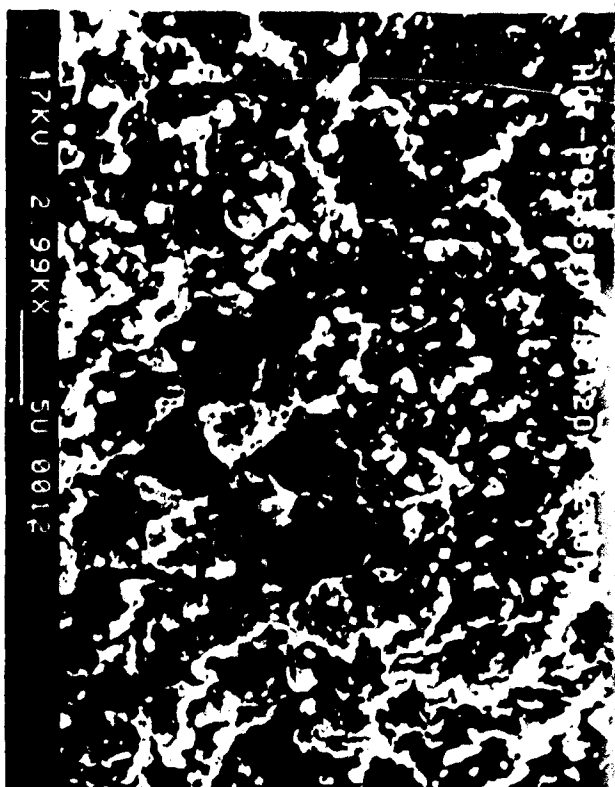
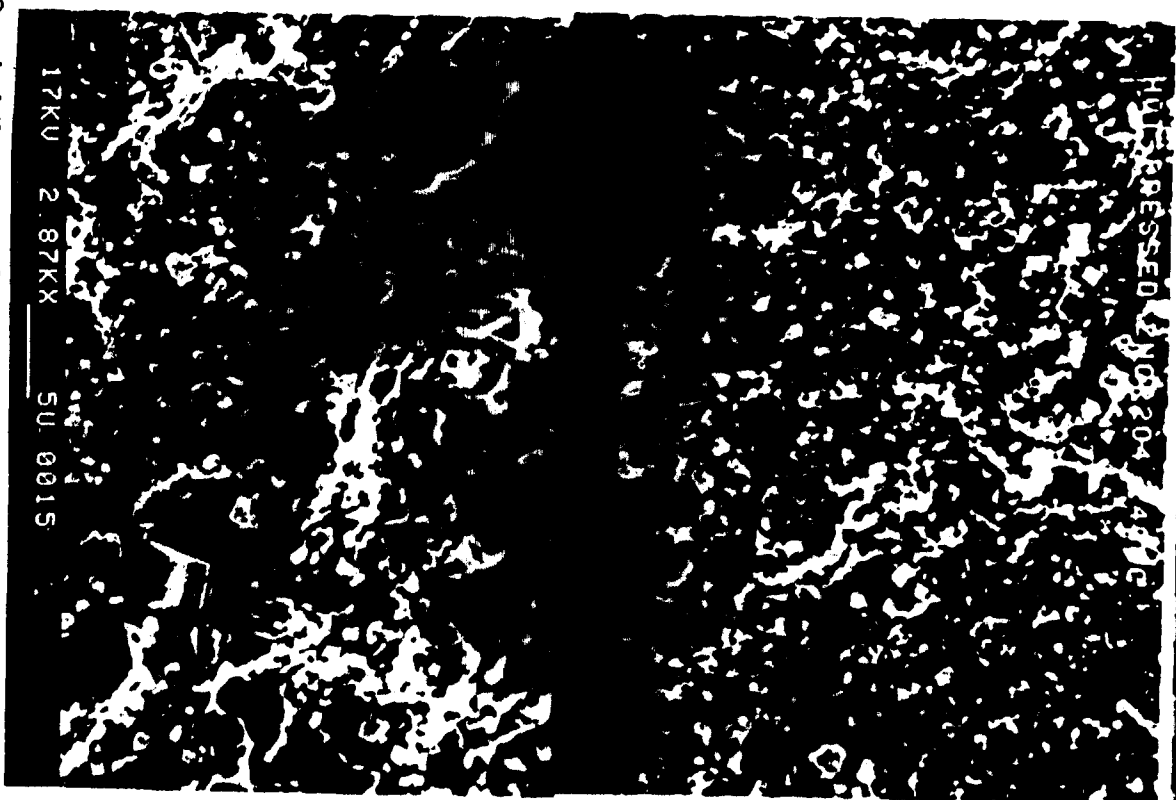


Figure 6.

SEM photomicrograph of hot uniaxially pressed ZnCr_2O_4 spinel (fractured surfaces). Top left: HUP @ 1250°C. Top right: HUP @ 1400°C. Bottom right: HUP @ 1450°C.



temperatures converts the dried salts to the desired oxide form. In the above method, the addition of the acetate solution to TEAH solution allows for excellent mixing because the TEAOH "complexes" with the acetates in solution. Without this step, segregation of the acetates would occur upon drying and the atomic-scale mixing would not be achieved. Using a similar method, the preparation of fine powders of CdCr_2O_4 were also prepared.

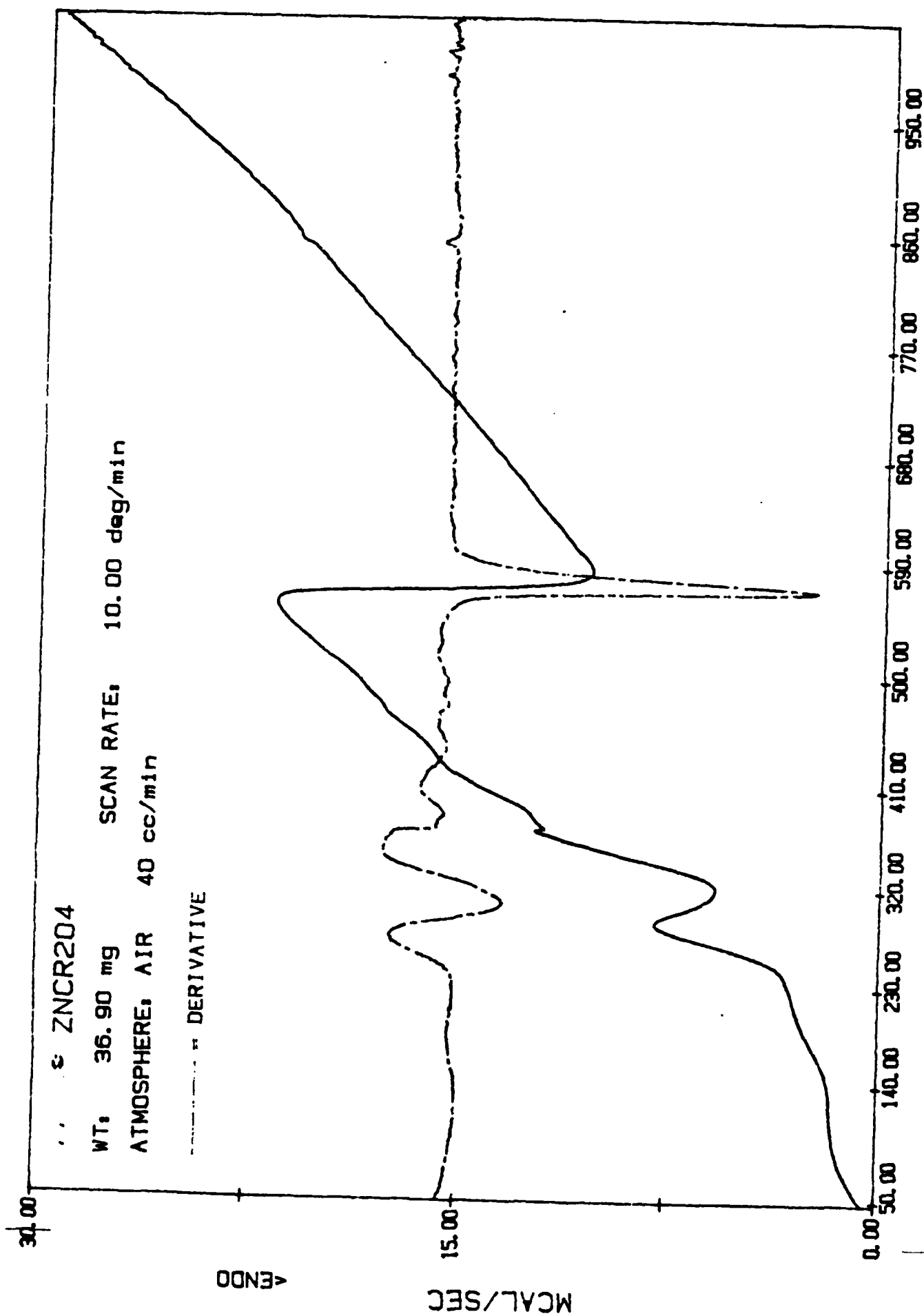
As prepared, the dark precipitated powders were amorphous to x-rays. To determine optimum calcination conditions in which to form the appropriate spinels both D.T.A.⁺--differential thermal analysis and T.G.A.⁺⁺--thermal gravitational analyses were performed. Figure 7 is a DTA pattern of the chemically prepared ZnCr_2O_4 powder showing several exothermic and endothermic reactions. The exotherms at low temperatures (250-350°C) are the result of organics being released as evident by the T.G.A. (Fig. 8) indicating a large weight loss at these temperatures. The large endothermic reaction around 590°C is believed to be the $\text{ZnO} + \text{Cr}_2\text{O}_3 \rightarrow$ spinel formation reaction. This is confirmed by the x-ray powder diffraction analysis shown in Fig. 9 clearly indicating single phase spinel for a calcine temperature of only 600°C. Powders calcined at 600°C, 700°C, and 800°C were characterized for specific surface area to determine the particle size with the results reported in Table VI. X-ray powder diffraction patterns for the 700°C and 800°C are shown in Figs. 9 and 10, respectively.

The DTA pattern for the chemically prepared CdCr_2O_4 powder is shown in Fig. 12, being somewhat different than that for ZnCr_2O_4 . As shown in Fig. 12, several exotherms and endothermic reactions occurred. The large exotherm(s) at low temperatures (250 - 350°C) are the result of organics being released as evident by TGA, shown in Fig. 13. An endothermic reaction around 530°C and perhaps 600°C could be associated to the $\text{CdO} + \text{Cr}_2\text{O}_3 \rightarrow$ spinel formation. Calcination studies of the chemically prepared powder at 500°C, 600°C, 700°C, and 800°C were performed. X-ray powder diffraction analyses shown in Figs. 13-15, clearly establishes that even at 500°C, single phase CdCr_2O_4 spinel was formed and from the sharpness of the peaks the powders were well crystallized. Virtually no difference in the x-ray powder patterns for the various calcinations were observed. As with ZnCr_2O_4 spinel, the calcined CdCr_2O_4 powders were characterized for specific surface area to determine the primary particle size with the results reported in Table VI. As presented with increasing calcination temperature surface area decreased and subsequently the particle size increased. Both powders were found to be significantly less

⁺Perkin Elmer, DTA 1700, Norwalk, CT 06856

⁺⁺Harrop Laboratories, Model T6716, Columbus, OH 43219

Figure 7. DTA pattern of chemically prepared ZnCr_2O_4 .



KGZ FILE: GZ749.DT

DATE: 00/00/17 TIME: 00:00

HARROP
INSTRUMENTS, INC.

SAMPLE: MODE: RUN NO.: REMARKS:

SIZE: RATE: OPERATOR:

TEST NO.: Y-AXIS SCALE: ATM.: DATE:

SOURCE:

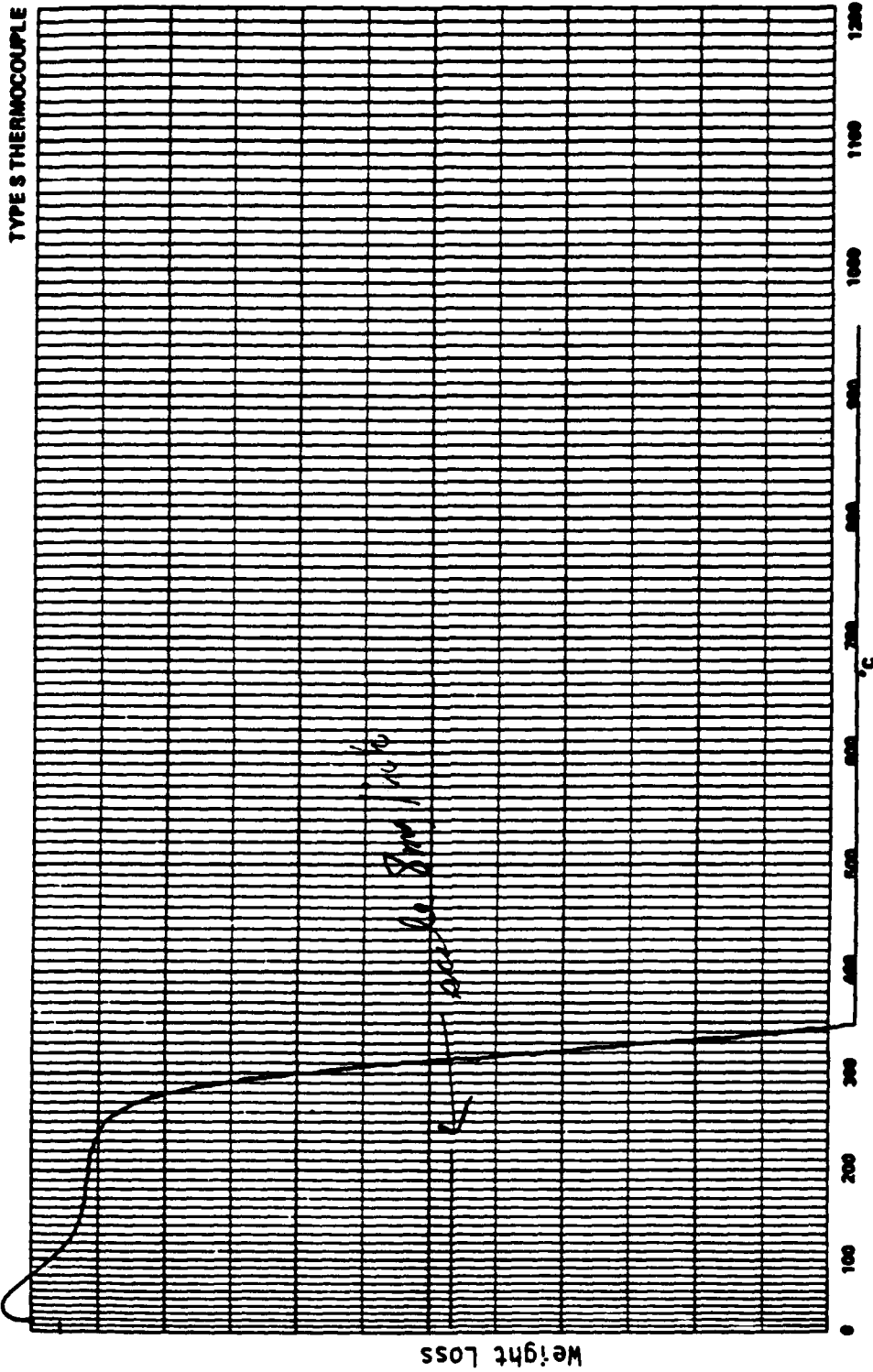


Figure 8. T.G.A. analysis of chemically prepared ZnCr_2O_4 powder.

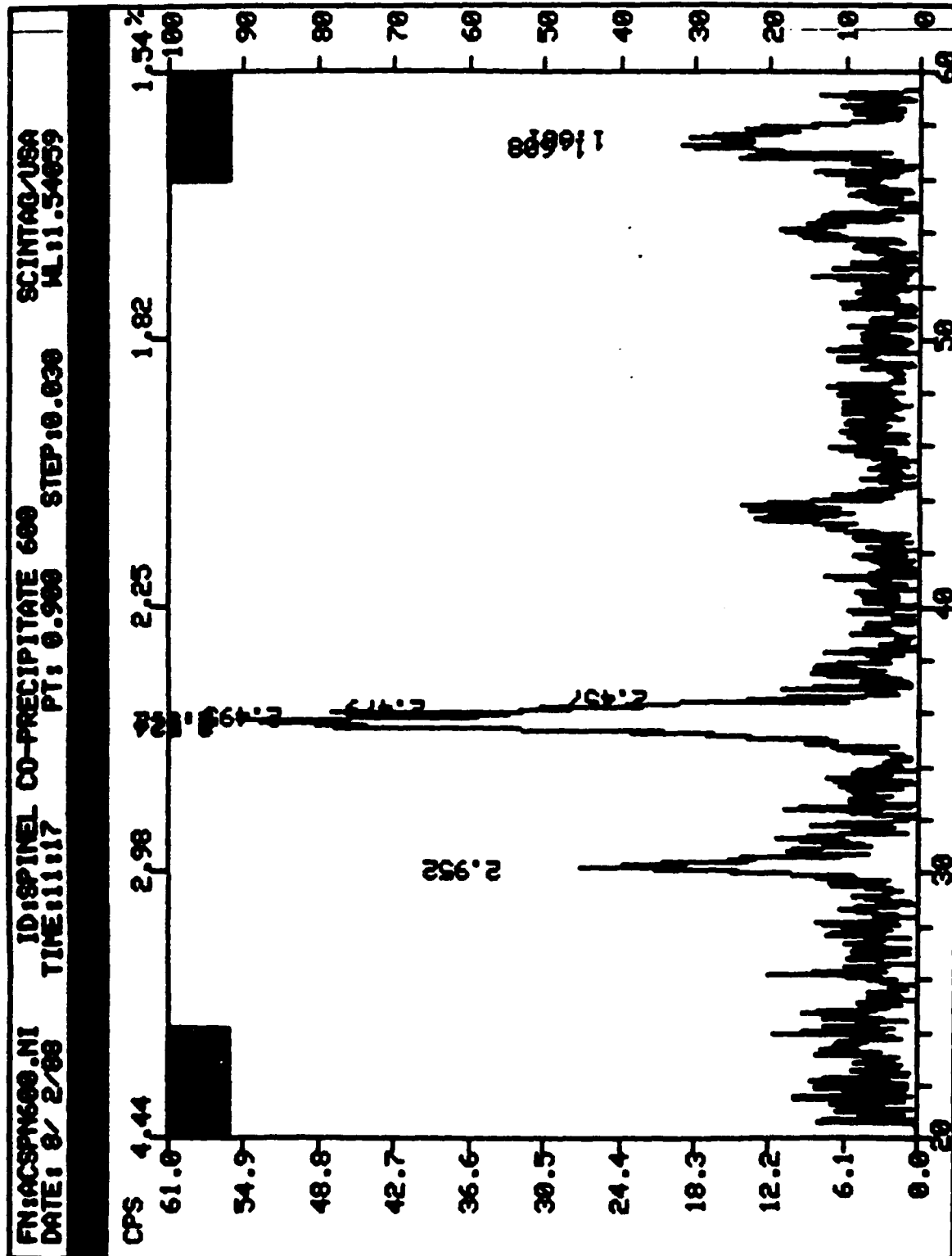
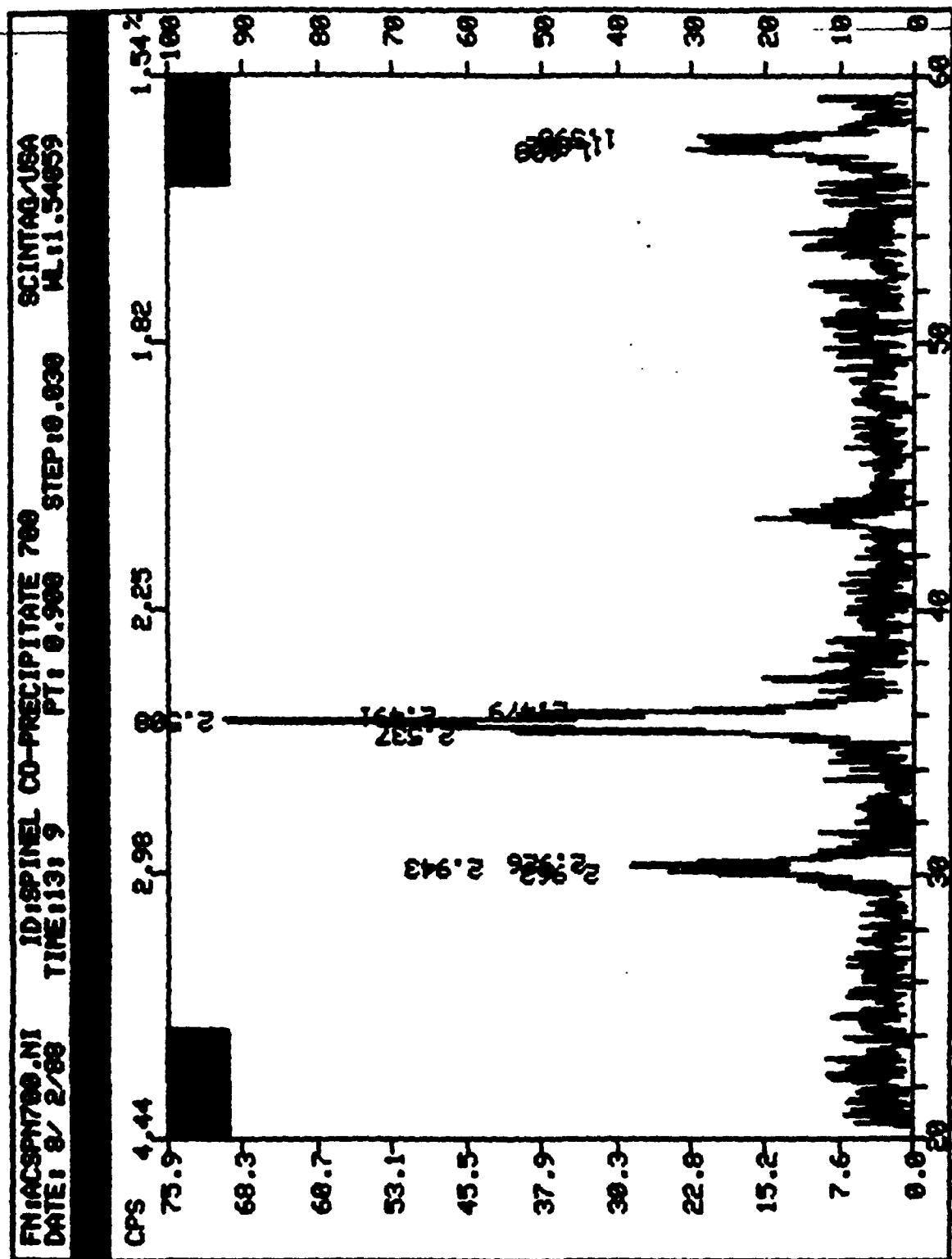


Figure 9. X-ray powder diffraction of chemically prepared ZnCr_2O_4 --calcined at 600°C.



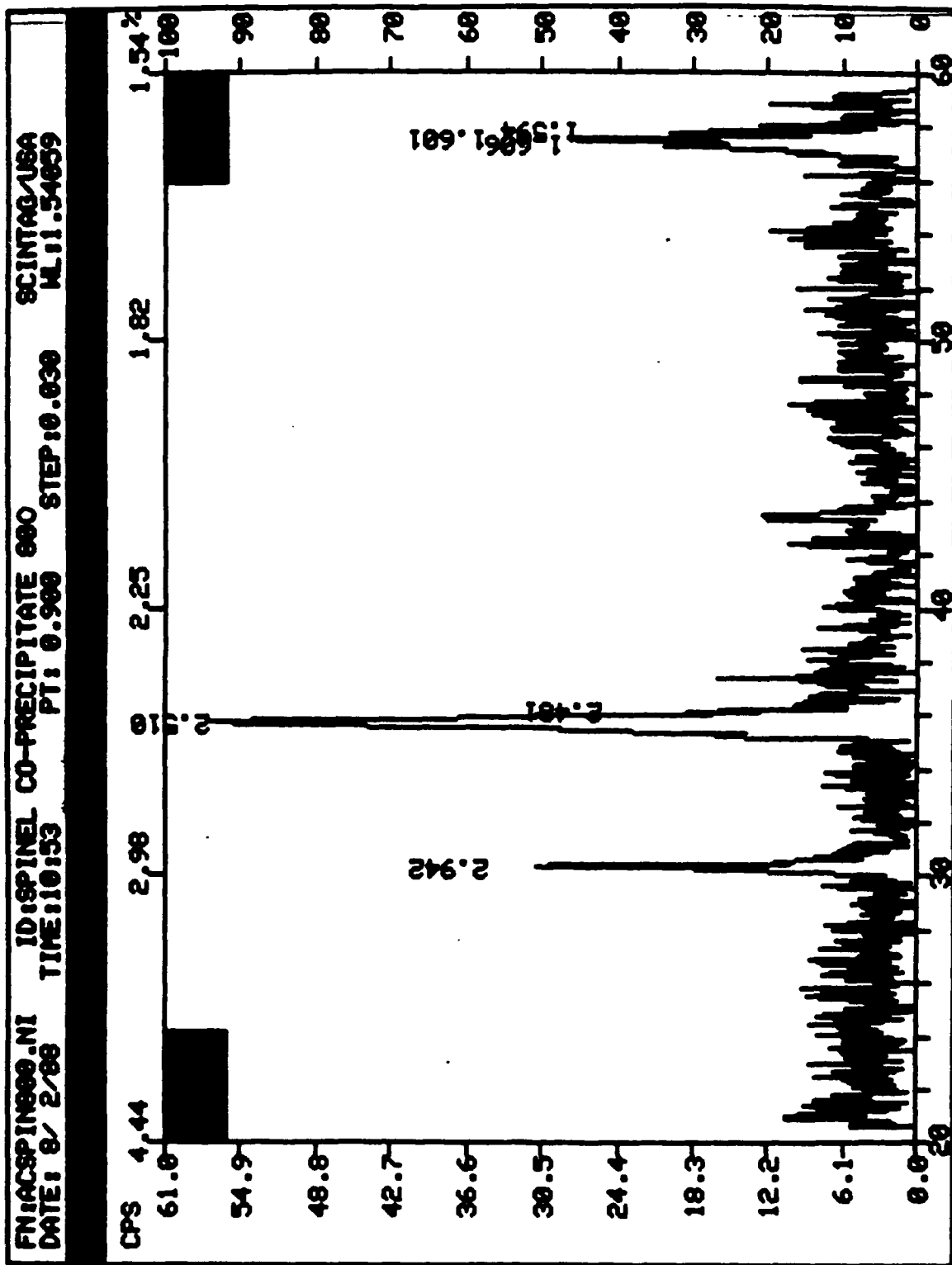
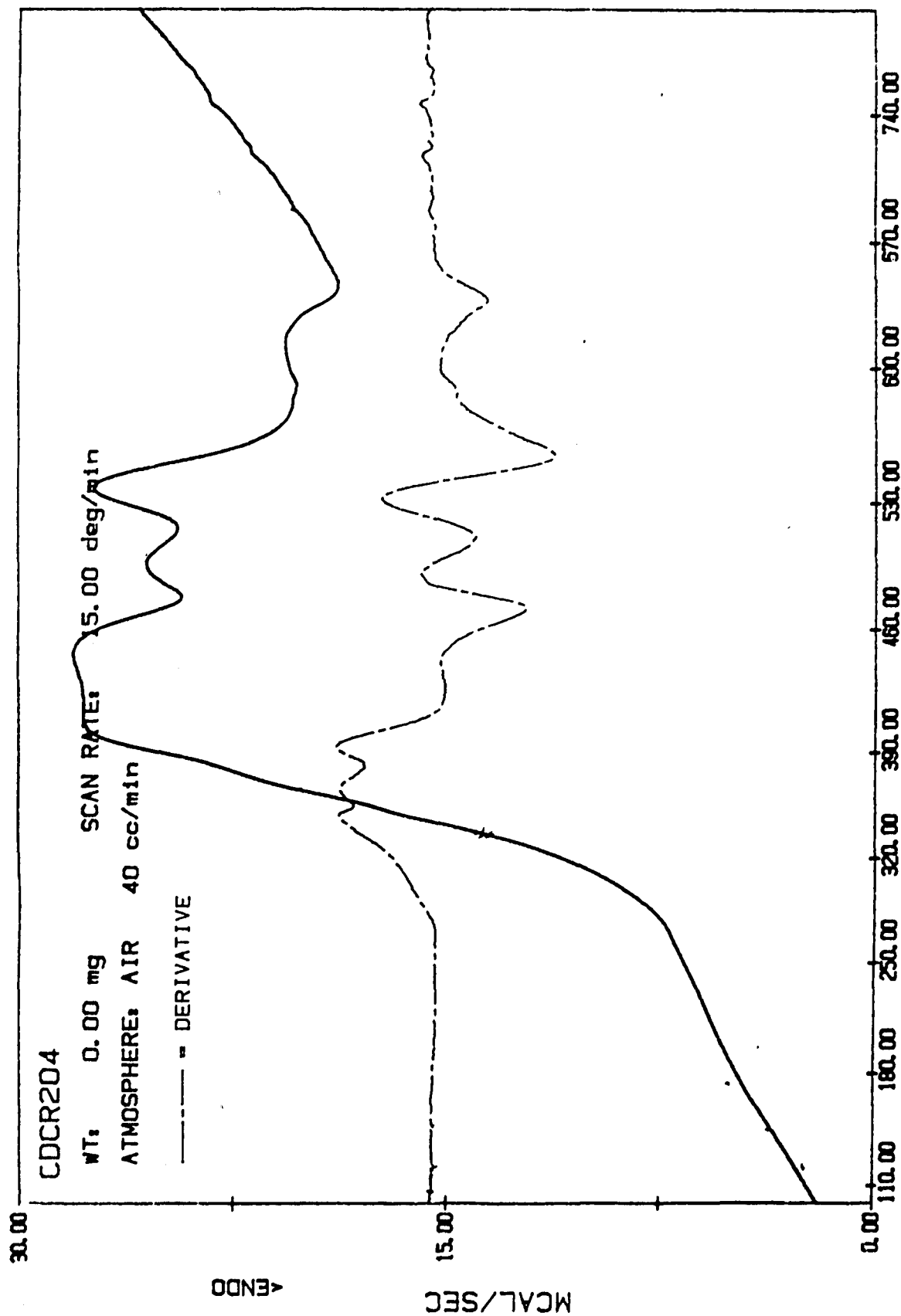


Figure 11. X-ray powder diffraction of chemically prepared ZnCr_2O_4 --calcined at 800°C.

Figure 12. D.T.A. of chemically prepared CdCr_2O_4 powder.



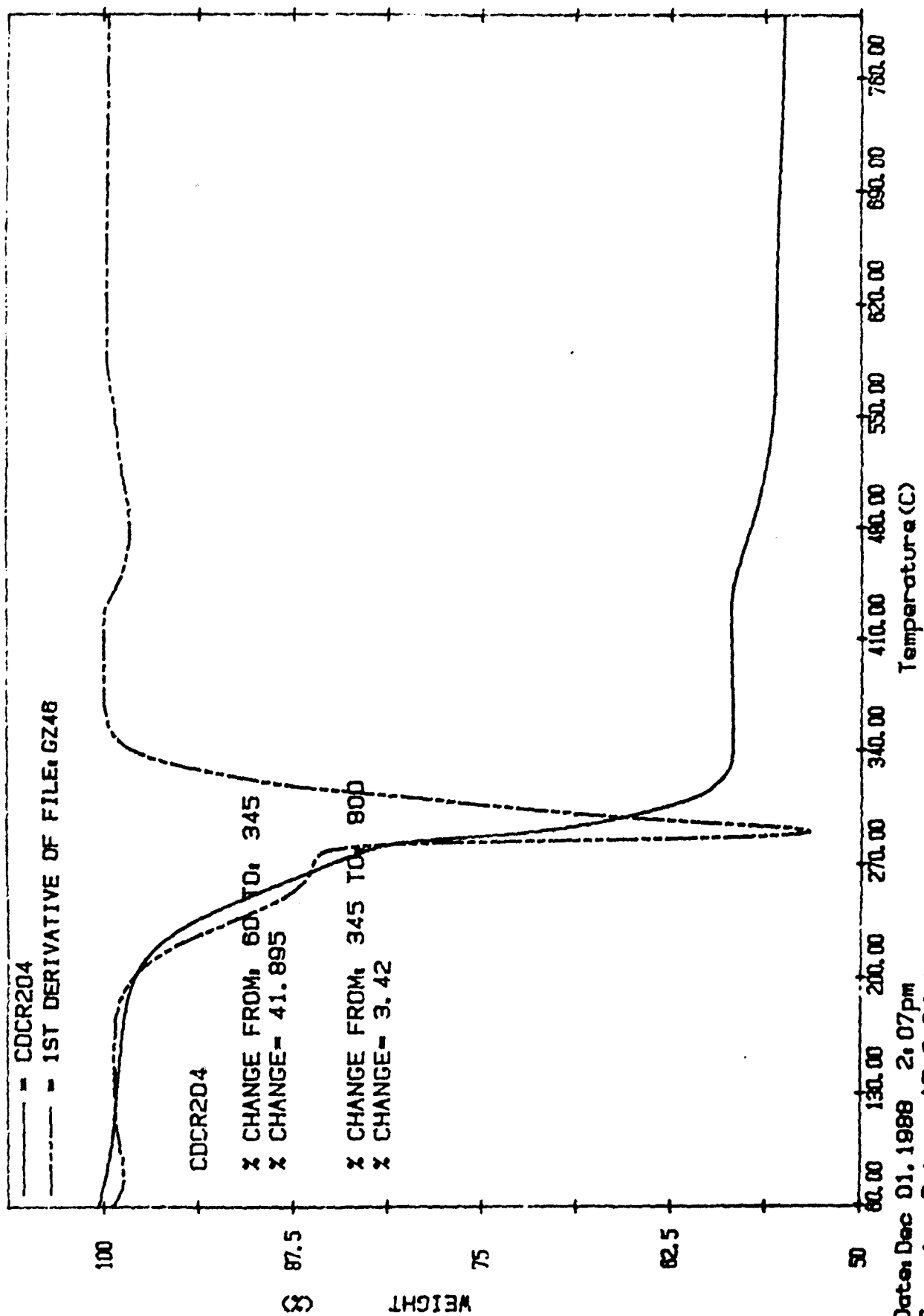
DTA

TEMPERATURE (C)

KGZ FILE: GZ801.DT

DATE: 88/12/01 TIME: 11.16

Figure 13. T.G.A. of chemically prepared CdCr_2O_4 powder.



Date: Dec 01, 1988 2:07pm
 Scanning Rate: 15.0 C/min
 Sample Wt: 8.517 mg Diek: PSTG
 File: GZ46 KCZ

DELTA SERIES TGA7

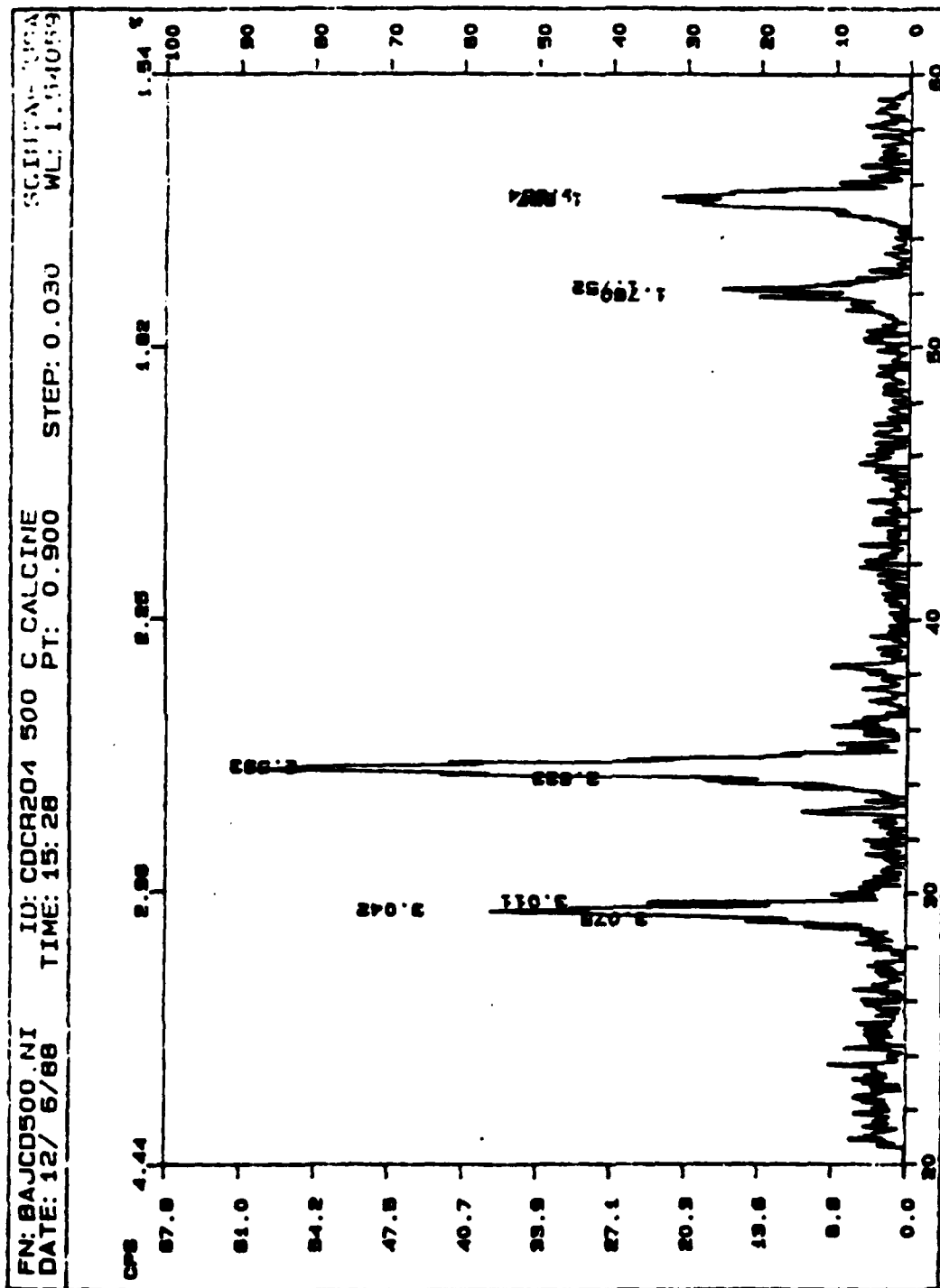


Figure 14. X-ray powder diffraction of chemically prepared CdCr_2O_4 ---calcined at 500°C.

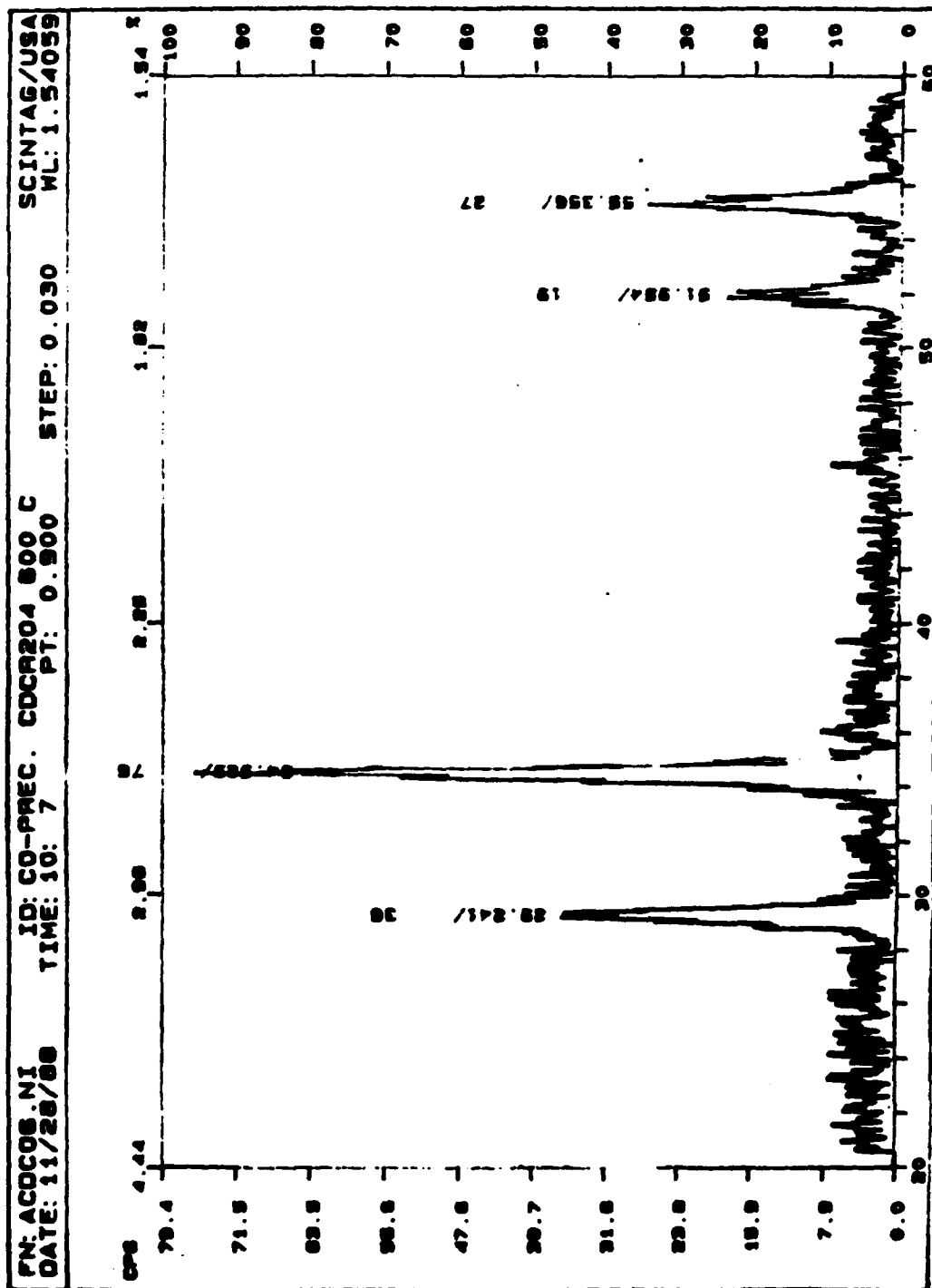


Figure 15. X-ray powder diffraction of chemically prepared CdCr₂O₄--calcined at 600°C.

FN: ACC0700.NI ID: C0-PREC. CDCR204 700 SCINTAG/USA
 DATE: 11/28/88 TIME: 13:59 PT: 0.900 STEP: 0.030 WL: 1.54059

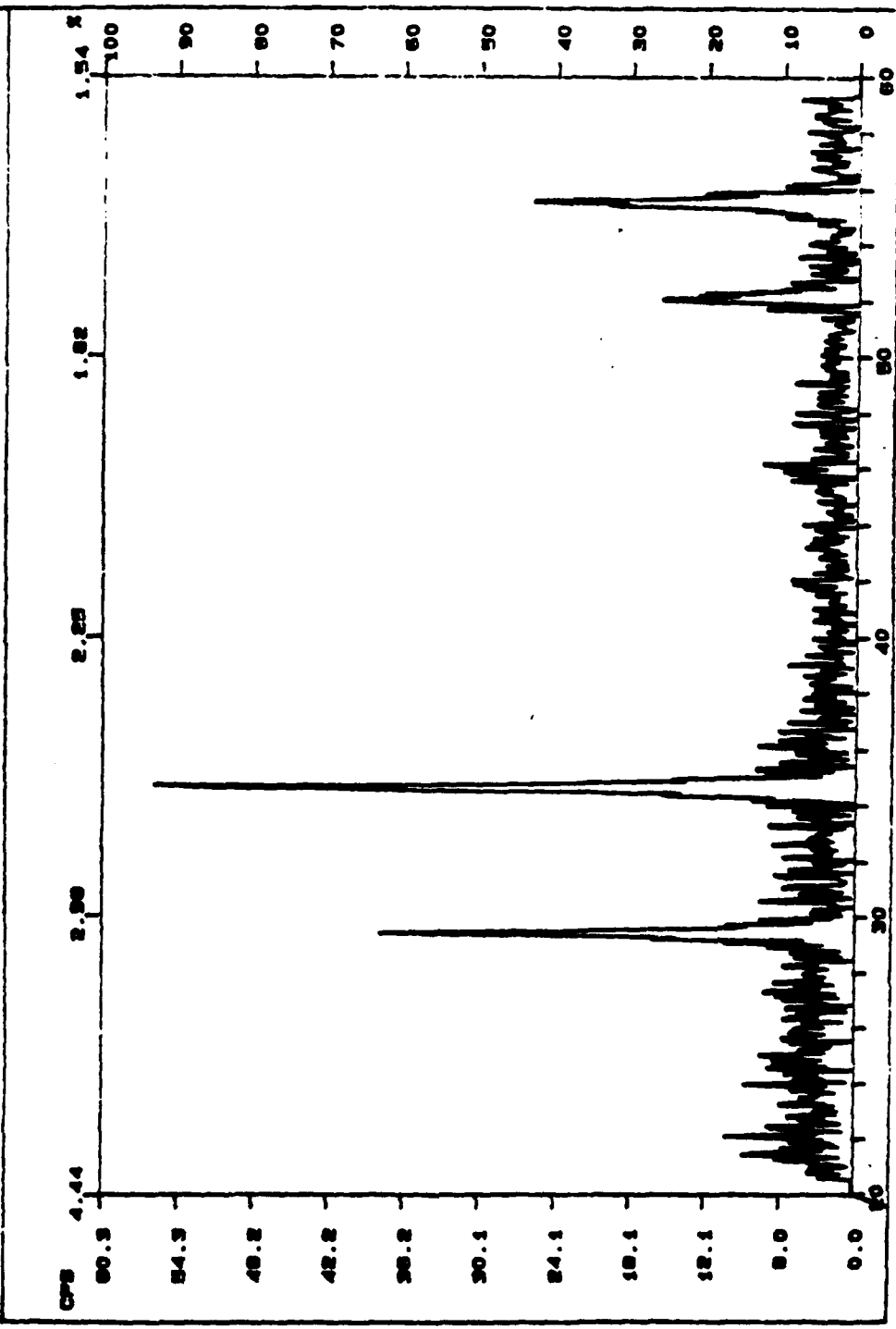


Figure 16. X-ray powder diffraction of chemically prepared CdCr₂O₄--calcined at 700°C.

than $0.1\ \mu$ as proposed in the work statement, with the ZnCr_2O_4 somewhat finer than the CdCr_2O_4 powder.

Obviously, the above powders were found to be much more reactive than the conventional oxide mixtures which require calcination temperatures greater than 900°C . However, no enhancement in terms of densification was observed. Green pressed samples of the coprecipitated spinel powders were sintered using appropriate firing sands at 1300°C and 1400°C for the CdCr_2O_4 and ZnCr_2O_4 , respectively. As reported in Table VII, the resulting densities were less than 50% of theoretical. The low densities were probably due to the inability to obtain well packed powder, a common problem in ultrafine powders and also perhaps the question of volatility is most severe in such high surface area powders.

Table VI
Powder Characteristics of Chemically Prepared ZnCr_2O_4 and CdCr_2O_4 Spinel.

Material	Calcine Condition	Phase	Specific Surface Area (m^2/g)	Primary Particle Size (μm)
ZnCr_2O_4	$600^\circ\text{C}/4\ \text{hrs}$	Spinel	79	0.014
	$700^\circ\text{C}/4\ \text{hrs}$	Spinel	82	0.014
	$800^\circ\text{C}/4\ \text{hrs}$	Spinel	64	0.018
CdCr_2O_4	$500^\circ\text{C}/4\ \text{hrs}$	Spinel	34	0.029
	$600^\circ\text{C}/4\ \text{hrs}$	Spinel	29	0.035
	$700^\circ\text{C}/4\ \text{hrs}$	Spinel	19	0.055

Table VII
Physical Characteristics of Sintered Spinel Using Coprecipitated Powders.

Material	Sintering Conditions	Density g/cc
ZnCr_2O_4	$1400^\circ\text{C}/4\ \text{hrs}$ in ZnCr_2O_4 sand	~ 2.4
CdCr_2O_4	$1300^\circ\text{C}/4\ \text{hrs}$ in CdCr_2O_4 sand	~ 2.5

Single Crystal Growth

As reported by Ferretti,⁽⁴⁾ Kino,⁽⁷⁾ and Leccabue,⁽⁵⁾ single crystals (millimeter sizes) could be grown using various flux growth techniques. In this section we will describe the methods and variations therein based on their work performed in exploring the possibility of growing single crystals of ZnCr_2O_4 . Much of the work presented was overseen by Dr. Z.P. Chang who has many years of experience in the growth of oxide crystals. Dr. Steven Markgraf who also has many years of experience in crystal growth, assisted in selection of fluxes as well as the growth techniques.

The flux growth techniques used involved the mixture of the spinel ZnCr_2O_4 or stoichiometric amounts of ZnO and Cr_2O_3 powder with varying amounts of fluxes. As reported, three families of fluxes were chosen: (1) combination of sodium tungstates $\text{Na}_2\text{W}_2\text{O}_7$ and Na_2WO_4 , (2) PbO and PbF_2 , and (3) Bi_2O_3 . In the first case, the sodium tungstate fluxes had to be prepared. Preparation involved standard mixing/calcination of stoichiometric amounts of Na_2O and WO_3 . X-ray powder diffraction was used to insure phase purity.

The various mixtures of flux and spinel powder were placed in a platinum crucible or an alumina crucible, both covered with a lid to help prevent volatilization.

The crucibles were then heated in an insulated furnace using silicon carbide rods as heating elements. A conventional type globar box furnace and a furnace specifically designed to grow crystals by the flux technique were used. Both types of furnaces were microprocessor controlled.

Flux growth variables included (1) flux type, (2) unreacted ZnO and Cr_2O_3 or calcined ZnCr_2O_4 spinel powder, (3) flux/spinel molar ratio, (4) soak temperature and time, and (5) cooling rate. In addition several runs were made in flowing nitrogen.

More than 30 flux growth runs were attempted with representative runs and associated variables summarized in Table VIII. As presented crystal growth runs were quite time consuming, generally taking more than 1 week to complete.

Initial growth runs using ZnO and Cr_2O_3 as starting materials with $\text{Na}_2\text{W}_2\text{O}_7$ and Na_2WO_4 fluxes were found to have problems. Using a NaOH solution to dissolve the flux, x-ray powder diffraction of the residual powder yielded a very complex pattern consisting of many diffraction peaks, shown in Fig. 17, none of which corresponded to ZnCr_2O_4 . Additional growth runs (e.g., #2 and 3) using unreacted ZnO and Cr_2O_3 did yield small crystals, and upon dissolving away the flux, submillimeter plate-like crystals were observed. Using the SEM, EDS (energy dispersive spectroscopy) analysis on the crystals was performed and shown in Fig. 18. Surprisingly, the major peaks corresponded to Cr only, with no peaks corresponding to Zn observed. A few of the crystallites were collected and placed on a microscope slide for x-ray diffraction analysis. The corresponding x-ray diffraction pattern is shown in Fig. 19. Because of the small number of crystallites, all in the form of platelets, only one peak corresponding to a d-

Table VIII. Flux Growth of ZnCr_2O_4 Crystals.

Run #	Starting Material	Flux	Molar Ratio (Spinel/Flux)	Soak Temp./Time	Cooling Rate	Comments
1	$\text{ZnO} + \text{Cr}_2\text{O}_3$	PbO	1:5	1150°C/5 hrs	1150°C-->890°C @ 10°C/hr	Did not see any crystals
2	$\text{ZnO} + \text{Cr}_2\text{O}_3$	$\text{Na}_2\text{W}_2\text{O}_7$ (0.6 mol%)	1:1.5	1250°C/5 hrs	1250°C-->1000°C @ 10°C/hr	Shiny crystals on wall of crucible observed
3	$\text{ZnO} + \text{Cr}_2\text{O}_3$	Na_2WO_4 (0.6 mol%)	1:1.5	1250°C/5 hrs	1250°C-->900°C @ 5°C/hr	Tiny rectangular platelet crystals. Composition Cr_2O_3
4	ZnCr_2O_4	$\text{Na}_2\text{W}_2\text{O}_7 + \text{Na}_2\text{WO}_4$	1:1.5	1250°C/4 hrs	1250°C-->900°C @ 5°C/hr	Dust like crystals
5	ZnCr_2O_4	$\text{Na}_2\text{W}_2\text{O}_7 + \text{Na}_2\text{WO}_4$	1:1.5	1300°C/3 hrs	1300°C-->1100°C @ 10°C/hr 1100°C-->900°C @ 20°C/hr	Very small shiny crystals
6	ZnCr_2O_4	$\text{Na}_2\text{W}_2\text{O}_7 + \text{Na}_2\text{WO}_4$	1:1.5	1250°C/24 hrs	1250°C-->R.T. @ 2.8°C/min	No crystals observed
7	ZnCr_2O_4	$\text{Na}_2\text{W}_2\text{O}_7 + \text{Na}_2\text{WO}_4$	1:1.5	1250°C/24 hrs in Nitrogen	1250°C-->R.T. @ 2.8°C/min	No crystals observed
8	ZnCr_2O_4	$\text{PbO} + \text{PbF}_2 + \text{MoO}_3$ (30%, 52.5%, 17.5%)	1:4	1220°C/5 hrs	1220°C-->1100°C @ 2°C/hr 1100°C-->900°C @ 5°C/hr	No crystals observed
9	ZnCr_2O_4	$\text{PbO} + \text{PbF}_2 + \text{MoO}_3$ (30%, 52.5%, 17.5%)	1:4	1220°C/8 hrs	1220°C-->1100°C @ 3°C/hr 1100°C-->900°C @ 5°C/hr	Tiny crystals observed
10	$\text{ZnO} + \text{Cr}_2\text{O}_3$ (excess ZnO added)	$\text{PbO}, \text{PbF}_2, \text{SiO}_2, \text{HBO}_3$ 1:4 (40%, 30%, 20%, 10%)		1200°C/5 hrs	1200°C-->850°C @ 3°C/hr	No crystals observed
11	ZnCr_2O_4	Bi_2O_3	25:75	1220°C/24 hrs	1220°C-->1000°C @ 2.2°C/hr 1000°C-->850°C @ 3°C/hr	Many tiny shiny crystals
12	ZnCr_2O_4	Bi_2O_3	30:70	1220°C/24 hrs	1220°C-->1000°C @ 2.2°C/hr 1000°C-->850°C @ 3°C/hr	~ 0.1 mm sized triangular crystals, Crystals were ZnCr_2O_4
13	ZnCr_2O_4	Bi_2O_3	35:65	1220°C/24 hrs	1220°C-->1000°C @ 2.2°C/hr 1000°C-->850°C @ 3°C/hr	Many tiny crystals

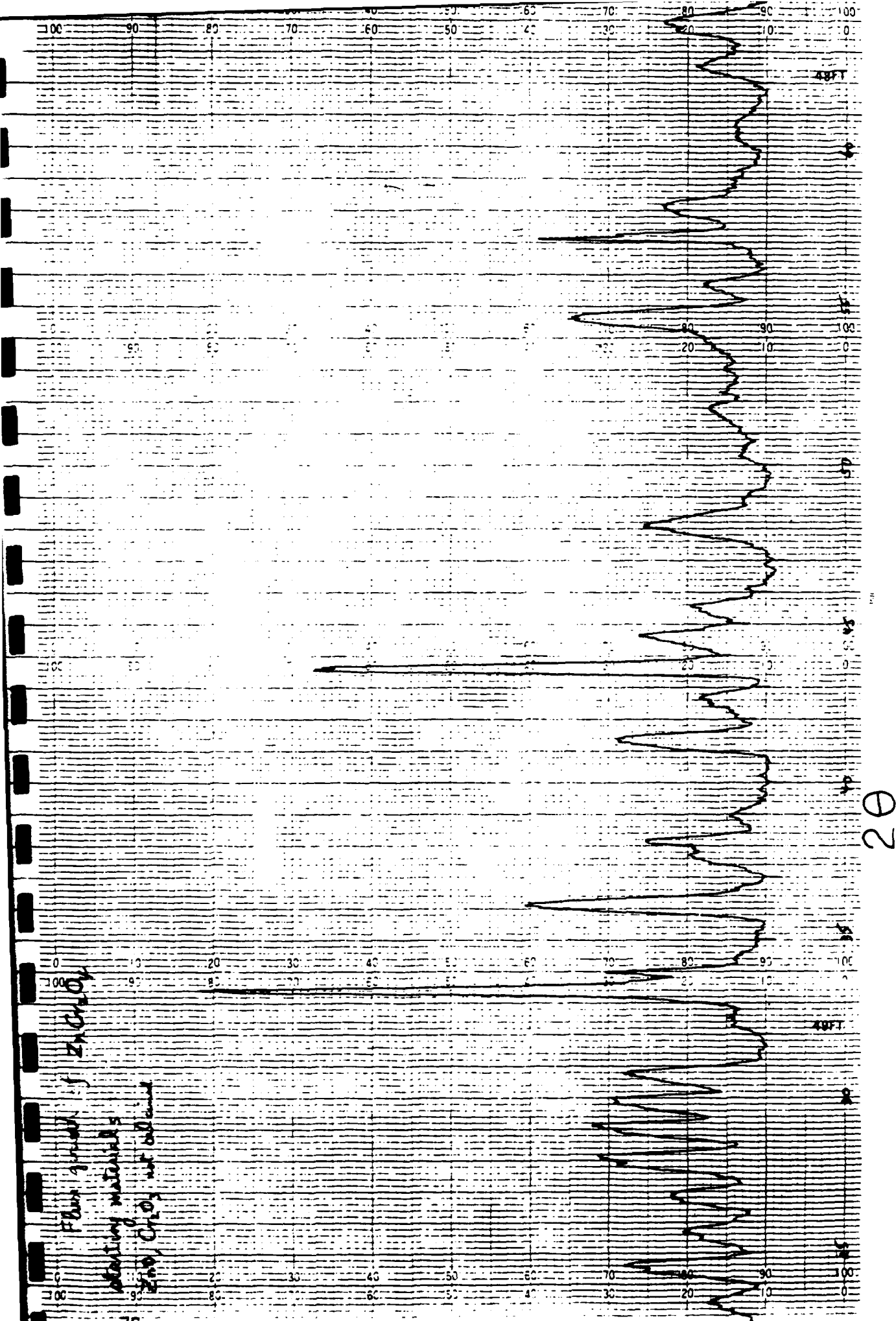
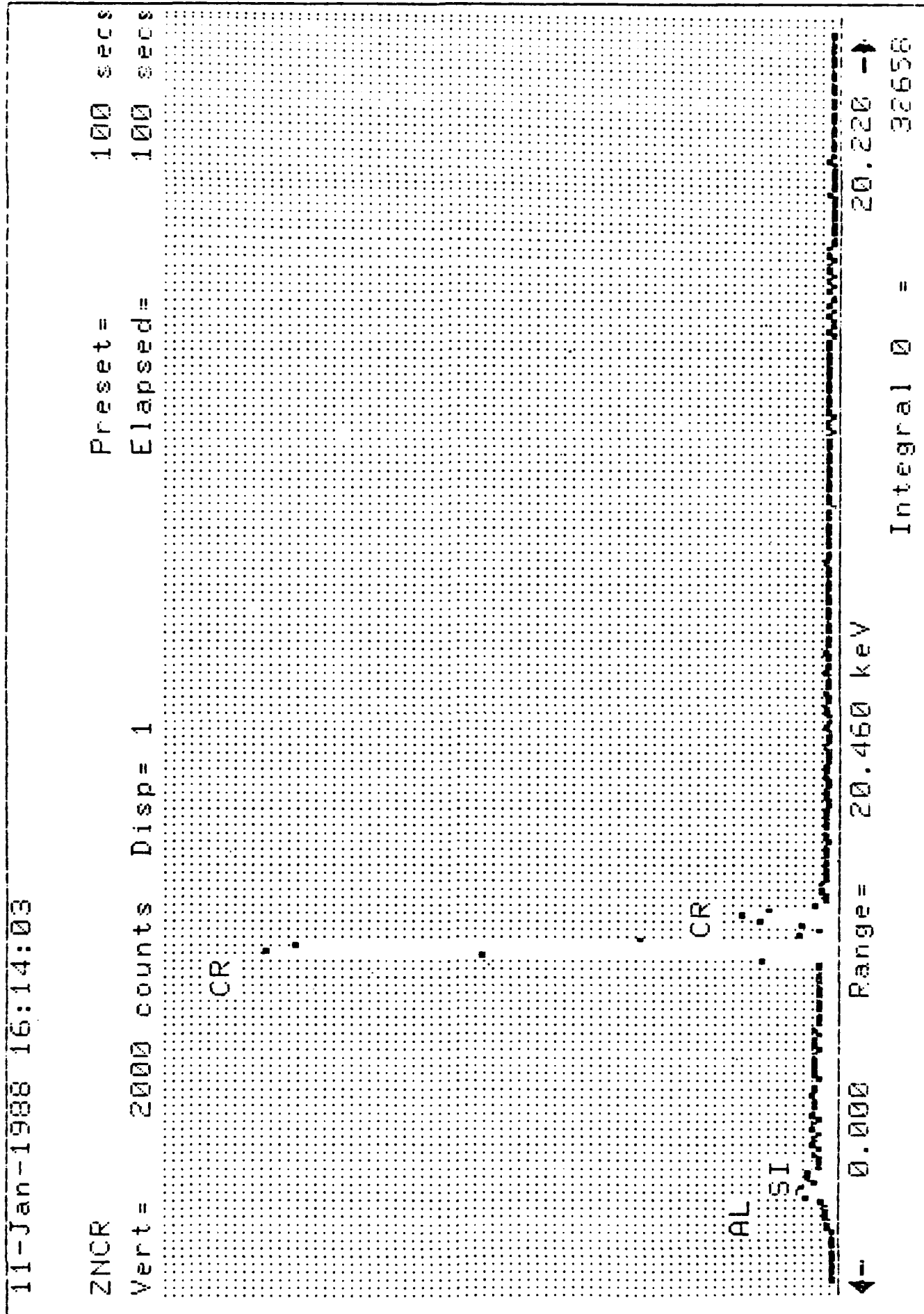


Figure 17. X-ray powder diffraction pattern of residual powder in early crystal growth run of ZnCr_2O_4 using ZnO and Cr_2O_3 starting materials.

Figure 18. EDS analysis of several small crystals from early crystal growth attempts of ZnCr_2O_4 .



spacing of 2.256 Å could be observed. This agrees well with the d-spacing of 2.264 for an hkl = 006 reflection of Cr_2O_3 .

The above results suggested a loss of ZnO occurred through evaporation. Hence, to reduce loss of ZnO, the component powders were prereacted. Crystal growth runs with prereacted ZnCr_2O_4 powder resulted in only very small crystals, but at least when washed with NaOH, x-ray diffraction analysis corresponded to the spinel structure (see Fig. 20) except for two lines, which are perhaps due to residual flux.

Crystal growth runs using Bi_2O_3 as a flux were generally more successful than the others. X-ray diffraction of ZnCr_2O_4 flux runs corresponded to the spinel phase as shown in Fig. 21.

X-ray diffraction using a Gandolfi camera, a technique designed for analysis of small single crystals, was performed on several shiny single crystals from Bi_2O_3 flux runs. From the diffraction film strip schematically shown in Fig. 22 and the associated tabulated data reported in Table IX, it is clearly evident that the crystals were ZnCr_2O_4 .

An optical photograph of some of the small crystals or crystallites is shown in Fig. 23. In summary, though many flux crystal growth parameters were used only a few tiny crystals of ZnCr_2O_4 spinel were successfully grown.

Doped Spinel and Spinel/Glass Composites

The effect of various dopants and/or stress effects on the undistorted spinel lattice and subsequent properties was originated under a separate Wright Patterson AFB (Contract # F33615-86-263715 B5871-0351) which ended September 30, 1987.

From this work it was felt that the basic physics discovered on these materials warranted further investigation at the request of Dr. William Lawless of CeramPhysics, Inc. and samples were prepared. Details of the basic physics results and their understanding were reported with much of the work performed at Ohio State University.

The fabrication and characterization of various doped spinels and spinel/glass composites will be presented in this section.

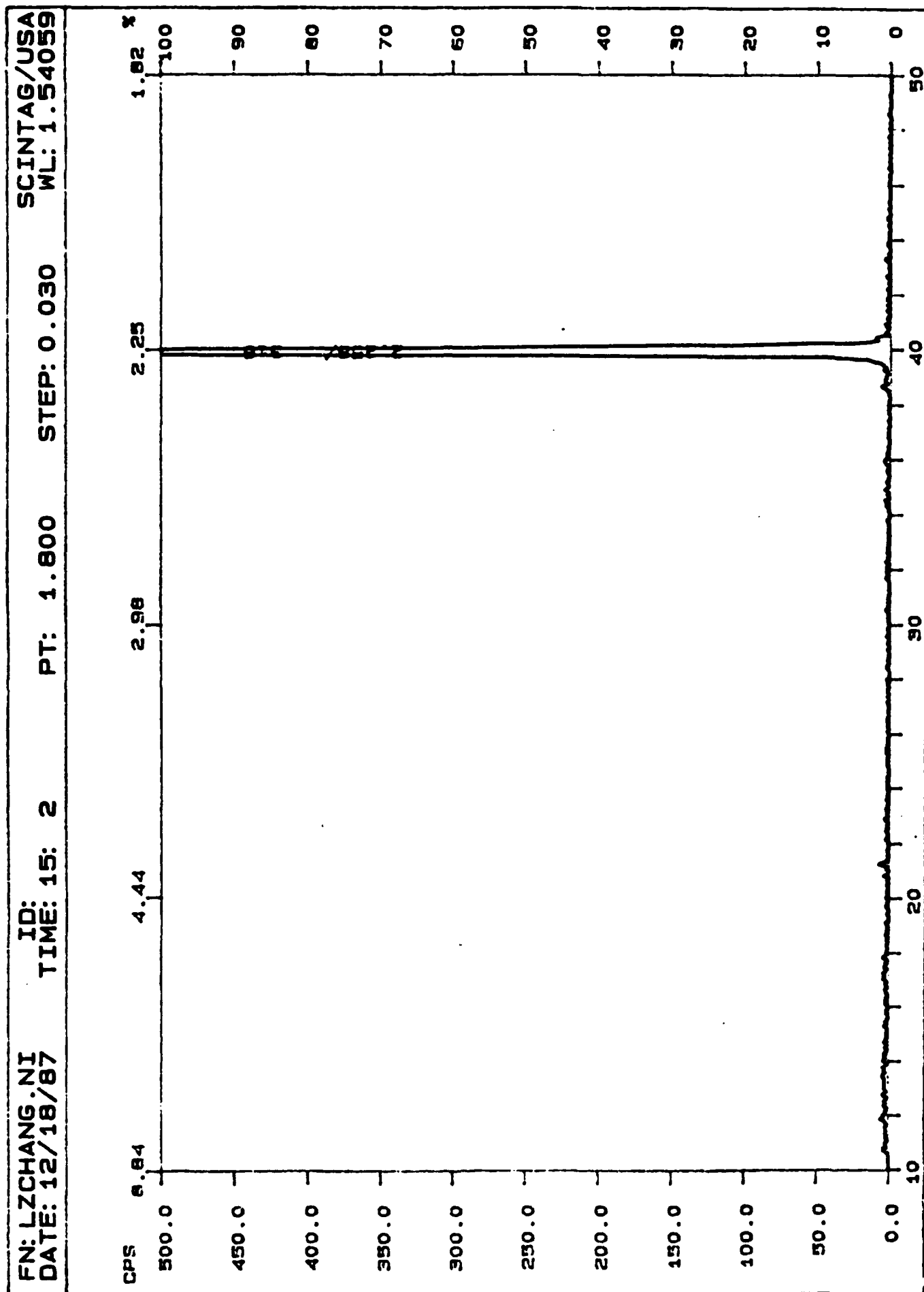
Fabrication and Characterization

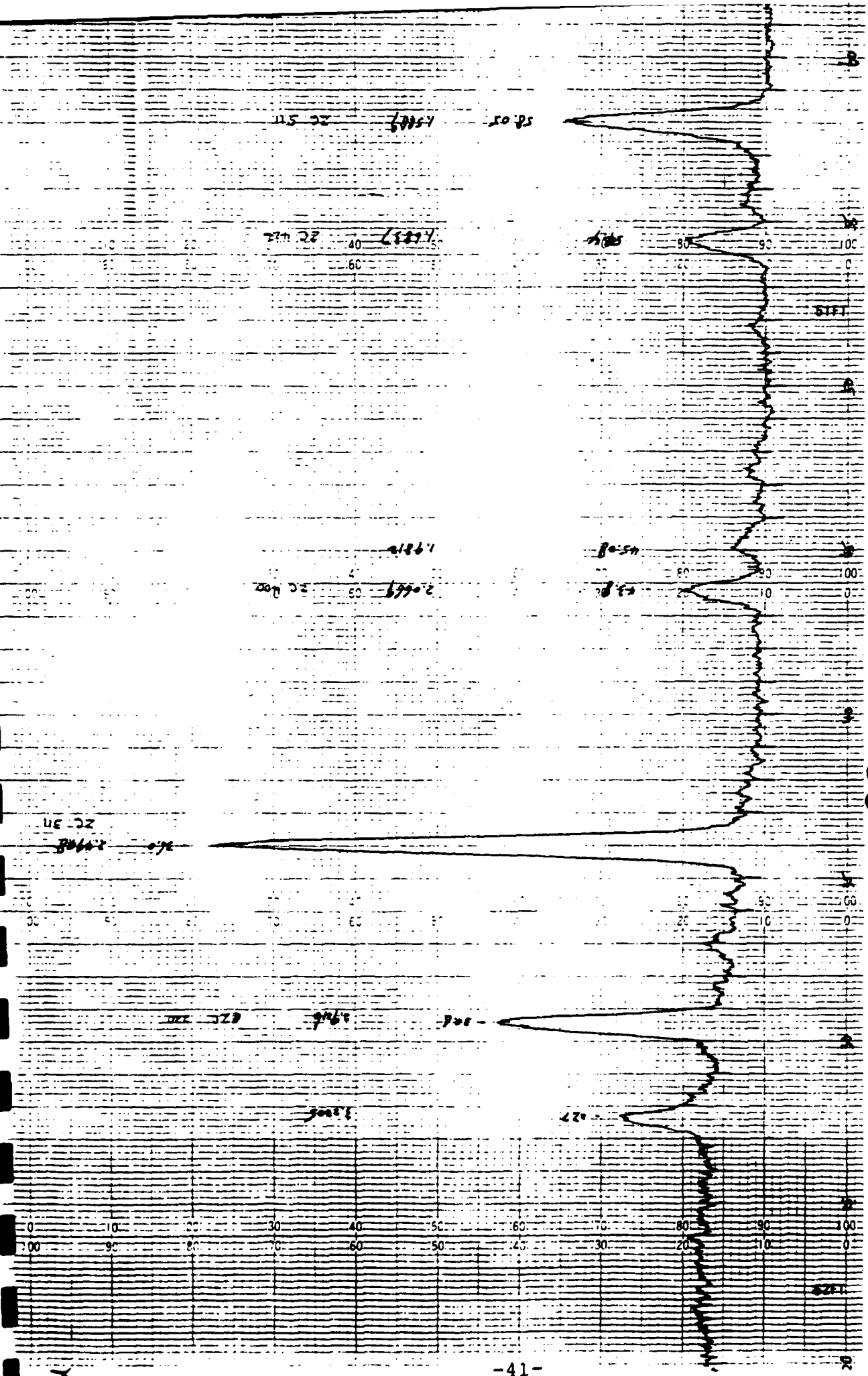
Doped Spinel

In the Wright Patterson AFB work, many dopants were suggested and tried, but in this work only Al^{+3} and Gd^{+3} dopants on the B-site replacing Cr^{+3} of the ZnCr_2O_4 spinel were used.

The dopant levels of Al_2O_3 used were 1, 3, 6, and 10 mole% with only one dopant level of Gd_2O_3 , that being 2 mole%. The component powders of ZnO and Cr_2O_3 and dopants were

Figure 19. X-ray powder diffraction of several small crystals grown in early flux growth runs of ZnCr_2O_4 .

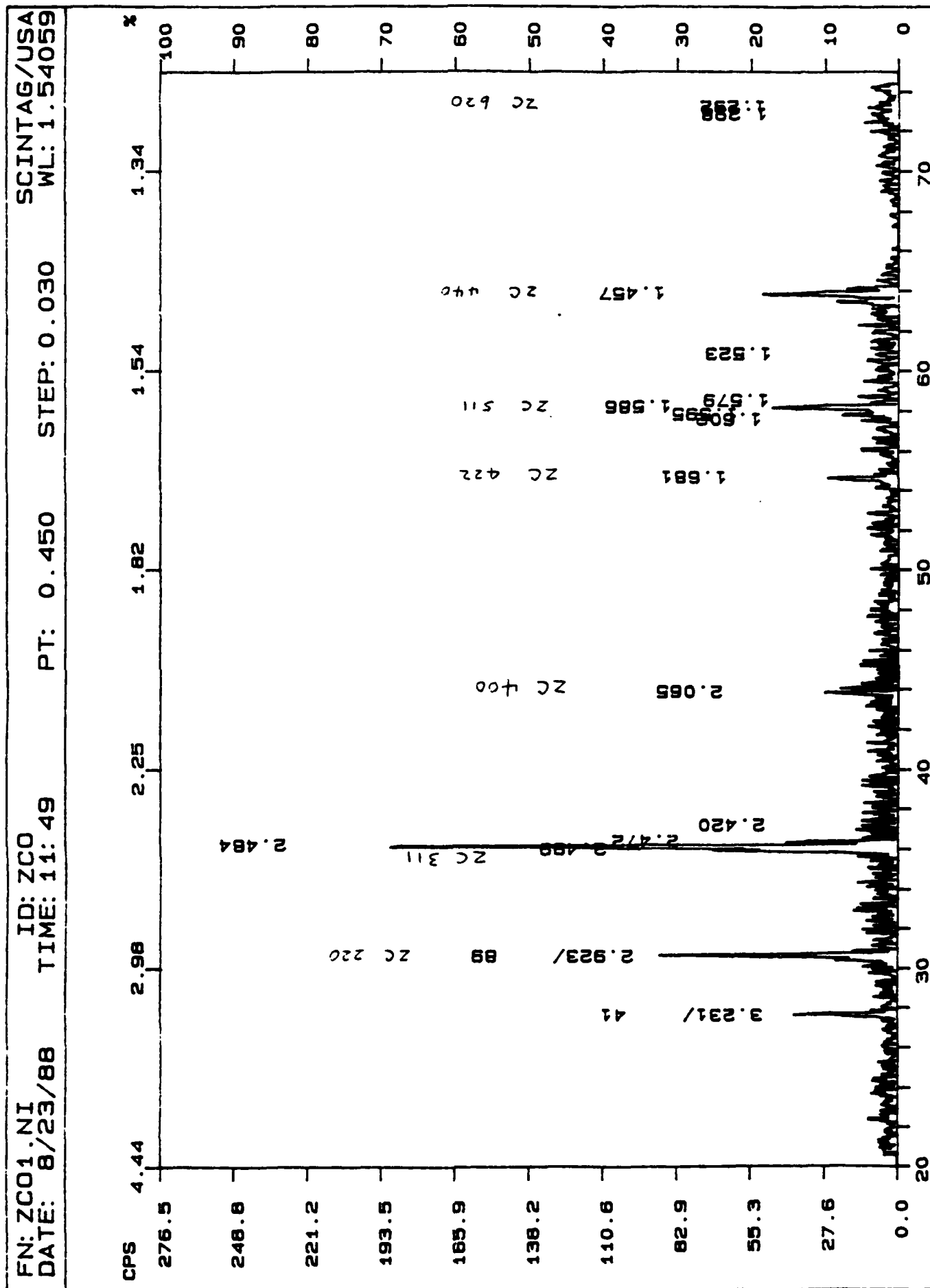




20

Figure 20. X-ray powder diffraction pattern of residual powder from ZnCr₂O₄ crystal growth run using prereacted powder.

Figure 21. X-ray powder diffraction of residual powder from crystal growth runs using Bi₂O₃ flux.



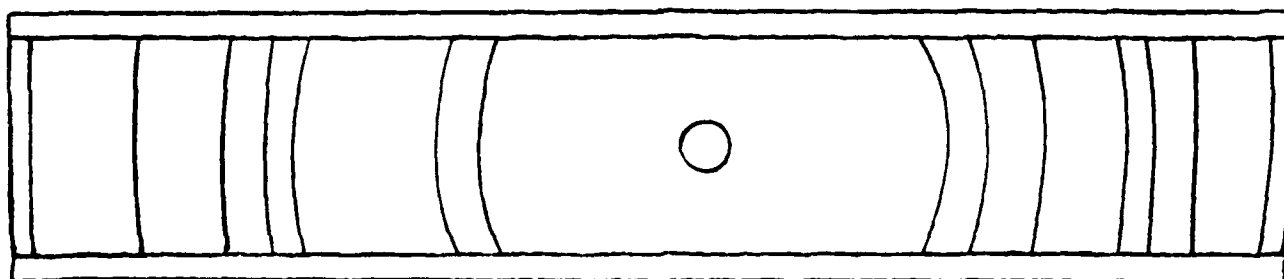


Figure 22. Representation of diffraction film strip obtained using Gandolfi camera.

Table IX
Tabulated data from Gandolfi x-ray diffraction pattern of ZnCr_2O_4 crystallites.

Left	Right	I (Intensity)	4θ	2θ	d Å	ZnCr_2O_4 hkl
96.60	152.10	W	55.50	27.75	3.2148	
93.40	155.25	M	61.85	30.925	2.8911	220
87.95	160.75	S	72.80	36.40	2.4682	311
86.66	162.45 (uncertain)	VW	75.79	37.895	2.3739	222
80.15	168.70	W	88.55	44.275	2.0456	400
76.1 (not sure)	173.00 (not sure)	VW	96.90	48.45	1.8788	331
69.8 (broad or double peak) 69.25	179.4	M	109.88	54.94	1.6712	422
66.00	183.10	S	117.10	58.55	1.5765	511
60.10	188.70	S	128.60	64.30	1.4487	440
51.60	197.70	W	146.10	73.05	1.2953	620
48.45	200.80	M	152.35	76.175	1.2497	533
43.90	205.80	VW	161.90	80.95	1.1876	444

VW--Very Weak
W--Weak
M--Medium
S--Strong

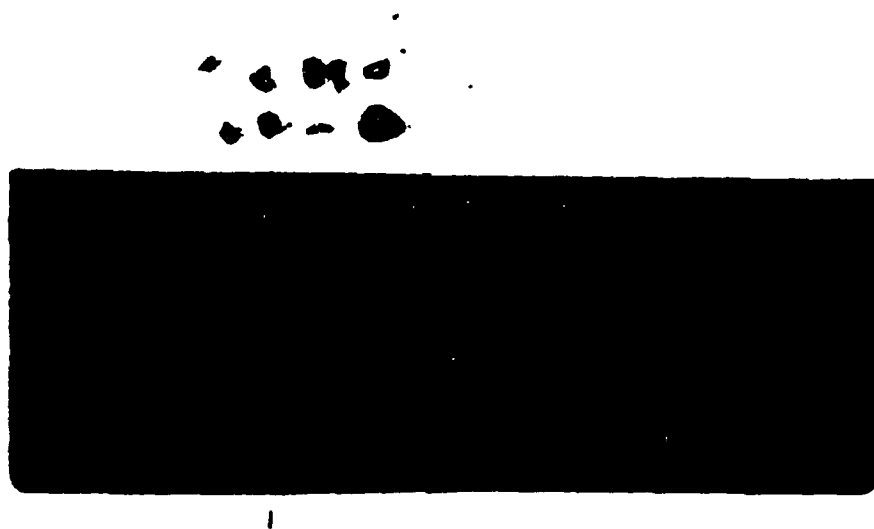


Figure 23. Optical photograph of several small crystals of ZnCr_2O_4 growth using Bi_2O_3 flux growth.

mixed/calcined as previously described. Upon calcination, the powders were characterized for phase purity using x-ray powder diffraction. See Appendix A for x-ray diffraction patterns of selected samples.

Due to the limitations of x-ray powder diffraction being typically ~ 2% it was difficult to determine whether or not the dopants successfully entered the spinel structure.

Disks were fabricated from the calcined powders and sintered at various temperatures. The samples were fired in a closed crucible to help prevent ZnO volatility and as expected the resultant densities were low. The sintered samples were characterized for phase purity, with the results reported in Table X. SEM analysis was used to investigate possible second phases and to determine the grain size. Representative SEM photomicrographs are shown in Fig. 24. From these results it appeared that the dopants went into the spinel structure. However, at high sintering temperatures (~ 1600°C) it appeared, based on x-ray diffraction, that Al₂O₃ possibly leached back out of the structure.

All in all, it was difficult to ascertain the degree or level of dopants actually incorporated into the spinel structure. Little or no effect of the dopants on sintering and the microstructure of the spinel ceramics were observed.

Glass/Spinel Composites

Two types of glasses (Corning #7052 and 7570) were used to fabricate various spinel/glass composites. Physical characteristics of the glasses are reported in Table XI. The glass/spinel composites were prepared by wet mixing various amounts of the selected glass and spinel powders, using a vibratory mill. The powder mixtures were then dried followed by green forming. The samples were then fired at 950°C/4 hrs. Due to the low working point of the glasses, the firing temperature used was relatively low as compared to the spinels themselves.

The fired composites were characterized for geometric density and x-ray diffraction was performed to look at possible chemical reactions between the spinels and the glasses. SEM microstructural analyses was performed on various composites. The physical characteristics of the composites are reported in Table XII, and representative SEM photomicrographs are shown in Fig. 25. The SEM photos revealed that the glasses appeared to wet the spinel powders. Naturally, at such low firing temperatures, no grain growth occurred, with the particle sizes of the spinels in the range of 1-3 μ. Based on x-ray diffraction little if any reaction between the glass and spinels was found to occur. See Appendix A for representative powder diffraction patterns.

Table X
Physical Characteristics of ZnCr_2O_4 Spinel with Various Dopants.

Material	Firing Conditions	Phase
$\text{ZnCr}_2\text{O}_4 + 1\% \text{Al}_2\text{O}_3$	1250°C/4 hrs	Spinel
	1400°C/4 hrs	""
	1600°C/2 hrs	""
+ 3% Al_2O_3	1250°C/4 hrs	Spinel
	1400°C/4 hrs	""
	1600°C/2.5 hrs	Spinel + Al_2O_3
+ 6% Al_2O_3	1400°C/4 hrs	Spinel
	1600°C/2.5 hrs	Spinel + Al_2O_3
+ 10% Al_2O_3	1250°C/4 hrs	Spinel
	1300°C/4 hrs	""
	1600°C/2.5 hrs	Spinel + Al_2O_3
$\text{ZnCr}_2\text{O}_4 + 2\% \text{Gd}_2\text{O}_3$	1150°C/4 hrs	Spinel

No additional characterization was performed on the composites.

To look at whether or not stress due to thermal expansion mismatch between the spinels and glasses actually occurred, the lattice parameter of the cubic spinel structure as determined by x-ray powder patterns (see Appendix A) were run on ZnCr_2O_4 powder and ZnCr_2O_4 /glass composite, both with Pt internal standards. No shift or splitting of diffraction peaks or the lattice parameter was observed.

Table XI
Physical Characteristics of Corning Glass #7570 and #7052

Material	Working Point	Density g/cc
7570 (High Lead Silicate)	560°C	5.42
7052 (Borosilicate)	1115°C	2.20

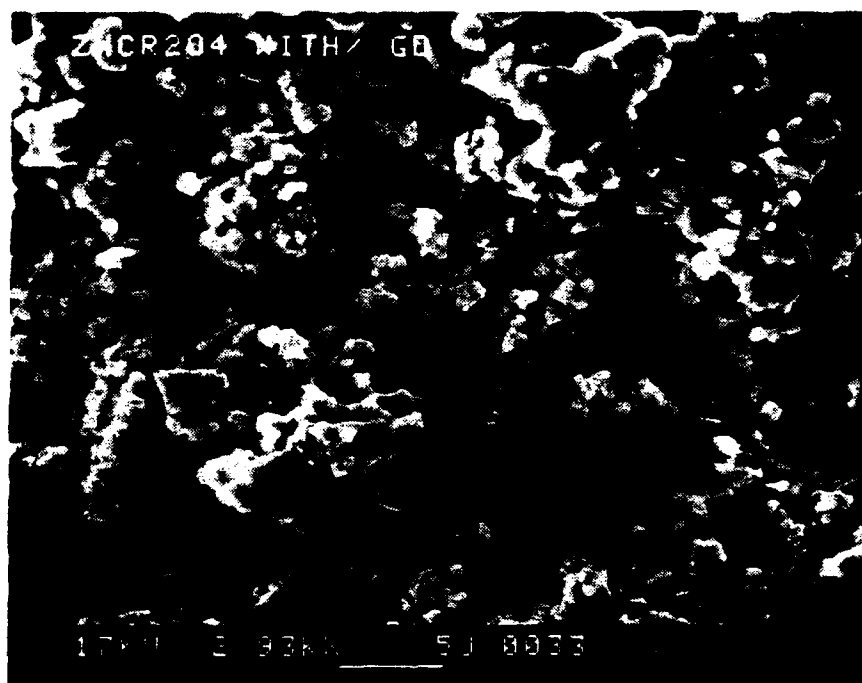
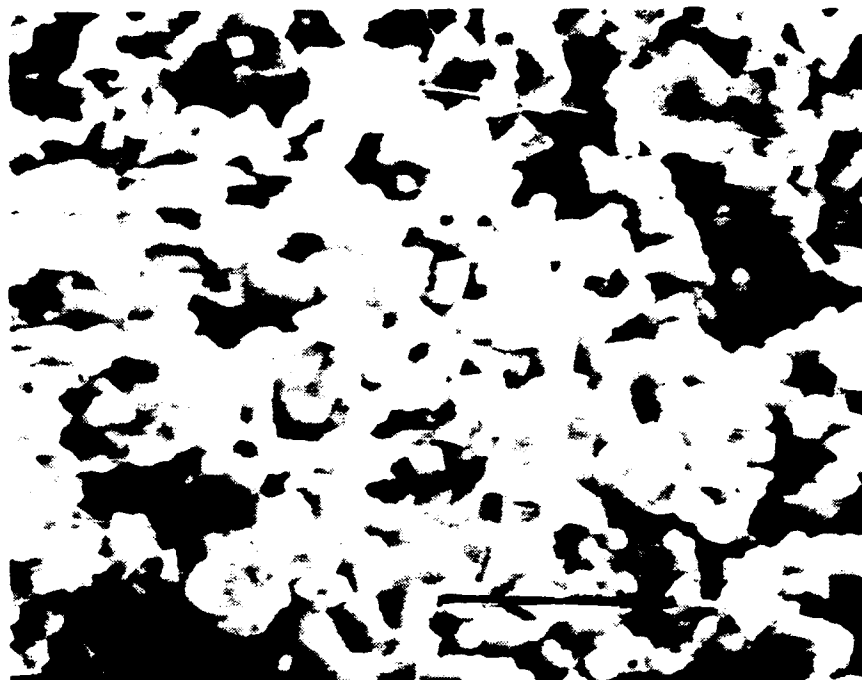


Figure 24. Representative SEM photomicrographs of sintered Al^{3+} (top) and Gd^{3+} doped ZnCr_2O_4 spinels (fractured samples). Note: Top photo--marker = 10 μ .

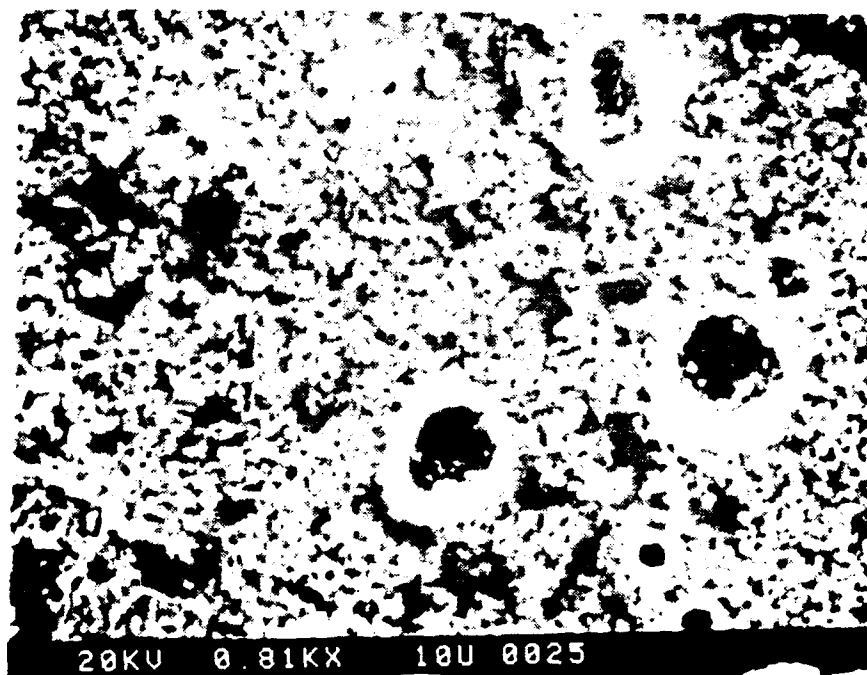
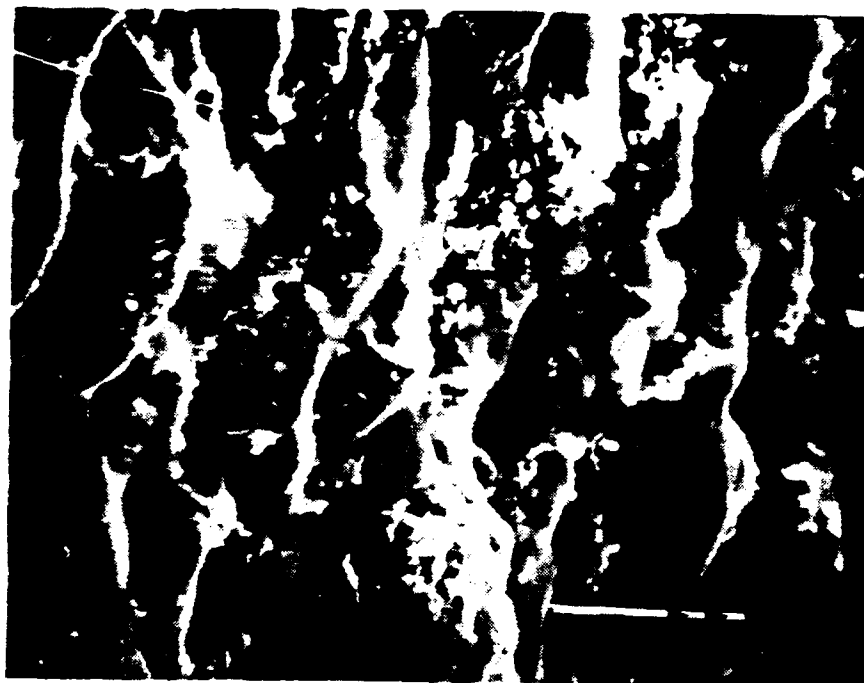


Figure 25. SEM photomicrographs of ZnCr_2O_4 spinel/glass. Top: 7570 glass. Bottom: 7052 glass (fractured surfaces).

Table XII
Physical Characteristics of Spinel/Glass Composites

Material Spinel/Glass (wt%)	Firing Condition	Density g/cc	Comment
ZnCr ₂ O ₄ + 50% 7570	950°C/2-4 hrs	~ 4.2	No Reaction
ZnCr ₂ O ₄ + 30% 7052	950°C/2-4 hrs	~ 2.6	No Reaction
+ 50% 7052	950°C/2-4 hrs	~ 2.9	""
+ 70% 7052	950°C/2-4 hrs	~ 2.4	""
CdCr ₂ O ₄ + 50% 7570	950°C/2-4 hrs	~ 3.6	No Reaction
CdCr ₂ O ₄ + 5% 7052	950°C/2-4 hrs		No Reaction
+ 10% 7052	950°C/2-4 hrs		""
+ 20% 7052	950°C/2-4 hrs		""
+ 30% 7052	950°C/2-4 hrs		""

SUMMARY

The role of Penn State University in the Air Force Program on "Research on High Specific Heat Dielectrics," was to explore and investigate new ceramic preparation methods for the highly frustrated spinels CdCr₂O₄ and ZnCr₂O₄. In particular, the concept of new preparation techniques arose from the need to prepare highly dense spinels without the use of columbite sintering aids. In addition to polycrystalline spinels, it was desired that PSU should explore the growth of single crystals using flux growth technique.

To achieve these goals the proposed work plan was presented in the letter proposed^(c) to the Air Force which included the following:

1. Explore flux growth techniques to fabricate single crystals.
2. Investigate both HIP (hot isostatic pressing) and HUP (hot uniaxial pressing) to fabricate dense polycrystalline samples without the columbite phase.
3. Investigate the fabrication of samples using chemical synthesis techniques such as hydrothermal growth and coprecipitation of alkoxides.

It was hoped that chemical fabrication techniques would result in very fine spinel powders with increased reactivity and thus enhanced densification.

It was a further goal to determine the effects of purity and particle and/or grain size of the spinels on their thermal and magnetic properties.

The program was conducted with all of the above goals in mind. The fabrication of spinels was investigated and the results presented and summarized in the following:

- 1) High purity spinel powders of ZnCr_2O_4 and CdCr_2O_4 were prepared using 99.999% pure component powders of ZnO , CdO and Cr_2O_3 . Sintered samples were prepared from the powders. Careful attention in the fabrication of these samples was taken to insure minimal contamination. In order to investigate the effect of purity on the properties, reagent grade conventional spinel powders and sintered samples were also prepared.
- 2) Highly dense (> 90%) polycrystalline disks of ZnCr_2O_4 without the columbite sintering aid, were achieved by controlling the ZnO volatility using a firing sand of the same composition. The samples could be densified over the range of 1600°C to 1700°C, resulting in grain sizes as large as 10 microns.
- 3) With respect to the densification of CdCr_2O_4 , by attempting to control the CdO volatility with firing sands, no enhancement in densification was observed. Severe CdO volatilization was found to occur, even when firing sands were used above 1300°C. No further attempts to control the CdO volatility were made owing to the fact of its carcinogenic nature.
- 4) Highly dense ZnCr_2O_4 spinels could also be achieved using hot uniaxial pressing (HUP) at temperatures as low as 1400°C. The samples were found to have grain sizes as small as 1-2 μm . The fact that densification could only be achieved around 1400°C, clearly indicated that hot isostatic pressing (HIP), which is limited to ~ 1200°C, would not be successful in producing dense samples.

Though hot uniaxial pressing was successful in enhancing densification of ZnCr_2O_4 , the question of ZnO volatility and contamination from the pressure vessels (graphite and Boron Nitride lubrication powder) remains a problem that needs to be addressed. In addition, hot pressing was performed in a vacuum which may have resulted in partial reduction of the ZnCr_2O_4 .

As such, the high volatility associated with CdO and its relative ease of reduction (CdO - Cd metal) made it impossible to attempt hot pressing.

- 5) Preparation of fine spinel powders using the hydrothermal technique was evaluated and it was determined that extremely high pHs > 12, would be required resulting in compromised purity due to severe reaction with the material of the containment vessel, namely the nickel liner of the autoclave. Hence, fine powders of both spinels with particle sizes (<< 0.1 μm) were prepared using a coprecipitation technique. The powders were found to react to form

the spinel phase at temperatures as low as 500°C to 600°C (CdCr_2O_4 and ZnCr_2O_4 , respectively) being significantly lower than that for reagent grade powders. However, enhancement of the sintering kinetics was not observed. Resulting densities of fired samples were extremely low (< 50% theoretical) possibly being the result of poor powder packing associated with ultrafine powders. In addition to poor packing efficiency, the high surface area of the powders may have led to a problem in volatilization.

- 6) A literature search on the growth of single crystal spinels, namely ZnCr_2O_4 and CdCr_2O_4 , using the flux growth technique was performed. Based on the search, several potential flux systems were selected including, 1) sodium tungstates $\text{Na}_2\text{W}_2\text{O}_7$ and Na_2WO_4 , 2) PbO and PbF_2 , and 3) Bi_2O_3 . Flux growth variables for the ZnCr_2O_4 spinel included: 1) flux type, 2) unreacted ZnO and Cr_2O_3 or calcined ZnCr_2O_4 powder, 3) flux/spinel molar ratio, 4) soak temperature and time, and 5) cooling rate. More than 30 flux growth runs were made generally taking more than one week to complete. Crystal growth using the Bi_2O_3 flux were generally more successful than the others. Small crystals (mm) were grown and their crystallinity and structure confirmed by x-ray diffraction using a Gandolfi camera.
- 7) To look at the effect of dopants and/or stress effects on the undistorted spinel lattice and subsequent properties several dopant levels of Al^{+3} and Gd^{+3} replacing the Cr^{+3} cation of the ZnCr_2O_4 spinel were proposed by Dr. William Lawless and samples fabricated. To examine possible stress effects various spinel (ZnCr_2O_4 and CdCr_2O_4) glass composites were made. Based on x-ray diffraction using internal standards no effect of stress (if present) was observed.

Samples prepared and fabricated at Penn State University that were delivered to CeramPhysics, Inc. are tabulated in Table XIII. Included are the time frame in which the samples were fabricated as well as delivered. In addition, PSU, CeramPhysics (CP) and subcontractors reports documenting these samples are referenced.

Table XIII
Delivered Samples.

Material	Time Frame Fabricated--Delivered	Report/Refs.
<u>High Purity Spinel</u>		
1. High Purity 99.999% CdCr ₂ O ₄	2-3/88--3/88	f,g,i,m,n,o,q
2. Reagent Grade--CdCr ₂ O ₄ (1250°C--closed crucible)	2-3/88--3/88	f,g,m,o,q
3. High Purity 99.999% ZnCr ₂ O ₄	11-12/87--2/88	f,g,i,m,n,o,q
4. Reagent Grade--ZnCr ₂ O ₄ (1600°C--closed crucible)	11-12/87--2/88	f,g,m,o,q
5. High Purity 99.999% CdCr ₂ O ₄ Powder	12/87--1/89	f,g,t
<u>Conventionally Sintered Spinel</u>		
ZnCr ₂ O ₄		
1500°C	12/88--1/89	t
1550°C	12/88--1/89	t
1600°C	6-8/88--8/88	o
1650°C	6-8/88--8/88	l,o,q
1700°C	6-8/88--8/88	l,o,q
<u>Hot Pressed Spinel</u>		
ZnCr ₂ O ₄		
1250°C	7-8/88--8/88	l,n,o,q
1400°C	7-8/88--8/88	l,n,o,q
1450°C	7-8/88--8/88	l,n,o,q
<u>Chemically Prepared Spinel</u>		
ZnCr ₂ O ₄ Powder		
Calcined 600°C	7/88--12/88	l,q,r,s
Calcined 700°C	7/88--8/88	l,q,s
Calcined 800°C	7/88--12/88	l,q,r,s

Material	Time Frame Fabricated--Delivered	Report/Refs.
CdCr₂O₄ Powder		
Calcined 500°C	11/88--12/88	r,t
Calcined 600°C	11/88--1/89	t
Calcined 700°C	11/88--1/89	t
ZnCr₂O₄ Bar		
Sintered 1400°C	12/88--1/89	t
CdCr₂O₄ Disk		
Sintered 1300°C	12/88--1/89	t
<u>Single Crystal Spinel</u>s		
ZnCr ₂ O ₄ /Bi ₂ O ₃ [flux 35/65]--single crystal(s)	9-11/88--1/89	o,q,t
ZnCr ₂ O ₄ /Bi ₂ O ₃ [flux 30-70]--single crystal(s)	9-11/88--1/89	o,q,t
ZnCr ₂ O ₄ /Bi ₂ O ₃ [flux 25/75]--single crystal(s) and flux	9-11/88--1/89	o,q,t
ZnCr ₂ O ₄ /Na ₂ W ₂ O ₇ -Na ₂ WO ₄ --single crystal(s) and flux		l,o,q,t
Doped Spinel and Glass/Spinel Composites (Total of ~ 20 samples)	10/87-3/88--3/88	g,h,i,m,n,p

REFERENCES

- 1) J.H. Adair, D.A. Anderson, G.O. Dayton, and T.R. Shrout. "A Review of the Processing of Electronic Ceramics with Emphasis on Multilayer Capacitor Fabrication," *The Journal of Materials Education*, **9**, 71-118 (1987).
- 2) J.H. Adair. Private Communication.
- 3) J.H. Adair, A.J. Rose, and L.G. McCoy. "Particle Size Analysis of Ceramic Powders," *Proc. Processing for Improved Productivity*, Amer. Cer. Soc. (1983).
- 4) A. Ferretti, R.J. Arnout, and D.B. Rogers. "Single Crystal Growth of Transition Metal Oxides from Polytungstate Fluxes," *Phys. Chem. Solids*, **26**, 311-314 (1965).
- 5) F. Leccabue and C. Pelosi. "Crystal Growth, Thermodynamical and Structural Study of CoGa_2O_4 and ZnCr_2O_4 Single Crystals," *J. of Crystal Growth*, **79**, 410-416 (1986).
- 6) Y. Kino, B. Luthi, M.E. Mullen. "Cooperative Jahn-Teller Phase Transition in Nickel-Zinc-Chromite System," *J. Phys. Soc. Jpn.*, **33**, 687 (1972).
- 7) Y. Kino and B. Luthi. "Magnetic and Elastic Properties of Zinc-Chromite," *Solid State Comm.*, **9**, 805-808 (1971).
- 8) A. Pajaczowska and W. Piekarczyk. "Growth on ZnCr_2O_4 Single Crystals by Chemical Transport," *Mat. Res. Bull.*, **16**, 1091-1097 (1981).

References—Reports and Documents

AFOSR Contract No. F49620-86-C-0049, "Research on High Specific-Heat Dielectrics"

- a) Annual Report. "Research on High Specific Heat Dielectrics," CeramPhysics, Inc., May 10, 1987.
- b) Research Proposal. "For Continuation of Subcontract Support under AFOSR Prime Contract No. F49620-86-C-0049," Penn State University, May 1987.
- c) Letter Proposal. "Extension of AFOSR Contract No. F49620-86-C-0049," CeramPhysics, Inc., May 1988.
- d) Documentation Page. "Research on High-Specific Heat Dielectrics," CeramPhysics, Inc., September 30, 1987.
- e) Progress Report. "Low Temperature Thermal Contraction and Dielectric Constant Measurements," CeramPhysics, Inc., January 20, 1988.
- f) Progress Report. "Processing of Single Crystal and Polycrystalline Spinels," Penn State University, February 3, 1988.
- g) Quarterly Report. "Quality Review," CeramPhysics, Inc., April 15, 1988.

- h) Progress Report. "Specific Heat Metrology," CeramPhysics, Inc., July 15, 1988.
- i) Quarterly Report. "Quarterly Review," CeramPhysics, Inc., July 15, 1988.
- j) Progress Report. "Thermal Contract Measurements on Ceramic Composites," CeramPhysics, Inc., August 12, 1988.
- k) Memo. "Research on High-Specific-Heat Dielectrics, September 1, 1987-February 28, 1989," CeramPhysics, Inc., August 15, 1988.
- l) Progress Report. "Processing of Single Crystal and Polycrystalline Spinel," Penn State University, August 22, 1988.
- m) Progress Report. "Broad Range Specific Heat Measurement," CeramPhysics, Inc., August 26, 1988.
- n) Progress Report. "Dielectric Constant Measurements," CeramPhysics, Inc., November 15, 1988.
- o) Progress Report. "Processing of Single Crystal and Polycrystalline Spinel," Penn State University, November 18, 1988.
- p) Progress Report. "Theoretical Studies I: Effects of Impurity Spin Doping on Undistorted Spinel Lattice," Ohio State University, December 7, 1988.
- q) Progress Report. "Processing of Single Crystal and Polycrystalline Spinel," CeramPhysics, Inc., December 9, 1988.
- r) Letter of Delivery. "Delivery of Co-Precipitated ZnCr_2O_4 and CdCr_2O_4 Powder," Penn State University, December 13, 1988.
- s) Progress Report. "Specific Heat Measurements on ZnCr_2O_4 Powders," CeramPhysics, Inc., December 22, 1988.
- t) Letter of Delivery. "Delivery of Completed Work on ZnCr_2O_4 and CdCr_2O_4 Samples," Penn State University, January 5, 1988.

III.B. SAMPLE PREPARATIONS AT WEST VIRGINIA UNIVERSITY

Introduction

This document details our recent experimental work on the growth of the spinels ZnCr_2O_4 and CdCr_2O_4 . This work was undertaken with the hope of growing large enough single crystal samples for specific heat (C_p), magnetic susceptibility (χ), and EPR measurements. The overall goal of this project was to obtain accurate C_p , χ , and EPR data on defect-free samples, which will help to understand the microscopic mechanism of the exceptionally high C_p peaks exhibited by these materials in the 4 - 16 K range (Lawless *et al.*, 1986-87). The need for C_p and χ data employing single crystals became even more urgent with the recent discovery by CeramPhysics that the C_p peaks are quite sensitive to the extent and type of doping (Lawless *et al.*, 1988). For example, the doping of ZnCr_2O_4 by even 2-3% of a non-magnetic impurity (such as Al_2O_3 , MoO_3 , or sulfur) causes a splitting of the C_p peak by up to 6 K (Lawless *et al.*, 1988). This effect has been confirmed by EPR and χ measurements (Dalal and Kahol, 1989; Dalal and DeLooze, 1989). In particular, EPR measurements have provided clear indications of some 'free' Cr^{3+} spins below the T_N of these materials (Dalal and coworkers, 1986-89). Moreover, the concentration of these 'free' Cr^{3+} spins was found to be higher in doped samples than in pure powders. These results were supported by dc susceptibility measurements on the same samples. On the other hand, theoretical (Monte Carlo) calculations by Patton and coworkers (Lin and Patton, 1986; Lu and Patton, 1986; Patton, Lin, and Lu, 1986) have indicated that the emergence of the free spins around the phase transitions of these materials is an inherent property of the spinel lattices. Discussions with Lawless, Clark, and their coworkers to the effect that C_p , χ , and EPR

measurements on single crystal samples could help provide clear-cut evidence for the role of lattice defects and impurities, and a sensitive check on theoretical models of the origin of the unusually high C_p values of these lattices provided the major impetus for the presently described single crystal growth endeavor.

Outline of Efforts in Single Crystal Growth

A. Initial Need of New Furnace

Efforts to synthesize single crystals of ZnCr_2O_4 along the lines of the work of Pajaczkowska and coworkers (Pajaczkowska, A. *et al.*, 1981) with the commercial high temperature furnace presently in our laboratory met with only limited success. Using high pressure, simultaneous halogen transport of Cr_2O_3 and ZnO with I_2 and Br_2 as described in our previous reports (Dalal and DeLooze, 1989), we continued to produce small granular structures with neither sufficient size nor orientable face to be experimentally useful. We feel that the cause of the failure lies in the lack of temperature control. Because of the large volume of our high temperature furnace, it is difficult to eliminate temperature fluctuations in the controlled slow cooling caused by the large 'dead volume' and latent thermal mass of the heating chamber. These temperature fluctuations in the furnace with the accompanying thermal gradients caused in the sample charge produce numerous small areas of crystal nucleation, with the result being a mass of fused microcrystals of little experimental use. Thus it was decided to design and construct a furnace with a better control of temperature, less 'dead volume'

(i.e., faster response to heater power), less thermal gradients, and sample mobility.

B. Furnace Design and Construction

To this end designs were drawn, taking into account the time and budgetary constraints, for a much-modified, conventional furnace. A modified Bridgman-Stockbarger (Mikkelsen, 1980) furnace was chosen. After the initial design of the system was approved by our machine shop engineers (e.g., Figures 26 and 27) and electronic technician (e.g., Figures 28 and 29), construction was begun. The furnace consists of two independently-controlled, nichrome resistance-heated Al_2O_3 tubular elements separated by a fused silica ring. In effect, the system is a large, vertical bore, two zone tube furnace with the heated fused silica ring in place to shape and control the gradients between the zones. The sample is moved between the two zones through the established temperature gradient by means of a stepping motor drive assembly and controller.

It was originally determined that the entire furnace, electronic as well as mechanical sub-assemblies, would be produced in our own shops; however, after giving due consideration to the time constraints for their construction and the need for immediate use and reliability with a minimum testing period, it was agreed upon that the electronic heater controls and heater elements should be produced by a commercial manufacturer. Four Lindbergh Model # 721410220AC elements encased in Carborundum Corp. FiberFrax[®] insulation with a dual aluminum sheath would make up

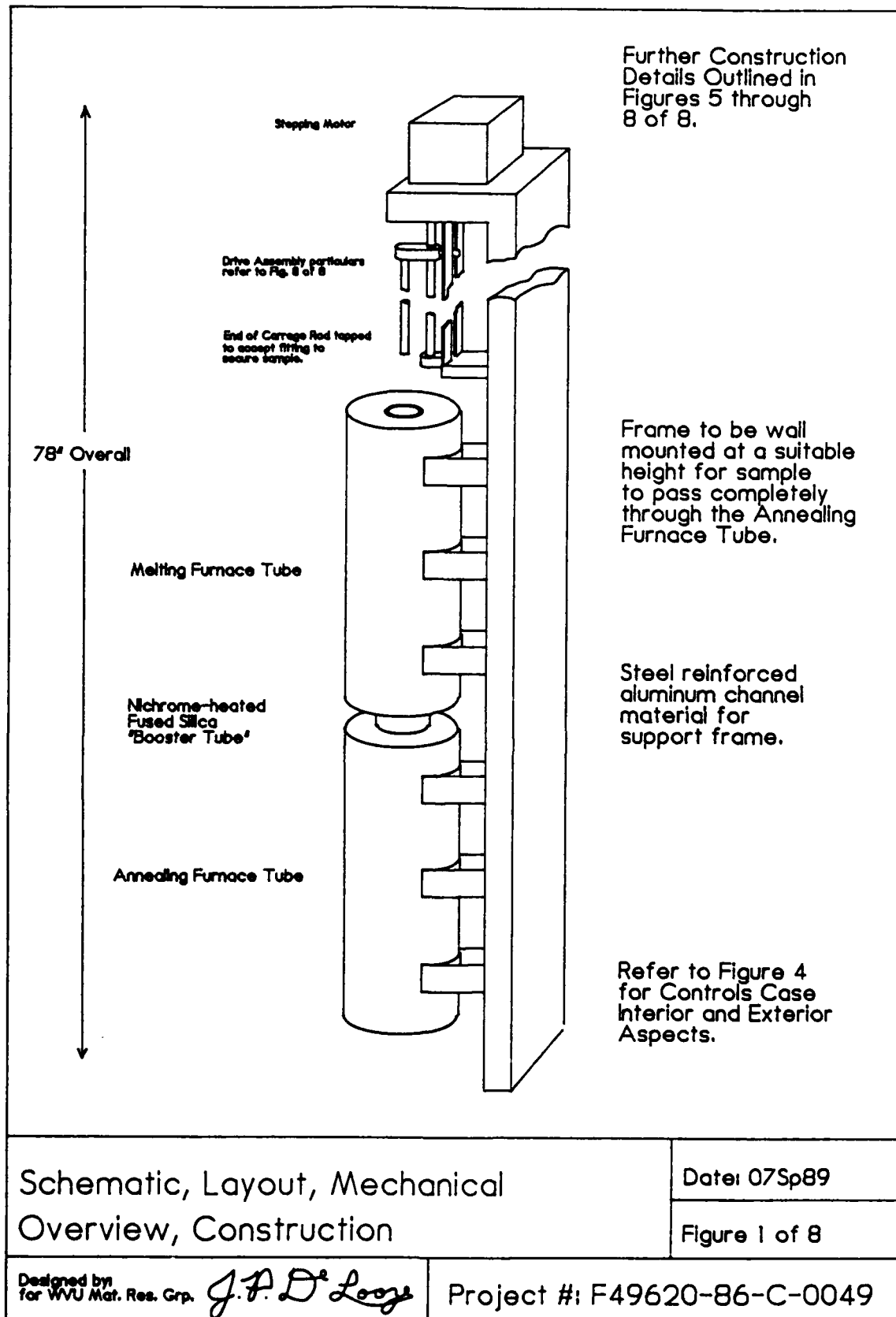


Figure 26. General overview of tube furnace construction. Drawing noted as Number 1 of 8.

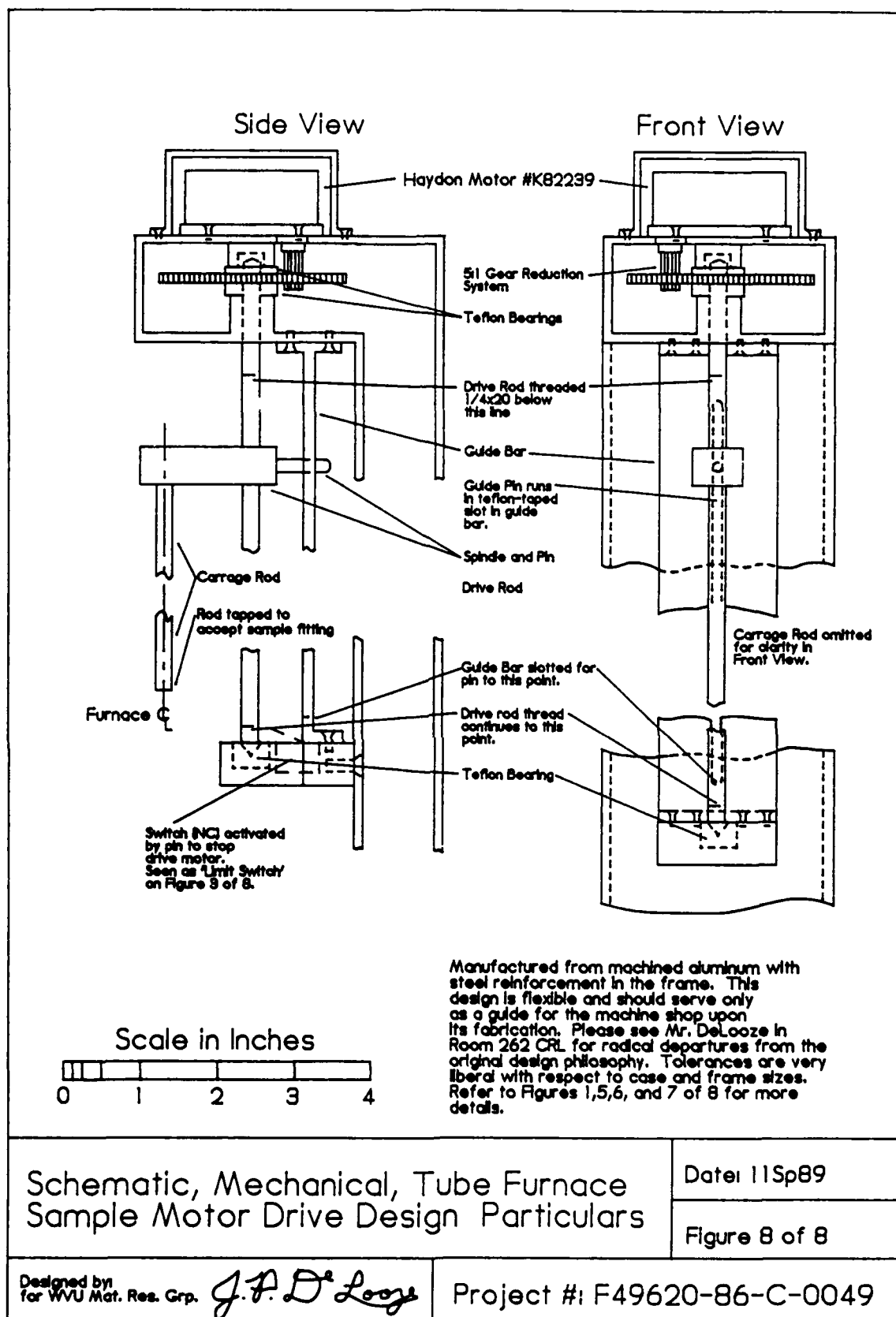
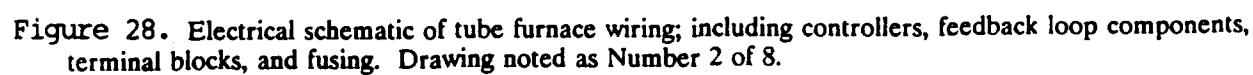


Figure 27. Sample motor drive design particulars providing general instruction and theory as to drive design.
Drawing noted as Number 8 of 8.



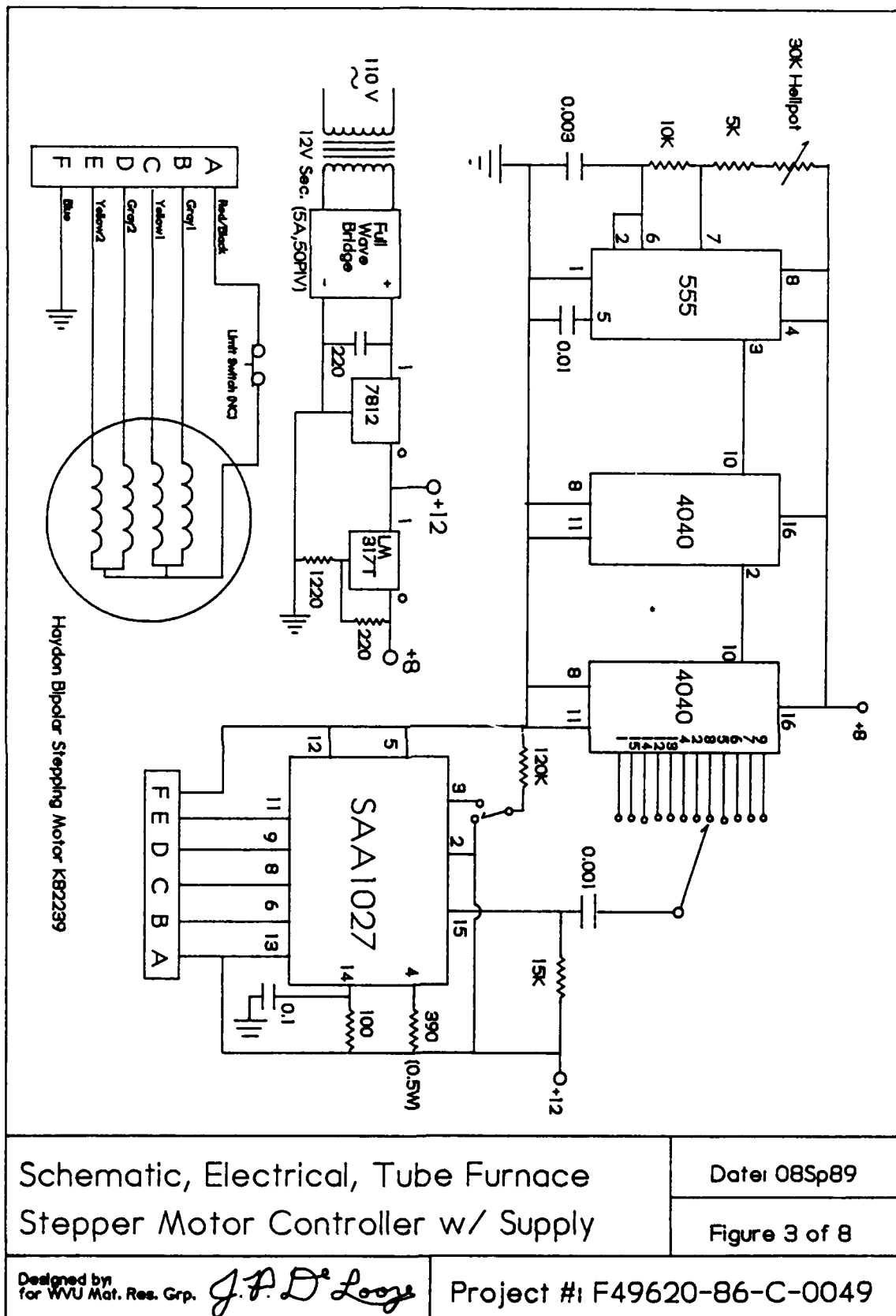


Figure 29. Electrical schematic of stepper motor controller, including power supply and motor wiring harness. Note from Figure 3 that the power supply is powered from TB1. Drawing noted as Number 3 of 8.

the two tube furnaces, providing a two inch diameter bore. Between the two furnace tubes is a 2" x 1" fused silica (or quartz) ring wrapped with 14ga nichrome (80/20) connected to a simple variac. This ring is designed to temper the transition from the melting tube (typically $1200^{\circ} \pm 50^{\circ} \text{ C}$) to the annealing tube (typically 800° C) and to insure uniformity in the melting tube profile. It, in conjunction with the stepping motor rate, also determines the speed and extent of the thermal gradient traversed in a given time by the sample and allows limited observation of the sample as it passes through the furnace.

Each furnace tube is connected to the line voltage by means of a KAX-25 cartridge fuse and a heavy-duty silicon gate relay (Omega SSR-240-D-25) actuated by 5V control pulses from the temperature controller. Each properly cooled solid state relay is designed to handle 25 amps of continuous load for 50,000,000 cycles. An Omega CN9121 temperature controller determines the duty cycle of the relay by means of a PID feedback loop formed by a K-type thermocouple imbedded in the tube wall at the center of each furnace section. Each furnace is independently controlled and is designed to shut down in the event of a sensor burnout or if a pre-set furnace over-temperature condition is reached.

The sample is lowered vertically through the tube via the gear, spindle, and drive rod assembly shown in **Figure 27**. A Haydon stepping motor (#K82239) operating through a one to five gear reduction system provides the torque to turn a $1/4 \times 20$ threaded rod between two teflon bearings. This rod, in turn, is threaded through a

spindle that carries the carriage rod on one end and a pin on the other. This pin rides in a teflon-taped guide bar that prevents the spindle from rotating with the drive rod. The system, therefore, converts high torque, rotary motion into very precise, well-regulated vertical displacement. The system exhibits no backlash and provides 1.25×10^{-4} inches of vertical displacement per step. The stepper motor controller (see Figure 29), the only electrical subassembly built in-house, is constructed around the SAA1027 Stepping Motor Controller integrated circuit. A LM-555 integrated circuit, configured as an 8-19 kHz variable frequency oscillator, is configured as a free-running astable multivibrator with the output being fed to two CD-4040 integrated circuits in series. The first CD-4040 operates in the divide by 64 (i.e., $\div 2^6$) mode, while the second CD-4040's division factor is determined by the SP12P switch, allowing division from 2^7 to 2^{18} of the original oscillators frequency. This allows as few as one step per half minute (2 days, 18.666 hours per linear inch) to as many as 150 steps per second (53 seconds per linear inch). The SAA1027 was ideal for our low-duty-cycle job as it provides the proper pulse sequence and timing to the motor without the need of additional current boosting transistors and allows for motor reversal as well.

During the initial testing of the furnace control system, however, an electrical short occurred. A short section of the upper heater experienced an current inrush of »25 amps before the KAX-25 fuse opened. This rapidly melted a portion of the upper heater assembly and ruined three of the heating elements. To date, we have not been able to secure the funding required to replace the three heating elements and their associated enclosures, because of the shortage of funds in the project. We thus decided

to investigate the possibility of improving our starting materials, with the hope of receiving some relief funding meanwhile.

C. Investigation of Chemical Routes to Spinel Synthesis

During the previous quarter, we outlined the production of finely-grained, low temperature-calcined ZnCr_2O_4 and CdCr_2O_4 powders by the application of chemical coprecipitation in a manner similar to members of the research initiative. We had hoped at that time that we could have utilized these powders to produce single crystal spinels using halogen transport of the finely divided solids themselves. This, however, was not the case. The same problems which plagued us during the halogen transport also prevents the use of the micro-crystalline solids.

At this point in the project, we began to investigate a new process with the hope that the single crystal spinels may be synthesized from a new type of starting material. In halogen transport, the sub-components of the system in the hot zone are dissolved in gaseous halogens and redeposited in a cooler zone due to the inherent heat of formation of the spinels in comparison with those of the gaseous complexes (Pajaczkowska, A. *et al.*, 1981). It is felt that perhaps lower temperature syntheses similar to those recently reported for perovskite-based single crystal ceramics (Murugaraj, Maier, and Rabenau, 1988-89) may be developed in which the spinel component precursors (*i.e.*, Cr_2O_3 and ZnO or CdO) are formed *in situ* from the thermal decomposition of Cr, Zn, or Cd compounds which contain oxygen bearing complex ions (*e.g.*, NO_3^- , CO_3^{2-} , $\text{C}_2\text{H}_3\text{O}_2^-$, *etc.*)

while in a molten, albeit evaporating, flux (*e.g.*, K_2CO_3).

References

- Lawless, W. N., Clark, C. F., and Munson, S. K., 1986a, "Magnetocaloric Measurements on CdCr_2O_4 , ZnCr_2O_4 , and MnNb_2O_6 Ceramics," Progress Report, AFOSR Contract No. F49620-86-C-0049, Research on High-Specific-Heat-Dielectrics, April 10, 1987.
- Lawless, W. N., and Clark, C. F., 1986, "Specific Heat and Dielectric Measurements on Compacted Disks of CdCr_2O_4 and ZnCr_2O_4 Spinel Powders," Interim Report, AFOSR Contract No. F49620-86-C-0049, Research on High-Specific-Heat-Dielectrics, April 10, 1987.
- Lawless, W. N., and Munson, S. K., 1987, "Thermodynamic Analysis of Magnetocaloric Data Measured on Compacted Disks of CdCr_2O_4 and ZnCr_2O_4 ," Interim Report, AFOSR Contract No. F49620-86-C-0049, Research on High-Specific-Heat-Dielectrics, January 9, 1987.
- Lawless, W. N., 1987a, "Analysis of Specific Heat Data Measured on Compacted Disks of CdCr_2O_4 and ZnCr_2O_4 ," Interim Report, AFOSR Contract No. F49620-86-C-0049, Research on High-Specific-Heat-Dielectrics, January 8, 1987.
- Lawless, W. N., and Hampton, S. K., 1988, "Broad-Range Specific Heat Measurements," Progress Report, AFOSR Contract No. F49620-86-C-0049, Research on High-Specific-Heat-Dielectrics, August 26, 1988.
- Kahol, P. K., Singh, K. and Dalal, N. S., 1986, "Magnetic Susceptibility and Resonance Studies," Progress Report, AFOSR Contract No. F49620-86-C-0049, Research on High-Specific-Heat-Dielectrics, September 30, 1986.
- Kahol, P. K. and Dalal, N. S., 1987, "Magnetic Susceptibility and Resonance Studies," Progress Report, AFOSR Contract No. F49620-86-C-0049, Research on High-Specific-Heat-Dielectrics, April 10, 1987.
- Dalal, N. S., and Kahol, P. K., 1989, "Magnetic Susceptibility and EPR Measurements: Direct Evidence for Free Spins," Progress Report, AFOSR Contract No. F49620-86-C-0049, Research on High-Specific-Heat-Dielectrics, May 8, 1989.
- Dalal, N. S., and DeLooze, J. P., 1989, "Magnetic Susceptibility Measurements and Crystal Growth Efforts," Quarterly Report, AFOSR Contract No. F49620-86-C-0049, Research on High-Specific-Heat-Dielectrics, September 27, 1989.
- Dalal, N. S., and DeLooze, J. P., 1989, "Comprehensive Magnetic Susceptibility and EPR Measurements on Pure, Doped, and Sulfur-exchanged ZnCr_2O_4 and CdCr_2O_4 ," Final Report, AFOSR Contract No. F49620-86-C-0049, Research on High-Specific-Heat-Dielectrics, December 22, 1989.

Lin, C., and Patton, B. R., 1986, "Spinel Studies IV. Ginzburg-Landau Theory of the Spinel Phase Transitions," Progress Report, AFOSR Contract No. F49620-86-C-0049, Research on High-Specific-Heat-Dielectrics, December 30, 1986.

Lu, Y., and Patton, B. R., 1986, "Spinel Studies III. Monte Carlo Studies on Undistorted Spinels," Progress Report, AFOSR Contract No. F49620-86-C-0049, Research on High-Specific-Heat-Dielectrics, December 15, 1986.

Patton, B. R., Lin, C. Y., and Lu, Y., 1986, "Spinel Studies II. Experimental Review and Theoretical Overview," Progress Report, AFOSR Contract No. F49620-86-C-0049, Research on High-Specific-Heat-Dielectrics, December 15, 1986.

Pajaczkowska, A., Piekarczyk, W., Peshev, P., and Toshev, A., *Mat. Res. Bull.* 16, 1091 (1981).

Mikkelsen, J. C., Jr., *Rev. Sci. Instrum.* 51, 1564 (1980).

Murugaraj, P., Maier, J., and Rabenau, A., *Solid State Commun.* 66, 735 (1988).

Murugaraj, P., Maier, J., and Rabenau, A., *Solid State Commun.* 71, 167 (1989).

IV. SPECIFIC HEAT STUDIES

Specific heat measurements at low temperatures reveal a rich spectrum of physical information, and these specific heat studies are described in this section. Specific heat measurements constitute the majority of the experimentation performed in this research program.

This Section is organized as follows: In Section IV.A. a broad-range (2 - 100 K) specific-heat measurement method is described, including thermometry calibrations. In Section IV.B. broad-range specific heat data on large variety of CdCr_2O_4 samples are reported -- doped and undoped ceramics and ceramic/glass composites, undoped ceramic/epoxy composites, and fine-grained powders. In Section IV.C. studies of latent heat phenomena are described, and in Section IV.D. a summary is given of the findings from all the thermal measurements in Section IV.

IV.A. Broad-Range (2 - 100 K) Specific Heat Metrology

We have been measuring specific heat for several years by the pulse-calorimetry method which is very labor-intensive at both the experimental level and the data-reduction level. Nonetheless, this method did lead to an apparent discovery at temperatures above the range of applicability (see below). Consequently, a decision was made to develop a broad-range calorimetry method that would take advantage of computer interfacing.

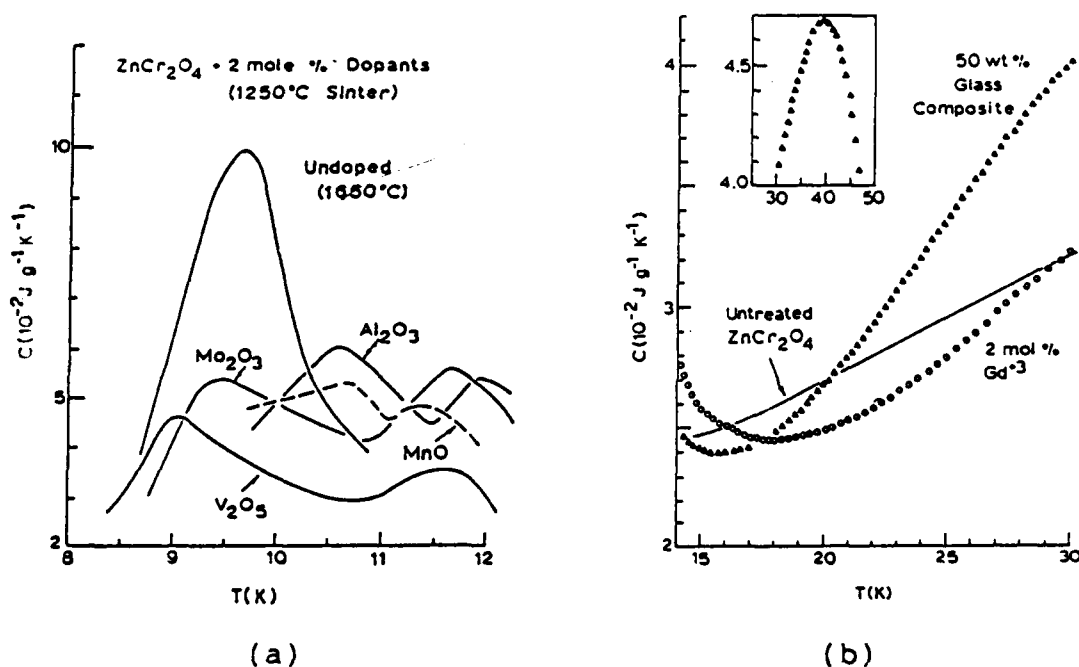


Figure 1. (a) Effect of 2 mole % dopants in ZnCr_2O_4 ; (b) Effect of stress in a composite of ZnCr_2O_4 and glass.

The discoveries found in the pulse method are illustrated in Fig. 1. The effects of dopants at the 2 mole % level in ZnCr_2O_4 are shown in Fig. 1(a) (Mo^{3+} , Al^{3+} , V^{5+} , Mn^{2+}), and in all cases the central maximum in the specific heat is split into two maxima. In contrast, for ZnCr_2O_4 in a 50/50 glass composite, a stress-induced maximum in the specific heat occurs at 39 K, inset in Fig. 1(b). Also shown in Fig. 1(b) are data for the Gd^{3+} -doped material above 15 K, and below 15 K this large-spin

dopant yields double maxima similar to those in Fig. 1(a).

It is immediately clear from Fig. 1 that basic discoveries are involved -- all dopants behave similarly, but the effect of (hydrostatic) stress is to induce a higher temperature transition.

It is also clear from Fig. 1 that specific heat measurements over a broader temperature range are required. In fact, the data in Fig 1(b) cannot be considered reliable above ~ 25 K due to addenda and thermometry calibrations.

In what follows, we describe the specific heat methodology developed for the temperature range up to about 80 K. This methodology consists of several parts: (1) Theory of the method; (2) Thermal link calibration; (3) Addenda; (4) Thermometry calibrations; (5) Thermal time constants; (6) Data smoothing; (7) Experimental techniques; and (8) Calibrations and Scaling.

Theory of the Method

A calibrated-link method is chosen, as illustrated in Fig. 2. The basic concept here is that if the sample (1) and reservoir (6) are at different temperatures, then the sample temperature will approach the reservoir temperature in a specific fashion which, when measured, will yield the specific heat.

A thermometer (2) is thermally anchored to the sample, as are the thermometer leads (7), and the sample is suspended from the reservoir by two links -- a mechanical-support link (4) and a thermal link (5), both of which are attached to a pin (3) embedded in the reservoir. This latter thermal link is the key to the method because it is through this link that the sample primarily exchanges energy with the reservoir.

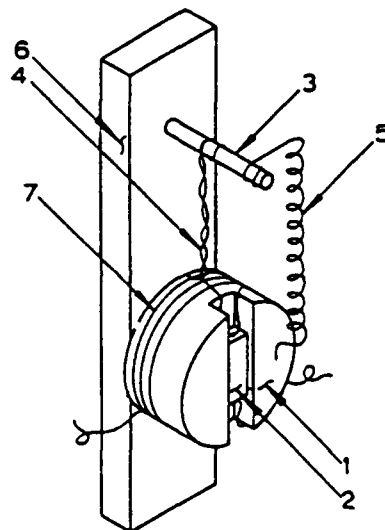


Figure 2. Schematic illustration of the calibrated-link method.

For good thermal anchoring, copper wire is attached to the thermometer (2) and heat sunk on the periphery of the sample (7). However, these copper thermometer leads cannot be used as hookup leads because they would constitute a strong thermal link (i.e., the pin connections in the calorimeter are approximately at the reservoir temperature). Consequently, fine manganin wires (0.004-cm diam) are used as hookup leads between the sample and the pin connections.

We begin with the energy-balance condition between the sample and the reservoir,

$$C_t(dT/dt) = -\int_{T_r}^T (KA/l)dT - A_r(T^4 - T_r^4) \quad (1)$$

where T and T_r are the sample and reservoir temperatures, respectively, C_t is the total heat capacity of the sample, K is the thermal conductivity of the copper link wire, and A/l is the area-to-length ratio of the wire. The A_r -coefficient is the radiation constant involving the emissivities of the sample and the reservoir. The meaning of Eq. (1) is that if $T > T_r$ the sample loses heat energy to the reservoir by thermal conduction and by radiation and $dT/dt < 0$. Convective heat losses are negligible because the experiment is carried out in a hard vacuum.

To implement Eq.(1), we first note that C_t is made up of two parts,

$$C_t = mC + \sum m_j C_j \quad (2)$$

where m and C are the mass and specific heat of the sample and the m_j and C_j are the addenda contributions. Next, we expand the product KA in a power series in temperature,

$$KA = \sum \beta_n T^n, \quad (3)$$

and substituting in Eq.(1) we have the final result,

$$(mC + \sum m_j C_j) l(dT/dt) = -\sum \beta_n (T^{n+1} - T_r^{n+1}) / (n+1) - A_r(T^4 - T_r^4) \quad (4)$$

The quantity of interest is the specific heat C in Eq.(4), and Eq.(4) shows that measurements of T , T_r , and dT/dt will yield C provided the $m_j C_j$, ℓ , A_r , and the β_n 's are known.

The length ℓ entering Eq.(4) is, of course, the length of the copper link (5) shown in Fig. 2, and Eq.(4) shows that adjusting this length will determine the overall cooldown time (thus, this wire is shown coiled in Fig. 2 to gain additional length). A subtlety enters here in that the manganin support link, (4) in Fig. 2, cannot contribute significantly to the heat exchange between the sample and the reservoir, and this condition will be met provided $\ell(\text{manganin}) > 0.1 \ell(\text{copper})$.

Thermal Link Calibration

The formalism above shows that the β_n -coefficients in Eqs.(3) and (4) calibrate the copper thermal-link wire, and this calibration is the heart of the method.

To calibrate the wire, the thermal conductivity was measured by the two-thermometer, linear-flow method on ten-strand bundles of the wire in different runs over different temperature ranges. The composite of all these data are shown in Fig. 3 where the product KA is plotted vs. temperature.

The KA -data were fitted to Eq.(3), and a sixth-order expansion gave the best fit; this fit is shown in Fig. 3. The coefficients are, for KA in units of $W \text{ cm K}^{-1}$:

$$\begin{aligned} \beta_0 &= -2.1620 \times 10^{-5} & \beta_4 &= 7.5361 \times 10^{-9} \\ \beta_1 &= 3.3477 \times 10^{-5} & \beta_5 &= -8.1509 \times 10^{-11} \\ \beta_2 &= 3.9112 \times 10^{-6} & \beta_6 &= 3.2590 \times 10^{-13} \\ \beta_3 &= -3.0167 \times 10^{-7} & & \end{aligned} \quad (5)$$

In the temperature range 4-80 K, this sixth-order fit describes the experimental data to within $\pm 5\%$.

Addenda

The addenda entering Eq.(4) as $m_j C_j$ are due to the thermometer, wires, etc. directly attached to the sample in Fig.

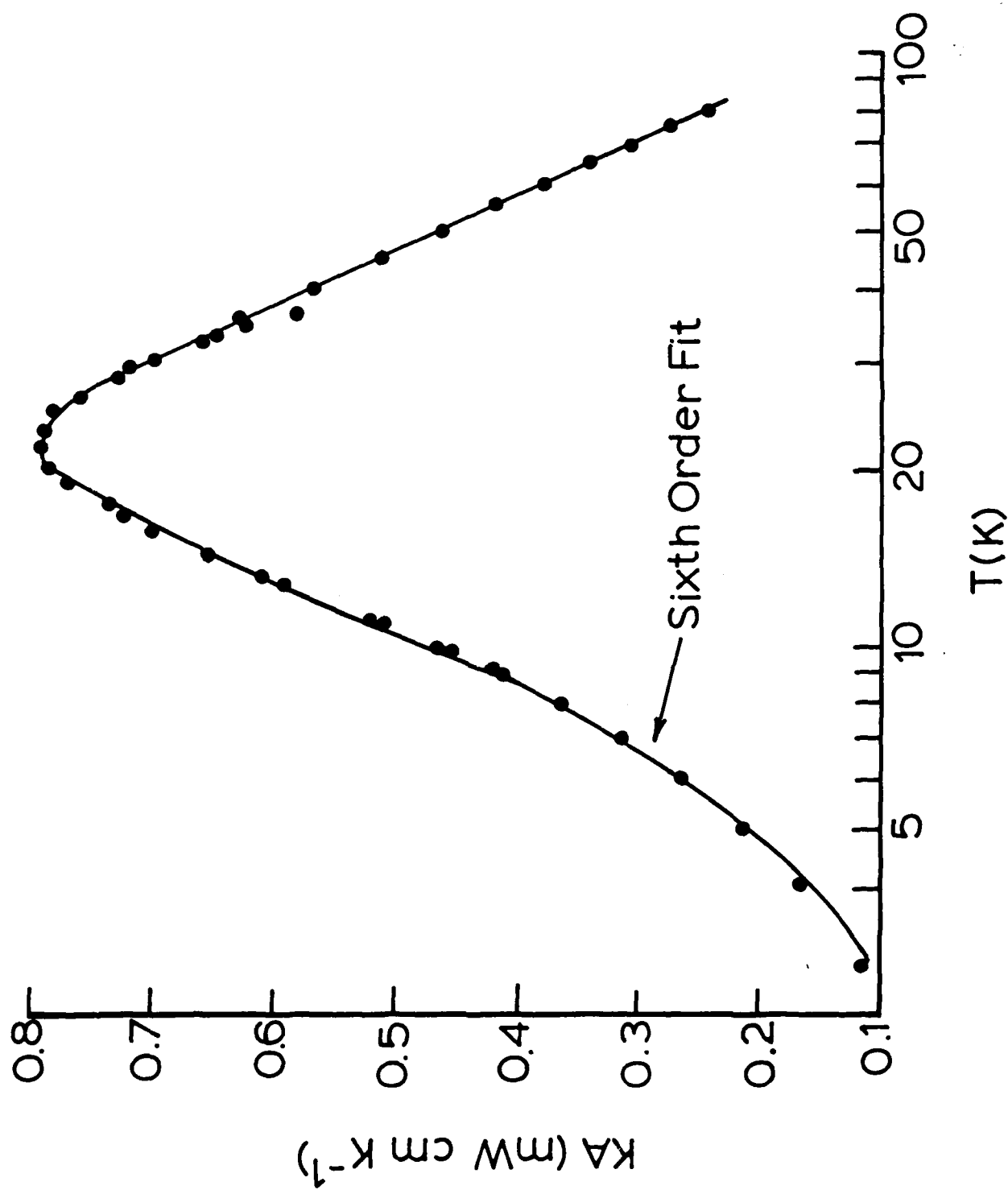


FIGURE 3

2, and the heat capacities of these components are the addenda correction.

A subtlety enters these correction terms regarding the wires running from the sample to the reservoir, for example, the copper link (5) in Fig. 2. It can be shown that one-half the mass of such wires constitute an addenda correction; consequently, the lengths of all such wires must be measured.

Four materials are involved in fixturing the samples for this method: (1) The copper in the thermometer pins, thermal link, and thermometer leads; (2) The carbon in the thermometer; (3) The G.E. 7031 varnish used to attach components to the sample; and (4) The insulated manganin wires used for the mechanical support link and for the thermometer leads between the sample and the pin connections. The individual masses m_j of these components are determined by cumulative weighings, and below we consider individually the specific heats C_j .

Copper. The NBS Tables were analyzed below 15 K and yield, in units of $J g^{-1} K^{-1}$,

$$T < 15 K: C_{\text{copper}} = (108.1T + 7.46T^3) \times 10^{-7} \quad (6)$$

Above 15 K the NBS Table is reproduced here in Table I.

The rationale for dividing these copper data into regions above and below 15 K is as follows: First, C changes very rapidly below 15 K, and the fitting equation, Eq.(6), gives a more accurate description than a table interpolation; and second, from Table I $\log C$ changes relatively slowly with T above 15 K, and the expansion

$$T > 15 K: \log C = \sum a_n T^n \quad (7)$$

gives an excellent sixth-order fit to the Table I data.

Table I

Specific Heat of Copper^(a)

<u>T(K)</u>	<u>C(J g⁻¹ K⁻¹)</u>
15	2.679x10 ⁻³
20	7.691
25	1.600x10 ⁻²
30	2.698
40	5.998
50	9.908
60	1.370x10 ⁻¹
70	1.730
80	2.050
90	2.320
100	2.540

(a) NBS Tables

Consequently, all the addenda terms are calculated according to this rational: Fitting equations at the lower temperatures, and Eq.(7)-type fits to table data at the higher temperatures.

Graphite. Following along the above lines for copper, we find, in units of J g⁻¹ K⁻¹,

$$T < 4 \text{ K: } C_{\text{graph}} = (60T + 18.75T^3) \times 10^{-7}$$

$$4 < T < 10 \text{ K: } C_{\text{graph}} = (208T + 9.5T^3 - 0.0018T^5) \times 10^{-7} \quad (8)$$

$$T > 10 \text{ K: } \log C_{\text{graph}} = \sum a_n T^n,$$

where the latter expansion fits the Table II data.

Table II
Specific Heat of Graphite^(a)

T(K)	C(J g ⁻¹ K ⁻¹)
10	1.140x10 ⁻³
15	3.304
20	6.295
25	1.030x10 ⁻²
30	1.549
40	2.698
50	4.198
60	5.794
70	7.691
80	9.705
90	1.180x10 ⁻¹
100	1.400

(a) NBS Tables

G.E. 7031 Varnish. A composite of literature data on the 7031 varnish yielded the following, in units of J g⁻¹ K⁻¹,

$$T < 4.5 \text{ K: } C_{7031} = [308T^3(1+0.0584T^2e^{-T/18})] \times 10^{-7},$$

$$4.5 < T < 7.6 \text{ K: } C_{7031} = [291T^3(1+0.0619T^2e^{-T/18})] \times 10^{-7}, \quad (9)$$

$$7.6 < T < 10 \text{ K: } C_{7031} = [309T^3e^{-(T-7.6)/11.5}] \times 10^{-7},$$

$$T > 10 \text{ K: } \log C_{7031} = \sum a_n T^n,$$

where the latter expansion fits the Table III data.

Table III

Specific Heat of G.E. 7031 Varnish ^(a)	
T(K)	C(J g ⁻¹ K ⁻¹)
10.63	2.844x10 ⁻²
13.44	4.276
15.39	5.129
16.90	6.180
22.62	9.750
24.58	1.103x10 ⁻¹
32.30	1.593
37.08	1.959
46.13	2.564
53.93	3.057
61.10	3.959
69.23	4.600
82.63	5.373

(a) Composite literature data

Manganin Wire. The specific heat of insulated manganin wire presents a complicating feature in that the organic insulation contributes a substantial portion of the specific heat. This is illustrated by the literature data reproduced in Fig. 4 where it is seen that the wire data exceeds the alloy data.

We have taken the following approach to this problem: First, we assume that the insulation can be taken as G.E. 7031 varnish; and second, we assume that the thickness of the insulation is a constant fraction of the total wire diameter.

The literature data in Fig. 4 were analyzed according to these

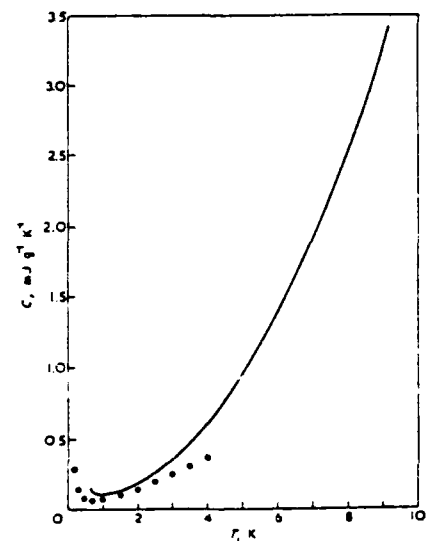


Figure 4. Specific heat of manganin alloy (circles) and manganin wire (solid curve).

assumptions, and it was found that these data could be accurately described using the 7031-varnish specific heat data above. The fitting results when coupled with the second assumption indicate that

$$\begin{aligned} m(\text{manganin alloy}) &= 0.956 m(\text{wire}) \\ m(7031) &= 0.0445 m(\text{wire}), \end{aligned} \tag{10}$$

independent of the wire diameter. Therefore, knowing the mass of the manganin wire, Eqs.(10) are used to determine the masses of the manganin alloy and effective 7031 varnish on the wire, and, of course, this 7031 component is added to the 7031 content determined by cumulative weighings.

For the manganin alloy, the literature data yield, in units of $\text{J g}^{-1} \text{K}^{-1}$,

$$\begin{aligned} T < 9 \text{ K}: \quad C_{\text{MA}} &= (595T + 29.4T^3) \times 10^{-7} \\ T > 9 \text{ K}: \quad \log C_{\text{MA}} &= \sum a_n T^n, \end{aligned} \tag{11}$$

where the latter expansion fits the Table IV data.

Table IV

Specific Heat of Manganin Alloy^(a)

T(K)	C(J g ⁻¹ K ⁻¹)
8	1.982x10 ⁻³
10	3.540
15	1.081x10 ⁻²
20	2.438
25	4.477
30	7.047
35	9.908
40	1.280x10 ⁻¹
45	1.558
50	1.817
55	2.049
60	2.255
65	2.437
70	2.598
80	2.867
90	3.074
100	3.234

(a) Composite literature data

Thermometry Calibrations

The thermometer attached to the sample, (?) in Fig. 2, has to meet three requirements: (1) Good sensitivity, 4-80 K; (2) Small and quantifiable addendum; and (3) Reliable calibration, 4-80 K. The second requirement eliminates commercially available thermometers (which are also very expensive.).

It is desirable to have inexpensive thermometers due to breakage, and we have selected 1 k Ω , BB, Allen Bradley resistors which easily satisfy the first and second requirements above. These resistors are small (~ 15 mg), inexpensive, and easily available.

It is well known, however, that these resistors do not retain a reliable calibration from run to run, thus necessitating an in situ calibration for each run. This presents a major

problem because the thermal link length, l in Eq. (4), is designed to yield slow drift rates, $dT/dt \sim 10$ mK/s (for thermal equilibration reasons, see below), and this means that long times are required for the sample to come to equilibrium with the reservoir. Consequently, the number of calibration points that can practically be measured is severely restricted.

We have conducted a systematic study of calibrating these 1 k Ω resistors, as described below.

Calibrations, 4-80 K. The first step in this study was to measure R-T calibration data, 4-80 K, on ten randomly selected 1 k Ω resistors. The resistors were color-coded for convenience and tempered by repeated dippings in liquid nitrogen. Calibration data were measured in a helium cryostat on the resistors by four-lead potentiometric methods against a calibrated Ge thermometer. Data were measured at 1 K intervals up to 10 K, 2 K intervals up to 25 K, and 5 K intervals above 25 K. A typical R-T calibration is shown in Fig. 5.

Various expansions of $\log R$ in $\log T$, $\log R$ in T , etc. were used to fit the calibration data, and satisfactory fits could be obtained in some cases. However, the number of coefficients involved (>8) proscribed a convenient in situ calibration procedure because of the number of calibration points required.

An alternate approach was attempted; namely, to begin with a simple fitting equation and to study successive approximations to this equation.

The simple, widely-used functional was adopted,

$$\log R = A + BT^{-P}, \quad (12)$$

and for the resistors the following scheme was employed: (1) An overall fit to Eq. (12) was obtained to determine A, B, and P; and (2) Using two of the fitted coefficients, the temperature dependence of the third coefficient was determined using the measured R-T data set in Eq. (12).

The typical T-dependence of the A-coefficient is shown in the inset of Fig. 5, and the B- and P- coefficients display

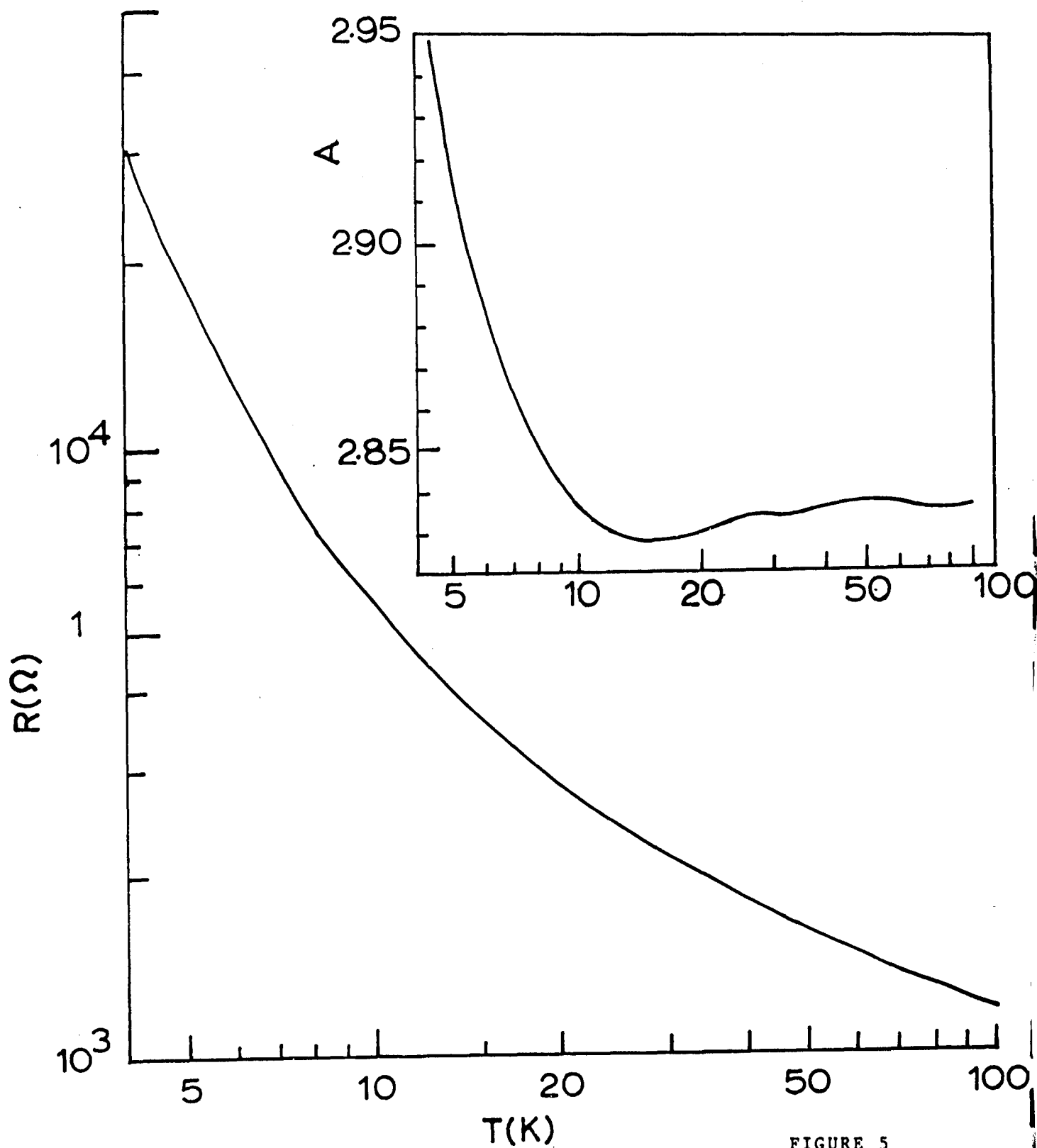


FIGURE 5

similar dependences (inverted in the case of the latter coefficient). In all cases, the coefficients appear constant above 25 K (a small, positive temperature dependence for A is suggested in the inset of Fig. 5, but this is specific to the resistor chosen in this example--other resistors appeared to have a small negative dependence or none at all).

We therefore look for a correction to Eq. (12) below 25 K, and for the first approximation we write

$$\log R = (\langle A \rangle + BT^{-P}) [1 + f(T)], \quad (13)$$

where $\langle A \rangle$ is the mean value of A in the 25-80 K range. Data for $f(T)$ are easily generated for an R-T data set, and typical $f(T)$ -data are shown in Fig. 6.

The $f(T)$ data have three characteristics: (1) $f=0$ at 10 K; (2) f has a minimum at about 15 K; and (3) $f \rightarrow 0$ at large T-values. The simplest function that satisfies these conditions is

$$f = \alpha/T^{n+1} - \beta/T^n, \quad (14)$$

where the condition that the exponents vary by unity insures a single-valued minimum.

Fitting studies of Eq. (14) showed that excellent fits up to about 15 K were obtained with $n=1$ for which $T^2 f = \alpha - \beta T$. A typical plot of $T^2 f$ vs. T is shown in the inset of Fig. 6.

Although Eq. (14) fits the $f(T)$ data very well up to about 15 K, this first approximation approaches zero very slowly with increasing temperature as shown by the dashed curve in Fig. 6. We therefore look for a second approximation above 15 K, $g(T)$, by writing

$$\log R = (\langle A \rangle + BT^{-P}) [1 + f(T) + g(T)], \quad (15)$$

and typical $g(T)$ -data above 15 K are shown in the inset of Fig. 6. A linear dependence is seen, $g \propto T$, and g approaches zero in the neighborhood of 16 K.

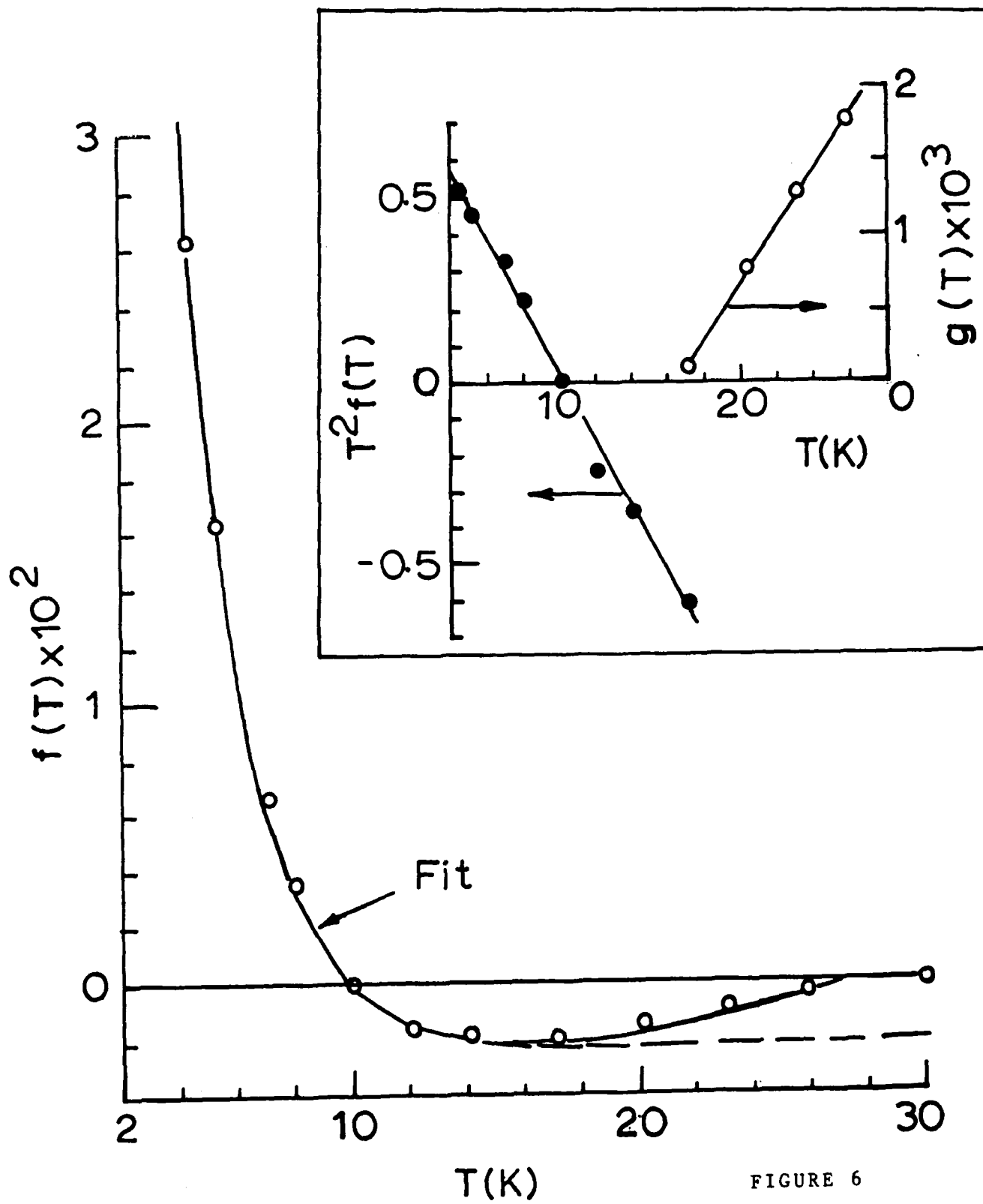


FIGURE 6

We note that $f(T)$ given by Eq. (14) has a minimum at

$$T_{\min} = 2\alpha/\beta, \quad (16)$$

and it is natural to select T_{\min} as the temperature below which $g=0$. Consequently,

$$g(T) = \gamma(T - T_{\min}), \quad T_{\min} \leq T < 25 \text{ K}. \quad (17)$$

As a final condition we require that the two successive approximations given by Eq. (15) be zero at 25 K, from which we obtain the relation for γ ,

$$\gamma = (\beta/25 - \alpha/625)/(25 - T_{\min}) \quad (18)$$

using Eq. (17) in Eq. (15).

Collecting, we have the final result,

$$\log R = (\langle A \rangle + BT^{-P}) [1 + \alpha/T^2 - \beta/T + \gamma(T - T_{\min})] \quad (19)$$

where:

$$\begin{aligned} T > 25 \text{ K}, \quad \alpha = \beta = \gamma = 0 \\ T_{\min} \leq T < 25 \text{ K}, \quad \alpha \neq \beta \neq \gamma \neq 0 \\ T < T_{\min}, \quad \alpha \neq \beta \neq 0, \quad \gamma = 0 \end{aligned} \quad (20)$$

Equation (19) involves seven coefficients, but we note that in principle only three calibration points are required to determine $\langle A \rangle$, B , and P because the remaining coefficients follow as successive correction terms.

We now examine how accurately Eqs. (19) and (20) describe the measured R - T calibration data for the ten resistors, and the first step is to study the minimum number of calibration points required. The cryogenic boiling points at 4.2 and 77 K are natural calibration points, and at least one point is required in the range 4.2-15 K to determine α and β . Arbitrarily selecting 12 K as the third calibration point and applying Eqs. (19) and (20) with $\langle A \rangle$ being the value of A at 77 K, we find that the

resulting $\Delta T/T$ -values range up to 6% (here ΔT is the difference between the measured and predicted temperature).

The reason this three-point procedure works poorly is because the constancy of the A-, B-, and P-coefficients in the 25-80 K range is not adequately represented. Consequently, we next examine a four-point procedure where the calibration point at 25 K is included. Again the point of 12 K is used, and $\langle A \rangle$ is the average of the A-values at 25 and 77 K. Applying Eqs. (19) and (20) to the R-T data sets for the ten resistors, we find the composite $\Delta T/T$ -data shown in Fig. 7. An excellent overall fit is obtained from this four-point procedure, as seen in Fig. 7, with $\Delta T/T < 0.5\%$ up to 30 K and $\Delta T/T < 1.7\%$ above 30 K. The mean value of $\Delta T/T$ from the fits shown in Fig. 7 is 0.51%.

The calibration point at 12 K has been chosen arbitrarily in the above studies, and we now examine this selection. Calibration points at 8, 10, and 12 K were selected (keeping the same points at 4.2, 25, and 77 K), and the resulting mean $\Delta T/T$ values were 0.46, 0.48, and 0.51%, respectively. This variation is not statistically meaningful, and the clear conclusion is that any convenient point in the 8-12 K range will suffice.

We observed an interesting consistency in T_{\min} as given by Eq. (16) in the course of examining these ten resistors. Namely, $T_{\min} = 13.867 \pm 0.122$ K when the 12 K point is used. When calibration points at 8 and 10 K are employed, $T_{\min} = 11.98$ and 13.16 K, respectively. These results favor the use of the 12 K calibration point to give the broadest range fit to the first approximation, Eq. (13).

Finally, we can identify a third successive approximation from the $\Delta T/T$ -data in Fig. 7. Namely, $\Delta T/T$ for all resistors has a bell-shaped maximum near 50 K which can be approximated by

$$\Delta T/T = 0.0165 \exp[-5.3 \times 10^{-3} (T-45)^2] \quad (21)$$

Equation (21) was obtained by a visual fit and is shown plotted

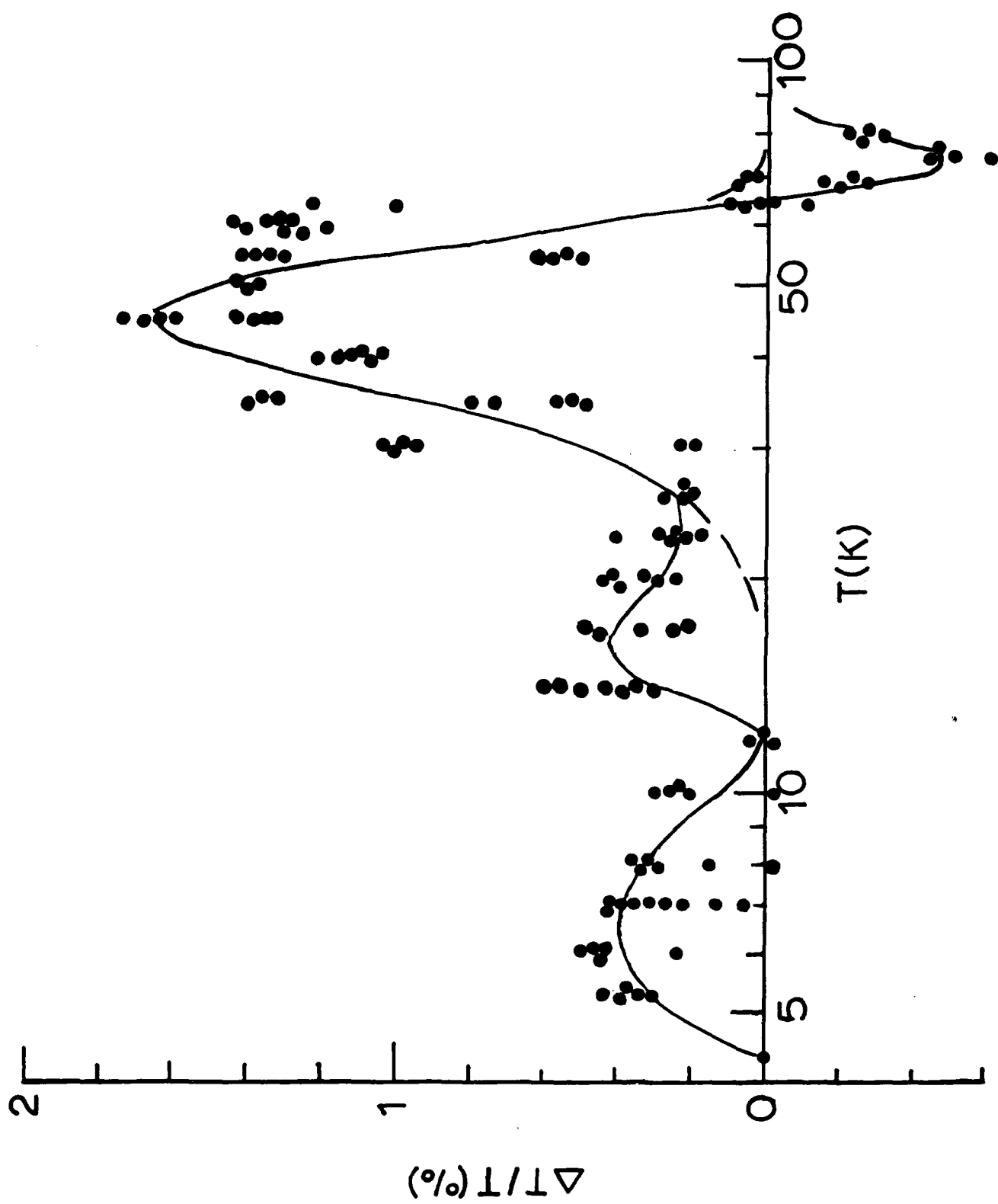


FIGURE 7

in Fig. 7 [note that Eq.(21) rapidly damps below 20 K and above 70 K].

We summarize this thermometer calibration procedure, as follows:

1. Calibration points are measured in situ at 4.2, 12, 25, and 77 K and fitted to Eq. (12).
2. The B- and P- coefficients are retained from the fit to Eq. (12), and $\langle A \rangle$ is taken as the average value of A at 25 and 77 K from Eq. (12).
3. Using $\langle A \rangle$, B, and P and the points at 4.2 and 12 K, the coefficients α and β are determined from Eqs. (13) and (14) with $n=1$, and T_{\min} is found from Eq. (16).
4. The coefficient γ is found from Eq. (18), and Eq. (19) is inverted to find T_{pred} according to the temperature ranges given in Eq. (20).
5. Finally, Eq. (21) is employed

$$T = T_{\text{pred}} \{1 + 0.0165 \exp[-5.3 \times 10^{-3} (T - 45)^2]\} \quad (22)$$

Except for the 55-65 K range, this four-point calibration procedure for tempered 1 k Ω Allen-Bradley resistors yields $\Delta T/T \leq 0.5\%$. In the 55-66 K range, $\Delta T/T \leq 0.8\%$, as may be judged from Fig. 7.

To put these results in perspective, we point out that in the case of commercially available calibrated Ge thermometers, $\Delta T/T \leq 0.1\%$ in the 42-100 K range.

Although the above procedure yields a reliable temperature calibration from four measured R-T points, the question of the derivative $d \log R / dT$ deserves special consideration because in the drift specific heat method we are interested in the temperature difference ΔT between adjacent points. Stated differently, the calibration procedure, Eqs. (19)-(21) above, introduces discontinuities in the derivative $d \log R / dt$ at 25 K and at T_{\min} .

To judge the gravity of these discontinuities, a pragmatic approach was adopted: A calculated R-t record was generated in the 10-30 K range using typical values for $\langle A \rangle$, B, etc., and the

software incorporating Eqs. (19)-(21) was used to compute a hypothetical specific heat-temperature record. These C-T data are shown in Fig. 8, and we note that the record is smooth through the break points at 25 K and T_{\min} , as shown. A data-smoothing routine discussed below has been employed here, but we point out that this routine will not smooth a substantial discontinuity in the time-temperature record.

Therefore, since the Fig. 8 data show that a smooth R-t record leads to a smooth C-T record, we conclude that special precautions regarding the discontinuities at 25 K and at T_{\min} are not warranted.

Calibration Method. The discussion above shows that four calibration points are involved -- 4.2, 12, 25, and 77.4 K. The latter point is easily obtained after an overnight cooldown in liquid nitrogen. However, the remaining points can be tedious due to the long-time-constant thermal link. We describe here a convenient method for taking these calibration points.

First, if the sample temperature T and reservoir temperature T_r differ by a small amount, then T will exponentially decay to T_r according to

$$T(t) - T_r = (T_0 - T_r)e^{-t/\tau} \quad (23)$$

where T_0 is the sample temperature at $t=0$. Note that $T=T_r$ is the calibration condition because T_r is determined from a calibrated Ge thermometer embedded in the temperature-controlled reservoir. This exponential-decay relation Eq.(23) shows that it is tedious to achieve calibration for long time constants, τ .

We now prove that if T_0 and T_r are not much different, Eq.(23) can be written in terms of the thermometer resistance R which is the measured quantity in the calibration procedure. At $t > 0$, let $R_0 + r$ be the resistance and $T_0 + \theta$ be the temperature. Substituting in Eq.(12)

$$\log (R_0 + r) = A + B (T_0 + \theta)^{-P},$$

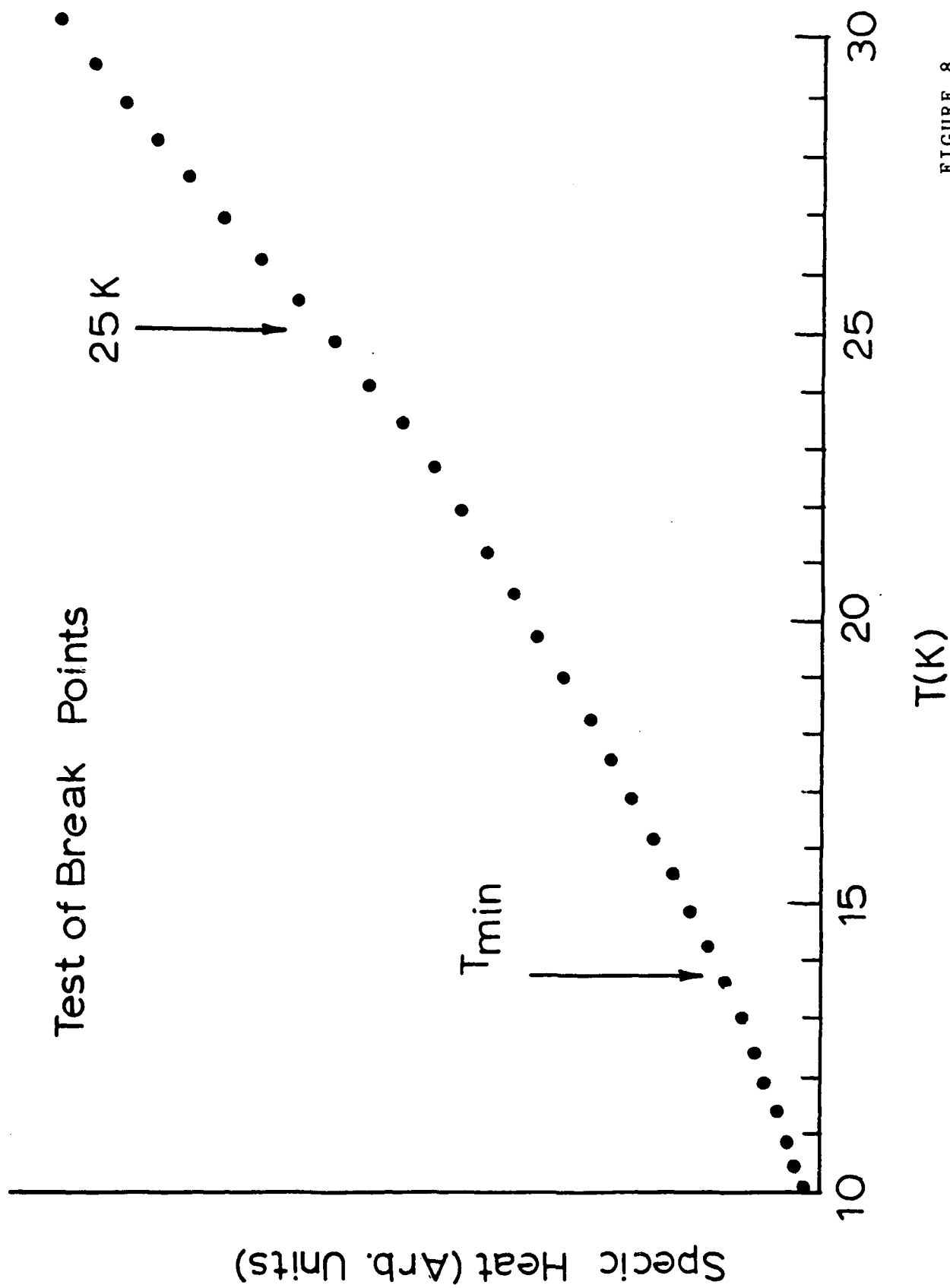


FIGURE 8

and employing Taylor expansions in the small quantities r/R_0 and θ/T_0 , we have

$$r = -(R_0 B P T_0^{-P-1}) \theta \propto \theta. \quad (24)$$

We have used Eq.(12) for convenience to show that $r \propto \theta$, but any R-T functional can be used to obtain this result.

Since the time $t = 0$ is arbitrary, we can write $T(t) = T_0 + \theta(t)$, and substituting in Eq.(23) we have

$$\theta(t) - \theta_\infty = (\theta_0 - \theta_\infty) e^{-t/\tau},$$

or, making use of Eq.(24),

$$r(t) - r_\infty = (r_0 - r_\infty) e^{-t/\tau}.$$

Finally, since $r(t) = R(t) - R_0$, we have the desired result,

$$R(t) - R_\infty = (R_0 - R_\infty) e^{-t/\tau}. \quad (25)$$

On comparing Eqs.(23) and (25) it is clear that R_∞ is the resistance of the thermometer at $t \rightarrow \infty$ when $T = T_r$ -- i.e., the calibration condition.

Consequently, the following calibration scheme is suggested: First, the sample temperature is brought very close to the reservoir temperature, $T \approx T_r$. Next, the reservoir is temperature-controlled to maintain T_r constant, and an $R(t)$ data record is measured where the interval between points is ~ 1 min. Finally, this record is curve-fitted to Eq.(25) to determine R_∞ and T_r is determined from the Ge thermometer.

Thermal Time Constants

The drift method here involves the time constant within the sample, and the longer is this thermal time constant, the slower must be the drift rate to maintain thermal equilibrium. In this section we will estimate this thermal time constant which, in

turn, will set upper bounds on the drift rate.

For thermal equilibration within the sample, the time constant is given by

$$\tau = d^2 \rho C / \pi^2 K \quad (26)$$

where ρ is the density of the ceramic sample, and d is a characteristic dimension (i.e., half thickness). This time constant translates into a temperature uncertainty δT given by

$$\delta T = (dT/dt) \tau. \quad (27)$$

For the materials of interest, $C \sim 0.3 \text{ J g}^{-1} \text{ K}^{-1}$, $\rho \sim 4 \text{ g/cm}^3$, and $K \sim 0.01 \text{ W cm}^{-1} \text{ K}^{-1}$. If we restrict $\delta T \sim 10 \text{ mK}$ in Eq.(27) for $dT/dt \sim 10 \text{ mK/s}$, then we find from Eq.(26) that $d \sim 3 \text{ mm}$, which experimentally is an achievable half thickness.

Consequently, thermal time constants here do not appear problematic. We remark that the use of copper foil or wires inside the sample can be used to improve thermal equilibration (see below).

A potentially worrisome condition arises when the specific heat C in Eq.(26) goes through a maximum. However, from Eq.(4), $dT/dt \propto C^{-1}$, so in this case the drift rate slows considerably. Going further, on combining Eqs.(26) and (27), the specific heat cancels.

Data Smoothing

The implementation of this method involves measuring the R - t record of the thermometer on the sample and the R_{Ge} - t record of the calibrated Ge thermometer embedded in the reservoir. These records are then converted to T - t and T_r - t records for solving Eq.(4) using the calibration procedures described above.

The primary measurement is that of resistance at specified intervals Δt using computer-interface methods. Due to electrical noise even in shielded cables within a screen room there is an unavoidable noise δR in a resistance measurement which translates

into a temperature noise δT . For a very slow drift and/or a small Δt , two subsequent T's may be sufficiently close (e.g., $\Delta T \sim 10$ mK) that the associated δT 's (e.g., $\delta T \sim 3$ mK) cause a significant scatter ($\sim \pm 10$ -20%) in dT/dt and hence also in the specific heat record.

A simple smoothing scheme has been developed based on the observation that over narrow regions (e.g., 10 points) the T-t record is linear. The method here consists of least-squares fitting the T-t record over the range of four points before to four points after the point in question, and then forming dT/dt from this fitting. Each point in the T-t record is handled in this fashion (except, of course, the first four and last four points). Because Δt is constant, this linearization method by least-squares fitting yields,

$$dT/dt = -(1/60 \Delta t) \sum_{m=n-4}^{n+4} (4-m) T_{m+n-4} \quad (28)$$

where n is the index number of the point in question and m is the summation index.

As an example of this method, a non-smoothed specific heat record contained a scatter $\delta C < \pm 12\%$ between adjacent points; smoothing by this linearization method reduced the scatter to $\delta C < \pm 1\%$.

This smoothing technique has a serious drawback, however, that has to be kept in mind in analyzing the final output data, as follows: If for whatever reason the thermometer resistance is incorrectly read at time t during the drift, then the resulting four specific heat points before and after this point will be incorrectly adjusted and a false minimum or maximum will appear in the plotted record. To correct this occurrence, the false resistance reading in the original data set is replaced with the interpolated value from the two adjacent readings.

Experimental Techniques

We review here the specialized experimental techniques used to implement this calorimetric method.

Copper Platforms. The schematic drawing in Fig. 2 illustrates an individually fixtured sample with an embedded thermometer. It is time-consuming and tedious to fixture samples individually, and a copper-platform technique has been developed.

The design of the copper platform is shown in Fig. 9(a) and consists of a copper cylinder with a copper cross-piece on the bottom. This forms a cup into which disc-shaped sample is placed, and the goal of this design is to minimize the mass of the platform. Toward this end the cylinder has a multitude of drill holes, and the bottom cross-piece is also drilled (varnish well, see below). Copper sheet, 0.13-mm thick, is used in the construction, and the solder used in the joints is held to a minimum by filing the joints after assembly. Ten platforms were fabricated, and the weight of each platform was in the range 150-160 mg.

Each platform was outfitted with a 1 k Ω Allen-Bradley thermometer, a manganin mechanical support coil, and a coiled copper thermal link wire, as shown in Fig. 9(a). A washer soldered to the mechanical support coil serves as a convenient hanger for bolt-mounting in the calorimeter. The length of the thermal link wire, l , attached to each platform was carefully measured (± 0.02 cm uncertainty) and ranged 19.5-20.5 cm.

Copper lead wires attached to the Allen-Bradley thermometer were heat sunk to the o.d. of the platform cylinder with cigarette paper to prevent shorting. Thin manganin hook-up leads were attached to these copper leads, as mentioned earlier.

The sample is mounted in the platform using a thin coating of G.E. 7031 varnish on the periphery of the varnish well in the bottom cross-piece, Fig. 9(a). For easy removal of the sample, a drop of the varnish solvent is placed in the varnish well to free the sample.

The i.d. of the platform is 1.11 cm, and the height of the platform, 0.64 cm. Cumulative weights of each platform and its components were made during assembly to determine addenda (see below).

Copper Platform

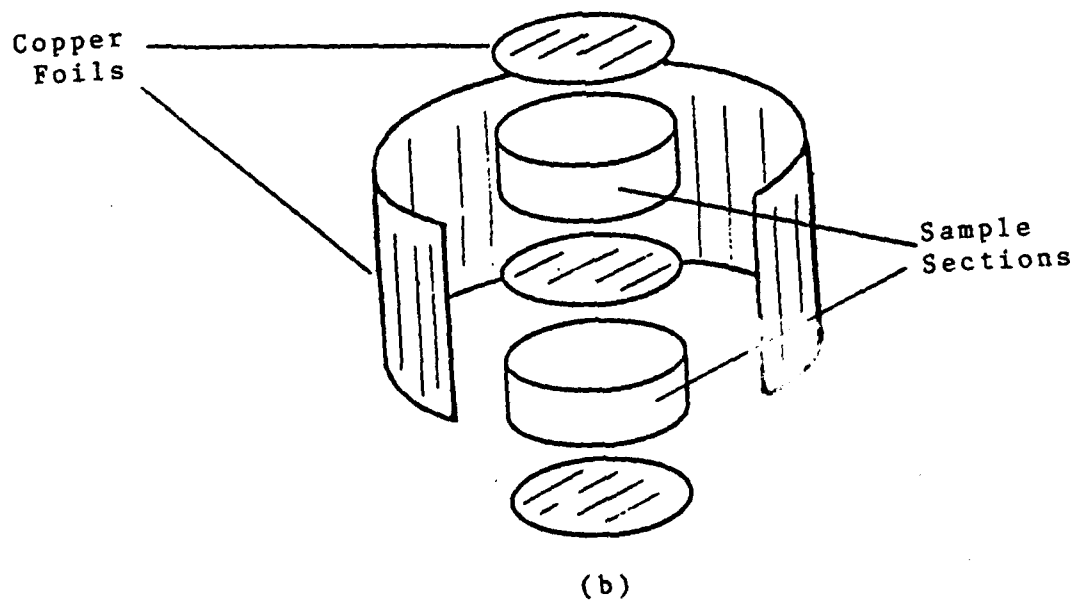
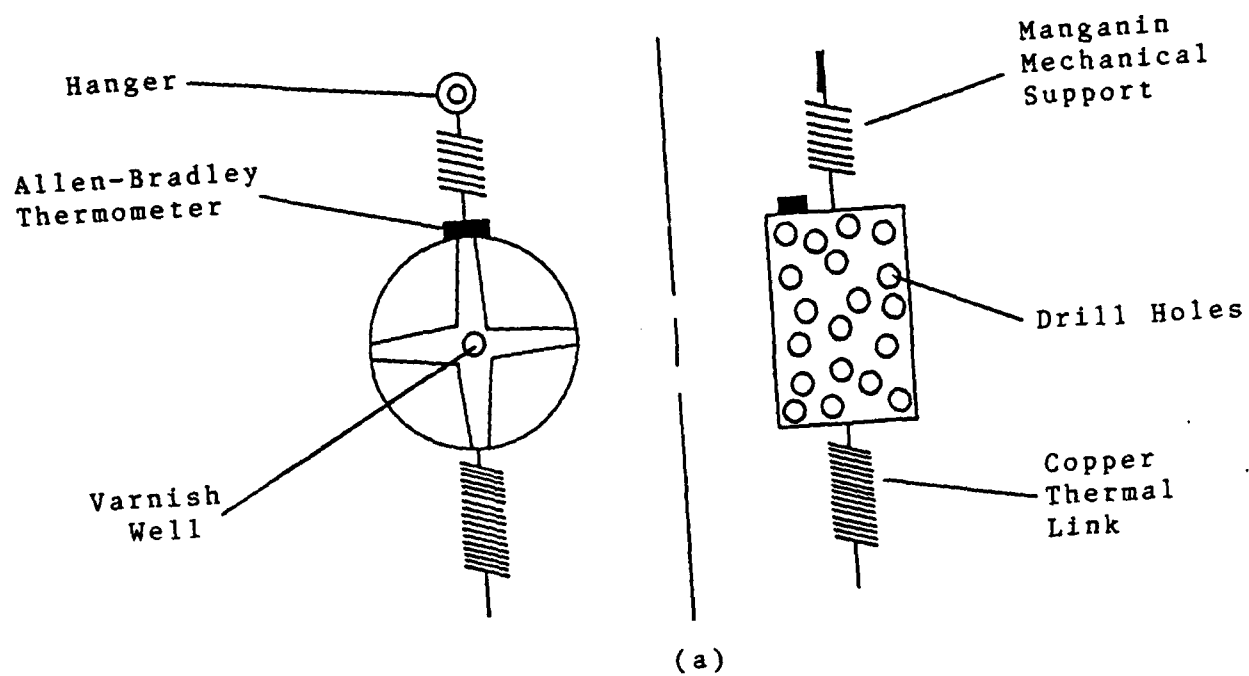


FIGURE 9

Sample Fixturing. Samples in the form of 1-cm diam discs were fixtured with copper foils as shown in Fig. 9(b). This fixturing served two purposes: (1) To insure good thermal equilibration within the sample (see above); and (2) To provide each platform + sample combination the same emissivity for applying the radiation coefficient, A_r in Eq. (4) (see below). The copper-foil used in this fixturing is 2×10^{-3} cm thick, and oxide layers were first removed with dilute hydrochloric acid. Fixturing was done with G.E. 7031 varnish and cumulative weights measured.

Disc samples were generally cut into two sections as shown in Fig. 9(b) according to the guideline above that no section be thicker than about 3 mm.

Miscellaneous. The calorimeter is evacuated at room temperature, and charcoal granules placed in the calorimeter assure a very hard vacuum at low temperatures.

The procedure for the thermometer-activation current is as follows: First, a 10-20 μ A current is applied during the overnight cooldown of the calorimeter in liquid nitrogen. Subsequently during the 80-4 K drift, the current is decreased in stages to avoid over-ranging the voltmeters (i.e., at 4 K the current should not exceed 1 μ A).

Following the overnight cooldown, the 77.4 K calibration point is measured. Next, the heater on the reservoir is used to bring the sample and the reservoir to about 90 K, and then this heating is stopped. Finally, the He transfer is started, and as soon as the sample displays cooling, the computer-interfaced data collection is begun (note that the procedure is calibrated in the range 4-80 K whatever the values of T and T_r are in this range).

The reason for activating the reservoir heater is to extend the measurement range above 77 K. However, experience shows that the initial data points are usually unreliable due to very small ΔT values (~ 1 -5 mK) at the beginning of the drift.

When the He transfer is completed, the He bath is pumped to about 3 K. The reason for this step is to provide a sizable

difference $T - T_r \approx 1$ K at the end of the drift run when the sample reaches 4 K. The point here is that the data for which $T \approx T_r$ are unreliable.

Experience has shown that for ceramic samples ~ 1 -2 g mounted in the copper platforms with thermal link lengths $l \approx 20$ cm, the 80-4 K drift times are 150-200 min, indicating average drift rates $dT/dt \approx 10$ mK/s which are slow enough to satisfy thermal-equilibration criteria (see below).

Finally, it is interesting that the reservoir temperature T_r slowly cools to 3 K in the drift experiment, and the difference $T - T_r$ is generally ~ 10 -40 K. The reasons for this are twofold: (1) The reservoir itself is not strongly linked thermally to the He bath in the double-can calorimeter; and, more importantly, (2) The high-specific-heat sample thermally loads the reservoir.

Calibrations and Scaling

The above discussions lay the detailed groundwork for this calorimetric drift method. We now take up actual measurements on a copper sample and on the copper platforms in order to calibrate the radiation coefficient, A_r in Eq. (4), to scale the method to the NBS data for copper (Table I), and to examine the addenda of the copper platforms.

Measurements on Copper. A disc of high-purity, ETP copper was loaded into a copper platform and drift data measured 75-4 K. The data were processed according to Eq. (4) with $A_r = 0$, and two features were found in the C-T data: (1) Below about 50 K, the drift C-data were $\sim 20\%$ larger than the NBS data for copper; and (2) Above 50 K, the drift C-data did not increase as rapidly with temperature as the NBS data and actually went through a maximum.

The explanation for these two features is straightforward: First, the radiation term in Eq. (4) becomes significant above 50 K, and ignoring this radiation-cooling has the effect of underestimating the specific heat, as can be seen from Eq. (4). And second, the $\pm 10\%$ spread between the drift data and the NBS data represents not only rather good agreement but also the sum

total of all the uncertainties in the method. In particular, the experimental KA-data in Fig. 3 have an uncertainty of $\pm 5\%$, and the integration of these data enter Eq. (4).

In reducing these copper drift data, the addenda of the copper platform were calculated using the formalism and addenda tables above; we shall return to this point below.

The following procedure was adopted to reconcile the drift C-data and the NBS data for copper: A scale factor is introduced, defined as $C(\text{NBS})/C(\text{Drift})$, to be applied to the drift data as an overall technique calibration. And a computer-based experiment was carried out to determine that value of the radiation coefficient A_r in Eq. (4) which brings the drift data into commensuration with the NBS data (primarily above 50 K).

The criterion used for determining the scale factor and A_r from the computer-based experiment was to vary A_r to find the minimum standard deviation in the scale factor (i.e., that value of A_r which yielded the tightest grouping of scale factors in the range 4-75 K). The A_r -values were stepped in increments of 5×10^{-13} beginning at $1 \times 10^{-11} \text{ W K}^{-4}$, and $A_r = 2.00 \times 10^{-11} \text{ W K}^{-4}$ yielded the smallest standard deviation in the scale factor at 0.7806 ± 0.0317 .

The results of these studies are summarized in Fig. 10. The upper plot compares the unscaled drift C-data to the NBS data, and the lower plot shows the empirical temperature variation of the scale factor, defined as the ratio of the two curves in the upper plot. As seen, the scale factor varies from 0.75 to 0.83, and this is a very rewarding result for a methodology covering such a broad temperature range.

The logic here is that the scale factor and A_r can be determined simultaneously according to the criterion that the drift data be matched most closely to the NBS data. A clear minimum in the standard deviation of the scale factor was found, and the A_r -value determined from this procedure agrees well with independent estimates. Therefore, there is good internal consistency with the procedure.

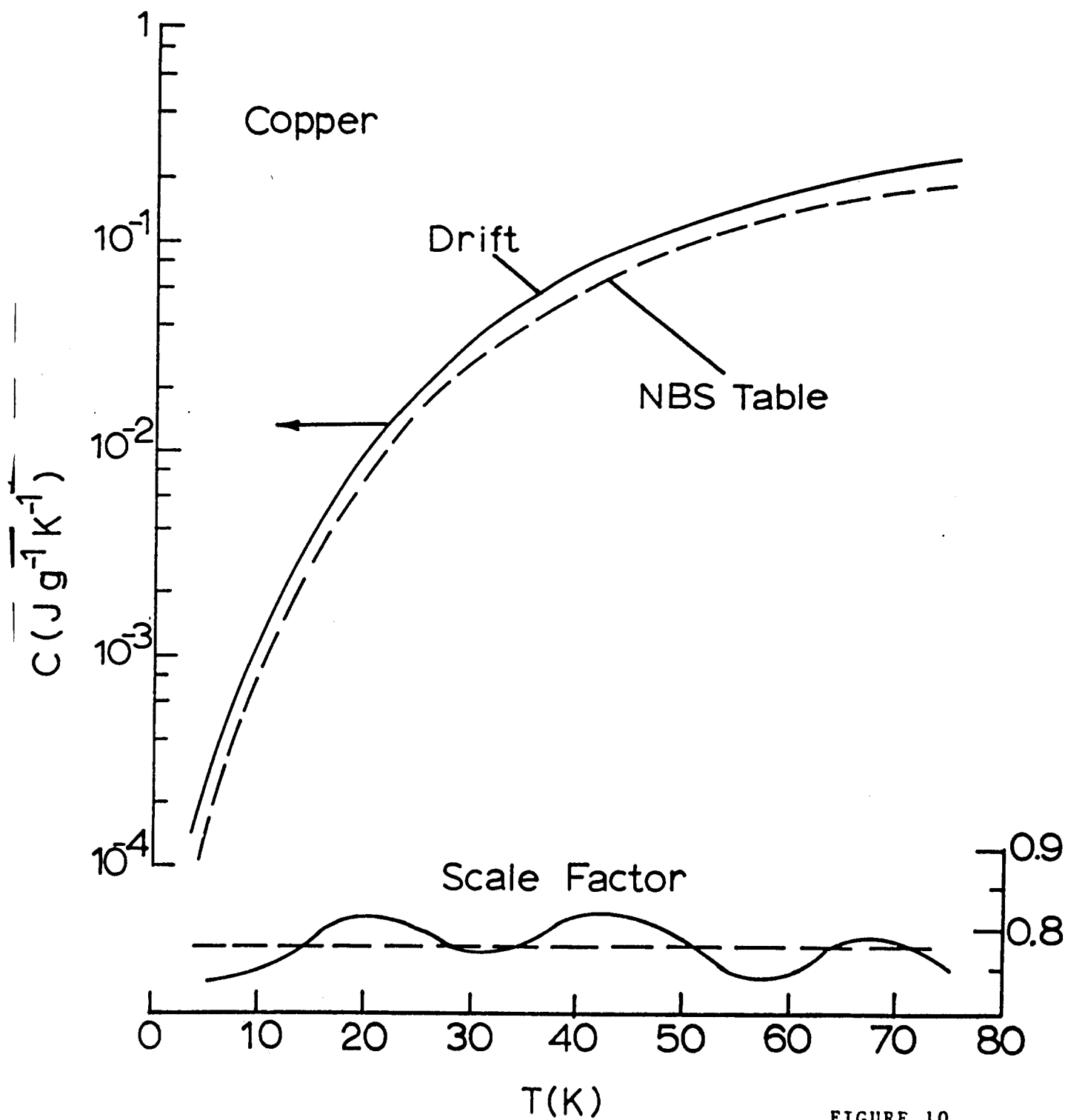


FIGURE 10

We now see the importance of wrapping the samples with copper foil as mentioned previously--namely, the A_r coefficient determined from the copper sample can also be applied to the copper-foil-wrapped samples because the emissivities are matched.

Measurements on Copper Platforms. The copper platforms constitute addenda in the sample measurements, and it is important to determine if the addenda formalism and tables discussed previously can be applied to these platforms. That is, although cumulative weights were measured on each platform during assembly, there are components not covered in the tables (i.e., the solder was included with the copper, and the phenolic resin on the $1\text{ k } \Omega$ resistor was included with the 7031 varnish as was the cigarette paper). Moreover, our addenda tabulations involve literature data from several sources, so that the studies here provide a good test of these tabulations.

Drift data were measured on all ten copper platforms (i.e., without samples in the platforms), and the scale factor and A_r -coefficient determined above were used in the data reductions.

The heat-capacity data for the platforms are summarized in Fig. 11 as bars at 5 K temperature intervals, and also shown in Fig. 11 is a typical heat-capacity curve for a platform calculated from the addenda formalism and tables.

There is excellent agreement between the measured and calculated data in Fig. 11 below 30 K, but between 40 and 60 K the calculated data are $\sim 20\%$ larger than the measured data. There is a possible experimental reason for this discrepancy: These drifts occurred very rapidly due to the small thermal loading, such that T and T_r were always very close, on the one hand; and on the other hand, the range 40-60 K is that range where our thermometer-calibration procedure leads to the largest $\Delta T/T$ discrepancies, as seen in Fig. 7. These latter discrepancies are not important if T and T_r are substantially separated, as in the case of the copper sample in Fig. 10.

We conclude that the agreement in Fig. 11 between the measured and calculated data is sufficiently good that the

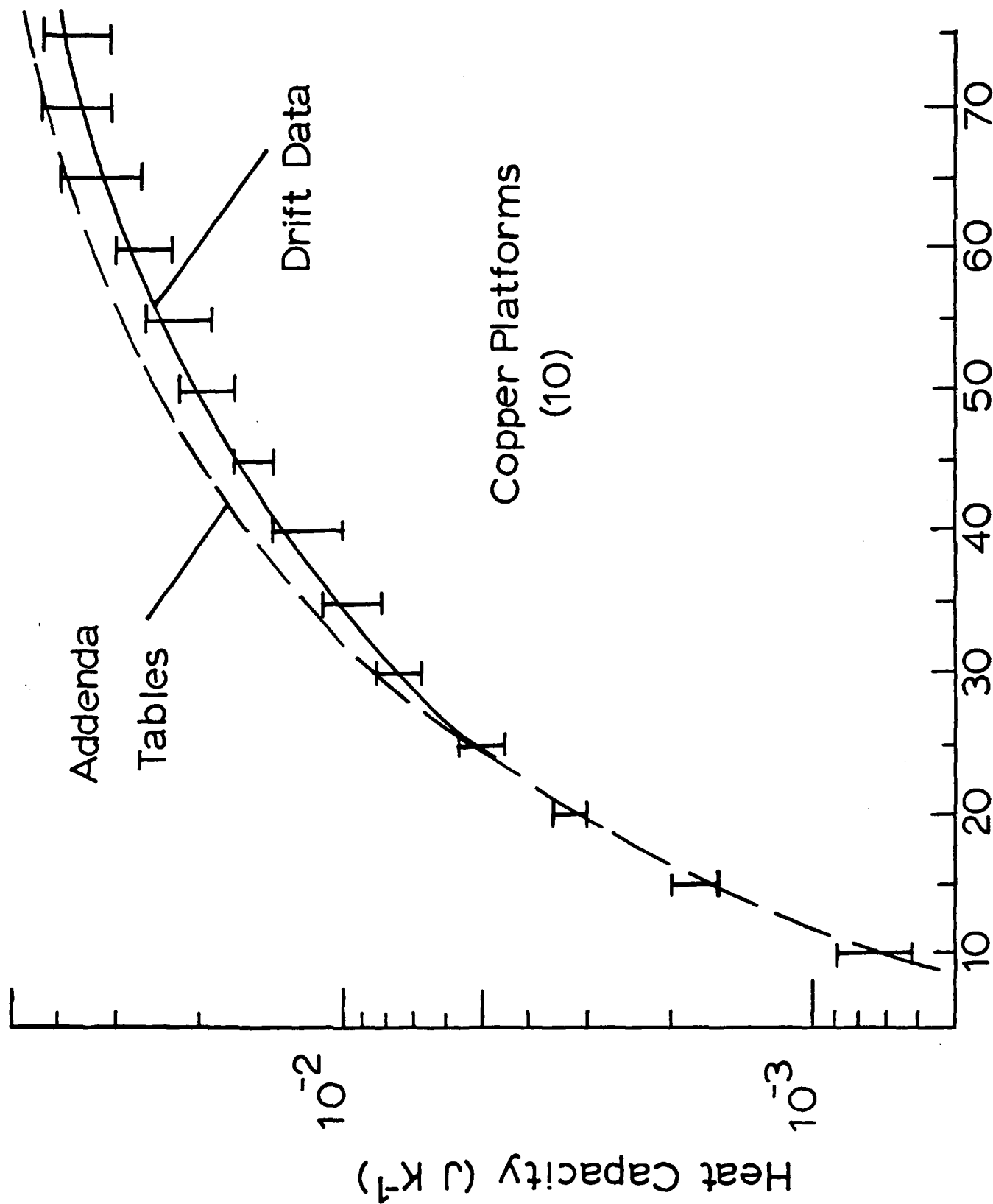


FIGURE 11

7778

addenda formalism discussed previously can be employed to calculate the addenda corrections for the copper platforms. Looked at differently, these addenda corrections in the case of a measured sample constitute $\sim 20\text{-}30\%$, so the $\pm 10\%$ discrepancy in Fig. 11, if real, translates into a 2-3% effect on the specific heat of the sample.

We also conclude that the addenda formalism and tables are reliable.

There are two important advantages to these findings. First, if a particular copper platform is modified or repaired, the new addenda for that platform can be determined from cumulative weights. And second, the addenda contributions from the copper foils and 7031 varnish on the sample can be calculated easily and reliably.

Conclusions

In this Report a calorimetric drift method for measuring specific heat in the 4-80 K temperature range has been documented. The theory of the method is straightforward, Eq. (4), and the calibrations and calibration procedures for the thermal link, addenda, thermometry, radiation coefficients, scale factor, and copper platforms have been determined. Specialized experimental techniques and a simple data-smoothing scheme have been described. Thermal equilibration time constants are not problematic for drift rates ~ 10 mK/s.

A high-purity copper sample was measured by the method, and with scaling the results match the NBS data for copper to within $\pm 4\%$ in the range 4-80 K. An upper limit of $\pm 3\%$ uncertainty in the specific heat has been estimated due to the addenda contributions from the copper platforms.

The method is ideally suited for a computer-interfaced, data-collection system, and a particularly attractive feature of the method is the resolution of a sharp maximum in the specific heat. Here the drift rate shows dramatically, and points within a few mK of the maximum are resolved. An example of this feature is shown in Fig. 12; here a Zn-based spinel ceramic with a

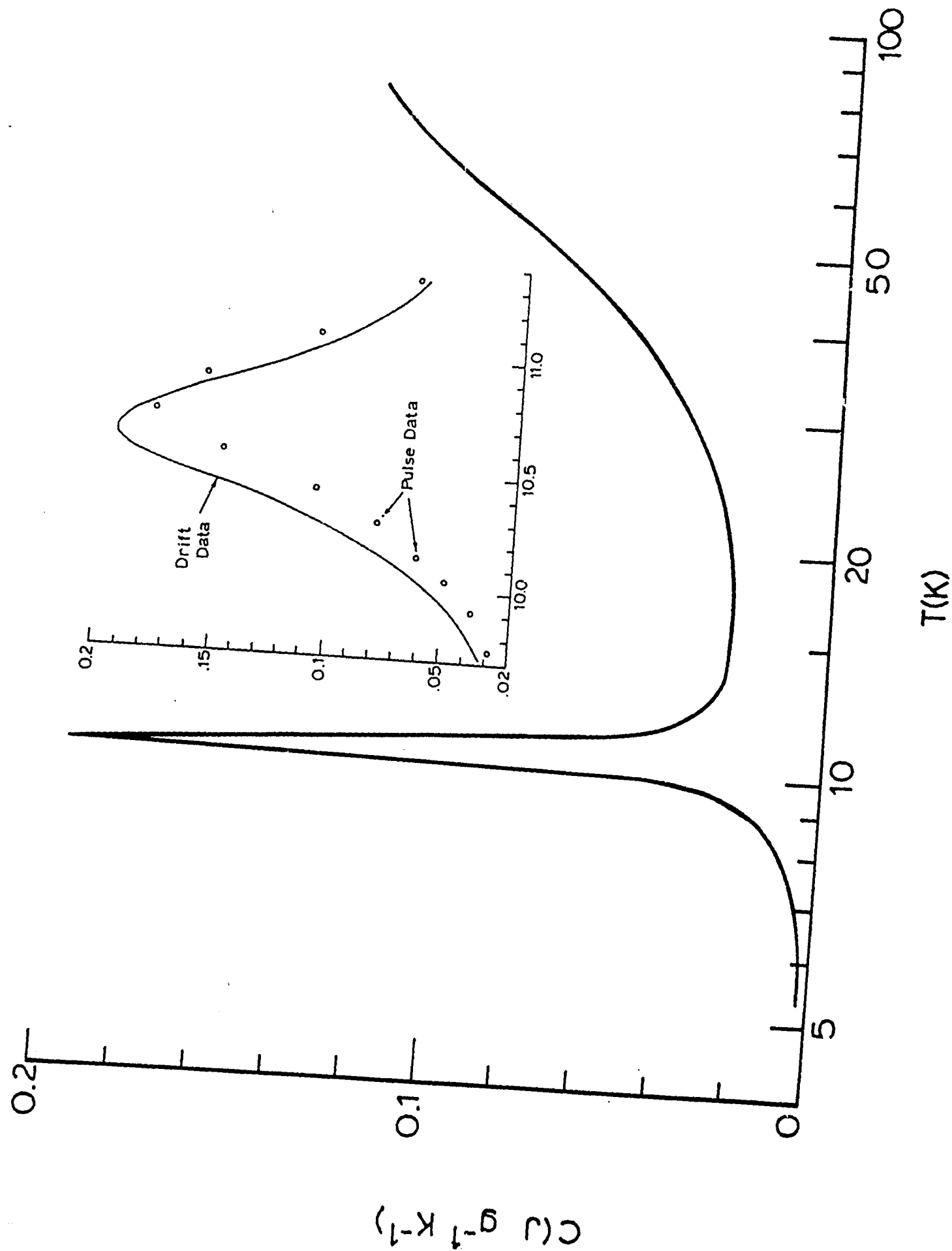


FIGURE 12

specific-heat peak at 10.7 K was measured. The inset in Fig. 12 shows both pulse and drift data in the neighborhood of the peak, and the drift method yields a continuous record ($dT/dt=0.4$ mK/s in the neighborhood of the peak) whereas for the pulse method $\Delta T \sim 300-500$ mK. The magnitude of these pulse ΔT 's probably explains the apparent temperature shift between the two data sets in the inset in Fig. 12.

IV.B. Broad-Range Specific Heat Measurements

The data in Fig. 1 above reveal potentially interesting phenomena: (1) Doping in ZnCr_2O_4 , Fig. 1(a), splits the specific-heat maximum into two components; and (2) The effect of stress in the glass composite with ZnCr_2O_4 induces a maximum at higher temperatures. Thus, doping and stress effects bear directly on the physics of these spinels.

In this Section we report specific heat measurements on the following generic categories of samples, using the broad-range methods described in Section IV.A.:

1. Undoped ceramic samples
2. Doped ceramic samples
3. Undoped ceramic powders in composites of both glass and epoxy.
4. Doped ceramic powders in glass composites.
5. Fine-grained powders, including Gd^{+3} doping.

Consequently, the effects of doping and stress will be examined both separately and together, and we shall focus on two temperature regimes: Above 15-20 K to see if new, high-temperature effects are induced [e.g., Fig. 1(b)]; and below 15 K to study induced changes in the basic transitions [e.g., Fig. 1(a)].

Some of the composites reported below were available from previous programs and are included here for completeness sake. In particular, the epoxy composites are included because, due to measured thermal-expansion mismatches,

1. The spinel powders are in compression in the epoxy composites; whereas,
2. The spinel powders are in tension in the glass composites.

In applying the new specific-heat method, the thermometry calibration technique adopted leads to an unavoidable discontinuity in the derivative $d\log R/dT$ at 25 K which may lead

to a slight shoulder in the specific heat in the neighborhood of 35 K. This effect will be seen in some of the C-T plots below, and the reader is cautioned that this is an artifact rather than a real effect.

The first issue to address is whether the specific heat maximum at 40 K in the ZnCr_2O_4 -glass composite in Fig. 1(b) is a real effect or an artifact of the previous metrology. The original sample and a duplicate sample were measured 4-70 K, and these data are shown in Fig. 13. In neither case does a maximum occur in the specific heat at 40 K. The difference between the C-T plots in Fig. 13 is probably due to the different preparation conditions: The original composite was prepared at 1050°C ($\rho = 3.976$) whereas the repeat sample was prepared at 950°C ($\rho = 4.211$).

The maximum in the specific heat of this composite shown in Fig. 1(b) is now seen to be spurious, and the probable cause is the addenda corrections (uncalibrated above 25-30 K in the previous method). That is, if the addenda extrapolations overestimated the addenda corrections above 30 K, this could lead to an apparent maximum in the specific heat. This suggestion, however, has not been pursued relative to the Fig. 1(b) data due to the compounding uncertainties in the thermometer calibration, etc. above 30 K.

UNDOPED CERAMIC SERIES

In the course of this research over several years different types of undoped ceramic samples of CdCr_2O_4 and ZnCr_2O_4 have been prepared under different conditions. All available types of samples have been measured and are reported below.

CdCr_2O_4

Four types of CdCr_2O_4 ceramic samples were measured:

1. Compacted CdCr_2O_4 , a large-grain-size ceramic fired at

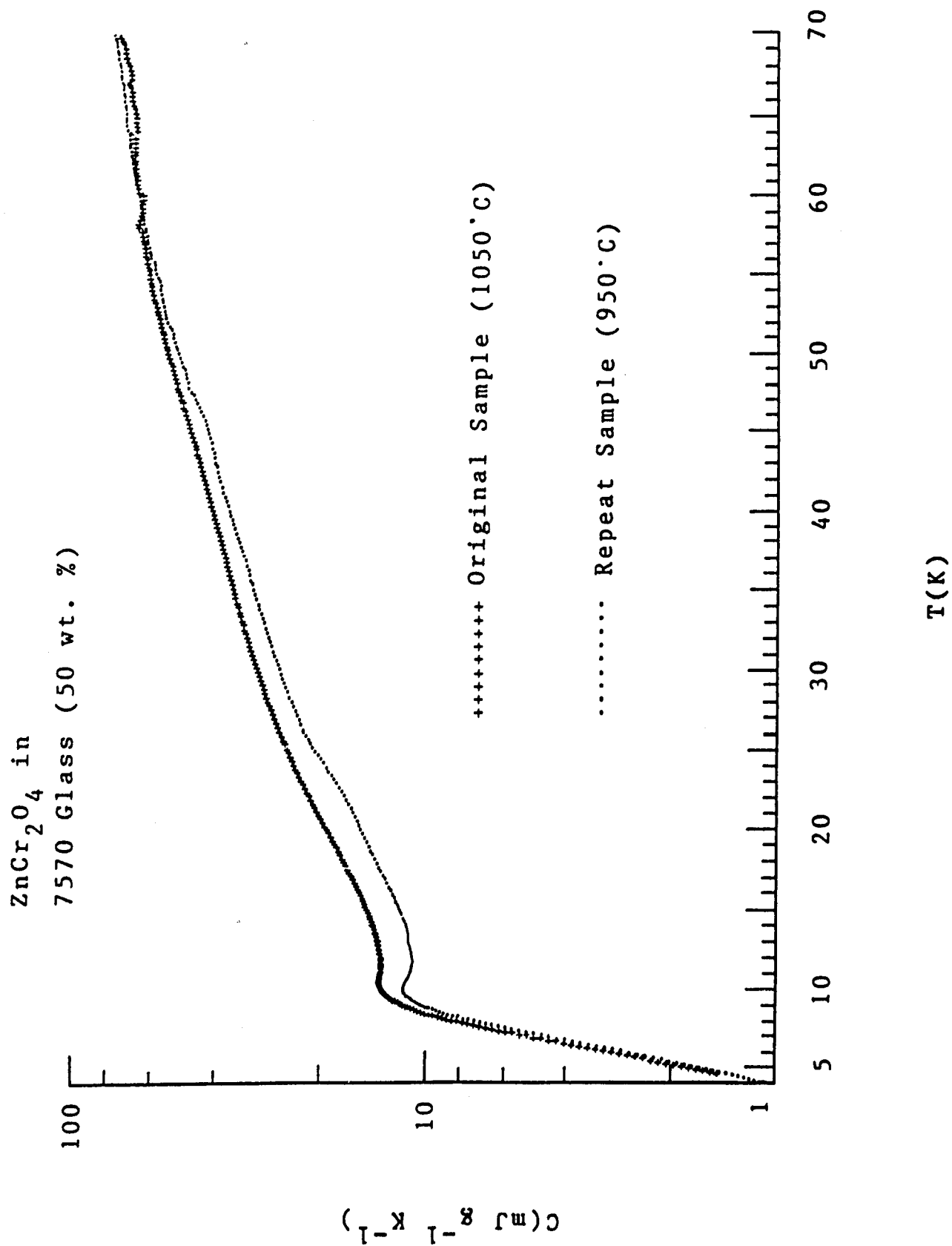


FIGURE 13

1250°C for 3 h following compaction in the green state.

2. Hi-Purity CdCr_2O_4 , a ceramic calcined at 1150°C for 2 h and sintered at 1250°C for 2 h. Very high purity starting powders were used to make this sample.
3. Conventional CdCr_2O_4 , a ceramic identical to the Hi-Purity sample above except that nominally pure starting powders were used.
4. CCN (9/1), a ceramic composed of 90 mol % CdCr_2O_4 and 10% CdNb_2O_6 and fired at 1350 °C wherein the CdNb_2O_6 acts as a mineralizer to promote densification and remains as a separate phase (i.e., the Nb^{5+} does not dope the CdCr_2O_4).

Except for sample 2. above, nominally pure starting powders were used to make these samples.

Specific heat data for these samples are shown in Fig. 14 over the 4-75 K range and in Fig. 15 over the 4-13 K range. We can draw the following conclusions from these data:

1. For all samples, there is no structure in the specific heat above 10 K.
2. The specific heat of the Conventional sample is about 20% smaller than the specific heats of the other samples above 30 K (note the convergence of the C-data for the latter samples in Fig. 14).
3. Only the Conventional and CCN (9/1) samples display maxima in the specific heat at 8 K, Fig. 15. The Compacted and Hi-purity samples display broad, flat specific heats 5-13 K.

It is significant that the Conventional and Hi-Purity samples are identical except for the purity of the starting powders, yet the specific heats of these samples are dramatically different, Fig. 15. This finding strongly suggests that minor impurities play a significant role in the physical properties of CdCr_2O_4 at low temperatures.

Undoped CdCr_2O_4 Ceramics

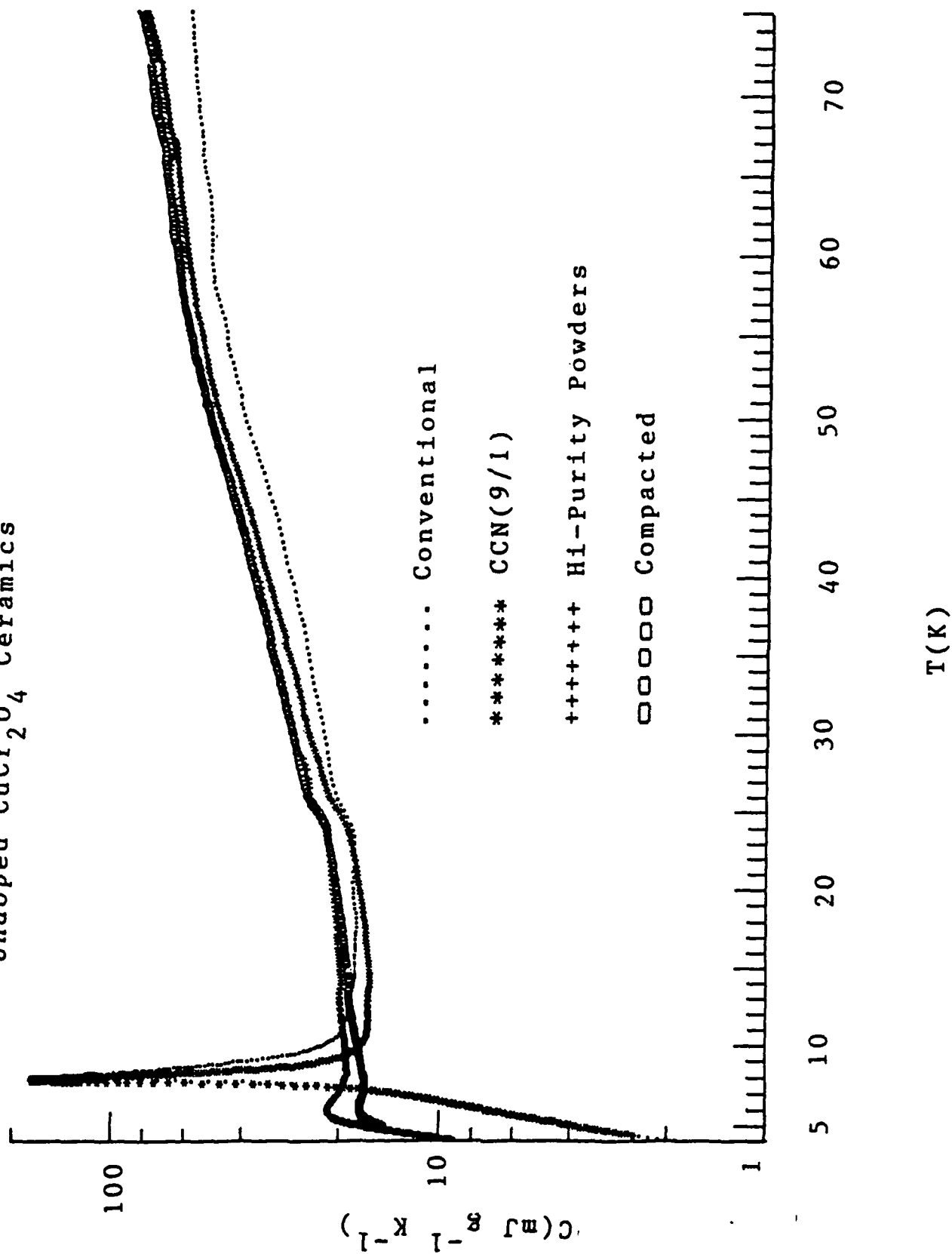


FIGURE 14

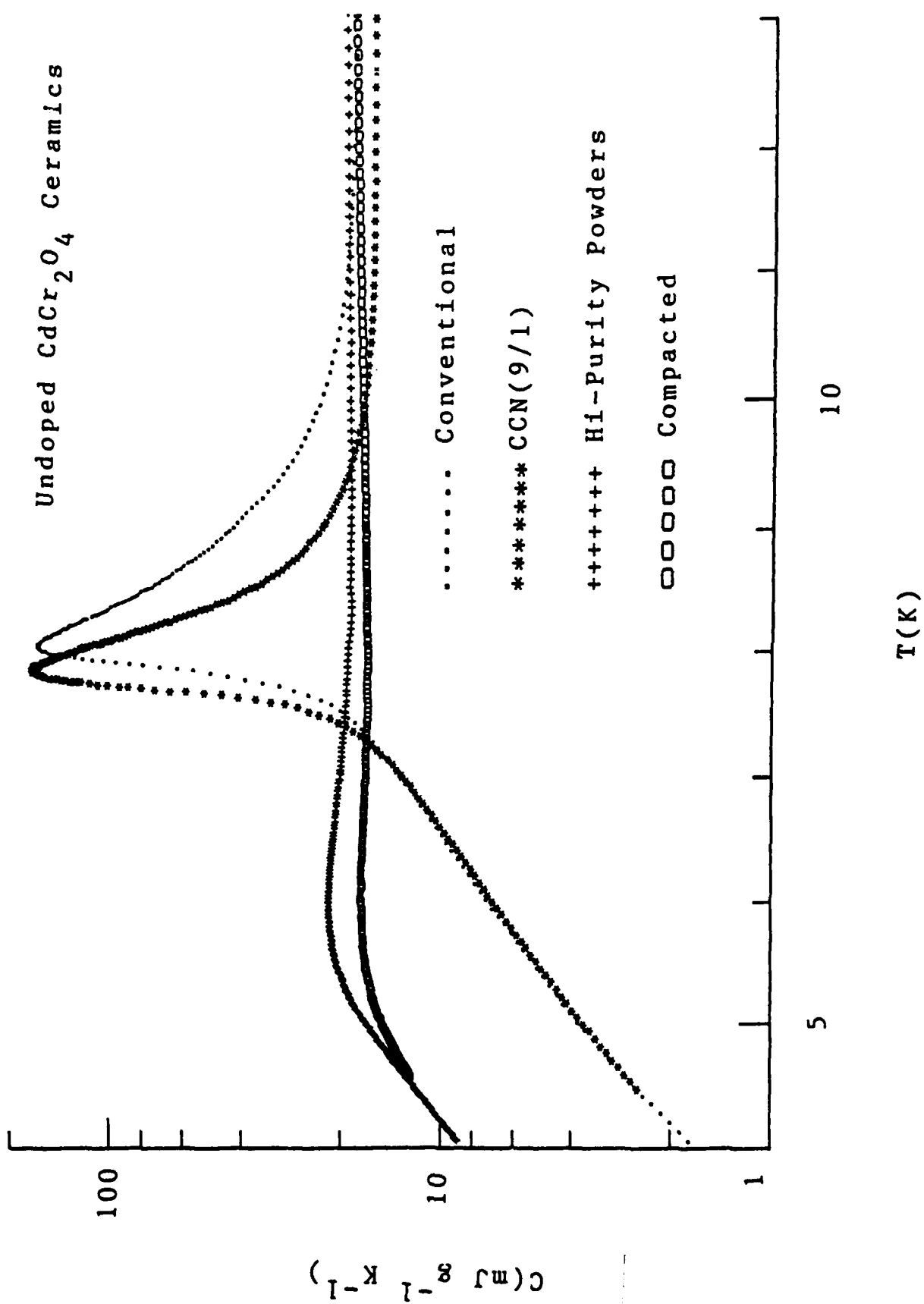


FIGURE 15

One would expect the Conventional and Compacted samples to behave identically because of the similarity in the preparation conditions (see above). However, from Fig. 15 the specific heats of these samples are markedly different. This is all the more surprising because coherence-length limitations are certainly missing in the large-grained Compacted sample in Fig. 15.

ZnCr₂O₄

As with the CdCr₂O₄ sequence above, a variety of ZnCr₂O₄-based ceramics (undoped) were measured, as follows:

1. Compacted ZnCr₂O₄, a ceramic fired at 1600°C for 1 h following compaction in the green state.
2. Hi-Purity ZnCr₂O₄, a ceramic fired at 1600°C for 4 h and prepared from very high purity starting powders.
3. ZCN (9/1), a ceramic composed of 90 mol % ZnCr₂O₄ and 10 mol % ZnNb₂O₆ and fired at 1350°C. As with CCN (9/1) above, the ZnNb₂O₆ acts as a mineralizer to promote densification and remains as a separate phase (i.e., the Nb⁵⁺ does not dope the ZnCr₂O₄).

Except for sample 2. above, nominally pure starting powders were used to make these samples.

Specific heat data for these samples are shown in Fig. 16 over the 4-75 K range and in Fig. 17 over the 4-18 K range, and we can draw the following conclusions from these data:

1. As with the ceramic CdCr₂O₄ sequence in Fig. 14, no specific heat features occur in Fig. 15 for the ZnCr₂O₄ ceramics above 15 K.
2. From Fig. 16, the specific heat of the Hi-Purity sample has the largest and sharpest specific heat maximum and also exceeds the specific heat of the other two samples at the higher temperatures. However, the specific heat

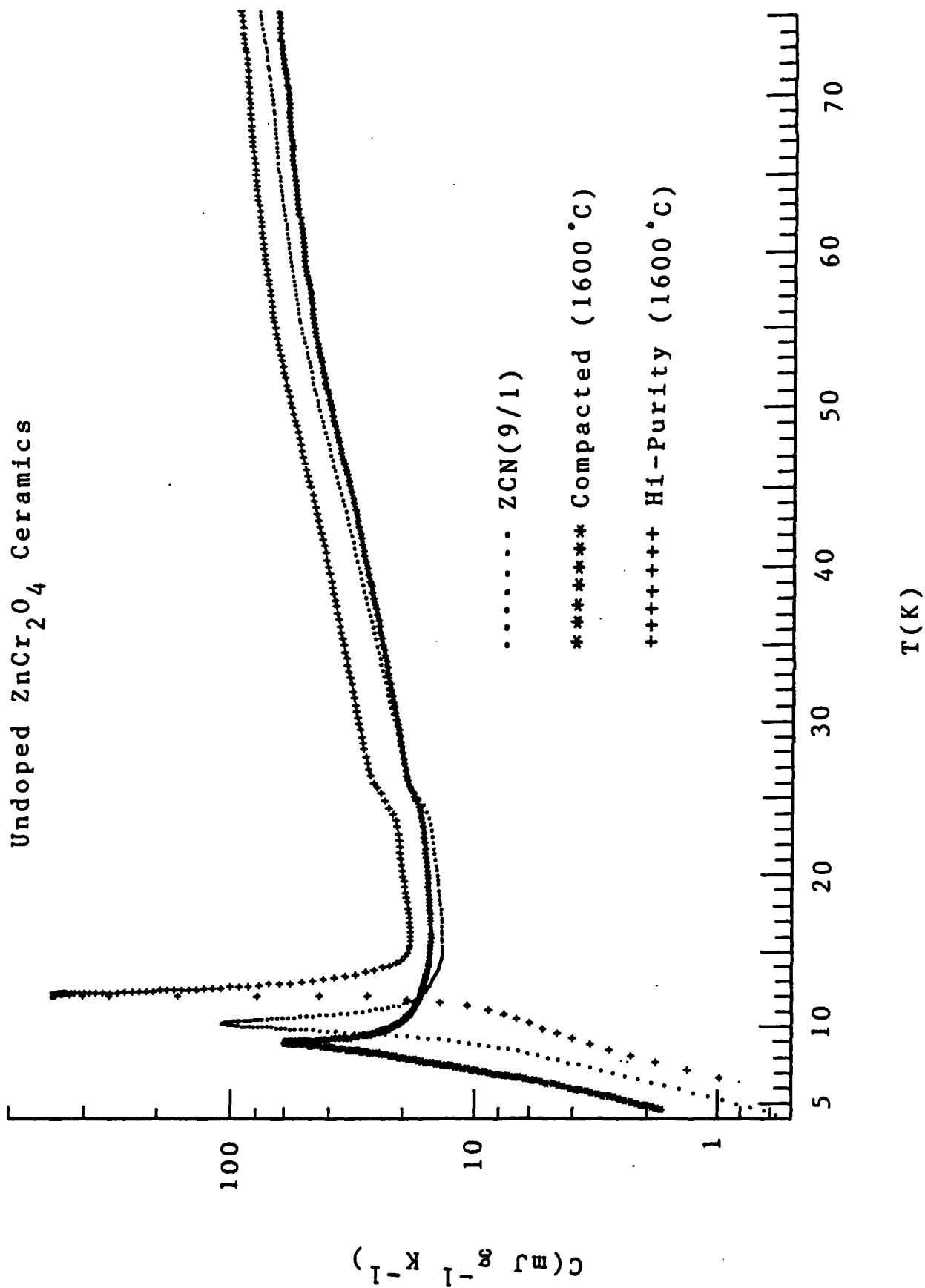


FIGURE 16

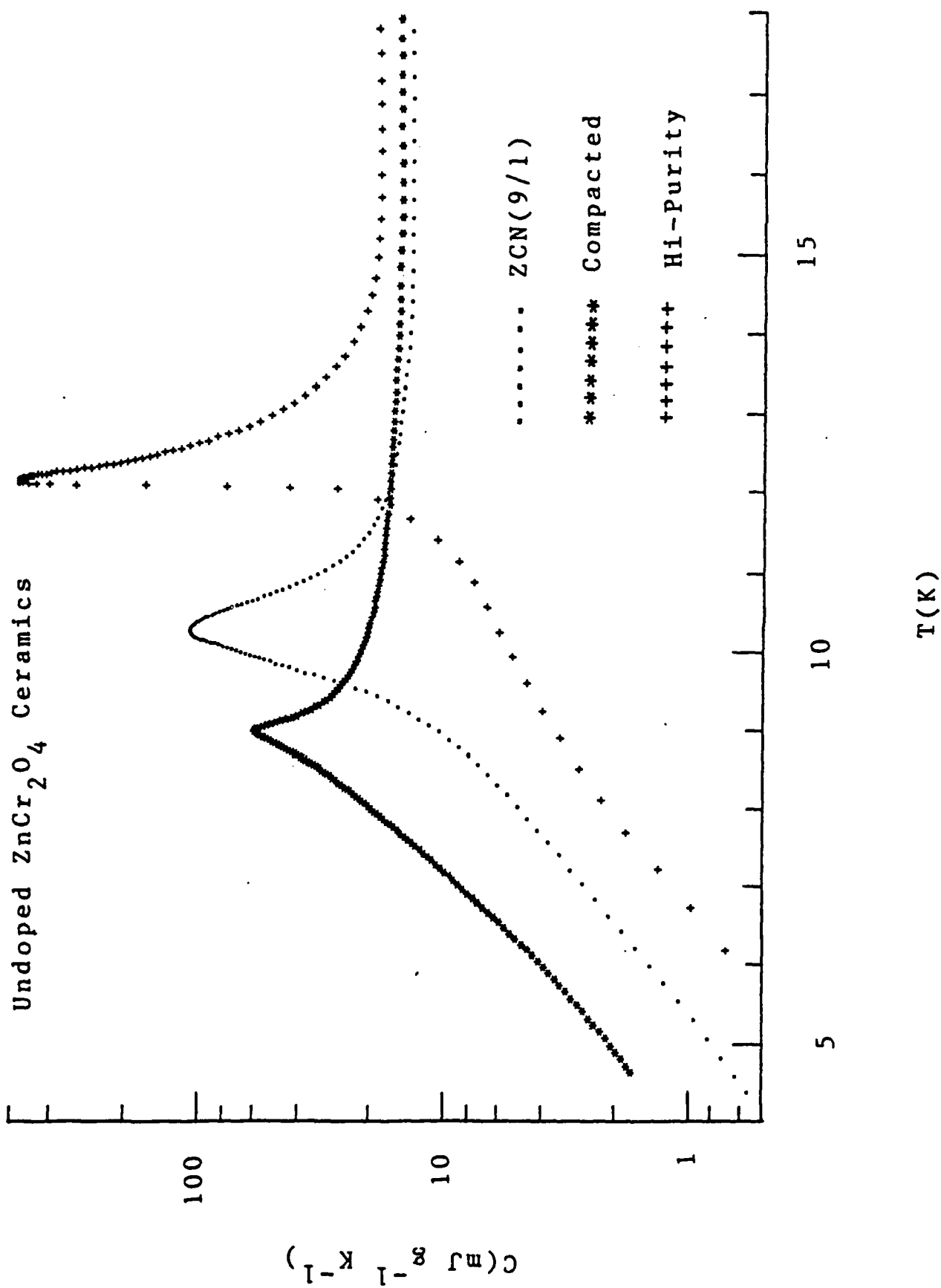


FIGURE 17

of this sample falls more rapidly below the peak than that of the other two samples.

3. From Fig. 17 there is a steady progression of the specific-heat peak height and temperature, as follows:

Hi-Purity, $600 \text{ mJ g}^{-1} \text{ K}^{-1}$ at 12.1 K

ZCN(9/1), $120 \text{ mJ g}^{-1} \text{ K}^{-1}$ at 10.1 K

Compacted, $60 \text{ mJ g}^{-1} \text{ K}^{-1}$ at 9.0 K

In contrast to the Hi-Purity CdCr_2O_4 sample in Figs. 14 and 15, the corresponding ZnCr_2O_4 sample in Figs. 16 and 17 displays a sharp transition. This finding suggests that impurity effects play a much more dominant role in CdCr_2O_4 than in ZnCr_2O_4 .

The progression of peak heights and temperatures in Fig. 17 might be explained by minor impurity effects in ZnCr_2O_4 , and it is interesting to observe that the peak heights in the Hi-Purity and Compacted samples differ by an order of magnitude (note the similar preparation conditions above).

It is rewarding that the ZCN(9/1) sample in Figs. 16 and 17 is intermediate between the other two samples, and this reinforces the observation above that there is minimal interaction between the ZnCr_2O_4 and ZnNb_2O_6 phases in this ceramic. We also remark that the stresses between these two phases is most probably unimportant (see below).

Comparison Data

The two spinels here differ by the cation on the A-site. Because Cd^{2+} and Zn^{2+} are chemically similar and also have similar ionic radii (0.97 and 0.74 Angstroms, respectively), it is interesting to compare data on these two spinels. The high-purity forms and the two-phase forms are selected for comparison from Figs. 14-17, and these comparative data are shown in Fig. 18 from 4 to 75 K and in Fig. 19 from 4 to 18 .

The specific heat data in Fig. 18 converge to $80\text{-}90 \text{ mJ g}^{-1} \text{ K}^{-1}$ at 75 K which is to be expected given the similarity of these spinels. However, the data at the lower temperatures in Fig. 19

Undoped Ceramics

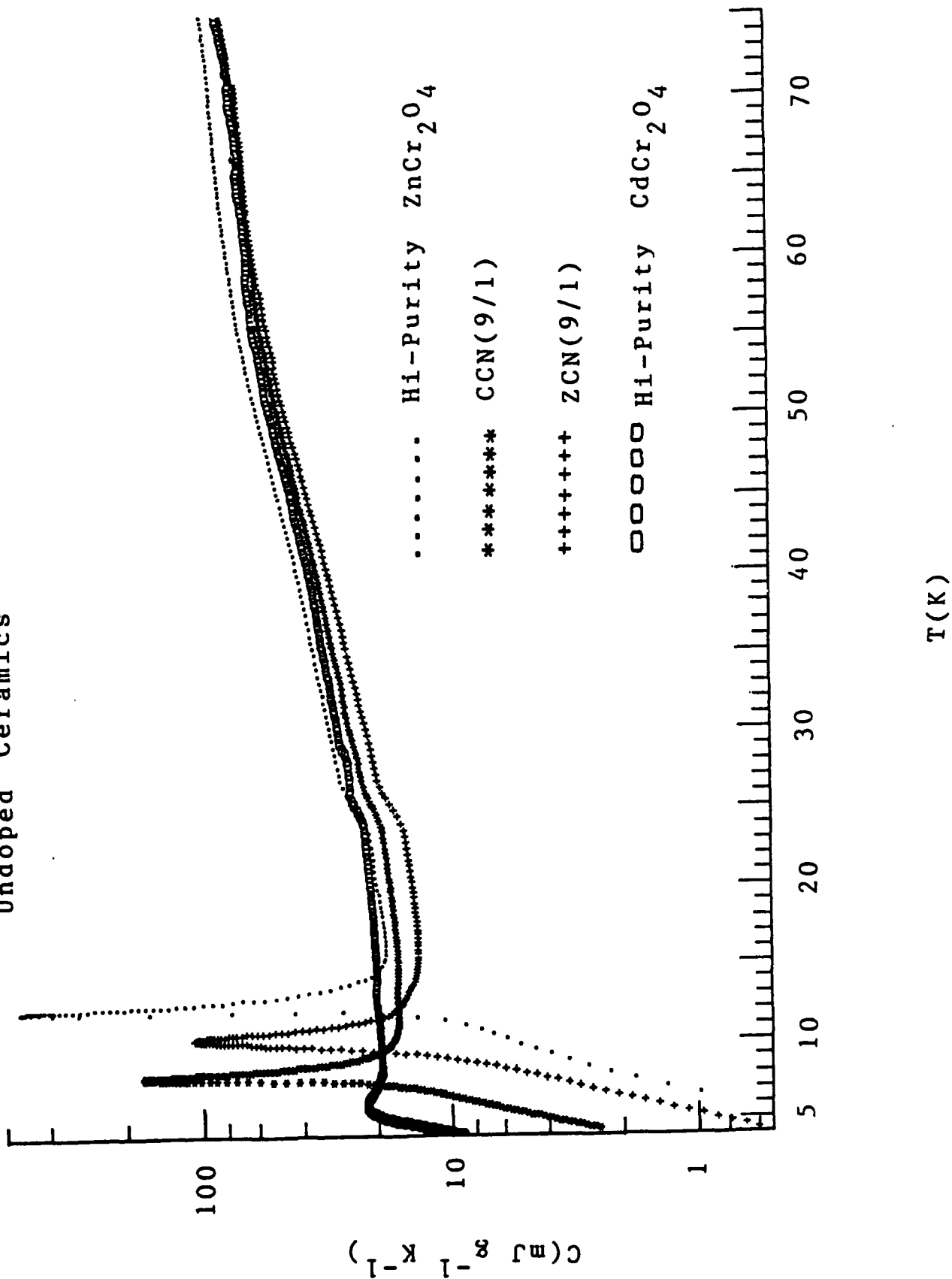


FIGURE 18

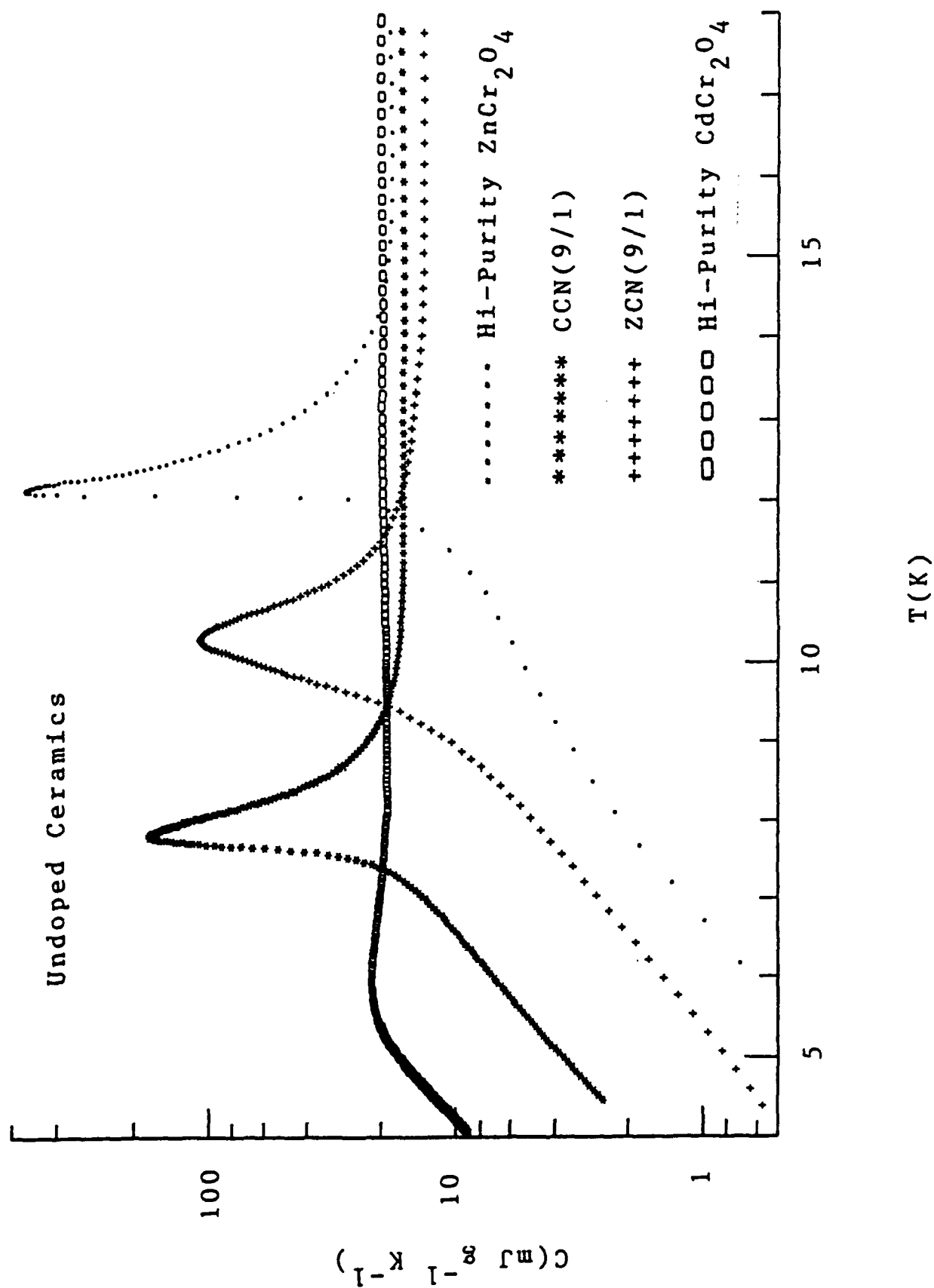


FIGURE 19

underscore the dramatic difference between high-purity forms of CdCr_2O_4 and ZnCr_2O_4 --the specific-heat peak in the former is quenched whereas the peak in the latter is enhanced.

It is also interesting to observe the similarities between the two-phase ceramics in Figs. 17 and 19--i.e., a temperature shift of about 2 K would appear to bring the CCN(9/1) and ZCN (9/1) curves into coincidence.

DOPED CERAMIC SERIES

The above series of data sets on undoped CdCr_2O_4 and ZnCr_2O_4 strongly suggest the important role of impurities in determining the low-temperature physical properties of these spinels, particularly in the case of CdCr_2O_4 . We now consider the effects of controlled doping in these spinels, and in particular we look for features in the specific heat above 20 K.

Doped CdCr_2O_4

Samples of ceramic CdCr_2O_4 doped with 2 mol % each of Mo^{+3} and V^{+5} were prepared identically with the undoped Conventional sample above (Figs. 14 and 15). These dopants are expected to enter the B-site in the AB_2O_4 spinel lattice. Specific heat data on these doped samples are shown in Fig. 20 over the 4-75 K temperature range and in Fig. 21 over the 4-15 K range. Data for the undoped Conventional sample are also shown for comparison.

The data in Fig. 20 show that no specific heat features appear in the doped samples up to 75 K, and the data in Fig. 21 show that the specific heat peak at 8 K is quenched by the dopants.

These are surprising results because the data in Fig. 15 strongly suggest that impurities must be present in CdCr_2O_4 in order for the specific heat peak at 8 K to appear.

In fact, the data in Figs. 20 and 21 for doped CdCr_2O_4 bear a striking resemblance to the data for the Hi-Purity CdCr_2O_4

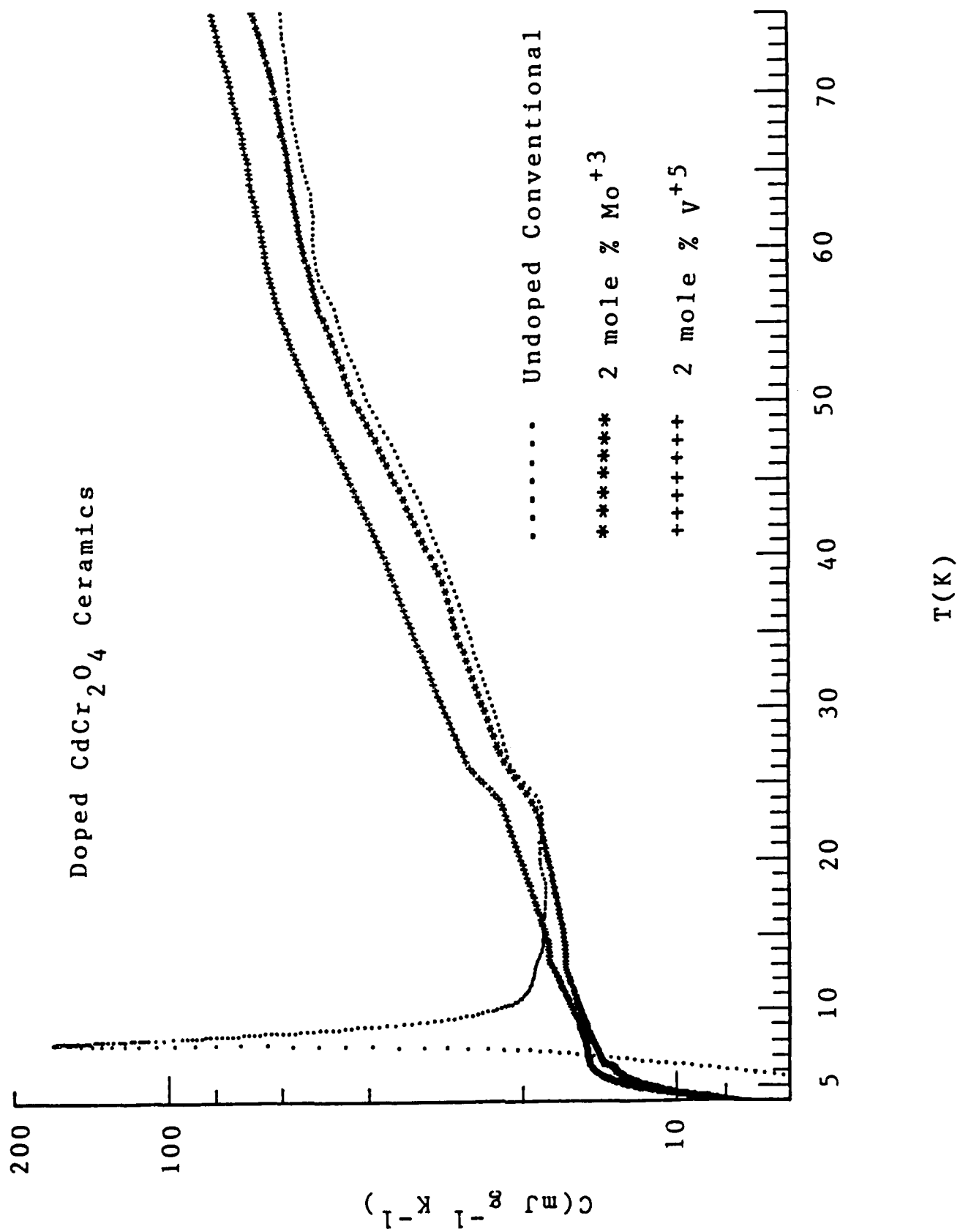
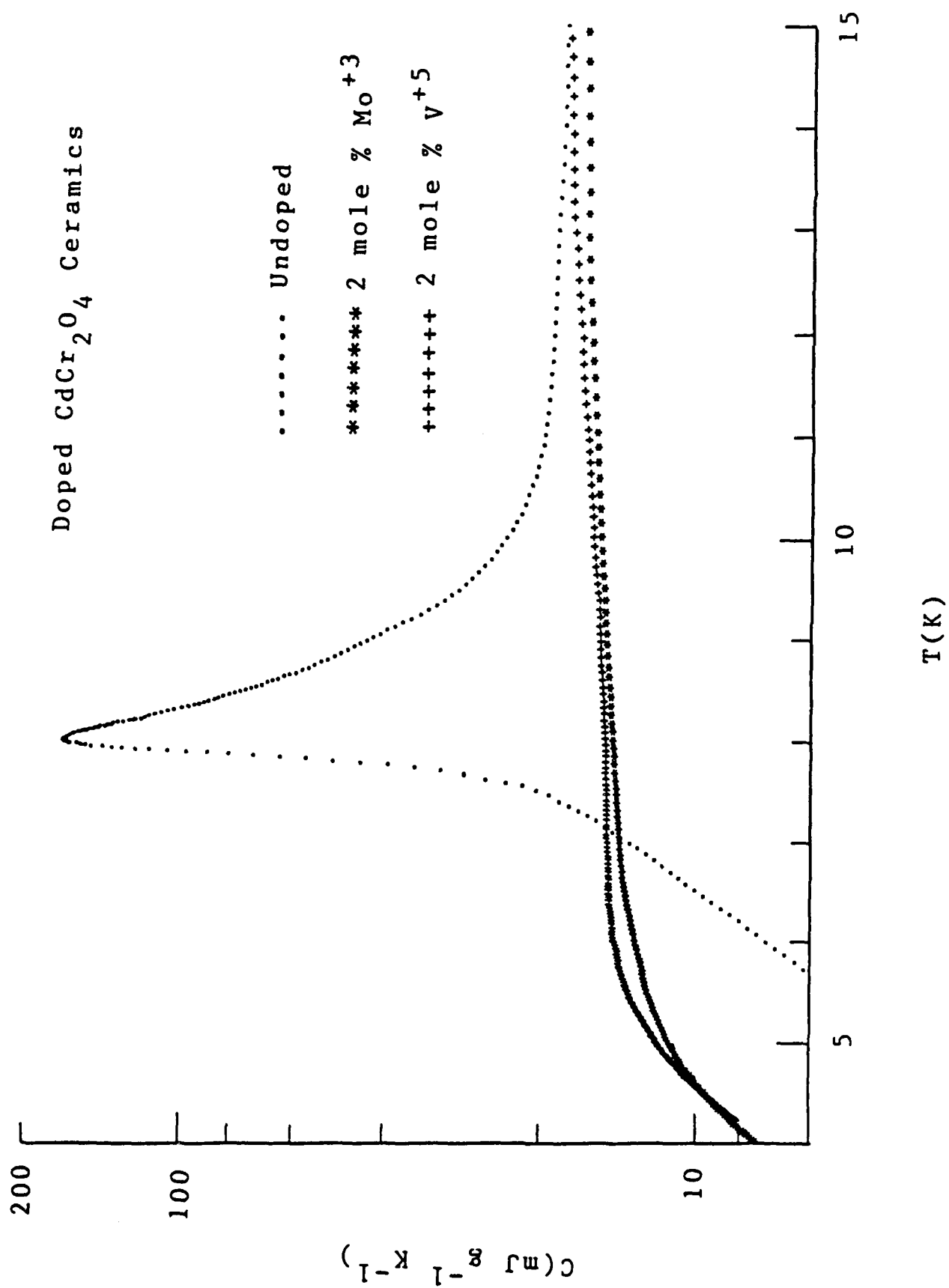


FIGURE 20



sample in Figs. 14 and 15. In Fig. 22 these doped and high-purity data are collected for the 4-75 K temperature range and in Fig. 23 for the 4-15 K range. The similarity in these data plots is striking considering the broad range of impurity levels represented. A clear but small maximum is seen for the high-purity CdCr_2O_4 , but this maximum is missing in both cases of doped CdCr_2O_4 .

The tentative conclusions from these data is that although some impurities must be present in CdCr_2O_4 for the 8 K specific-heat peak to appear, the range of impurities to cause this peak is apparently limited to relatively small levels. This observation may also explain the anomalous behavior of the Compacted sample in Fig. 15--we might speculate that the impurities in this sample were either too low or too high.

Along this line, we point out that the CCN(9/1) ceramic (Figs. 14 and 15) has been shown historically to be invariant to the purity of the starting powders used (i.e., this ceramic has been prepared at several laboratories using powders from different suppliers). We conjecture that the grain boundaries in this two-phase ceramic absorb any excess impurities present.

Doped ZnCr_2O_4

We have already seen in Fig. 1(a) that dopants in ZnCr_2O_4 have the effect of splitting the 9.5 K specific heat peak in the undoped ceramic. Here we consider broad-range specific heat data for selected dopants in ZnCr_2O_4 .

Previous measurements below 15 K [e.g., Fig. 1(a)] have shown the universality of peak splitting in ZnCr_2O_4 due to dopants. Consequently, three dopants were selected for further studies here: (1) The Al^{+3} dopant, $\text{spin}=0$; (2) The Gd^{+3} dopant, $\text{spin}=7/2$; and (3) The intermediate V^{+5} dopant. All three dopants are expected to enter the B-site in the AB_2O_4 spinel lattice. The ceramic samples here were prepared comparably to the Compacted sample of undoped ZnCr_2O_4 in Figs. 16 and 17.

Specific heat data for these doped ceramic samples of

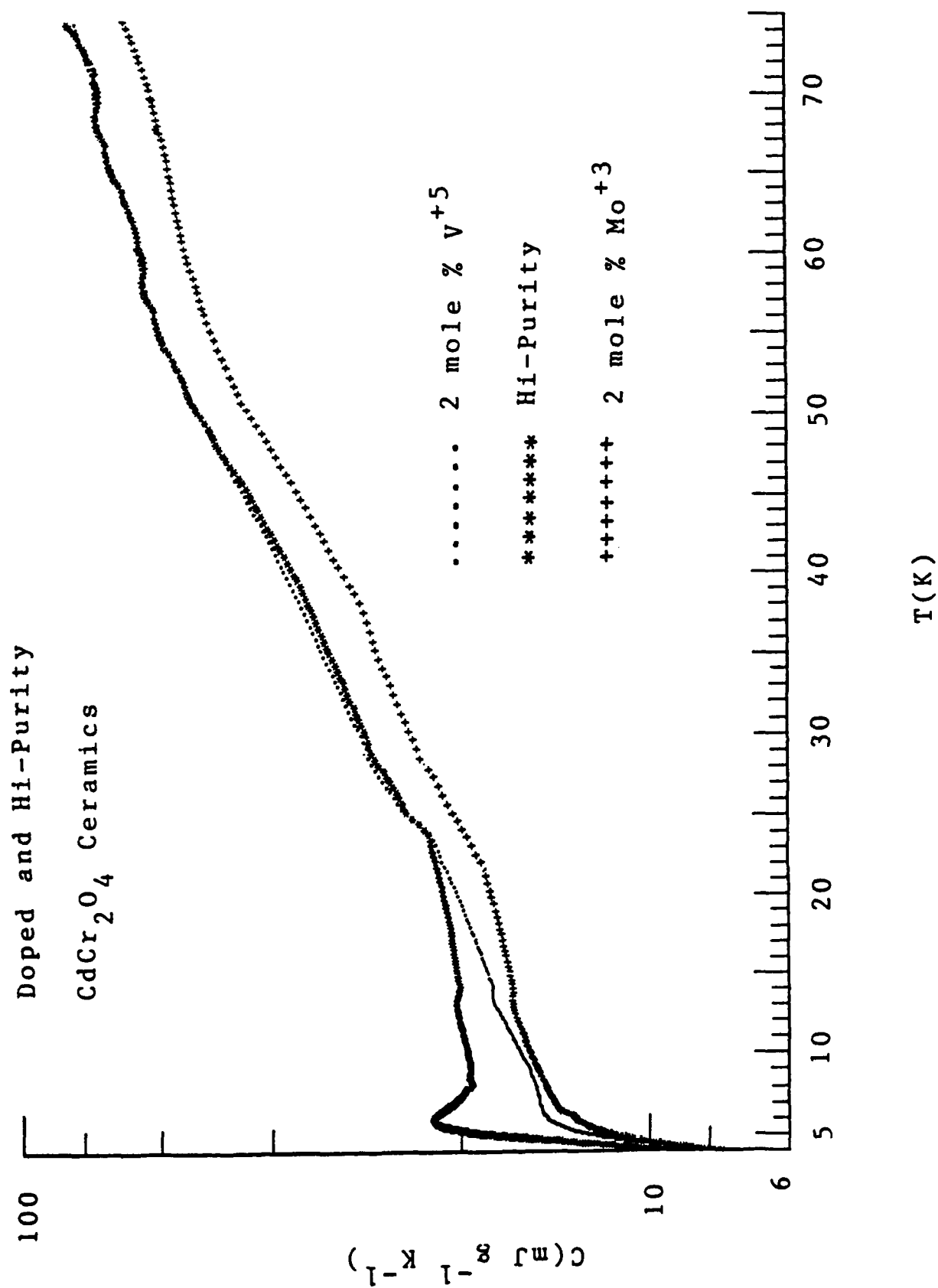


FIGURE 22

Doped and Hi-Purity
CdCr₂O₄ Ceramics

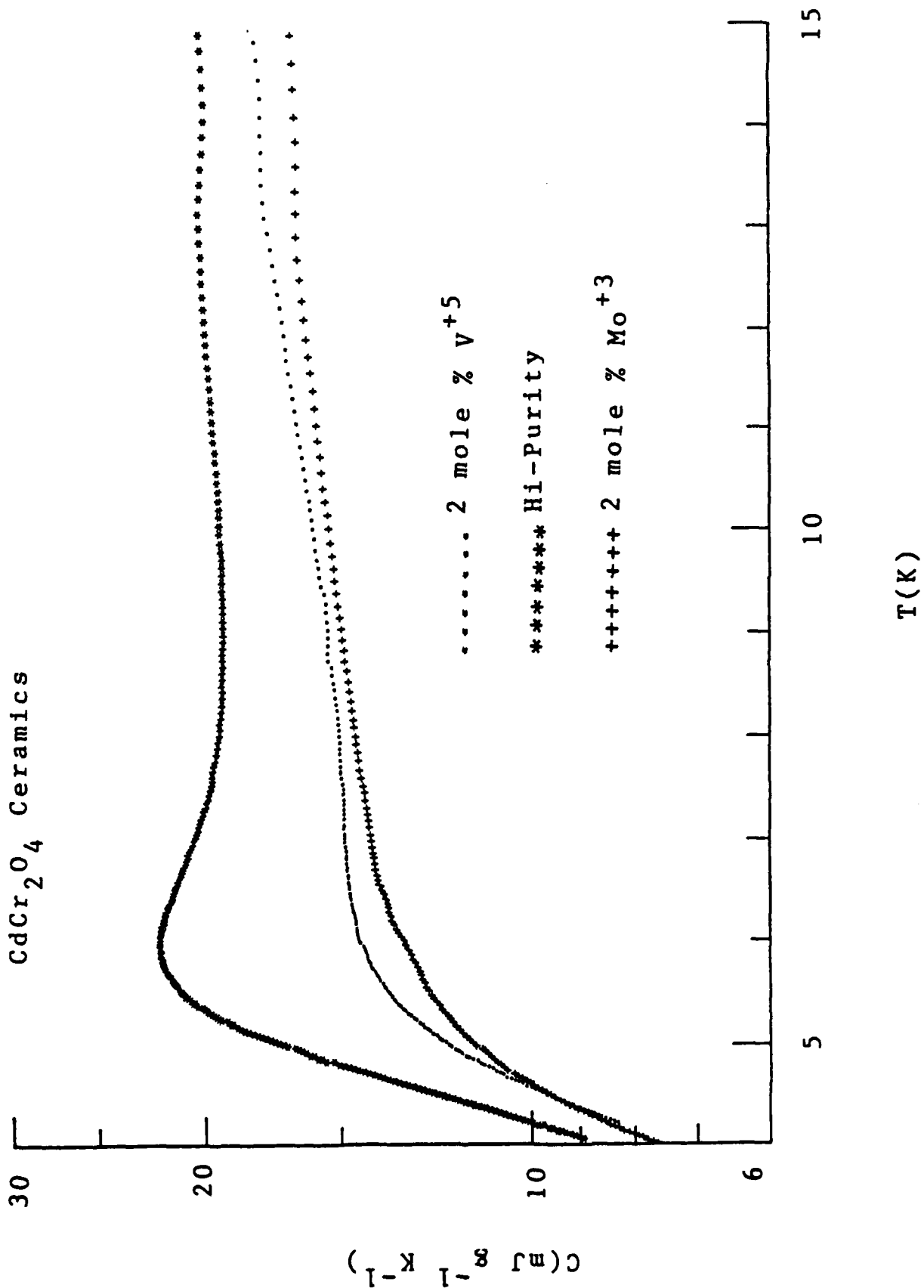


FIGURE 23

ZnCr_2O_4 are shown in Fig. 24 for the 4-75 K temperature range and in Fig. 25 for the 4-17 K range. Data for the compacted sample of undoped ZnCr_2O_4 are shown in Figs. 24 and 25 for comparison.

The splitting of the peak by the dopants is clearly seen in the lower-temperature data in Fig. 25, and it is interesting to observe that the intermediate V^{+5} dopant leads to a peak at the same temperature as the peak of the undoped compacted sample. We also draw attention to the fact that the second peaks in the doped samples all occur at about 12 K.

We are left with the surprising conclusion that the spin of the dopant on the B-site is immaterial in the splitting of the low-temperature specific heat peak and does not lead to higher temperature transitions.

A certain connection can be drawn between the doped samples in Fig. 25 and the undoped samples in Fig. 17. Namely, the transition temperature of the high-purity sample of ZnCr_2O_4 in Fig. 17 is 12 K, whereas the Compacted sample in Fig. 17 has a transition at about 9 K. Consequently, the double maxima for the doped samples in Fig. 25 appear to be super-positions of the maxima in Fig. 17 for the undoped samples. Entropy estimates here would prove illuminating (see below).

Sulfurized ZnCr_2O_4

The inability of the dopants in Figs. 24 and 25 to raise the transition temperature of ZnCr_2O_4 is surprising and led to an alternate suggestion: It is well known that replacing oxygen with sulfur in normal spinels generally leads to a dramatic increase in the transition temperature.

Consequently, a ceramic of ZnCr_2O_4 was prepared from nominally pure powders (similar to the compacted sample in Figs. 16 and 17) and subsequently subjected to an H_2S sulfurizing atmosphere for 60 h at 920°C. Substantial grain growth was observed after sulfurization, and from color and weight changes it was concluded that a nearly complete exchange of sulfur for oxygen had taken place. The analogous CdCr_2O_4 case was not

Doped ZnCr_2O_4 Ceramics

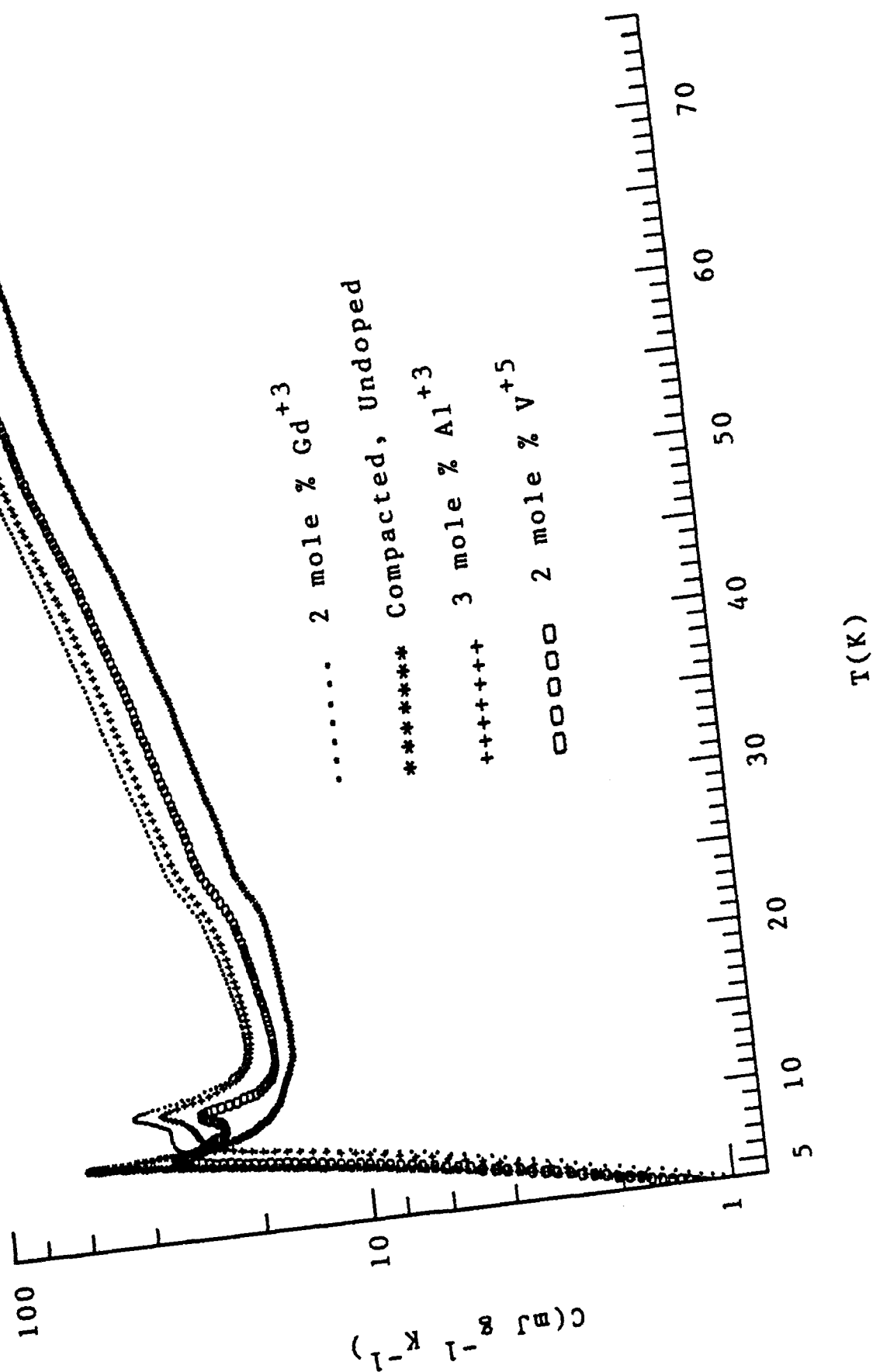


FIGURE 24

Doped ZnCr_2O_4 Ceramics

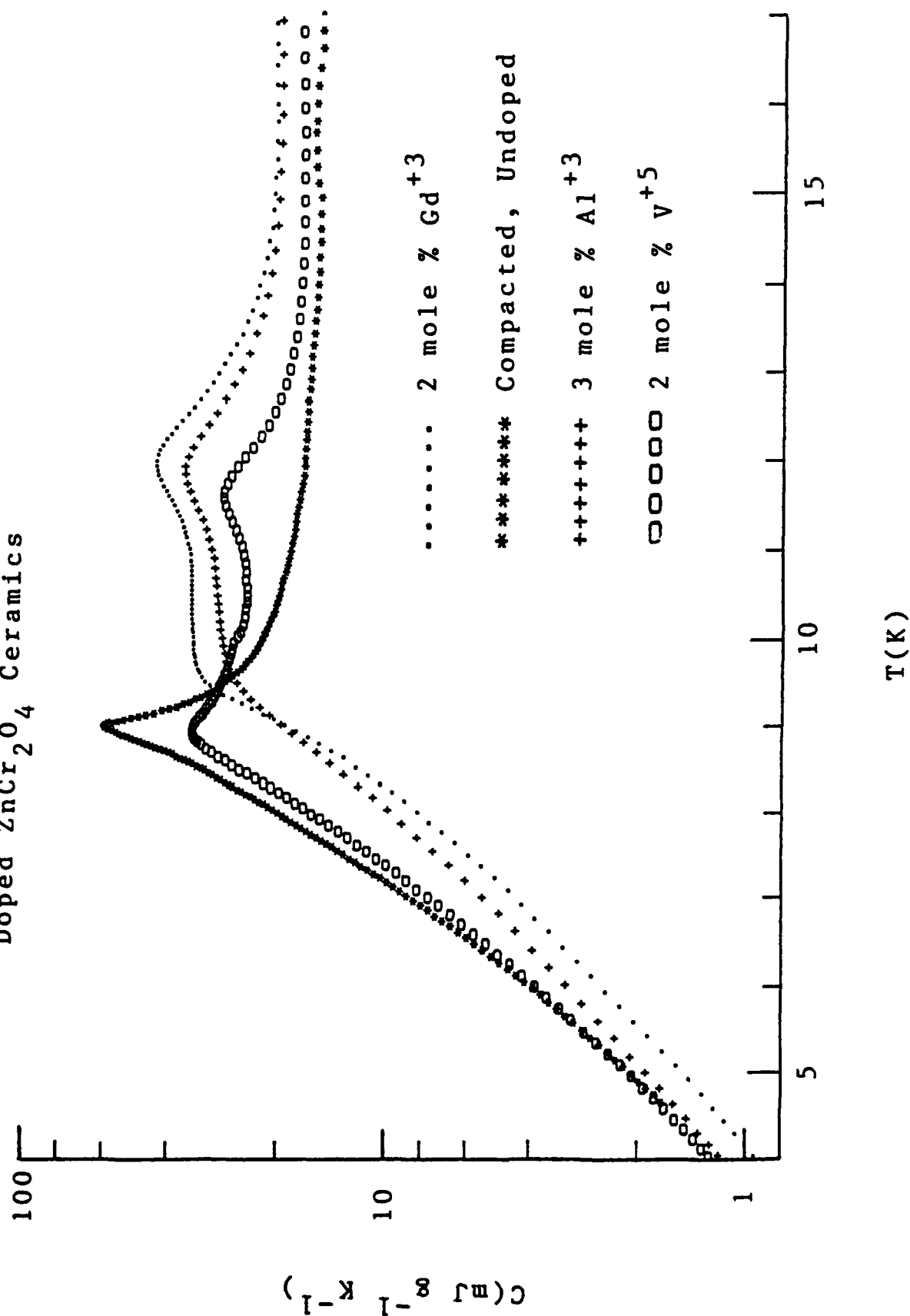


FIGURE 25

pursued due to anticipated loss of cadmium.

Specific-heat data on this sulfurized sample of ZnCr_2O_4 are shown in Fig. 26 for the 4-75 K temperature range and in Fig. 27 for the 4-13 K range. Data for the analogous Compacted sample of ZnCr_2O_4 are also shown in Figs. 26 and 27 K.

The Fig. 26 data show that higher temperature transitions in ZnCr_2O_4 are not induced by sulfurization; rather, a double maxima is induced around 9 K, as seen in Fig. 27, similar to the effects of the various dopants displayed in Fig. 25.

Conclusions from Doping/Sulfurization Studies

A surprisingly rich picture emerges from these measurements:

1. The CdCr_2O_4 spinel has low-temperature properties that are delicately dependent upon impurity levels. Under restrictive conditions, a specific-heat maximum occurs at 8 K, and once these conditions are undermet or overmet, no specific heat features occur up to 75 K.
2. The ZnCr_2O_4 spinel, by contrast, appears more forgiving in that specific-heat features are always seen in the range 9-12 K regardless of the impurity or dopant types or levels (see below, also). Also independent of the types or levels of impurities or dopants, no specific heat features are seen at higher temperatures.

STRESSED CERAMIC SERIES

In order to gain further insight into the unusual low-temperature properties of these CdCr_2O_4 and ZnCr_2O_4 spinels, studies of controlled stress effects were undertaken. The original motivation for these studies was the (apparent) maximum observed in Fig. 1(b) for a ZnCr_2O_4 -glass composite. However, as we have seen above, Fig. 13, this maximum is an artifact of the previous metrology (uncalibrated above 25-30 K).

Sulfurized ZnCr_2O_4 Ceramic

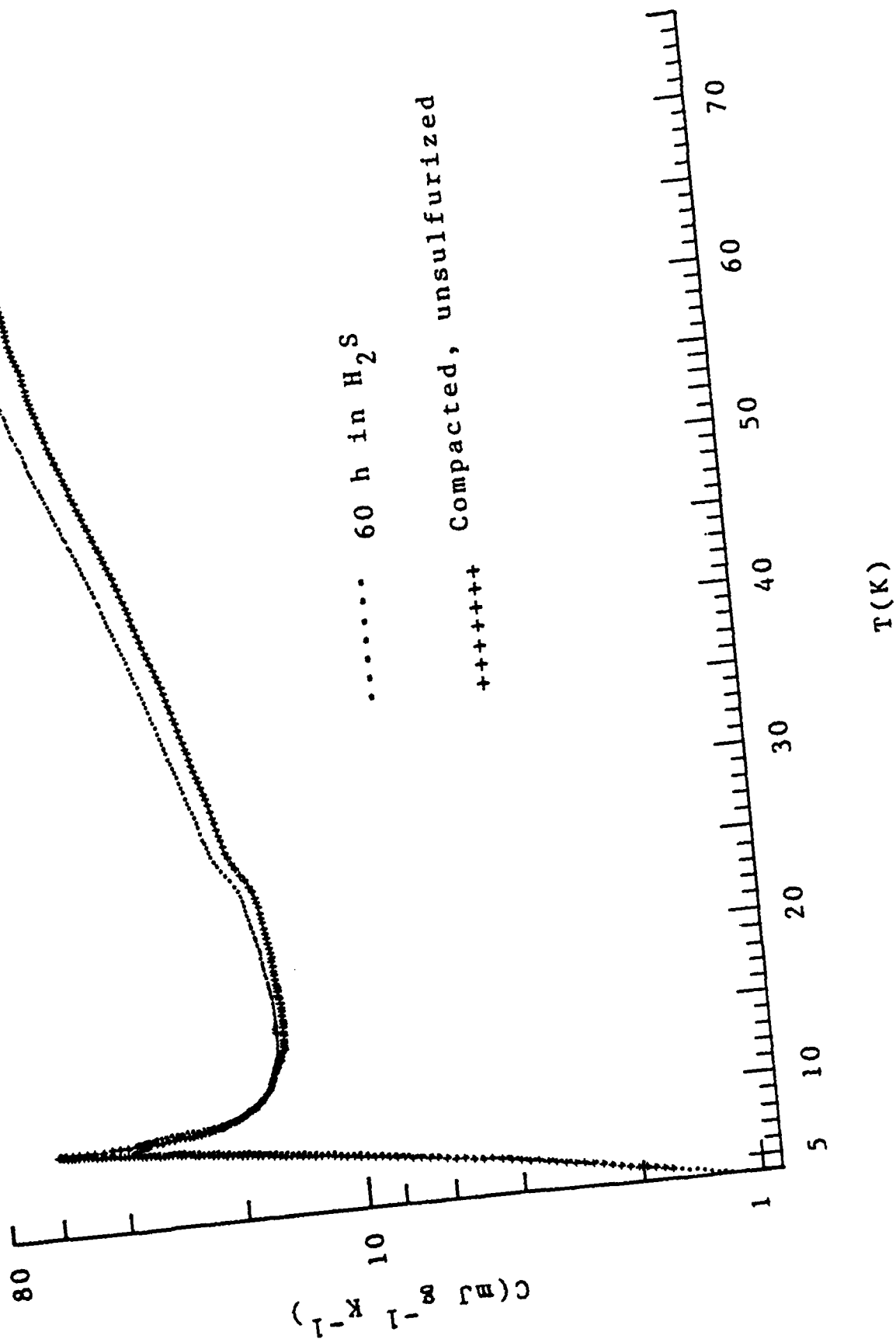
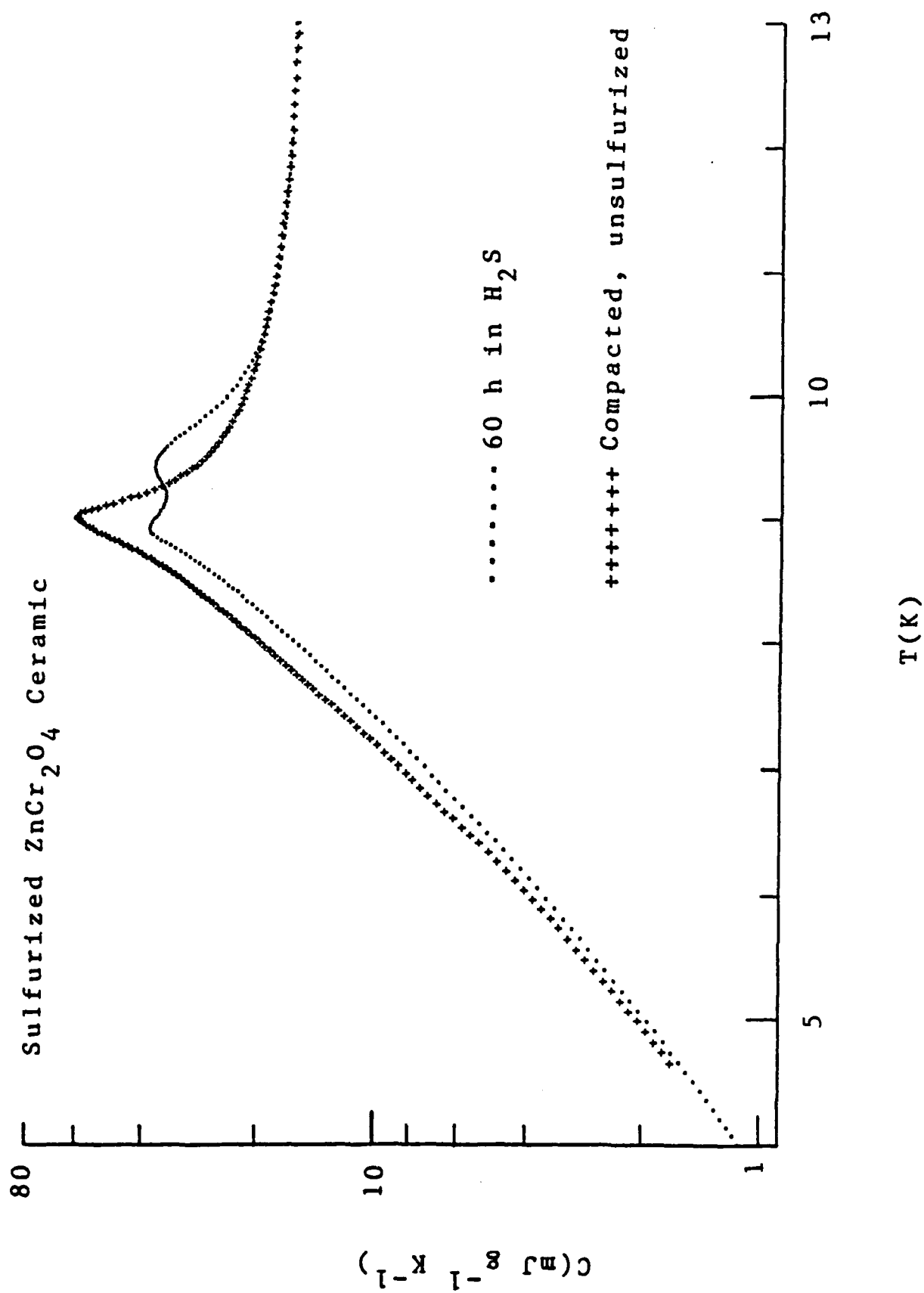


FIGURE 26



Stress effects can be controlled as follows, as mentioned above: Thermal expansion measurements (see below) show that ceramic grains of the spinels are in compression in epoxy composites and in tension in glass composites (The glasses here are Corning 7570 and 7052). Most probably these are hydrostatic stresses if the vol. % of ceramic powder is below about 35%, the connectivity limit. At higher vol. %'s and in the presence of large porosity, the stress levels deviate from hydrostatic to uniaxial.

Complete series of CdCr_2O_4 and ZnCr_2O_4 powders in all of these amorphous matrices over a broad range of filling ratios were unavailable. Rather, in what follows below, we have measured samples available from the applied WPAFB program and from previous programs.

Stressed CdCr_2O_4

Two series of samples were investigated: CdCr_2O_4 in 7570 glass and in an industrial epoxy (Envirotex). The composites here involve both CdCr_2O_4 powders and powders of the two-phase ceramic CCN(9/1) (see above). However, in light of the data in Figs. 14 and 15 we shall assume that these two powders are essentially identical in their low temperature physical properties.

Glass Composites

The three available composites with 7570 were: 50 wt. % CdCr_2O_4 , and 30 and 60 wt. % CCN(9/1). The former composite was prepared at 540°C whereas the latter two composites were prepared at 850°C.

The densities of 7570 glass and CdCr_2O_4 are nearly identical, so the above wt. %'s are approximately the vol. %'s also. This however, neglects the effects of porosity, and density measurements reveal that these composites are about 30 % porous. Consequently, the tensile stresses here are only

approximately hydrostatic.

Specific heat data on these three composites are shown in Fig. 28 over the 4-70 K temperature range and in Fig. 29 over the 4-15 K range. These data reveal the following features:

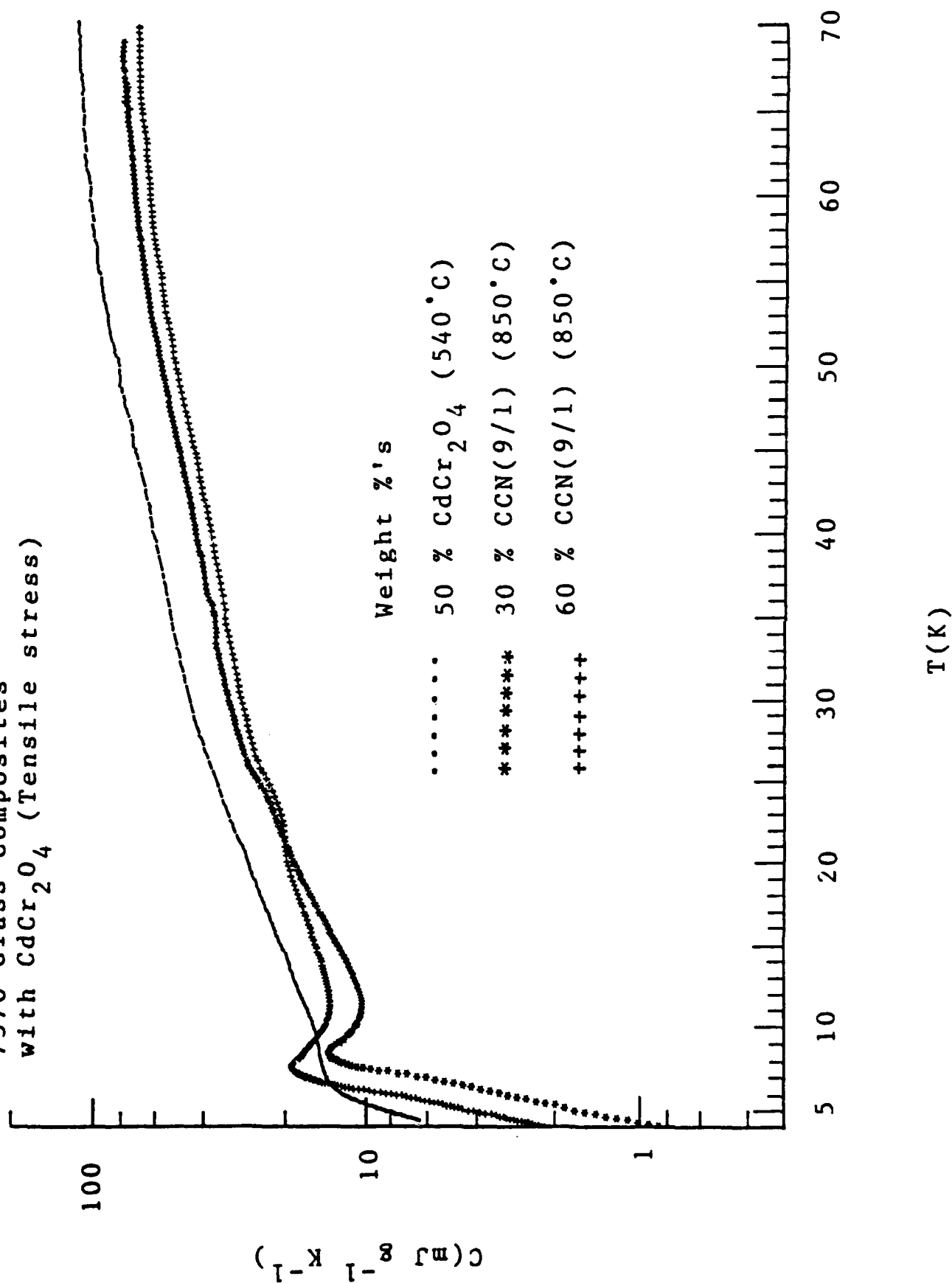
1. Tensile stresses do not induce features in the specific heat above 10 K.
2. The 50% CdCr_2O_4 composite has the largest specific heat 10-70 K but otherwise displays no specific-heat structure near 8 K.
3. The 30 and 60% CCN(9/1) composites have specific heats that order according to the powder contents below 20 K in Fig. 29, suggesting that these powders enter additively into the glass matrix. However, above 20 K in Fig. 28, a reverse ordering of these data is observed.
4. In Fig. 29 the 60% CCN(9/1) composite has a 7.7 K transition whereas the 30% CCN(9/1) composite has an 8.5 K transition. From Fig. 15, the CCN(9/1) ceramic has a transition at 8.0 K

It is surprising that the 50% CdCr_2O_4 composite in Fig. 29 displays no specific-heat structure near 8 K. In light of our findings above we can suggest that the high-Pb glass 7570 introduces too high a level of impurities into the spinel for any specific heat structure to develop (It is, however, surprising that this can happen at the relatively low 540°C).

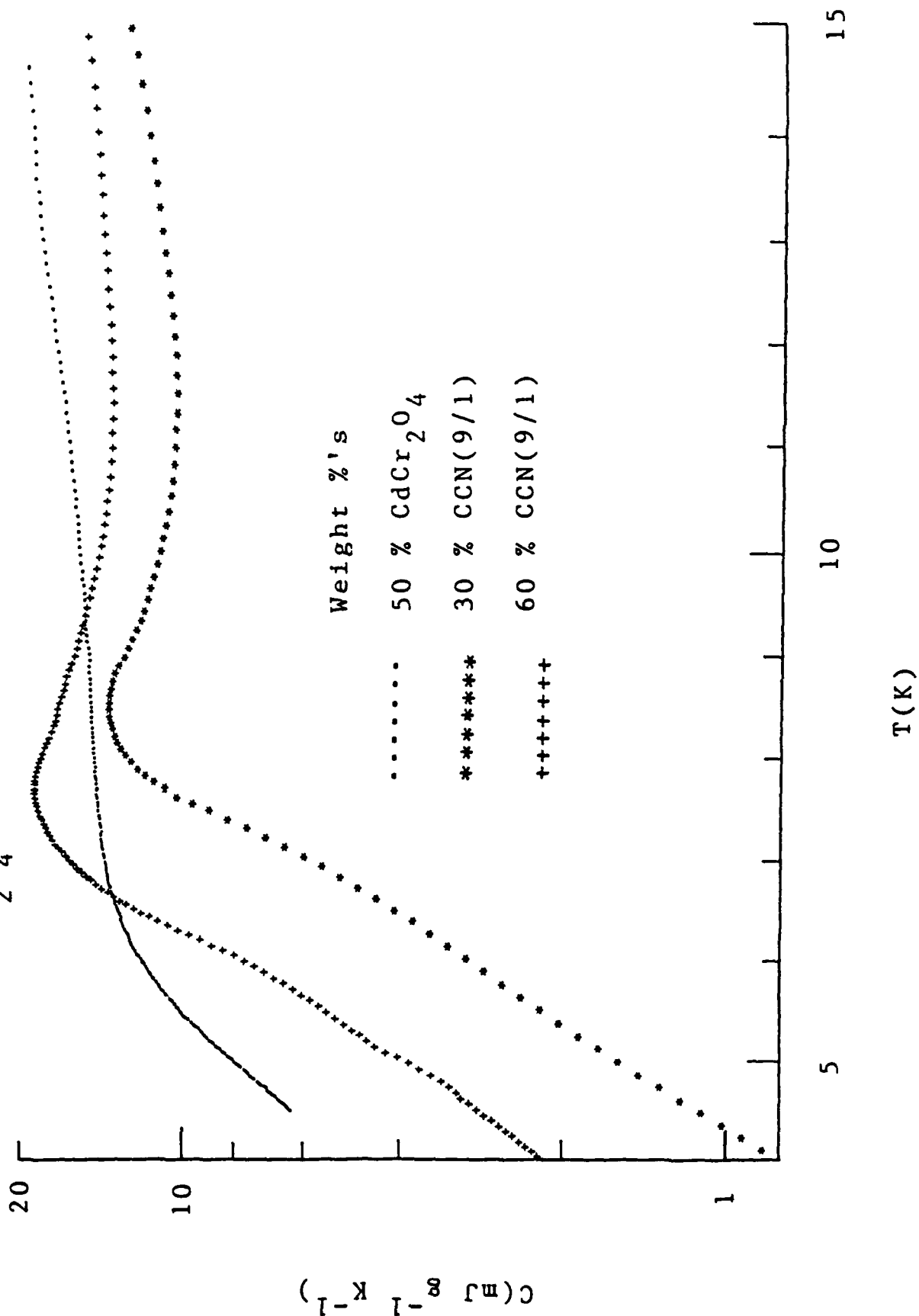
In contrast, the presence of the 10% mineralizer in CCN(9/1) may buffer this ceramic against the incorporation of additional impurities from the 7570 glass, thus leading to the features in Fig. 29. The scaling of these composite data with ceramic powder content supports this conjecture.

The data in Figs. 28 and 29 suggest that stress effects in CdCr_2O_4 are very minor (note that the stress levels here can be huge). Only the 30% CCN(9/1) composite approaches hydrostatic tensile stress, and here the shift of the transition temperature is only about 0.5 K.

7570 Glass Composites
with CdCr_2O_4 (Tensile stress)



7570 Glass Composites
with CdCr_2O_4



Epoxy Composites

Turning next to the epoxy composites with the associated compressive stresses on the ceramic grains, the situation here is more straightforward than in the glass composites, for two reasons: (1) Composites are formed at room temperature where chemical reactions between the epoxy and ceramic powders are negligible; and (2) The porosity levels in the epoxy composites are relatively modest, ~ 10%.

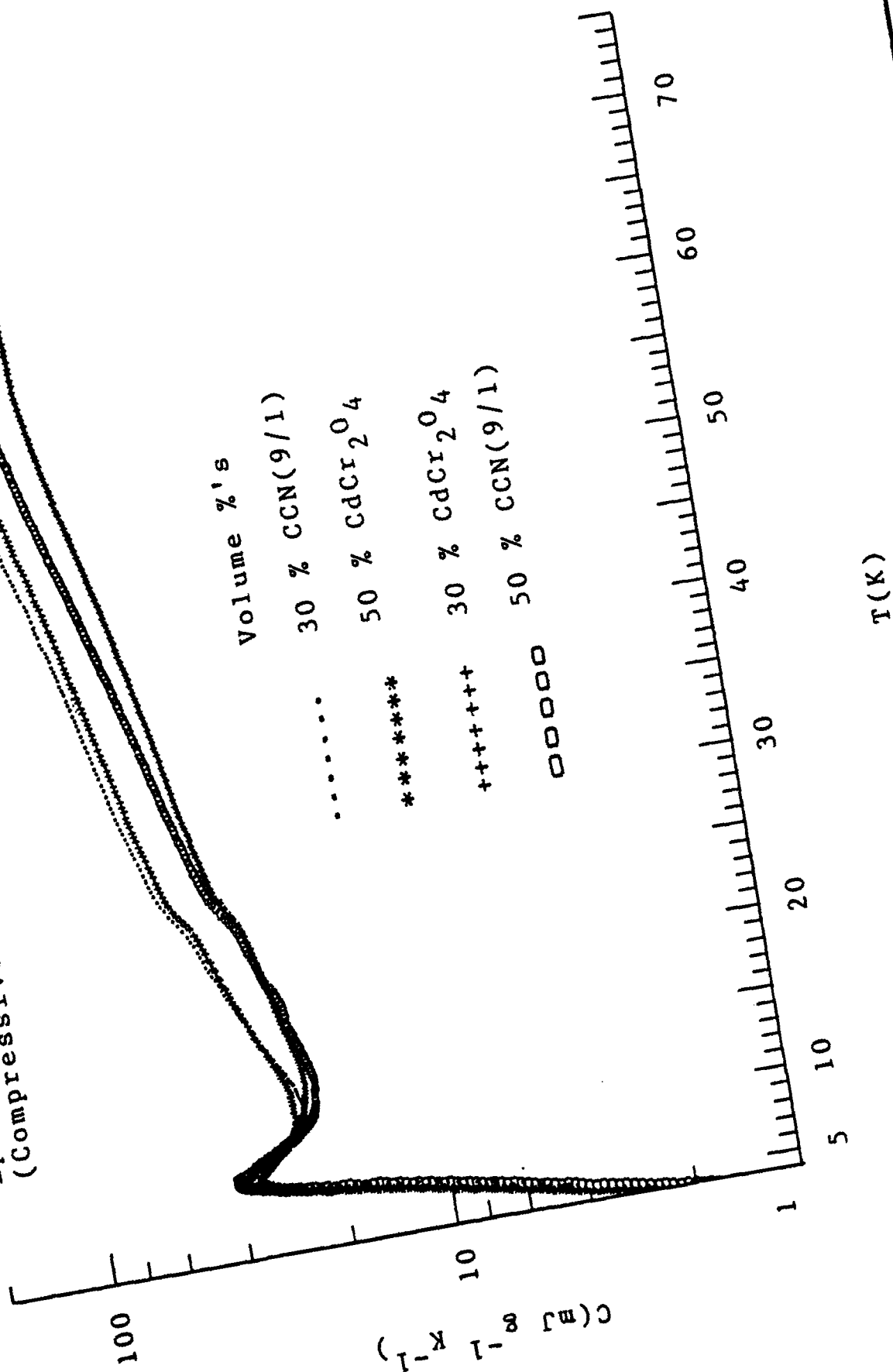
Four epoxy-composite samples were available from a previous program: 30 and 50 vol. % each of CdCr_2O_4 and CCN(9/1) in the same industrial epoxy (Envirotext).

Specific heat data on these composites are shown in Fig. 30 over the 4-75 K temperature range and in Fig. 31 over the 4-16 K range. These data reveal several interesting features:

1. Compressive stresses in CdCr_2O_4 do not induce specific-heat features above 10 K, as was also seen to be the case for tensile stresses above.
2. All composites display specific-heat maxima at 8.5 K in Fig. 31.
3. An unusual ordering of the magnitudes of the specific heats is seen in Fig. 30 above 15 K; namely, for both CdCr_2O_4 and CCN(9/1), the 30 vol. % composites have larger specific heats than the 50% composites--note that based on the additivity of specific heats, exactly the opposite trend would be expected. Along this line, we point out that at the 8.5 K maxima in Fig. 31, the data are ordered proportionally to the ceramic content.

In all of these measurements on composites with CdCr_2O_4 , the only clear correlation found between stress and specific heat is the reverse ordering of the curves above 15 K in Fig. 30 due to compressive stresses and the reverse ordering above 20 K in Fig. 28 for tensile stresses. In the neighborhood of the specific

Epoxy Composites with CdCr_2O_4
(Compressive Stress)



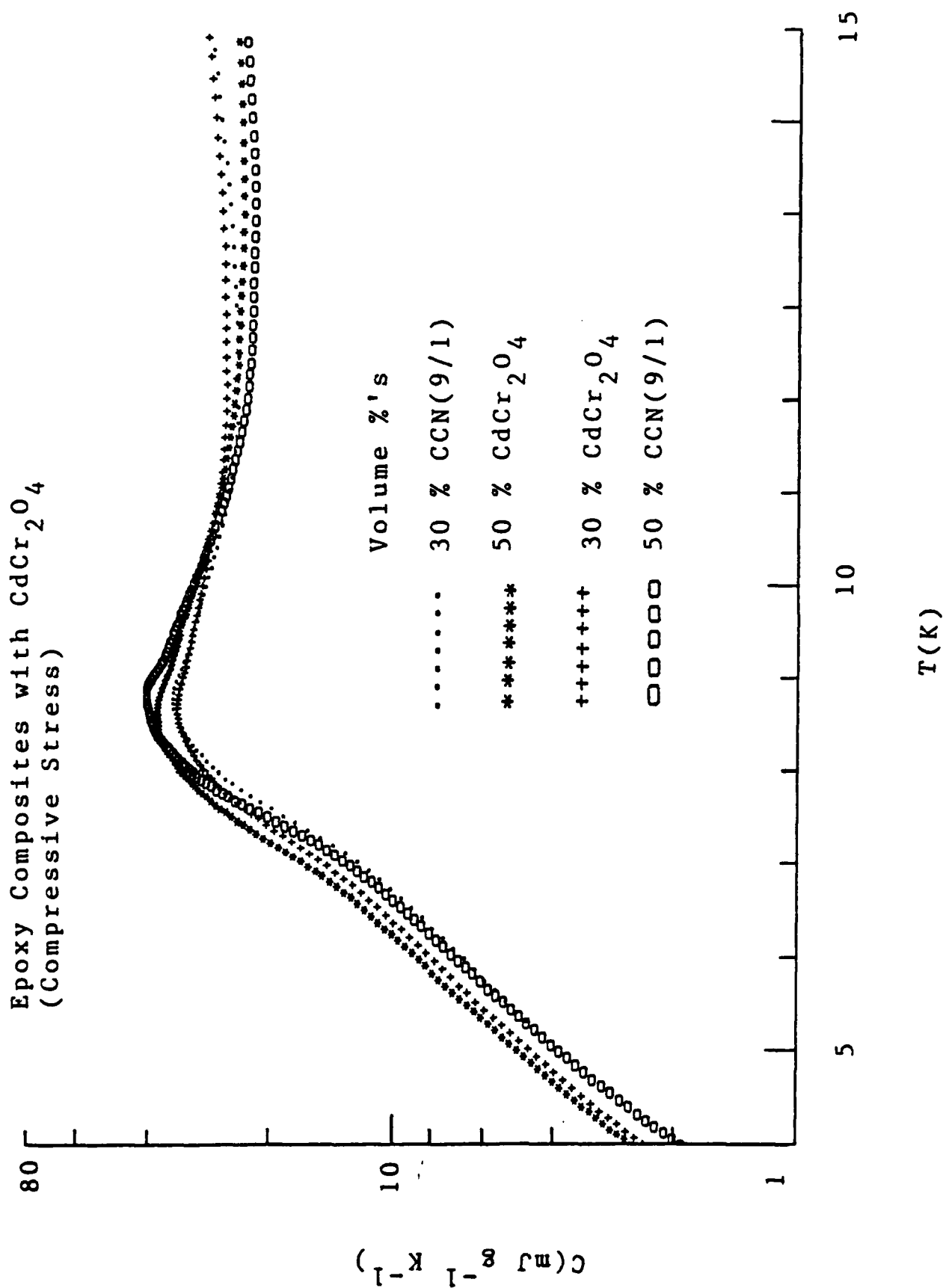


FIGURE 31

heat maxima at about 8-9 K, however, this reverse ordering is not observed.

Stressed ZnCr_2O_4

Two types of glass composites with ZnCr_2O_4 powders were prepared, one with 7570 glass, the other with 7052 glass. In each case, composites were prepared with 30, 50, and 70 wt. % ZnCr_2O_4 . As with the glass composites involving CdCr_2O_4 above, these ZnCr_2O_4 composites had measured porosities ~ 30%. Both the 7570 and 7052 glass matrices result in tensile stresses on the ceramic grains as shown by the previously reported thermal expansion measurements.

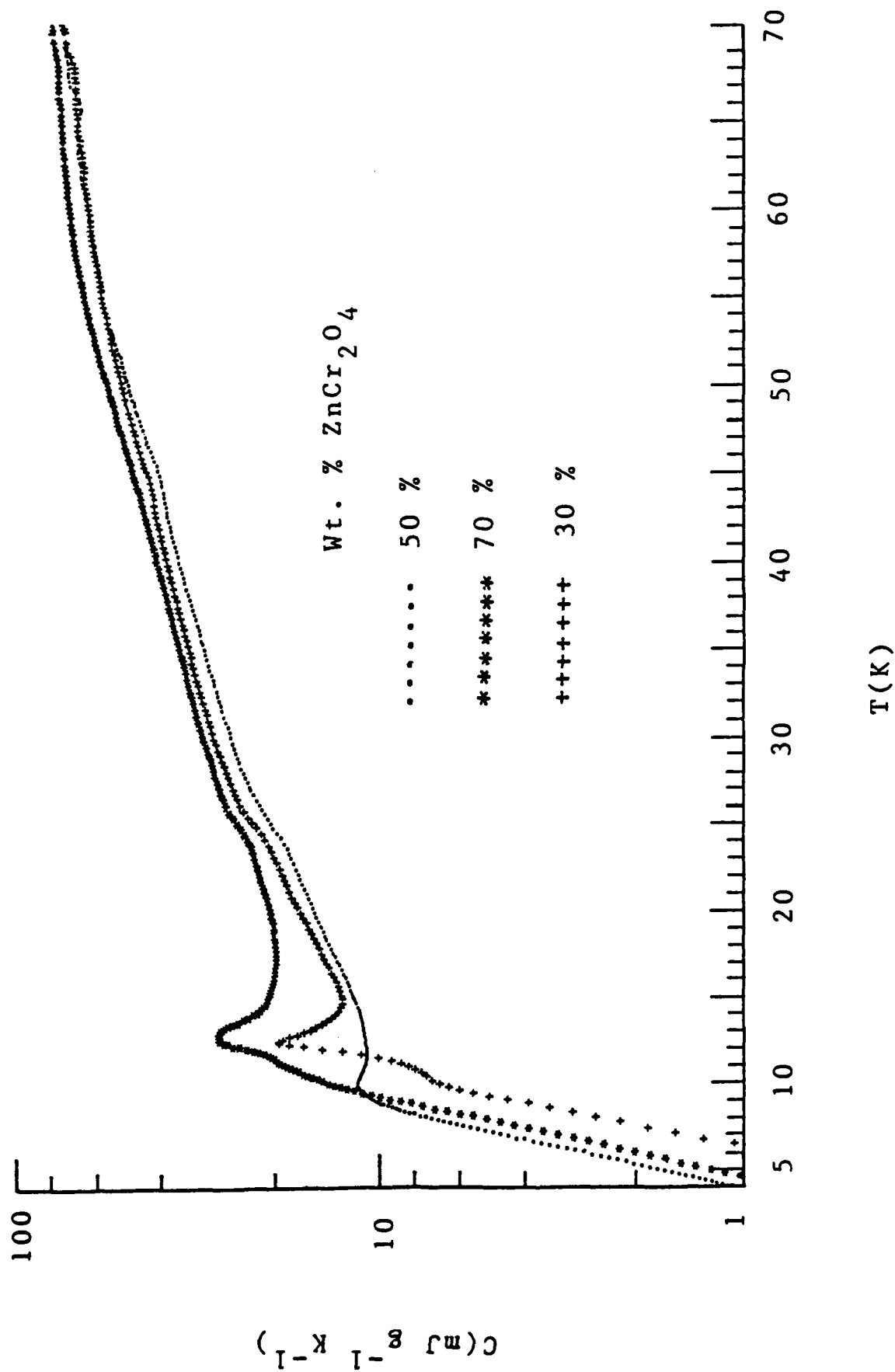
Epoxy composites with ZnCr_2O_4 were unavailable

7570 Glass Composites. The 30, 50, and 70 wt. % ZnCr_2O_4 composites with 7570 glass were formed at 470, 1050, and 950 °C, respectively. As in the case of the glass composites with CdCr_2O_4 , the wt. %'s and vol. %'s are nearly identical for these ZnCr_2O_4 composites, except for the porosity levels noted above.

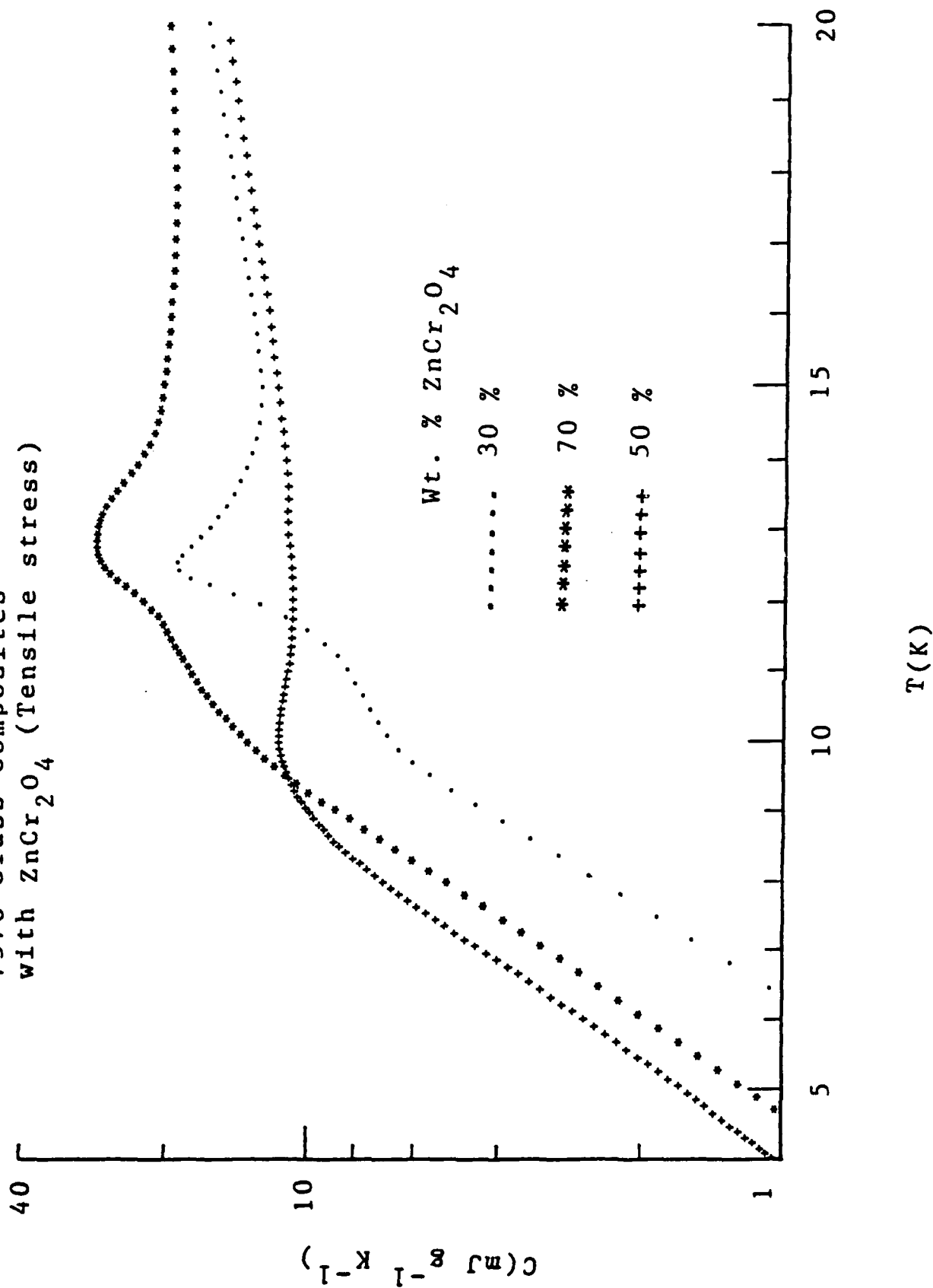
Specific heat data for these composites are shown in Fig. 32 over the temperature range 4-70 K and in Fig. 33 over the 4-20 K range. Here we observe both similarities and dissimilarities compared to the glass composites with CdCr_2O_4 shown in Figs. 28 and 29, as follows:

1. Tensile stresses do not induce any specific heat features above 15 K in ZnCr_2O_4 , Fig. 32.
2. All three composites display specific heat maxima, Fig. 33, but the temperatures of these maxima do not scale proportionally with the ceramic content: 30%, 12.5 K; 50%, 9.7 K; and 70%, 13.0 K. The peak heights in Fig. 33 also do not scale with the powder contents.
3. At the higher temperatures in Fig. 32, the data for the 70% composite are everywhere the largest in magnitude, whereas there is a reversal for the 30 and 50% composite data up to about 50 K. We have seen this reversal

7570 Glass Composites
with ZnCr_2O_4 (Tensile stress)



7570 Glass Composites
with ZnCr_2O_4 (Tensile stress)



effect for the CdCr_2O_4 composites above (Figs. 28-31).

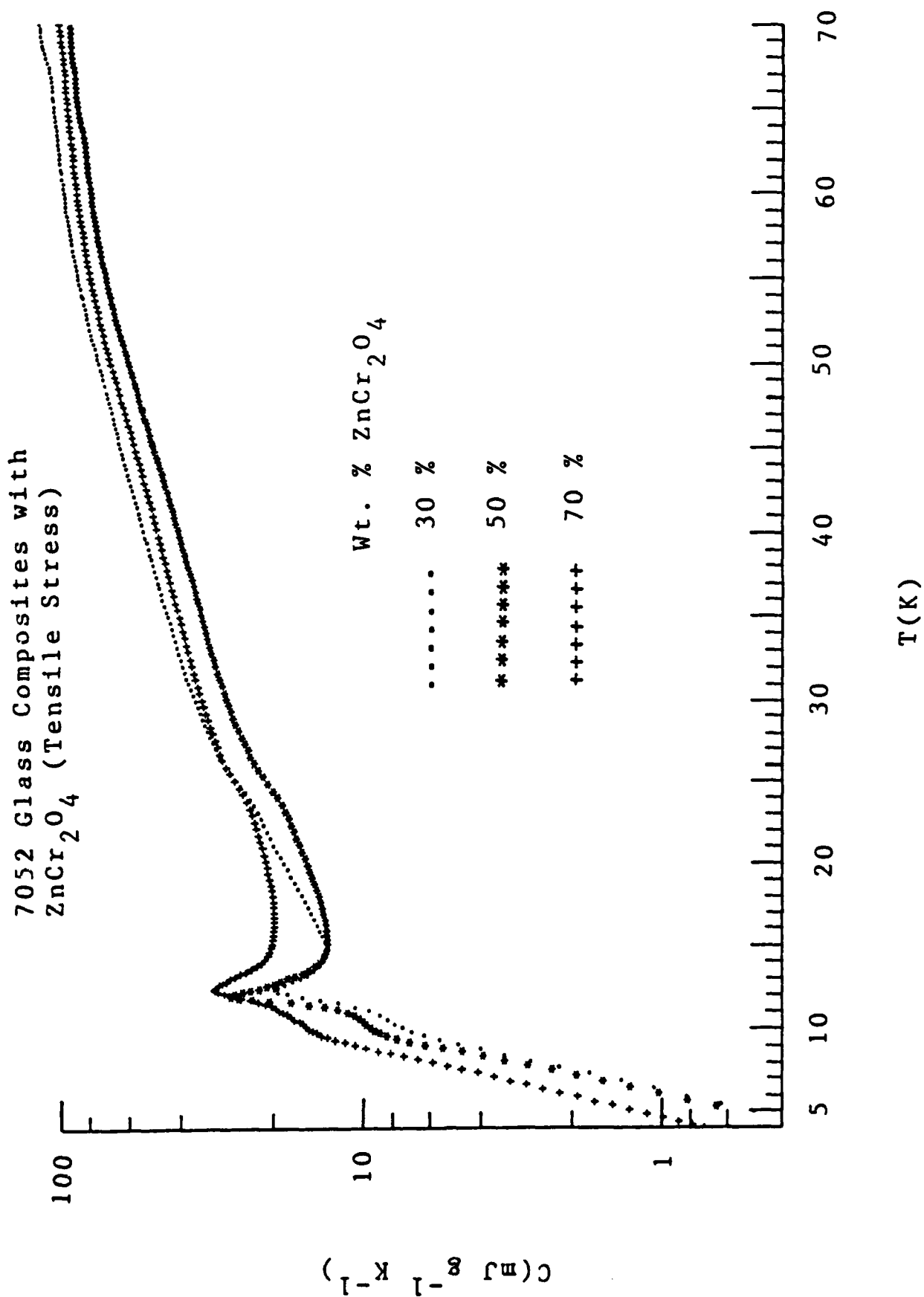
Perhaps the most striking feature of these data for the ZnCr_2O_4 composites is seen in Fig. 33--namely, the suggestion of incipient double maxima for the 30 and 70% composites and the near quenching of the maximum for the 50% composite. These effects may be due either to tensile-stress phenomena or to impurities entering the ZnCr_2O_4 from the 7570 glass matrix (note that the 50% composite was prepared at the highest temperature). The evidence to date suggest the latter, but the data on composites with the 7052 glass below shed light on these phenomena.

7052 Glass Composites. The 30, 50, and 70 wt. % ZnCr_2O_4 composites with 7052 were all prepared at 800°C for 4 h, and as with the 7570 composites above the porosity levels in these composites were about 30%.

Due to the large difference in density between ZnCr_2O_4 (5.367) and the 7052 glass (2.28), the 30, 50, and 70 wt. %'s of ZnCr_2O_4 correspond to 15.4, 29.8, and 49.8 vol. %'s, respectively. However, these vol. %'s are substantially decreased by the large porosity levels.

Specific heat data for these ZnCr_2O_4 composites with 7052 are shown in Fig. 34 over the 4-70 K temperature range and in Fig. 35 over the 7-17 K range. There is a striking similarity between Figs. 32 and 34 and between Figs. 33 and 35 for the 7570 and 7052 composites, respectively, and we can draw the following comparisons between these sets of composites:

1. Tensile stresses arising from the 7570 matrix (Fig. 32) and from the 7052 matrix (Fig. 34) do not induce specific heat features above 20 K, despite the broad range of ZnCr_2O_4 vol. %'s represented in these composites.
2. All three 7052 composites display specific heat maxima, Fig. 35, and as with the 7570 composites the peak temperatures do not scale with the ceramic content: 30%, 12.5; 50%, 12.1 K; 70%, 12.5 K. However, the peak



7052 Glass Composites with
 ZnCr_2O_4 (Tensile Stress)

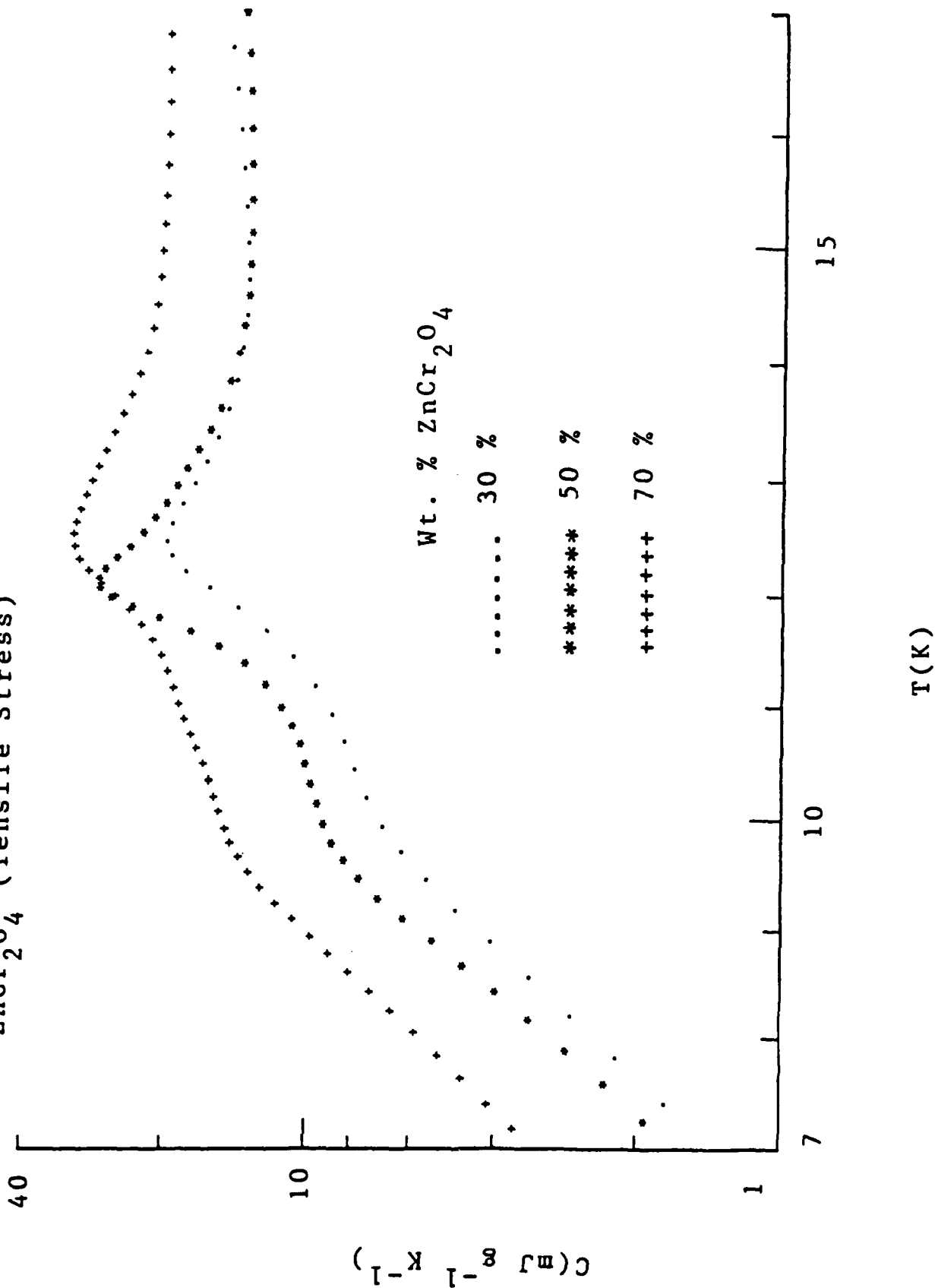


FIGURE 35

heights in Fig. 35 do scale with the ceramic content in contrast to the 7570 composites, Fig. 33.

3. At temperatures above 25 K in Fig. 34, the composite with the lowest ceramic content has the largest specific heat whereas the 50 and 70 % composites are ordered according to the ceramic content. These reversal effects are seen in all composites regardless of whether the stresses are compressive or tensile.

Once again in Fig. 35 we see the same suggestion of imminent double maxima as seen in Fig. 33 for the 7570 composites. However, all 7052 composites in Fig. 35 display clear maxima whereas the 50% composite in Fig. 33 has a very weak maximum.

Conclusions from Stress Studies

In light of the doping studies in ZnCr_2O_4 , we believe that some of the findings on stressed CdCr_2O_4 and ZnCr_2O_4 can be explained in a straightforward fashion.

We begin by comparing the 50 wt. % composites of ZnCr_2O_4 in 7570 and 7052 in Fig. 36, where data for the undoped Compacted ceramic sample are also shown. We propose that impurities from the glass phases are responsible for all specific heat features observed in the CdCr_2O_4 and ZnCr_2O_4 composites near the transition temperatures, as follows:

1. The impurities in ZnCr_2O_4 in the 50% 7052 composite of Fig. 36 have induced the 12 K transition, by comparison with the 12 K upper transitions in Fig. 25 for Gd, Al, and V doped ZnCr_2O_4 . However, these impurity levels may not be large enough to induce the lower transition (see below).
2. In contrast, the impurity levels in ZnCr_2O_4 in the 50% 7570 composite of Fig. 36 may be so large due to the elevated preparation temperature (1050°C) that the transition is quenched, as in the case of doped CdCr_2O_4 in Fig. 23.

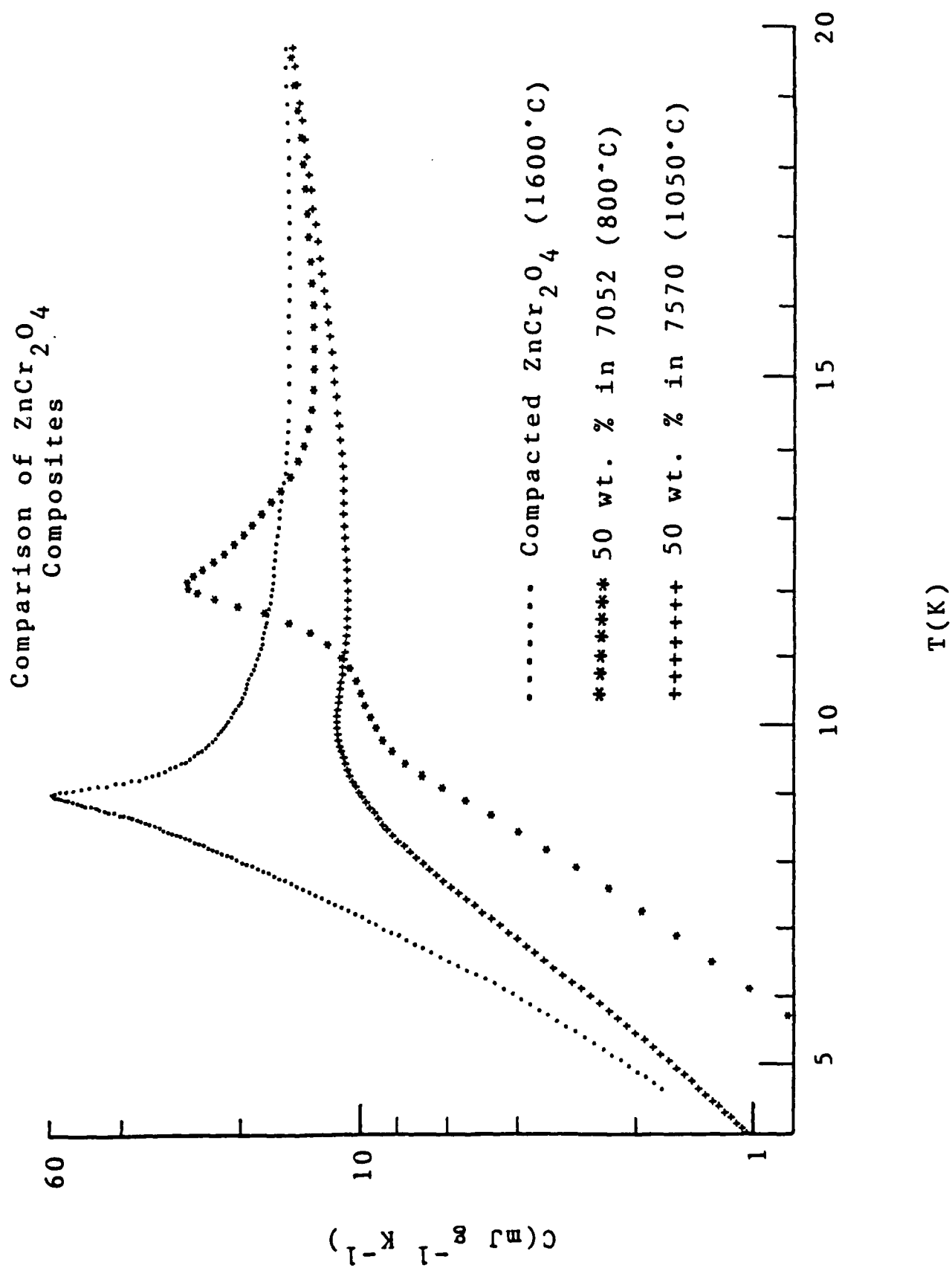


FIGURE 36

3. With the exception of the 50% ZnCr_2O_4 composite in 7570, all other ZnCr_2O_4 composites display maxima at 9-10 K (Figs. 33 and 35). It is appealing to suggest that these lower transitions are quenched by the tensile stresses, but this argument appears implausible in view of the broad range of stresses involved in going from the 15.4 vol. % (30 wt. %) 7052 composite (Fig. 35) to the 70 vol. % (70 wt. %) 7570 composite (Fig. 33). Conceivably, however, some relatively small threshold stress could be involved in quenching these lower transitions (see below).
4. These observations are useful in explaining the findings on the CdCr_2O_4 composites. The absence of any structure in the 50% CdCr_2O_4 composite with 7570 in Fig. 29 is most probably due to impurities from the glass phase. This explanation is fortified by the epoxy-composites data in Fig. 31: Impurities from the epoxy phase are negligible, and all composites display identical behavior (i.e., taking ceramic content into account).

We are left with the conclusion that the low-temperature transitions in CdCr_2O_4 and ZnCr_2O_4 are unaffected by stress, tensile or compressive. Stated differently, no effects have been observed that cannot be plausibly explained as impurity effects.

It deserves mentioning that the stresses involved in these composites are both hydrostatic and partially uniaxial. Only four composites approach hydrostatic conditions--30% composites of CdCr_2O_4 and CCN(9/1) in epoxy, Figs. 30 and 31, and the 30 % composites of ZnCr_2O_4 in 7570 and 7052, Figs. 32-35. In all other cases, the effects of connectivity and porosity result in non-hydrostatic conditions.

Although stress effects do not appear to affect the transitions in CdCr_2O_4 and ZnCr_2O_4 , we have firm evidence that in all composites above 20 K there is a reversal in the ordering of the magnitudes of the specific heat data--i.e., the lower-ceramic-content composites have the largest specific heats. We suggest

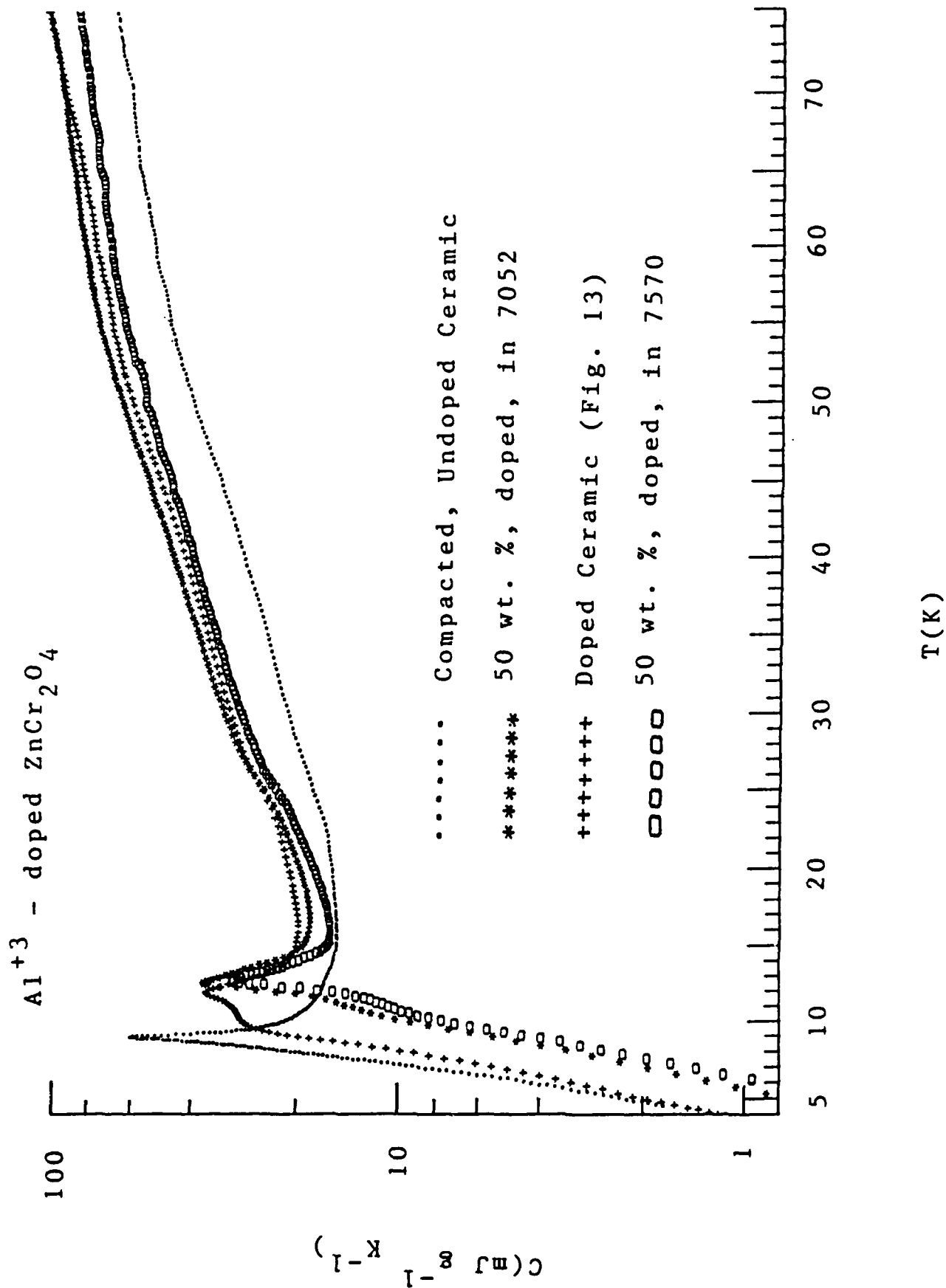
that this may be associated with the changeover from hydrostatic to uniaxial stress conditions, independent of whether the stresses are tensile or compressive.

DOPED AND STRESSED CERAMIC SERIES

In the above sections, specific heat measurements were reported on CdCr_2O_4 and ZnCr_2O_4 in three forms: Pure samples, doped samples, and composite samples. Explanations were put forward to correlate the stress effects seen in composites with the doping effects.

To complete this picture, it was decided to combine the doping and stress effects by putting doped ceramic powders into glass matrices. The ZnCr_2O_4 spinel was selected because dopants at the 2 mole % level do not quench the transition (Fig. 25), in contrast to the CdCr_2O_4 case (Fig. 23).. The Al^{+3} and Gd^{+3} dopants were selected because of the large disparity in spin values ($s=0$ and $7/2$, respectively), and both the 7570 and 7052 glasses were selected for comparison purposes. Ceramic powders of ZnCr_2O_4 doped at the 2 mole % level with Al^{+3} and Gd^{+3} were prepared, and these powders were then used to make composites with the glasses 7052 and 7570 at the 50 wt. % level. Preparation firings were kept at or below 850°C to avoid introducing quenching levels of impurities from the glass phase (as happened with the 50% composite at 1050°C in Fig. 36). The porosity levels in the resulting composites were comparable to those encountered earlier, about 30%.

Broad-range specific heat data for the Al^{+3} and Gd^{+3} doped composites are shown in Figs. 37 and 38, respectively. Also shown are data for the undoped compacted ceramics and for the doped ceramics from Fig. 24. Two features are evident in Figs. 37 and 38: (1) The combined effects of doping and stress do not induce specific heat features above 20 K; and (2) These combined effects do, however, lead to substantially larger specific heats above 20 K compared to the undoped, Compacted ceramic.



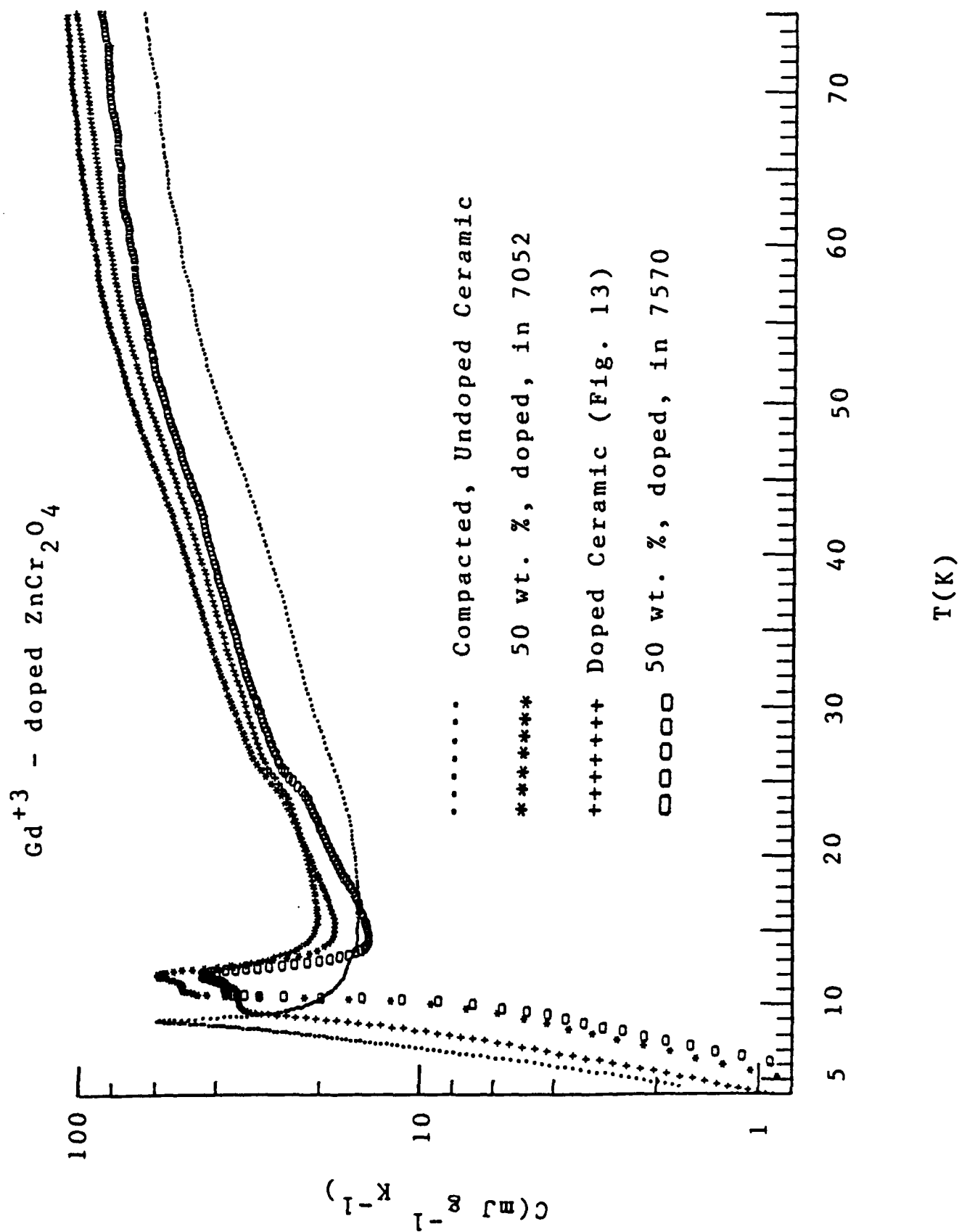


FIGURE 38

This latter effect is particularly noteworthy for the cases of the two 7052 composites which have the largest specific heats above 25 K in Figs. 37 and 38. The point here is that if the additivity rule for the specific heats of components were to apply, one would expect the specific heats of these composites to be one-half that of the undoped, Compacted ceramic (ignoring doping effects). Instead, these composites have specific heats 50 % larger than that of the Compacted sample.

The specific heats of these composites below 20 K are shown in Figs. 39 and 40, again compared to the undoped, Compacted sample and to the doped ceramic samples. Two interesting features are seen in Figs. 39 and 40: (1) The lower transition seen in the Al^{+3} doped ceramic is missing in the doped-and-stressed case of both composites, Fig. 39; and (2) In all cases involving the Gd^{+3} dopant, the double-maxima feature appears. We note in particular that the effect of stress in the composites with 7570 and 7052 in Fig. 40 is to narrow the difference in the two transition temperatures compared to the case of the doped ceramic.

The finding in Fig. 40 that clear double maxima occur in the glass composites disproves the suggestion made above that stress conditions might quench the lower transition in doped ZnCr_2O_4 .

We also draw attention to the features in Figs. 39 and 40 for the 50% 7570 composite which are missing from the analogous, undoped composite in Fig. 36 prepared at 1050°C. This observation supports the suggestion above that in the latter composite the ingestion of impurities from the glass phase quenched the ZnCr_2O_4 transition.

ADDITIONAL BROAD-RANGE MEASUREMENTS

In the above specific heat data, 4-75 K, were reported on about thirty samples of CdCr_2O_4 and ZnCr_2O_4 under a variety of conditions: (1) Pure, undoped samples, including very high purity conditions; (2) Doped samples with broad variations in the spin of the dopants; (3) Stressed samples incorporating both

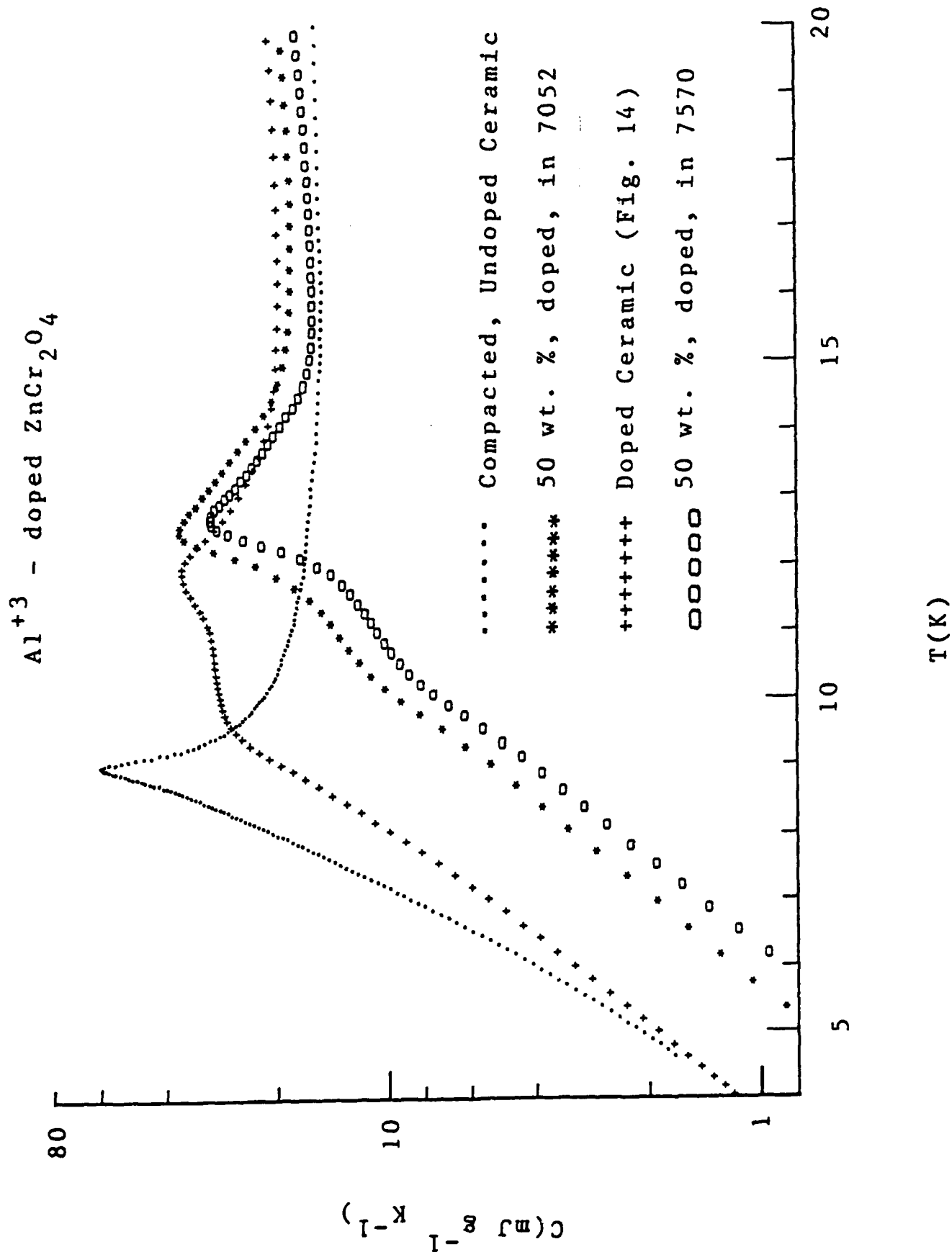
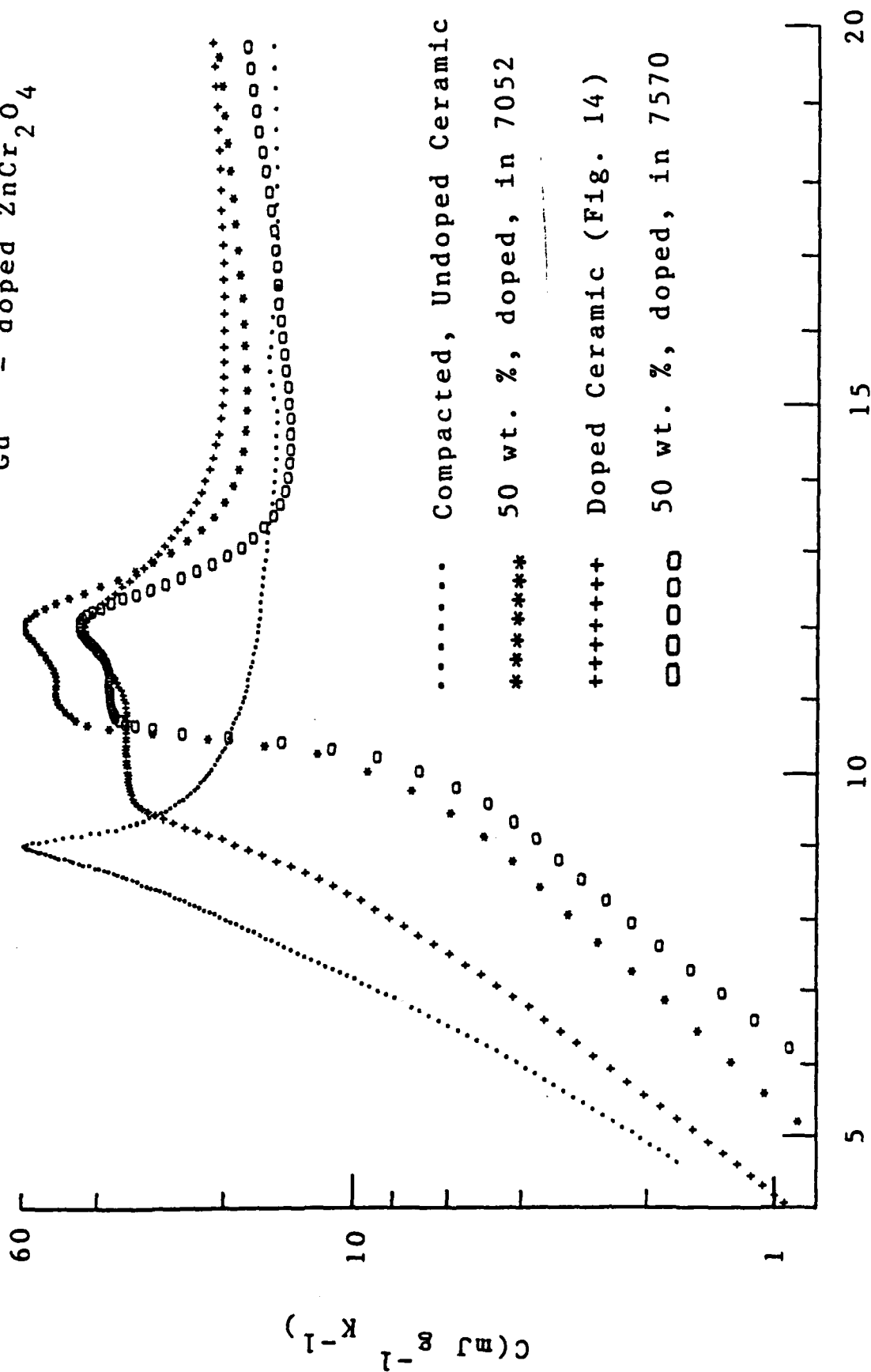


FIGURE 39

Gd³⁺ - doped ZnCr₂O₄



tensile and compressive, hydrostatic and uniaxial stresses; and (4) Combined doping and stress conditions.

This broad survey of these spinels yielded rich and unusual findings: (1) No structures in the specific heats are induced above 15 K by doping or stress; (2) The 8 K C-peak in CdCr_2O_4 is quenched if no impurities are present, whereas the 10.5 K C-peak in ZnCr_2O_4 is not quenched unless large impurity levels are present; (3) At moderate doping levels the C-peak in ZnCr_2O_4 splits into two peaks; (4) The C-peak in the CdCr_2O_4 spinel is unaffected by stress; and (5) The spin densities contributing to the C-maxima in both spinels are nearly independent of doping or stress conditions.

Here we document additional specific heat measurements, 4-75 K, on the ZnCr_2O_4 spinel prepared under the following, new conditions:

1. Hot uniaxially pressed, 1400°C, $\rho = 5.15$
2. Sintered 1650°C, 4 h, in ZnCr_2O_4 sand, $\rho = 4.81$
3. 2 mole % Gd^{+3} doped, sintered 1250°C, 48 h, $\rho = 3.17$
4. 50 wt. % powder in 8161 glass, 900°C, 2 h, $\rho = 3.6$

The rationale for these preparations was as follows: Hot uniaxial pressing leads to both better control of microstructure and improved densification, on the one hand, and sintering in a ZnCr_2O_4 sand minimizes ZnO volatility, on the other hand. The previously studied Gd^{+3} doped ZnCr_2O_4 was sintered for 2 h, and it was felt that this dopant may not have been fully incorporated into the spinel--hence, the 48 h sinter was explored. Finally, the 8161 glass has a larger thermal expansion coefficient (90×10^{-7}) than the two previous glasses used with ZnCr_2O_4 powder (7052, 46×10^{-7} and 7570, 84×10^{-7}). The spinel powders are in tension in these glass composites.

Specific heat data on the hot-uniaxially-pressed sample are shown in Fig. 41. Two maxima occur near 10-12 K, and there are no other features seen up to 75 K.

Specific heat data on the sand-sintered sample are shown in

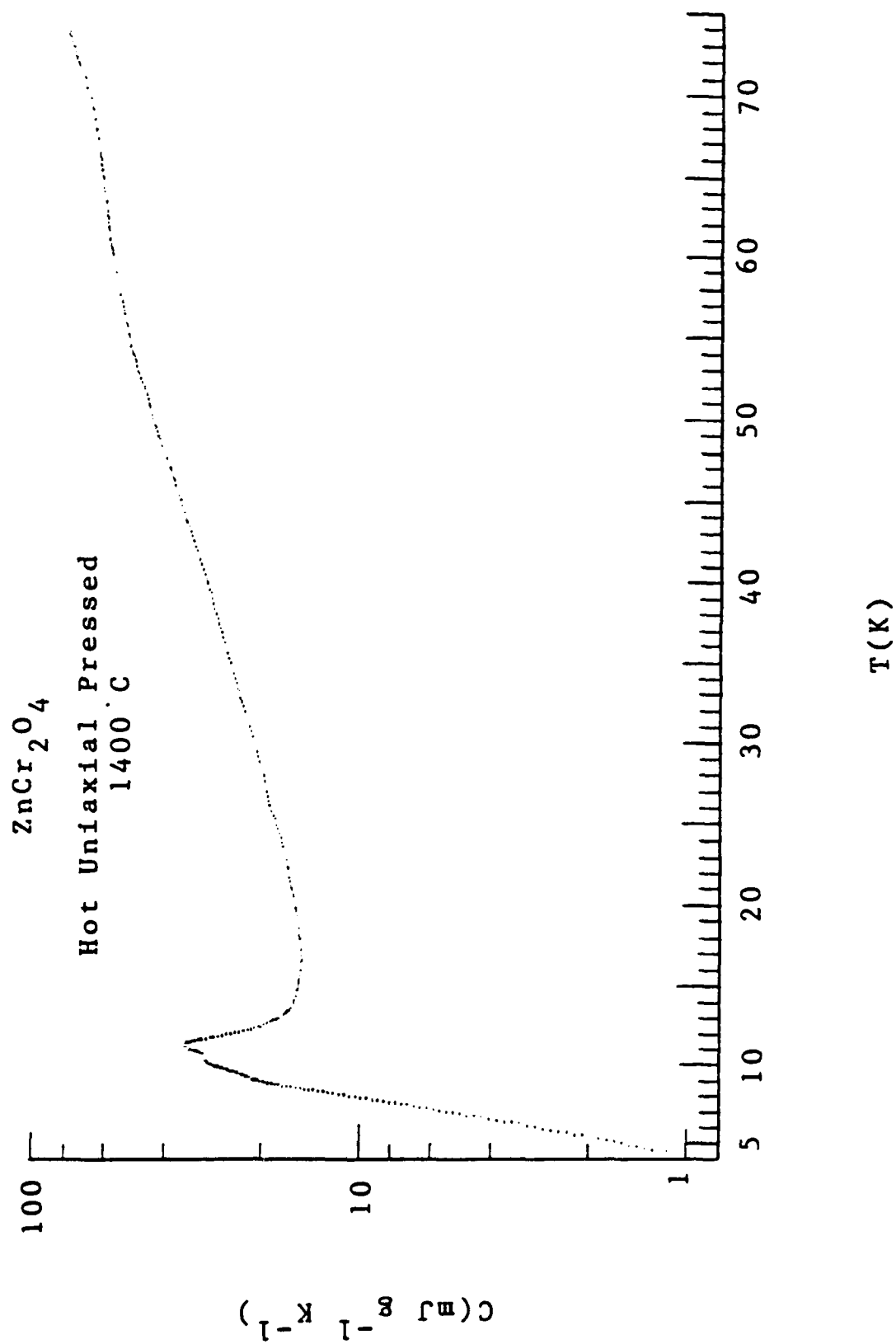


FIGURE 41

Fig. 42. A sharp C-maxima is seen at about 9 K, and a shoulder feature appears at 10-11 K. This shoulder feature was checked with the original data record and is a real feature. No other features appear up to 75 K.

A composite plot of specific heat data in the range 4-16 K is shown in Fig. 43 for the uniaxially pressed sample, the sand-sintered sample, and a compacted sample sintered at 1600°C, 1 h measured previously. These data show little difference between the latter two samples (except for the shoulder at 10 K for the sand-sintered sample). However, the uniaxially pressed sample displays two broad maxima at 10.2 and 11.5 K.

Specific heat data for the 48-h-sintered Gd^{+3} sample are shown in Fig. 44. A double maximum in C occurs near 10 K, but otherwise no structure appears at higher temperatures.

A comparison of the C-data, 4-16 K, for the 2-h and 48-h sintered, Gd^{+3} doped samples is shown in Fig. 45. Both samples show basically the same behavior of double C-maxima but with one interesting difference: There is a reversal of the magnitudes of the maxima between the two samples.

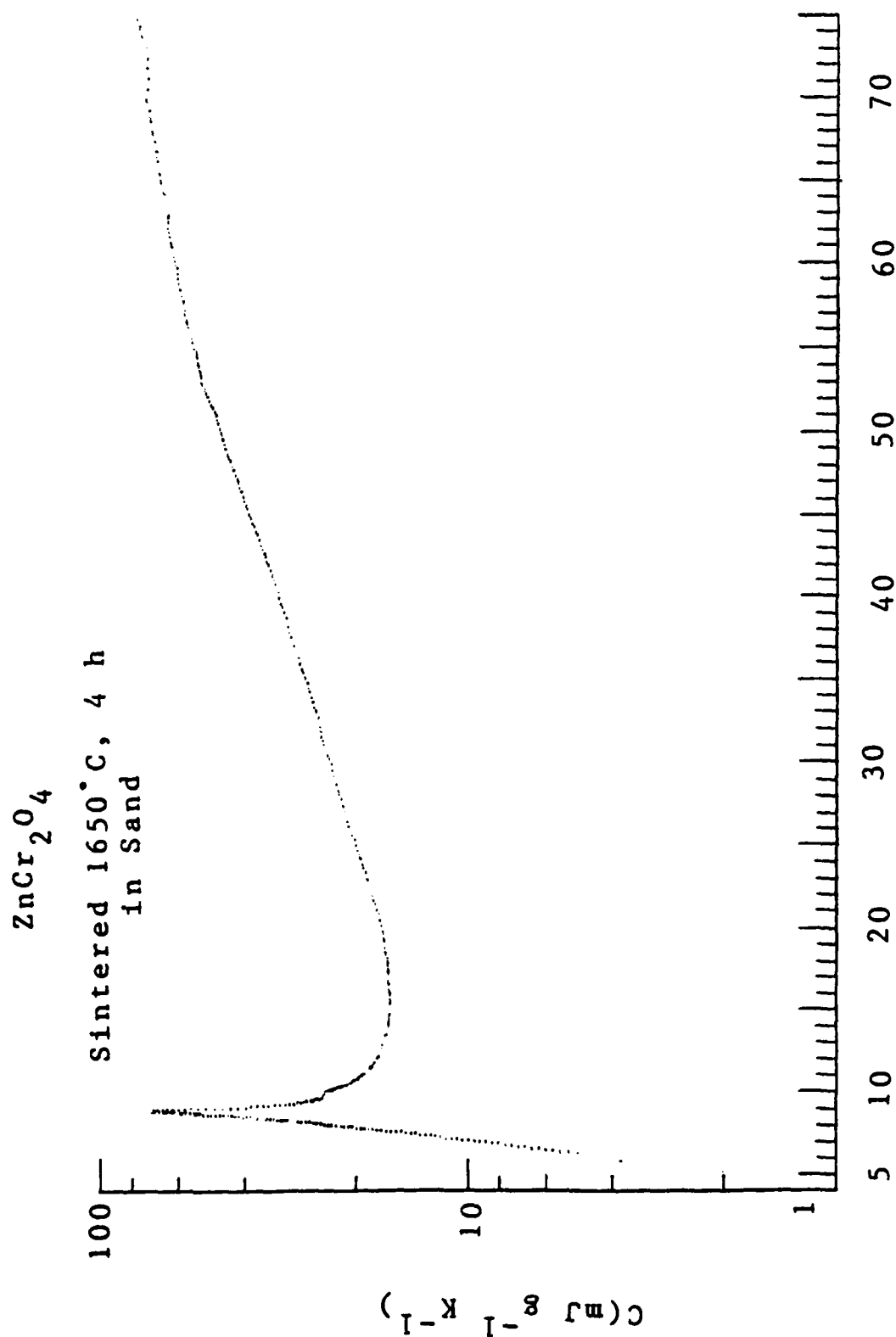
Specific heat data for the 50 wt. % composite with the 8161 glass are shown in Fig. 46, and double maxima are seen around 11 K but no features appear at higher temperatures.

Comparison plots are shown in Fig. 47 for 50 wt. % composites of $ZnCr_2O_4$ in 7052, 7570 and 8161 glasses. The tensile stress on the spinel grains here increases in going from 7052 to 7570 to 8161, but no stress correlations appear in Fig. 47. In fact, it is interesting to observe that the smallest stress (7052) and largest stress (8161) cases are very similar.

We now offer tentative explanations for these new findings based on the previous measurements.

Perhaps the most interesting sample in this set is the uniaxially hot pressed sample which displays double C- maxima, Fig. 43. This is the first case we have encountered of a nominally pure sample of $ZnCr_2O_4$ displaying double maxima.

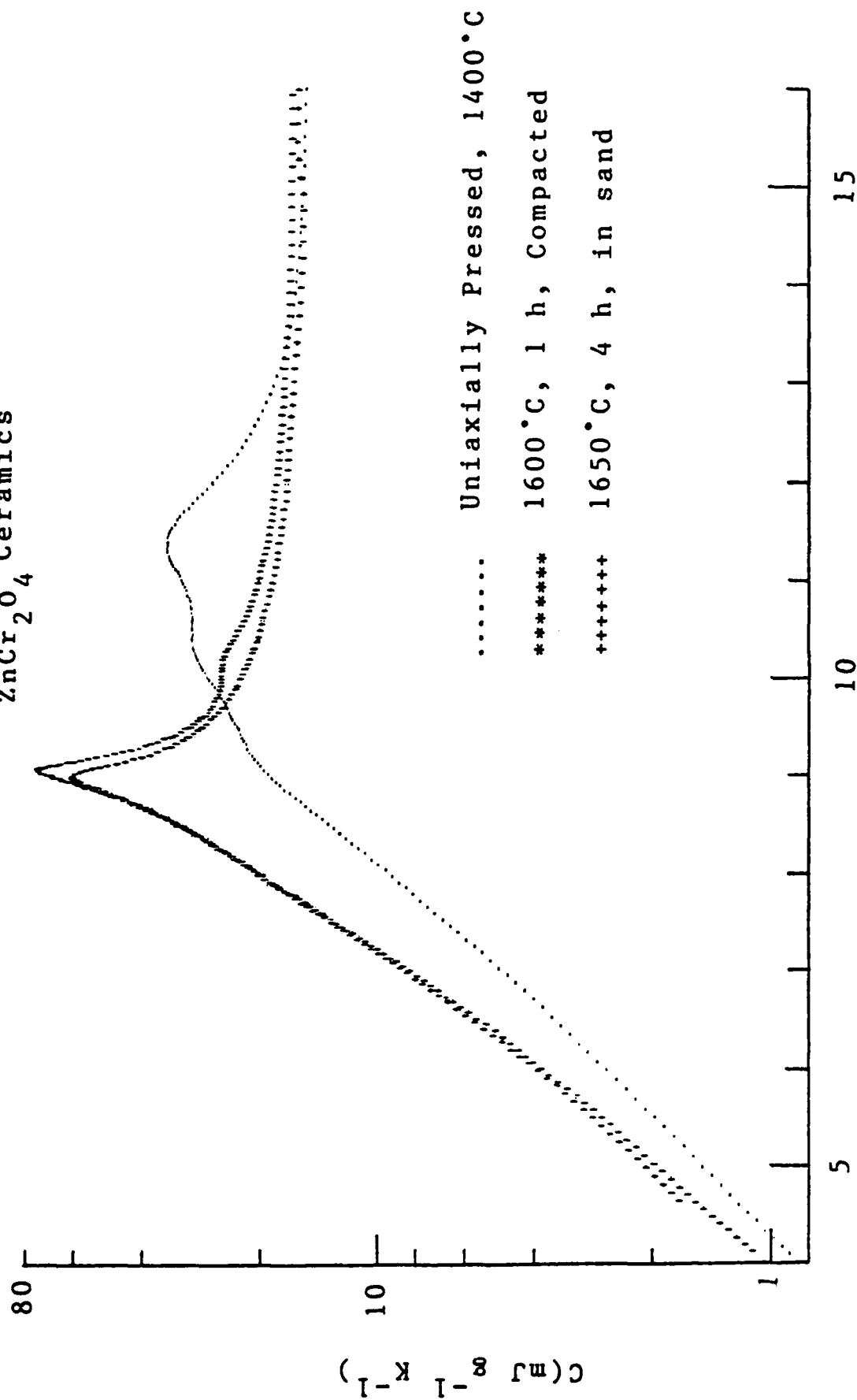
Two phenomena may be occurring in the uniaxially-pressed sample: The hot-pressing operation may (1) result in residual



T(K)

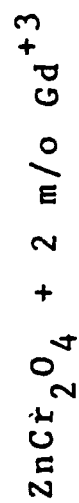
FIGURE 42

ZnCr₂O₄ Ceramics



T(K)

FIGURE 43



1250°C, 48 h

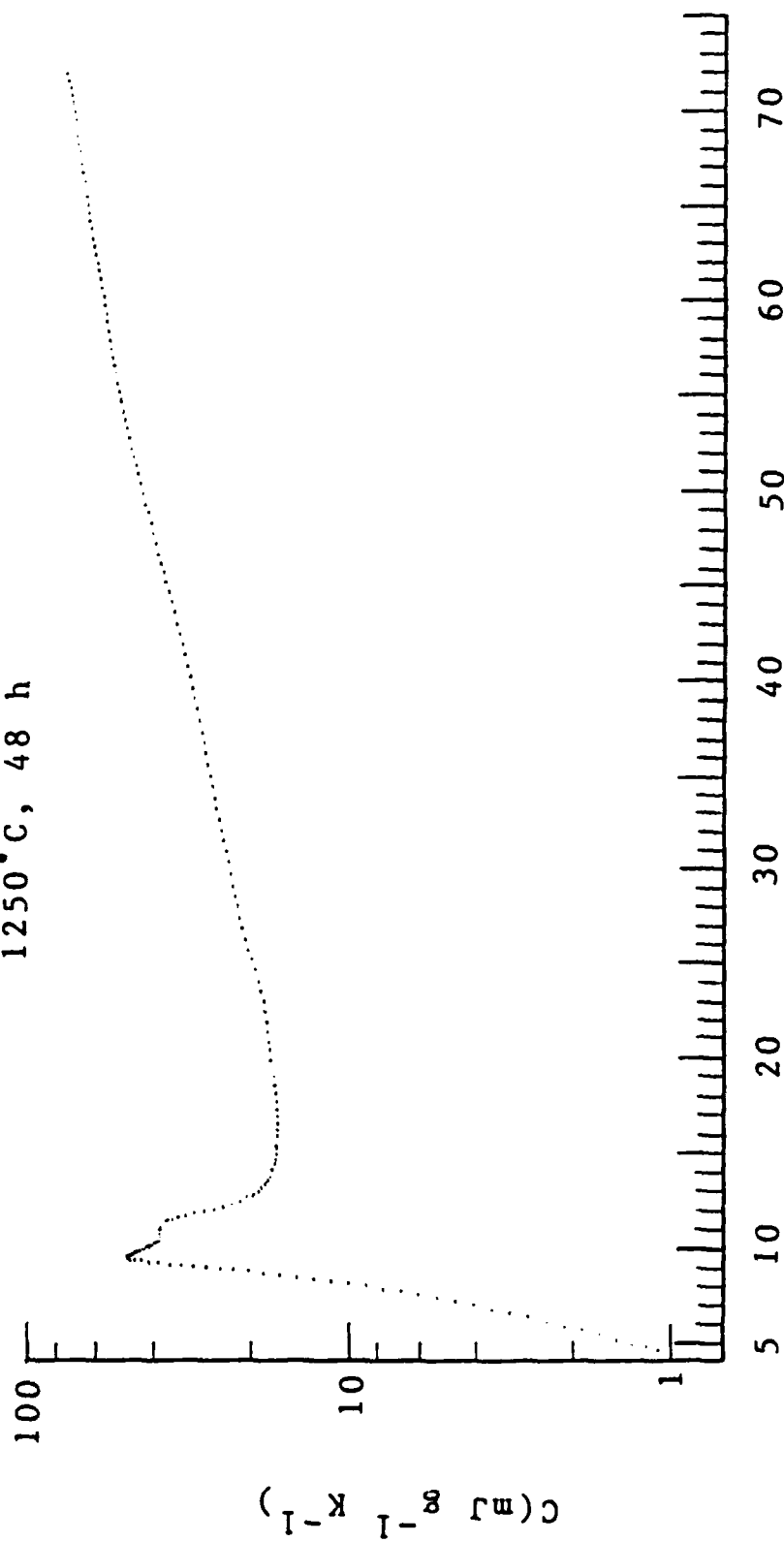


FIGURE 44

T(K)

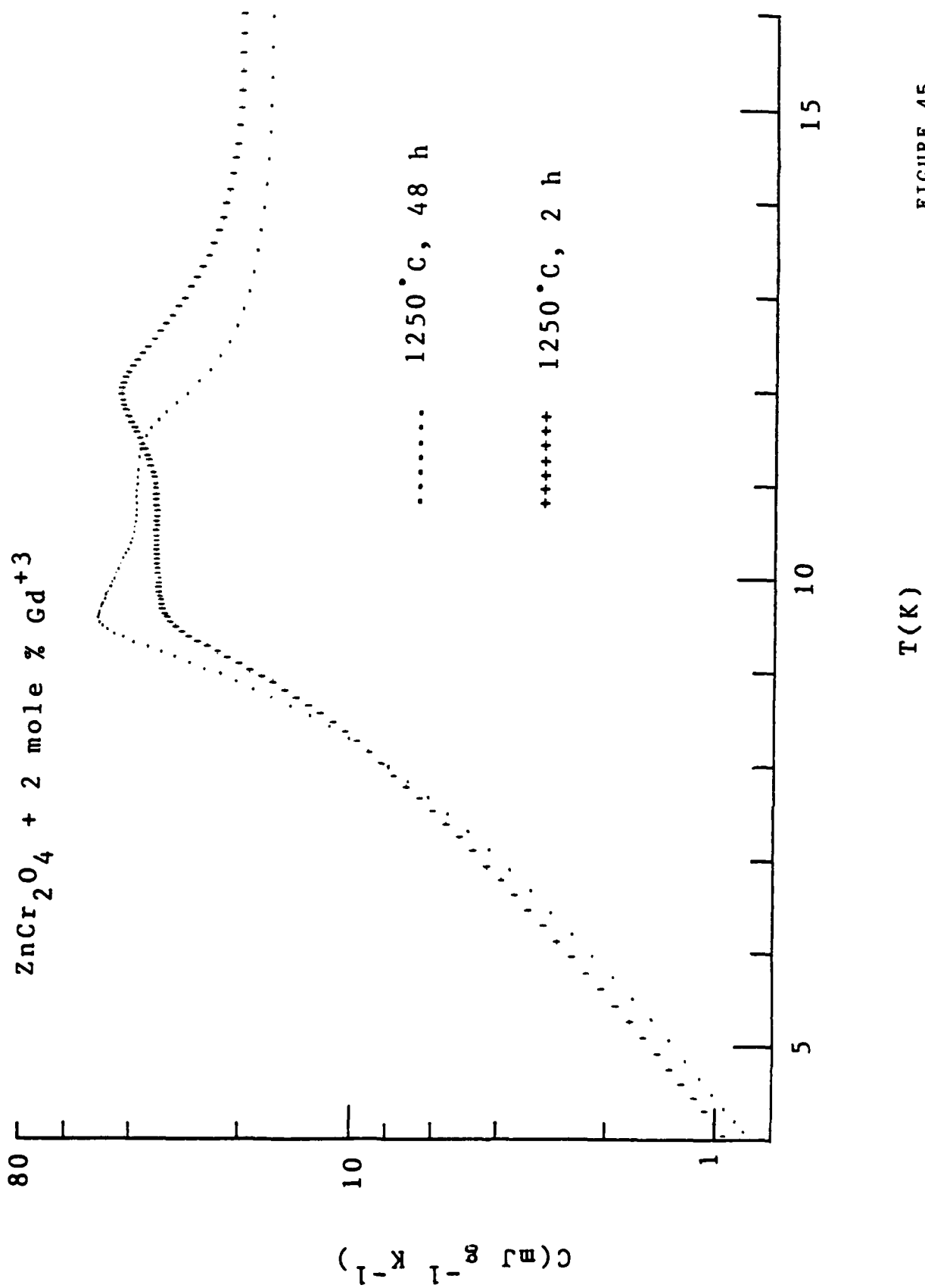
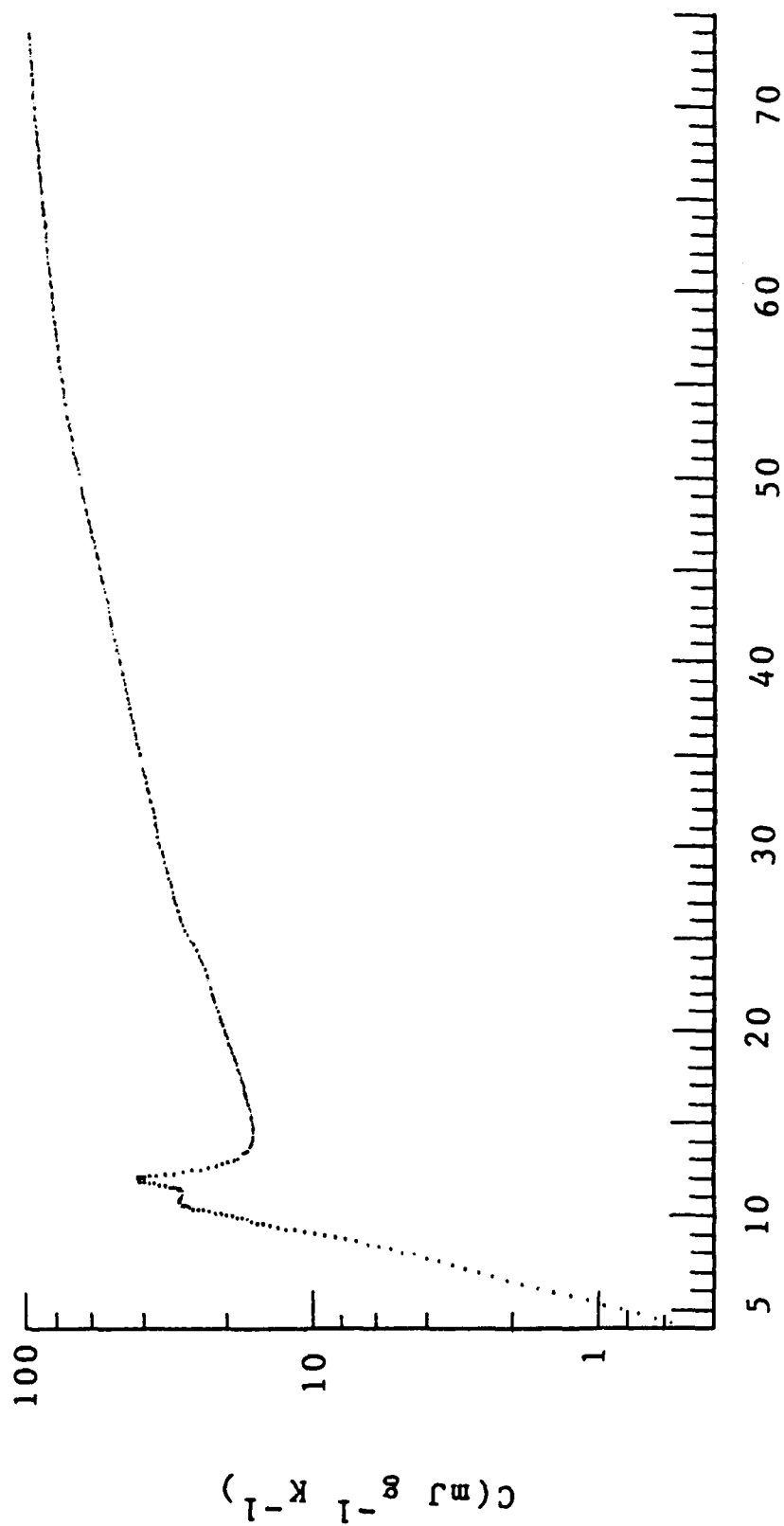


FIGURE 45

50 wt % ZnCr_2O_4
in 8161 Glass (900°C, 2 h)



T(K)

FIGURE 46

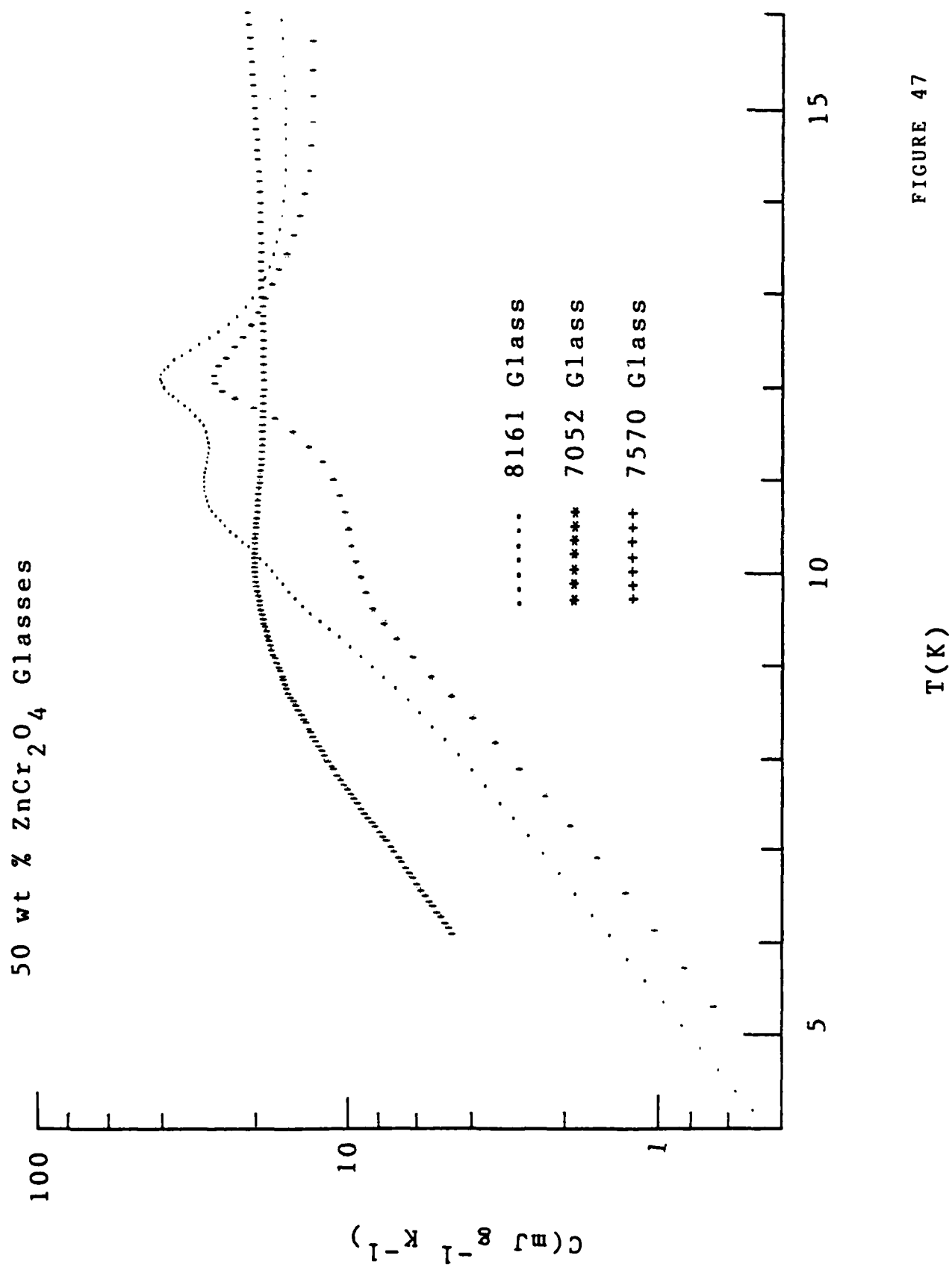


FIGURE 47

stresses or (2) drive minor impurities from the grain boundaries into the spinel lattice. Neither of these explanations is satisfactory. Microstructural examination of the nominally pure samples in Fig. 43 would be useful.

The uniaxially pressed sample has the largest density of all the nominally pure samples studied to date. We point out, however, that the samples of ZnCr_2O_4 prepared over the past several years with the 10% columbite mineralizer have the largest densities yet achieved by any preparation method, and these samples always display single, sharp C-maxima. Thus, density itself cannot be invoked as an explanation.

The results here for the uniaxially pressed sample are puzzling because the C-data in Fig. 43 for this sample fall more in line with the doped samples and the glass composite samples. An interesting experiment is suggested, however--namely, embedding ZnCr_2O_4 powder in an epoxy-type matrix at room temperature would produce pure stress effects. We remark in this regard that embedding CdCr_2O_4 in epoxy matrices does not induce double C-maxima.

The Gd^{+3} doping results in Fig. 45 appear to have a straightforward explanation: We speculate that two spin mechanism cause the two C-maxima, and the different sintering times shift the spin populations. Going further, the longer sintering time appears to exsolve the Gd^{+3} dopant from the spinel grains because the dominant C-peak in the 48-h sample in Fig. 45 coincides with the undoped C-peaks in Fig. 43.

Finally, the similarity between the 7052 and 8161 glass composites in Fig. 47 is interesting because of the markedly different thermal expansion coefficients of the glasses (46×10^{-7} and 90×10^{-7} , respectively). Moreover, we note that 7052 is a borosilicate glass whereas 8161 is a potash lead glass, and therefore it seems unlikely that the same doping level of the same dopant is involved. Two possibilities exist: (1) Only stress effects are involved above some threshold value; or (2) Similar double C-maxima occur in ZnCr_2O_4 essentially independent of the type or concentration of dopants. Here also we see the

need for studying pure stress effects in an epoxy-type composite.

In the glass composites one cannot discount dopants entering the spinel from the glass phase, and the featureless data for the 7570 composite in Fig. 47 have been previously explained as a dopant rather than stress effect. We point out here that all other glass composites studied to date display double maxima, as in Fig. 47.

FINE-GRAIN CERAMIC POWDERS

The measurements above involve samples wherein the CdCr_2O_4 and ZnCr_2O_4 ceramic grains are mechanically constrained in one fashion or another. We now consider measurements on unconstrained ceramic powders, and three types of powders have been investigated:

1. Relatively coarse grain size powder, $\sim 1\text{-}2\ \mu\text{m}$;
2. Very small grain size powder, $\sim 100\text{ - }200\ \text{\AA}$;
3. 5% Gd-doped, small grain size powder.

The reason for selecting the $1\text{-}2\ \mu\text{m}$ grain-size powder is because all samples measured above were prepared by starting with such powder. And the reason for selecting the Gd dopant is because the doping studies above show that this dopant always splits the specific heat peak.

It is an experimental challenge to perform dynamic specific heat measurements on powders, for two reasons: (1) The powder has to be contained in such a way as to minimize mechanical constraint (e.g., potting the powder in an epoxy introduces constraints); and (2) The powder has to be well coupled thermally to the measuring apparatus.

To accommodate these two boundary conditions, the following procedure was used. The powder was loaded directly into the copper cup illustrated in Fig. 9 (cigarette paper varnished to the periphery of the cup covered the drill holes in the cup). The powder was hand-tamped in the cup using finger pressure, and eight copper foils were used as spacers in this tamping operation. These foil spacers were distributed uniformly in the

comcompact about 0.05 cm apart, and the o.d. of these spacers was cut slightly larger than the i.d. of the cup so as to force a crimping between the outer edge of the spacer and the cup to improve thermal coupling. It was later determined experimentally that good thermal coupling between the powder and the cup was achieved (see below). Of course, these copper foil spacers were carefully weighed and included in the addenda correction.

Undoped Powders

The fine-grained powders of ZnCr_2O_4 and CdCr_2O_4 ($\sim 100\text{-}300$ Å) were prepared by co-precipitation from acetate solutions as explained in Section III.A. The coarse-grained powders of these spinels ($\sim 1\text{-}2$ μm) were available from the ceramic processing.

The results of the specific heat measurements on the ZnCr_2O_4 powders are shown in Fig. 48; also shown for comparison are previous data for a consolidated ceramic pellet, and these data show the very sharp maximum at about 8-9 K. The data for the coarse-grained powder in Fig. 48 also show a sharp maximum at about 12 K plus a shoulder feature at about 10 K. However, below about 6 K the specific heat of the coarse-grained powder increases very rapidly, and for this reason the data could not conveniently be measured below 4.5 K due to the very slow drift rate that occurred.

The fine-grained powder in Fig. 48 shows a broad specific heat maximum centered at about 15 K and here it proved inconvenient to measure the specific heat below 7 K due to the very slow drift rate (note in Fig. 48 that the specific heat of this powder achieves enormous values below 20 K).

The results of the specific heat measurements on the CdCr_2O_4 powders are shown in Fig. 49, and also shown for comparison are data previously measured on a consolidated ceramic pellet. The consolidated-pellet data show the sharp maximum at about 8 K followed by a rapid descent at lower temperatures. In contrast, the data for the coarse-grained powder exhibit a maximum at about 7 K followed by a steep rise below 5 K. In the

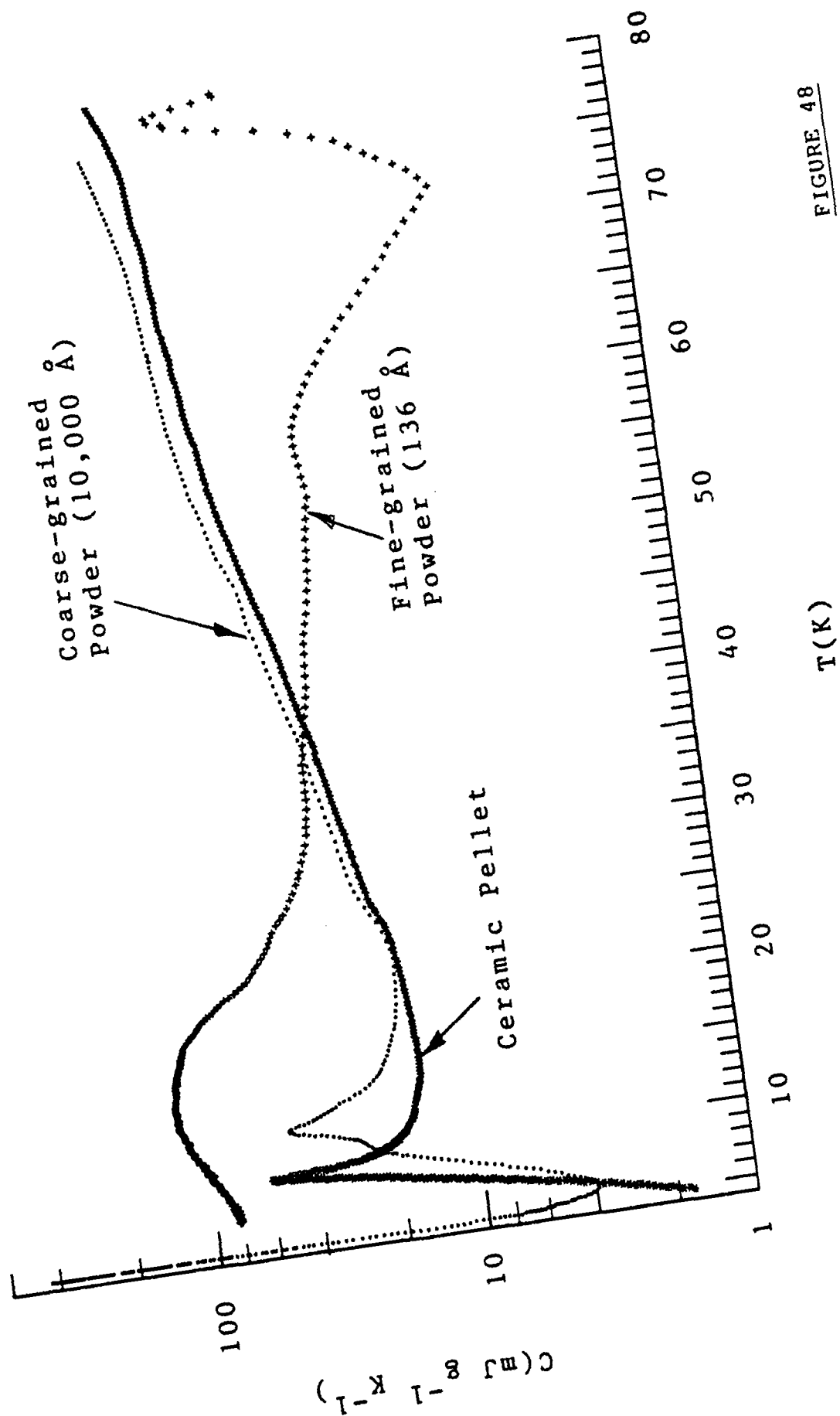
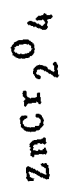


FIGURE 48

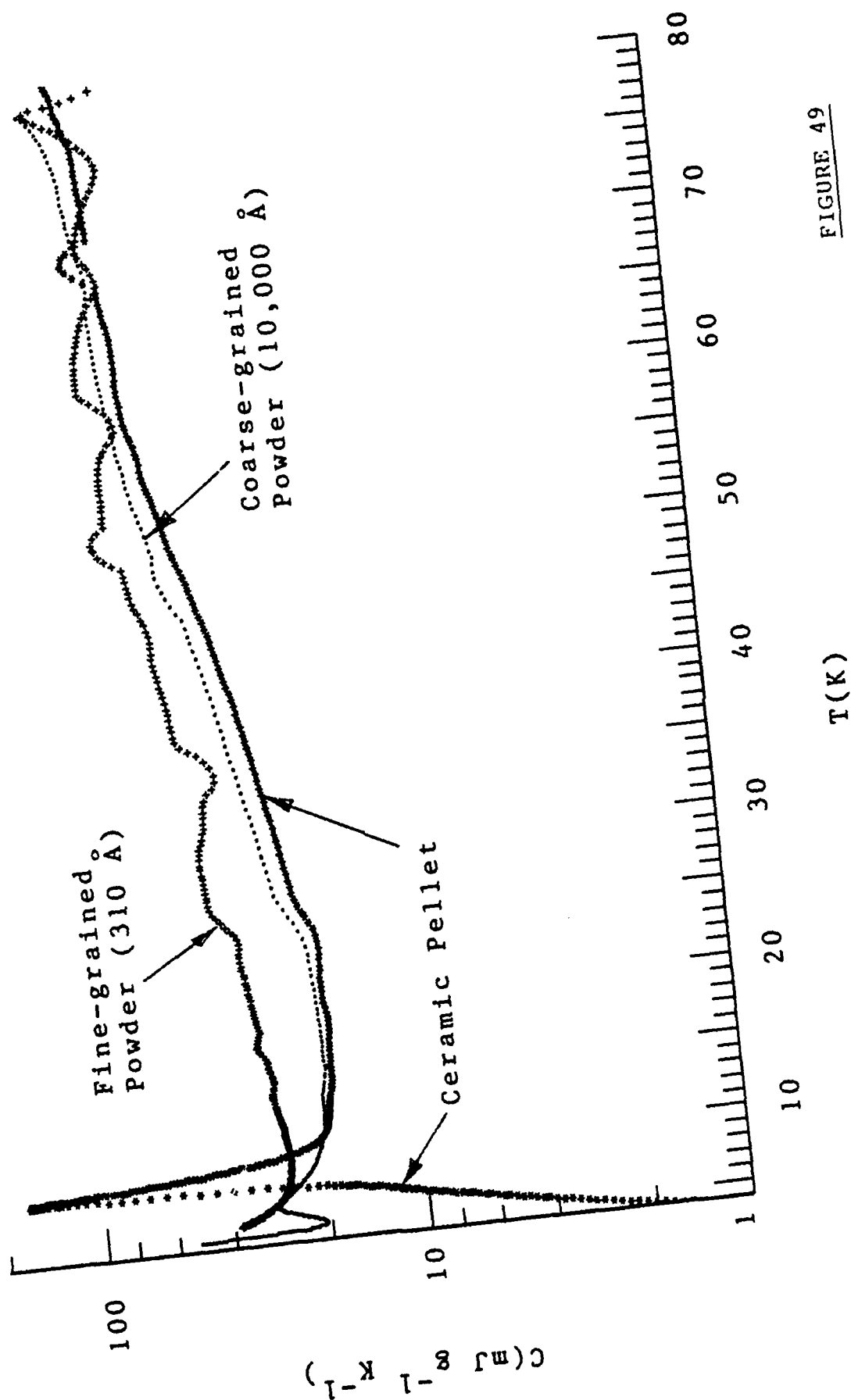
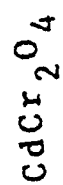


FIGURE 49

fine-grained powder data in Fig. 49 a maximum is not observed in the neighborhood of the maximum in the consolidated pellet. These fine-grained data increase with decreasing temperature below 15 K, and here also the drift rate became so slow that measurements could not be made below 5.5 K.

The specific heat data in Figs. 48 and 49 are for the temperature range 4-80 K. The powder data from these plots are collected in Fig. 50 on the range 4-15 K (here ZC and CC refer to the zinc and cadmium spinels, respectively). The Fig. 50 data show that the coarse-grained powders have specific heats that increase very rapidly with decreasing temperature below 5 K, and the maximum in the coarse-grained ZC powder at 12 K is clearly evident in Fig. 50. It is also seen in Fig. 50 that the fine-grained powders have specific heats that are increasing with decreasing temperature below 6 K, and it is apparent that very large values are achieved below 5 K.

The experiments on these ZC and CC powders point to the presence of a large density of free surface spins that lead to a rich variety of phenomena at low temperatures. The density of these free spins is much larger in the fine-grained powders than in the coarse-grained powders. The powders studied to date represent particle sizes that differ by about a factor of 100 for both spinels.

The specific heats of the coarse-grained powders of both spinels display maxima, but the coarse-grain CC powder has a muted maximum compared to the coarse-grain ZC powder (Figs. 48-50). A very broad maximum occurs in the specific heat of the fine-grain ZC powder (Fig. 48), but the fine-grain CC powder does not display a maximum (Figs. 49 and 50).

All powder samples show a rapid rise in the specific heat with decreasing temperature below 5-6 K, Fig. 50. Here we must consider the effect of the particle sizes involved in discussing these results. It is well known that for very finely divided powders there is a specific-heat contribution from the surface, and this contribution varies as T^2 . Therefore, while this contribution is certainly significant for the fine-grain ZC and CC

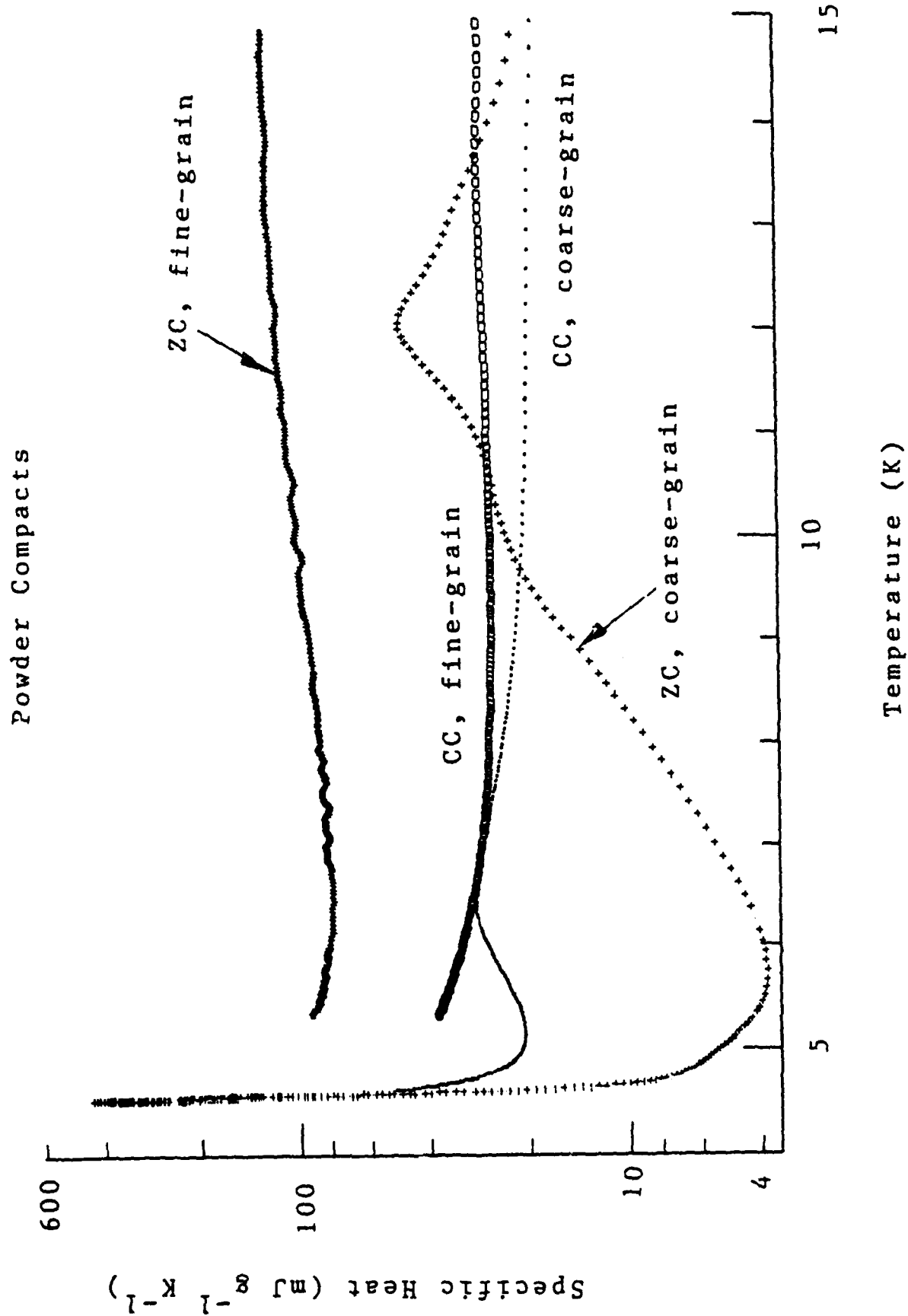


FIGURE 50

powders here, it cannot explain the rise in the specific heat with decreasing temperature. We are left with the conclusion that this effect is due to an ordering of the free surface spins. Measurements down to 1.8 K are needed to resolve this issue, and it is expected that a Schottky term will be seen, the amplitude of which will scale with the surface area of the powders. The analysis of such a term will, however, be complicated by the T^2 surface term.

Doped Powders

Fresh batches of fine-grained powders of ZnCr_2O_4 and CdCr_2O_4 were prepared with 5% Gd doping by the method of co-precipitation from acetate solutions. Fresh batches of the undoped powders were also prepared at the same time, and specific heat measurements were performed on all four of these new powder batches. In these measurements, attention was focused on the 2-20 K temperature range based on the above findings with the first batches of powders (Figs. 48-50). The grain sizes in these second-generation powders are given in Table VI.

Table VI
Grain Sizes in the
Second Generation of Fine-Grained Powders

<u>Powder</u>	<u>Grain Size (\AA)</u>
Undoped ZnCr_2O_4	87
Undoped CdCr_2O_4	108
5% Gd-doped ZnCr_2O_4	99-247
<u>5% Gd-doped CdCr_2O_4</u>	<u>164</u>

For these measurements, the powders were hand-tamped into the copper cups with foil spacers, as discussed above. Since the 2-20 K range was of primary interest, the AB thermometers on the cups were calibrated in this range according to Eq. (12).

The specific heat data measured on the doped and undoped

ZnCr_2O_4 powders are shown in Fig. 51, and on the corresponding CdCr_2O_4 powders, in Fig. 52. We immediately see that the undoped powders display broad specific heat maxima, but only in ZnCr_2O_4 does the Dd-doping induce a sharp specific heat peak at 11.7 K (Fig. 51).

The data for the undoped ZnCr_2O_4 powder in Fig. 51 agrees qualitatively with the corresponding data in Figs. 48 and 50 regarding the presence of a broad specific heat maximum centered around 15 K; quantitatively, however, the magnitudes of these maxima differ by about an order of magnitude. (~ 0.1 in Fig. 48, ~ 0.01 in Fig. 51, in units of $\text{J g}^{-1} \text{K}^{-1}$). This large discrepancy is too large not to be real, but it is surprising that decreasing the particle size from 136 to 87 Å would suppress the specific heat by an order of magnitude.

The data for the undoped CdCr_2O_4 powders in Figs. 49 (310 Å) and 52 (108 Å) are in qualitative disagreement -- the former data do not display a specific-heat maximum, but the latter data display a broad maximum centered around 12-15 K. Here also it is surprising that decreasing the grain size would cause the maximum to occur [Note in this regard that the coarse-grain CdCr_2O_4 powder ($\sim 10,000$ Å) in Figs. 49 and 50 displays a muted maximum near 6.5 K]. Finally, we point out that the 310 Å powder in Fig. 50 has $C = 0.03 \text{ J g}^{-1} \text{K}^{-1}$ at 10 K.

There may be an explanation for these experimental discrepancies based on the thermal equilibration within the powder compacts, as follows: In the case of the powders shown in Figs. 48-50, the compacts cooled overnight (~ 15 h) from room temperatures to 77 K prior to the drift measurement. In contrast, the powder compacts in Figs. 51 and 52 cooled overnight to 4.2 K prior to the drift measurement. As a general rule, thermal equilibration is a longer process at the higher temperatures because specific heats are larger but thermal conductivities (of metals) are smaller. Therefore, there is the possibility that in the drift experiments of Figs. 48-50 the powders were not at thermal equilibrium, and this situation would be exacerbated the finer the grain size of the powder. There is some evidence for

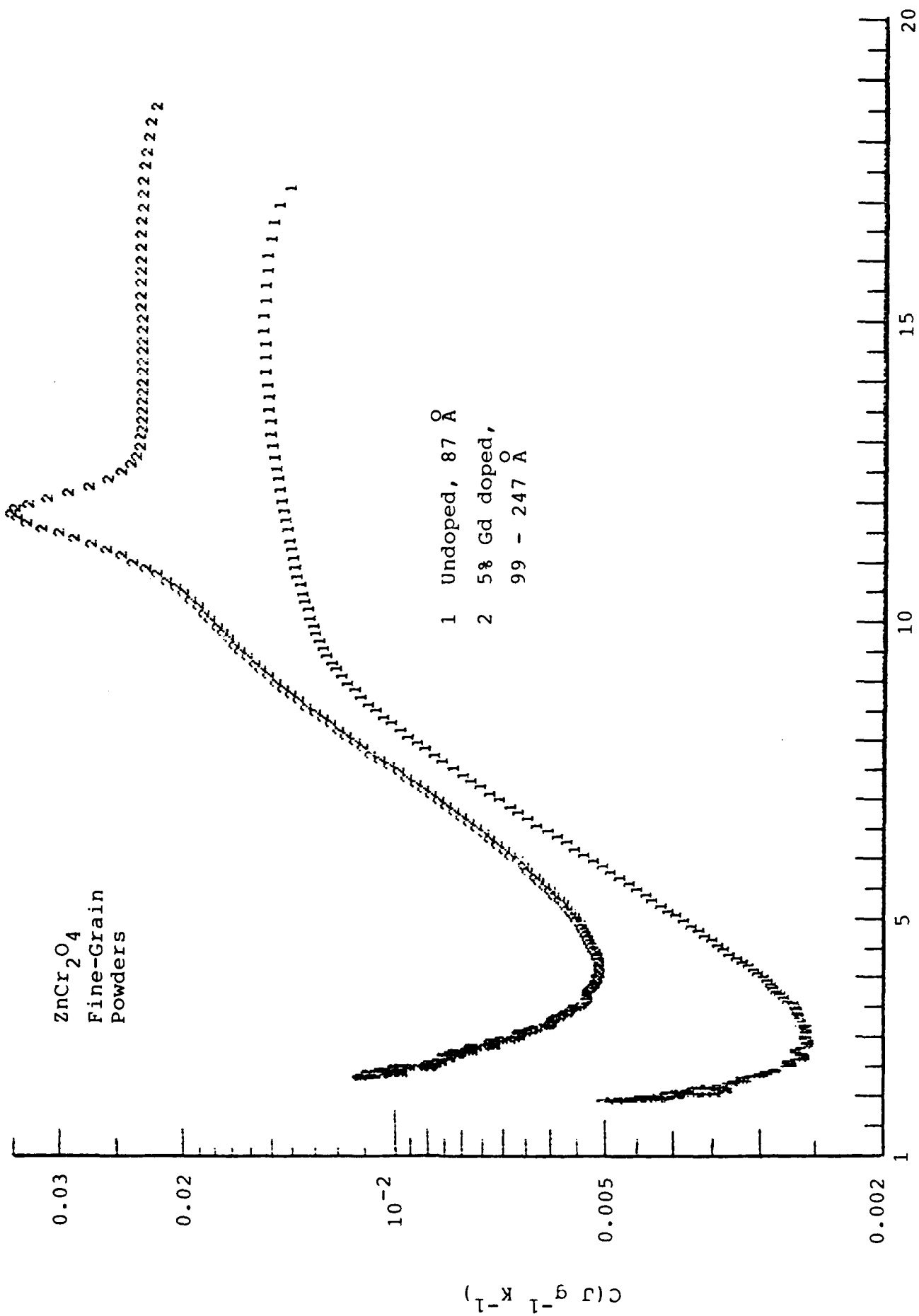


FIGURE 51

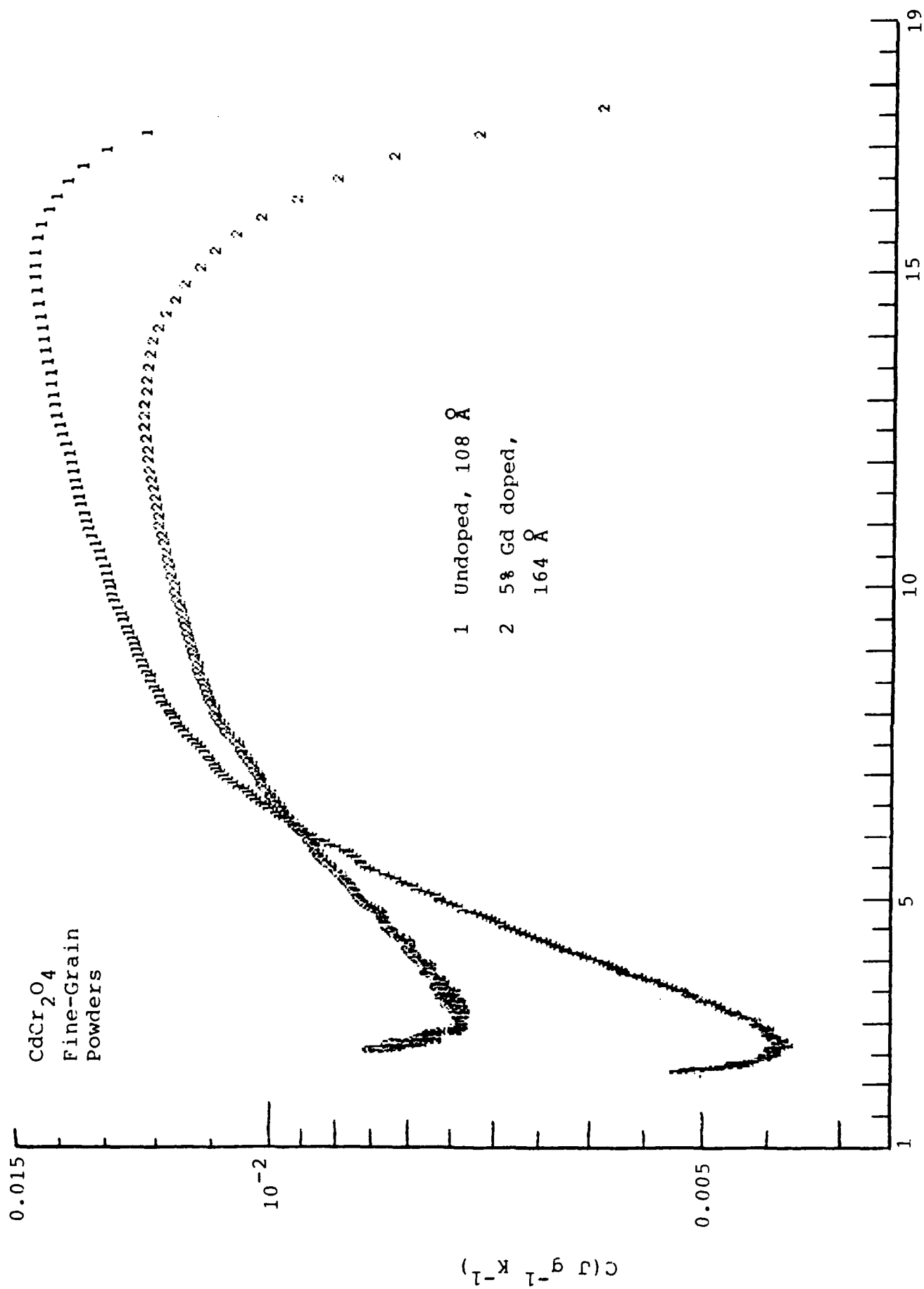


FIGURE 52

this Figs. 48 and 49 in that records for the fine-grain powders display erratic peaks and valleys whereas the coarse-grain powders display smooth records. Consequently, the data in Figs. 51 and 52 probably represent the more reliable data from the standpoint of thermal equilibration, 2-20 K.

Along this line, we remark that following the 20+2 K drift of the second-generation powder compacts, these samples were heat-pulsed at 2 K and the decay back to the reservoir temperature recorded. This experiment yielded the thermal time constant of the powder compact, and time constants ~ 5 -10 s were found. This result reinforces the observations made above regarding thermal equilibration.

The most striking feature in Figs. 51 and 52 is that the Gd doping induces a sharp specific heat peak in fine-grain ZnCr_2O_4 but not in CdCr_2O_4 . There is a real concern here that the Gd^{+3} dopant entered the B-site of ZnCr_2O_4 in preparation, but possibly not in the case of CdCr_2O_4 . The X-ray diffraction patterns of these doped powders were so particle-size-broadened that lattice constant shifts indicating successful doping could not be resolved.

Therefore, concentrating only on the ZnCr_2O_4 case, the Gd doping induces a single specific heat peak at 11.7 K, Fig. 51, whereas the undoped powder of comparable grain size does not display this peak (thermal equilibration concerns do not affect this intercomparison because the two powders were prepared and measured identically). The coarse-grained powder in Fig. 48 displays this same specific-heat peak, and these peak heights agree reasonably well (~ 0.05 in Fig. 48, ~ 0.035 in Fig. 51, in units of $\text{J g}^{-1} \text{K}^{-1}$).

Therefore, the spin-frustration that leads to a large, sharp specific heat peak in consolidated samples of ZnCr_2O_4 and in coarse-grain powder of ZnCr_2O_4 is dramatically altered in very fine powders ($\sim 100 \text{ \AA}$), resulting in a very broad specific heat maximum. However, Gd-doping on the B-site in the fine-grain powder restores the original spin-frustration. The same Gd-doping in coarse-grain ZnCr_2O_4 powders, however, induces

double peaks in the specific heat. These findings clearly indicate that the spin-frustration in ZnCr_2O_4 represents a delicate balance.

It deserves mentioning that stresses are certainly absent in the measurements on these powder compacts.

Finally, a very interesting feature is seen at the lowest temperatures for all the powders in Figs. 48-51 -- namely, there is a rapid rise in the specific heat with decreasing temperature. This effect leads to very large specific heat values at these temperatures (the magnitude of this effect prevented some of the powder data in Figs. 48-50 from being measured down to 2 K).

This feature in the powder data suggests a Schottky contribution to the specific heat, according to

$$C = mT^3 + nRg_0g_1(g_0 + g_1)^{-2} (\delta/T)^2 \quad (29)$$

where mT^3 is the Debye term, and the Schottky term is written for the case that $T \gg \delta$ for a two-level system, g_0 and g_1 being the degeneracies of the ground state and first excited state (see below, also). The important quantity is n , the number of Schottky systems per formula weight, as we shall see below.

In to test the validity of the Schottky model for these powder data, we plot CT^2 versus T^5 (We remark that the multilevel Schottky term in the general case is also proportional to n/T^2). The powder data in Figs. 51 and 52 are probably the most reliable experimentally for the reasons discussed above, and CT^2 vs. T^5 for these four powders are shown in Fig. 53.

Reasonably good data representations are seen in Fig. 53, indicating the essential validity of the Schottky model for these powder data. Another good indication of the validity of the model comes from the fact that the ZnCr_2O_4 plots in Fig. 53 are parallel, as are the CdCr_2O_4 plots. That is, the slopes of these curves are related to the Debye temperature, $m \propto \theta_D^{-3}$.

The data in Fig. 53 were fitted to Eq. (29), and the results of these analyses are given in Table VII.

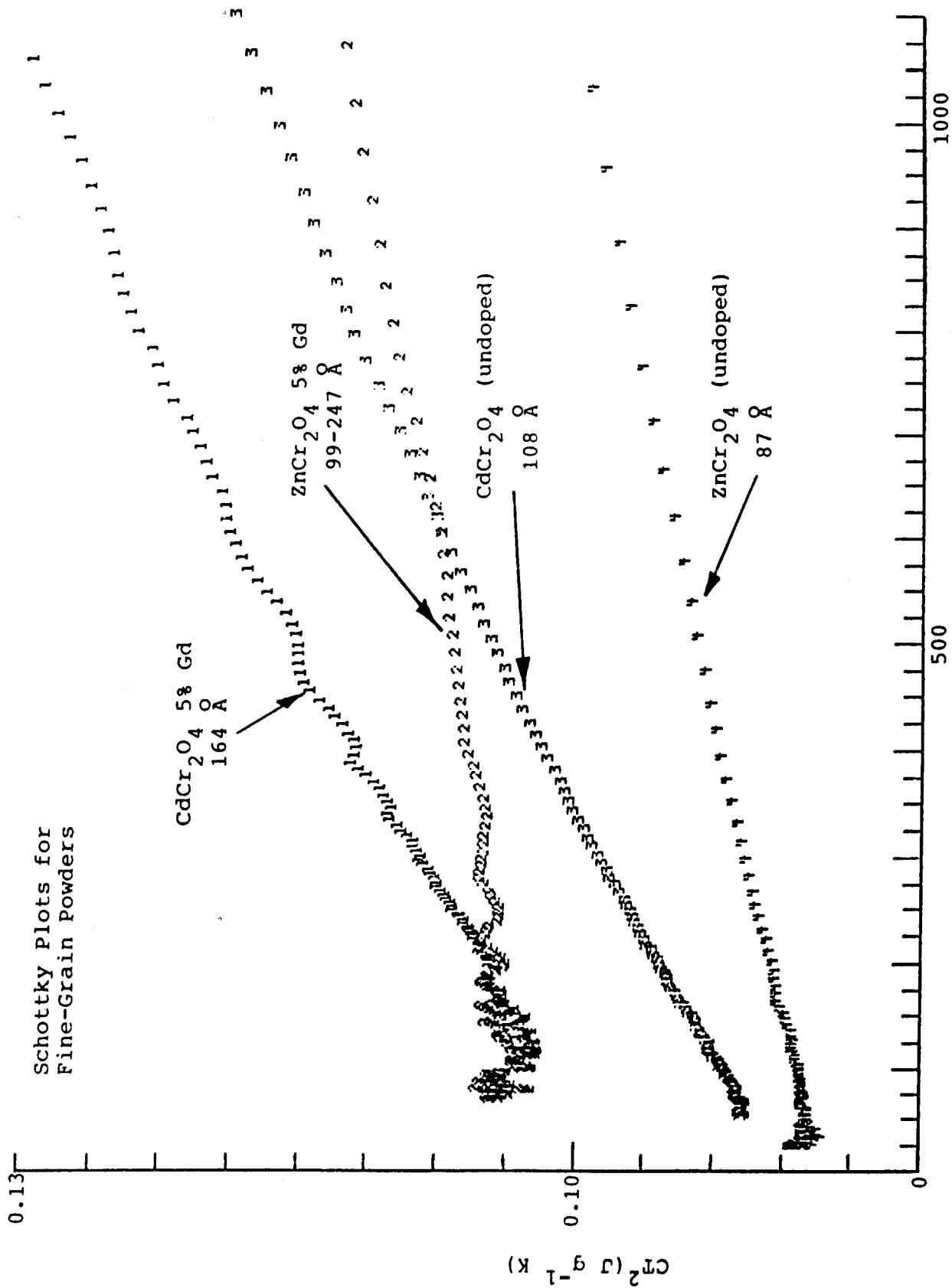


FIGURE 53

T^5 (K⁵)

Table VII
Schottky Analyses of Power Data

Powder	Grain Size	θ_D	$n\alpha$
Undoped ZnCr_2O_4	87 Å	122.3 K	0.431
ZnCr_2O_4 5% Gd	99-247	134.7	1.673
Undoped CdCr_2O_4	108	86.75	0.742
CdCr_2O_4 5% Gd	164	84.06	1.681

From Eq. (29), α has been defined as $\alpha = g_0 g_1 \delta^2 / (g_0 + g_1)^2$ (i.e., to convert the Schottky term to the general, multilevel case), and the Debye temperatures are normalized to one atom per formula weight. In reducing the experimental data, the molecular weight have been calculated based on the assumption that the Gd dopant enters the spinel B-site (This assumption, however has a minor effect on θ_D and $n\alpha$ for the doped powders in the above Table).

We notice that there is reasonably good agreement between the Debye temperatures in Table VII: ZnCr_2O_4 , 128.5 ± 8.8 K; CdCr_2O_4 , 85.41 ± 1.90 K. These are effective Debye temperatures and are unusually small for the following reason: Below the transition temperature in an antiferromagnet, there is a T^3 spin-wave contribution to the specific heat that is indistinguishable from the Debye term due to the lattice contribution. In fact, the smallness of the effective θ_D 's in Table VII confirms that antiferromagnet transitions have taken place in these fine-grained powders.

The $n\alpha$ -values in Table VII clearly show that the effect of Gd-doping is to dramatically increase the amplitude of the Schottky term in these powders.

Analyses similar to those in Fig. 53 and Table VII have, in the previous AFOSR-sponsored research programs, been performed using specific heat data for compacted discs of ZnCr_2O_4 and CdCr_2O_4 and for these spinel phases in the two-phase materials ZCN(9/1) and CCN(9/1). The results of all these analyses are collected in Table VIII.

Table VIII
Schottky Analyses for ZnCr_2O_4 and
 CdCr_2O_4 in Various Forms

<u>ZnCr_2O_4</u>	θ_D (a)	$n\alpha$
Undoped Powder, 87 Å	122.3	0.431
Gd-doped Powder, 99-247 Å	134.7	1.673
Compacted Disc	139	0.159
Phase in ZCN(9/1)	162	0.034
 <u>CdCr_2O_4</u>		
Undoped Powder, 108 Å	86.75	0.742
Gd-doped Powder, 164 Å	84.06	1.681
Compacted Disc	56.	0.190
Phase in CCN(9/1)	101.	0.027

(a) Effective Debye temperature below ~ 5 K.

The results in Table VIII show a remarkable variety in the specific heats of ZnCr_2O_4 and CdCr_2O_4 prepared under different conditions. The grain sizes of these spinels in the compacted discs and in the two-phase materials were ~ 10,000 Å. The density of free spins in both spinels drops precipitously in progressing from the fine powder to the compacted ceramic to the two-phase material, and in both cases the doped powders have the highest densities of free spins.

Results for the effective Debye temperatures in Table VIII are also interesting. First we note that the smaller is θ_D , the larger is the density of antiferromagnetic spins contributing to the T^3 spin wave term. For ZnCr_2O_4 , the density of these correlated spins is approximately the same for the two powders and the compacted disc, but this density drops in the two-phase material. For CdCr_2O_4 , in contrast, the correlated-spin density is very large in the compacted disc but drops dramatically in the other three forms. Going further, these results suggest that a compacted disc made from fine powders of Gd-doped CdCr_2O_4 would have an enormous specific heat below 15 K.

LATENT HEAT MEASUREMENTS

The question of whether or not a transition is accompanied by a latent heat is of fundamental importance. In the most straightforward case, a first-order transition has a latent heat, a second-order transition does not. In the case of the CdCr_2O_4 and ZnCr_2O_4 spinels, the question of the presence or absence of latent heats at the transitions is of great theoretical interest. In this report, we document attempts to measure latent heats in these spinels.

The method for measuring a latent heat is easily grasped: If the spinel sample is suspended on a long-time-constant thermal link within an adiabatic calorimeter in a hard vacuum, and if the heater on the sample is used to heat the sample to, say, $T_N + 5$ K, then the sample temperature will slowly drift down to, say, $T_N - 5$ K according to

$$C(dT/dt) = -\int_T^{T_0} GdT \quad (30)$$

where T_0 is the reservoir temperature ($T_0 < T_N - 5$ K in this example), C is the heat capacity of the sample, and G is the thermal conductance of the thermal link. Of particular importance here, if a latent heat is dissipated at T_N , then $dT/dt = 0$ until this heat is transported from the sample to the reservoir through the thermal link. This simple technique is used to calibrate thermocouples, for example, at the ice point, the Sn point, the Pb point, etc. Denoting Q_L as the latent heat, we have from Eq.(30)

$$Q_L = \Delta t \int_T^{T_0} GdT \quad (31)$$

where Δt is the length of time that $dT/dt = 0$ at T_N . Thus, a latent heat experiment consists simply of monitoring $dT/dt = 0$ and measuring Δt .

We have repeatedly performed time-temperature drifts near T_N on CdCr_2O_4 - and ZnCr_2O_4 -containing materials in zero magnetic

field and in intense magnetic fields, as summarized in Table IX.

Table IX
Time-Temperature Drifts, CdCr_2O_4 and ZnCr_2O_4 Spinels

Sample	H-field Range
9:1 Spinel:Columbite Ceramics	0-10 T
9:1 Powders in Glass Matrix*	0-10 T
9:1 Powders in Epoxy Matrix*	0-10 T
Pure Spinel Ceramics	0-10 T
Loosely compacted pure spinel powders	0-15 T

* CdCr_2O_4 only

In all of these experiments, we have never seen evidence of a latent heat (i.e., $dT/dt \neq 0$ near T_N).

We must, however, consider the possibility that the latent heat may be too small to be resolved by our experimental dT/dt -methods. Stated differently, we now consider an upper bound to the latent heat corresponding to experimental non-detectability.

Two types of drift measurements have been performed: (1) Computer-interfaced experiments wherein the time between consecutive readings is ~ 10 - 20 s; (2) Chart-trace recordings which are continuous records.

An example of a chart-trace record is shown in Fig. 54, in this case for ZnCr_2O_4 powder at 15 T. As seen in Fig. 54, there is no evidence of $dT/dt = 0$ in the neighborhood of T_N .

To estimate an upper bound for Q_L from Eq.(31) means first estimating a Δt -value that represents the minimum of detectability. The Fig. 54 trace, which is typical of the continuous measurements made, has a minimum division of the time scale of 6 s, and the trace width is ~ 0.5 s. It therefore is reasonable to select

$$\Delta t(\text{minimum}) \approx 1 \text{ s.}$$

The conductance G in Eq.(31) is $G = \kappa A/l$ where A and l are

ZnCr_2O_4
Powder

Current =
 $20.47 \mu\text{A}$

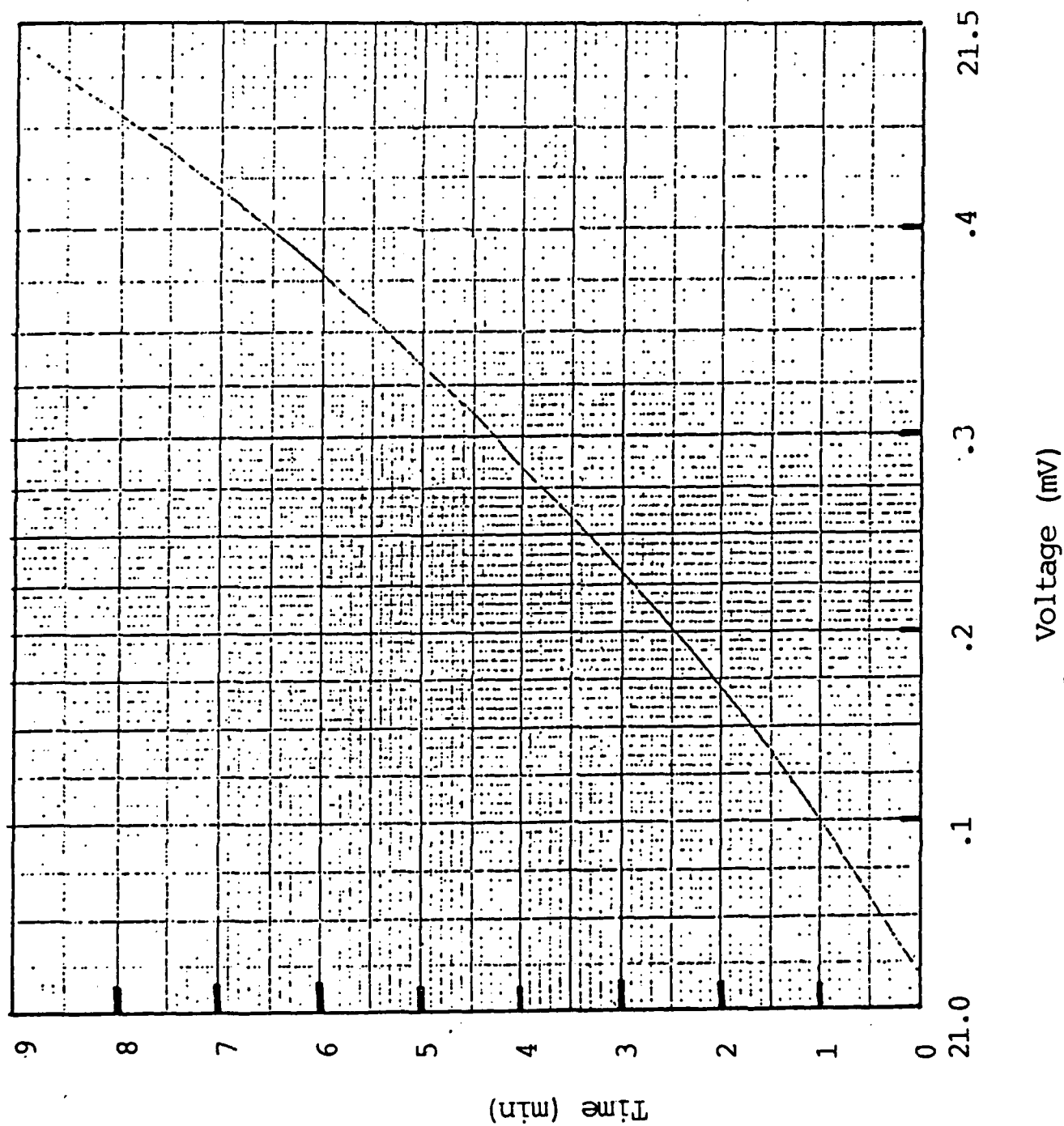


FIGURE 54

the cross-section area and length of the copper wire used. This wire has a diameter 0.005 cm, and typically $l \approx 20$ cm, so that $A/l \approx 10^{-6}$ cm. For commercial grade copper, $\kappa \approx T$ in units of $\text{W cm}^{-1} \text{K}^{-1}$. The reservoir temperature T_0 is typically 4.2 K, and T_N for CdCr_2O_4 and ZnCr_2O_4 is 8.0 and 10.5 K, respectively. Substituting in Eq.(31) we find that

$$\begin{aligned} \text{CdCr}_2\text{O}_4 : \text{Maximum } Q_L &\approx 120 \text{ erg/g} \approx 650 \text{ erg/cm}^3 \\ \text{ZnCr}_2\text{O}_4 : \text{Maximum } Q_L &\approx 230 \text{ erg/g} \approx 1300 \text{ erg/cm}^3. \end{aligned}$$

These are extremely small upperbound values for the latent heats in these spinels. For example, we note that these Q_L -values are about five orders of magnitude smaller than the specific heats of these spinels near T_N .

Going further, the specific-heat drift technique described in Section IV.A. also provides a very sensitive, computer-interface method for observing latent heats. In all the drift experiments on all of the ZnCr_2O_4 and CdCr_2O_4 samples reported in this Section IV.B., no discernible evidence of a latent heat has been observed.

ENTROPY CONSIDERATIONS

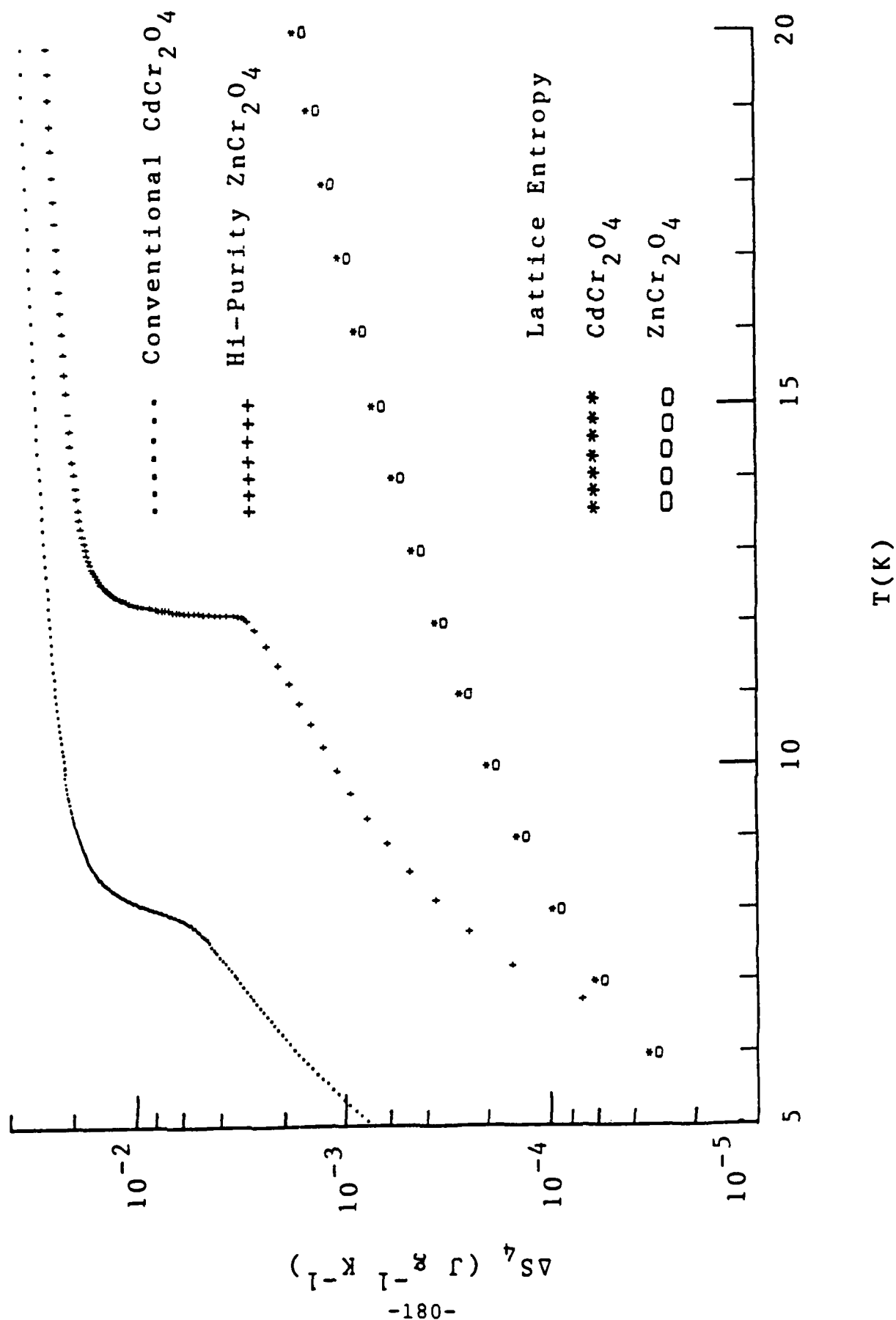
In conclusion of this Section, we consider the entropy of the spin system, ΔS_M , in these frustrated spinels, according to the well-known relation

$$\Delta S_M = nR \ln(2s + 1) \quad (32)$$

where s is the spin and n is the number of contributing spins per formula weight.

Entropies are easily obtained by numerically integrating C/T data, and the specific heat data above can be considered to have two parts: The lattice contribution and the contribution from the spin system. For the lattice contribution we employ our previously reported Debye temperatures for CdCr_2O_4 and ZnCr_2O_4 ,

Entropy Comparisons



420 and 463 K, respectively.

Examples of entropy data calculated relative to 4 K are shown in Fig. 55: Total entropy data for the Conventional CdCr_2O_4 ceramic (Fig. 14) and the Hi-Purity ZnCr_2O_4 ceramic (Fig. 16) are shown, as are the lattice contributions for CdCr_2O_4 and ZnCr_2O_4 estimated from the above Debye temperatures. The transitions at 8 and 12 K in the ceramics are clearly evident in Fig. 55, and it is also seen that the lattice contributions are relatively minor in this temperature range.

To evaluate Eq. (32) properly, C/T data should be integrated from near absolute zero to very high temperatures and the lattice contribution subtracted accordingly. Since our specific heat data do not extend below 4 K, we will approximate ΔS_M using data in the 4-20 K range. There are several justifications for employing this approximation: (1) As seen in Fig. 55 the dominant contribution to ΔS_M comes from C/T near the transition; (2) At 4 K the lattice specific-heat contribution ($\sim 0.1 \text{ mJ g}^{-1} \text{ K}^{-1}$) is much smaller than the total specific heat ($\sim 1 \text{ mJ g}^{-1} \text{ K}^{-1}$), but we assume that the contribution to the entropy from this and the lower temperatures is relatively minor; and (3) At 20 K the lattice and total specific heats are relatively commensurate (~ 5 and $10 \text{ mJ g}^{-1} \text{ K}^{-1}$).

Given these approximations, the procedure is straightforward: Measured C/T data are integrated 4-20 K, the respective lattice-contribution entropy over the same range is subtracted, and we solve for n in Eq. (32), the density of contributing spins. A spin value $s=3/2$ is adopted (Cr^{+3}).

The results of these entropy analyses are given in Table X where the samples are arranged according to the ordering shown in Figs. 13-27 for easy reference. The composite samples in Figs. 28-40 were not analyzed because of the complicating feature of the specific heats of the epoxy and glass matrices; nor where the powder data in Figs. 41 and 42.

We immediately see a remarkable result in Table X -- namely, for all of these samples the spin densities are tightly grouped, $0.54 < n < 0.81$. Note that if all the chromite spins contribut-

ed, then $n=2$. For example, referring to Fig. 14 for the undoped CdCr_2O_4 ceramics, the Conventional and CCN(9/1) ceramics display large C-maxima, whereas the Hi-Purity and Compacted ceramics do not. Yet the n -values in Table X for this group are not much different. The reason here is that, referring to Fig. 15, the latter two ceramics retain very large specific heats below 7 K, and this contribution to the entropy offsets the lack of a C-maximum. This same reasoning applies to the doped CdCr_2O_4 ceramics in Figs. 20 and 21.

It is interesting to note that the undoped ZnCr_2O_4 ceramics in Fig. 17 have much different peak heights (60 to 600 $\text{mJ g}^{-1} \text{K}^{-1}$) occurring at different temperatures, but from Table X n does not vary that much ($\sim \pm 15\%$ about the average).

Doping in ZnCr_2O_4 leads to an interesting discovery in Table X: Referring to Fig. 25, the double-maxima feature arising from the Gd^{+3} , Al^{+3} , and V^{+5} dopants leads to larger n -values ($0.631 \pm 5\%$) than in the undoped case (compacted sample, $n = 0.579$). Presumably, the excess spin density here may account for the lower transition. Nonetheless, in the ZnCr_2O_4 series, the Hi-Purity case has the largest density, $n = 0.696$.

These spin-density estimates are most reliable in a relative rather than an absolute sense because of the approximations involved. Nevertheless, the findings here are very valuable and lead to additional insights that are richly complementary to the conclusions reached above regarding doping and stress effects. Namely, in both CdCr_2O_4 and ZnCr_2O_4 only about 30 % of the free spins (Table X) cause the specific heat maxima; these spin densities are approximately invariant to impurity, doping, or stress effects, but the manner in which these spins become aligned as reflected in the specific heat are strongly influenced by impurity and doping effects.

Table X
Spin Densities from ΔS_M

Sample	$\Delta S_M(4-20 \text{ K})$ ($\text{J g}^{-1} \text{ K}^{-1}$)	n
Conventional CdCr_2O_4	3.33×10^{-2}	0.810
CCN(9/1)	2.85	0.695
Hi-Purity CdCr_2O_4	2.87	0.699
Compacted CdCr_2O_4	2.46	0.597
ZCN(9/1)	1.95×10^{-2}	0.546
Compacted ZnCr_2O_4	2.06	0.579
Hi-Purity ZnCr_2O_4	2.48	0.696
$\text{CdCr}_2\text{O}_4 + 2 \text{ m/o Mo}^{+3}$	2.23×10^{-2}	0.542
$\text{CdCr}_2\text{O}_4 + 2 \text{ m/o V}^{+5}$	2.24	0.545
$\text{ZnCr}_2\text{O}_4 + 2 \text{ m/o Gd}^{+5}$	2.37×10^{-2}	0.665
$\text{ZnCr}_2\text{O}_4 + 3 \text{ m/o Al}^{+3}$	2.21	0.620
$\text{ZnCr}_2\text{O}_4 + 2 \text{ m/o V}^{+5}$	2.17	0.608
ZnCr_2O_4 , 60 h in H_2S	1.99×10^{-2}	0.559

IV.C. SUMMARY OF SPECIFIC-HEAT STUDIES

A rich variety of new physical phenomena in CdCr_2O_4 and ZnCr_2O_4 are found from broad-range specific heat measurements (4-75 K) on samples representing a wide variety of conditions: pure samples, including very high purity conditions; doped conditions with broad variations in the spin of the dopants; stress conditions, incorporating both tensile and compressive, hydrostatic and uniaxial; combined doping and stress conditions, and doped and undoped fine-grain-size powders.

The central findings are as follows:

1. No structures in the specific heats of CdCr_2O_4 or ZnCr_2O_4 are induced above 15 K by purity, doping, stress conditions, or grain size.
2. The 8 K specific-heat peak in CdCr_2O_4 is quenched if no impurities are present or if the impurity levels are too large (2 mole %). In contrast, the peak in ZnCr_2O_4 is not quenched unless large impurity levels are present (~10 mole %). These findings are limited to consolidated samples (see below).
3. Dopants in ZnCr_2O_4 induce double maxima in the specific heat (9-12 K) regardless of the spin or site occupancy of the dopant. Hot-pressing also induces double maxima.
4. Doping in both CdCr_2O_4 and ZnCr_2O_4 universally induces larger specific heat values 20-75 K.
5. The specific-heat peaks in CdCr_2O_4 and ZnCr_2O_4 (8-12 K) are unaffected by stress magnitudes or types (compressive or tensile, hydrostatic or uniaxial).
6. Stress conditions in both CdCr_2O_4 and ZnCr_2O_4 composites universally lead to a reverse-ordering of specific heat magnitudes above 20 K based on the ceramic content of the composites. A crossover from hydrostatic to uniaxial stress conditions is suggested to explain this reversal.
7. In free, unstressed coarse-grain powders of ZnCr_2O_4 and

CdCr_2O_4 , single specific-heat peaks occur as in the corresponding consolidated samples. In very fine grain powders ($\sim 100 \text{ \AA}$), however, these peaks are broadened over a large temperature range and are associated with antiferromagnetic transitions (as evidenced by Schottky fits to the data at lower temperatures).

8. A 5% Gd doping in fine-grain ZnCr_2O_4 restores the single sharp specific heat peak but does not induce double peaks as in consolidated samples. The 5% Gd doping in fine-grain CdCr_2O_4 induces neither a sharp peak nor double peaks.
9. All ZnCr_2O_4 and CdCr_2O_4 samples exhibit Schottky specific heat terms below 4-6 K due to free spins, and these spin densities are largest in the case of Gd-doping in both spinel powders.
10. There is no evidence of a latent heat in all of the samples of ZnCr_2O_4 and CdCr_2O_4 measured.
11. Entropy analyses of the measured data on consolidated samples reveal that about 30 % of the free spins in CdCr_2O_4 and ZnCr_2O_4 contribute to the specific heat maxima, and these spin densities are nearly independent of purity, doping, or stress effects. However, the manner in which these spins align as reflected in the specific heat are strongly influenced by purity and doping.

V. THERMAL EXPANSION, DIELECTRIC CONSTANT, AND AC CONDUCTIVITY STUDIES

V.A. THERMAL EXPANSION AND DIELECTRIC CONSTANT STUDIES OF CERAMICS

Measurements are reported here of the low temperature thermal contraction of CCN(9/1) and ZCN(9/1) from 2-20 K and from 15-300 K, along with the dielectric constant of both of these materials in the same temperature range. The dielectric constant of CCN(1/0) has also been measured at 4.2 K under hydrostatic pressure from 0 to 9250 kPa.

The thermal contraction measurements were made on the apparatus shown in Fig. 1. The capacitance of a small gap between the silvered sample end and the copper electrode is monitored with a capacitance bridge and changes in this capacitance as the temperature is changed indicate differences in contraction between the sample and the copper fixture. When these differences are added to the known (from NBS tables) contraction of copper as a function of temperature, then the length changes in the sample can be calculated.

These relative length changes for CCN(9/1) and ZCN(9/1) are shown in Fig. 2(A) as a function of temperature. In both materials there is an anomalous "knee" in the contraction at ~ 150-160 K for CCN(9/1) and ~ 130-140 K for ZCN(9/1). The knee is not due to any systematic measurement error since the system has been well-tested with other materials (e.g., Al and nylon) with no similar result. Magnetic susceptibility measurements by Dalal and Kahol at West Virginia University show no anomalies at these temperatures.

The possibility exists that these knees can be explained by some previously unrecognized structural change within these materials which might also appear as anomalies in the dielectric constants. To test this theory, $\epsilon(T)$ for both materials was measured over the temperature range 40-240 K and the result is shown in Fig. 3. While there is a minimum in the dielectric

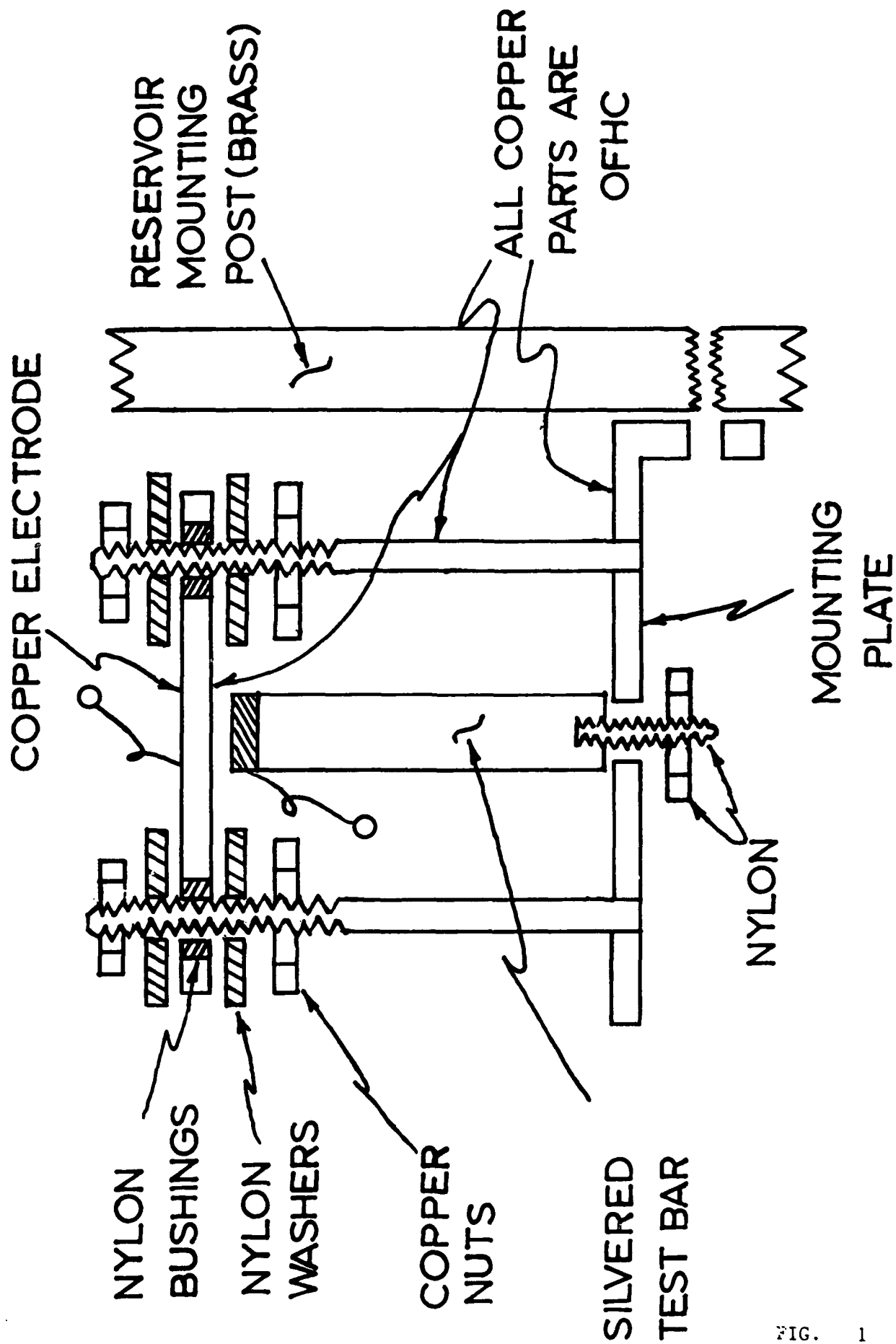


FIG. 1

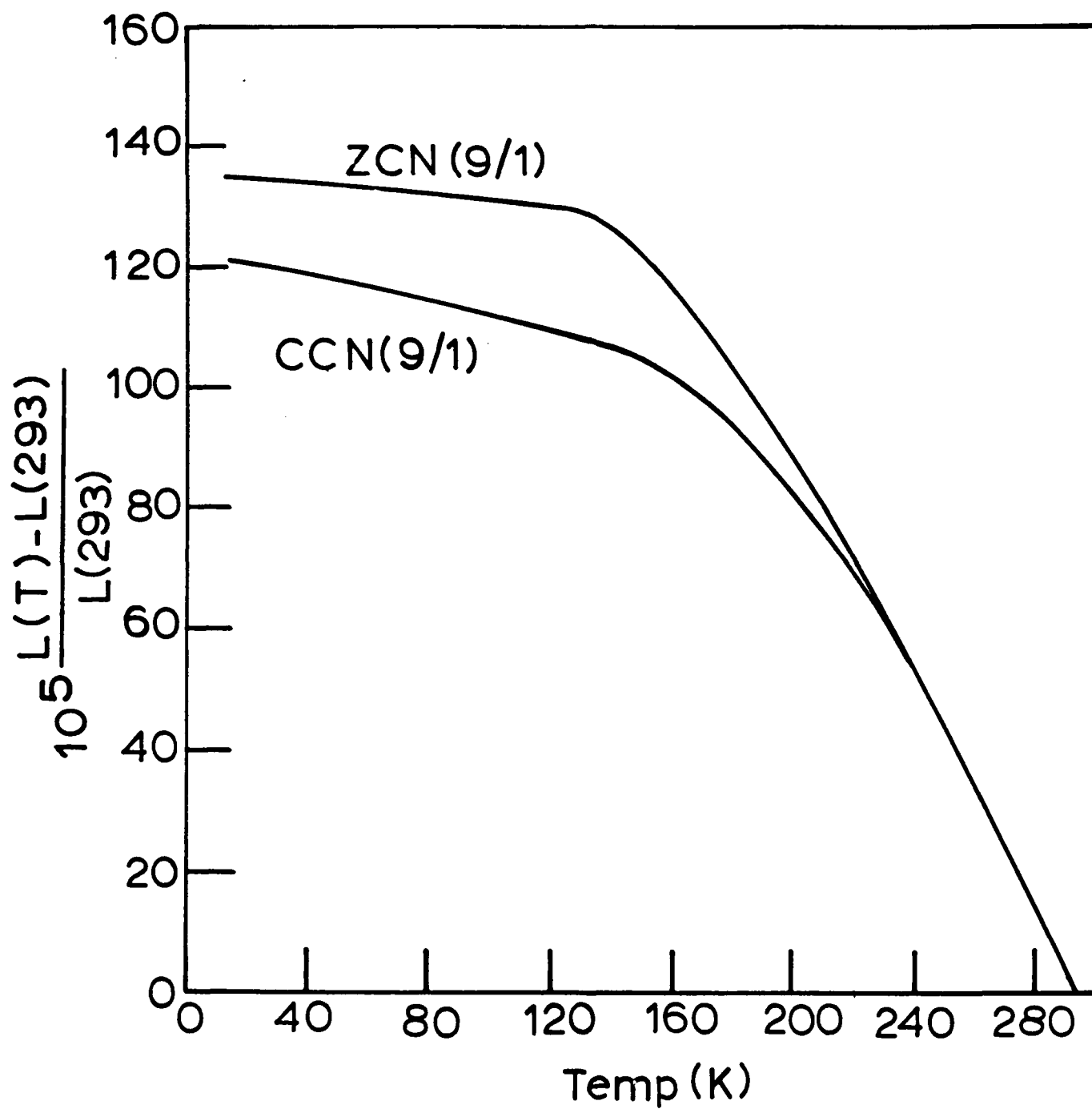


FIG. 2(A)

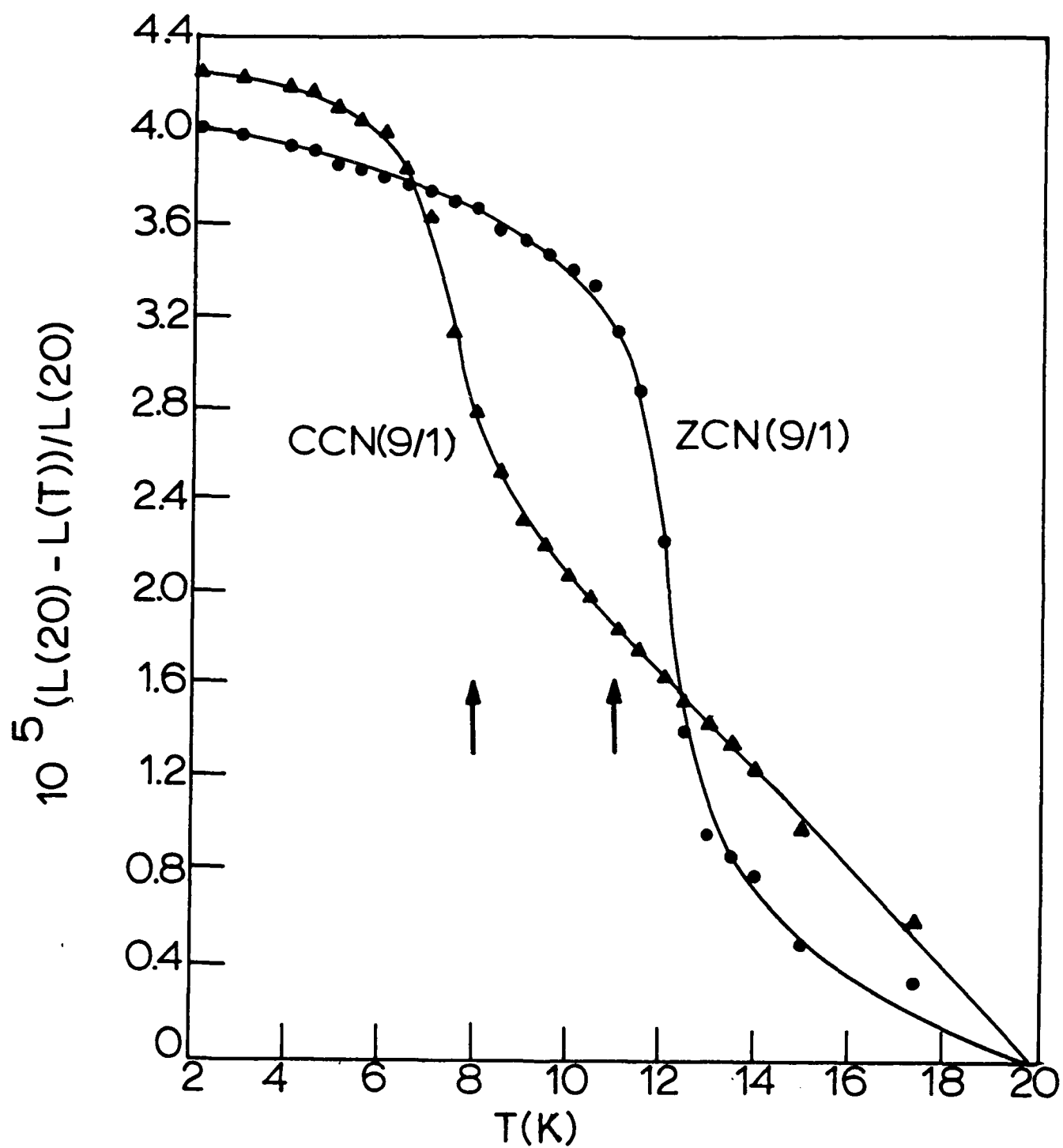
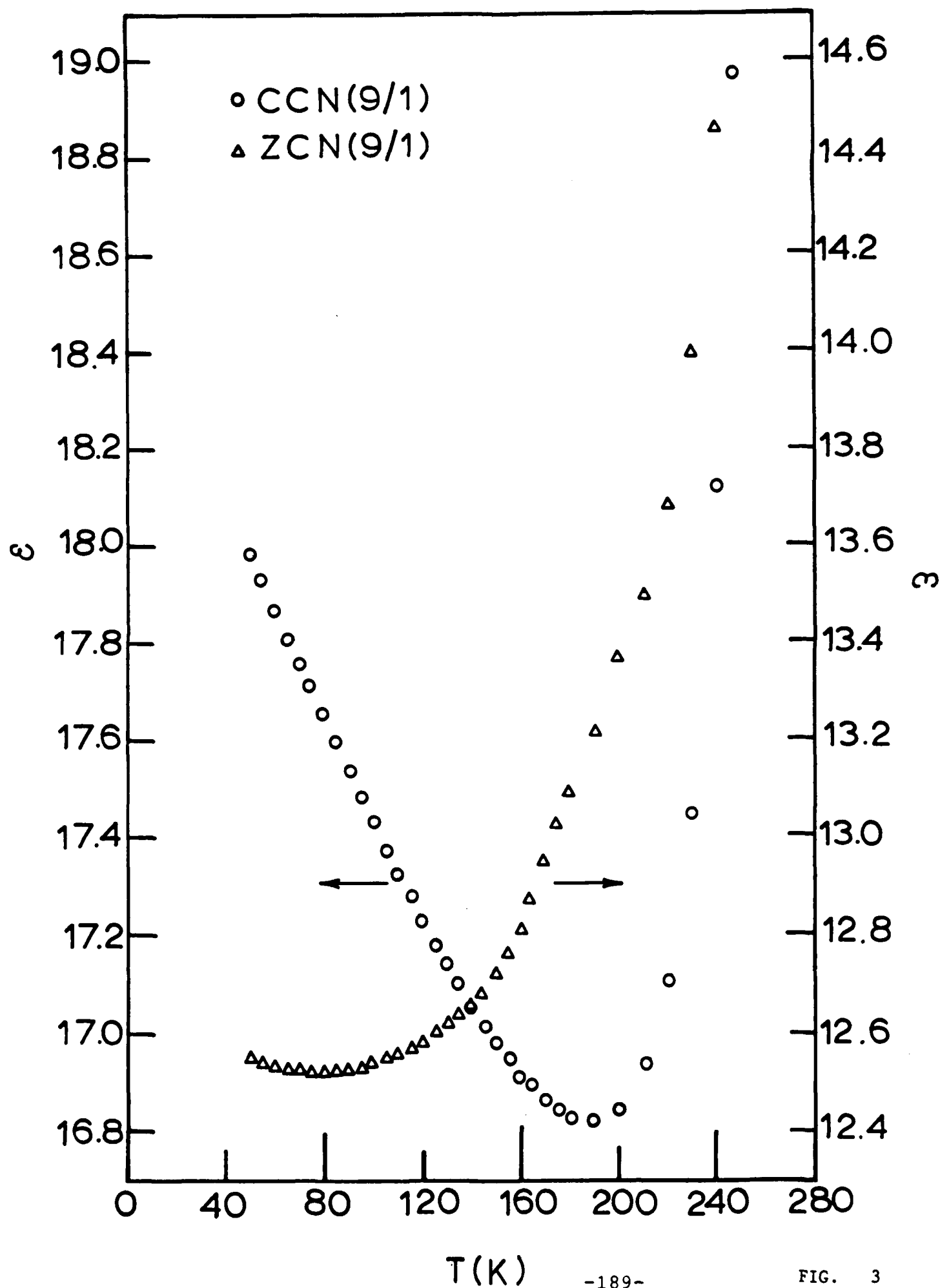


FIG. 2 (B)



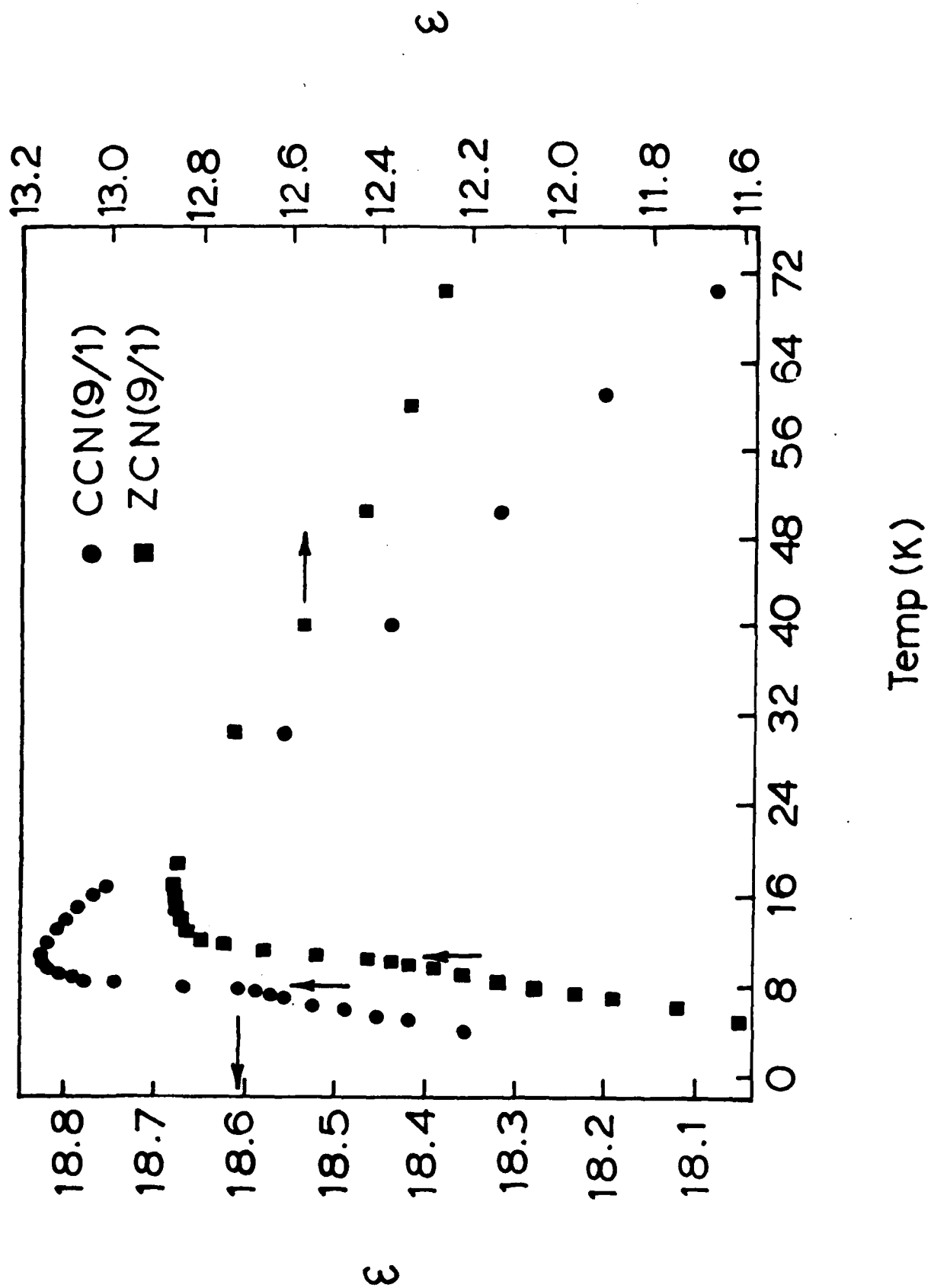
constants of both CCN and ZCN, these minima bear no obvious relation to the knees in the thermal contraction data.

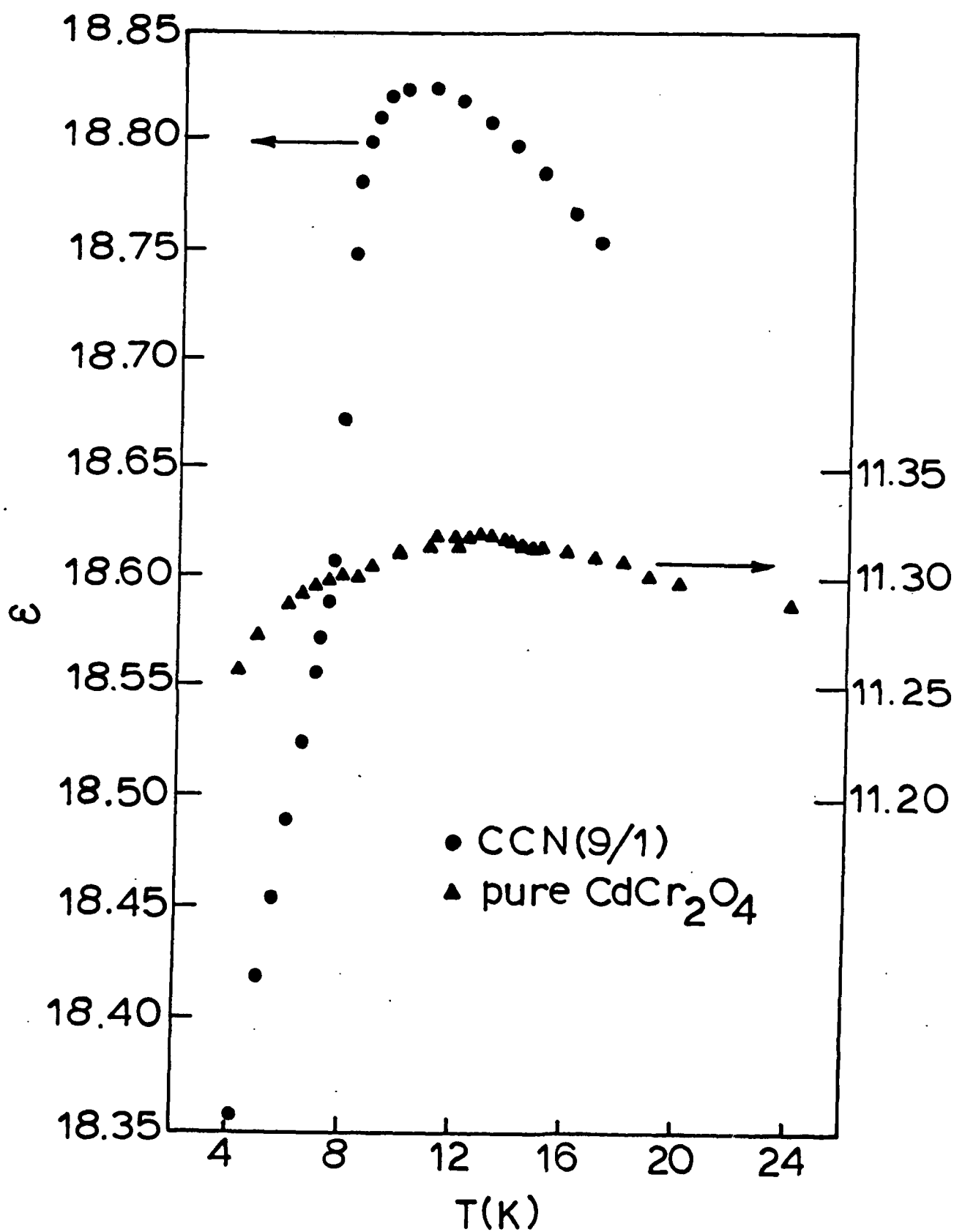
As discussed in Section VII, if there are tetragonal distortions of the materials as they pass through their transition temperatures, these distortions would have profound impact on the properties of the materials. Figure 2(B) shows the thermal contraction of CCN(9/1) and ZCN(9/1) ceramics as a function of temperature from 2-20 K. The positions of the antiferromagnetic transitions for each material are shown by the arrows. Figure 2(B) indicates that there are distortions, and that there must be a preferred (but unknown) direction for the grain orientations within the ceramics. Extrapolating the high and low temperature straight sections of the thermal contractions of each material in Fig. 2(B) to the respective transition, there is an additional relative contraction due to the distortion of 2.7×10^{-5} and 1.6×10^{-5} for ZCN and CCN respectively.

Previously in this program, anomalies in the dielectric constants of CCN(9/1) and ZCN(9/1) have been discovered at the same temperatures as the antiferromagnetic transitions (report dated 9/4/86). These data are shown in Fig. 4 where the arrows indicate the temperatures of the respective antiferromagnetic transitions and the temperatures of the anomalous peaks in $\Delta\epsilon/\Delta T$.

Dr. Bruce Patton of Ohio State University has adequately explained these anomalies as coupling between the magnetic order parameter and the band gap separating the valence and conduction bands which is related to the polarization (see the Annual report for this program dated 5/11/87, p. 131 ff). The combination of these couplings and the shifts of the materials from insulators to semiconductors at higher temperatures probably accounts for the minima in the dielectric constants, but the knees in the thermal contraction remain unexplained.

Dielectric measurements of pure CdCr_2O_4 were reported earlier in the temperature range of the antiferromagnetic transition (~ 8 K) and the data are shown in Fig. 5 compared to CCN(9/1). Here, instead of a sharp peak in ϵ and $\Delta\epsilon/\Delta T$, there is a broad maximum indicating that the coupling between the magnetic





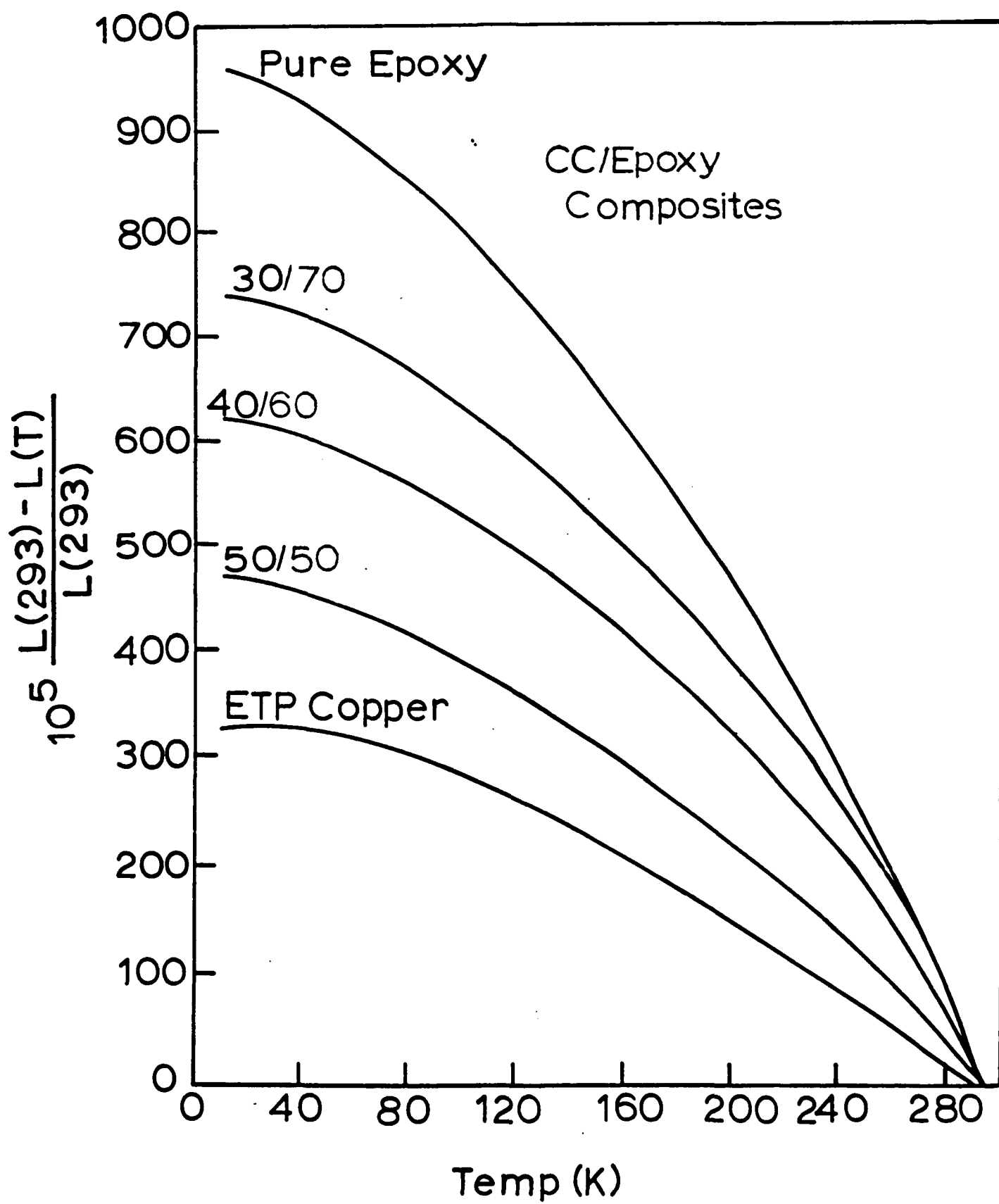
order parameter and the band gap is not nearly as strong as in CCN(9/1). However, it is not clear whether the broadening is due to the fact that the CdCr_2O_4 sample has 46% porosity or whether the columbite phase is absent. The presence of this non-magnetic phase may increase the coupling between the magnetic order parameter and the band gap by applying hydrostatic pressure to the spinel phase at low temperatures due to differential thermal contraction.

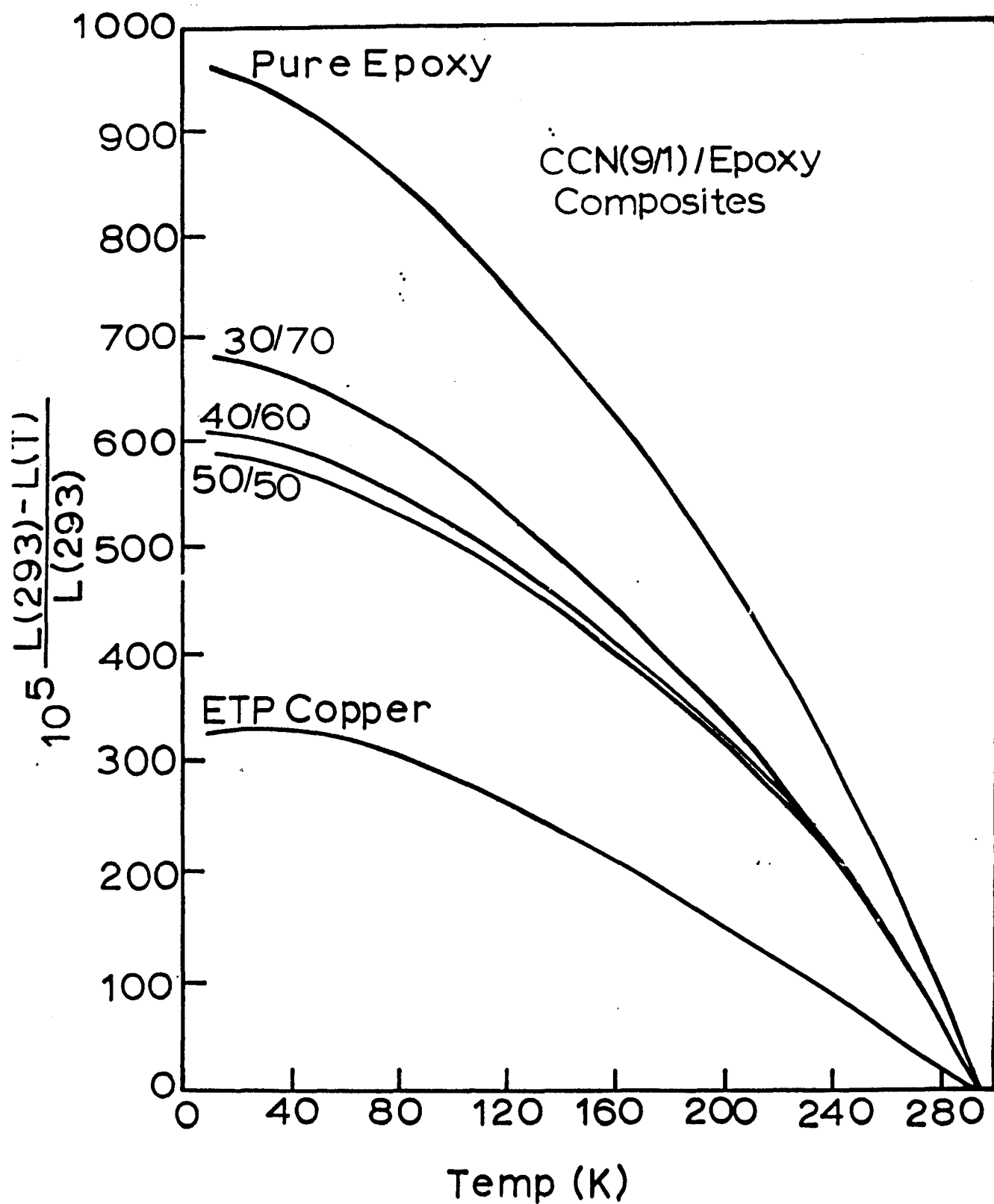
To test this theory, the same sample of pure CdCr_2O_4 used for the data in Fig. 5 was put under hydrostatic pressure in liquid helium at 4.2 K and the dielectric constant was measured as a function of pressure from 0 to 9250 kPa (0 to ~ 92 atm). Over this pressure range there was a small (0.5 %) increase in dielectric constant which can be accounted for by the change in density of the liquid helium within the pores of the sample. The null results of this experiment do not disprove the theory that the columbite phase exerting pressure on the spinel causes the anomaly in the dielectric constant, but it does put a lower limit on the pressure needed to cause the effect.

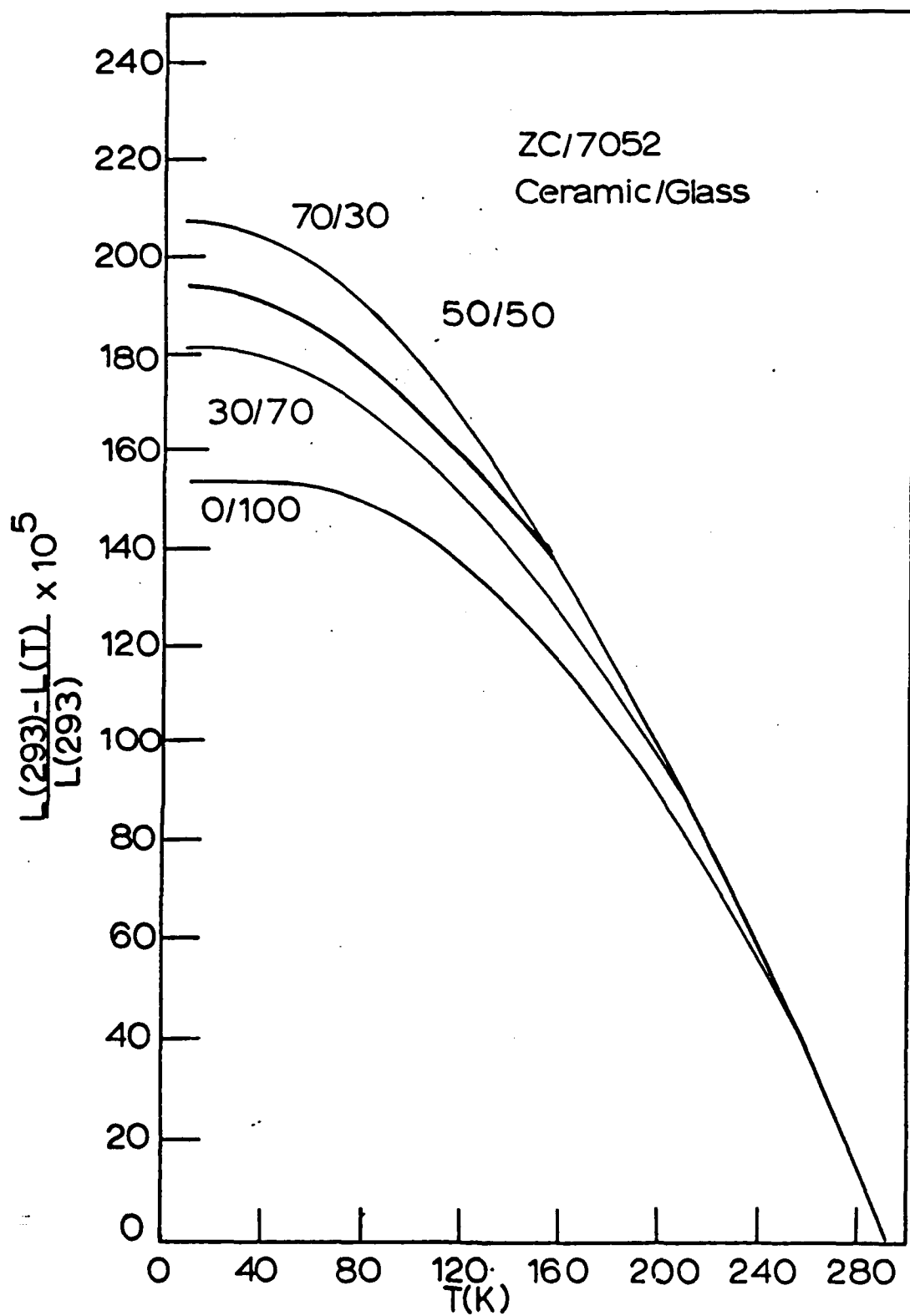
V.B. THERMAL CONTRACTION - COMPOSITE SAMPLES

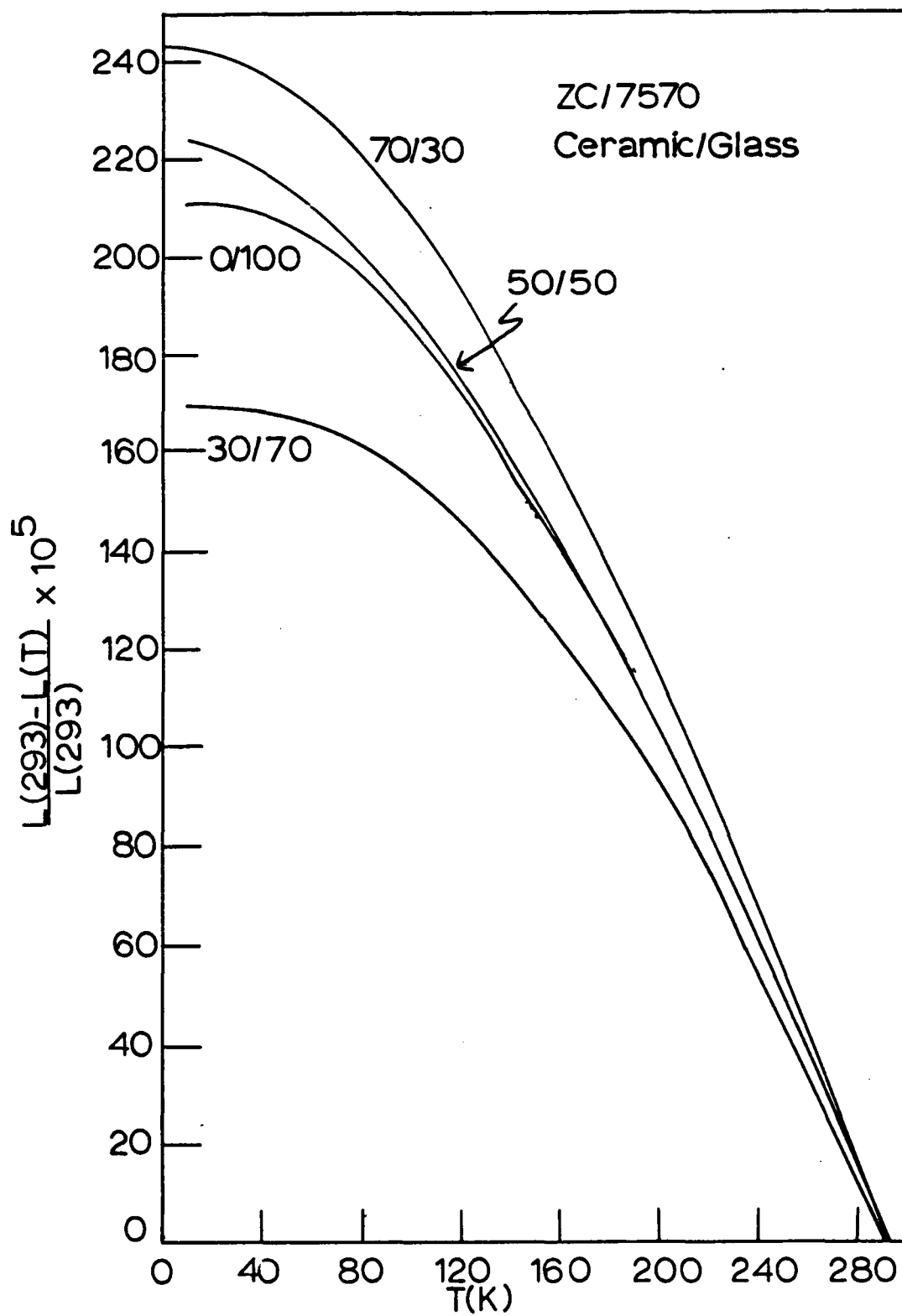
Here we report thermal contraction measurements on several of the glass and epoxy composites with ZnCr_2O_4 (ZC) and CdCr_2O_4 (CC) on which specific-heat measurements were reported in Section IV.B.

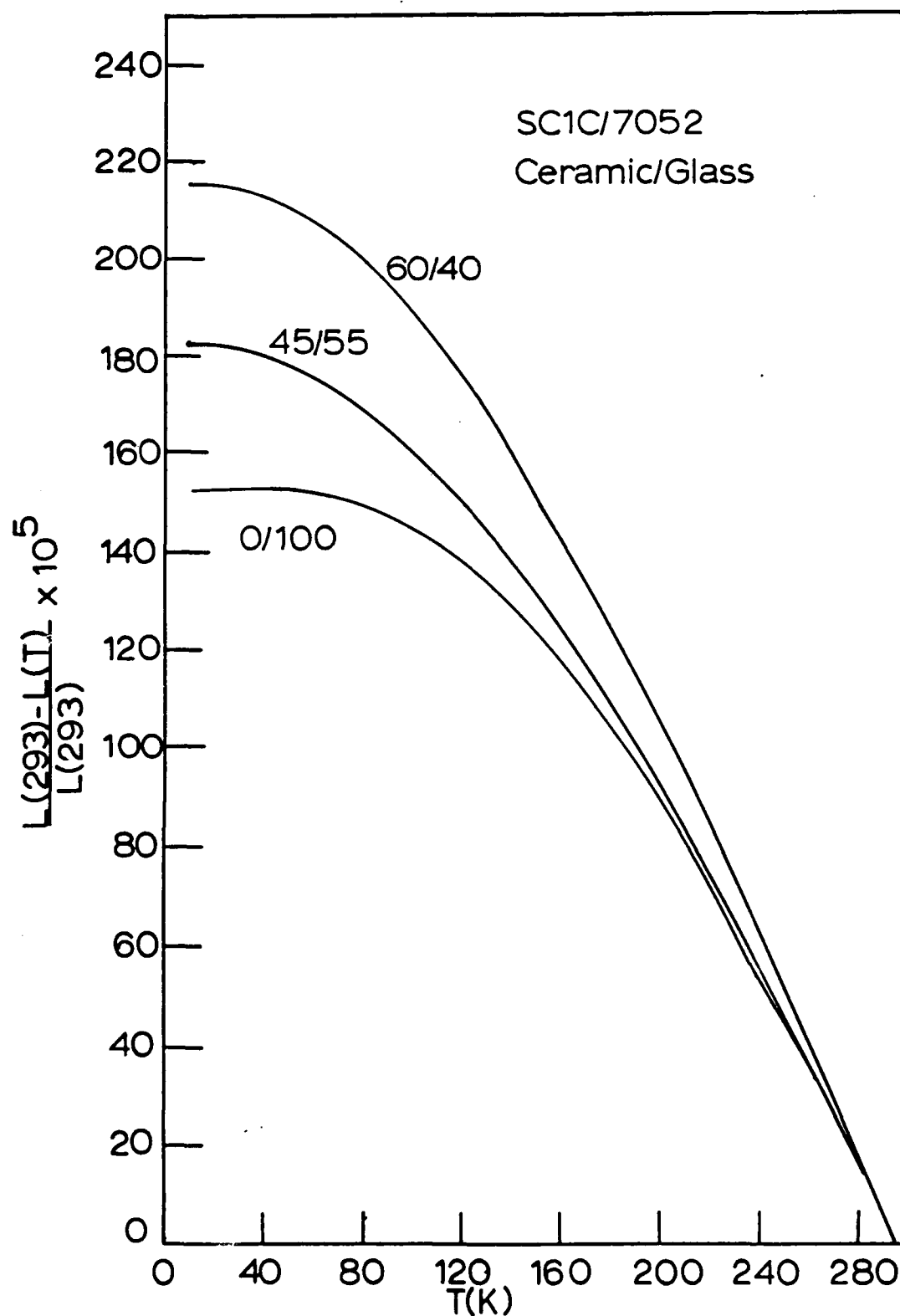
The results of the measurements are shown Figs. 6-11. Figure 6 and 7 show the contractions of CC and CCN(9/1) as varying volume percentages in epoxy. The thermal contraction of the pure epoxy is shown in both figures, and the thermal contraction of ETP copper is also shown for comparison. Figures 8-11 show the thermal contraction of ZC/7052 mixtures, ZC/7570 mixtures, CCN(9/1)/7052 mixtures, and CCN(9/1)/7570 mixtures respectively. On these graphs, the thermal contraction of the pure glasses are indicated by the lines labeled 0/100 (i.e. 100% glass). The thermal contract of a sample of CC/7570 is shown in

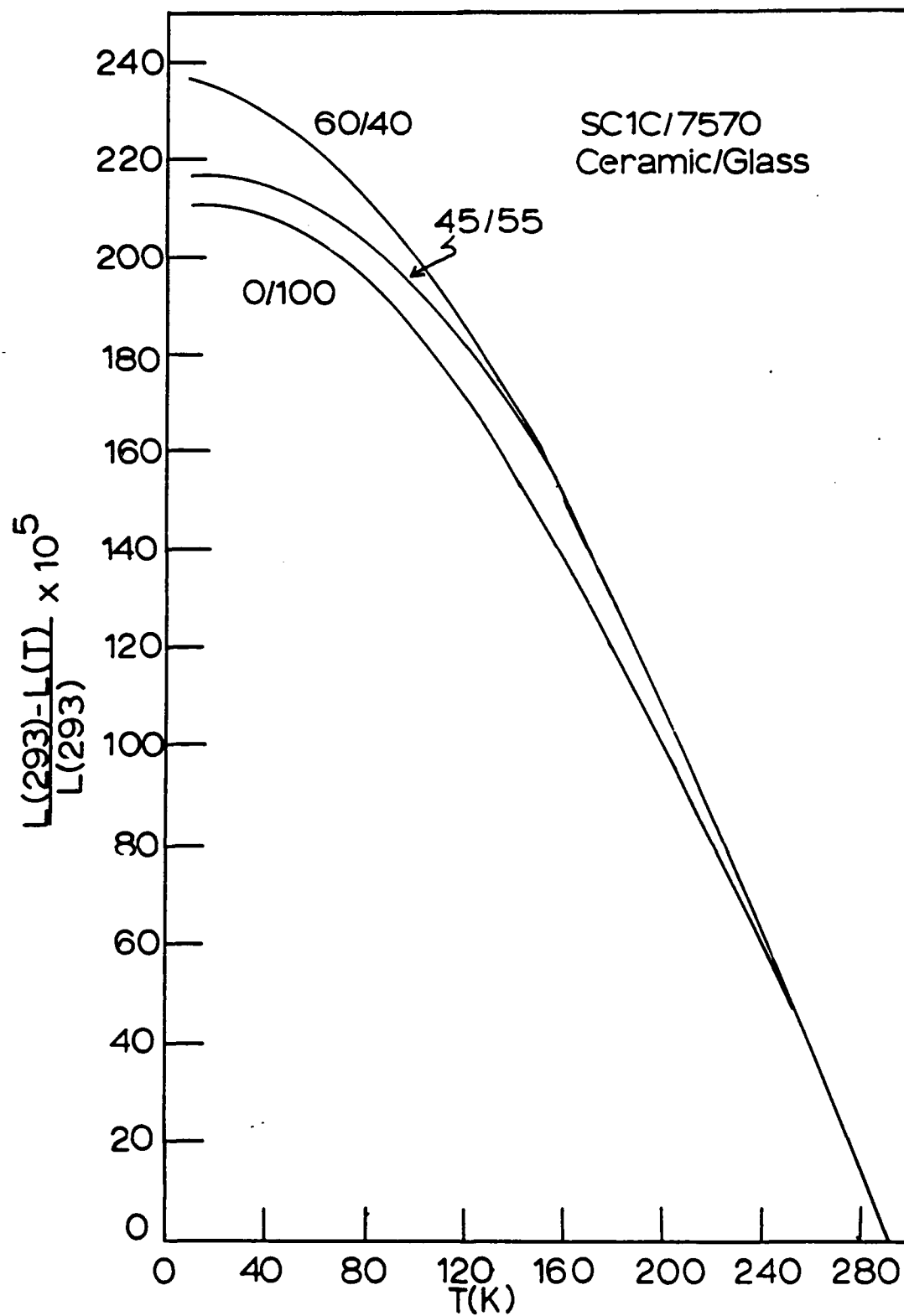












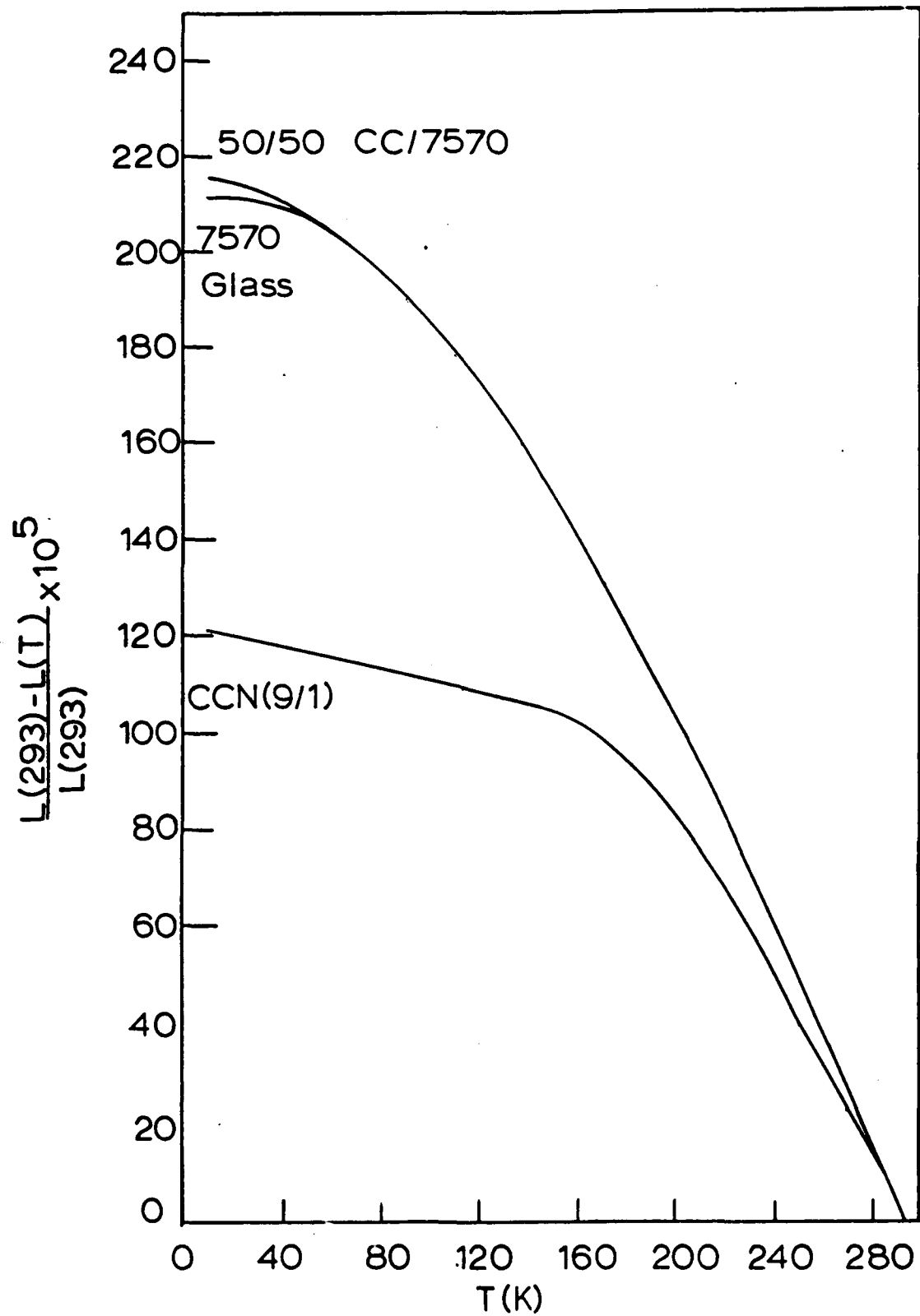


FIGURE 12

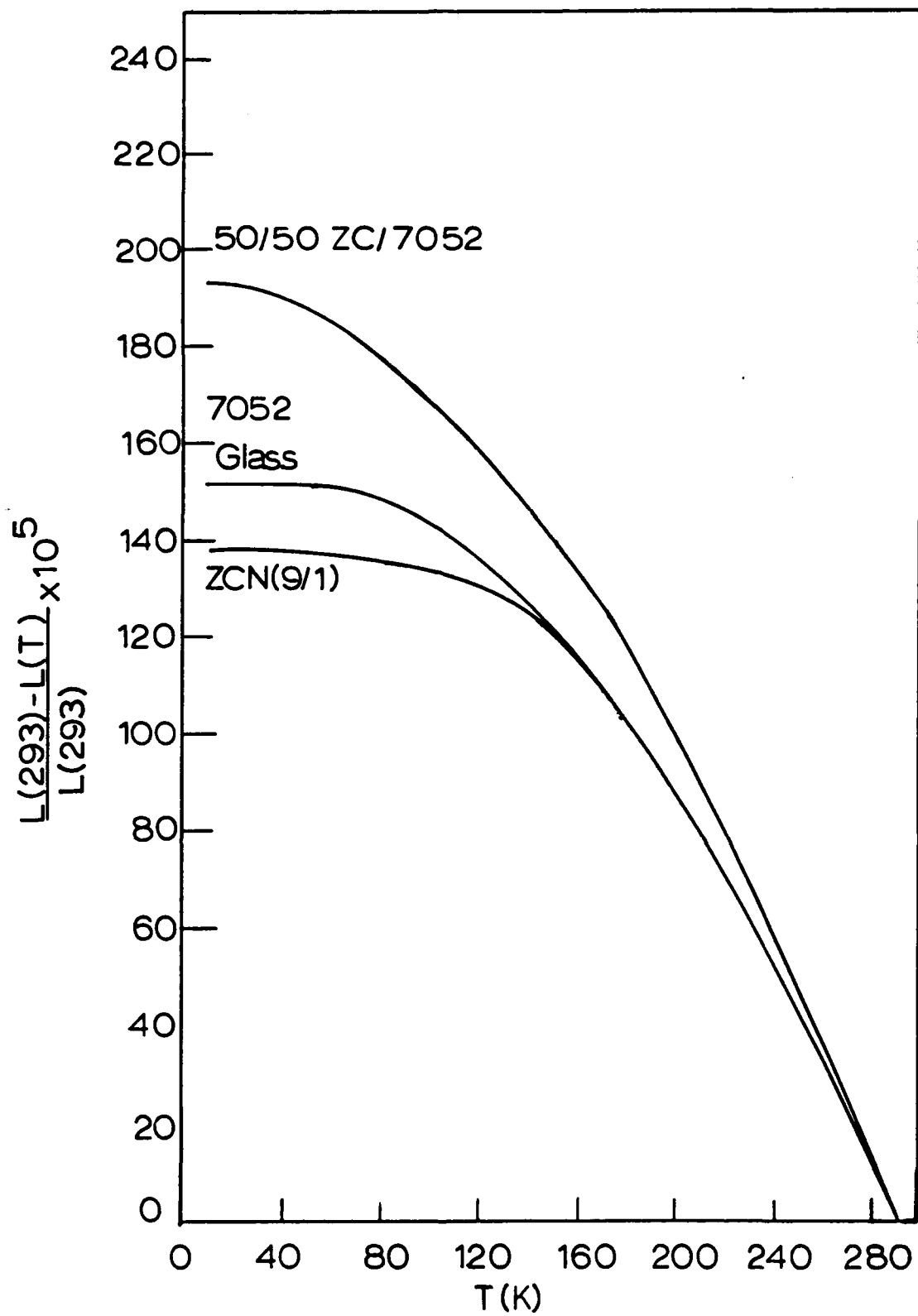


FIGURE 13

Fig. 12 compared to pure 7570 glass and CCN(9/1). Likewise, the thermal contraction of a sample of ZC/7052 compared to pure 7052 glass and ZCN(9/1) is shown in Fig. 13.

There are a number of conclusions that can be drawn from these data. First note that the thermal contraction of the epoxy is large and that increasing percentages of ceramic consistently decrease the contraction; thus, the thermal contractions of the ceramics are less than that of the epoxies. On the other hand, increasing the percentage of a ceramic in the glasses consistently increases the contraction (the one exception is discussed below), thus implying that the thermal contraction of the ceramics is greater than that of the glasses. Therefore, mixing ceramics in epoxy will place them in compression, while mixing them in 7052 and 7570 glasses will place them in tension.

There are two anomalies in these data which should be noted. First in Fig. 9, the thermal contraction of 30/70 ZC/7570 is not consistent with other mixtures of these materials. It is possible there was a confusion during sample preparation (note the similarity of the curves labeled 30/70 in Figs. 8 and 9) although this is unproven and will not be pursued at this point because it does not change the overall conclusions.

More worrisome is the inconsistency between Figs. 10 and 11 compared to Fig. 12 and by implication to Fig. 13. If Figs. 10 and 11 were considered alone, it would be concluded that the glasses contract less than CCN(9/1), i.e., adding ceramic raises the curve. Yet the direct comparison of glass and CCN(9/1) in Fig. 12 indicates the opposite. At present there is no known explanation for this discrepancy.

Note that there have been no samples of pure CC or pure ZC which have been dense enough to use in thermal contraction measurements. It is very possible that pure CC and ZC spinels have a larger contraction than the CCN(9/1) and ZCN(9/1) spinel/columbite mixtures and therefore Figs. 8, 9, 12 and 13 are internally consistent.

V.D. DIELECTRIC CONSTANT MEASUREMENTS ON DOPED AND

HUP'ED SAMPLES

Dielectric constant measurements have been made on disks of materials which became available late in the program. These include disks of ZC and CC were produced in a variety of ways, including disks from very high purity powders, a disk of ZC compacted using hot uniaxial-pressing (HUP) techniques and disks sintered from powders of ZC and CC with various doping substitutions. These latter include ZC doped with 2% Gd^{+3} and 3% Al^{+3} on the A-site, ZC exposed to H_2S for 60 hrs to replace O with S, and CC with 2% V^{+5} on the A-site.

The samples were all disks with widely varying porosities and diameters of ~ 1 cm and thicknesses of 2-3 mm. Electrodes were applied on the faces with a Dupont silver paste fired at 595°C . Measurements were made in a special probe using shielded co-axial leads to eliminate lead-to-lead capacitance. Since the samples had significant porosity, and since the silver in the electrodes may have penetrated a small but unknown amount into the samples, it was impossible to determine the absolute dielectric constant. Instead all the data below are presented as normalized to the dielectric constant at 8 K for each sample.

In the previous dielectric constant measurements in CCN(9/1), ZCN(9/1), CC and ZC, it was shown that there was a relationship between the dielectric constant peaks and the specific heat peaks caused by the antiferromagnetic transition in these materials. In the materials chosen for additional dielectric constant measurements, the specific heat peaks all showed some type of anomalous behavior. Therefore the discussion of the dielectric constant measurements also involves a discussion of the specific heat measurements which are reported in another section.

Figure 17 of Section IV.B. shows the measured specific heat of high purity ZC powder. The peak which occurs at 12.15 K is larger by a factor of six compared to the specific heat peak in ZCN(9/1), i.e., 600 mJ/gmK compared to 100 mJ/gmK respectively. The relative dielectric constant of this material is shown in

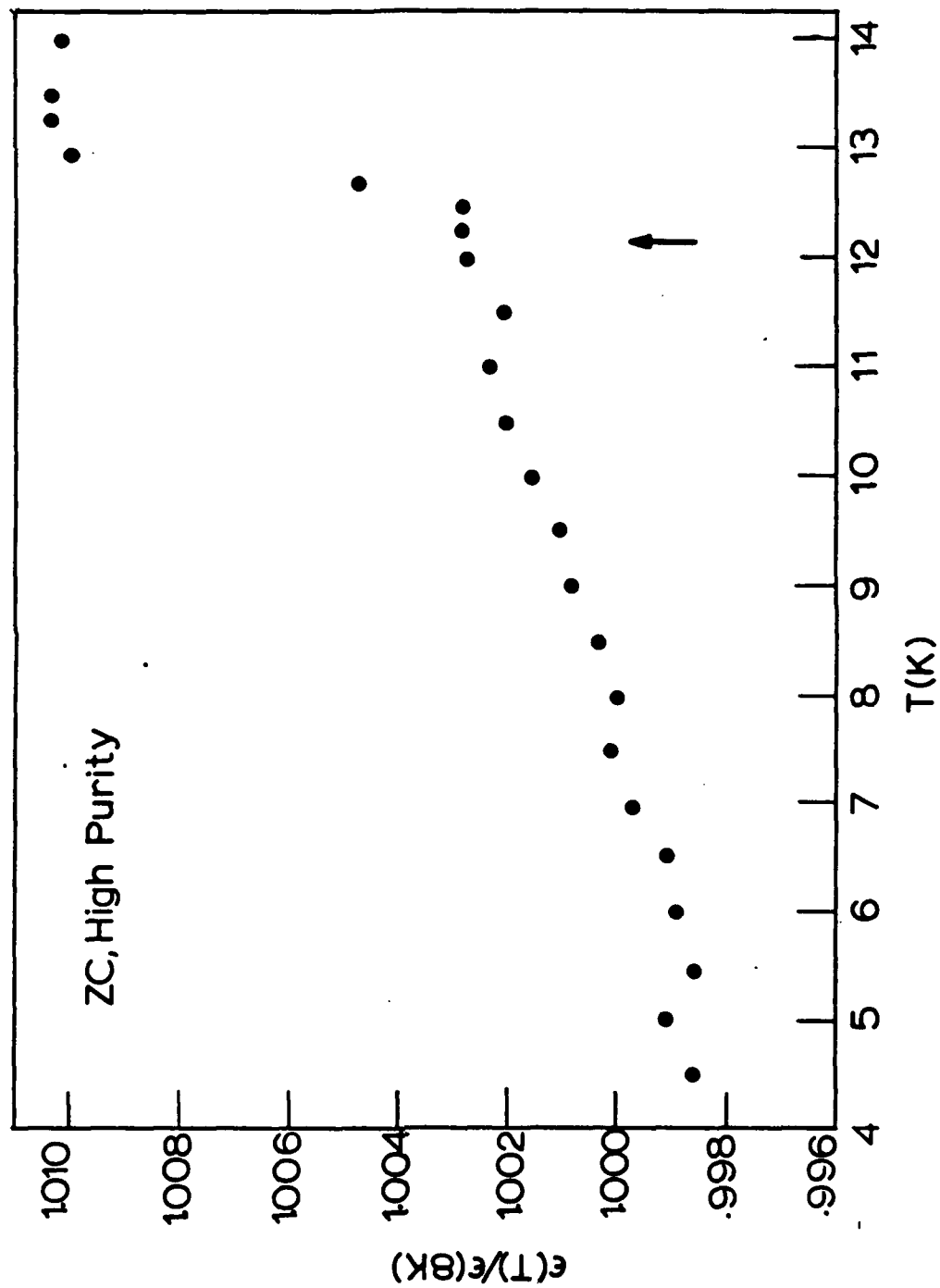


FIGURE 14

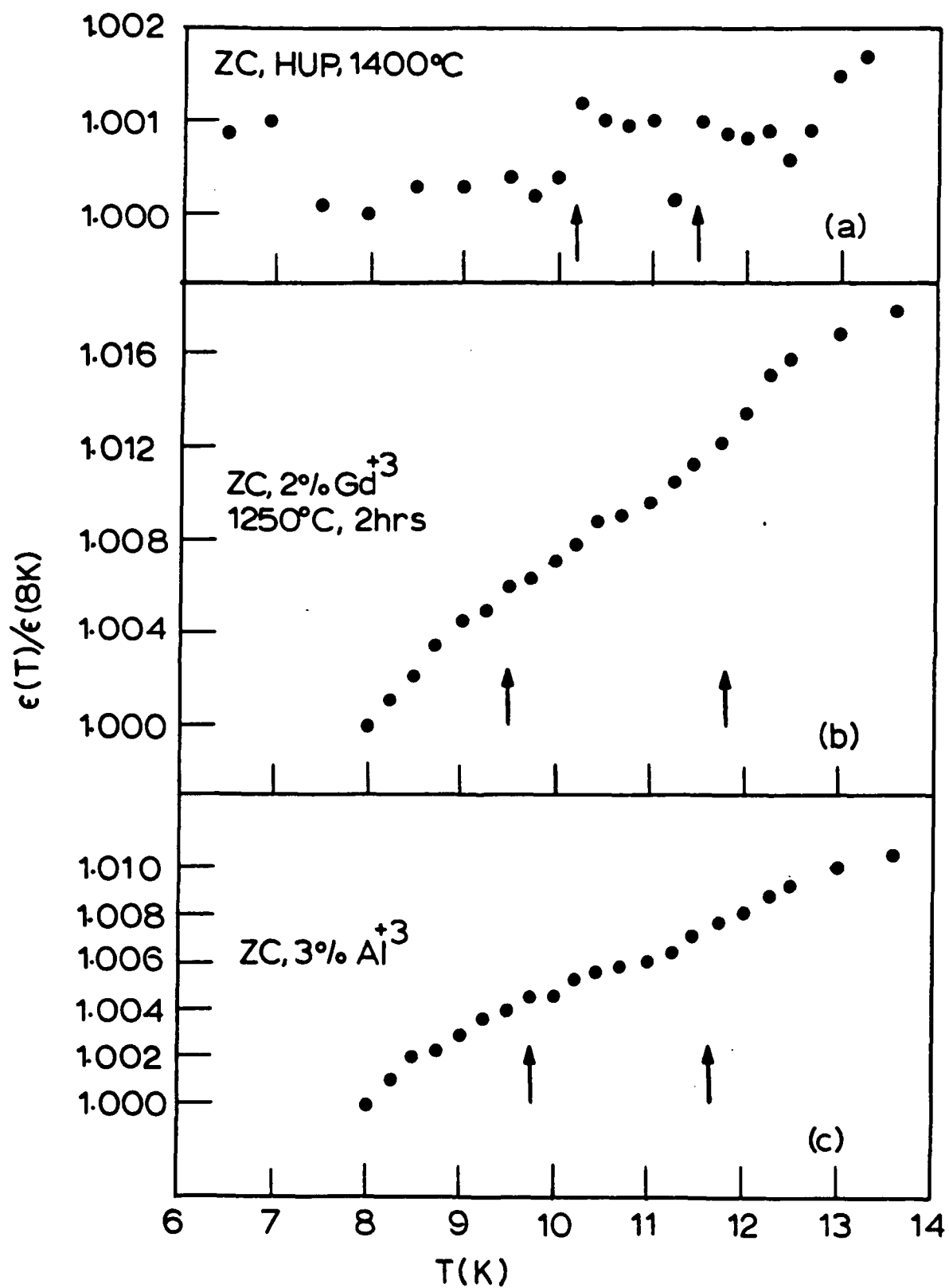


FIGURE 15 a,b,c

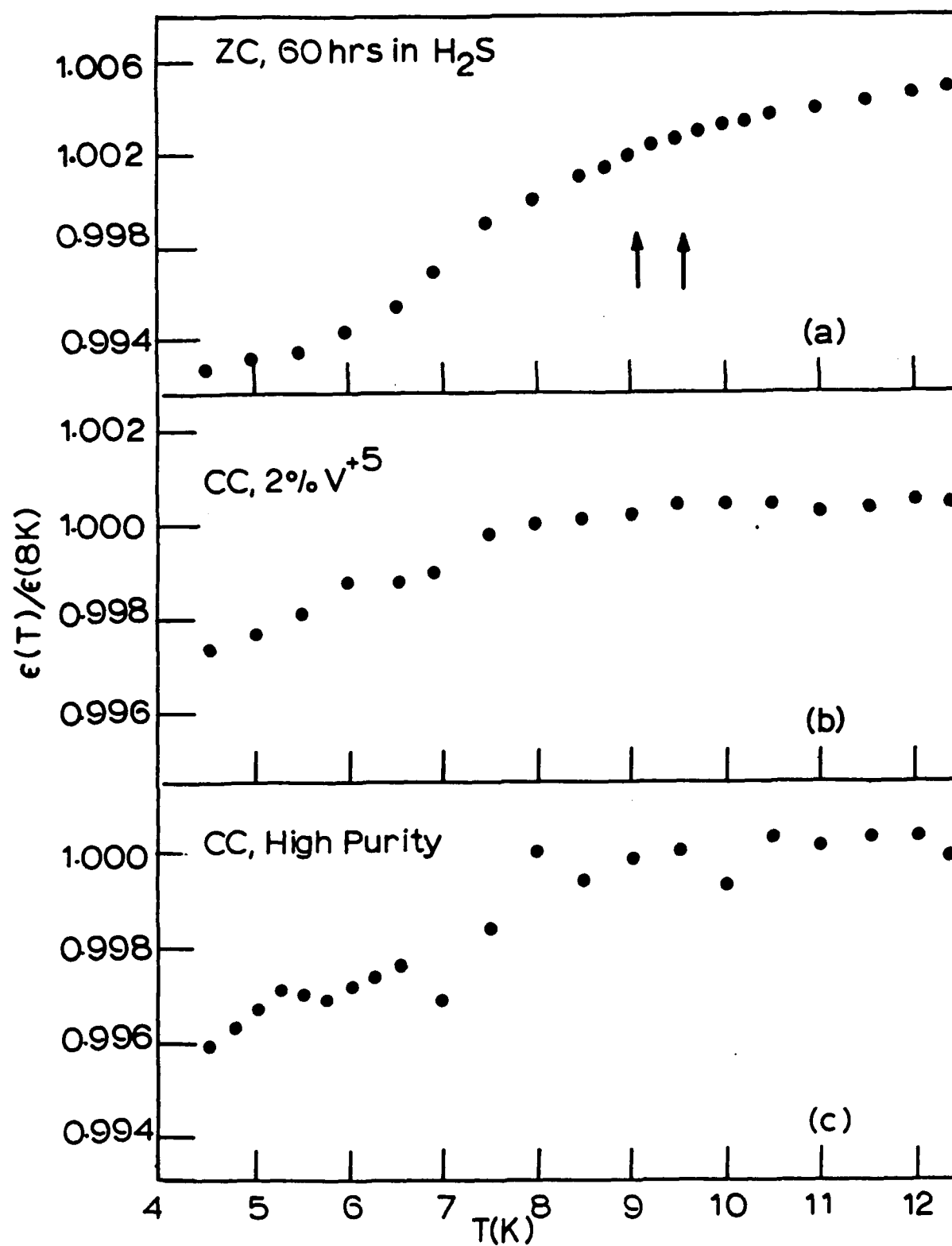


FIGURE 16 a, b, c

Fig. 14 and shows a large rise near the maximum specific heat temperature indicated by the arrow. This result is consistent with the data previously reported in this section for CCN(9/1), ZCN(9/1), CC and ZC powders which all have well-defined, large specific heat peaks, and dielectric constant anomalies associated with them.

In all the other samples of ZC listed above, the substitutions, HUP'ing, and sulfurization all result in a splitting of the specific heat peak and a drastic decrease in the magnitude of the peak as shown in Figs. 43 and 25-27 of Section IV.B.. Note that all the specific heat peaks lie between ~ 60 - 70 mJ/gmK or a factor of 10 lower than the peak of high purity ZC. The dielectric constants for these same four samples are shown in Figs. 15 a, b, c and 16a. There are no evident sharp increases in the dielectric constants with the possible exception of the HUP'ed sample (Fig. 15a) where there is a small increase at the first peak. However the magnitude of the jump is not much different from the noise in the system as indicated by the bounce in the points. In all the dielectric constant graphs (Figs. 15 a, b, c and 16a), the specific heat peak temperatures are indicated by arrows.

Figure 15 of Section IV.B. shows the specific heat of CCN(9/1) and CC high-purity samples and Fig. 23 of Section IV.B. shows the specific heat of CC doped with 2% V^{+5} . In both the high purity and doped samples, the peak is completely washed out. Likewise, there is no peak in the dielectric constant data for either sample as shown in Figs. 16 b,c.

All of these samples had densities of no more than 60-70% of theoretical. It is likely that the combination of decreased measurement sensitivity due to the porosity prevented the detection of any dielectric anomalies which were present in the samples. In addition, as discussed below, the magnitude of the dielectric anomaly is probably related to the magnitude of the specific heat peak and since the peaks were all lower in these materials, the anomaly was also probably lower.

V.D. AC CONDUCTIVITY MEASUREMENTS

AC conductivity measurements were performed on disk samples of CCN(9/1) and ZCN(9/1) at 4.2 K and 77 K from 0.6Hz to 10^5 Hz. There were no interesting features to the measurements; the circuit response was that of a single capacitor, i.e., the capacitor formed by the electrodes on the disk sample.

V.E. SUMMARY AND CONCLUSIONS FOR THERMAL EXPANSION AND DIELECTRIC CONSTANT MEASUREMENTS

The thermal expansion measurements as reported here are generally straightforward, well-behaved and internally consistent with one main exception. The thermal contraction of CCN(9/1) as shown in Fig. 2(A) and the thermal contractions of this ceramic mixed with glass are inconsistent as shown in Figs. 10 and 11. The thermal contraction of glass is larger than that of CCN(9/1), yet additions of ceramic to glass increased the thermal expansion of the mixture above either pure material.

The primary motivation in making thermal contraction measurements was to indicate whether samples of ceramic in epoxies and glasses were in compression or tension. Stresses in the ceramic coupled with the antiferromagnetic transitions are a potential source of the large specific heats found in these materials and the specific anomalies found in mixtures of ceramics with glasses and epoxies. The results indicate that mixing ceramics in epoxy places them in compression, while mixing them with glasses will place them in tension.

The low temperature thermal contraction measurements have shown that both CCN(9/1) and ZCN(9/1) undergo a lattice distortion as the materials pass through their antiferromagnetic transition temperatures. This result has important ramifications for a theoretical understanding of the materials.

The dielectric constant measurements show the only known example at cryogenic temperatures of a coupling between a magnetization and polarization. Bruce Patton of Ohio State Univer-

sity has derived a theoretical expression for the dielectric constant using three adjustable parameters (see the Annual Technical Report for this program dated 5/11/87, pp 131-145) and this expression agrees quite well with experimental data for CCN(9/1). The derivation assumes there is a coupling between the polarization P and the sublattice magnetization L . This sublattice magnetization arises due to a large amount of frustration in the undistorted spinel lattice and leads under the right conditions to the large specific heat peaks observed. It is the distortions of the lattice to reduce this frustration that leads to changes in the dielectric constant. From a simple argument it would appear that in the samples above with greatly reduced specific heat peaks and the absence of a dielectric anomaly that L (or at least the average L) is decreased due to the presence of doping impurities.

However this explanation is an oversimplification since Dr. Patton has also shown that the splitting of the specific heat peaks can be explained by certain types of lattice distortions due to clustering of doping defects. Furthermore, this clustering argument is not readily applicable to the high purity CC nor the HUP'ed ZC samples.

It is likely that dielectric anomalies exist in all of the samples which show specific heat peaks, but in the measurements shown in Figs. 15 and 16 the anomalies are smaller than the sensitivity of the measurements. All of the samples of Figs. 15 and 16 had smaller specific heat peaks than those of CCN(9/1) and ZCN(9/1) which also implies that the sublattice magnetization and the coupling to the polarization would be weaker. In addition, all of the samples of Figs. 15 and 16 were porous, which lowers the capacitance and sensitivity of the measurements on the samples.

VI. MAGNETIC SUSCEPTIBILITY AND EPR MEASUREMENTS

VI.A. INTRODUCTION

This report summarizes our comprehensive magnetic susceptibility (χ) and electron paramagnetic resonance (EPR) measurements on eighteen judiciously selected samples of CdCr_2O_4 and ZnCr_2O_4 over a wide (1.8 - 300 K) temperature range. The measurements span a period of over 12 months because of the iterative nature of the results obtained. While we had earlier reported (Kahol et al., 1986; Kahol and Dalal, 1987; Dalal and Kahol, 1989) the susceptibility and EPR measurements on a variety of ceramic powders and disks of CdCr_2O_4 and ZnCr_2O_4 , the results needed further work in several respects. First, the earlier work was done mostly in the spirit of preliminary explorations so as to determine the scope of the methodologies. However, both the susceptibility and the EPR measurements yielded some new clues (e.g., possibility of some 'free' spins) to the mechanism of the cooperative phenomena and hence the enormous specific heat (C_p) peaks exhibited by these lattices (Lawless et al., 1986-88). The next step was to make detailed susceptibility and EPR measurements on some selected samples on which the extensive C_p , magnetocaloric and dielectric measurements have been made by Lawless, Clark and Hampton at CeramPhysics, Inc. Second, it was important that the earlier EPR measurements be extended from 77 K to the liquid helium range, in particular below 4.2 K. The

need for the EPR measurements below 4.2 K was indicated by the susceptibility data, since it was below 4.2 K that the data had indicated the emergence of Curie-like tails (*i.e.* the 'free' spins). We note here that while susceptibility measurements can detect the presence of 'free' spins, such data generally cannot unambiguously identify the origin of the spins, for example, whether the spins reside on the grain boundary $S = \frac{1}{2}$ defects or on Cr^{3+} ($S = \frac{3}{2}$). In this case EPR is the technique of choice because the EPR signal line shape and line position are characteristic of the 'free' spin undergoing resonance absorption⁴. EPR is thus the most direct method of detecting and identifying the chemical species (or ions) responsible for any 'free' paramagnetic spins in a given sample. In certain cases, however, the EPR signals might not be detectable because of the possible very short ($< 10^{-10}$ s) electron spin-lattice relaxation time (T_1) of the 'free' spins. In such cases one must resort to the susceptibility measurements which are independent of the spin-lattice relaxation processes. In principle, therefore, for the detection and identification of any new paramagnetic species, one must make both the susceptibility and the EPR measurements. The results of such measurements on eighteen CdCr_2O_4 , ZnCr_2O_4 , and ZnCr_2S_4 samples are the subject of this report.

VI.B. EXPERIMENTAL METHODOLOGY AND SAMPLE DETAILS

Experimental details of the susceptibility and EPR measurements have been given in our earlier reports (Kahol et al., 1986; Kahol and Dalal, 1987; Dalal and Kahol, 1989), and will be only briefly summarized here.

A portion of the susceptibility measurements were made at the National Magnet Laboratory of the Massachusetts Institute of Technology (MIT), using a SQUID magnetometer designed by the SHE corporation, and the remainder were performed at WVU using a SQUID magnetometer designed by the Quantum Corporation. The sample temperature was varied from 1.8 to 300 K in any desired step to within 0.1 K or better. The EPR measurements were made at West Virginia University using a Brüker X-band (model ER 200D) EPR spectrometer, operating normally at 9-10 GHz. The spectrometer is controlled by an ASPECT 2000 microcomputer for data acquisition and line shape simulations. The sample temperature was again controlled to within 0.1 K, using an Oxford ESR-900/ DTC-2 helium-flow cryostat. For the EPR measurements, the magnetic field was calibrated with a Brüker model ER-035M NMR fluxmeter and the microwave frequency was measured with a Hewlett-Packard HP5409A digital frequency counter.

The eighteen samples selected to be investigated are described below, with the numeration corresponding to the approximate order in which the results will be presented:

<u>Sample #</u>	<u>Base Material - Comments</u>
1	CdCr_2O_4 - undoped CeramPhysics sample
2	CdCr_2O_4 - 5% Nb_2O_5 , CeramPhysics sample
3	ZnCr_2O_4 - high purity ceramic
4	ZnCr_2O_4 - 5% Nb_2O_5 , CeramPhysics sample
5	ZnCr_2O_4 - sulfur exchanged
6	ZnCr_2O_4 - 2 molar percent Gd_2O_3
7	CdCr_2O_4 - 2 molar percent V_2O_5
8	ZnCr_2O_4 - 3 molar percent Al_2O_3
9	ZnCr_2O_4 - high purity ceramic
10	CdCr_2O_4 - high purity ceramic
11	ZnCr_2O_4 - hot pressed at $\approx 1400^\circ \text{C}$
12	ZnCr_2O_4 - nominal Gd^{3+}
13	ZnCr_2O_4 - 2% Gd_2O_3
14	ZnCr_2O_4 - MoO_3
15	ZnCr_2O_4 - 2 molar percent V^{5+}
16	ZnCr_2O_4 - MnO
17	CdCr_2O_4 - 2 molar percent Mo^{3+}
18	ZnCr_2O_4 - 2% V_2O_5

VI.C. EXPERIMENTAL RESULTS

Magnetic susceptibility (χ) measurements - indication for 'free' spins below T_N

The results of the dc (0.2 kG) magnetic susceptibility (χ) measurements on CdCr_2O_4 undoped ceramic (conventional) are shown in Fig.1 (full circles). Similar data for a CdCr_2O_4 ceramic compacted using 5% Nb_2O_5 are also shown in Fig. 1 (open circles). The (slow) exponential increase in susceptibility with decreasing temperature, a small, rounded peak around 8 K and then a rapid decrease with further temperature decrease is the direct evidence that these lattices undergo antiferromagnetic transitions. The antiferromagnetic transition temperature, i.e. the Néel temperature, T_N , was determined by plotting $d\chi/dT$ vs. T and defining T_N as the temperature corresponding to the maximum of $d\chi/dT$, as discussed in detail in our earlier report (Kahol and Dalal, 1987): T_N was found to be 8.0 ± 0.5 K for both samples. This value is a reasonably good agreement with that (7.9 ± 0.1 K) reported by Lawless and coworkers (1986-88) via specific heat (C_p) measurements, attesting to the consistency of magnetic (χ) and thermodynamic (C_p) data and their analysis procedures.

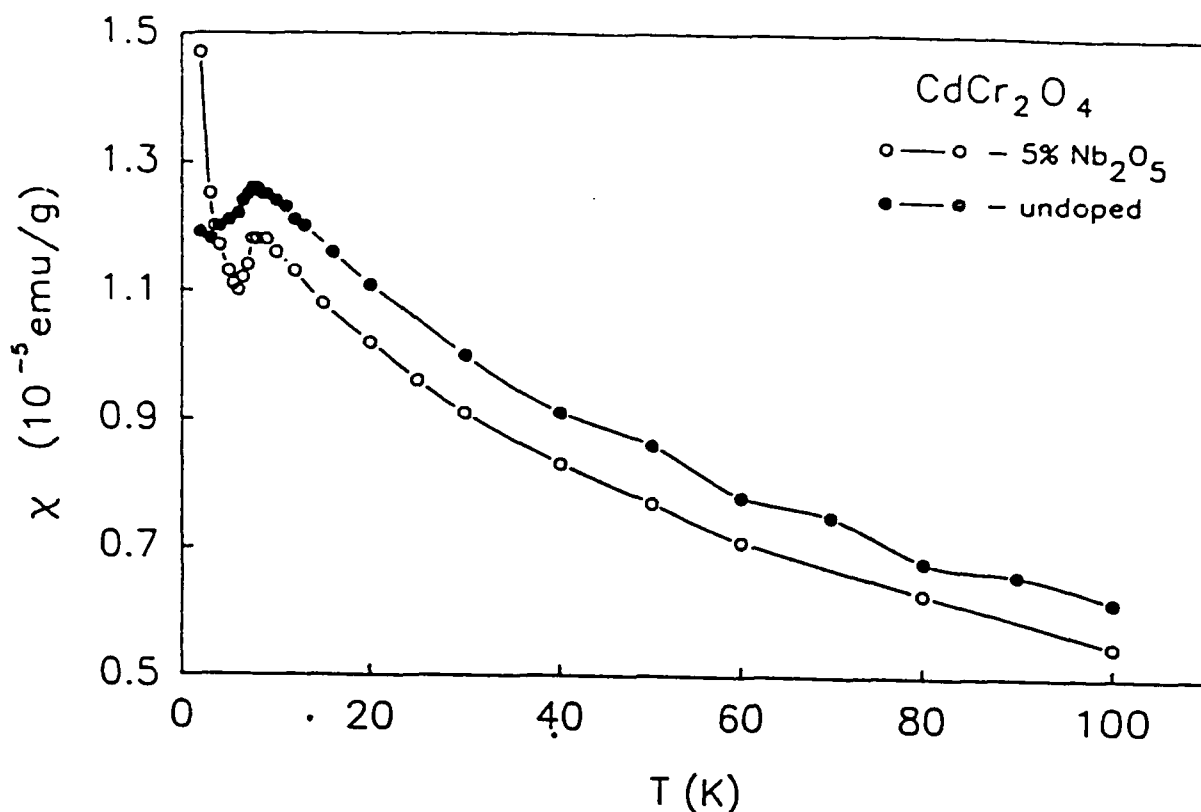


Figure 1. Temperature dependence of the magnetic susceptibility (χ) of CdCr_2O_4 .

The results of the susceptibility measurements, in static field of 0.2 kG for the undoped, conventional ceramic of ZnCr_2O_4 are shown in Fig.2 (full circles). The corresponding data for the compacted ceramic disk of ZnCr_2O_4 prepared with 5% Nb_2O_5 are shown in Fig.2 (open circles). Again, both of these samples exhibit (nearly) second order antiferromagnetic transitions at the Néel temperature $T_N \approx 11.5$ K. This value compares favorably with the more precise value of 10.7 ± 0.1 K as determined by Lawless and coworkers from their specific heat measurements. These

results underscore the fact that the huge specific heat peaks of the CdCr_2O_4 as well as ZnCr_2O_4 ceramics are intimately related to the antiferromagnetic ordering of these lattices.

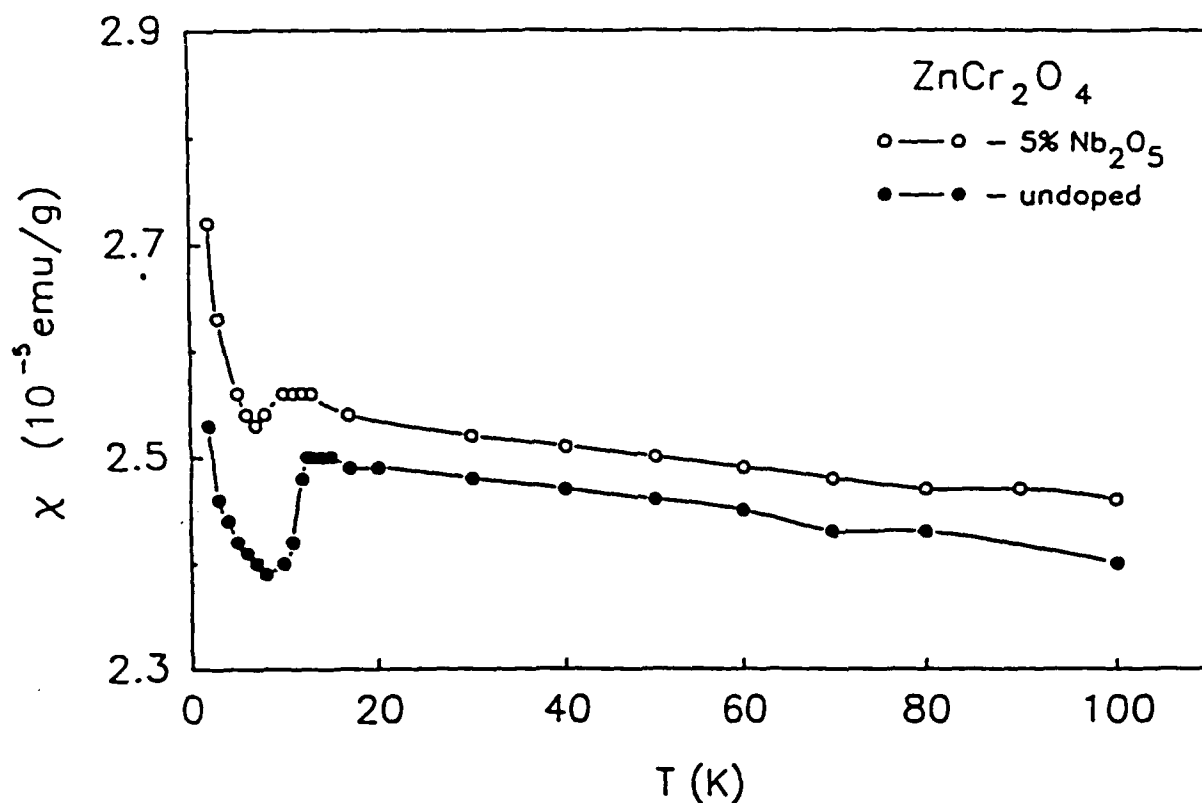


Figure 2. Magnetic susceptibility (χ) versus temperature for ZnCr_2O_4 .

A significant new result to be noted from Figures 1 and 2 was the strong increase in susceptibility with decreasing temperatures below the T_N values. An increase in

susceptibility below the T_N of an antiferromagnet must reflect either a re-entrant, ferri- or ferromagnetic phase, or simply the emergence of some 'free' spins. As mentioned earlier, the specific heat (C_p) measurements (Lawless, W.N. et al., 1986-1988.) below T_N had indicated, a significant contribution of some type of 'free' spins to the C_p of these lattices. In order to discriminate between the 'free' spin vs. ferri- or ferromagnetic type of interactions we analyzed the temperature dependence of the susceptibility, especially in the liquid helium temperature range. Since the behavior appeared to be Curie-like, we fitted the experimental data to the following expression:

$$\chi = \chi_0 \text{ (antiferro)} + C_{\text{free}} / T \quad (1)$$

where χ_0 is the extrapolated value of χ at $T = 0$ K and $C_{\text{free}} = N\mu^2/3k_B$, the Curie constant for the 'free' spins. N is the number of spins, μ is the magnetic moment per spin, and k_B is the Boltzmann constant. Thus, if the susceptibility increase were due to the free spins, then a plot of χ versus $1/T$ would be linear, with a slope equal to C_{free} , from which the number of 'free' spins can be estimated. Figures 3 and 4 show such plots for CdCr_2O_4 and ZnCr_2O_4 , respectively. All of the plots do indeed seem to be fairly linear, implying that the Curie-like tails in Figures 1 and 2 are likely to be due to the emergence of some sort of 'free' spins. Table 2 lists the fitting

parameters obtained and the estimated number of 'free' spins.

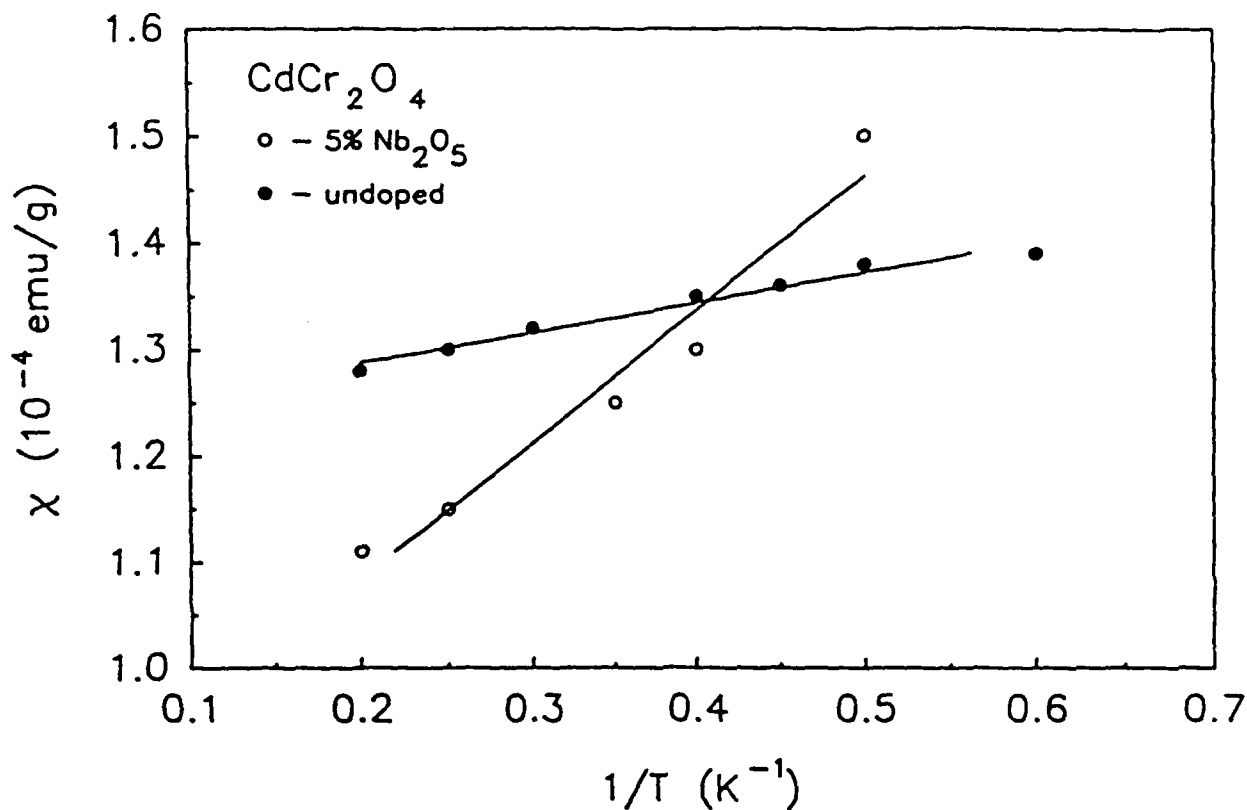


Figure 3. χ vs. $1/T$ plots for CdCr_2O_4 below T_N (≈ 8 K)

From the results entered in Table 2, it seemed that Lawless' postulate of the existence of a significant amount of 'free' spins below the T_N was quite reasonable, as also noted in our earlier report (Kahol et al., 1986; Kahol and Dalal, 1987). It was, nonetheless, thought desirable to search for direct evidence such as is obtainable via electron paramagnetic resonance (EPR) spectroscopy. Perhaps

an equally compelling reason for undertaking EPR measurements was that the EPR signal line shapes and positions could also unravel the puzzle concerning the identification of the ion (or ionic complex) bearing the 'free' spins. Thus, a detailed EPR study of all four samples was undertaken.

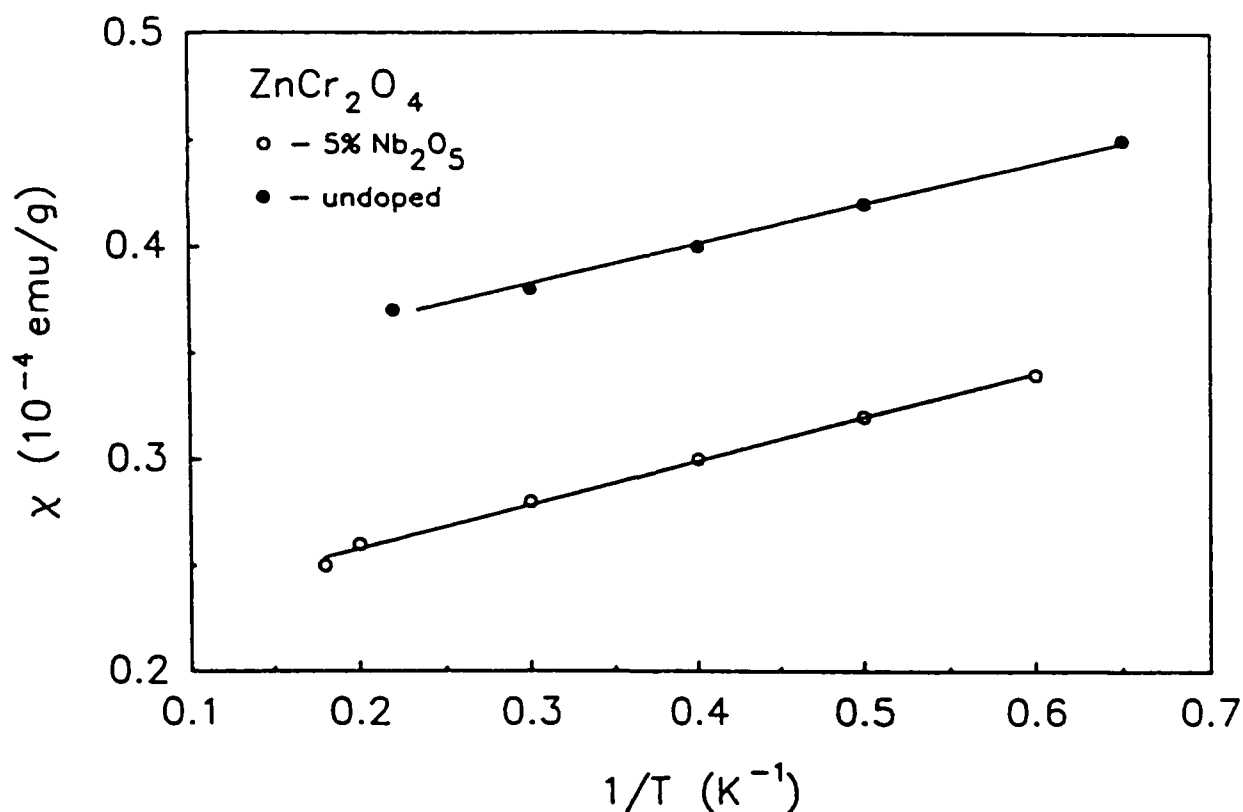


Figure 4. χ vs. $1/T$ plots for ZnCr_2O_4 below T_N (≈ 12 K)

Table 1. The parameters χ_0 , C_{free} and N as obtained by fitting Equation (1) to the χ data below T_N . The samples are listed as Samples 1-4 in Section II.

Sample	χ_0 (emu·g ⁻¹)	C_{free} (emu·K·g ⁻¹)	N (%)
CdCr ₂ O ₄	0.95×10^{-4}	1.0×10^{-4}	0.6 ± 0.5
CdCr ₂ O ₄ + 5% Nb ₂ O ₅	1.30×10^{-4}	2.5×10^{-5}	8.0 ± 2.0
ZnCr ₂ O ₄	0.25×10^{-4}	2.5×10^{-6}	0.6 ± 0.5
ZnCr ₂ O ₄ + 5% Nb ₂ O ₅	0.23×10^{-4}	2.0×10^{-5}	3.0 ± 2.0

EPR Measurements - direct evidence for the 'free'
spins

Figures 5 and 6 show some typical EPR spectra for the CdCr_2O_4 (conventional ceramic disk) and ZnCr_2O_4 (high purity ceramic disk), respectively. As usual, each spectrum is a plot of the first derivative of the (microwave) power absorbed with respect to an applied magnetic field H (i.e. $\partial P / \partial H$) at a given temperature T . The sample temperature was varied from room temperature down to 1.8 K. Approximately five hundred spectra were taken for each sample. The temperature steps were in increments of 0.05 K near the T_N for each sample. Each spectrum shown here is labeled according to the temperature of measurement, which is the only variable between these spectra.

Several important features are evident from a comparison of the temperature dependence of the EPR spectra shown in Figures 5 and 6:

(a) With a decrease in temperature (T), the peak-to-peak line width, ΔH_{p-p} , increases. In particular, ΔH_{p-p} diverges as $T \rightarrow T_N$ for each sample. Figures 7 and 8 show the temperature dependence of ΔH_{p-p} for CdCr_2O_4 and ZnCr_2O_4 , respectively. The T_N values deduced from the critical divergence of ΔH_{p-p} agree within ± 0.2 K of the values derived from the magnetic susceptibility (χ) as well as the specific heat data.

EPR SPECTRA, CdCr_2O_4 —COMPACTED CERAMIC

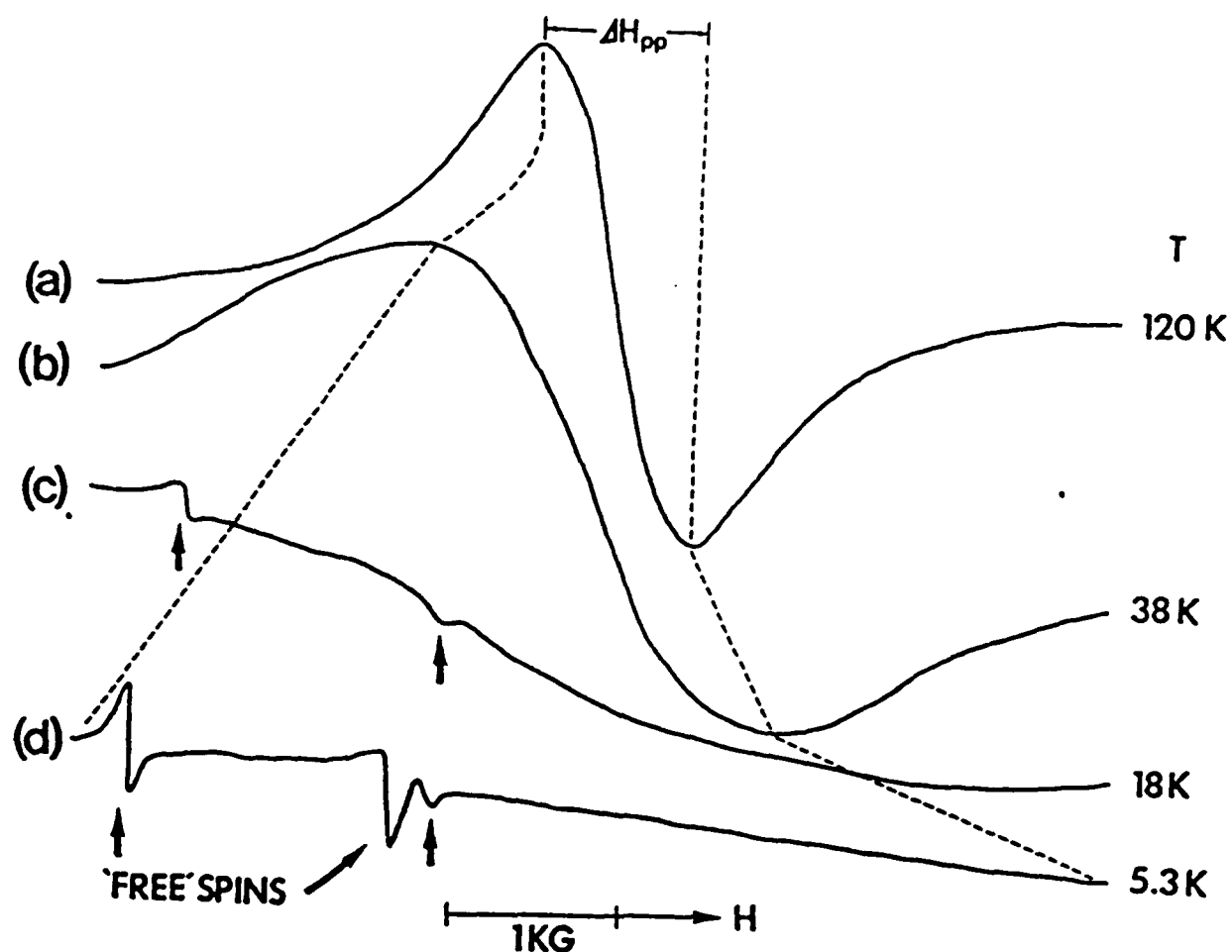


Figure 5. Temperature dependence of the first-derivative EPR spectra for the CdCr_2O_4 compacted disk. Note the rapid increase of the peak-to-peak line width, ΔH_{pp} , of the high temperature ($T > T_N$) signals and the emergence of the sharp Cr^{3+} 'free' spin peaks highlighted by the arrows as the temperature is lowered below the T_N (≈ 8 K) of the sample.

EPR SPECTRA, ZnCr_2O_4 COMPACT CERAMIC

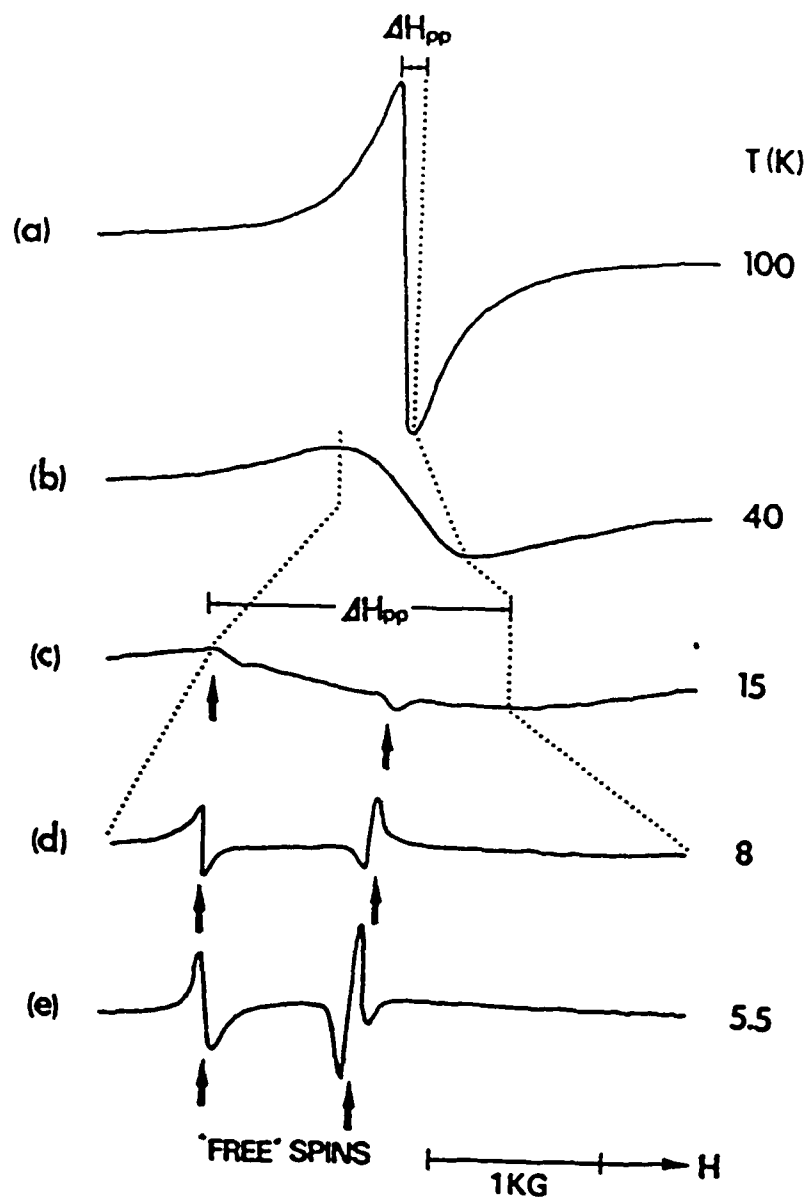


Figure 6. Temperature dependence of the first-derivative EPR spectra for the ZnCr_2O_4 compact ceramic (undoped). Note the rapid increase in the peak-to-peak width, ΔH_{pp} , as the temperature is lowered towards T_N (≈ 12 K). The new signals assigned to the 'free' Cr^{3+} spins are indicated by the arrows at the bottom.

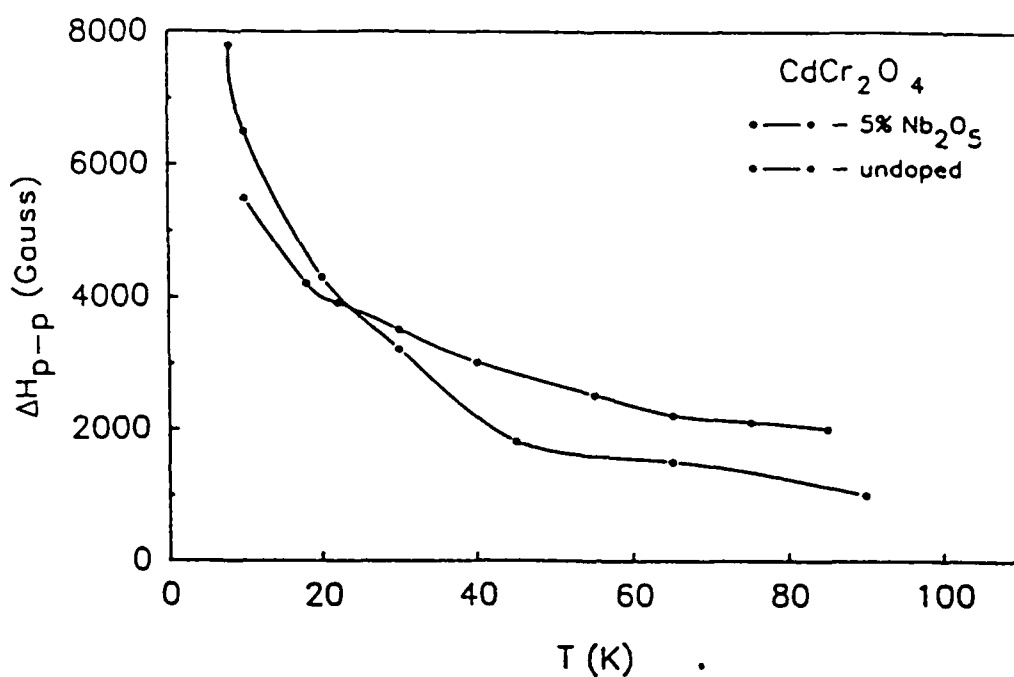


Figure 7. ΔH_{pp} vs. T for CdCr_2O_4

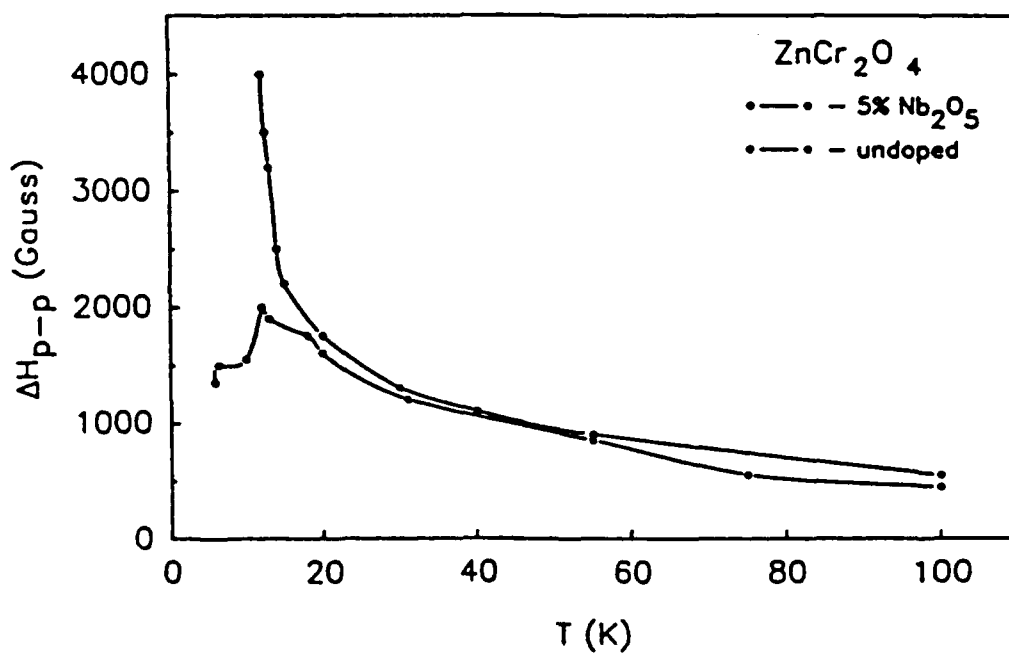


Figure 8. ΔH_{pp} vs. T for ZnCr_2O_4

The divergent behavior of ΔH_{p-p} and the disappearance of the main EPR line signal below the critical temperature is another piece of direct evidence for the antiferro- magnetic phase transitions at the T_N values of ≈ 8 K and 12 K for CdCr_2O_4 and ZnCr_2O_4 , respectively.

(b) A most significant result is the emergence of new, sharp EPR signals in the vicinity of T_N , as marked by the arrows in Figures 5 and 6. From the narrower width (≈ 50 Gauss) as compared to that ($\approx 1000 - 8000$ Gauss) corresponding to the $T > T_N$ phases, and the increase of their intensities essentially as $1/T$, they directly demonstrate that these signals originate from some 'free', Curie-like spins, such as are indicated by both the magnetic susceptibility and specific heat data.

(c) The overall intensities of the EPR signals assigned to the 'free' spins are consistent with their concentration being $\approx 1-10$ % of the total number of spins giving the signals above T_N , in agreement with the susceptibility data.

(d) Their positions and the powder-like shapes (asymmetric derivatives) are completely consistent (Abragam and Bleaney, 1970) with their being localized on the Cr^{3+} ions.

While the EPR results provide unequivocal evidence for the presence of the 'free' spins below the T_N of these lattices, it is still not clear as to what causes the emergence of the 'free' spins. Theoretical calculations by

Patton and coworkers (Lin and Patton, 1986; Lu and Patton, 1986; Patton et al., 1986) indicate that the 'free' spins are a consequence of the inherent magnetic frustrations in these (approximately) triangular lattices. The present EPR studies indicate that the lattice defects due to the strains and imperfections at the grain boundaries help to pin these spins, because the samples prepared with 5% Nb_2O_5 definitely contains at least 50% more Cr^{3+} spins, as well as some additional 'free' spins which might be centered on Nb^{4+} at the grain boundaries. For example, Figure 9 shows the EPR spectra for the 5% Nb_2O_5 -prepared CdCr_2O_4 ceramic disk. As done in Figures 5 and 6, the arrows here indicate the 'free' Cr^{3+} -based spins. Comparison of the spectra in Figures 5 (Nb_2O_5 free) and 9 show that there is an intense EPR signal located at $g \approx 1.95$ (the broad signal at the center of the 5.3 K spectrum) which is extra to the Nb_2O_5 -prepared sample. These spectra clearly demonstrate that the grain boundaries are not inert; they contribute to the 'free' spin pool.

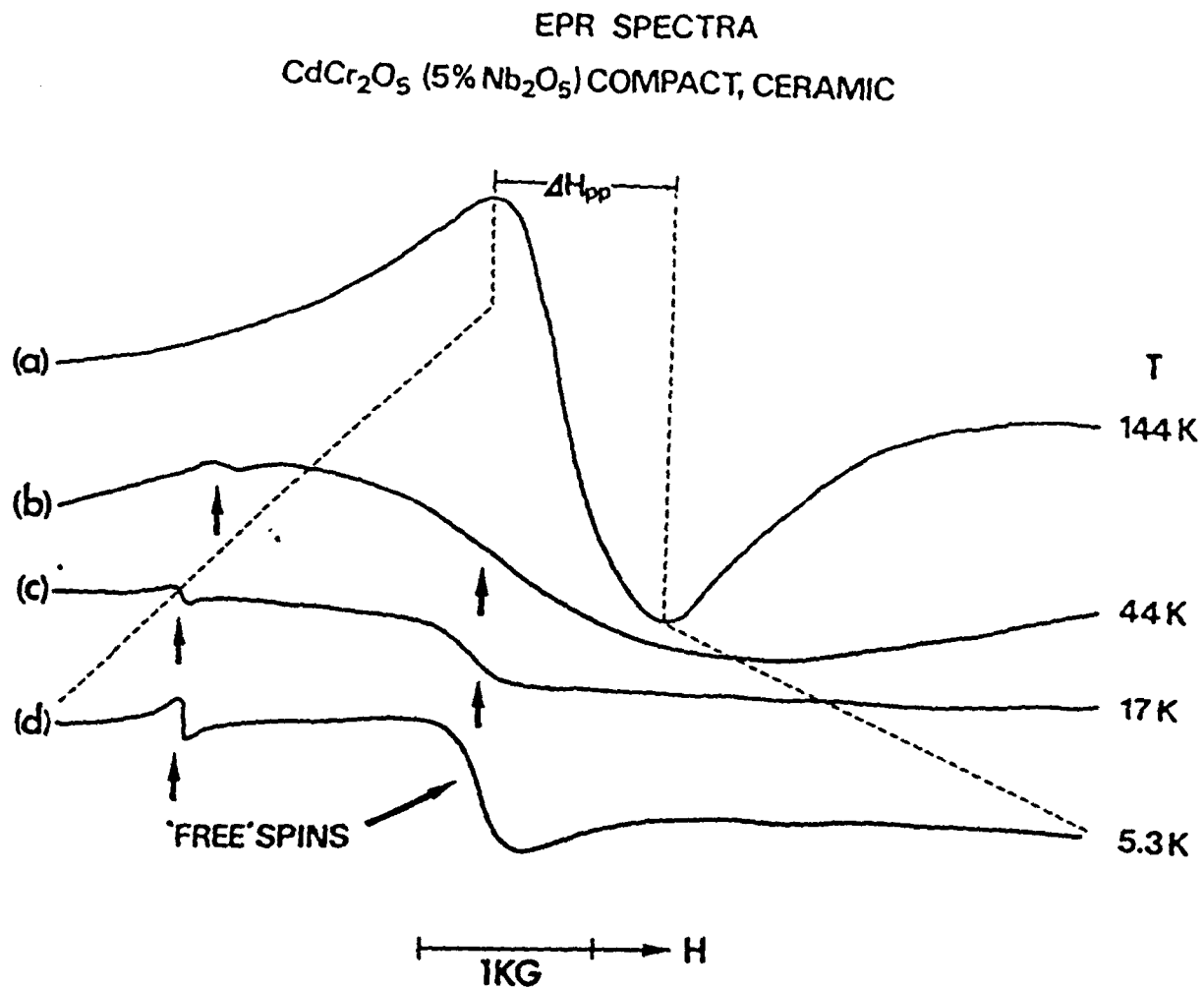


Figure 9. Temperature dependence of the EPR spectra of CdCr₂O₄ compact disk prepared with 5% Nb₂O₅. Note the emergence of the Cr³⁺-based 'free' spins (sharp line marked by the vertical arrow) and the Nb⁴⁺-related 'free' spins, the broad signal in the 5.3 K spectrum (highlighted by the slanted arrow).

VI.D. Effect of Process Variables on χ : Peak Splitting and Broadening

Additional, detailed χ measurements were performed on fourteen new samples (listed previously as numbers 5 - 18) of CdCr_2O_4 and ZnCr_2O_4 which were prepared by CeramPhysics under judiciously selected process-variable conditions. The variables investigated were: sulfur exchange (# 5); iso-static pressing (# 11); Gd-doping (#'s 6, 12, and 13); V-doping (#'s 7, 15, and 18); Al-doping (# 8); Mo-doping (#'s 14, and 17); and Mn-doping (# 16). These results are summarized below:

Transition Peak Splitting due to Sulfur Exchange

Figure 10 shows the temperature dependence of χ for sulfur-exchanged ZnCr_2O_4 (sample # 5) over the broad range of 1.8 - 100 K. A salient feature of this plot is the presence of two peaks at 9.0 ± 0.1 K and 16.5 ± 0.1 K, highlighted by the arrows in the figure. This result is significant because unsubstituted ZnCr_2O_4 exhibits only a single peak at about 12.5 K, as may be noted from Figure 2. Thus, a comparison of the plots in Figures 2 and 10 clearly shows that sulfur substitution of ZnCr_2O_4 causes a doubling of the peak corresponding to the antiferromagnetic transition of this lattice. These results confirm a similar

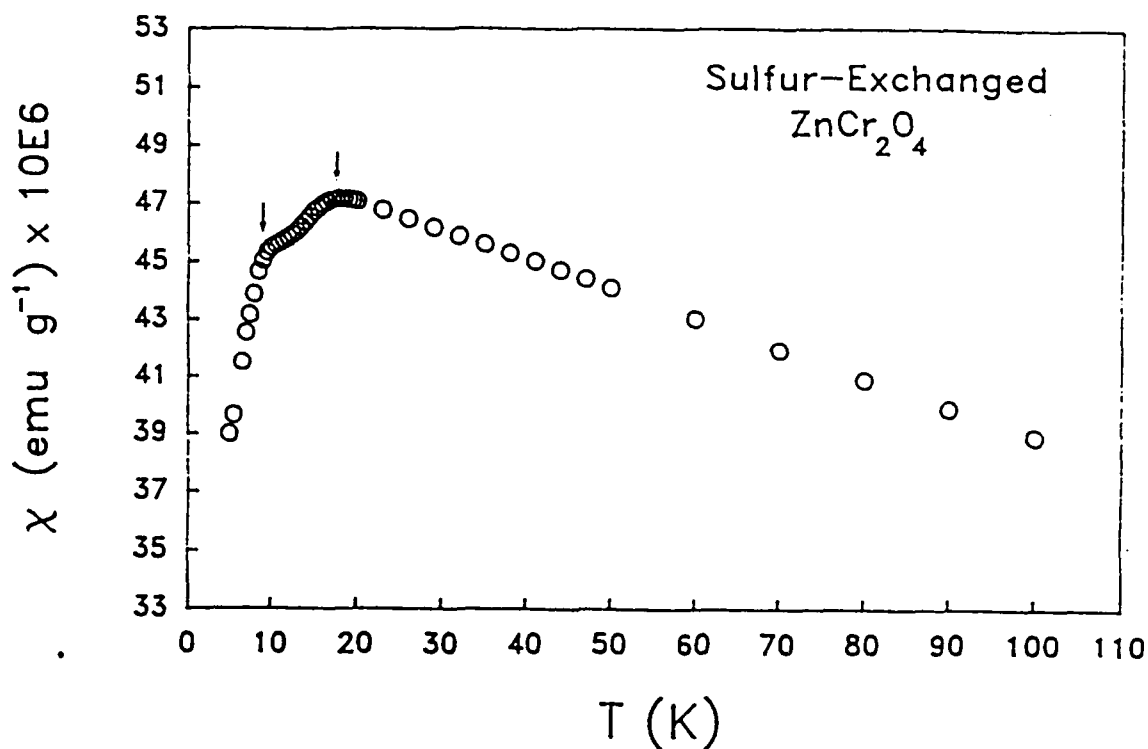


Figure 10. Temperature dependence of χ for sulfur-exchanged ZnCr_2O_4 . Note the doublet structure in the peak as highlighted by the arrows.

phenomenon noted by Lawless and coworkers in their specific heat C_p data (Lawless et al. 1988).

Effect of hot pressing on $\text{ZnCr}_{2-4}\text{O}_4$

Figure 11 (a) shows the temperature dependence of the χ for a hot-pressed ZnCr_2O_4 ceramic pellet over the 1.8-110 K range. This plot also exhibits signs of two peaks, as highlighted by the arrows. To obtain more definitive evidence,

the measurements were made at 0.1 K intervals over a narrower range of 1.8 - 20 K. These data are plotted in Figure 11 (b) from which the anticipated doublet of peaks can be clearly seen.

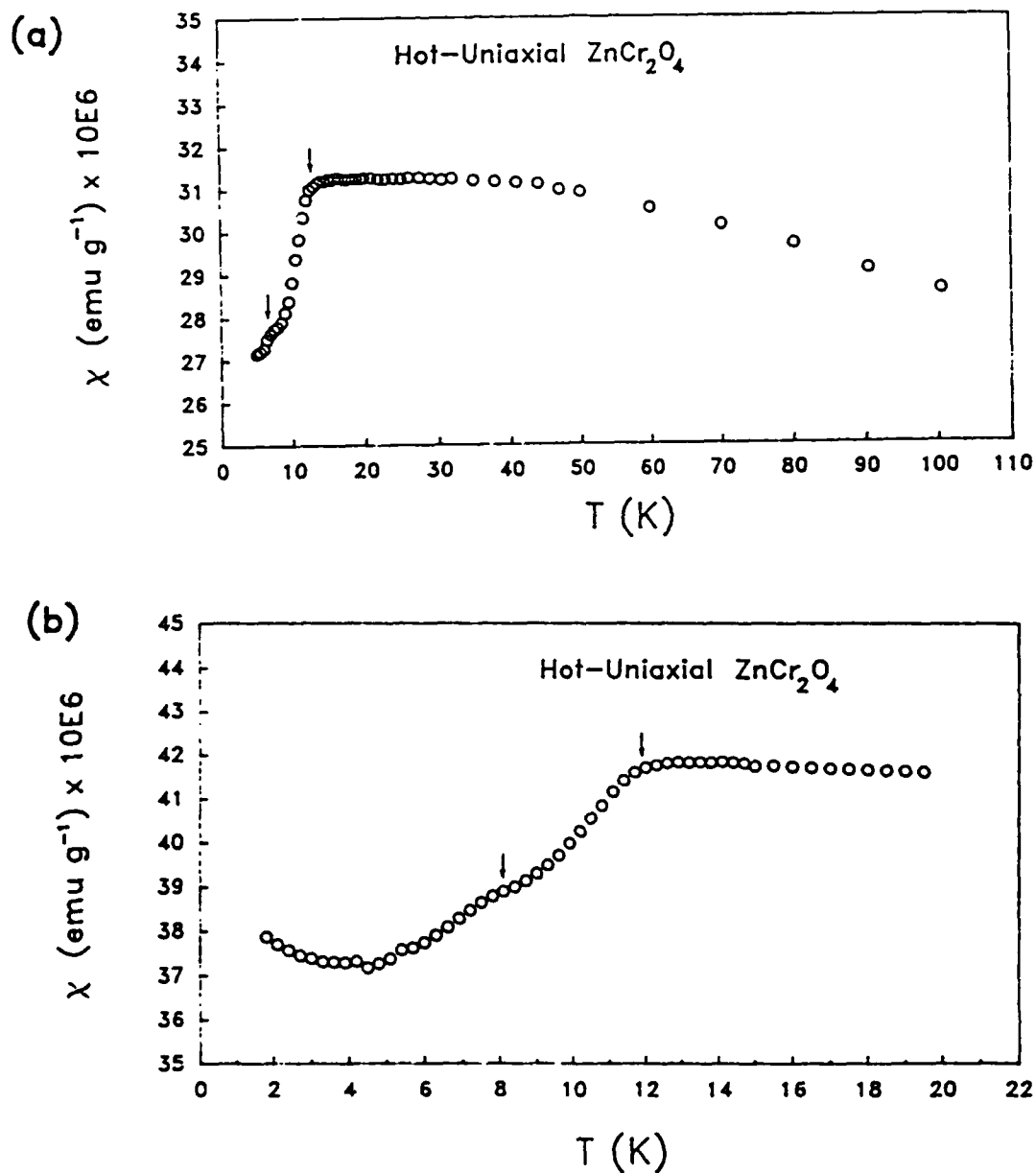


Figure 11. Plots of χ versus T over a broad (a) and narrow (b) temperature range. The arrows indicate the split peaks.

Peak Splitting by Non-magnetic Doping

In order to find if the peak splitting is a general phenomenon and if the transitions could be shifted to even higher temperatures, we measured χ for both ZnCr_2O_4 and CdCr_2O_4 doped with various metal ions in the form of oxides. Figures 12, 13, and 14 show the χ versus T plots for ZnCr_2O_4 doped with Al_2O_3 , V_2O_5 (V^{5+}), and MoO_3 , respectively.

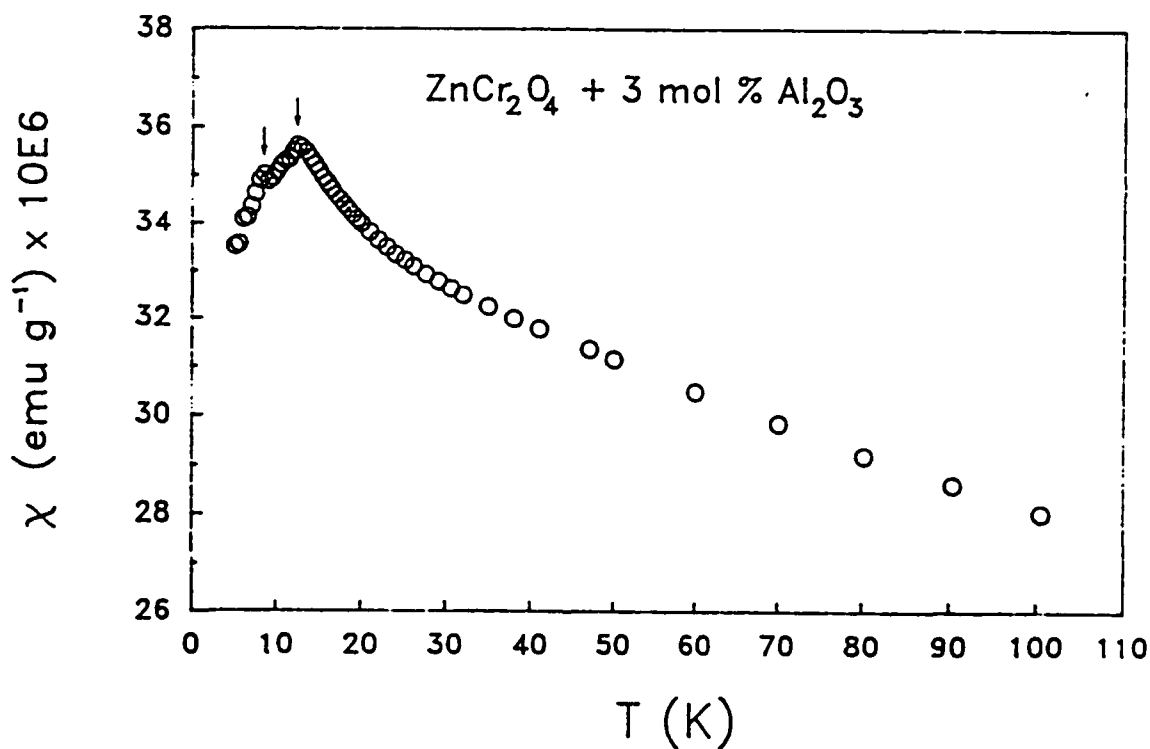


Figure 12. Temperature dependence of χ for ZnCr_2O_4 doped with 3 molar % Al_2O_3 . The arrows indicate the positions of the two peaks mentioned in the text.

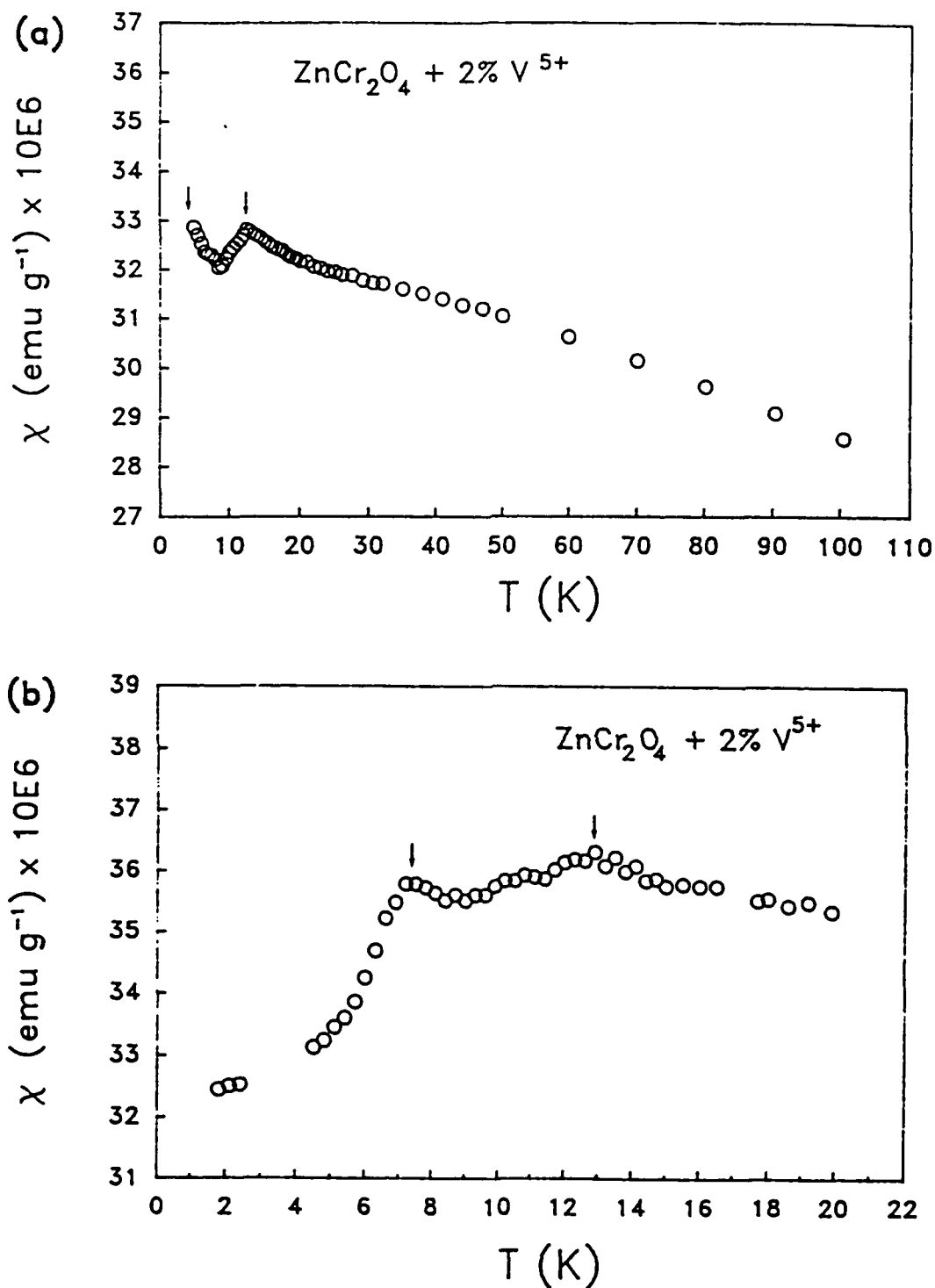


Figure 13. χ versus T plots for ZnCr_2O_4 doped with V_2O_5 (V^{5+}) over (a) broad range of 1.8- 110 K and (b) 1.8- 20 K, expanded scale. The arrows indicate the peak doublets.

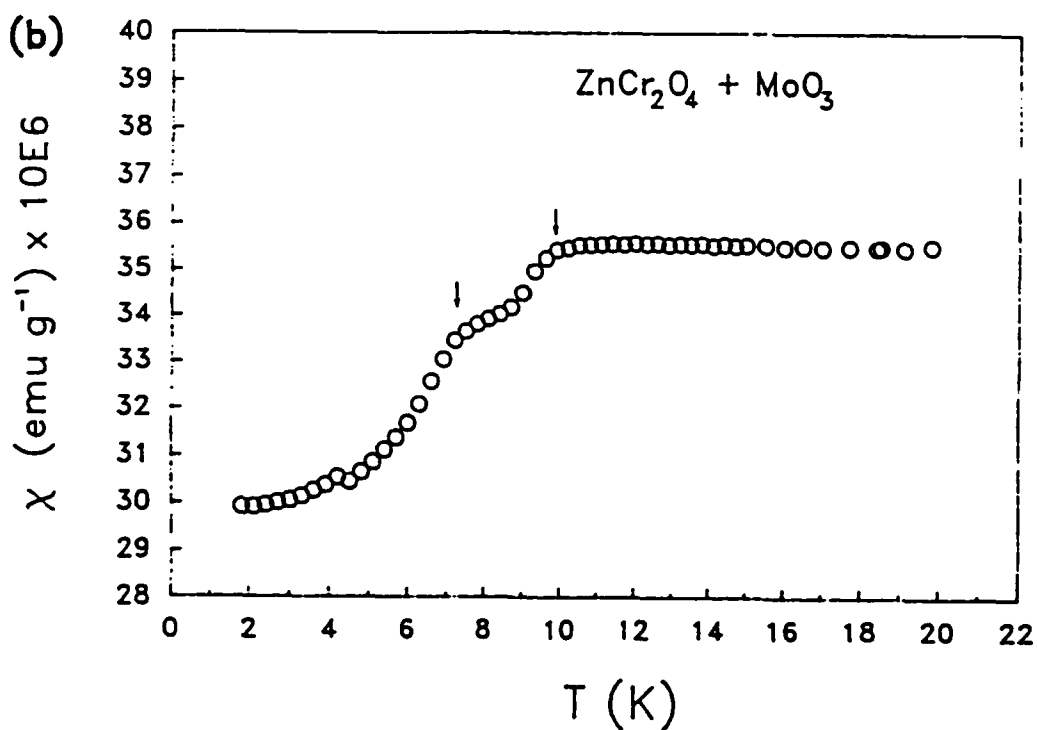
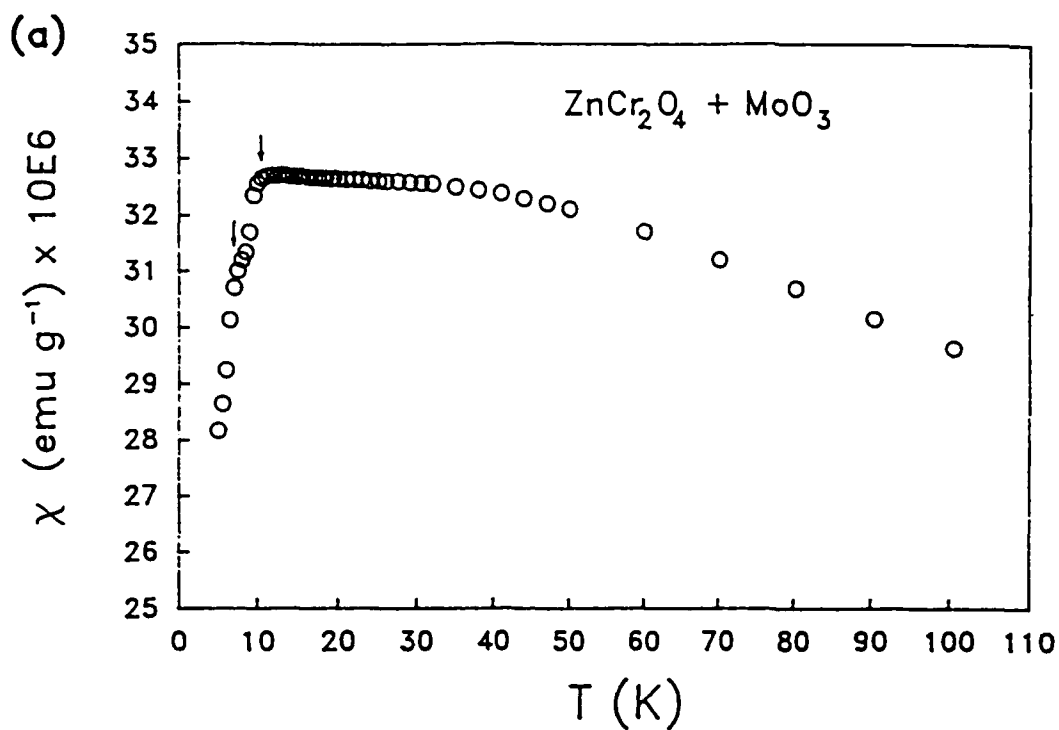


Figure 14. Temperature dependence of χ versus T for MoO_3 -doped ZnCr_2O_4 over (a) 1.8 - 110 K and (b) 1.8 - 20 K (expanded scale). The arrows indicate the peak doublets.

Figure 15 (a) shows a χ versus T plot for CdCr_2O_4 doped with 2 molar % Mo^{3+} while Figure 15 (b) shows a similar plot for CdCr_2O_4 doped with 2 molar % V_2O_5 .

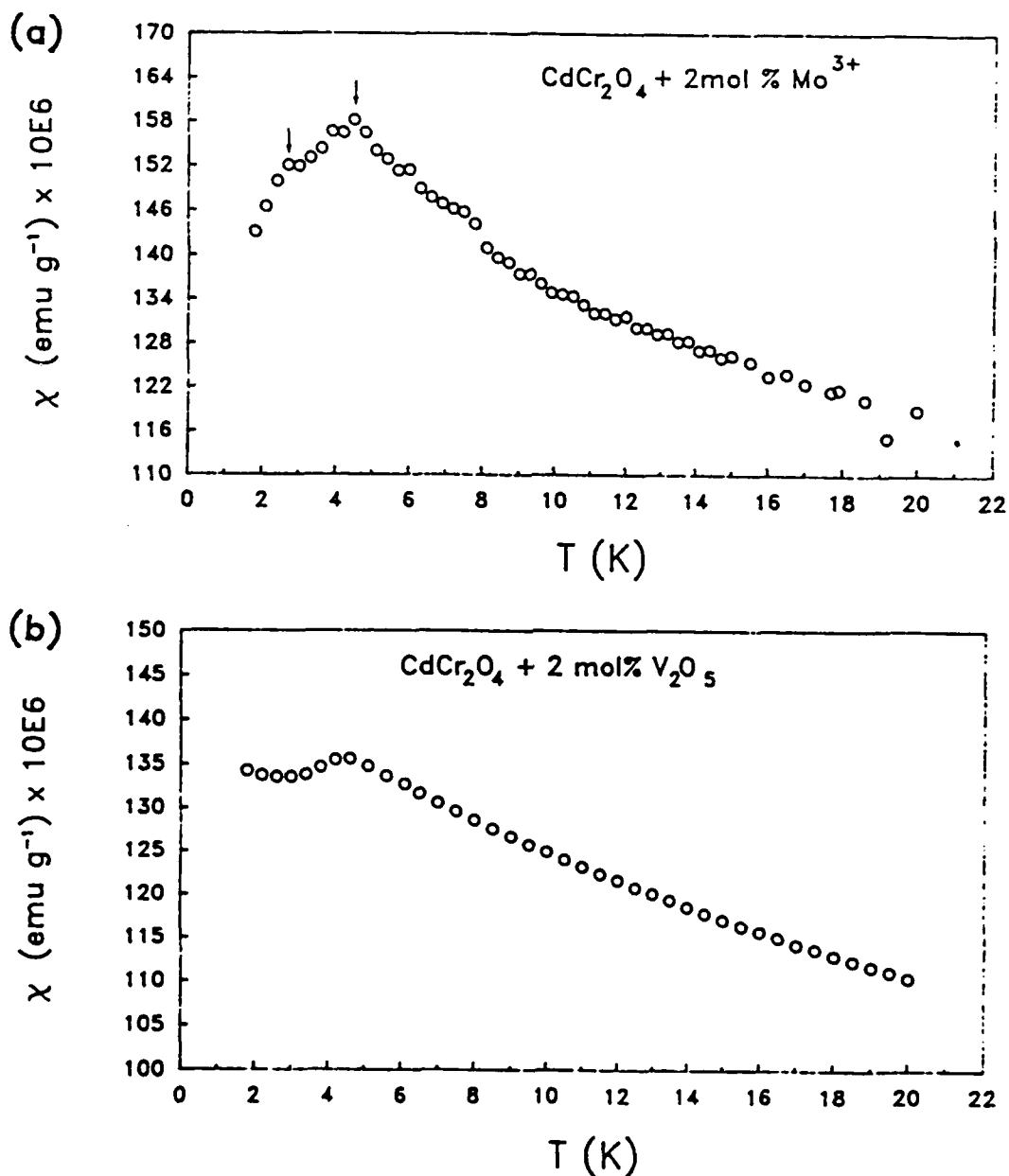


Figure 15. Plots of χ versus T for CdCr_2O_4 doped with (a) 2 mol % Mo^{3+} and (b) 2 mol % V_2O_5 . The arrows correspond to the split peaks.

It is seen that the doping is much less effective in causing the splitting for the CdCr_2O_4 lattice, although it does cause an apparent broadening of the susceptibility (χ) versus temperature peaks.

Effect of Doping with Magnetic Ions

In order to determine if spin-spin interactions might be the cause of the peak splitting, the χ measurements were made on ZnCr_2O_4 doped with the high spin transition metal ion Mn^{2+} ($S = \frac{5}{2}$) and the rare earth ion Gd^{3+} ($S = \frac{7}{2}$). Figure 16 (a) shows the temperature dependence of the χ for ZnCr_2O_4 doped with MnO (i.e., Mn^{2+}), while Figure 16 (b) shows the data over the narrow temperature range of 1.8 to 20 K.

It is seen that the observed χ is simply the sum of that expected from the undoped lattice and that from MnO itself. Thus, the peak splitting observed from other samples perhaps does not involve antiferromagnetic interactions involving dopants.

To investigate if ferromagnetic interactions involving the dopants might be the cause of the peak splitting, χ measurements were made on ZnCr_2O_4 doped with various amounts of Gd_2O_3 . Figure 17 (a) shows the χ versus T plot for a

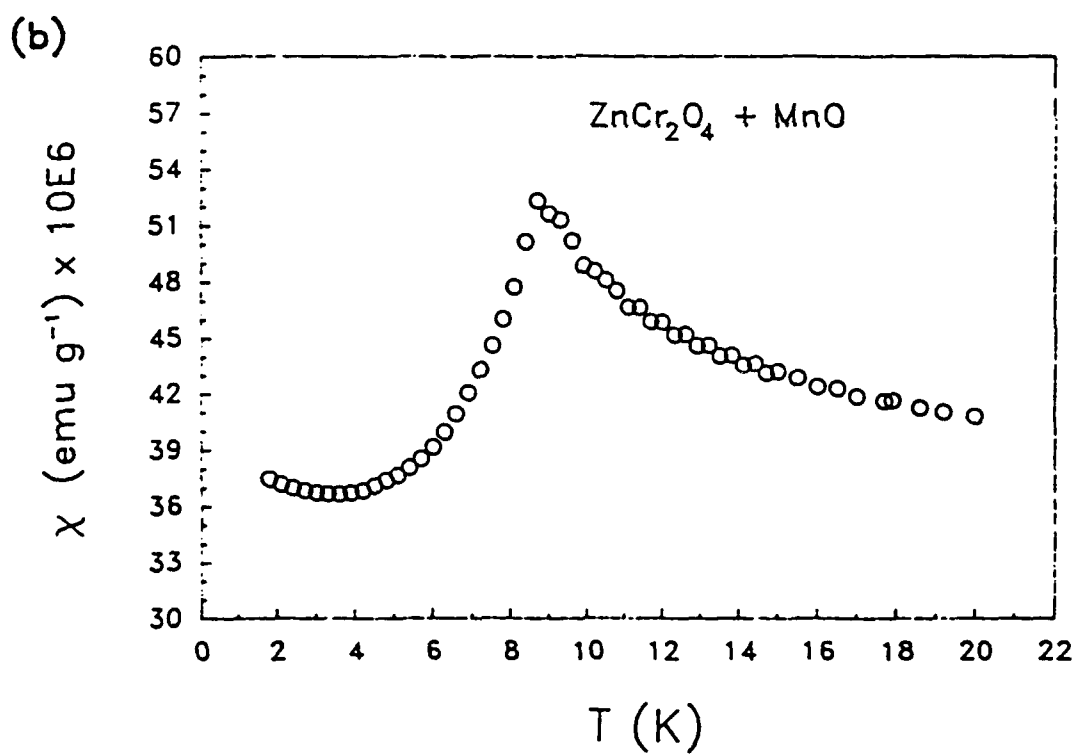
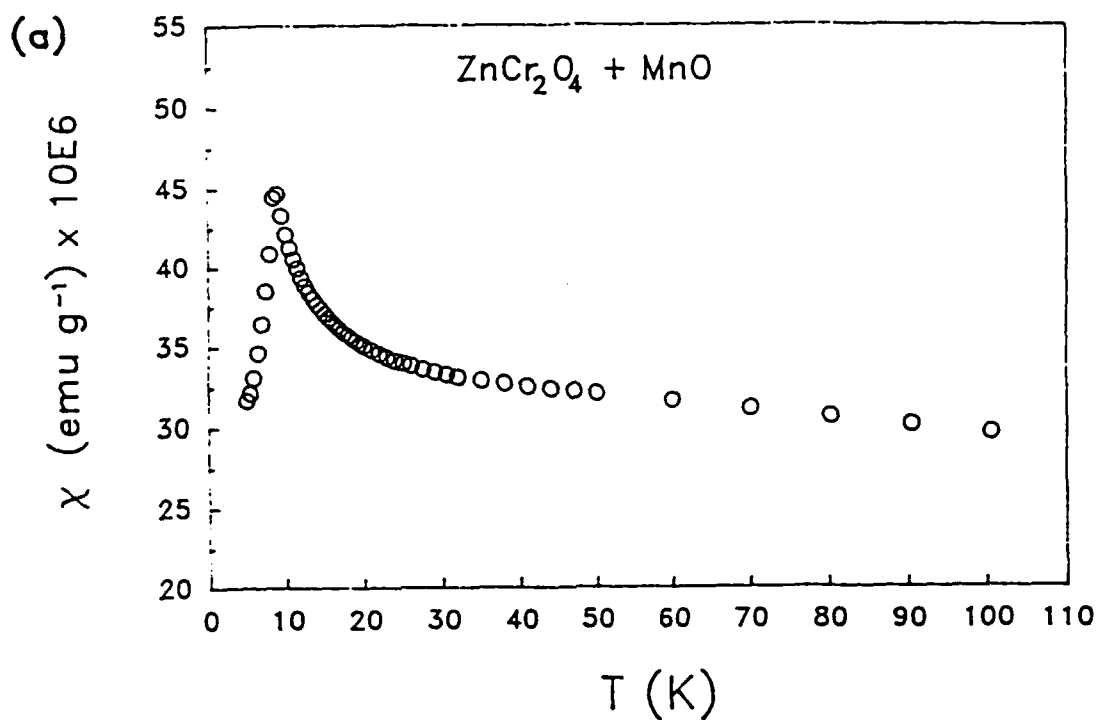


Figure 16. Temperature dependence of χ for ZnCr_2O_4 doped with MnO over a (a) wide and (b) narrow temperature range.

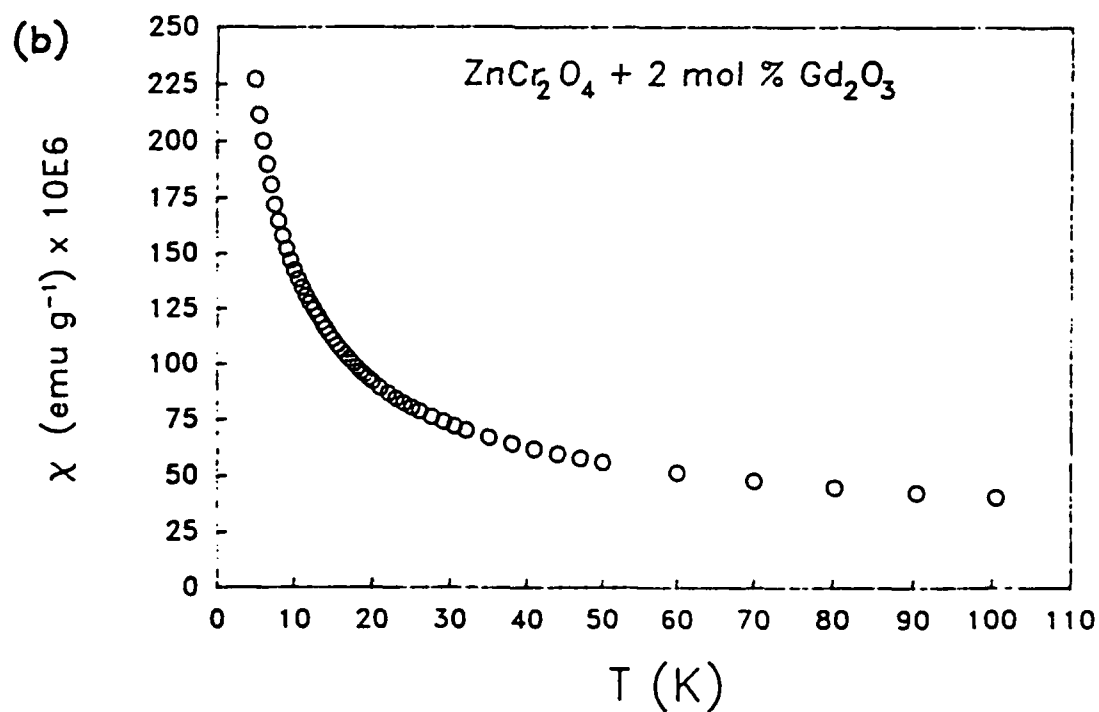
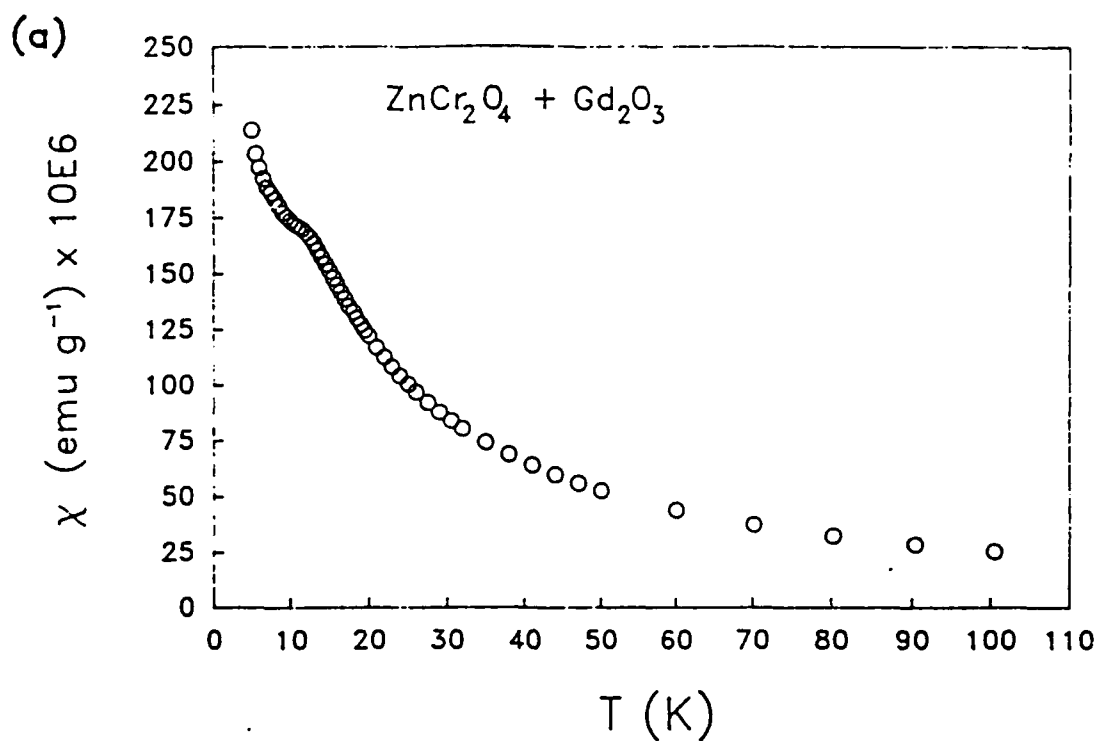


Figure 17. Temperature dependence of χ for ZnCr_2O_4 doped with (a) nominal and (b) 2 mol % Gd_2O_3 .

sample doped with only a nominal amount of Gd_2O_3 . It is seen again that the measured susceptibility is the sum of those from the undoped ZnCr_2O_4 and Gd^{3+} . Measurement on more strongly doped samples supported this conjecture. For example, the χ data for a 2 molar % Gd_2O_3 -doped sample are shown in Figure 17 (b). The absence of a peak in Figure 17 (b) is completely consistent with the fact that the peak is buried within the much higher susceptibility expected from the Gd^{3+} dopant spins. These results indicate that the aforementioned peak splitting phenomena cannot be attributed to any simple ferromagnetic coupling introduced by the dopant spins.

VI.E. Conclusions

From the presently reported EPR and magnetic susceptibility (χ) measurements on ZnCr_2O_4 and CdCr_2O_4 and their comparison the C_p data of CeramPhysics, Inc. as well as related thermodynamic properties, we infer the following conclusions:

1. The exceptionally high C_p peaks for ZnCr_2O_4 and CdCr_2O_4 in the 2 - 17 K range are intimately related to critical spin fluctuations accompanying their anti-ferromagnetic ordering at their Neél temperatures (T_N).
2. The T_N values are found to be very sensitive to the sample processing variables such as hot, uniaxial pressing, doping with non-magnetic ions, and oxygen-sulfur exchange; with ZnCr_2O_4 exhibiting a higher sensitivity. For ZnCr_2O_4 , these variables induce a splitting in the T_N values up to over 6 K and a broadening of the corresponding χ peaks. CdCr_2O_4 is found to exhibit primarily the broadening, with only minor signs of splitting.
3. Doping by magnetic ions causes the T_N peaks in susceptibility to be swamped by that of the magnetic ions. Our conclusion is that the C_p peak splitting and

broadening phenomenon discovered by CeramPhysics and the analogous results obtained for χ in this research are not (dominantly) caused by any spin-spin interactions introduced by the dopant.

4. EPR measurements support the χ and C_p data and, in addition, provide direct evidence for the emergence of 'free' Cr^{3+} spins below T_N in CdCr_2O_4 and ZnCr_2O_4 powders as well as ceramic pellets prepared with 5 % Nb_2O_5 . The density of the 'free' spins is significantly higher in the Nb_2O_5 -doped samples, indicating that their concentration is sensitive to doping.
5. C_p , thermocaloric, χ , and EPR measurements on single crystal samples are needed for delineating the various interrelated parameters causing the exceptionally high C_p values and their sensitivity to process variables. The results obtained might lead to new technologies based on these highly unusual materials.

REFERENCES

- Abragam, A., and Bleaney, B., 1970, Electron Paramagnetic Resonance of Transition Ions, Clarendon Press, Oxford.
- Dalal, N. S., and Kahol, P. K., 1989, "Magnetic Susceptibility and EPR Measurements: Direct Evidence for Free Spins," Progress Report, AFOSR Contract No. F49620-86-C-0049, Research on High-Specific-Heat-Dielectrics, May 8, 1989.
- Kahol, P. K., Singh, K. and Dalal, N. S., 1986, "Magnetic Susceptibility and Resonance Studies," Progress Report, AFOSR Contract No. F49620-86-C-0049, Research on High-Specific-Heat-Dielectrics, September 30, 1986.
- Kahol, P. K. and Dalal, N. S., 1987, "Magnetic Susceptibility and Resonance Studies," Progress Report, AFOSR Contract No. F49620-86-C-0049, Research on High-Specific-Heat-Dielectrics, April 10, 1987.
- Lawless, W. N., Clark, C. F., and Munson, S. K., 1986a, "Magnetocaloric Measurements on CdCr_2O_4 , ZnCr_2O_4 , and MnNb_2O_6 Ceramics," Progress Report, AFOSR Contract No. F49620-86-C-0049, Research on High-Specific-Heat-Dielectrics, April 10, 1987.
- Lawless, W. N., and Clark, C. F., 1986, "Specific Heat and Dielectric Measurements on Compacted Disks of CdCr_2O_4 and ZnCr_2O_4 Spinel Powders," Interim Report, AFOSR Contract No. F49620-86-C-0049, Research on High-Specific-Heat-Dielectrics, April 10, 1987.
- Lawless, W. N., and Munson, S. K., 1987, "Thermodynamic Analysis of Magnetocaloric Data Measured on Compacted Disks of CdCr_2O_4 and ZnCr_2O_4 ," Interim Report, AFOSR Contract No. F49620-86-C-0049, Research on High-Specific-Heat-Dielectrics, January 9, 1987.
- Lawless, W. N., 1987a, "Analysis of Specific Heat Data Measured on Compacted Disks of CdCr_2O_4 and ZnCr_2O_4 ," Interim Report, AFOSR Contract No. F49620-86-C-0049, Research on High-Specific-Heat-Dielectrics, January 8, 1987.

- Lawless, W. N., and Hampton, S. K., 1988, "Broad-Range Specific Heat Measurements," Progress Report, AFOSR Contract No. F49620-86-C-0049, Research on High-Specific-Heat-Dielectrics, August 26, 1988.
- Lin, C., and Patton, B. R., 1986, "Spinel Studies IV. Ginzburg-Landau Theory of the Spinel Phase Transitions," Progress Report, AFOSR Contract No. F49620-86-C-0049, Research on High-Specific-Heat-Dielectrics, December 30, 1986.
- Lu, Y., and Patton, B. R., 1986, "Spinel Studies III. Monte Carlo Studies on Undistorted Spinel," Progress Report, AFOSR Contract No. F49620-86-C-0049, Research on High-Specific-Heat-Dielectrics, December 15, 1986.
- Patton, B. R., Lin, C. Y., and Lu, Y., 1986, "Spinel Studies II. Experimental Review and Theoretical Overview," Progress Report, AFOSR Contract No. F49620-86-C-0049, Research on High-Specific-Heat-Dielectrics, December 15, 1986.

VII. THEORETICAL STUDIES

Theoretical studies of the ZnCr_2O_4 and CdCr_2O_4 spinels were performed at Ohio State Univ., approximately in parallel with much of the experimental data reported above. Consequently, the theoretical studies were evolutionary in nature and are presented here in this spirit.

The following section topics are as follows:

- VII.A. Impurity Spin Doping on Undistorted Lattice
- VII.B. Impurity Spin Doping on Distorted Lattice, $c < a$
- VII.C. Impurity Spin Doping on Distorted Lattice, $a < c$
- VII.D. Ginzburg-Landau Analysis of Magnetic Transitions
- VII.E. Monte Carlo Calculations of Magnetic Phase Diagrams
- VII.F. Splitting of Specific Heat Peaks
- VII.G. Summary of Theoretical Studies

The subsections constitute separate theoretical investigations; consequently, each subsection has been written as a stand-alone study in what follows below. A decision was made not to number the equations, figures, and tables sequentially throughout this entire Section VII, and, therefore, the figure numbers is subsection VII.B., for example, refer only to that subsection. This codification leads to some duplication in the literature references cited.

I. Introduction

In this report we summarize our results on Monte Carlo simulations of the undistorted spinel lattice doped with various spin impurities. The origin of this work began with related work carried out under separate Wright Patterson AF support. The aim of that work was to investigate the possibility of raising the transition temperature of the high specific heat dielectric materials based on the chromite spinels, CdCr_2O_4 and ZnCr_2O_4 , by introduction of other spin species like Fe, Al, V, etc.

In order to better understand the effects of frustration in the spinel lattice, which we have previously shown are important for the large specific heat anomalies in these systems, we have undertaken a more extensive study of the role of substituted impurity spins on the magnetic ordering of the spinel materials.

For completeness, we review the role of dopants on frustration in the spinel lattice in Section II, then summarize the expected effect of various chemical substitutions in Section III. Section IV presents our Monte Carlo results for small and large spin impurities, followed by a summary in Section V.

II. Effect on Impurity Doping on Frustration of Spinel Lattice

As can be seen in Fig. 1, the spinel lattice with B site spin occupation only (A site unoccupied) involves triangular loops connecting adjoining spins. This is the origin of the frustration of the spin ordering since, with antiferromagnetic

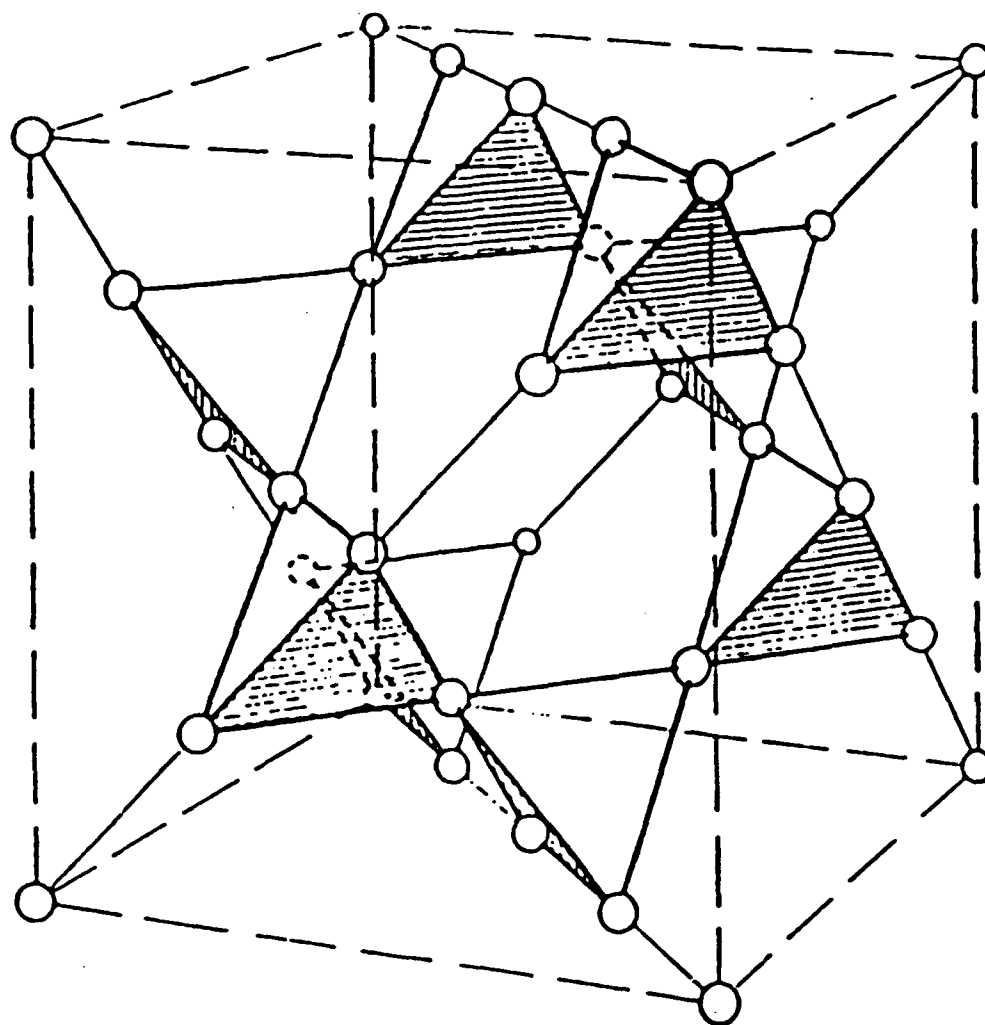


Fig. 1. Magnetic spinel lattice showing location of the spins and the tetrahedral coordination with neighboring spins.

interactions, all spins in a triangular loop cannot be anti-aligned with its two neighbors.

As a result, this perfect frustration in the ordering gives rise to many fluctuating spins at low temperatures which directly results in a large broad specific heat. In contrast, in a normal antiferromagnet the spins order below the transition and the specific heat becomes very small. One of the purposes of the theoretical calculations in this research is to explore the consequences of modifying or reducing the frustration in the spinel lattice for the physical properties of the material.

One way to modify the frustration in the spinel lattice is to introduce spin impurities, magnetic ions with either larger or smaller values of spin than the host Cr^{3+} atom, which has spin $S = 3/2$. The interaction Hamiltonian is given by

$$H = \sum_{\langle ij \rangle} J_{ij} S_i S_j \quad (1)$$

where J_{ij} is the exchange interaction between the spin S_i and the spin S_j and the sum $\langle ij \rangle$ runs over nearest neighbors in the lattice shown in Fig. 1.

Since the effective coupling between two spins from Eq. (1) is JS^2 , replacing one of the spins with a larger or smaller value then changes the coupling between those spins. This may change the frustration in the system, for example if the substituted spin is large enough, all its neighboring spins will line up opposite to it in order to minimize the energy. This removes the spin frustration, at least locally, since all the spins now have a unique preferred orientation.

III. Chemical Doping Effects in Spinel Lattice

The effect of substituting a magnetic ion in the spinel lattice is complicated, depending on the preferred valance state as well as the orbital symmetry of the ion with respect to the site where it goes. Divalent ions prefer the A site on the spinel, while trivalent ions prefer the B site. In addition, the middle of the transition series, like Fe^{3+} with a $3d^5$ configuration strongly prefers the tetrahedral symmetry of the A site, while configurations near the beginning and end of the series, like $3d^3$ or $3d^7$ prefer the octahedral B sites. In the following table we summarize the expected locations for the various ions:

Ion	Ti	V	Cr	Mn	Fe	Co	Ni
Spin	1/2	1	3/2	2	5/2	2	3/2
3+ config	3d ¹	3d ²	3d ³	3d ⁴	3d ⁵	3d ⁶	3d ⁷
Site pref by symmetry	small	~B	B	small	A	~A	~B
Valence prefer in order	4,3,2	5,4,3 2	3,6,2 5	2,7,6 4,3	3,2	2,3	2,3
Site pref by valence	~B	~B	B	A	~B	~A	~A
Dopes on B site?	may	may	yes	no	no?	no	?

Table I. Site Preference for 3d Substitutional Impurities

We note from examining this table that the one 3d transition series ion with strong preference for the B site in the spinel lattice is Cr^{3+} ; this verifies the fact that the chromite spinels, CdCr_2O_4 and ZnCr_2O_4 , are the best candidates for a system in which the spins populate only the B sites (and are therefore frustrated). This explains why the CdCr_2O_4 and ZnCr_2O_4 systems are unique in their properties. As a consequence the other transition metal ions have a lower tendency to go onto the B sites, but the best possibility would be V, followed by Ti. The other ions have a good chance of going into the A site, which

Ion	Al	Mo	Gd
Spin	0	3/2	5/2
3+ config	[Ne]	4d ³	5f ⁷
Site pref by symmetry	none	B	small
Valence prefer in order	3	6,5	3,6,2
Site pref by valence	B	B	B
Dopes on B site?	may	yes	may

Table II. Site Preferences for Additional Substitutional Impurities.

should give rise to strong antiferromagnetic ordering at high temperature with a high enough concentration of dopant. One question of interest is whether a small concentration of spins on the A site could increase the transition temperature while not completely eliminating the frustration. In the present numerical work we consider only doping on the B site.

In Table II we give several additional possibilities for doping, corresponding to zero spin (Al) and large spin (Gd), as well as the same spin as the host (Mo, $S = 3/2$).

From these tables we see that impurity dopants like Al, Ti, V, Mo, and Gd may tend to go into the B site of the spinel and therefore disrupt the spin ordering. These ions have a spin of 0, $1/2$, 1, $3/2$, and $5/2$, respectively, compared to the host spin $3/2$ of the Cr ion. Thus we expect the Al ($S=0$) and the Gd ($S=5/2$) to have the largest effects, while Mo ($S=3/2$) should have little effect since it has the same spin as Cr.

IV. Monte Carlo Results for dopants with large and zero spin.

In order to determine the effect of the various substitutional spins on the magnetic ordering we carried out extensive Monte Carlo simulations. The computational techniques have been discussed in our earlier reports on this contract.¹ In order to obtain an overall picture, we first considered a broad range of dopings from 20%, 40%, 60% and 80%. The results for the specific heat versus temperature (in units of the host coupling JS^2 with $S=3/2$) are shown in Fig. 2 for a lattice of 2000 spins.

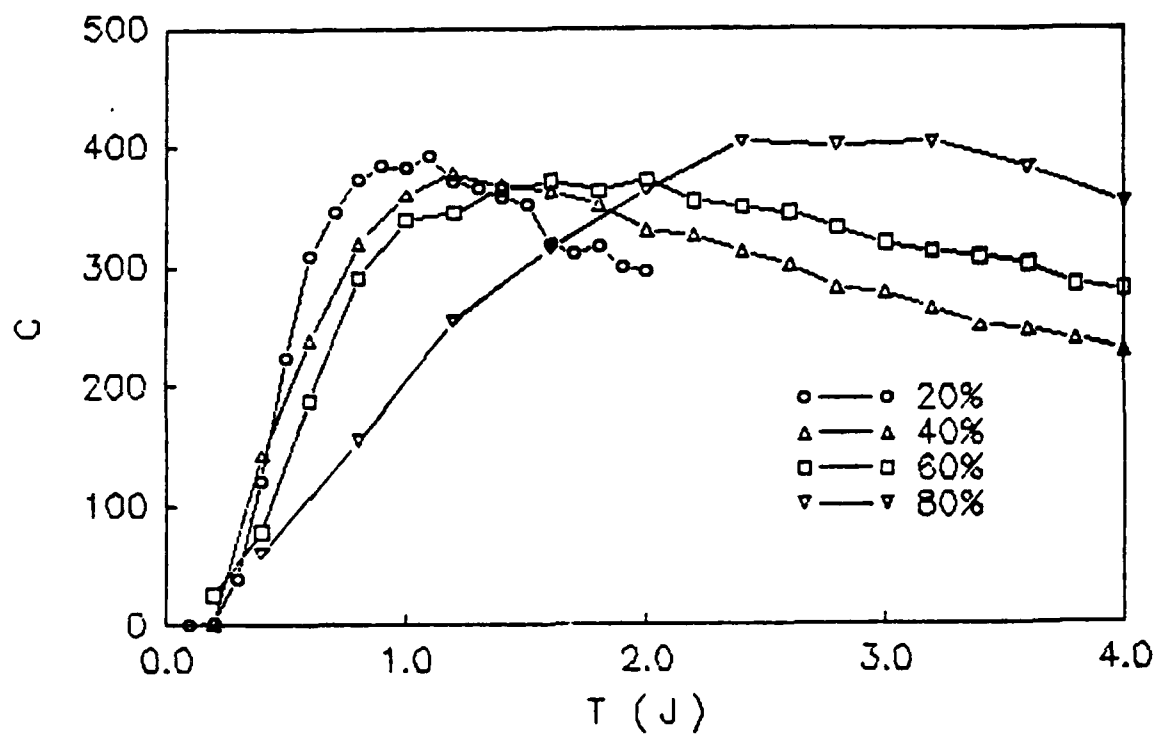


Fig. 2. Heat capacity vs. T for spinel lattice of 2000 spins with various doping fractions of spin 3 random impurity.

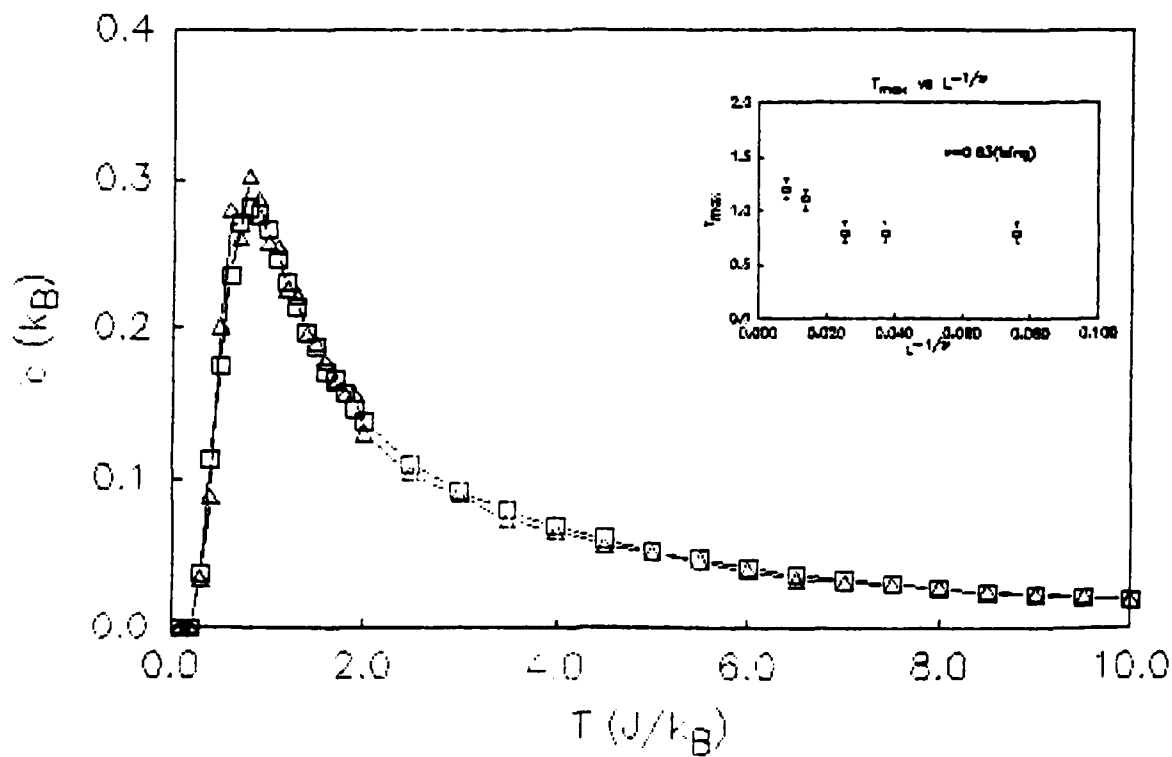


Fig. 3. Specific heat for pure spinel lattice with spin 3/2.

In comparison with our earlier results for the undoped system shown in Fig. 3, it is clear that the effect of the impurity is to broaden and move the peak in the specific heat to higher temperatures: for the undoped lattice the maximum in C is at $T \sim 0.8$ (in units of the host JS^2), while for 20% spin 3 it is at $T \sim 1.0$, and moves steadily up to $T \sim 2.9$ for 80% doping. For 100% spin 3 we would have a system identical to the original undoped lattice but with a spin twice as large; thus, since the peak should scale with $T_C \sim J \cdot S^2$, the peak would be at $2^2 \cdot 0.8 = 3.2$. However the peak for 60% doping is somewhat below the average of the temperatures of the two pure phase peaks and is closer to the geometric mean of the two temperature peaks. This indicates that the spin is playing some role in changing the frustration in the system as we expected, but the effect is small.

A second key feature is that the dopants have greatly changed the shape of the specific heat. The peak height has been reduced from about $560k_B$ ($0.28k_B$ per spin) to about $400k_B$, but more strikingly, the high temperature tail has been greatly increased. At $T = 4.0$ (in units of the host JS^2), the specific heat has risen from $140k_B$ to about $250k_B$ for 40% and $300k_B$ for 60% doping. This indicates an increased number of higher energy excitations as a result of the impurity doping.

Finally, we note that the doping has not produced long range spin order in the system below the peak temperature. This is clear from the low specific heat per spin, which is even lower than in the undoped lattice, which also does not have long range order due to frustration.

The reason that random doping does not completely remove the frustration may be seen in Fig. 4 where several elementary tetrahedra are shown with differing numbers of impurity spins (large arrows). Configurations (a) and (c) contain frustrated triangles of spins, and thus eliminate the long range order.

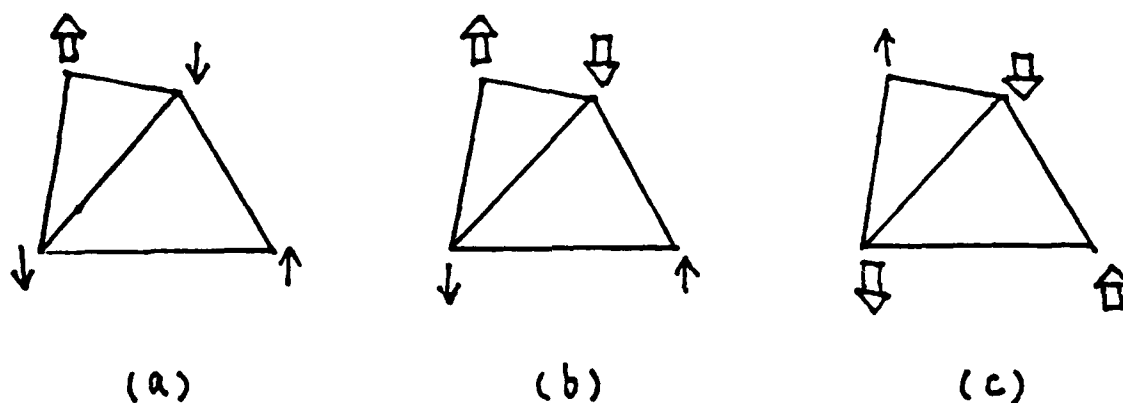


Fig. 4. Different impurity spin configurations on elementary tetrahedron.

The magnetic susceptibility for the spin 3 dopant is shown in Fig. 5 for dopant concentrations of 20%, 40%, 60% and 80%. Fig. 6 shows our previous results for the pure spinel lattice for comparison (note that the temperature range extends to much higher values in Fig. 6).

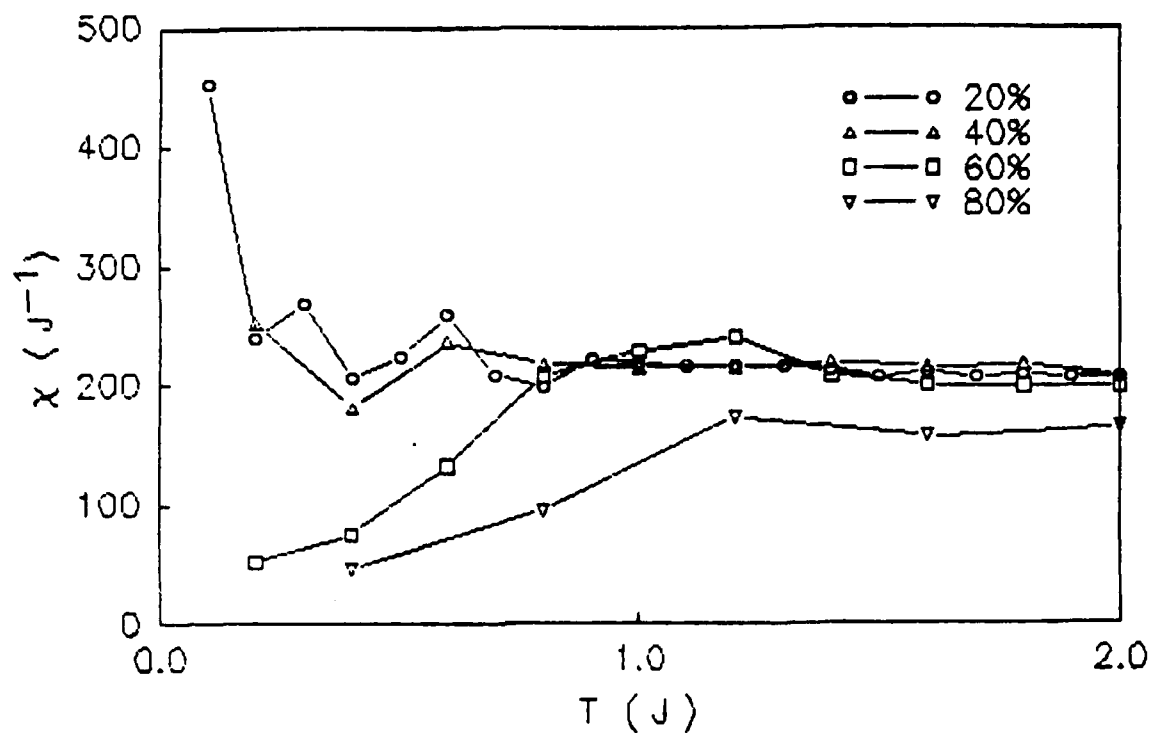


Fig. 5. Susceptibility for vs. T for spinel lattice with various fractions of spin 3 randomly distributed impurity.

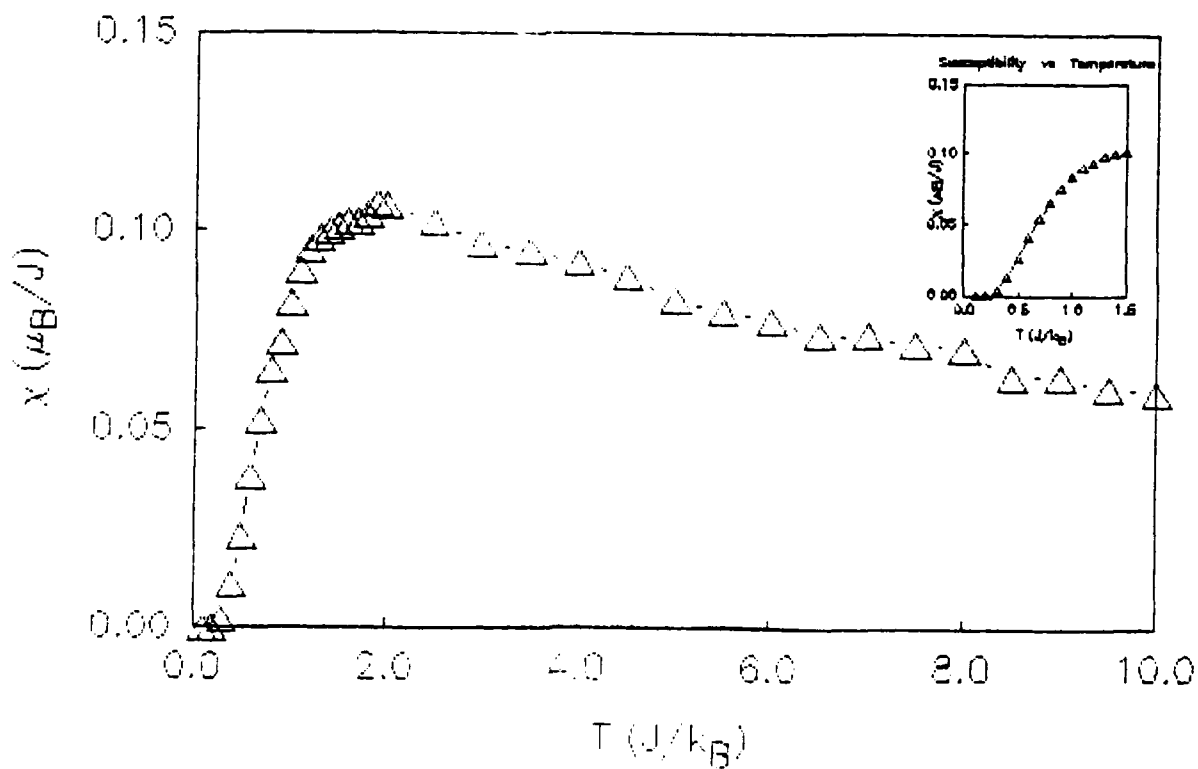


Fig. 6. Susceptibility for pure spinel lattice with spin $3/2$.

From the downturn in the susceptibility for 60% and 80%, it is clear that, as in the specific heat, the transition temperature increases with increasing amount of a larger spin. However, a novel feature occurs for lower concentrations at 20% dopant. A large paramagnetic tail causes the susceptibility to increase for the lowest temperatures, indicating that some spins remain free and unfrozen. Fig. 7 indicates the origin of this paramagnetic tail by displaying a common spin configuration when the concentration is 20-30%.

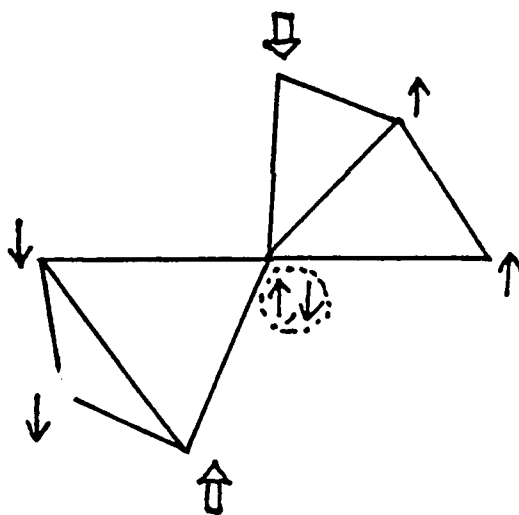


Fig. 7. Typical spin configuration for 20-30% spin 3 dopant.

The spin in the circle at the intersection of two tetrahedra with one large spin each is in a zero net field and can easily flip in a field, giving rise to the low temperature Curie contribution to the susceptibility proportional to $1/T$. Other spin

configurations due not allow a single spin to move and thus the paramagnetic tail disappears at higher and lower concentrations.

One feature seen in the specific heat data measured at CeramPhysics is the development of a splitting into two peaks with some impurity dopings.² From the Monte Carlo results shown in Figs. 2 and 5, it is clear that no splitting has developed in the case of randomly quenched impurities which we have considered. We will see in our finite cluster calculations that a splitting is obtained in that case, indicating that clustering effects may play the important role in producing the split transitions.

We now consider the case of doping with a spin 0 impurity such as Al. In this case the net effect is to remove the spin from the lattice, in effect diluting the lattice. We expect that the transition should go down due to reduction in the number of bonds contributing, but up due to the possible reduction in frustration. The key question here is whether the second effect, reduction of frustration, could dominate giving a net increase in the transition temperature.

Fig. 8 shows the Monte Carlo specific heat results for a spin 0 impurity with 20% to 80% concentration. The reference pure specific heat is given in Fig. 3. The effect of the spin 0 impurity is to decrease the magnitude of the specific heat, reflecting the dilution of the spin lattice, namely, there are fewer spins to order. The transition temperature does not change very much in comparison, which reflects the fact that the coupling energy per spin is essentially unchanged in the diluted system. This behavior is characteristic of the frustrated system

and is quite different from what happens in a ordinary magnet when the transitions drops rapidly with dilution. Another way of seeing this is to note that for the pure spinel lattice the ground state energy is $-JS^2$ per spin, while an isolated cluster of three spins in a row has an energy $-2JS^2/3$ per spin and even a cluster of two spins has an energy of $-JS^2/2$ per spin. The conventional (unfrustrated) ferromagnet or antiferromagnet in contrast starts with a ground state energy of $-zJS^2/2$ per spin where z is the number of nearest neighbors, 6, 8 or 12, depending on lattice structure; thus the effects of dilution are more serious for it.

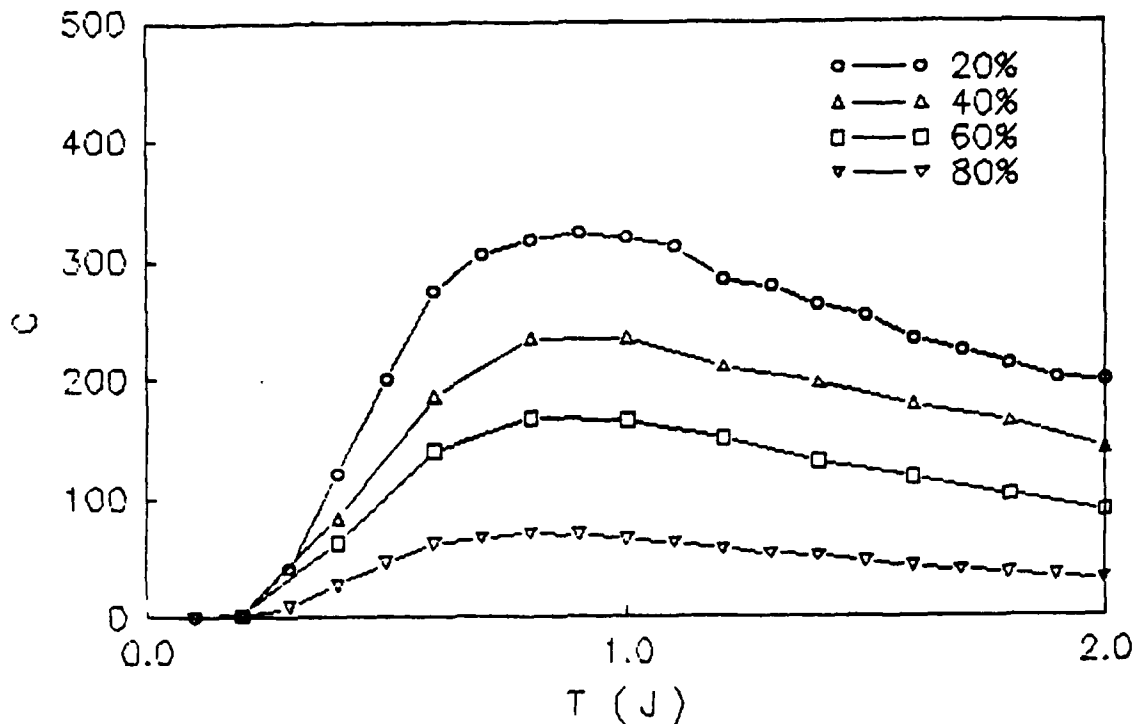


Fig. 8. Specific heat vs. T for spinel lattice with various doping fractions of spin 0 randomly distributed impurity.

The susceptibility is plotted in Fig. 9 for the spin 0 dopant. The most obvious feature is the presence of a low temperature Curie tail proportional to $1/T$ for all impurity doping levels. This indicates the presence of free spins at all concentrations and may be understood by considering Fig. 10, where two typical spin 0 configurations are shown. For these configurations, the spin in the circle may point either up or down with no change in coupling to the other spins, thus it behaves like a free spin. In addition, the configuration in Fig. 10(a) is predominant at lower concentrations while that in 10(b) is dominant at higher concentrations, thus the number of free spins produced by a spin 0 impurity is roughly independent of concen-

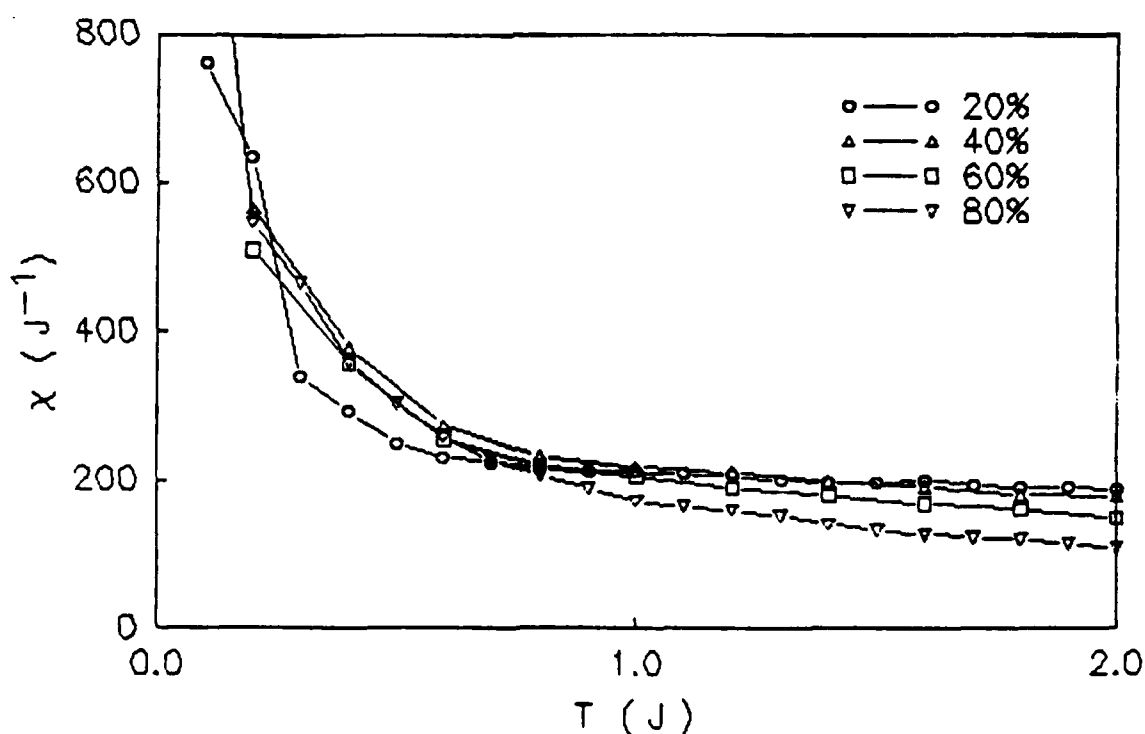


Fig. 9. Susceptibility for vs. T for spinel lattice with various fractions of spin 0 randomly distributed impurity.

tration, unlike the case of the large spin dopant, as shown in Fig. 5.

The effect of the spin 0 impurity is somewhat analogous to the introduction of free surfaces which we showed in our previous work led to the presence of free paramagnetic spins at the surfaces.

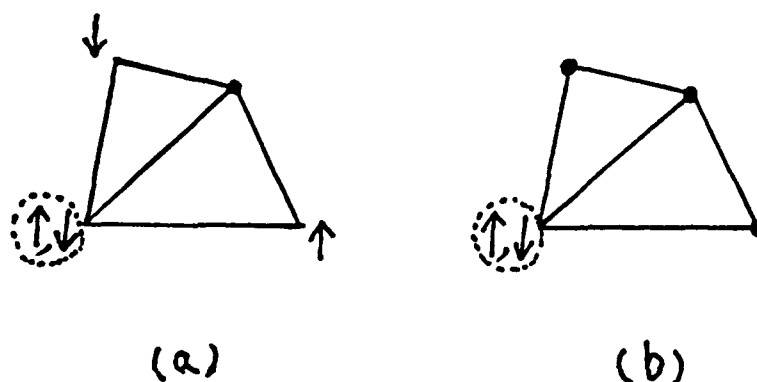


Fig. 10. Typical spin configurations for low (a) and high (b) concentration of spin 0 dopant.

We consider now a comparison with recent experimental data on the doped spinels.² Fig. 11 shows data on Gd, Al, and V doped samples at low concentrations, which corresponds to $S = 5/2$ (Gd^{+3}), $S = 0$ (Al^{+3}), and $S = 1$ (V^{+3}). Although the doping fractions in Fig. 11 are much smaller than the values in our initial calculations reported above, we may compare the general trends.

As mentioned previously the splitting in the peaks arises from finite cluster effects which were not included in the pre-

sent Monte Carlo calculations. However, if we look at the movement of the lowest peak in C with doping, we see that the V with a slightly smaller spin of 1 compared to the host Cr spin of $3/2$ moves the lower peak down, while Gd with a larger spin moves the peak up, as the Monte Carlo calculations show.

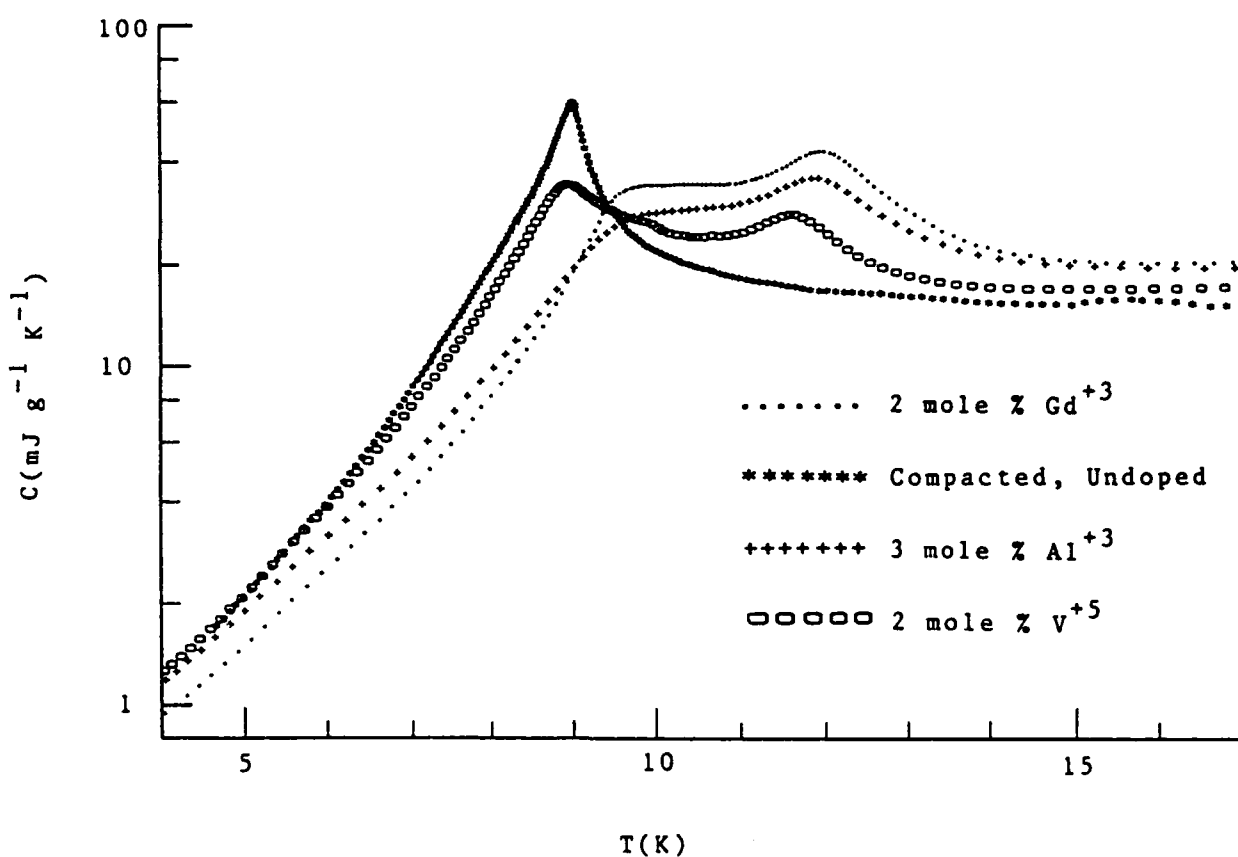


Fig. 11. Experimental specific heat data on doped ZnCr_2O_4 from Ref.2 (Fig. 14). If V is on the B site then it is likely V^{+3} with $S = 1$, not V^{+5} , which is the preferred valence (see Table I).

But a puzzling anomaly is the Al effect, which moves up, although our calculations showed that for the $S = 0$ case the peak should be almost unchanged, with a drop in height only. This result suggests a careful examination of the finite clustering effects in the $S = 0$ case is necessary, since the Al shows a strong tendency to reduce the frustration, and therefor raise the transition.

V. Summary

We have found that the results of Monte Carlo calculations on the undistorted cubic spinel lattice for randomly quenched impurities indicate the following characteristic features:

1. A large spin impurity causes the peak in the specific heat to move up in temperature roughly in proportion to the average increase in S^2 , indicating that the frustration is not changed dramatically by the doping.
2. The large spin dopant broadens the specific heat significantly, greatly increasing the high temperature value of the specific heat.
3. The large spin impurity for small concentrations initially produces a large number of free spins (Curie tail), which disappears for concentrations above 50%.
4. A spin 0 impurity simply dilutes the spin lattice, giving rise to no shift in the transition, indicating that the effects of dilution and reduction in frustration produced by the doping cancel.
5. The spin 0 dopant of concentration x reduces the magnitude of the specific heat peak roughly by a factor of $(1-x)$,

which corresponds to the number of remaining host spins.

6. A spin 0 impurity gives rise to free spins (Curie tail) at all concentrations, which may be used to distinguish the behavior from that produced by a large spin impurity where the Curie tail disappears at high concentrations.
7. Neither large nor zero spin impurities have led to a large increase in the ordering temperature, although the large spin in reasonable concentration gives rise to a high temperature increase in the specific heat tail which may prove useful.
8. Experimental data are in general agreement with this picture, **except** for the case of Al^{+3} $S = 0$ dopants, for which clustering effects may be important.

Several interesting questions remain after these calculations. The effects of distorting the spinel lattice from the cubic into the tetragonal phase, with both $c > a$ and $c < a$, may give interesting effects upon doping, in view of our previous Monte Carlo work which has shown that the transition may be raised dramatically by such a lattice distortion. In this connection the effects of smaller doping concentrations may be explored. Finally, the splitting in the transition seen in the experimental specific heat measurements at CeramPhysics needs to be considered in connection with the finite cluster effects for a more complete picture.

REFERENCES

1. Annual Technical Report, Research on High-Specific-Heat Dielectrics, AFOSR Contract F49620-86-C-0049, May 11, 1987. In brief summary the simulations used the Ising model in which each spin takes the possible values $\pm S$, where S is the magnitude of the spin. The spins are set on the B sites of a cube of the spinel lattice 5 unit cells on a side containing 2000 spins. Periodic boundary conditions are used to eliminate boundary effects. After equilibration, 2000 Monte Carlo steps per spin are used at each temperature.
2. CeramPhysics, Inc. Progress Report, Research on High-Specific-Heat Dielectrics, AFOSR Contract F49620-86-C-0049, August 26, 1988.

VII.B. EFFECTS OF IMPURITY SPIN DOPING ON TETRAGONALLY DISTORTED SPINEL LATTICE - $c < a$ Case

I. Introduction

Following our previous report on Monte Carlo simulations of the undistorted spinel lattice doped with various spin impurities,¹ we consider in the present report our results for the tetragonally distorted spinel lattice for $c < a$ ($= b$), where a , b , and c are the three lattice constants in the tetragonal phase. The case of the $c > a$ tetragonal distortion is completely different and will be reported separately.

The origin of this work was to investigate the possibility of raising the transition temperature of the high specific heat dielectric materials based on the chromite spinels, CdCr_2O_4 and ZnCr_2O_4 , by introduction of other spin species like Fe, Al, V, Gd, or other ions, as well as to understand the role played by the frustration in the magnetic ordering properties of these very unusual materials.

For the undistorted lattice case, we found that a large spin like $S = 3$ increased the transition temperature and broadened the specific heat curve. A small spin like $S = 0$ had little effect on the ordering temperature and simply diluted the spin lattice. In addition both the large spin and the small spin produced a large low T Curie tail in the susceptibility.¹

In order to examine the importance of frustration in the spinel lattice, which we have previously shown is important for the large specific heat anomalies in these systems,² we have examined the interplay between the role of substituted impurity spins and a lattice distortion on the magnetic ordering of the

spinel materials.

In Section II, we review the role of doping in the undistorted spinel lattice. The results of the Monte Carlo calculations for the large spin case ($S = 3$) are reported in Section III. Section IV presents our Monte Carlo results for small spin ($S = 0$) impurities, followed by a summary in Section V.

II. Effect on Impurity Doping on Spin Ordering of the Undistorted Spinel Lattice: $c = a$ or $J_{\perp} = J_{\parallel} = J_0$.

We briefly summarize here the key results of our broad range doping calculations for the undistorted cubic spinel lattice, since the differences in the tetragonal cases are important. As pointed out in our previous work, the spinel lattice with B site spin occupation only (A site unoccupied) involves triangular loops connecting adjoining spins and is a totally frustrated spin system with antiferromagnetic interactions.²

The results of our Monte Carlo calculations on the undistorted cubic spinel lattice for a wide concentration range of randomly quenched impurities indicate the following characteristic features:¹

1. A large spin impurity causes the peak in the specific heat to move up in temperature roughly in proportion to the average increase in S^2 , indicating that the frustration is not changed dramatically by the doping.
2. The large spin dopant broadens the specific heat significantly, greatly increasing the high temperature value of the specific heat.

3. The large spin impurity for small concentrations initially produces a large number of free spins (Curie tail), which disappears for concentrations above 50%.
4. A spin 0 impurity simply dilutes the spin lattice, giving rise to no shift in the transition, indicating that the effects of dilution and reduction in frustration produced by the doping cancel.
5. The spin 0 dopant of concentration x reduces the magnitude of the specific heat peak roughly by a factor of $(1-x)$, which corresponds to the number of remaining host spins.
6. A spin 0 impurity gives rise to free spins (Curie tail) at all concentrations, which may be used to distinguish the behavior from that produced by a large spin impurity where the Curie tail disappears at high concentrations.
7. Neither large nor zero spin impurities have led to a large increase in the ordering temperature, although the large spin in reasonable concentration gives rise to a high temperature increase in the specific heat tail which may prove useful.
8. Experimental data are in general agreement with this picture, **except** for the case of Al^{+3} $S = 0$ dopants, for which clustering effects may be important.

We know that a distortion into the tetragonal phase reduces the frustration and, in the case $c < a$, can completely remove the frustration. Thus the effects of distorting the spinel lattice from the cubic into the tetragonal phase, with both $c > a$ and $c < a$, may give interesting effects upon doping, since our previous Monte Carlo work which has shown that the transition may be raised dramatically by such a lattice distortion. Since the

lattice transition is stabilized by the lattice distortion, we will concentrate on the effects of smaller doping concentrations in the present report.

III. Monte Carlo Calculations of Large Spin Dopants in the $c < a$ Tetragonally Distorted Spinel Lattice: $J_{\perp} > J_{\parallel}$.

In the following discussion the c axis will be taken in the vertical direction and the equivalent a, b axis of the tetragonal phase will be taken in the horizontal plane (Fig. 1). The spin exchange Hamiltonian, given in Eq. (1), is correct in both the cubic and tetragonal phases, as long as the proper values are taken for the values of the exchange couplings, J_{ij} .

$$H = \sum_{\langle ij \rangle} J_{ij} S_i S_j \quad (1)$$

In the cubic phase, as shown in Fig. 1, symmetry requires all the J_{ij} to have the same value. The effect of a tetragonal distortion on the cubic spinel lattice, is to bring the horizontal planes of spins close together. As a result the exchange constant between spins in the z direction, J_{\perp} , then becomes in general larger than the coupling among the spins within the x - y plane, J_{\parallel} . In the Monte Carlo calculations, the effect of the lattice distortions is then to introduce two exchange couplings into the Hamiltonian (1).

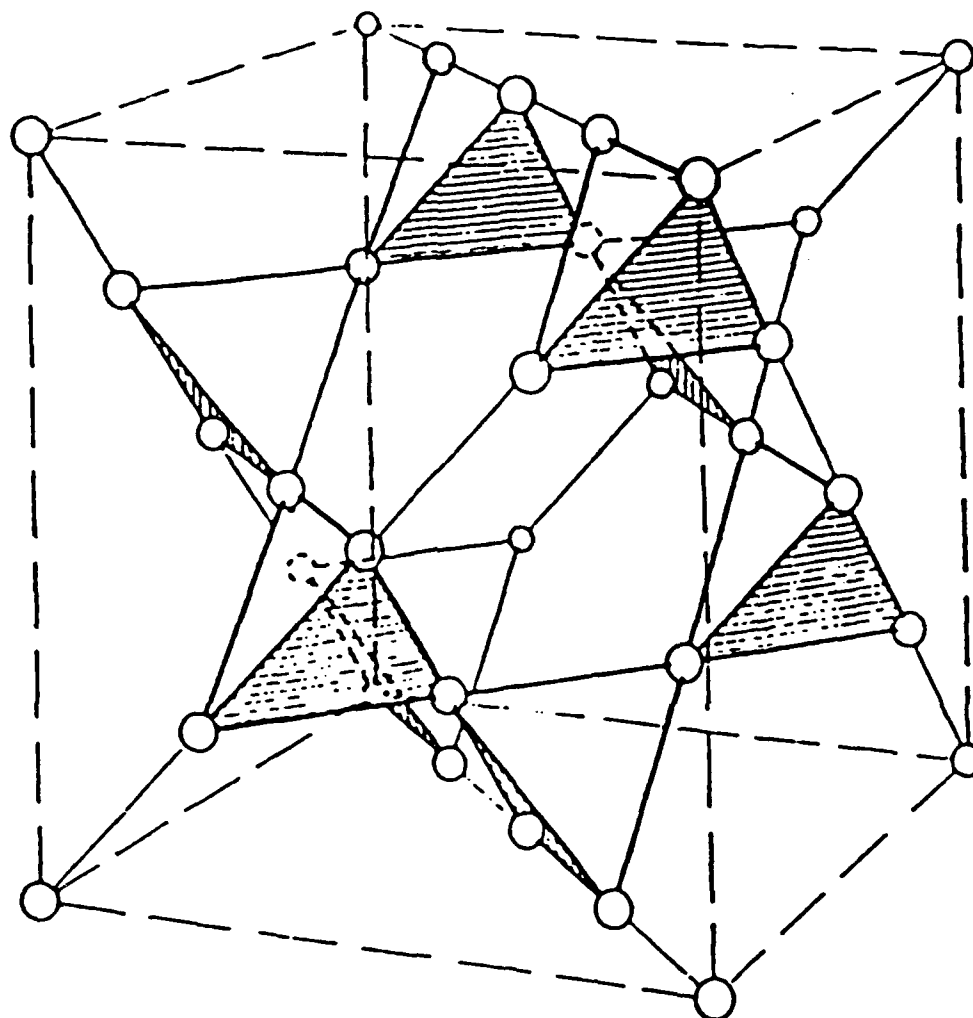


Fig. 1. Magnetic spinel lattice showing location of the spins and the tetrahedral coordination with neighboring spins.

Using lattice sizes and Monte Carlo cycle times comparable to our previous work to facilitate comparison with our previous results, we have carried out numerical simulations for concentra-

tions x of a large spin ($S = 3$) between $x = 1\%$ and $x = 20\%$. The ratio of J_{\perp} to J_{\parallel} was taken to be 1.1, corresponding to a modest tetragonal distortion. The specific heat calculations are shown in Fig. 2 for a lattice of 2000 spins, in units of the average spin coupling JS_0^2 with $S_0 = 3/2$, where $J = (2J_{\perp} + J_{\parallel})/3$ is the average exchange interaction.

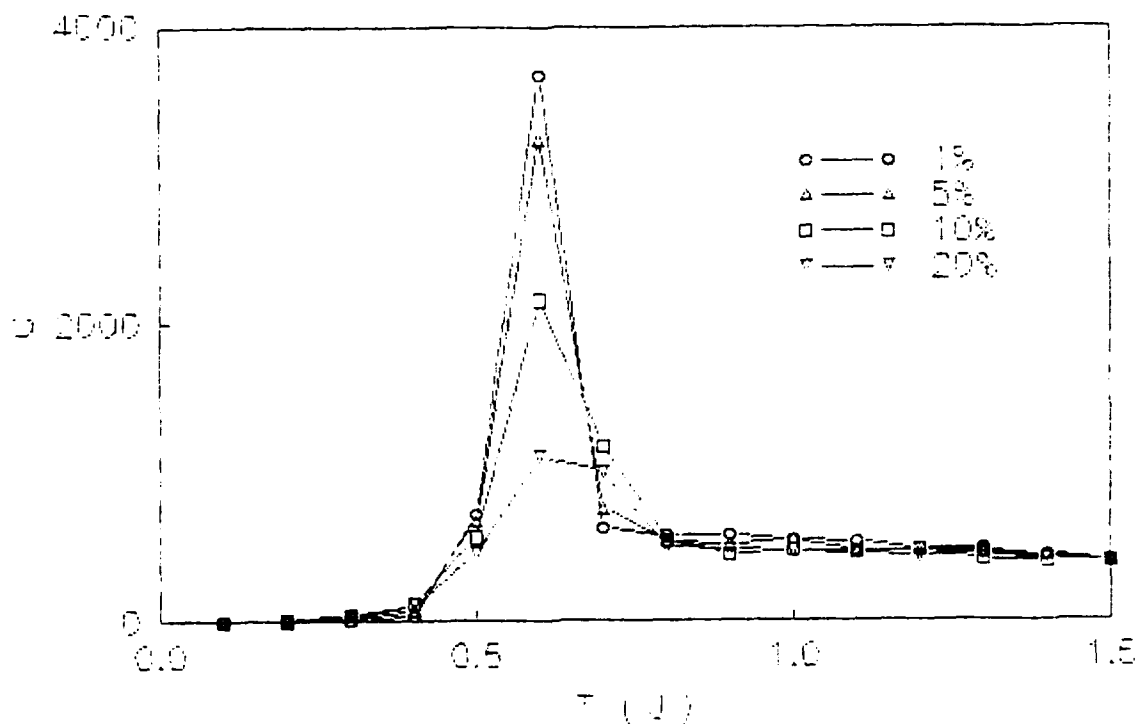


Fig. 2. Heat capacity vs. T for $c < a$ tetragonal spinel lattice of 2000 spins with various doping fractions of spin 3 random impurity.

For $x = 1\%$, the peak in the specific heat occurs near $T \sim 0.6J$, in good agreement with our previous calculations with no impurities. As the $S = 3$ impurity concentration increases to 5%,

10%, and 20%, the peak drops in height and moves slightly in temperature. We may compare the width of the specific peak at 20% $S = 3$ dopant with the undistorted lattice, F for the same dopant concentration. The distorted case has sharper specific heat, approximately twice as high and half width of $\sim 0.3J$ compared to $\sim 2J$ for the undistorted case. Thus the lattice distortion produces a much sharper transition in the magnetic ordering, which remains even after a fraction $\sim 20\%$ of spins has been replaced with a larger spin

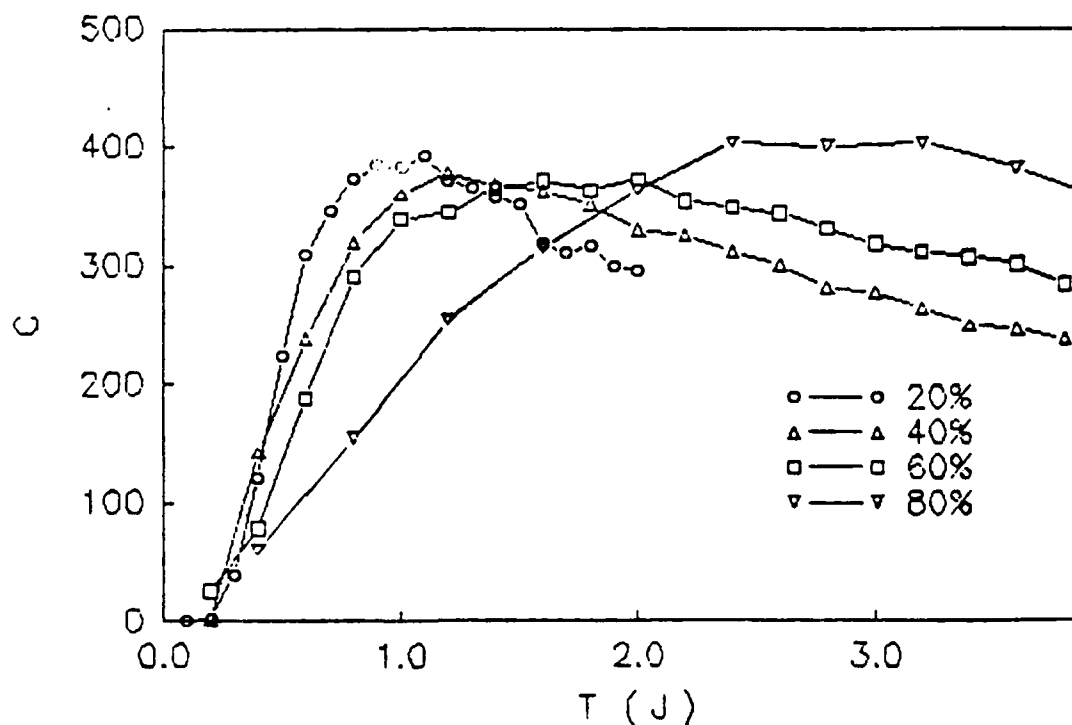


Fig. 3. Heat capacity vs. T for spinel lattice of 2000 s with various doping fractions of spin 3 random impuri

The susceptibility is shown in Fig. 4 for the same conditions: $J_{\perp}/J_{\parallel} = 1.1$, $S = 3$, and impurity concentrations from $x = 1\%$ to 20% . The overall effect of the impurity is to raise the susceptibility and shift the curve to lower temperature. It is interesting to note this occurs in the susceptibility even though the peak in the specific heat has been shifted to higher temperatures, as shown in Fig. 2. In addition, it is interesting to note that no low temperature Curie tail shows up even for substantial doping concentrations, unlike the case for the cubic undistorted lattice.

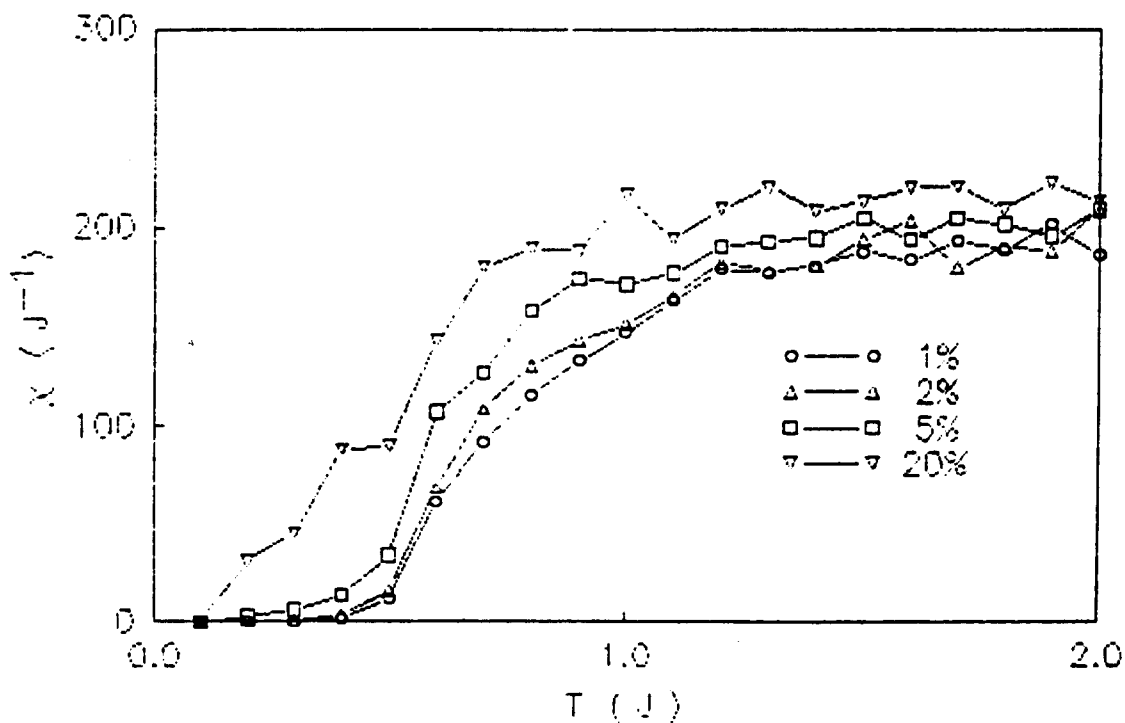


Fig. 4. Susceptibility vs. T for $c < a$ tetragonal spinel lattice with various fractions of spin 3 randomly distributed impurity.

The origin of these effects of doping with a larger spin in the $c < a$ distorted spinel lattice may be understood by considering the configurations shown in Fig. 5. For the case $J_{\perp} > J_{\parallel}$, a totally unfrustrated ordering is possible for the spinel lattice, as indicated in Fig. 5(a). The largest antiferromagnetic interaction, namely J_{\perp} , is satisfied first, resulting in antiferromagnetic coupling of the spins in the z direction. The smaller antiferromagnetic interaction, J_{\parallel} , is not satisfied, but the net energy of this state is lower than the cubic case by the difference $J_{\perp} - J_{\parallel}$ per spin. Thus a long range antiferromagnetic order parameter exists, corresponding to sheets of ferromagnetically oriented spins in the x - y planes which are then antiferromagnetically ordered in the z direction.

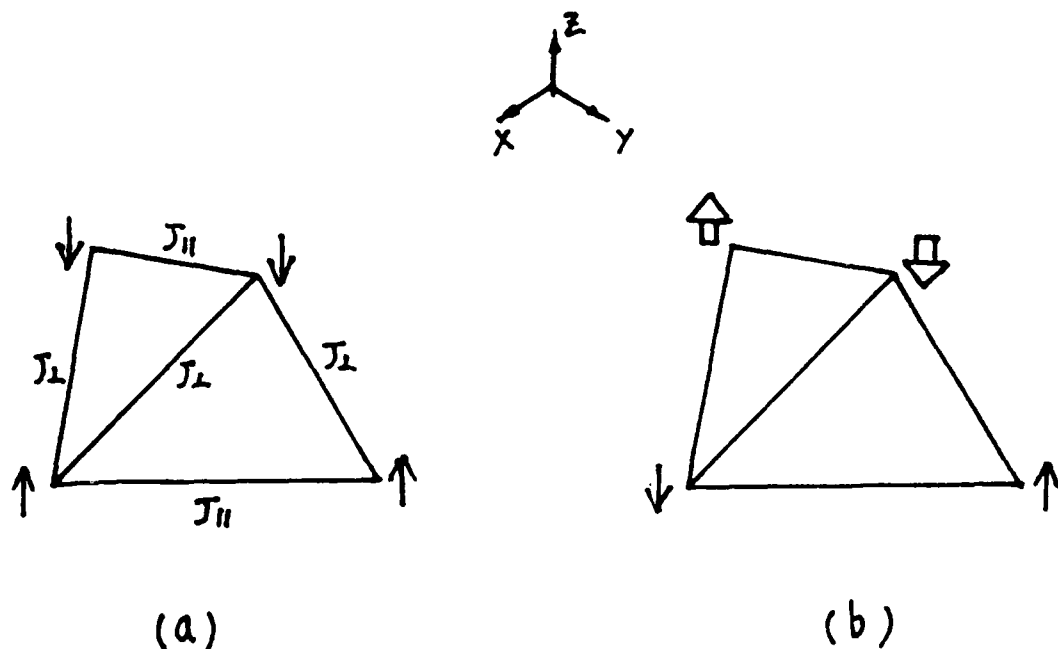


Fig. 5. Large spin configurations in $c < a$ tetragonal spinel lattice.

The effect of doping with a larger spin is shown in Fig. 5(b). For those impurity spins going into neighboring sites in an x-y plane, which constitute a large fraction of the possible configurations, the large coupling between the dopant spins ($= J_{\perp} S^2$) must be satisfied first. This reduces the antiferromagnetic order of the undoped crystal (Fig. 5(a)). This effect depends on the fact that the total exchange, proportional to JS^2 , is larger for the in-plane impurity spins than for one impurity and one host spin between planes. This is true as long as the ratio of the exchange interactions $J_{\perp}/J_{\parallel} = 1.1$ is smaller than the ratio of the impurity spin, $S = 3$, here, to the host Cr^{3+} spin, $S_0 = 3/2$. This will be the case, as in our calculations, whenever the lattice distortion is small and the substituted spin large.

The absence of a low temperature Curie tail may be understood by considering Fig. 6, which represents the most common configura-

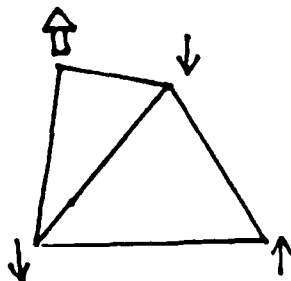


Fig. 6. Impurity configuration giving Curie tail in cubic case.

ration for small concentration x . In the cubic case for our spin values, the tetrahedral spin arrangement is frustrated, on spin has a net exchange field of zero, thus giving rise to Curie-like "free spins" which remain unordered. However, when the lattice is distorted such that $c < a$ or $J_{\perp} > J_{\parallel}$, the symmetry is broken and the frustration is removed, thus causing all the spins to order at low temperatures and removing the low T Curie tail.

Thus the large spin impurity broadens and reduces the specific heat peak, but actually shifts it higher in temperature. This arises because the average exchange coupling is increased as we saw in the undistorted case, discussed in our previous report. The impurity reduces the degree of antiferromagnetic order, however, which leads to increased spin fluctuations, and an increased value of the susceptibility below the transition (Fig. 4). The low temperature Curie tail is eliminated by the breaking of lattice symmetry which removes the up-down spin symmetry of the basic tetrahedral unit.

IV. Monte Carlo Calculations of Zero Spin Dopants in the $c < a$ Tetragonally Distorted Spinel Lattice: $J_{\perp} < J_{\parallel}$.

We now consider the case of a small spin, $S = 0$, impurity. As seen in the calculations reported previously for the cubic lattice, the $S = 0$ dopant does not lower the temperature of the peak in the specific heat but merely reduces it in magnitude.

In Fig. 7 we show the Monte Carlo specific heat results for the $c < a$ tetragonal spinel lattice for a concentration of $S = 0$

randomly distributed impurities ranging from $x = 1\%$ to $x = 20\%$. The most striking feature is the lowering of the transition temperature from about $0.6J$ for $x = 1\%$ to about $0.3J$ for $x = 20\%$. This is in sharp contrast to our Monte Carlo results on the undistorted lattice², as may be seen in Fig. 8 of Reference 2 where a concentration from 20% up to 60% spin zero impurities leaves the peak at virtually the same point. This is also completely different from the case of the large spin impurity for the tetragonal lattice reported above (Fig. 2) where the peak moved slightly up rather than down. We note that the magnitude of the specific heat is much larger in the tetragonal case at all impurity concentrations for the $S = 0$ spin dopant.

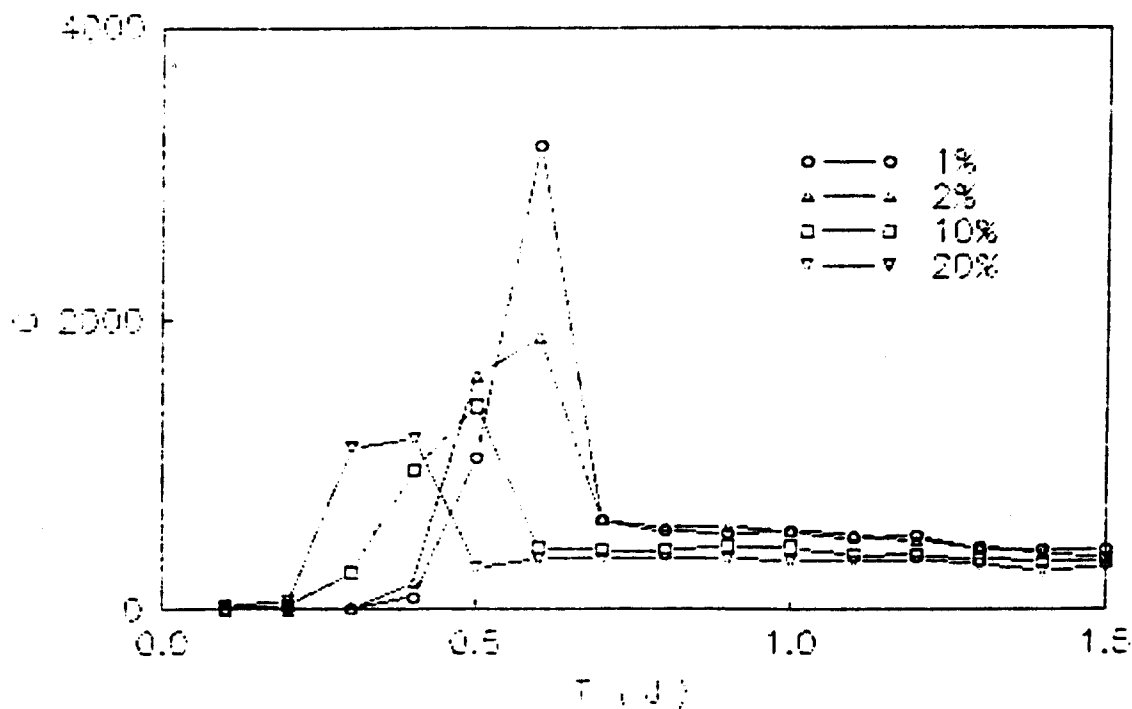


Fig. 7. Specific heat vs. T for tetragonal spinel lattice ($c < a$) with spin 0 randomly distributed impurities.

The Monte Carlo susceptibility for the corresponding case of the $c < a$ tetragonal lattice is shown in Fig. 8 for $x = 1\%$ to $x = 10\%$, since in this case the susceptibility becomes flat for larger dopant concentrations. The severe effects of the doping are clear in the susceptibility which shows both the suppression of the transition temperature as well as the disorder effects of the impurities on the long range magnetic order. The weaker antiferromagnetic order leads weaker antiferromagnetic order leads directly to large spin fluctuations and an increase in the susceptibility at all temperatures. In addition, there is clear evidence of free spins persisting down to a temperature of order $T \sim 0.4J$ for $x \sim 5-10\%$. This point will be discussed below.

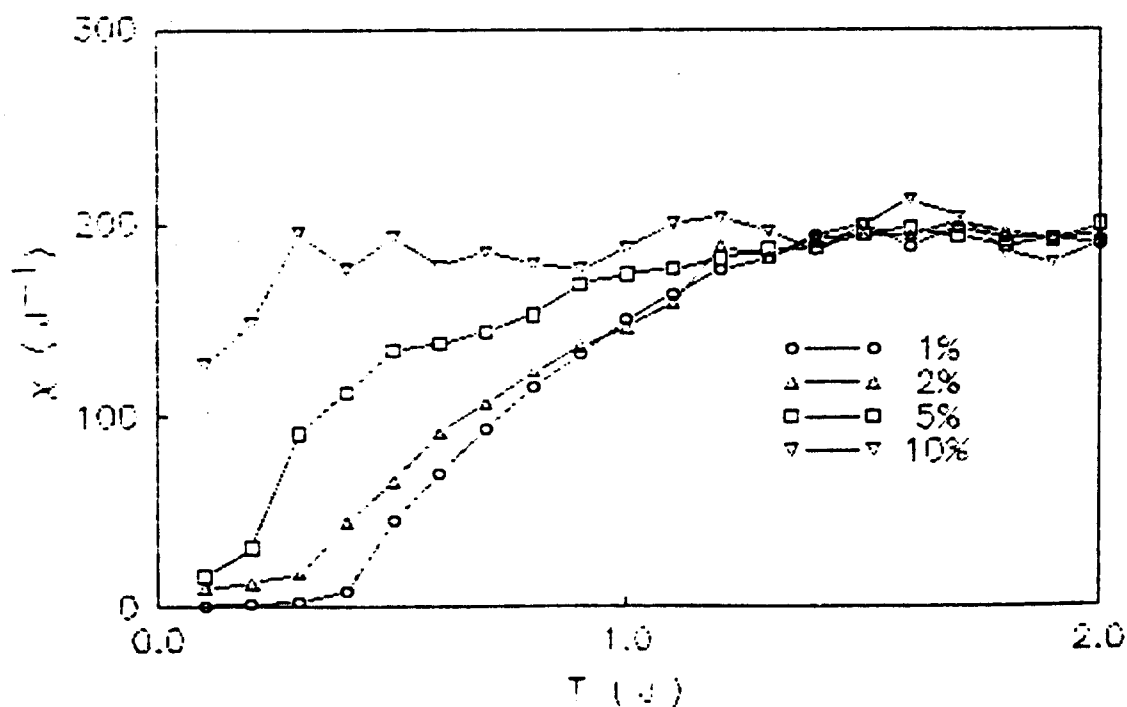


Fig. 8. Susceptibility vs. T for tetragonal spinel lattice with spin 0 randomly distributed impurities.

These results may be understood by considering the effects the $S = 0$ spin impurity has on typical spin ordering configurations. As we noted in our calculations on the cubic lattice, the effect of a spin zero impurity is to decouple the tetrahedral units, as shown in Fig. 9(a), where the missing spin at the intersection of the two tetrahedra separates the remaining triangles of spins on each tetrahedra. In the case of the frustrated cubic lattice this had little effect, since the order is basically local involving the freezing of the spins on a tetrahedra into a two-up two-down configuration. In the $c < a$ tetragonal lattice, however, as shown in Fig. 5(a) true long range spin ordering occurs; this long range order is severely impacted by the severing of connections between neighboring tetrahedra,

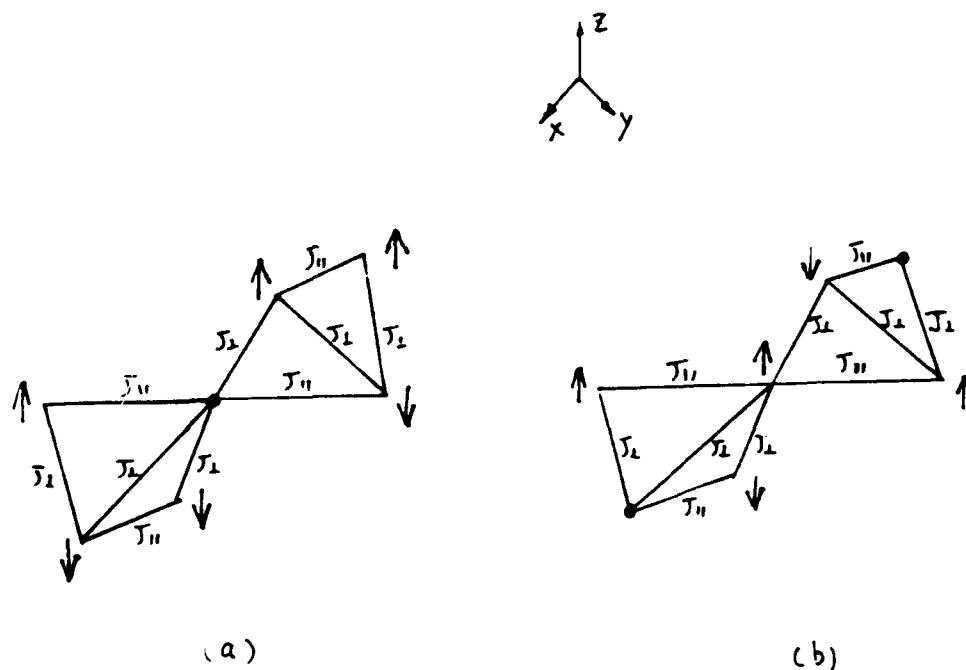


Fig. 9. Spin configurations important in the $S = 0$ impurity in the tetragonal spinel lattice with $c < a$.

unlike the frustrated cubic case. The difference between the frustrated system and the unfrustrated one are made very clear in this example.

The tendency to develop isolated free spins occurs in the tetragonal spinel lattice as it did in the cubic case reported previously. We recall from those considerations that a spin zero impurity removes a spin from a local tetrahedra (Fig. 10 of Reference 2) and leaves an isolated spin sitting in zero exchange field, much like the introduction of a free surface at the boundary of a finite spinel grain. In the tetragonally distorted spinel lattice, however, the degeneracy is removed by the difference in couplings J_{\perp} and J_{\parallel} as shown in Fig. 9(b). In the present calculations, $J_{\perp} = 1.1J_0$ and $J_{\parallel} = J_0$, where J_0 is the exchange interaction in the cubic phase (Note $J = (2J_{\perp} + J_{\parallel})/3 = 1.067 J_0$). The spin in the center of the two tetrahedra has a net change in energy when it flips of

$$\Delta E_{loc} = 2(J_{\perp} - J_{\parallel})S_0^2 = 0.2J_0S_0^2, \quad (2)$$

thus the spin at the center will display free spin characteristics, such as an increased contribution to the susceptibility, down to a temperature $T \sim 0.4 J$, at which point it will order. This is the origin of the enhanced susceptibility at intermediate temperatures in the tetragonal spinel. The local ordering energy (2) goes to zero in the cubic phase, giving rise to extended $1/T$ Curie tails in the susceptibility for the undistorted lattice as shown in our earlier work (Fig. 9 in Reference 2).

V. Summary of Results for $c < a$ Tetragonal Spinel Lattice

The results of our Monte Carlo calculations on the tetragonal spinel lattice with randomly quenched impurities and $J_1/J_2 = 1.1$ have provided the following important observations:

1. The tetragonal lattice for all spin impurity concentrations has a much larger and sharper specific heat feature, corresponding to the presence of true long range antiferromagnetic ordering.
2. The large spin dopant broadens and lowers the specific heat peak significantly, but moves the peak slightly up due to the increase in the average exchange interaction, while leaving the high temperature value of the specific heat virtually unchanged.
3. The large spin impurity for concentrations up to 20% increases the susceptibility due to spin fluctuations but produces no free spins (Curie tail), due to the breaking of symmetry between the c axis and the a - b plane by the tetragonal distortion.
4. A spin 0 impurity does not simply dilute the spin lattice, unlike the cubic frustrated or large spin distorted cases, but instead causes a sharp drop in transition temperature by a factor of two with only 20% dopant, as well as peak height, indicating the severe decoupling effect of the $S = 0$ impurity on the long range antiferromagnetic order.
5. The spin 0 impurity gives rise to a weak tendency toward free spins (Curie tail) in the temperature range between the original transition temperature and a lower temperature determined by twice the difference in the exchange interactions, $2(J_1 - J_2)$. As the tetragonal lattice distortion is reduced the Curie tail becomes more pronounced.

The present calculations indicate an interesting interplay between the effects of substitutional spin doping and lattice distortions on the frustrated spin ordering of the spinel lattice. The presence of both a lattice distortion and a spin impurity gives rise to unexpected consequences, such as the striking effect of $S = 0$ impurities is reducing the transition temperature, and of both large and small spin impurities in removing the low temperature $1/T$ Curie tails in the susceptibility.

It is clearly of major interest to examine in detail the case of the $c > a$ tetragonal distortion, since the effect is to reduce the frustration, but not to remove it completely. Thus the results may be intermediate between the cases considered so far.

REFERENCES

1. OSU Progress Report, Research on High-Specific-Heat Dielectrics, Theoretical Studies I: Effects of Impurity Spin Doping on Undistorted Spinel Lattice, AFOSR Contract F49620-86-C-0049, August 31, 1988.
2. Annual Technical Report, Research on High-Specific-Heat Dielectrics, AFOSR Contract F49620-86-C-0049, May 11, 1987. In brief summary the simulations used the Ising model in which each spin takes the possible values $\pm S$, where S is the magnitude of the spin. The spins are set on the 8 sites of a cube of the spinel lattice 5 unit cells on a side containing 2000 spins. Periodic boundary conditions are used to eliminate boundary effects. After equilibration, 2000 Monte Carlo steps per spin are used at each temperature.

VII.C. EFFECTS OF IMPURITY SPIN DOPING ON TETRAGONALLY DISTORTED SPINEL LATTICE - $a < c$ Case

I. Introduction

Our previous reports on Monte Carlo simulations of the spinel lattice doped with various spin impurities have considered the cases of the undistorted or cubic lattice,¹ and the tetragonally distorted spinel lattice for $c < a$, where a , b , and c are the three lattice constants in the tetragonal phase and $a = b$.² The case of the $c > a$ tetragonal distortion involves qualitatively different physical effects and is discussed in the present report.

This work arose from the attempt to understand the role played by frustration in the magnetic ordering properties of the very unusual dielectric materials with high specific heat based on the chromite spinels, CdCr_2O_4 and ZnCr_2O_4 . In addition, the possibility of raising the transition temperature of the magnetic ordering by introduction of other spin species like Fe, Al, V, Gd, or other ions was of interest.

For the undistorted lattice case, we found that a large spin like $S = 3$ increased the transition temperature and broadened the specific heat curve. A small spin like $S = 0$ had little effect on the ordering temperature and simply diluted the spin lattice. In addition both the large spin and the small spin produced a large low T Curie tail in the susceptibility.

In the case of the $c < a$ tetragonal spinel lattice, the results were surprisingly different. The pure tetragonal lattice showed good long range antiferromagnetic order, while a large spin reduced and broadened the peak, but without reducing the

transition temperature. A small spin impurity like $S = 0$ strongly suppressed the antiferromagnetic order, in sharp contrast to the cubic lattice case. The magnetic susceptibility displayed no $1/T$ Curie tail behavior as a signature of free spins, again in sharp contrast to the undistorted cubic results. The role of the reduction in symmetry produced by the tetragonal distortion was a key factor leading to these results.

Since our previous work has shown the importance of frustration in the large specific heat anomalies in these systems,³ we report here our investigations of the $c > a$ tetragonally distorted spinel lattice, which has an intermediate degree of frustration compared to the totally frustrated cubic lattice and the unfrustrated $c < a$ tetragonal lattice.

In Section II, we review the role of doping and lattice distortions in our previous calculations on the spinel lattice. The new results for the $c > a$ Monte Carlo calculations for the large spin case ($S = 3$) are reported in Section III. Section IV presents the analogous Monte Carlo results for small spin ($S = 0$) impurities, followed by an interpretive summary in Section V.

II. Effect of Impurity Doping and $c < a$ Lattice Distortion on Spin Ordering of the Spinel Lattice

We briefly summarize here the key results of our broad-range doping calculations for the undistorted cubic spinel lattice, as well as the result for the $c < a$ tetragonal lattice, since the differences in the tetragonal cases are important. As pointed

out in our previous work, the spinel lattice with B site spin occupation only (A site unoccupied) involves triangular loops connecting adjoining spins and is a totally frustrated spin system with antiferromagnetic interactions.³

The results of our Monte Carlo calculations on the undistorted cubic spinel lattice for a wide concentration range of randomly quenched impurities indicate the following characteristic features:¹

1. A large spin impurity causes the peak in the specific heat to move up in temperature roughly in proportion to the average increase in S^2 , indicating that the frustration is not changed dramatically by the doping.
2. The large spin dopant broadens the specific heat significantly, greatly increasing the high temperature value of the specific heat.
3. The large spin impurity for small concentrations initially produces a large number of free spins (Curie tail), which disappears for concentrations above 50%.
4. A spin 0 impurity dilutes the spin lattice, giving rise to no shift in the transition, indicating near cancellation of the effects of dilution and reduction in frustration produced by the doping.
5. The spin 0 dopant of concentration x reduces the magnitude of the specific heat peak roughly by a factor of $(1-x)$, which corresponds to the number of remaining host spins.
6. A spin 0 impurity gives rise to free spins (Curie tail) at all concentrations, which may be used to distinguish the behavior from that produced by a large spin impurity where the Curie tail disappears at high concentrations.

7. Neither large nor zero spin impurities have led to a large increase in the ordering temperature of the undistorted cubic lattice, although the large spin in reasonable concentration gives rise to a high temperature increase in the specific heat tail which could prove useful.
8. Experimental data are in general agreement with this picture, except for the case of Al^{+3} $S = 0$ dopants, for which clustering effects may be important.⁴

We know that a distortion into the tetragonal phase reduces the frustration and, in the case $c < a$, can completely remove the frustration. Thus the effects of distorting the spinel lattice from the cubic into the tetragonal phase, with both $c > a$ and $c < a$, may give interesting effects upon doping, since our previous Monte Carlo work has shown that the transition may be raised dramatically by such a lattice distortion. Because the antiferromagnetic transition is stabilized by the lattice distortion, we have focused on the effects of smaller doping concentrations in the tetragonal lattices.

In order to facilitate comparison with our Monte Carlo results on the $c < a$ tetragonal lattice with randomly quenched impurities we summarize the key findings here:²

1. The tetragonal lattice for all spin impurity concentrations has a much larger and sharper specific heat feature, corresponding to the presence of true long range antiferromagnetic ordering.
2. The large spin dopant broadens and lowers the specific

heat peak significantly, but moves the peak slightly up due to the increase in the average exchange interaction, while leaving the high temperature value of the specific heat virtually unchanged.

3. The large spin impurity for concentrations up to 20% increases the susceptibility due to spin fluctuations but produces no free spins (Curie tail), due to the breaking of symmetry between the c axis and the a-b plane by the tetragonal distortion.
4. A spin 0 impurity does not simply dilute the spin lattice, unlike the cubic frustrated or large spin distorted cases, but instead causes a sharp drop in transition temperature by a factor of two with 20% dopant, as well as decreasing the peak height, indicating the severe decoupling effect of the $S = 0$ impurity on the long range antiferromagnetic order.
5. The spin 0 impurity gives rise to a weak tendency toward free spins (Curie tail) in the temperature range between the original transition temperature and a lower temperature determined by twice the difference in the exchange interactions, $2(J_{\perp} - J_{\parallel})$. As the tetragonal lattice distortion is reduced the Curie tail becomes more pronounced.

In the present report we observe that the frustration of the cubic spinel lattice may also be reduced by a tetragonal distortion with increased lattice constant in the z direction, $c > a$, corresponding to $J_{\perp} < J_{\parallel}$. In this case, however, unlike the case $c < a$ discussed above, the distortion does not completely remove the frustration. The largest interaction, now J_{\parallel} , is satisfied first, leading to antiferromagnetically ordered chains in the x-y plane. The remaining interaction between planes in the z direc-

tion, J_{\perp} , in the present case does not lead to a unique ordering of the antiferromagnetic x-y chains; the interplane interaction is still frustrated.

III. Monte Carlo Calculations of Large Spin Dopants in the $c > a$ Tetragonally Distorted Spinel Lattice: $J_{\perp} < J_{\parallel}$.

Following our previous work,² the c axis will be taken in the vertical direction and the equivalent a, b axis of the tetragonal phase will be taken in the horizontal plane. The spin exchange Hamiltonian, Eq. (1), is correct in both the cubic and tetragonal phases, with the proper anisotropic values taken for the exchange couplings, J_{ij} :

$$H = \sum_{\langle ij \rangle} J_{ij} S_i S_j \quad (1)$$

As discussed in our previous reports, in the cubic phase, symmetry requires all the J_{ij} to have the same value. The effect of a $c > a$ tetragonal distortion on the cubic spinel lattice is to move the horizontal planes of spins farther apart. Thus the exchange constant between spins in the z direction, J_{\perp} , becomes smaller than the coupling among the spins within the x-y plane, J_{\parallel} . In our Monte Carlo calculations, the $c > a$ lattice distortion requires two exchange couplings in the Hamiltonian (1), with $J_{\perp}/J_{\parallel} < 1$. In the following numerical simulations, a reasonable lattice distortion corresponding to $J_{\perp}/J_{\parallel} = 0.9$ was assumed.

Using lattice sizes and Monte Carlo cycle times comparable to

our previous work to facilitate comparison with our previous results,³ we carried out numerical simulations for concentrations x of a large spin ($S = 3$) between $x = 0.05\%$ and $x = 20\%$. The heat capacity calculations are shown in Fig. 1 for a lattice of 2000 spins, in units of the average host spin coupling JS_0^2 with $S_0 = 3/2$, where $J = (2J_L + J_I)/3$ is the average exchange interaction.

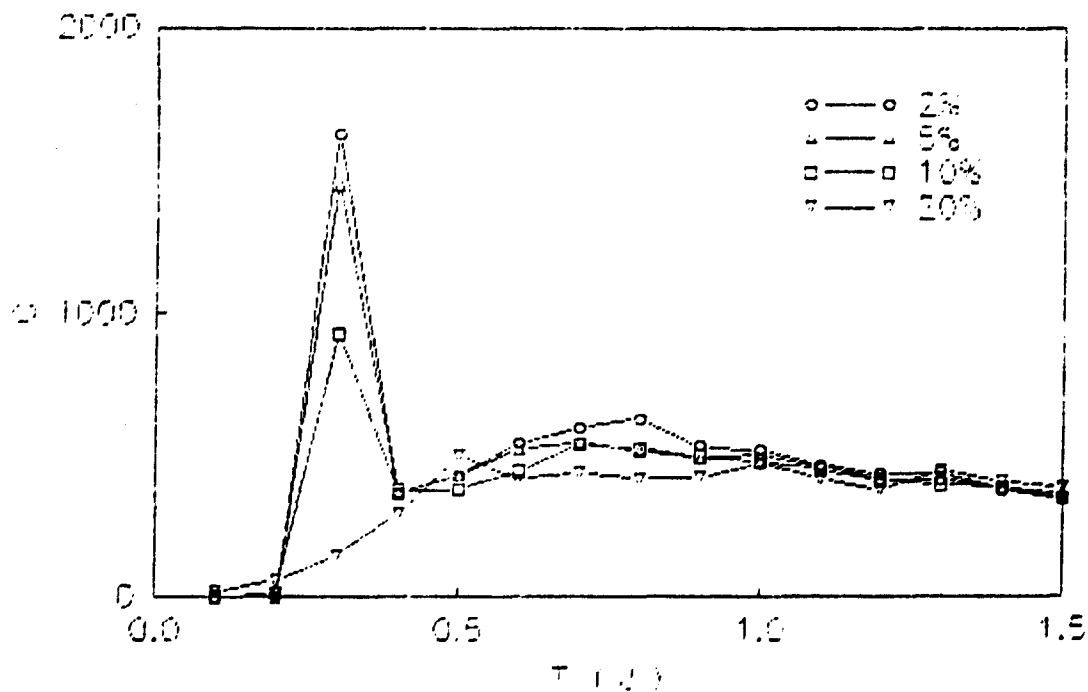


Fig. 1. Heat capacity vs. T for $c > a$ tetragonal spinel lattice of 2000 spins with spin 3 random impurities.

For the smallest spin concentration $x = 2\%$, the peak in the specific heat occurs near $T \sim 0.3J$, a value which in good agreement with our previous calculations for the $c > a$ lattice with no

impurities.³ As the $S = 3$ impurity concentration increases to 5% and 10%, the peak drops in height but remains unchanged in temperature location. The width of the specific heat peak is rather narrow up to 10% dopant, much like the $c < a$ lattice case. The magnitude of the heat capacity is very large compared to the undistorted lattice, although not quite as large as the unfrustrated $c < a$ lattice. This corresponds to good long range magnetic order of magnitude intermediate between the fully frustrated $c = a$ and the unfrustrated $c < a$ cases, which agrees with the fact that the $c > a$ lattice has an intermediate degree of frustration. For a concentration of 20% the peak becomes rather broad and shows some indication of a shift to higher temperatures, a feature which we have seen in all our results for a large spin in both tetragonally distorted phases as well as the cubic phase.

The disappearance of the long range magnetic order in this case appears to be more subtle than the other cases we have investigated. It does not appear possible to identify simple dominant spin configurations that explain the Monte Carlo results. Arguments on small spin clusters in fact suggest that the impurity spins should not destroy the long range magnetic order of the ground state. Thus the Monte Carlo calculations in this case may reveal delicate cancelations of interactions which could be studied in more detail.

The magnetic susceptibility is shown in Fig. 2 for the same set of parameters as the heat capacity of Fig. 1: $J_{\perp}/J_{\parallel} = 0.9$, $S = 3$, and impurity concentrations from $x = 1\%$ to 20% . As seen

before in both the cubic and the $c < a$ lattices, the effect of the impurity doping is to raise the susceptibility and shift the curve to lower temperature. For a large spin concentration of $x = 20\%$, however, a peak in the susceptibility appears, a qualitatively different result from the other cases. The peak occurs around $0.4J$, just below the broad peak in the heat capacity near $0.5J$. The increased value of the susceptibility reflects the increased fluctuations in the spin ordering caused by the impurities, but the sharp cusp at $T \sim 0.4J$ for $x = 20\%$ spin 3 impurities indicates the presence of free spins which freeze out suddenly at that temperature.

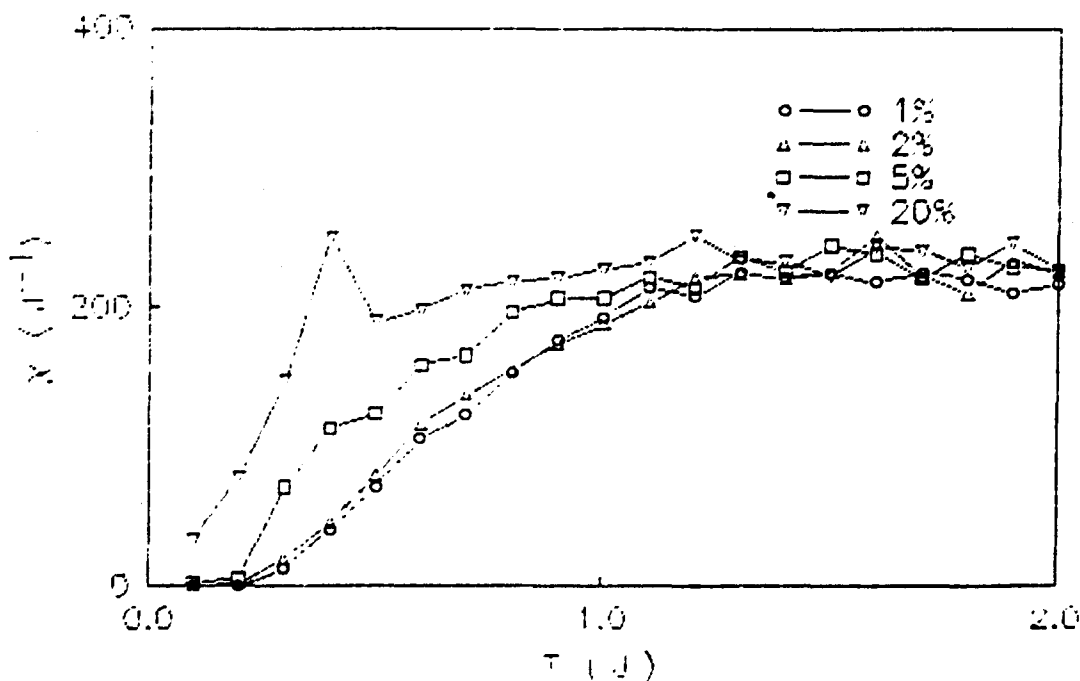


Fig. 2. Susceptibility vs. T for $c > a$ tetragonal spinel lattice with spin 3 randomly distributed impurities.

We have been able to identify the origin of these effects of large spin doping in the tetragonal spinel lattice by considering the ground state configurations shown in Fig. 3. Fig. 3(a) represents the ground state spin configuration for $J_{\perp} < J_{\parallel}$ (with $c > a$), while Fig. 3(b) depicts the ground state for the case $J_{\perp} > J_{\parallel}$. For the exchange coupling used in our Monte Carlo calculations, $J_{\perp} = 0.9J_0$ and $J_{\parallel} = J_0$, and an impurity spin-host spin ratio of $S/S_0 = 3/(3/2) = 2$, the energy of the central spin in Fig. 3(a) increases by $4(J_{\parallel} - J_{\perp}) = 0.4J_0$ upon flipping over. Thus for temperatures above $T \sim 0.4J_0$, these spins are effectively free, but order below that temperature, giving rise to the cusp in the susceptibility for large concentrations seen in Fig. 2.

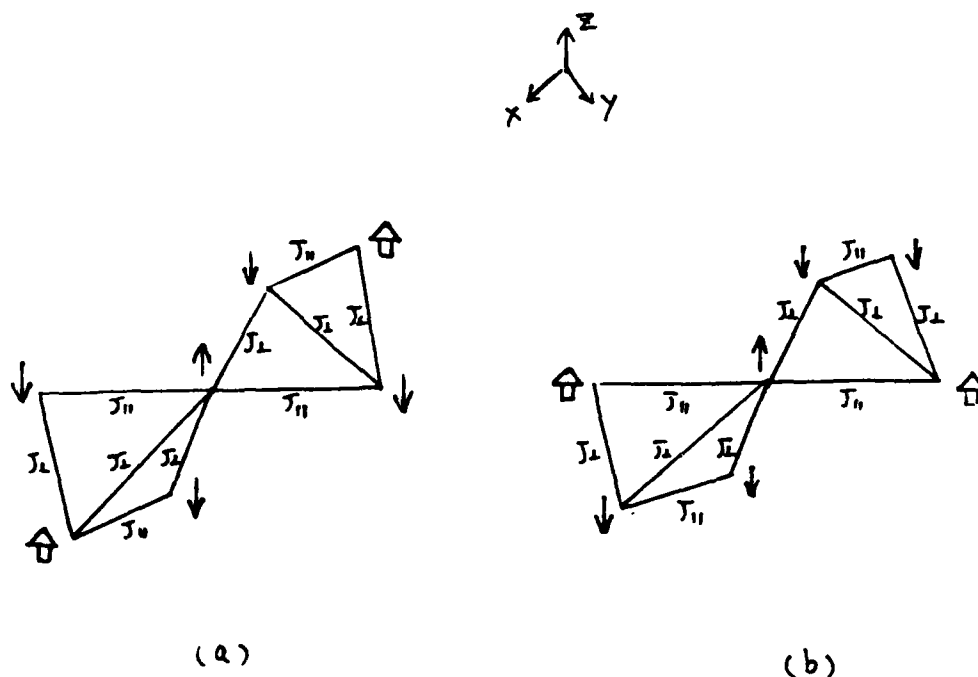


Fig. 3. Impurity configuration giving (a) cusp in $c > a$ tetragonal case, and (b) no cusp in $c < a$ case.

It is interesting to consider the other tetragonal phase, with $c < a$, since no cusp in the susceptibility was found in the Monte Carlo calculations.² Fig. 3(b) shows that a spin flip of the central spin involves a change in energy of $8(J_{\perp} - J_{\parallel}) = 0.8J_0$, since for $c < a$ we used $J_{\perp} = 1.1J_0$ and $J_{\parallel} = J_0$. Thus the excitation energy is twice as large for the $c < a$ lattice as for the case considered in this report, and is of order the transition temperature which makes the effect much weaker and explains why we did not find a cusp in the susceptibility in the earlier calculations for $c < a$.

IV. Monte Carlo Calculations of Zero Spin Dopants in the $c > a$ Tetragonally Distorted Spinel Lattice: $J_{\perp} < J_{\parallel}$.

The next set of calculations concern the case of a small spin, $S = 0$, impurity. In the cubic lattice, our results showed the $S = 0$ dopant did not lower the temperature of the peak in the specific heat but merely reduces it in magnitude, while for the $c < a$ lattice the spin zero impurity had a severe effect on the transition temperature.

Fig. 4 shows the Monte Carlo heat capacity results for the $c > a$ tetragonal spinel lattice for a concentration of $S = 0$ randomly distributed impurities ranging from $x = 0.05\%$ to $x = 20\%$. Although the peak is high, indicating good long range magnetic order, the impurities do not reduce the ordering transition, but merely reduce the height of the peak. This is in striking contrast to the $c < a$ case where the transition was reduced by half

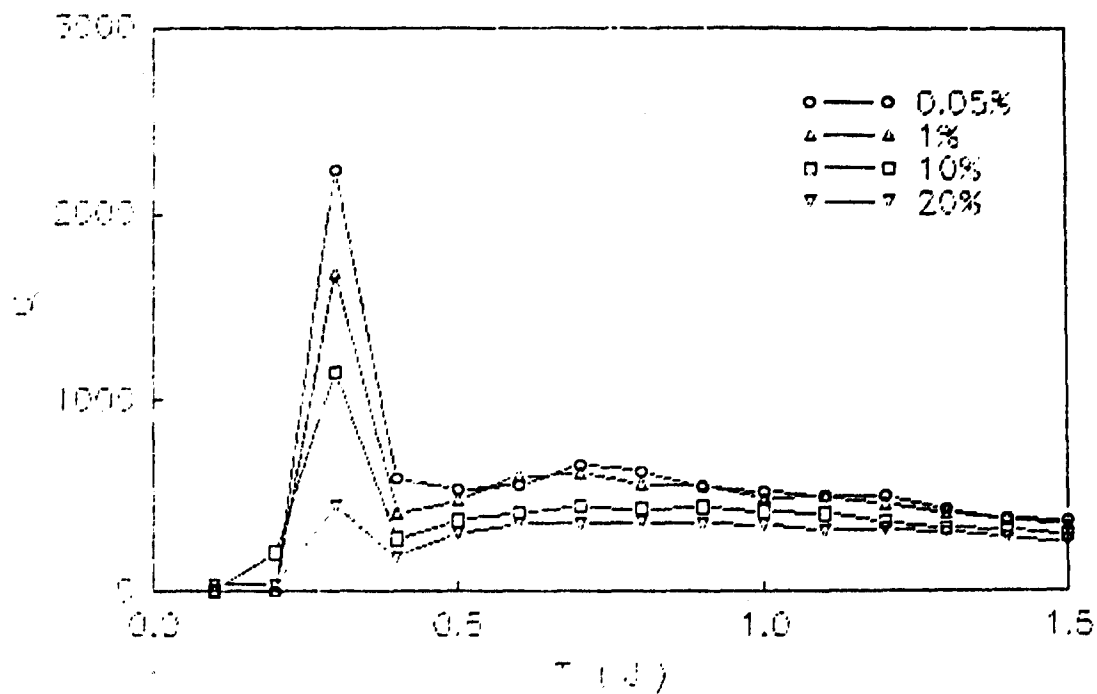


Fig. 4. Heat capacity vs. T for tetragonal spinel lattice ($c > a$) with spin 0 randomly distributed impurities.

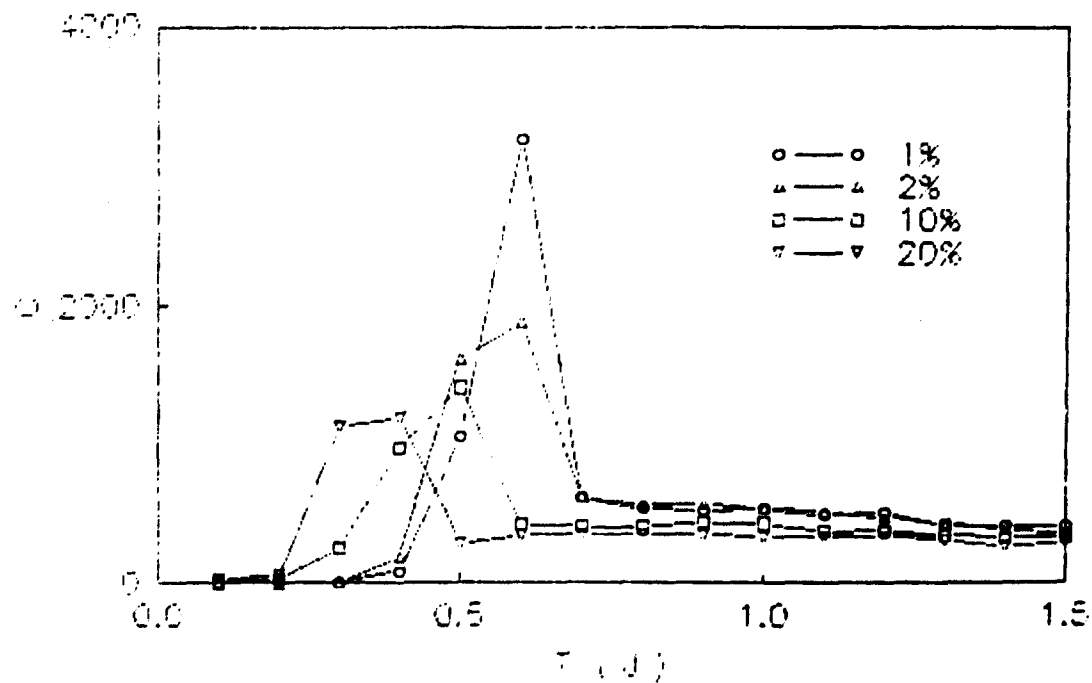


Fig. 5. Specific heat vs. T for tetragonal spinel lattice ($c < a$) with spin 0 randomly distributed impurities.

with the same 20% concentration of impurities as shown in Fig. 5. In fact the results in Fig. 4 are similar to the case of the cubic lattice in so far as the ordering transition is almost independent of impurity concentration. The magnitude of the specific heat is much larger in the tetragonal cases than in the cubic case, while the peak height is reduced more for the $c > a$ tetragonal lattice than it is for the $c < a$ case by a concentration of 20% impurities.

The susceptibility obtained from the Monte Carlo calculations for the case of the $c > a$ tetragonal lattice is shown in Fig. 6 for $x = 1\%$ to $x = 20\%$. These remarkable results are completely different from the susceptibility for the other cases. For low concentrations of $S = 0$ impurities the susceptibility drops monotonically to zero, with no indication of free spins present. However, for concentrations between $x = 5\%$ and $x = 20\%$, substantial structure appears in the vicinity of the specific heat peak. For 5% the susceptibility displays a cusp near $T \sim 0.4J$, while for a larger concentration of 20% a large Curie $1/T$ tail appears. To compare the differences with the $c < a$ tetragonal phase we reproduce the susceptibility for that case in Fig. 7, where it can be seen that the structure around $T \sim 0.4J$ is completely missing for the larger spin concentrations. In particular, there is no evidence of the cusp or $1/T$ Curie tail of the $c > a$ case (Fig. 6) in the corresponding curves for the $c < a$ case (Fig. 7).

We have been able to understand these unusual features of the partially frustrated $c > a$ lattice in terms of the excitations from the ground state and the effect that the $S = 0$ spin impurity

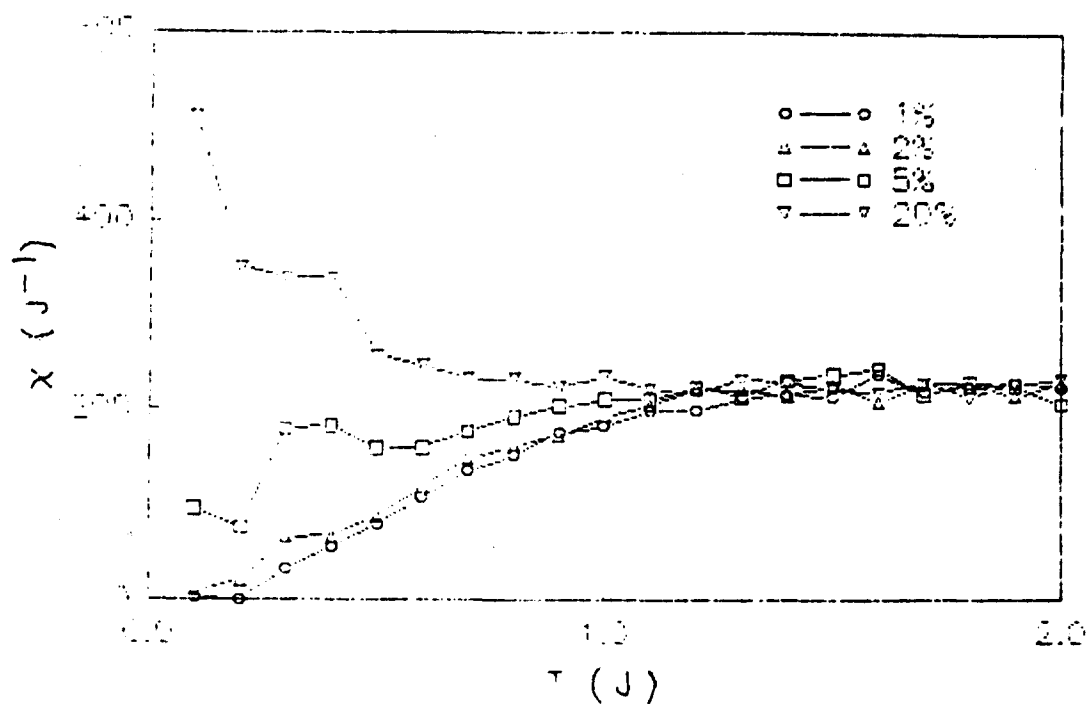


Fig. 6. Susceptibility vs. T for $c > a$ tetragonal spinel lattice with spin 0 randomly distributed impurities.

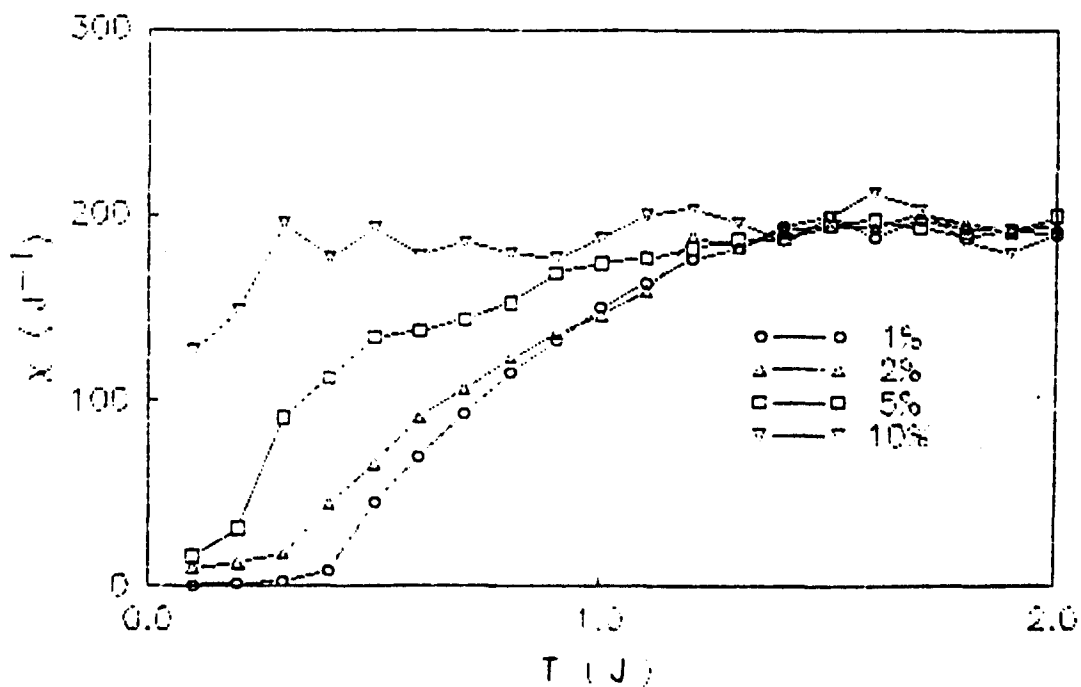


Fig. 7. Susceptibility vs. T for $c < a$ tetragonal spinel lattice with spin 0 randomly distributed impurities.

has on typical spin ordering configurations. Fig. 8 shows low lying excitations present for zero spin impurities and the $c > a$ ground state. When two $S = 0$ impurities lie along the same chain in the a - b plane as shown in Fig. 8(a), the spin at the center is fully frustrated, i.e., completely free, despite the lack of symmetry produced by the tetragonal distortion. This is the origin of the $1/T$ Curie tail in the susceptibility. The cusp, however, arises from the configuration shown in Fig. 8(b), in which the $S = 0$ impurities lie in the z direction with respect to the spin at the center. The energy change for a spin flip is $4(J_{\parallel} - J_{\perp}) = 0.4J_0$. Thus the configurations of Fig. 8(b) order below $T \sim 0.4J$ and give a cusp in the susceptibility at that temperature.

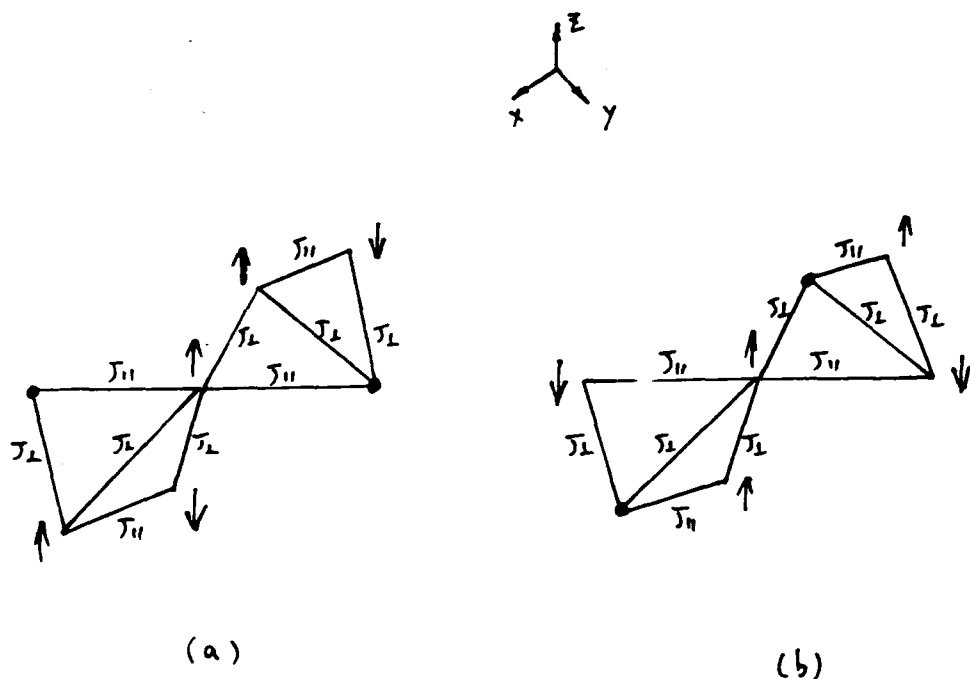


Fig. 8. Spin configurations important in the $S = 0$ impurity in the tetragonal spinel lattice with $c < a$. (a) $\Delta E = 0$, (b) $\Delta E = 0.4J$.

Finally, we consider a puzzling question concerning the nature of the specific heat curve in the presence of impurities. The basic question is that given the disordering effect of random spin impurities, why is the $S = 0$, $c < a$ ($J_{\perp}/J_{\parallel} = 1.1$) case the only one in which the peak in the specific heat shifts down?

To answer this question, it is important to realize that in order to move the specific heat peak down it is necessary to have excitations with an energy less than that of the ordering temperature. The basic answer to the above puzzle is that only the $S = 0$ and $c < a$ case has an excitation energy introduced by the impurity which is much lower than the transition temperature. To see this we consider the configurations of the ground state spins with one impurity spin present shown in Fig. 9. Fig. 9(a) and 9(b) correspond to the case $J_{\perp}/J_{\parallel} = 1.1$ and impurity spin $S = 3$ and $S = 0$, respectively, while Fig. 9(c) and 9(d) correspond to the case $J_{\perp}/J_{\parallel} = 0.9$ and impurity spin $S = 3$ and $S = 0$, respectively. The energy of the lowest excitation energy obtained by flipping the spin(s) in the dotted circles is given in Table I, along with the transition temperature T_N .

As may be easily seen from the table, the only case in which the excitation energy is much lower than the ordering temperature of the undoped lattice is case 9(b), corresponding to a $c < a$ tetragonal distortion with spin zero dopant impurities. The presence of these low energy excitations produces a large contribution to the specific heat at low temperature, and effectively shifts the peak to lower temperatures, unlike the other three cases where the excitation energies and T_N are comparable.

Fig.	J_{\perp}/J_{\parallel}	doped spin	lowest excitation energy	T_N
9(a)	1.1	3	$4(J_{\perp} - J_{\parallel}) = 0.4J_0$	$0.6J$
9(b)	1.1	0	$2(J_{\perp} - J_{\parallel}) = 0.2J_0$	$0.6J$
9(c)	0.9	3	$2(J_{\parallel} - J_{\perp}) = 0.2J_0$	$0.3J$
9(d)	0.9	0	$2(J_{\parallel} - J_{\perp}) = 0.2J_0$	$0.3J$

Table I. Excitation energies and transition temperatures T_N for different combinations of dopant spins and tetragonal lattice distortions with a host spin $S_0 = 3/2$. $J = (2J_{\perp} + J_{\parallel})/3 \sim J_0$.

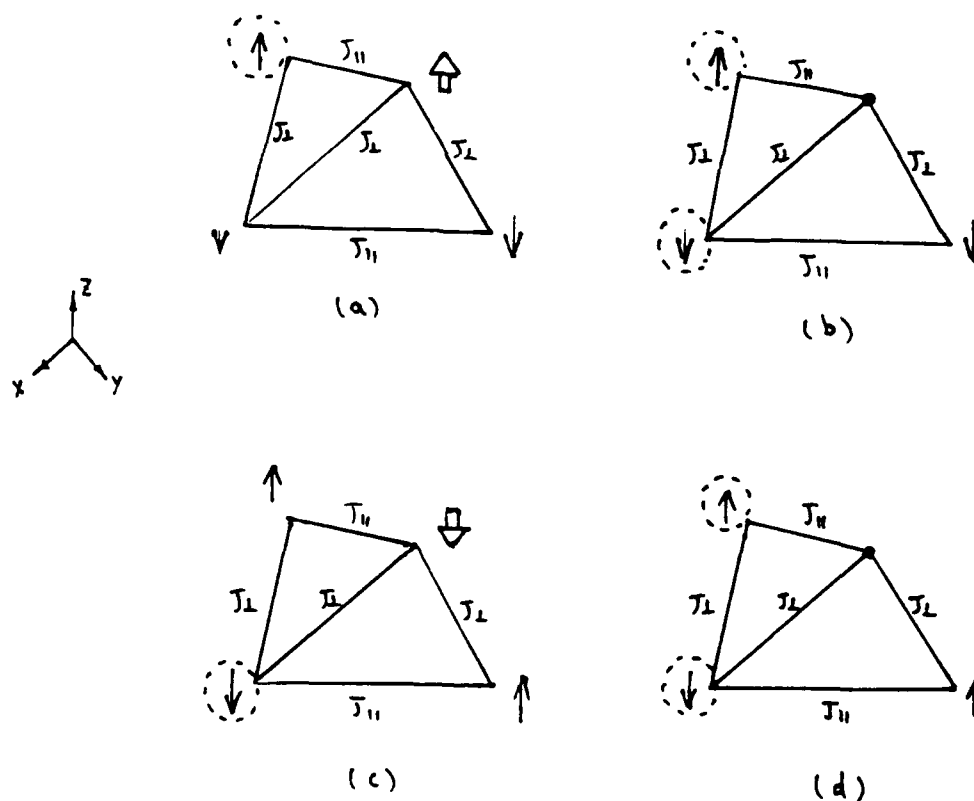


Fig. 9. Ground state spin configurations for (a) $J_{\perp}/J_{\parallel} = 1.1$ and $S = 3$, (b) $J_{\perp}/J_{\parallel} = 1.1$ and $S = 0$, (c) $J_{\perp}/J_{\parallel} = 0.9$ and $S = 3$, and (d) $J_{\perp}/J_{\parallel} = 0.9$ and $S = 0$. Spin 3 is denoted by a large arrow, spin 0 is denoted by dot.

V. Summary of Results for Tetragonally Distorted Spinel Lattice

The results of our Monte Carlo calculations on the tetragonal spinel lattice with randomly quenched impurities and $J_{\perp}/J_{\parallel} = 0.9$ ($c > a$) combined with our previous results may be summarized as follows:

1. The tetragonal lattice for all spin impurity concentrations has a much larger and sharper specific heat feature than the undistorted cubic lattice; the specific heat is larger for the unfrustrated $c < a$ case than the $c > a$ partially frustrated case.
2. For both tetragonal distortions, the large spin dopant broadens and lowers the specific heat peak by a factor of 2 at 10% dopant, but moves the peak slightly up due to the increase in the average exchange interaction, while leaving the high temperature value of the specific heat virtually unchanged.
3. For $c < a$, the large spin impurity for concentrations up to 20% increases the susceptibility due to spin fluctuations but produces no free spins (Curie tail), while for $c > a$, free spins down to $2(J_{\parallel} - J_{\perp}) = 0.4J$ produce a cusp for $x = 20\%$.
4. For $c < a$, a spin 0 impurity causes a sharp drop in transition temperature by a factor of two with 20% dopant, while for $c > a$ the transition temperature is unchanged, due to the difference in the low energy excitations above the ground state.
5. In both tetragonal lattices the spin 0 impurity gives rise to a weak tendency toward free spins (Curie tail) in the temperature range between the original transition temperature and a lower temperature determined by twice the difference in the exchange interactions, $2(J_{\perp} - J_{\parallel})$, which can give rise to a cusp. For the case $c > a$,

however, impurities produce additional spins sitting in zero exchange field, giving a strong $1/T$ Curie tail.

The Monte Carlo calculations described in our recent reports have revealed an interesting interplay between the effects of substitutional spin doping and lattice distortions on the frustrated spin ordering of the spinel lattice. The presence of both a lattice distortion and a spin impurity gives rise to unexpected consequences, such as the striking effect of $S = 0$ impurities in reducing the transition temperature for the $c < a$ lattice, and of both large and small spin impurities in removing the low temperature $1/T$ Curie tails in the susceptibility for $c < a$, while for $c > a$ both large and small impurities give rise to cusps in the susceptibility. The key to understanding the effects of dopants and lattice distortions on the spin ordering of the spinel lattice lie in the nature of the low energy excitations available to the system.

REFERENCES

1. OSU Progress Report, Research on High-Specific-Heat Dielectrics, Theoretical Studies I: Effects of Impurity Spin Doping on Undistorted Spinel Lattice, AFOSR Contract F49620-86-C-0049, August 31, 1988.
2. OSU Progress Report, Research on High-Specific-Heat Dielectrics, Theoretical Studies II: Effects of Impurity Spin Doping on Tetragonally Distorted Spinel Lattice - $c < a$ Case, AFOSR Contract F49620-86-C-0049, September 30, 1988.
3. Annual Technical Report, Research on High-Specific-Heat Dielectrics, AFOSR Contract F49620-86-C-0049, May 11, 1987. In brief summary the simulations used the Ising model in which each spin takes the possible values $\pm S$, where S is the magnitude of the spin. The spins are set on the B sites of a cube of the spinel lattice 5 unit cells on a side containing 2000 spins. Periodic boundary conditions are used to eliminate boundary effects. After equilibration, 2000 Monte Carlo steps per spin are used at each temperature.
4. CeramPhysics, Inc. Progress Report, Research on High-Specific-Heat Dielectrics, AFOSR Contract F49620-86-C-0049, August 26, 1988.

I. Introduction

One of the key questions in the AFOSR program on the high specific heat dielectrics based on the chromite spinels, CdCr_2O_4 and ZnCr_2O_4 , has been the precise nature of the phase magnetic transition, including the determination of what causes the high value of the specific heat near the transition as well as what determines the magnitude of the transition temperature, which is only about 10K in the pure phases of these materials.

In our Monte Carlo simulations of the spinel lattice for different possible low temperature lattice structures, we have found evidence for a variety of behaviors: 1) a spin glass-like freezing transition in the cubic structure, 2) a antiferromagnetic transition in the $c < a$ tetragonal structure, and 3) a partially frustrated antiferromagnetic transition in the $c > a$ tetragonal structure.^{1,2,3,4}

In addition, we found some evidence that the transition might be first order with a discontinuous change in properties at the transition temperature in some cases, and second order, or continuous, in other cases.^{4,5} The evidence from available experiments is also not clear since it is often hard to distinguish between a large specific heat at a second order transition and a small latent heat at a first order transition.^{4,6}

The question of a first or second order transition is not only of fundamental importance in understanding the unusual phase transition and large specific heats of these materials, but also in utilizing and manipulating the properties of the materials.

One consequence of a first order transition, for example, is the introduction of a certain amount of hysteresis in the temperature and magnetic field dependent properties of the material.

In order to clarify the nature of the transition, we have carried out several lines of investigation. The first, involving a Ginzberg-Landau (G-L) analysis of the degree of the phase transition based on a microscopic model of the ordered state of the tetragonal spinel lattice, will be reported here. The second approach, involving a new high efficiency Monte Carlo technique, will be summarized in our next progress report.⁵

The G-L approach is based on a model we used to successfully calculate an unusual coupling of the dielectric polarizability to the magnetic ordering in the spinel materials CdCr_2O_4 and ZnCr_2O_4 . The theory appears to account for the unusual dielectric anomalies seen experimentally at the magnetic phase transition as well as accounting for the shift to lower temperatures in a magnetic field of the structure in the dielectric constant.^{4,7}

In Section II we review the current evidence on the nature of the phase transition in the spinels. The G-L model is defined in Section III and the connection between the structure of the free energy and the order of the phase transition is made. In Section IV we derive the G-L functional from a microscopic model and connect the coefficients in G-L expansion with microscopic parameters, which shows that the transition is second order for the $c < a$ tetragonal phase. Finally, summary and conclusions are provided in Section V.

II. Available Evidence on the Nature of the Transition in the Spinel Materials CdCr_2O_4 and ZnCr_2O_4 .

In our previous work under this contract we developed a model which successfully accounted for the unusual dielectric anomaly at the magnetic transition in the spinels.⁴ This model assumed an antiferromagnetic symmetry for the magnetic order parameter, which experimental work carried out under this contract suggested was possible, though not certain.⁴ Some questions on the nature of the transition were also raised by our own Monte Carlo calculations which suggested that a first order transition might occur for slightly tetragonally distorted spinel structures.^{4,5}

The cubic phase of the spinel lattice is perfectly frustrated since the nearest neighbors are arranged in triangles in which the spins can not be all mutually antiferromagnetically aligned as shown in Fig. 1. As a result, this perfect frustration in the ordering gives rise to many fluctuating spins at low temperatures which directly results in a large broad specific heat. In contrast, in a normal antiferromagnet the spins order below the transition and the specific heat becomes very small. Our theoretical calculations have shown that modifying or reducing the frustration in the spinel lattice has a very sensitive effect on nature of the phase transition.

The frustration of the cubic spinel lattice may be changed by a tetragonal distortion with decreased lattice constant in the z direction, $c < a$, corresponding to $J_{\parallel} > J_{\perp}$. The distortion in this case completely removes the frustration. The largest inter-

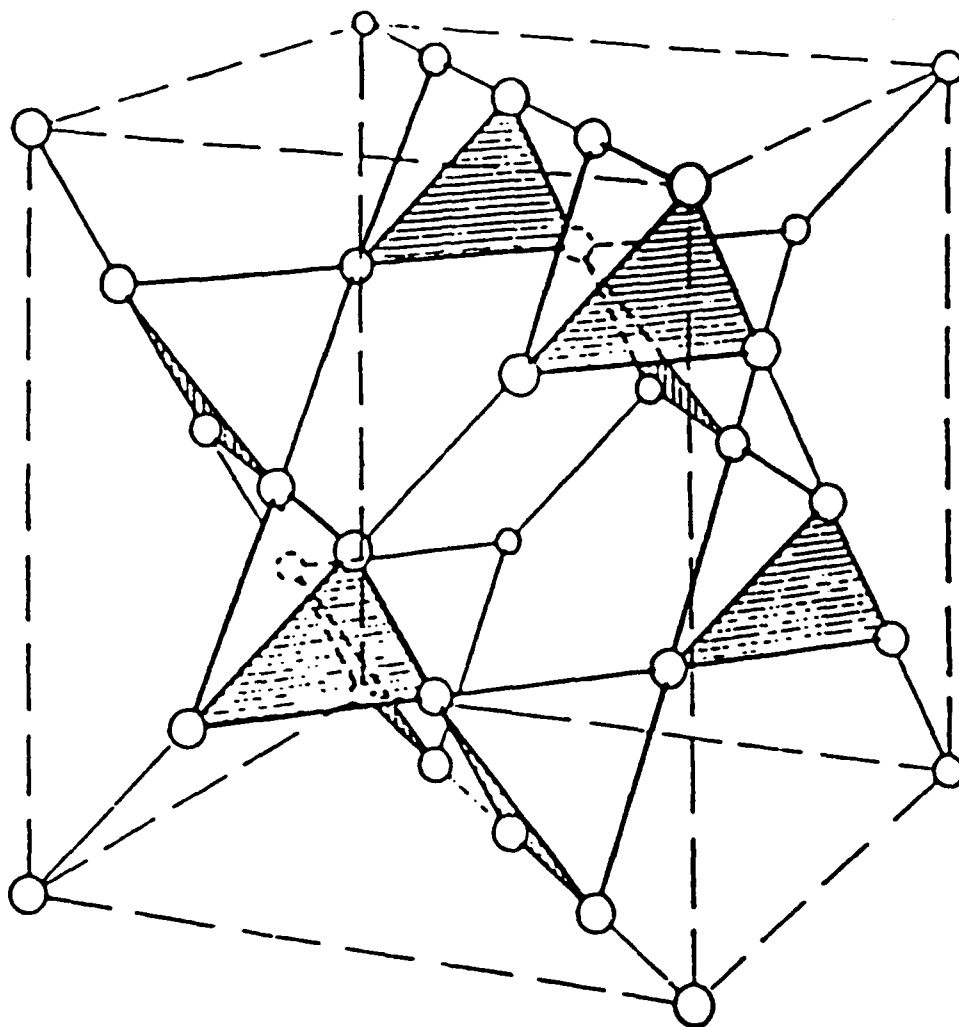


Fig. 1. Magnetic lattice of the B-site spinel materials CdCr_2O_4 and ZnCr_2O_4 .

action, J_1 , is satisfied first, leading to antiferromagnetically ordered spins between the x-y planes. This produces a non-degenerate ground state in which the x-y planes are ordered in

ferromagnetic sheets with an antiferromagnetic coupling in the z direction as indicated in Fig. 2.

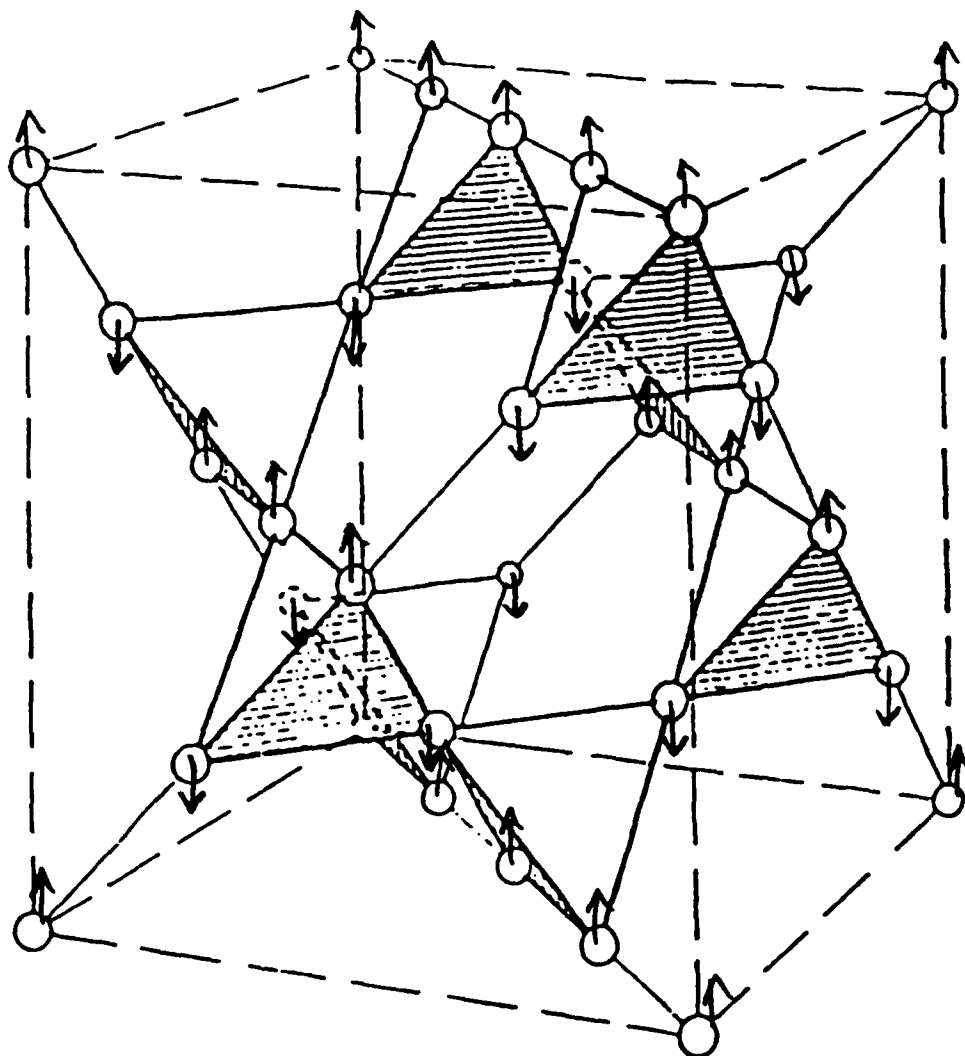


Fig. 2. Long range antiferromagnetic spin order for $c < a$ tetragonal lattice of the B-site spinel materials CdCr_2O_4 and ZnCr_2O_4 .

The frustration of the cubic spinel lattice may also be reduced by a tetragonal distortion with increased lattice constant in the z direction, $c > a$, corresponding to $J_{\perp} < J_{\parallel}$. In this case, however, unlike the case $c < a$ discussed above, the distortion does not completely remove the frustration. The largest interaction, now J_{\parallel} , is satisfied first, leading to antiferromagnetically ordered chains in the x - y plane. The remaining interaction between planes in the z direction, J_{\perp} , in the present case does not lead to a unique ordering of the antiferromagnetic x - y chains; the interplane interaction is still frustrated.

In confirmation of this difference in the reduction of frustration, in the case of the $c < a$ tetragonal spinel lattice, our Monte Carlo results indicate that the pure tetragonal lattice showed good long range antiferromagnetic order, while the $c > a$ case displayed less clear evidence for long range order.

Our Monte Carlo calculations, reported here in Fig. 3, suggest that the phase diagram of the magnetic transition temperature vs. lattice distortion (or equivalently the ratio J_{\perp}/J_{\parallel}) has a minimum for the cubic phase, where $J_{\perp}/J_{\parallel} = 1$, with a dramatic increase in transition temperature as the lattice is distorted, either for $c < a$ or $c > a$.^{1,2,3,4} In addition, some evidence, in the form of hysteresis in simulations done in warming and in cooling mode, was found for certain regions of the phase diagram as indicated, especially near the cubic phase where $J_{\perp} = J_{\parallel}$. This could be evidence of a first order transition, although the difference between a weak first order transition and a second

order transition is difficult to detect using standard Monte Carlo techniques.

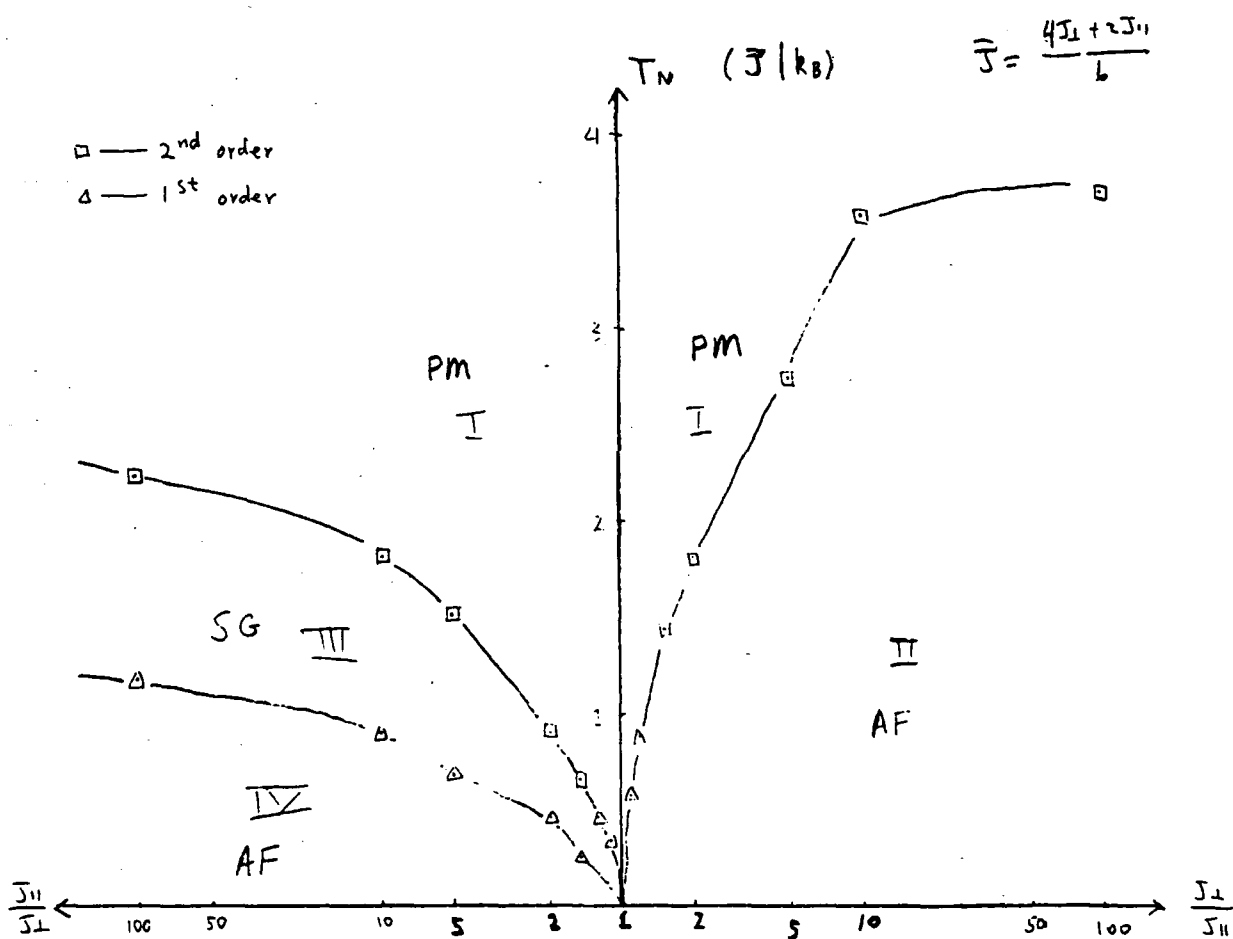


Fig. 3. Magnetic phase diagram of the B-site spinel materials CdCr_2O_4 and ZnCr_2O_4 from Monte Carlo simulations.

Finally, we should note that, beyond the effects of lattice distortion reported above, in addition the Monte Carlo calculations described in our recent reports have revealed an interesting interplay between the effects of substitutional spin doping and lattice distortions on the frustrated spin ordering of the spinel lattice.^{1,2,3} The presence of both a lattice distortion and a spin impurity gives rise to unexpected consequences, such as the striking effect of $S = 0$ impurities in reducing the transition temperature for the $c < a$ lattice, and of both large and small spin impurities in removing the low temperature $1/T$ Curie tails in the susceptibility for $c < a$, while for $c > a$, both large and small impurities give rise to cusps in the susceptibility. We found the key to understanding the effects of dopants and lattice distortions on the spin ordering of the spinel lattice was in the nature of the low energy excitations available to the system.

III. Ginzburg-Landau Theory of the Magnetic Ordering of the Spinel Lattice: Connection to First-Order Transition.

In order to derive the proper G-L description of the spinel materials, we observed that since the experimental susceptibility and adiabatic demagnetization are both characteristic of an antiferromagnetic system, the natural long range order parameter of the system is the sublattice magnetization. Furthermore, with both magnetic and electric fields present, then the sublattice magnetization, the total magnetization, and the polarization

should all appear as relevant order parameters. We have proposed a G-L theory with a free energy containing couplings of these order parameters and have used it to calculate experimental properties of the system.^{4,7}

In the present work we wish to examine the question of a first order or second order transition in the spinels. In order to analyze the nature of the magnetic phase transition, we focus on the dependence of the free energy functional F on the order parameters L and M , which are the difference of sublattice magnetic moments and the total magnetic moment, respectively, and suppress the dependence on the electric polarization. The G-L free energy is

$$F = F_{af}[L] + F_{pm}[M] + F_{ap}[L,M] \quad (1)$$

where the antiferromagnet contribution

$$F_{af}[L] = \int d\vec{r} \left[a|L|^2 + \frac{b}{2}|L|^4 + \xi^2|\vec{\nabla}L|^2 \right] \quad (2)$$

is the energy associated with the sublattice magnetization and near the Néel temperature T_N we have $a = a_0(T - T_N)$. The ferromagnetic contribution

$$F_{pm}[M] = \int d\vec{r} \left[\alpha|M|^2 - H \cdot M \right] \quad (3)$$

is the magnetization energy (with $\alpha > 0$) including that associated with the external magnetic field H . Finally, we took the interaction between L and M to be

$$F_{ad}[L,M] = \int d\vec{r} G |L|^2 |M|^2 \quad (4)$$

Eq. (4) gives the coupling between the magnetic order parameters L and M ; we have $G > 0$ since the antiferromagnetic and ferromagnetic states tend to exclude each other. This coupling is required by the behavior of the magnetic susceptibility.

The structure of the free energy (1) is revealed by the plot shown in Fig. 4 which displays the free energy as a function of the order parameter L . For $T > T_N$ ($a > 0$), the free energy has a parabolic shape with a minimum at the origin, while for $T < T_N$ (or $a < 0$), the free energy has a characteristic double minimum structure, with the minimum corresponding to (two) finite values

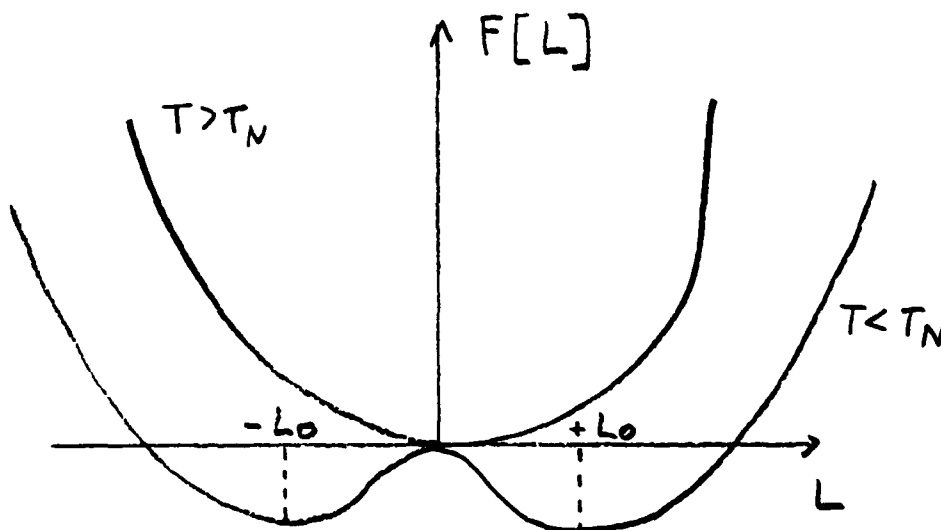


Fig. 4. Free energy functional vs. magnetic order parameter for second order transition: Eq. (1).

of the sublattice magnetization $\pm L_0$. The key point here is that the free energy F is symmetric for $L \rightarrow -L$; this requires that the minimum L_0 move away from zero continuously as the parameter a becomes negative.

This behavior is obtained explicitly by finding the solution to the minimization problem:

$$\frac{\partial F}{\partial M} = \frac{\partial F}{\partial L} = 0 \quad (5)$$

which yields the two equations

$$2\alpha M - H + 2G|L|^2 M = 0 \quad (6)$$

$$2aL + 2b|L|^2 L + 2G|M|^2 L = 0 \quad (7)$$

If $M = 0$, then Eq. (7) has the solution

$$|L|^2 = \pm[-a/b]^{1/2} \quad (8)$$

These equations give rise to a second order transition in which the magnetic order specified by L decreases continuously to zero as $a \rightarrow 0$ from below T_N .

In contrast, a first order transition may arise if the free energy contains additional terms of the form

$$cL^3 + dL^3 M \quad (9)$$

In this case the free energy as a function of L for various temperatures looks like that shown in Fig. 5.

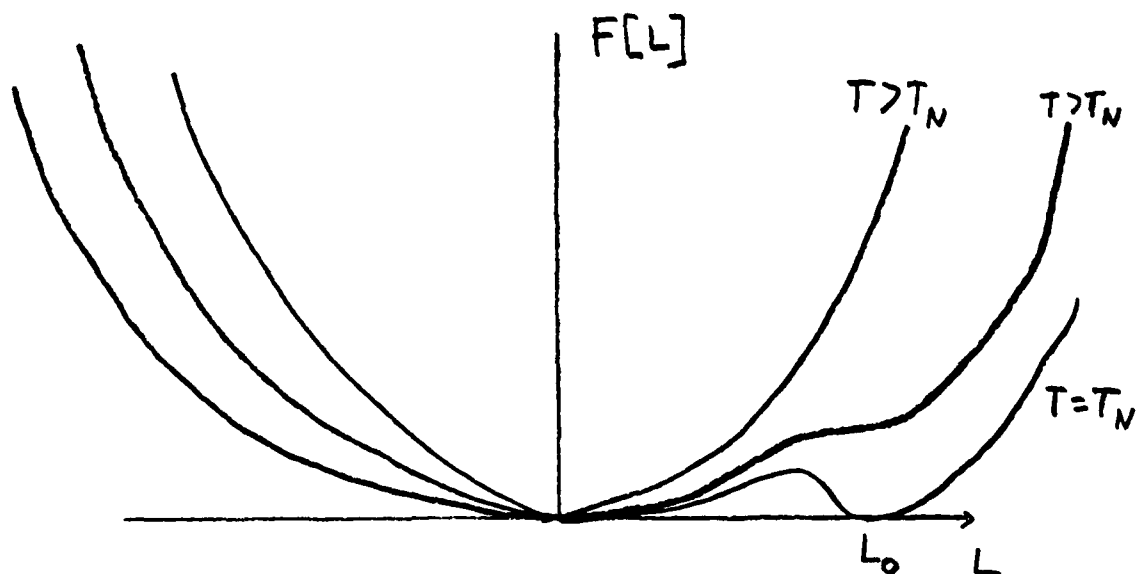


Fig. 5. Free energy functional vs. magnetic order parameter for first order transition: Eq. (1) plus Eq. (9).

In this case the symmetry for positive and negative L is lost and the free energy goes negative at a finite value of the magnetic order parameter L_0 . Thus the key question for the nature of the phase transition is the presence or absence of terms of the form (9). In the following section we evaluate the free energy directly from an explicit model of the spinel lattice. We find that terms like (9) which would lead to a first order transition are not present.

IV. The Ginzberg-Landau Free Energy Derived from Microscopic Theory

We now carry out an explicit evaluation of the G-L free energy starting from a correct microscopic exchange Hamiltonian representing the lattice symmetry. The procedure is to divide the spin degrees of freedom into a local averaged value of the magnetization (coarse grained average) which represents the long range G-L value of the spin magnetization, plus a short range contribution representing the local spin fluctuation. The latter short range spin fluctuations are integrated out, leaving a free energy functional which depends only on the long range part. This is the G-L free energy functional. First we review the lattice structure and symmetry of the exchange Hamiltonian.

Following our previous work,² the c axis will be taken in the vertical direction and the equivalent a, b axis of the tetragonal phase will be taken in the horizontal plane. The spin exchange Hamiltonian, Eq. (10), is correct in both the cubic and tetragonal phases, with the proper anisotropic values taken for the exchange couplings, J_{ij} :

$$H = \sum_{\langle ij \rangle} J_{ij} S_i S_j \quad (10)$$

As discussed in our previous reports, in the cubic phase, symmetry requires all the J_{ij} to have the same value. The effect of a $c < a$ tetragonal distortion on the cubic spinel lattice is to move the horizontal planes of spins close together. Thus the exchange constant between spins in the z direction, J_z , becomes

larger than the coupling among the spins within the x-y plane, J_{\parallel} . In our Monte Carlo calculations, the $c > a$ lattice distortion requires two exchange couplings in the Hamiltonian (10), with $J_{\perp}/J_{\parallel} < 1$. For the case $c < a$, the frustration of the cubic spinel lattice is totally removed and a unique antiferromagnetic order is produced, shown in Fig. 2, where the c direction is vertical. Our Monte Carlo calculations have verified this type of order. Thus, the G-L model of antiferromagnetic order given in Eq. (1) is a proper model of the ground state.

In the case of a $c > a$ tetragonal distortion, the situation is reversed and the result is that J_{\perp} becomes smaller than J_{\parallel} . For this situation the frustration, though reduced, is not eliminated and a unique ground state configuration of the spins is not present. This means that the order is not that of a simple antiferromagnet, and therefore, the G-L model proposed above is not applicable. Further careful work with numerical simulations are required to determine the nature of the phase transition in this case.⁵

We proceed to analyze the first case, a tetragonal distortion with $c < a$, to determine the nature of the transition, whether first or second order. The G-L free energy can be derived from microscopic model using a statistical coarse graining technique. Following this procedure, we derive a set of equations for the magnetic order parameters l and m , which can be expanded as a power series near the transition. By comparing these equations with those from minimizing the G-L free energy, we obtain the structure of the G-L free energy as well as the coefficients of

the G-L expansion as explicit functions of temperature and microscopic coupling constants. For simplicity, we do not include the coupling between spins and electric charges in our microscopic theory, so the coefficients of the terms involving the electric polarization in the G-L free energy will not be derived here.

We start with the Ising Hamiltonian (10) plus an external magnetic field

$$H = \sum_{\langle i,j \rangle} J_{ij} S_i S_j - H_0 \sum_i S_i \quad (11)$$

where the J_{ij} are the exchange couplings between nearest neighbors $\langle i,j \rangle$ on the spinel spin lattice shown in Fig. 2, and H_0 is the applied magnetic field.

We replace S_i with its coarse-grained average $\langle S_i \rangle$ and then trace over the short-range spin fluctuations. The G-L order parameters l and m are related to $\langle S_i \rangle$; by expanding our result in powers of $\langle S_i \rangle$ we can obtain the microscopic equivalent of Eqs. (8) and (9). Let $S_i = \langle S_i \rangle + (S_i - \langle S_i \rangle) = \langle S_i \rangle + \delta S_i$, to the first order in δS_i , we have

$$\begin{aligned} H &= \sum_{\langle i,j \rangle} J_{ij} [\langle S_j \rangle S_i + \langle S_i \rangle S_j] - H_0 \sum_i S_i \\ &= \sum_i \left(\sum_{j=n.n.} J_{i,j} \langle S_j \rangle - H_0 \right) S_i \end{aligned} \quad (12)$$

where the constant term $\langle S_i \rangle \langle S_j \rangle$ in H has been suppressed since it drops out of the thermal average.

To express $\langle S_j \rangle$ in the terms of the order parameters l and m correctly, we need to use knowledge of the symmetry of the

ordered phase. From previous results of Monte Carlo studies, the B-site spinel can be understood as a tetragonally distorted version of the spinel lattice shown in Fig. 1 with slightly larger coupling constant out of crystalline a-b plane than within the plane.⁴ The resulting low temperature ordered phase then has the same spin orientation within each spin plane but alternates along the c-axis as indicated in Fig. 2. Thus the two magnetic order parameters can be written as

$$m = \frac{1}{N} \left(\sum_{i \in \text{odd}} \langle S_i \rangle + \sum_{i \in \text{even}} \langle S_i \rangle \right) = \frac{(\langle S_i \rangle_{\text{odd}} + \langle S_i \rangle_{\text{even}})}{2} \quad (13)$$

and

$$l = \frac{1}{N} \left(\sum_{i \in \text{odd}} \langle S_i \rangle - \sum_{i \in \text{even}} \langle S_i \rangle \right) = \frac{(\langle S_i \rangle_{\text{odd}} - \langle S_i \rangle_{\text{even}})}{2} \quad (14)$$

where the sum over i is taken over the odd and even spin layers along the c-axis, and N is the total number of spins.

Solving (13) and (14) for $\langle S_i \rangle_{\text{odd}}$ and $\langle S_i \rangle_{\text{even}}$ in terms of l and m gives

$$\langle S_i \rangle_{\text{odd}} = m + l \quad (15)$$

$$\langle S_i \rangle_{\text{even}} = m - l \quad (16)$$

Considering the fact that each spin has 2 nearest neighbors within the plane and 4 in adjacent planes (Fig. 2), and letting J_{\parallel} and J_{\perp} be the in-plane and out-of-plane couplings, respectively, then the Hamiltonian (11) becomes

$$H = \sum [J_{\parallel} \cdot 2 \cdot (m+l) + J_{\perp} \cdot 4 \cdot (m-l) - H] S_i$$

$i \in \text{odd}$

$$+ \sum_{i \in \text{even}} [J_{\parallel} \cdot 2 \cdot (m-1) + J_{\perp} \cdot 4 \cdot (m+1) - H] S_i. \quad (17)$$

From (17), m and l can be calculated within the canonical ensemble as

$$m = \frac{1}{N} \frac{\text{Tr}[e^{-\beta H} (\sum_{i \in \text{odd}} S_i + \sum_{i \in \text{even}} S_i)]}{\text{Tr}(e^{-\beta H})} \quad (18)$$

and

$$l = \frac{1}{N} \frac{\text{Tr}[e^{-\beta H} (\sum_{i \in \text{odd}} S_i - \sum_{i \in \text{even}} S_i)]}{\text{Tr}(e^{-\beta H})}. \quad (19)$$

Carrying out the trace over $S_i = \pm 1$ for all S_i yields,

$$\begin{aligned} m = & -\frac{1}{2} \cdot \tanh\{\beta[2J_{\parallel}(m+1) + 4J_{\perp}(m-1) - H]\} \\ & -\frac{1}{2} \cdot \tanh\{\beta[2J_{\parallel}(m-1) + 4J_{\perp}(m+1) - H]\} \end{aligned} \quad (20)$$

and

$$\begin{aligned} l = & -\frac{1}{2} \cdot \tanh\{\beta[2J_{\parallel}(m+1) + 4J_{\perp}(m-1) - H]\} \\ & +\frac{1}{2} \cdot \tanh\{\beta[2J_{\parallel}(m-1) + 4J_{\perp}(m+1) - H]\} \end{aligned} \quad (21)$$

Near the transition temperature T_N , the antiferromagnetic order parameter l is small. If the applied field H is small, then the magnetization is also small, and we may expand the two equations (20) and (21) up to fourth order in l and second order

in m (or H), yielding two coupled equations for m and l . The higher order term in l is needed for stability as may be seen from Eq. (9). The expansion gives

$$1 + 2\beta(2J_{\perp} + J_{\parallel})m + 4\beta^2(2J_{\perp} + J_{\parallel})^2 m l^2 - \beta H = 0 \quad (22)$$

$$[1 - 2\beta(2J_{\perp} - J_{\parallel})] + 2\beta(2J_{\perp} - J_{\parallel})m^2 + \frac{8}{3}\beta^3(2J_{\perp} - J_{\parallel})^3 l^3 = 0 \quad (23)$$

Comparing Eqs. (22) and (23) with Eqs. (8) and (9) in the previous section, and noting that $L^2 = n_0^2 l^2$ and $M^2 = n_0^2 m^2$, where n_0 is the number of spins per unit volume, we may identify the following coefficients:

$$a = \frac{[1 - 2\beta(2J_{\perp} - J_{\parallel})](2J_{\perp} - J_{\parallel})}{n_0} \quad (24)$$

$$b = \frac{8\beta^3(2J_{\perp} - J_{\parallel})^4}{3n_0^3} \quad (25)$$

$$\alpha = \frac{1 + 2\beta(2J_{\perp} + J_{\parallel})}{2\beta n_0} \quad (26)$$

$$G = \frac{2\beta(2J_{\perp} - J_{\parallel})^2}{n_0^3} \quad (27)$$

Therefore, in terms of microscopic parameters, the Ginzburg-Landau free energy per unit volume can be written as

$$\begin{aligned} \frac{F}{V} = & \frac{[1 - 2\beta(2J_{\perp} - J_{\parallel})](2J_{\perp} - J_{\parallel})}{n_0} \cdot L^2 \\ & + \frac{4\beta^3(2J_{\perp} - J_{\parallel})^4}{n_0} \cdot L^4 + \frac{1 + 2\beta(2J_{\perp} + J_{\parallel})}{2\beta n_0} \cdot M^2 \\ & - M \cdot H + \frac{2\beta(2J_{\perp} - J_{\parallel})^2}{n_0^3} \cdot L^2 \cdot M^2 \end{aligned}$$

$$+ \lambda \cdot p^2 - p \cdot E + \Gamma \cdot L^2 \cdot p^2 \quad (28)$$

where V is the total volume. As mentioned above, the coefficients λ and Γ are not derived here.

The transition temperature T_N is determined by the condition

$$a = \frac{[1 - 2\beta(2J_{\perp} - J_{\parallel})](2J_{\perp} - J_{\parallel})}{n_0} = 0 \quad (29)$$

which gives the mean field transition temperature of

$$T_N = 4J_{\perp} - 2J_{\parallel} \quad (30)$$

Assuming the tetragonal distortion is small, i.e. $J_{\parallel} \sim J_{\perp}$, we have $J_{\parallel} \sim J_{\perp} \sim 0.5T_N$. Thus we can calculate the coefficients a , b , α , and G using experimentally known values of T_N and n_0 , which determine the electric, magnetic, and thermodynamic properties of the system.

In addition, we have found from this microscopic analysis that the G-L free energy has the structure corresponding to a second order transition; i.e. no third order invariants of the form given in Eq. (9), which would enter Eq. (23) as l^2 or l^2_m , were obtained which could lead to a first order transition.

V. Summary of Results for Tetragonally Distorted Spinel Lattice

A key question in determining the nature of the very unusual magnetic phase transition in the CdCr_2O_4 and ZnCr_2O_4 spinel materials has been to ascertain the order of the phase transition, whether of first or second order. The work reported here has shown that the phase transition may be analyzed with a Ginzburg-Landau approach when the frustration of the cubic spinel phase has been removed by a $c < a$ tetragonal distortion.

Our results show that the phase transition is expected to be second order in all cases, although the proximity of the frustrated phases may affect the experimental properties in unusual ways. The maximum transition temperature of the $c < a$ tetragonal phase may be as large as approximately $T_N^{\text{max}} \sim 4 J_1$, from twice to four times the transition temperature of the undistorted cubic structure, depending on the magnitude of the tetragonal distortion.

For the $c > a$ tetragonal lattice, the G-L approach is not justified since the ground state remains frustrated, without a unique antiferromagnet order parameter. A new Monte Carlo technique is being developed to determine the order of the phase transition in this case.

REFERENCES

1. OSU Progress Report, Research on High-Specific-Heat Dielectrics, Theoretical Studies I: Effects of Impurity Spin Doping on Undistorted Spinel Lattice, AFOSR Contract F49620-86-C-0049, August 31, 1988.
2. OSU Progress Report, Research on High-Specific-Heat Dielectrics, Theoretical Studies II: Effects of Impurity Spin Doping on Tetragonally Distorted Spinel Lattice - $c < a$ Case, AFOSR Contract F49620-86-C-0049, September 30, 1988.
3. OSU Progress Report, Research on High-Specific-Heat Dielectrics, Theoretical Studies III: Effects of Impurity Spin Doping on Tetragonally Distorted Spinel Lattice - $c > a$ Case, AFOSR Contract F49620-86-C-0049, October 30, 1988.
4. Annual Technical Report, Research on High-Specific-Heat Dielectrics, AFOSR Contract F49620-86-C-0049, May 11, 1987. In brief summary the simulations used the Ising model in which each spin takes the possible values $\pm S$, where S is the magnitude of the spin. The spins are set on the B sites of a cube of the spinel lattice 5 unit cells on a side containing 2000 spins. Periodic boundary conditions are used to eliminate boundary effects. After equilibration, 2000 Monte Carlo steps per spin are used at each temperature.
5. OSU Progress Report, Research on High-Specific-Heat Dielectrics, Theoretical Studies: First Order Transition in Tetragonally Distorted Spinel Lattices, AFOSR Contract F49620-86-C-0049, in preparation.
6. CeramPhysics, Inc. Progress Report, Research on High-Specific-Heat Dielectrics, AFOSR Contract F49620-86-C-0049, Latent Heat Measurements, November 11, 1987.
7. C.-Y. Lin, Y. Lu, and B.R. Patton, to be submitted for publication.

VII.E. MONTE CARLO CALCULATIONS OF MAGNETIC PHASE DIAGRAM OF SPINEL CHROMITE MATERIALS

I. Introduction

One of the key questions in the AFOSR program on the high specific heat dielectrics based on the chromite spinels, CdCr_2O_4 and ZnCr_2O_4 , has been the precise nature of the magnetic phase transition, including the determination of what causes the high value of the specific heat near the transition as well as what determines the magnitude of the transition temperature, which is only about 10K in the pure phases of these materials.

In our Monte Carlo simulations of the spinel lattice for different possible low temperature lattice structures, we have found evidence for a variety of behaviors: 1) a spin glass-like freezing transition in the cubic structure, 2) a antiferromagnetic transition in the $c < a$ tetragonal structure, and 3) a partially frustrated antiferromagnetic transition in the $c > a$ tetragonal structure.^{1,2,3,4}

In addition, we found some evidence that the transition might be first order with a discontinuous change in properties at the transition temperature in some cases, and second order, or continuous, in other cases.⁴ The evidence from available experiments is also not clear since it is often hard to distinguish between a large specific heat at a second order transition and a small latent heat at a first order transition.⁶

The question of a first or second order transition is not only of fundamental importance in understanding the unusual phase transition and large specific heats of these materials, but also in utilizing and manipulating the properties of the materials.

One consequence of a first order transition, for example, is the introduction of a certain amount of hysteresis in the temperature and magnetic field dependent properties of the material.

In order to clarify the nature of the transition, we have carried out several lines of investigation. The first, involving a Ginzburg-Landau analysis of the degree of the phase transition based on a microscopic model of the ordered state of the tetragonal spinel lattice, has been reported previously.^{7,10} Results on the second approach, involving a new high resolution Monte Carlo procedure, will be presented in this progress report.

In Section II we review the current evidence on the nature of the phase transition in the spinels. Our Monte Carlo results on quenched lattices calculated in warming mode are presented in Section III. In Section IV we report results in cooling mode for annealed samples. Finally, a summary and conclusions are provided in Section V.

II. Review of Evidence on the Nature of the Transition in the Spinel Materials CdCr_2O_4 and ZnCr_2O_4 .

Some experimental evidence is available on the structure of the spinel materials.⁹ This data, summarized in Table I, shows that the magnetic transition is generally accompanied by a small lattice distortion from the cubic into the tetragonal phase.

	Y	=	V	Cr	Mn
	Mg		-0.7%	-0.2%	
$\frac{c-a}{a}$	X = Zn		-?% (c<a)	0.2%	14%
	Cd			?	
	Mg		45	15	
T_N	X = Zn		45	12	?
	Cd			8	

Table I. Lattice distortion parameter $(c-a)/a$ and Néel temperature for spinel materials with formula XY_2O_4 in the magnetic phase at low temperatures. All compounds with negative $(c-a)/a$ have higher magnetic transition temperatures.⁹

This correlation suggests that the spin ordering drives a lattice transformation which lowers the total spin energy. As a result, we had proposed to study the general phase diagram which would give the behavior of transition temperature T_N as the

structure or lattice constants are varied. In particular, we would like to understand why a distortion with $c < a$ gives a higher transition temperature than $c > a$.

The cubic phase of the spinel lattice is perfectly frustrated since the nearest neighbors are arranged in triangles in which the spins can not be all mutually antiferromagnetically aligned as shown in Fig. 1. As a result, this perfect frustration in the ordering gives rise to many fluctuating spins at low temperatures which directly results in a large broad specific heat. In contrast, in a normal antiferromagnet the spins order below the transition and the specific heat becomes very small. Our theoretical calculations have shown that modifying or reducing the frustration in the spinel lattice has a very sensitive effect on nature of the phase transition.

In our previous work under this contract we developed a model which successfully accounted for the unusual dielectric anomaly at the magnetic transition in the spinels.^{4,6,10} This model assumed an antiferromagnetic symmetry for the magnetic order parameter, which experimental work carried out under this contract suggested was possible, though not certain.⁴ Some questions on the nature of the transition were also raised by our own Monte Carlo calculations which suggested that a first order transition might occur for slightly tetragonally distorted spinel structures.⁴ As a result of these calculations experimental investigations were initiated to determine the effects of stress or other ways of distorting the lattice.¹¹

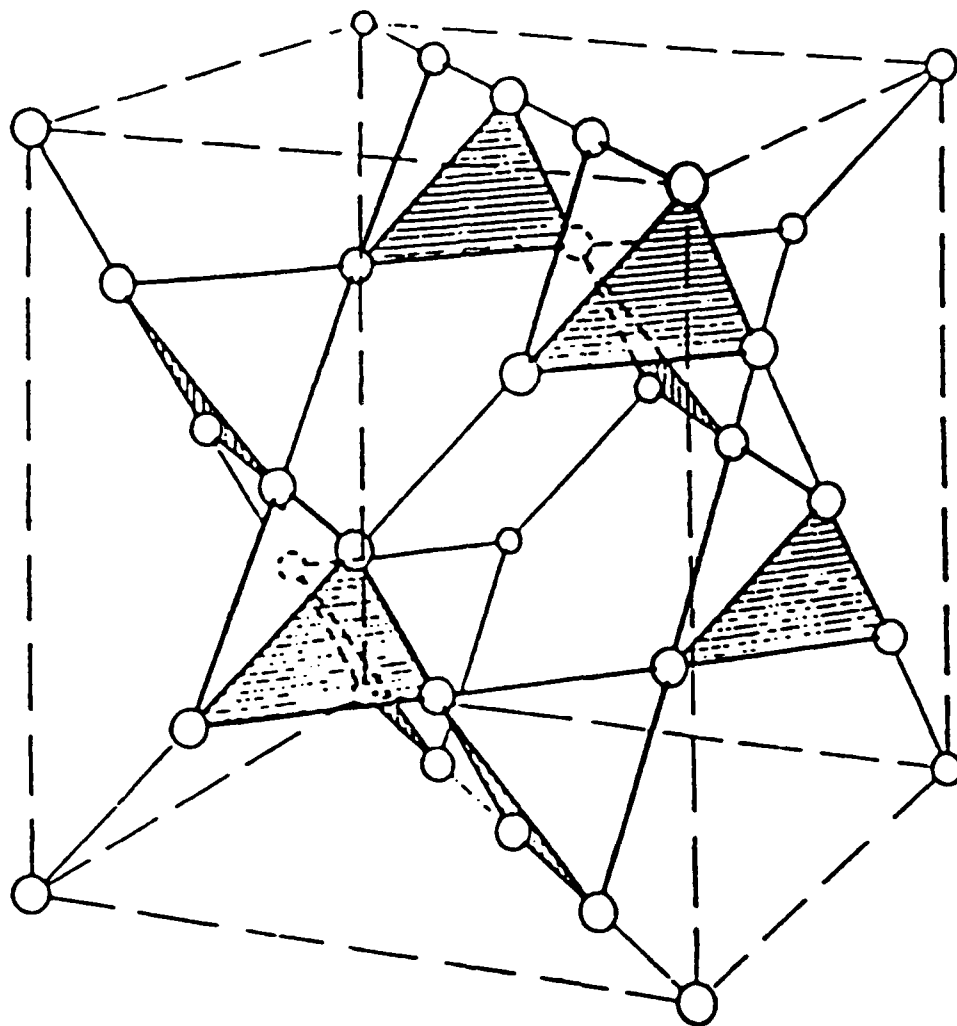


Fig. 1. Magnetic lattice sites of the B-site spinel materials CdCr_2O_4 and ZnCr_2O_4 .

Our previous Monte Carlo calculations suggested that the phase diagram giving the magnetic transition temperature vs. lattice distortion has a minimum for the cubic phase, where $c = a$, with a dramatic increase in transition temperature as the lattice is distorted, either for $c < a$ or $c > a$.^{1,2,3,4} In addition, some evidence, in the form of hysteresis in simulations done in warming and in cooling mode, was found for certain regions of the phase diagram especially for $c > a$ near the cubic phase. This behavior could be taken as evidence of a first order transition, although the difference between a weak first order transition and a second order transition is difficult to detect using standard Monte Carlo techniques.

Finally, beyond the effects of lattice distortion reported above, additional Monte Carlo calculations described in our recent reports have revealed an interesting interplay between the effects of substitutional spin doping and lattice distortions on the frustrated spin ordering of the spinel lattice.^{1,2,3} The presence of both a lattice distortion and a spin impurity gives rise to unexpected consequences, such as the striking effect of $S = 0$ impurities in reducing the transition temperature for the $c < a$ lattice, and of both large and small spin impurities in removing the low temperature $1/T$ Curie tails in the susceptibility for $c < a$, while for $c > a$, both large and small impurities give rise to cusps in the susceptibility.

III. Monte Carlo Calculations on Quenched Samples of Spinel Lattice: Splitting in Specific Heat Peaks and Possibility of First-Order Transition.

In order to determine the effects of lattice distortions on the phase transition in the spinel lattice, a systematic study was carried out to find the transition temperature as a function of the tetragonal lattice distortion parameter c/a . The difference in the lattice constants a ($= b$) and c implies a difference in the exchange couplings J_{ij} in the x - y plane $J_1 = J_{\parallel}$ and the coupling $J_2 = J_{\perp}$ the z direction entering the spin Hamiltonian⁸

$$H = \sum_{\langle ij \rangle} J_{ij} S_i S_j \quad (1)$$

The frustration of the cubic spinel lattice may be changed by a tetragonal distortion with decreased lattice constant in the z direction, $c < a$, corresponding to $J_2 > J_1$. The distortion in this case completely removes the frustration. The largest interaction, J_2 , is satisfied first, leading to antiferromagnetically ordered spins between the x - y planes. This produces a non-degenerate ground state in which the x - y planes are ordered in ferromagnetic sheets with an antiferromagnetic coupling in the z direction as indicated in Fig. 2.

The frustration of the cubic spinel lattice may also be reduced by a tetragonal distortion with increased lattice constant in the z direction, $c > a$, corresponding to $J_2 < J_1$. In this case, however, unlike the case $c < a$ discussed above, the distortion does not completely remove the frustration. The

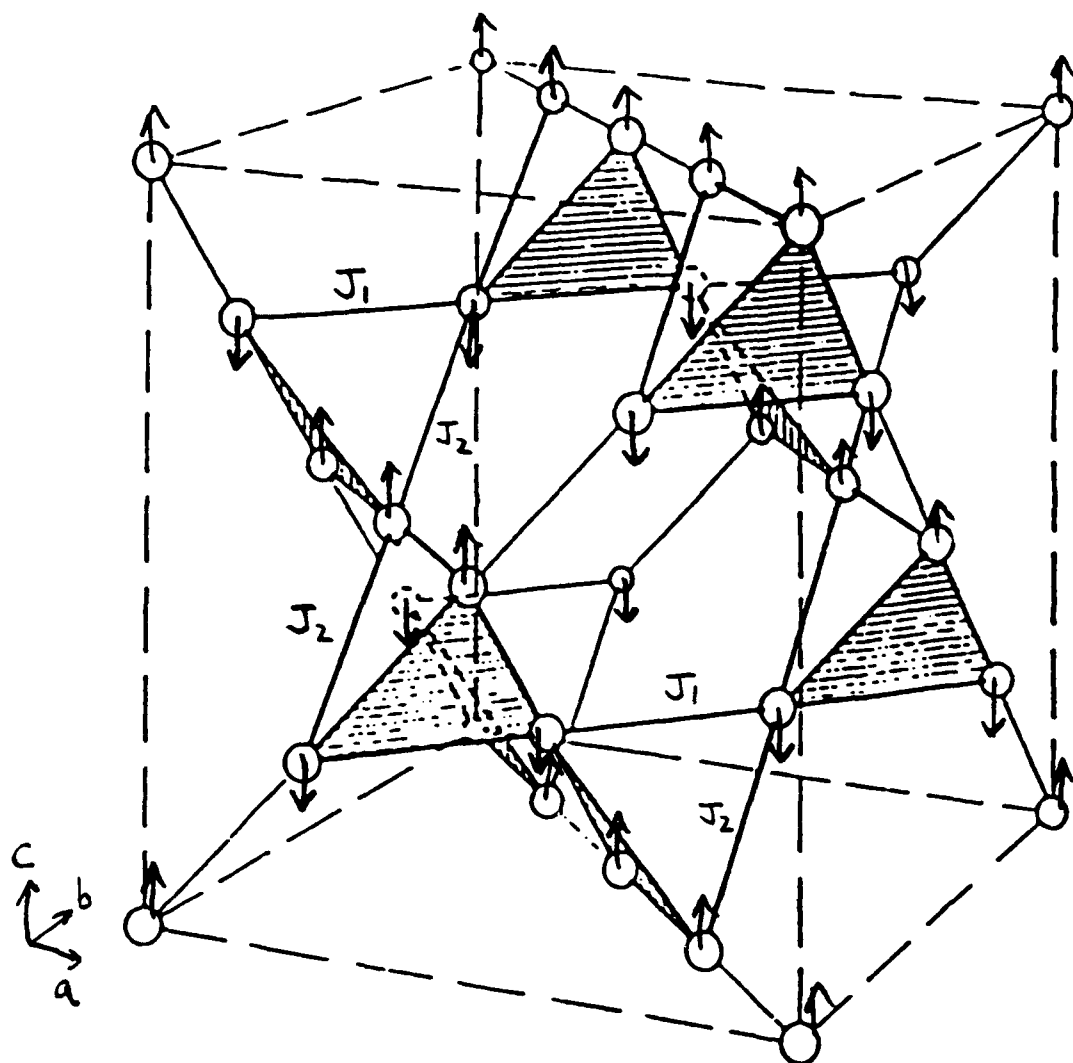


Fig. 2. Long range antiferromagnetic spin order for $c < a$ tetragonal lattice of the B-site spinel materials CdCr_2O_4 and ZnCr_2O_4 .

largest interaction, now J_1 , is satisfied first, leading to antiferromagnetically ordered chains in the x-y plane. The remaining interaction between planes in the z direction, J_2 , in the present case does not lead to a unique ordering of the antiferromagnetic x-y chains; the interplane ferromagnetic x-y chains; the interplane interaction is still frustrated.

In confirmation of this difference in the reduction of frustration, in the case of the $c < a$ tetragonal spinel lattice, our Monte Carlo results indicate that the pure tetragonal lattice showed good long range antiferromagnetic order, while the $c > a$ case displayed less clear evidence for long range order. This is also associated with the fact that, from Table I, the $c < a$ spinels experimentally have a higher transition temperature.

In general, since the exchange coupling occurs via super exchange, the magnitude of the coupling varies inversely with the lattice constant. Due to the exponential dependence of the coupling on distance, a small change in the lattice constant gives rise to a large change in the values of J_1 and J_2 .

In order to simulate the effects of doing an experiment by cooling to low temperature, then making measurements as the temperature is raised, we carried out our Monte Carlo calculations by first cooling the sample to the lowest temperature, usually about 0.1J, corresponding to less than 10 or 20% of the transition temperature T_N . The temperature was then raised, carrying out Monte Carlo simulations at successively higher temperatures until the maximum in the specific heat was reached and continuing until well above the maximum. The next Section presents results

obtained in cooling runs. Our previous Monte Carlo simulations have shown that for a lattice of 2000 spins such as we used, the maximum in the specific heat correlates well with the transition as measured by the susceptibility and, for $c < a$, the development of an antiferromagnetic order parameter.

We present first the calculations for Phase I, with $J_1 < J_2$ (or $c < a$). Our previous results have indicated that the transition in this case is a second order one to a state with long-range antiferromagnetic order along the c direction, as shown in Fig. 2.^{7,10}

The thermal and magnetic properties were obtained using high resolution temperature scans. Considerable calculational time was required to locate the transitions with the degree of accuracy desired. The transitions were studied for values of J_2/J_1 ranging from 1.1 to 100; the heat capacity vs. temperature are plotted in Fig. 3 to Fig. 9, where the temperature is measured in units of J_1 . One of the most striking features shown is the rapid increase in the transition temperature as the ratio J_2/J_1 increases. The transition temperature reaches the maximum asymptotic value of approximately $2.6 J_2$ for values of J_2/J_1 larger than about 10.

Another measure of the quality of the phase transition is the height of the specific heat peak at the transition. This quantity, in units of k_B per spin, also increases rapidly as J_2/J_1 increases from a value one, as shown in Fig. 10.

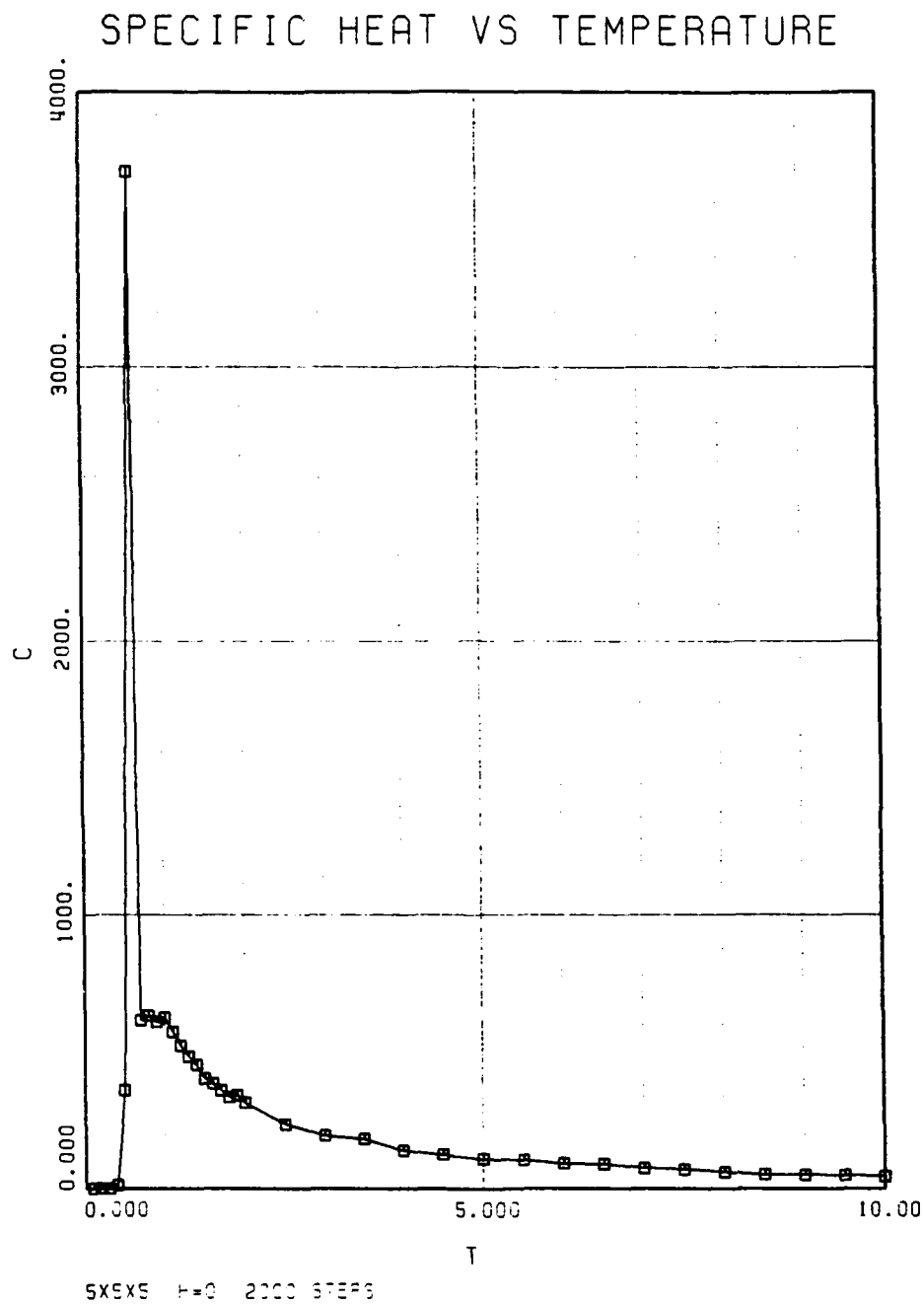


Fig. 3. Heat capacity vs. temperature T for quenched sample obtained for increasing T with $J_2/J_1 = 1.1$.

SPECIFIC HEAT VS TEMPERATURE

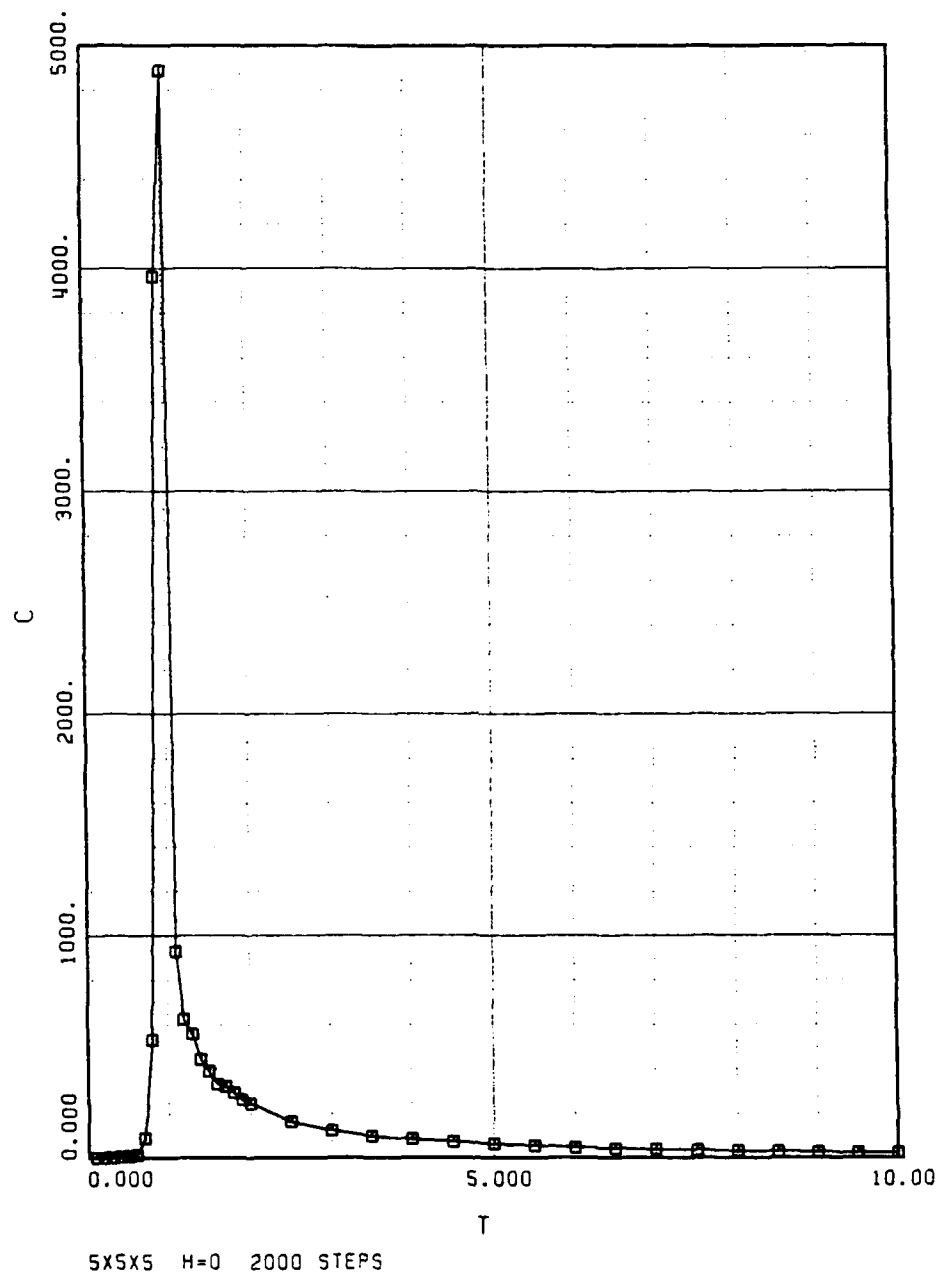


Fig. 4. Heat capacity vs. temperature T for quenched sample obtained for increasing T with $J_2/J_1 = 1.2$.

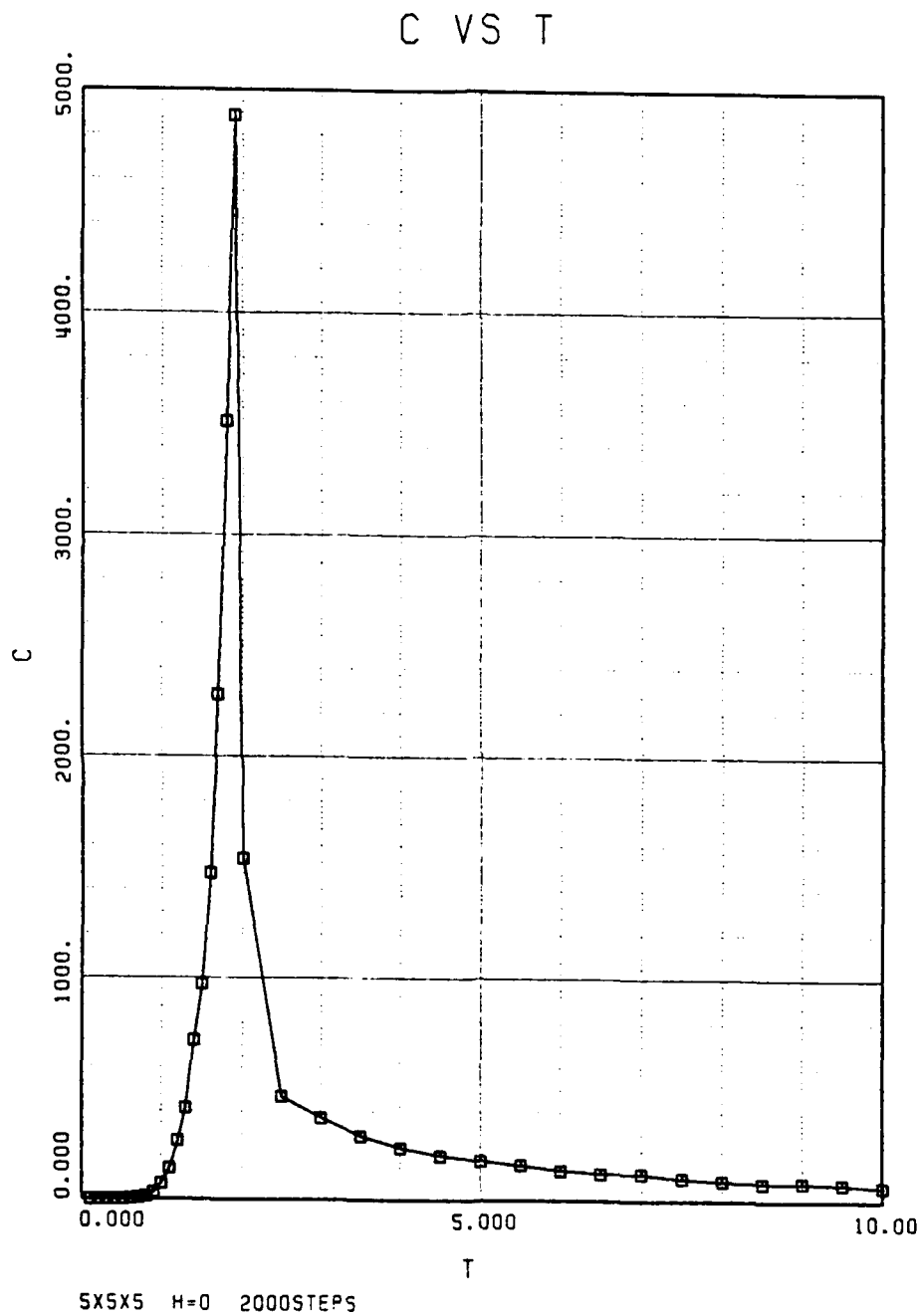


Fig. 5. Heat capacity vs. temperature T for quenched sample obtained for increasing T with $J_2/J_1 = 1.5$.

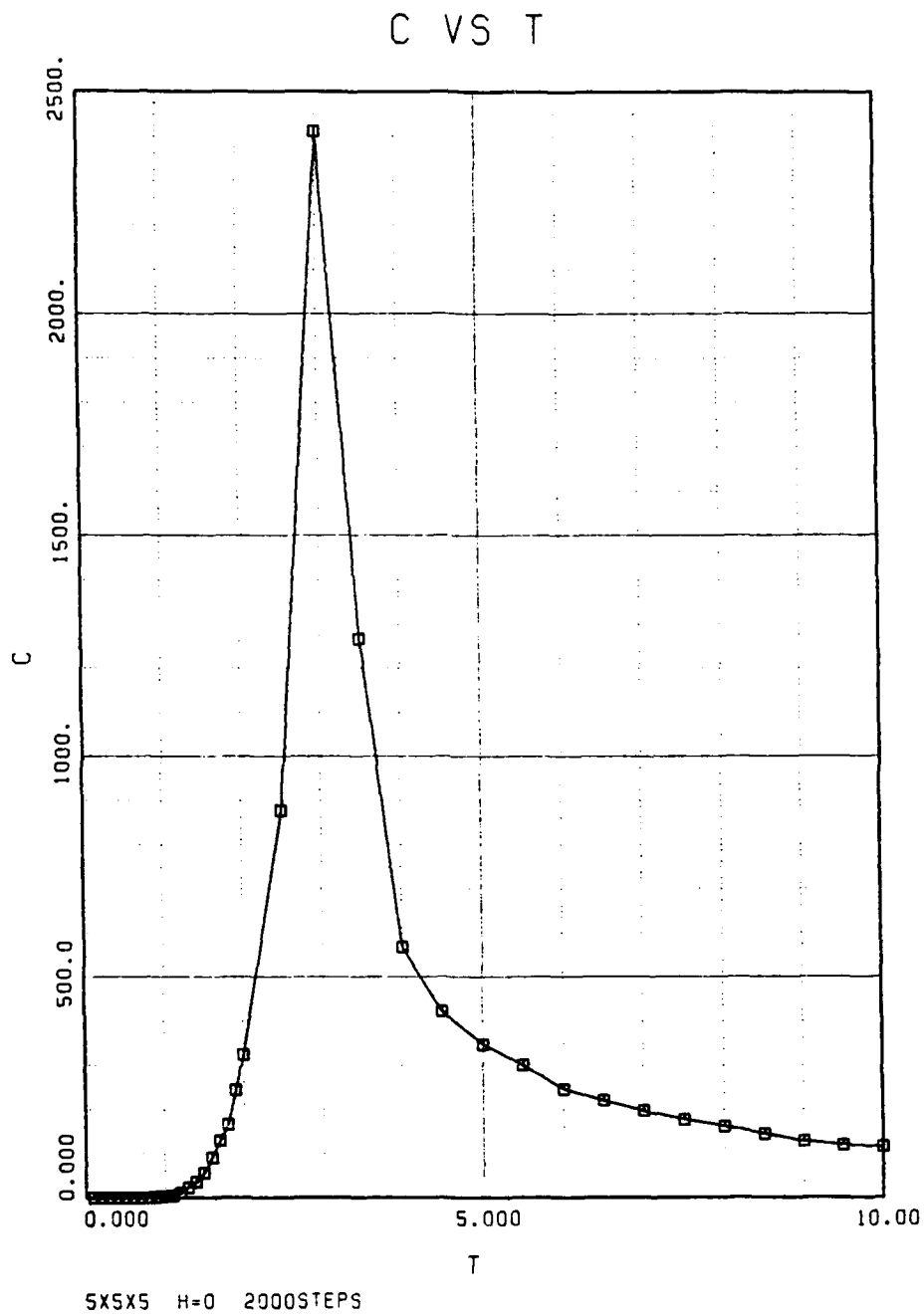


Fig. 6. Heat capacity vs. temperature T for quenched sample obtained for increasing T with $J_2/J_1 = 2$.

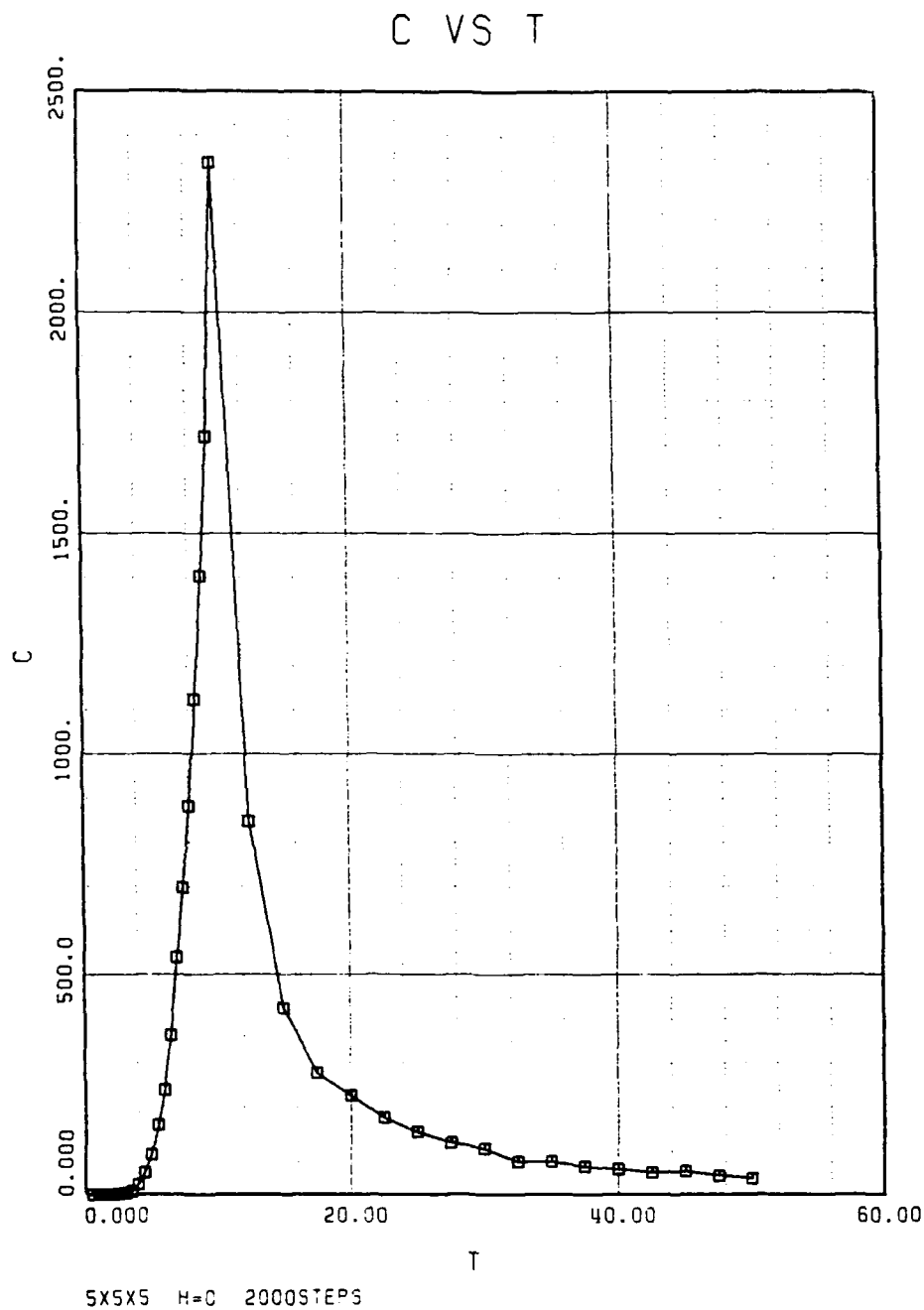


Fig. 7. Heat capacity vs. temperature T for quenched sample obtained for increasing T with $J_2/J_1 = 5$.

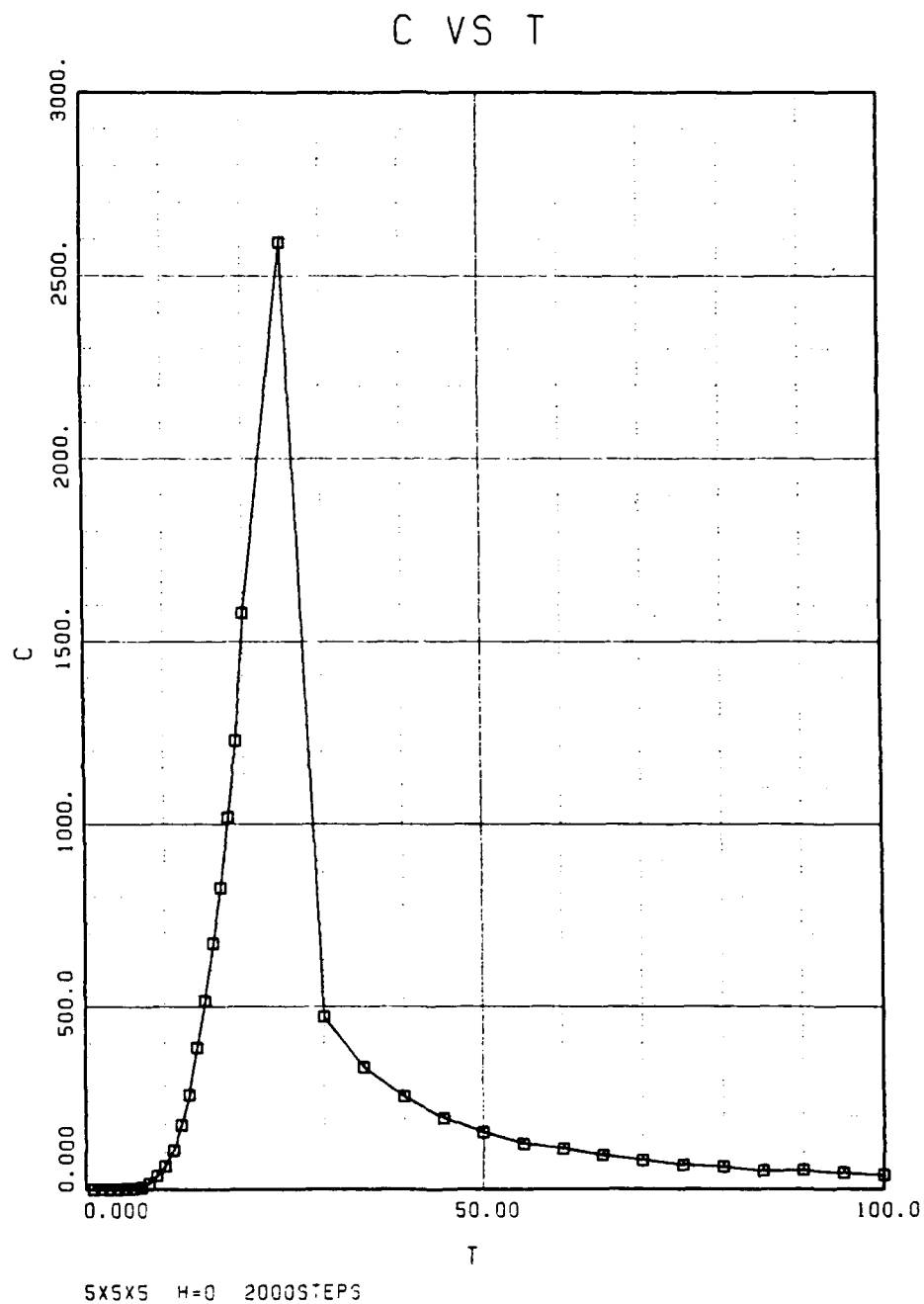


Fig. 8. Heat capacity vs. temperature T for quenched sample obtained for increasing T with $J_2/J_1 = 10$.

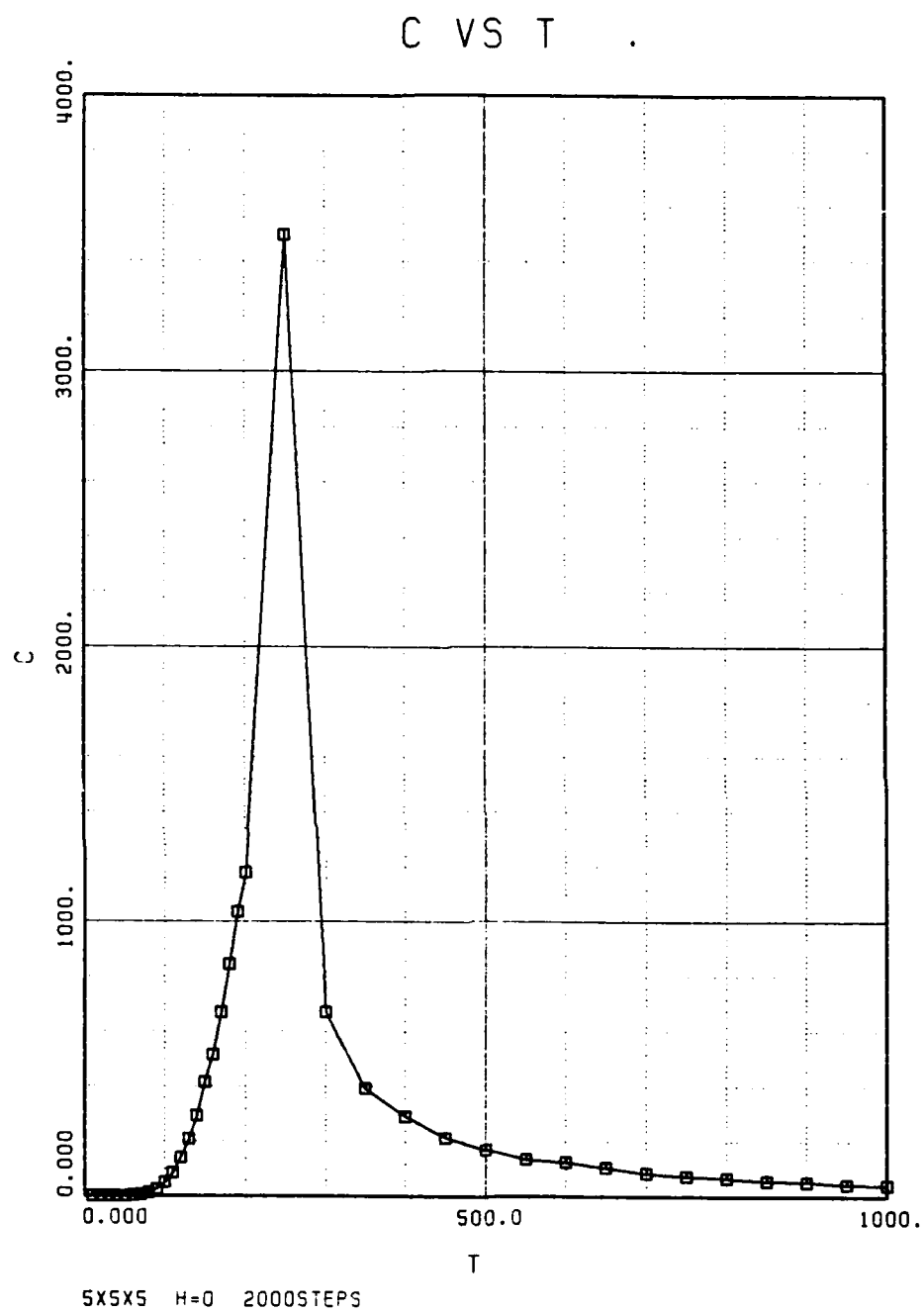


Fig. 9. Heat capacity vs. temperature T for quenched sample obtained for increasing T with $J_2/J_1 = 100$.

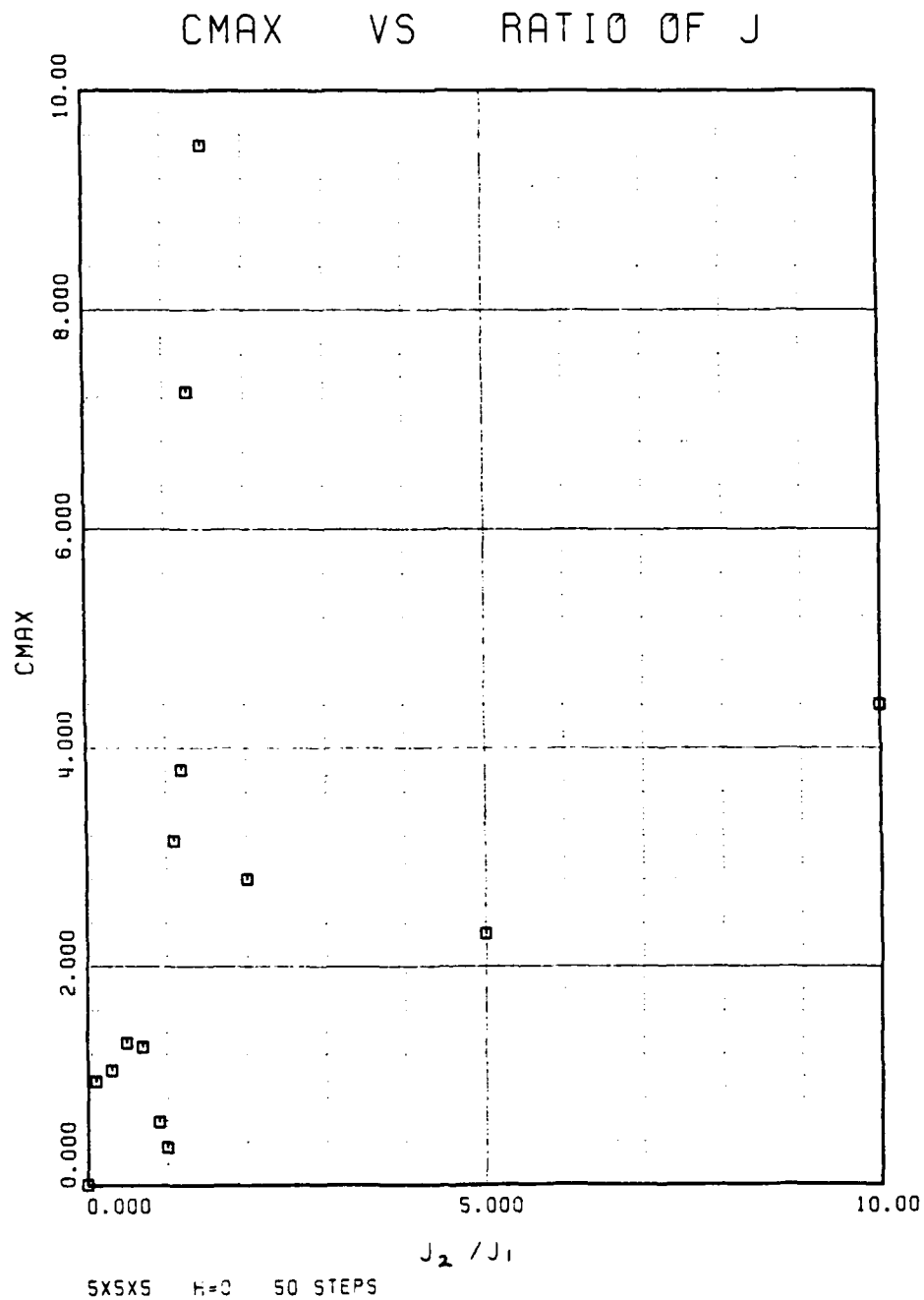


Fig. 10. Maximum of specific heat vs. ratio J_2/J_1 for quenched sample obtained for increasing T.

Similar simulations have been carried out for the case of the opposite tetragonal distortion, i.e., when $c > a$, or $J_2/J_1 < 1$. As discussed above, in this case the tetragonal distortion does not completely remove the frustration in the lattice and the ground state does not have a unique spin configuration.

The results of our extensive Monte Carlo simulations for $J_1/J_2 > 1$ are shown in Figs. 11 through 17, for values of the coupling ratio J_1/J_2 from 1.1 to 100. We note immediately that the results are completely different from the case $J_2/J_1 > 1$ considered above. The most striking feature is the development of two peaks in the specific heat. However, the location of the peaks in temperature does move up as the ratio J_1/J_2 increases from the value unity, just like the behavior for $J_2/J_1 > 1$. But the maximum value of the transition reached for large J_1/J_2 is much less than the case $J_2/J_1 > 1$ (compare Figs. 9 and 17). The maximum value of the transition temperature reached for large J_1/J_2 is about $T_N = 0.8 J_1$.

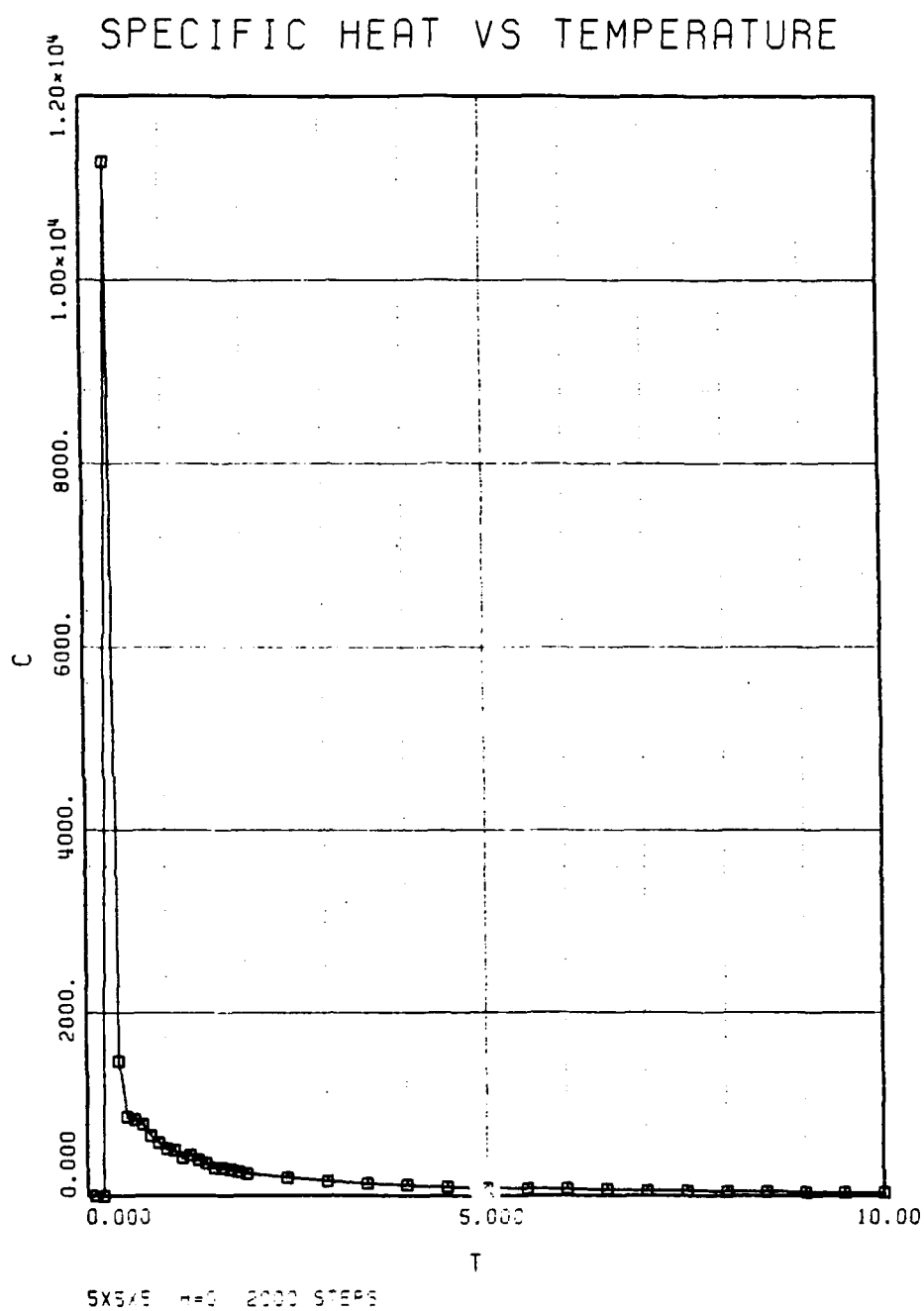


Fig. 11. Heat capacity vs. temperature T for quenched sample obtained for increasing T with $J_1/J_2 = 1.1$.

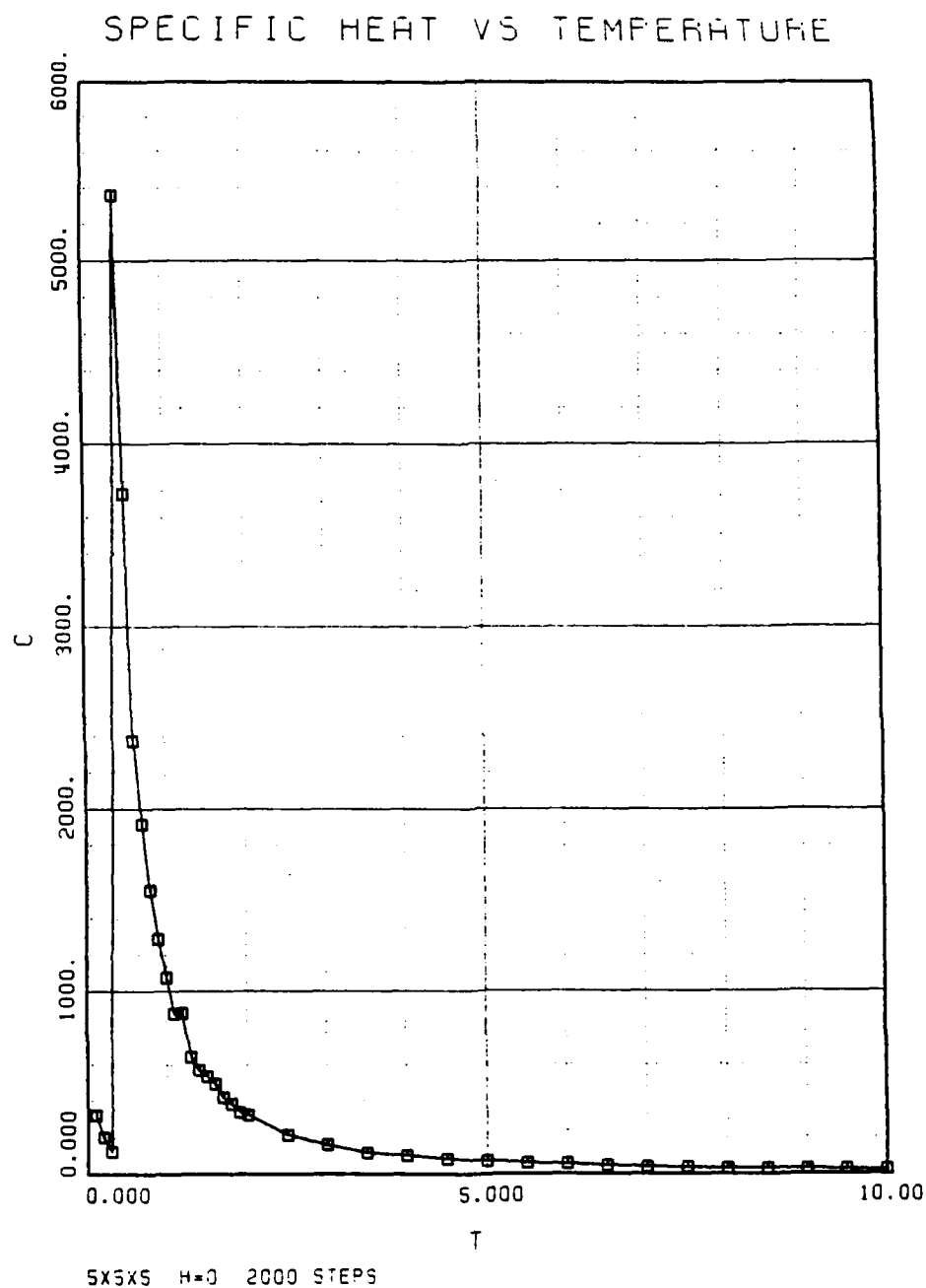


Fig. 12. Heat capacity vs. temperature T for quenched sample obtained for increasing T with $J_1/J_2 = 1.2$.

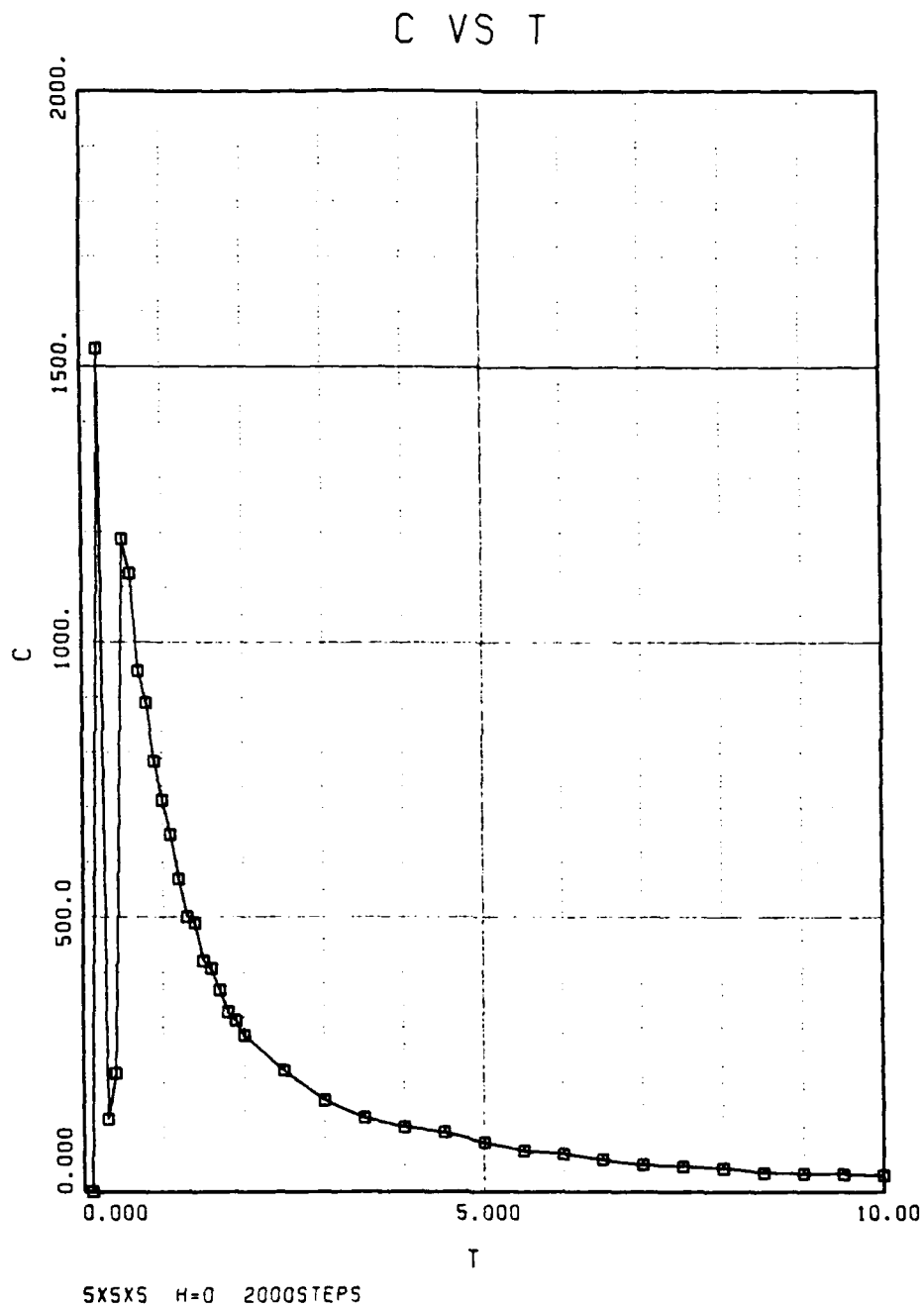


Fig. 13. Heat capacity vs. temperature T for quenched sample obtained for increasing T with $J_1/J_2 = 1.5$.

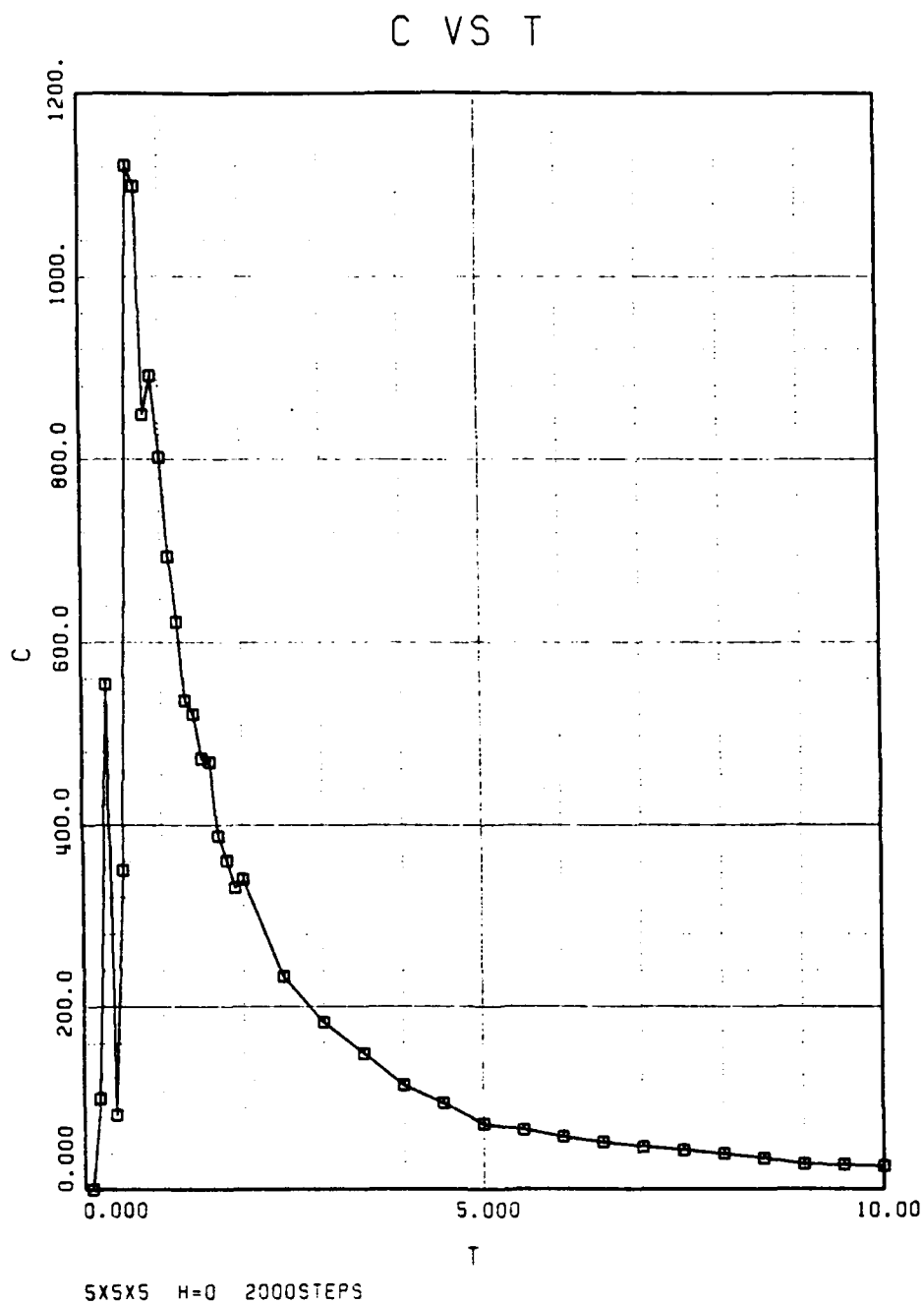


Fig. 14. Heat capacity vs. temperature T for quenched sample obtained for increasing T with $J_1/J_2 = 2$.

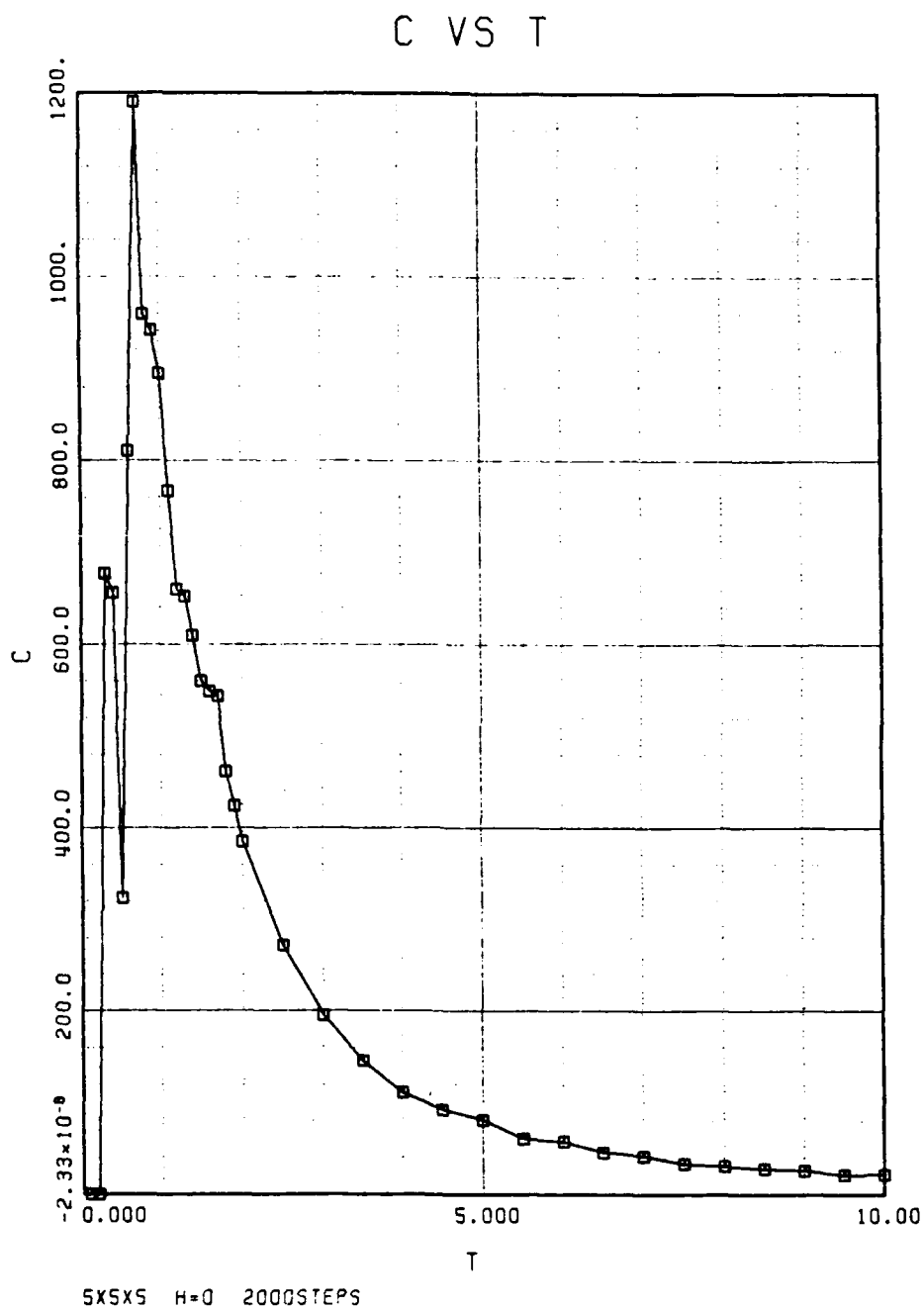


Fig. 15. Heat capacity vs. temperature T for quenched sample obtained for increasing T with $J_1/J_2 = 5$.

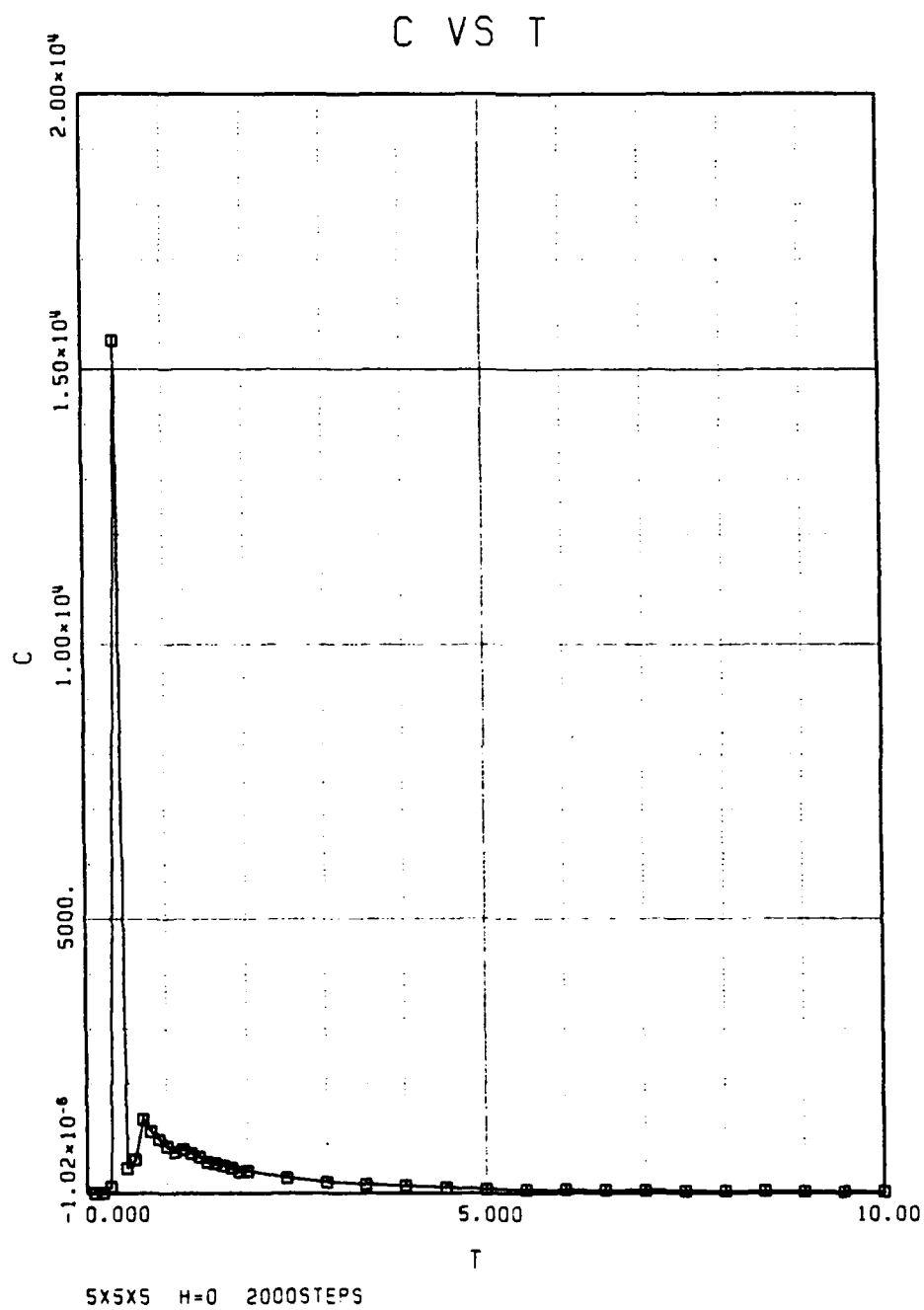


Fig. 16. Heat capacity vs. temperature T for quenched sample obtained for increasing T with $J_1/J_2 = 10$.

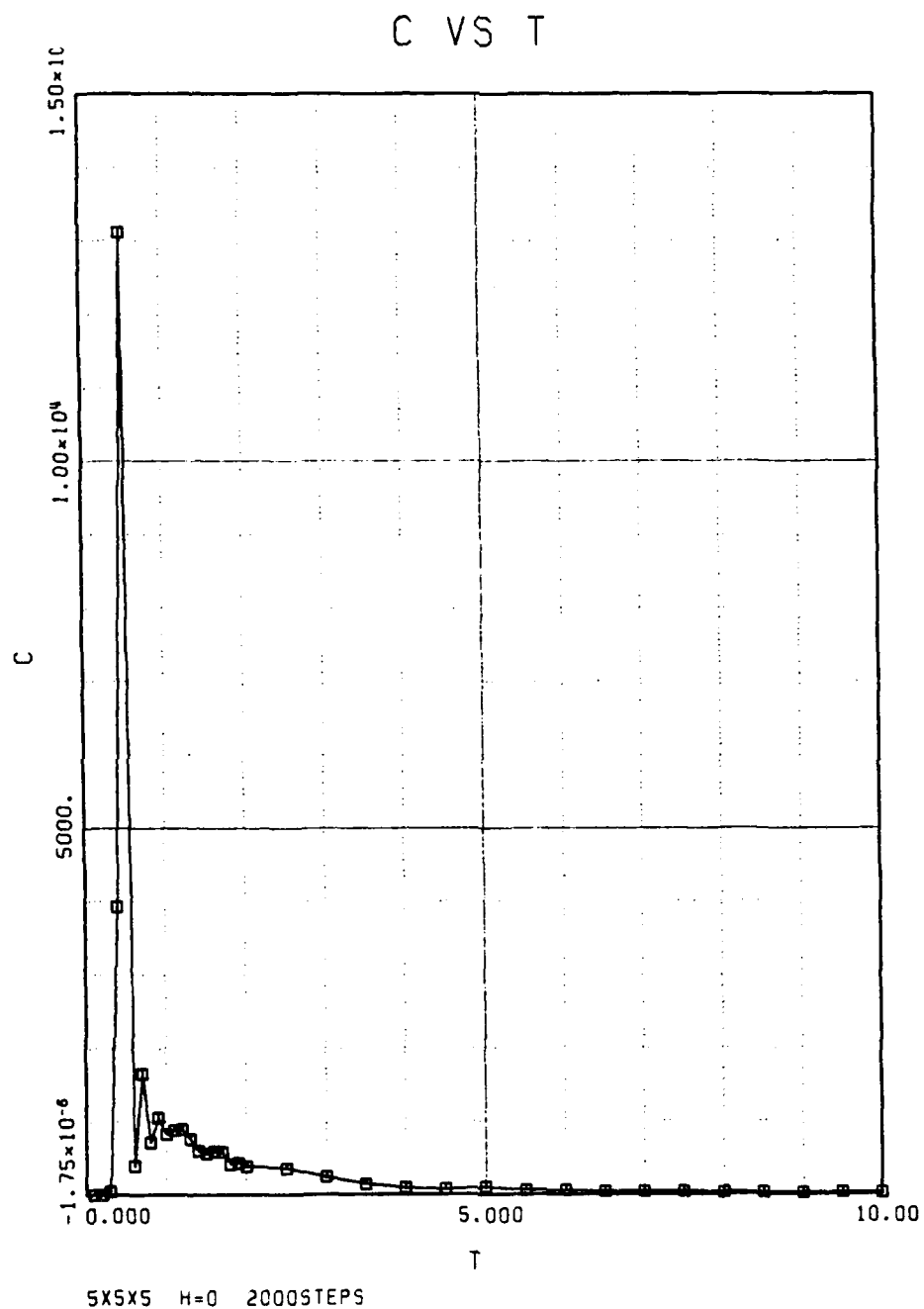


Fig. 17. Heat capacity vs. temperature T for quenched sample obtained for increasing T with $J_1/J_2 = 100$.

From the data calculated in the previous figures the location of the transition may be accurately estimated from the maximum in the specific heat. For the $J_2/J_1 > 1$ tetragonal spinel lattice this gives a single transition line dividing a paramagnetic high temperature region from a low temperature region, denoted by Phase I, as shown in Fig 18. For $J_1/J_2 > 1$, however, we have two transitions in the data of Figs. 11 to 17; in Fig. 18 only the higher one is plotted.

An alternative representation of the phase diagram is obtained by rescaling the variables in Fig. 18. The transition temperature is better measured in units of the average exchange coupling $\langle J \rangle$ where

$$\langle J \rangle = \frac{2J_1 + 4J_2}{6} \quad (2)$$

The factors of 2 and 4 come from the fact that the six nearest neighbors are divided into 2 in-plane and 4 out-of-plane neighbors.

The phase diagram becomes more symmetrical when expressed in terms of $\langle J \rangle$. To emphasize this symmetry we plot the Phase I, with $c < a$, (to the right in Fig. 18) vs. J_2/J_1 , and Phase II, with $c > a$, (to the left in Fig. 18) vs. J_1/J_2 . Fig. 19 shows the resulting phase diagram with both peaks in the specific heat indicated for Phase II.

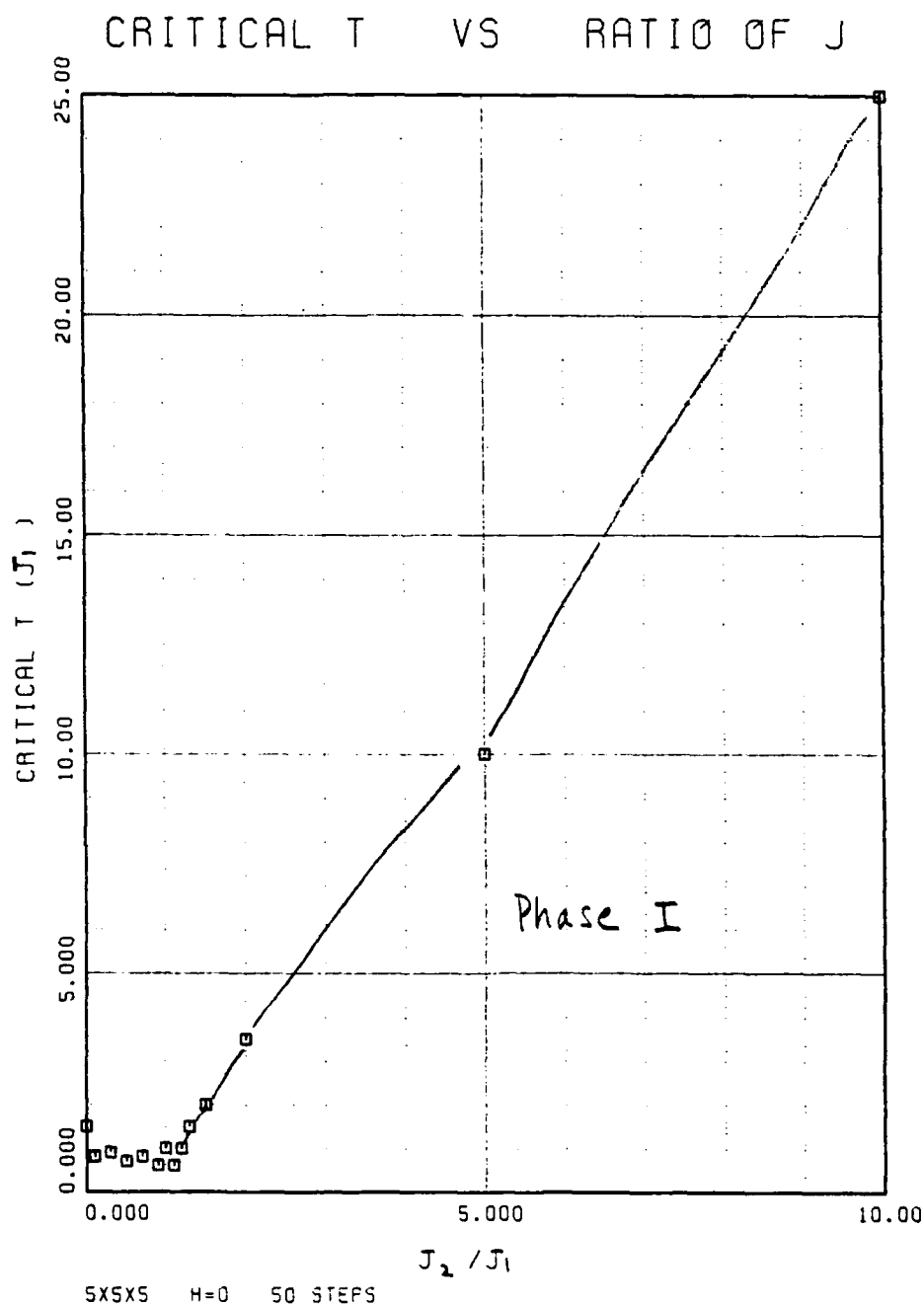


Fig. 18. Magnetic phase diagram of the B-site spinel materials CdCr_2O_4 and ZnCr_2O_4 from Monte Carlo simulations for quenched sample. Data obtained in rising T runs. T_N is measured in units of J_1 .

Initially, we interpreted the splitting in the peaks in Phase II as evidence for a first order transition. The cooling run results reported in the next Section provide a different interpretation. For Phase I, however, our previous report⁷ has provided a proof that the transition to Phase I must be second order, a result which is born out by these Monte Carlo results presented here. The presence of two peaks for the Phase II region suggests that a more detailed examination of that region would be useful. These results are presented in the next Section.

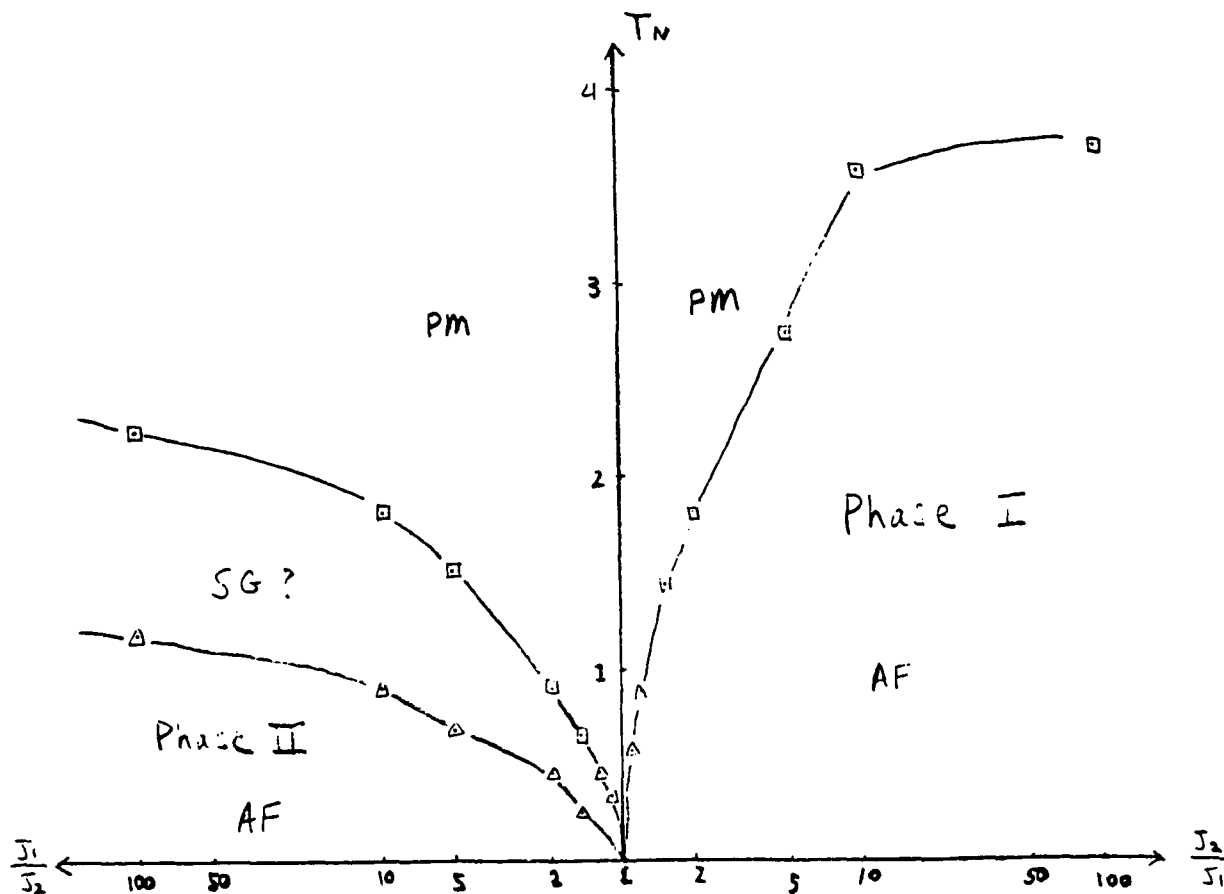


Fig. 19. Rescaled plot of phase diagram of the B-site spinel materials CdCr_2O_4 and ZnCr_2O_4 from Monte Carlo simulations for quenched sample. Data obtained in warming T runs. T_N in units of $\langle J \rangle$ from Eq. (2).

IV. Monte Carlo Calculations on Equilibrated (Annealed) Spinel Samples: Single Peak Specific Heat.

Because of the important question of the exact nature of the transition for the Phase II region of the phase diagram, we undertook more detailed Monte Carlo calculations of the $J_1/J_2 > 1$ tetragonal spinel lattice. In an extensive series of additional simulations we prepared the system at high temperatures, then slowly cooled the sample, calculating the thermal properties at each successively lowered temperature. This corresponds to experimental data taken in equilibrium or with decreasing temperature on an annealed sample, unlike the simulations described above in Section III which correspond to experiments on a quenched sample, which is rapidly cooled and then measured with increasing temperature.

For an ordinary second-order magnetic transition, there is essentially no difference between Monte Carlo simulations run with increasing and those run with decreasing temperature. However, the splitting in the specific heat into two peaks for $J_1/J_2 > 1$ indicates that the left side of the phase diagram, Phase II, shown in Fig. 19 may not be an ordinary second-order transition.

In addition, we extended the computer runs to insure that equilibrium was reached in the simulations and verified that the free energy and entropy displayed proper convergence.

Although Phase II was of primary interest, we also checked the results for Phase I to determine whether there was any evi-

dence of first order behavior or hysteresis. The results of the cooling cycle (annealed) Monte Carlo runs were identical to the results presented in Figs. 3 to 9, to within the rather small numerical noise. Thus we have not included separate graphs of those calculations. The location of the specific heat peaks were identical; the transition curves plotted in Figs. 3-9 therefore represent data obtained on both heating and cooling runs. As a consequence, the right hand side of the phase diagram in Fig. 19 is identical upon heating or cooling. This is consistent with our other analytic results indicating that this region, $J_2/J_1 > 1$, must be second order.^{7,10}

However, we obtained completely different results for the Phase II region of Fig. 19, $J_1/J_2 > 1$. A plot of the specific heat for a characteristic value of $J_1/J_2 = 5$ is presented in Fig. 20. The striking feature is that the split peaks seen in the warming Monte Carlo run have disappeared in the cooling run. Using our recalculated cooling-run Monte Carlo data obtained for seven values of the ratio J_1/J_2 from 1.1 to 100, we may obtain the phase diagram for an annealed spinel lattice, which is given in Fig. 21.

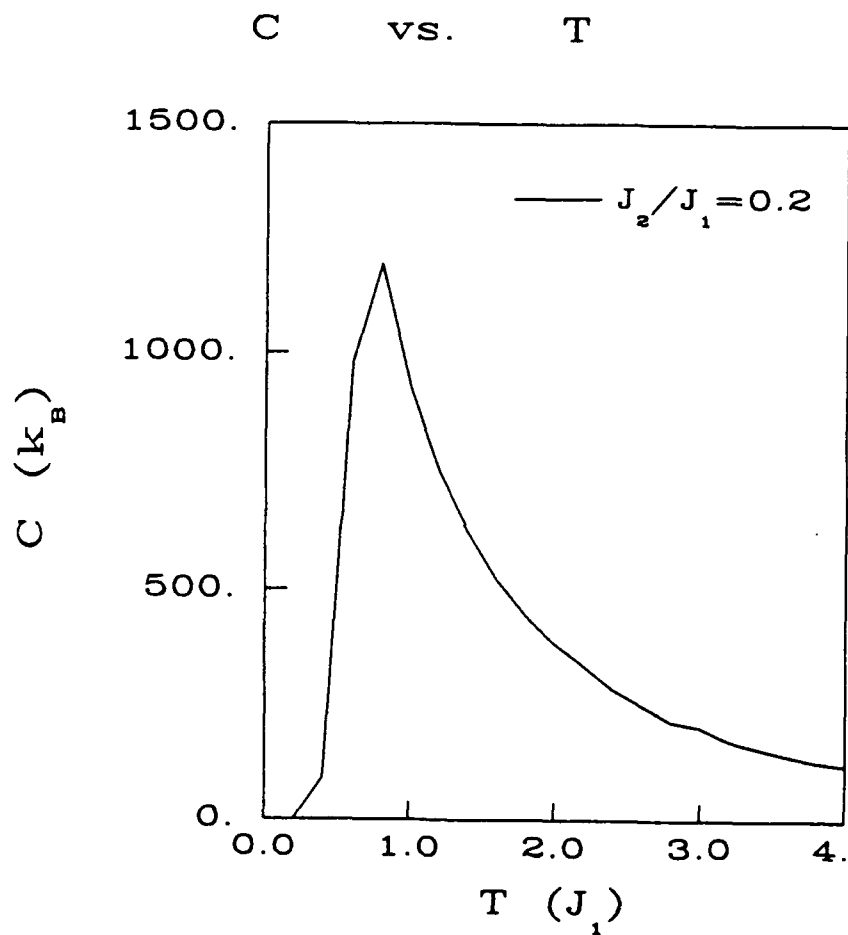


Fig. 20. Heat capacity vs. temperature T for annealed sample obtained for decreasing T with $J_1/J_2 = 5$.

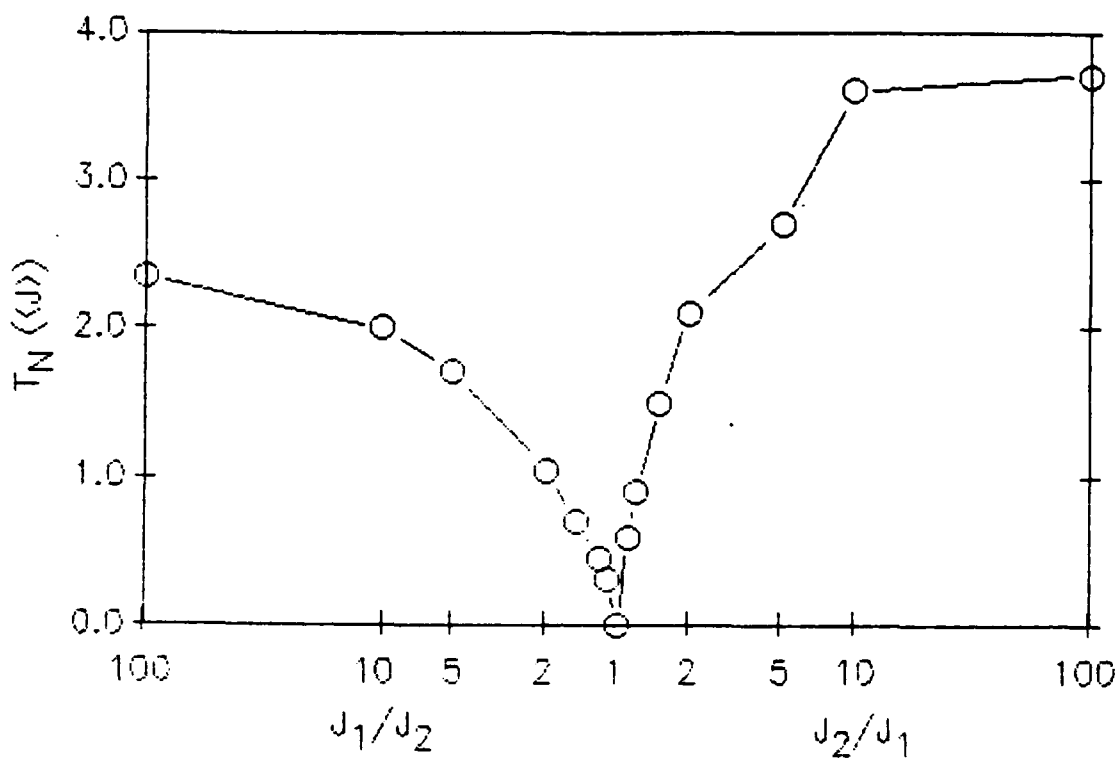


Fig. 21. Phase diagram of the B-site spinel materials CdCr_2O_4 and ZnCr_2O_4 from Monte Carlo simulations for annealed sample. Data obtained in cooling T runs. T_N is measured in units of $\langle J \rangle$ from Eq. (2).

The main feature of the phase diagram from cooling runs in Fig. 21 is the absence of two peaks in the Phase II region $J_1/J_2 > 1$, leaving only a single transition line, unlike the phase diagram for warming runs, Fig. 19. Analysis of these results is provided in the next section.

V. Summary of Results for Magnetic Phase Diagram of Tetragonally Distorted Spinel Lattice.

A key question in determining the nature of the very unusual magnetic phase transition in the CdCr_2O_4 and ZnCr_2O_4 spinel materials has been to ascertain the order of the phase transition, whether of first or second order. The work reported here has shown that when the frustration of the cubic spinel phase has been removed by a $c < a$ tetragonal distortion the phase transition is a second order one in the Monte Carlo simulations, in agreement with the analytic results based on the Ginzburg-Landau model.⁷

For the $c > a$ tetragonal lattice, the G-L approach was not justified since the ground state remains frustrated, without a unique antiferromagnet order parameter. Thus the new Monte Carlo calculations are particularly relevant in this case, Phase II. The Monte Carlo simulations reveal a difference between the quenched and annealed sample cases, a difference which does not exist for the $c < a$ case.

In analyzing the results of our extensive Monte Carlo simulations on the cubic and tetragonal spinel lattices, it is useful to make connections with several limiting cases. When $J_2 = 0$ there is no coupling between the vertical layers as shown in Fig. 2. The spinel spin lattice then reduces to independent one-dimensional (1D) chains of spins running along the 110 axis in the a - b plane. It is well known that a 1D chain has no phase transition at finite temperature, but instead displays a broad

bump in the vicinity of $T \sim J_1$. This is consistent with our Monte Carlo results which show a peak at $T \sim 0.8 J_1$.

For $J_1 = 0$ the x-y plane interaction vanishes and from Fig. 2 it may be seen that each spin is now coupled via J_2 to four spins above and below it. This is equivalent to a two-dimensional (2D) Ising spin model, which has a true long-range phase transition at a temperature $T_N = 2.269 J_2$, consistent with our value determined from the specific heat peak of $T_N \sim 2.6 J_2$ for large values of J_2/J_1 , i.e., when $J_1 = 0$.⁵

Thus our results are consistent with existing models at the boundaries of the phase diagram, $J_1/J_2 = 0$ and $J_2/J_1 = 0$. However, the actual magnitude of the transition temperature in Fig. 21 is expressed in terms of the average interaction $\langle J \rangle$, which is not known from experiment at present.

It is therefore useful to introduce a simple model of the exchange couplings in the tetragonal spinel lattice which will enable us to relate the transition temperatures of the tetragonally distorted lattices to that of the undistorted lattice.

The exchange coupling depends on distance between spins in the lattice, usually in an exponential fashion

$$J_{ij} = C e^{-(r_{ij}/a_0)} = J_0 e^{-(r_{ij}-a_0)/a_0} \quad (3)$$

where in the cubic lattice the spin distances are $r_{ij} = a_0$ and the exchange couplings are all $J_{ij} = J_0$.

We consider now the tetragonal phase transition in the spinel lattice. Generally, for small distortions from the cubic phase the volume of the unit cell remains constant, since the soft mode

corresponds to a transverse phonon in the a-b plane, not to a softening of the bulk modulus. As a result we have

$$V = (a_0 + \delta a)(b_0 + \delta b)(c_0 + \delta c) = V_0 = a_0 b_0 c_0 \quad (4)$$

This, with the tetragonal symmetry $a = b$ and the cubic symmetry $a_0 = b_0 = c_0$, implies that a relation exists between the change of the lattice constant in the a (or b) direction and the change along the c direction

$$\delta a = \delta b = -\delta c/2 \quad (5)$$

Using (5) in the expression for the exchange constants (3) yields the following useful relation

$$\delta J_1 = -\delta J_2/2 \quad (6)$$

Thus the average interaction $\langle J \rangle$, which scales the transition temperature in our phase diagram Fig. 21, may be written

$$\langle J \rangle = J_0 + \delta J \quad (7)$$

where

$$\delta J = -\delta J_1 = \delta J_2/2 \quad (8)$$

From these relations we may express the ratio J_1/J_2 as

$$\frac{J_1}{J_2} = \frac{J_0 + \delta J_1}{J_0 - 2\delta J_1} \quad (9)$$

As $J_1/J_2 \rightarrow \infty$, $\delta J_1 \rightarrow J_0/2$, which gives us the final result

$$J_1 \rightarrow 3J_0/2 \quad \text{as } J_1/J_2 \rightarrow \infty \quad (10)$$

Repeating the analysis for the ratio J_2/J_1 gives

$$\frac{J_2}{J_1} = \frac{J_0 + \delta J_2}{J_0 - \delta J_2/2} \quad (11)$$

As a result, when $J_2/J_1 \rightarrow \infty$, we have $\delta J_2 \rightarrow 2J_0$, and therefore

$$J_2 \rightarrow 3J_0 \quad \text{as } J_2/J_1 \rightarrow \infty \quad (12)$$

The two results (10) and (12) allow us to relate the scale of the phase transition temperatures to the cubic coupling J_0 since in Phase I, T_N asymptotically approaches

$$T_N \rightarrow 2.6 J_2 = 7.8 J_0 \quad \text{as } J_2/J_1 \rightarrow \infty \quad (13)$$

Similarly, for Phase II, the specific heat peak is given by

$$T_N \rightarrow 0.8 J_2 = 1.2 J_0 \quad \text{as } J_1/J_2 \rightarrow \infty \quad (14)$$

Using these results we may present the phase diagram with the transition temperature in terms of J_0 as in Fig. 22 using a simple interpolation factor to renormalize the transition temperatures.

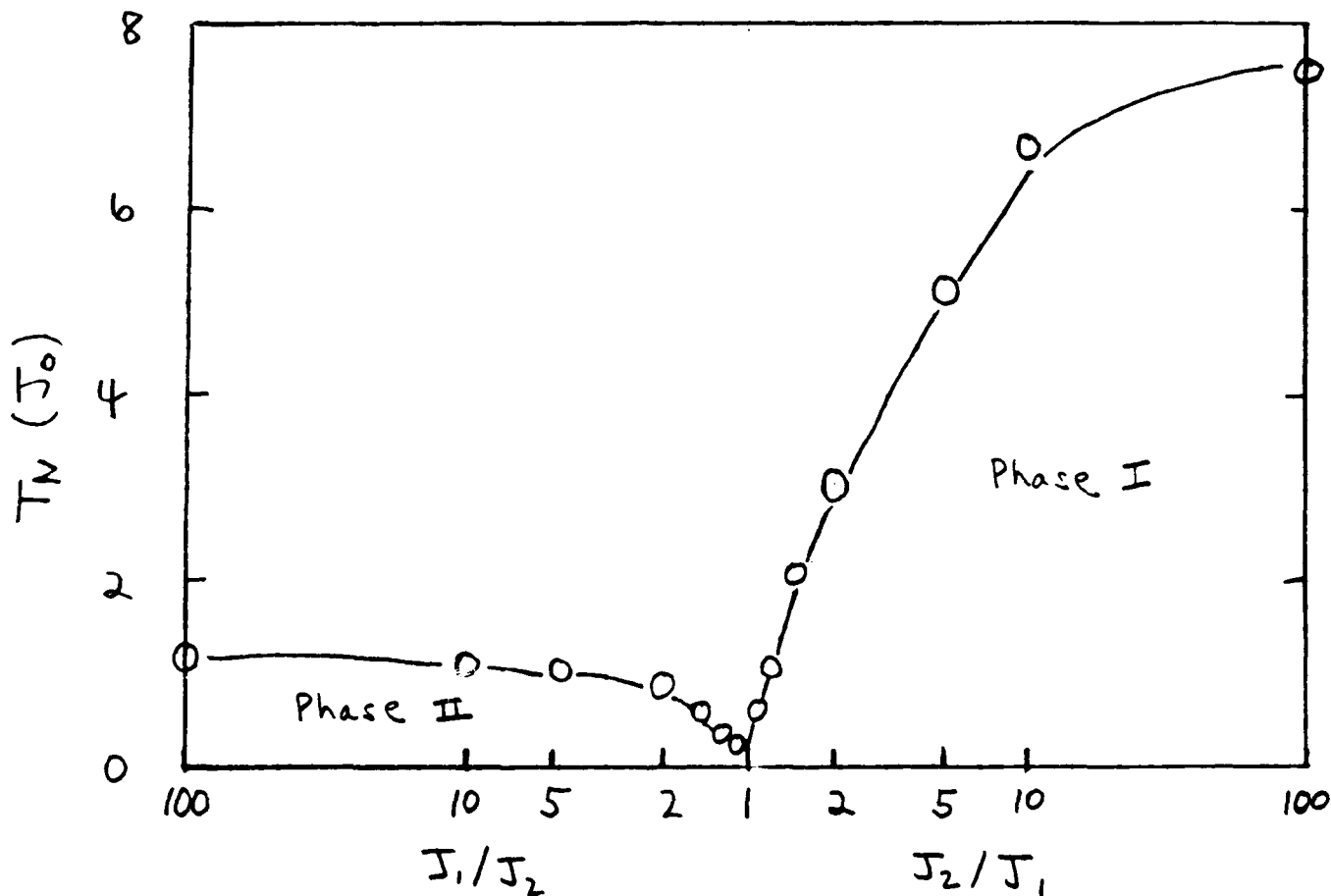


Fig. 22. Phase diagram of the B-site spinel materials CdCr_2O_4 and ZnCr_2O_4 from Monte Carlo simulations for annealed sample. Data obtained in decreasing T runs. T_N is measured in units of J_0 .

The final version of our phase diagram, Fig. 22, shows a large asymmetry for the two tetragonal phases. Phase I, with $c < a$, has a potential transition temperature about six times higher

than does Phase II, with $c > a$. The reason is associated with several factors

- the reduction in frustration by breaking the cubic symmetry,
- the fact that the $c < a$ phase corresponds for large a/c ratio to a 2D spin model, while the $c > a$ phase becomes a 1D spin system for large c/a . Other considerations being the same, 2D models always have higher transitions than the corresponding 1D system,
- the fact that to first order the change in the c axis lattice constant is twice as large as that in the a - b plane, favoring Phase II, which depends primarily on the c axis interaction, J_2 .

Thus, the experimental data on the different spinel systems are now easily explained. From Table I, the systems which distort for $c < a$ at the magnetic transition would lie in Phase I, while the compounds with $c > a$ lie in the Phase II region. Thus, from Fig. 22, the transition temperatures of the $c < a$ compounds would be expected to be higher.

These results may also account for the effects of varying preparation conditions on the location of the specific heat peak in ZnCr_2O_4 . Data taken at CeramPhysics indicate that high purity ZnCr_2O_4 has a sharp transition at 12K, while the 9-to-1 composite ZCN(9/1) has a transition at about 10K, and compacted ZnCr_2O_4 has a transition at 9K.¹¹ Since impurities are expected to broaden and split the transition^{1,2,3}, the high purity sample with a slight lattice distortion (Table I) at the transition has the highest transition, in the region of Phase II of Fig. 22. The

ZCN(9/1) sample is believed not to be under stress due to the similar expansion coefficients of the two constituents.¹¹ However, in a composite, the ability to deform into the tetragonal phase is inhibited compared to the high purity form, thus T_N is lower. Finally the compacted form is most severely restricted from distorting due to the random close-packed nature of the polycrystals involved. This is quite different from a single crystal in which the grains, in effect, are able to distort coherently, producing the largest possible transition temperature.

Finally, in CdCr_2O_4 , as noted from Table I, a lattice distortion has not yet been found from scattering experiments at low temperature. This may indicate a more rigid lattice with respect to a tetragonal distortion, and therefore a more delicate balance between the spin and lattice energies. Thus the experiments indicate a relatively sharp transition occurs in the conventional and CCN(9/1) samples but not in the high-purity and compacted forms.¹¹ Variation in preparation conditions, especially in view of the volatility of the Cd, may cause enough vacancies to affect the tetragonal transition. The Cd-O bond length is under considerable compression in CdCr_2O_4 , being 8% smaller than the sum of the ionic radii, while in ZnCr_2O_4 , for comparison, the Zn-O bond is essentially uncompressed, being just 1% smaller in length than the sum of the ionic radii.¹² Thus the presence of vacancy defects would have a sensitive effect on the possibility of a tetragonal lattice distortion, a sensitivity which is reflected in the experiments.

REFERENCES

1. OSU Progress Report, Research on High-Specific-Heat Dielectrics, Theoretical Studies I: Effects of Impurity Spin Doping on Undistorted Spinel Lattice, AFOSR Contract F49620-86-C-0049, August 31, 1988.
2. OSU Progress Report, Research on High-Specific-Heat Dielectrics, Theoretical Studies II: Effects of Impurity Spin Doping on Tetragonally Distorted Spinel Lattice - $c < a$ Case, AFOSR Contract F49620-86-C-0049, September 30, 1988.
3. OSU Progress Report, Research on High-Specific-Heat Dielectrics, Theoretical Studies III: Effects of Impurity Spin Doping on Tetragonally Distorted Spinel Lattice - $c > a$ Case, AFOSR Contract F49620-86-C-0049, October 30, 1988.
4. Annual Technical Report, Research on High-Specific-Heat Dielectrics, AFOSR Contract F49620-86-C-0049, May 11, 1987.
5. K. Huang, Statistical Physics, 2nd Ed., Wiley, 1987, p. 390.
6. CeramPhysics, Inc. Progress Report, Research on High-Specific-Heat Dielectrics, AFOSR Contract F49620-86-C-0049, Latent Heat Measurements, November 11, 1987.
7. OSU Progress Report, Research on High-Specific-Heat Dielectrics, Theoretical Studies IV: Ginzburg-Landau Analysis of Nature of Magnetic Phase Transitions in Spinel Chromite Materials, AFOSR Contract F49620-86-C-0049, November 30, 1988.
8. In some of our previous reports the notation $J_{\parallel} = J_1$ for the coupling within the x-y plane and $J_{\perp} = J_2$ for the coupling in the z direction was used. The Monte Carlo simulations used the Ising model in which each spin takes the possible values $\pm S$, where S is the magnitude of the spin. The spins are set on the B sites of a cube of the spinel lattice 5 unit cells on a side containing 2000 spins. Periodic boundary conditions are used to eliminate boundary effects.

9. A. Oles, F. Kajzar, M. Kubab, and W. Sikora, Magnetic Structures Determined by Neutron Diffraction, Panstwowe Wydawnictwo Naukowe, Warsaw, 1976.
10. C.-Y. Lin, Y. Lu, and B.R. Patton, to be submitted for publication.
11. CeramPhysics, Inc. Progress Report, Research on High-Specific-Heat Dielectrics, AFOSR Contract F49620-86-C-0049, Broad-Range Specific Heat Measurements, August 26, 1988, see Fig. 4 and Fig. 6.
12. J.C. Slater, Symmetry and Energy Bands in Crystals, McGraw-Hill, 1965, Appen. 1.

VII.F. SPLITTING OF SPECIFIC HEAT PEAKS IN SPINEL MATERIALS:
EFFECTS OF SPIN CLUSTERING

I. Introduction

The key questions in the AFOSR program on the high specific heat dielectrics based on the chromite spinels, CdCr_2O_4 and ZnCr_2O_4 , has been the precise nature of the magnetic phase transition, including the determination of what causes the high value of the specific heat near the transition as well as what determines the magnitude of the transition temperature.

In order to investigate these questions, doping with spin impurity ions has been explored both experimentally and theoretically.^{1,2,3,4} One of the characteristic features found in the experiments by CeramPhysics was a splitting of the specific heat peak when impurity spins were added.

In our Monte Carlo simulations of the spinel lattice for different possible low temperature lattice structures, we found evidence for a variety of behaviors: 1) a spin glass-like freezing transition in the cubic structure, 2) a antiferromagnetic transition in the $c < a$ tetragonal structure, and 3) a partially frustrated antiferromagnetic transition in the $c > a$ tetragonal structure.^{2,3,4}

However, none of our Monte Carlo calculations produced a splitting of the specific heat peak. We believe this is due to the fact that we have assumed a completely random distribution of the impurity spins in doing the simulations, while correlations between impurity spins leading to clustering effects are present in the samples.

This report summarizes our calculations on cluster models. The results we obtain explain the puzzling features of the experimental data obtained on the doped ZnCr_2O_4 spinel materials where the specific heat peak splits into two peaks by the introduction of spin impurities.

In Section II we review the current evidence on the effects spin doping on the phase transition in the spinels. Section III discusses our calculations on spin clusters, while Section IV provides a summary.

II. Experimental Results on Spin Doping

The recent measurements of specific heats on a wide variety of spinel materials including pure, doped, and composite forms of the spinel system have provided a rich variety of phenomena. A characteristic result is shown for the ZnCr_2O_4 system in Fig. 1, taken from a recent CeramPhysics report.¹ The data reveal a single peak in the pure ZnCr_2O_4 material, and a split peak structure in samples which are doped with various impurities of different spin. The data indicate a split peak occurs for all three dopants, including Gd, with a larger spin than the host Cr, as well as V and Al, with smaller spins than Cr.

In our extensive Monte Carlo doping studies, reported earlier,^{2,3,4} we found shifts in the peaks of the specific heat curves that we in excellent agreement, both in magnitude and direction, with the experimental trends in Fig. 1 and other CeramPhysics measurements.¹ However, one feature which did not

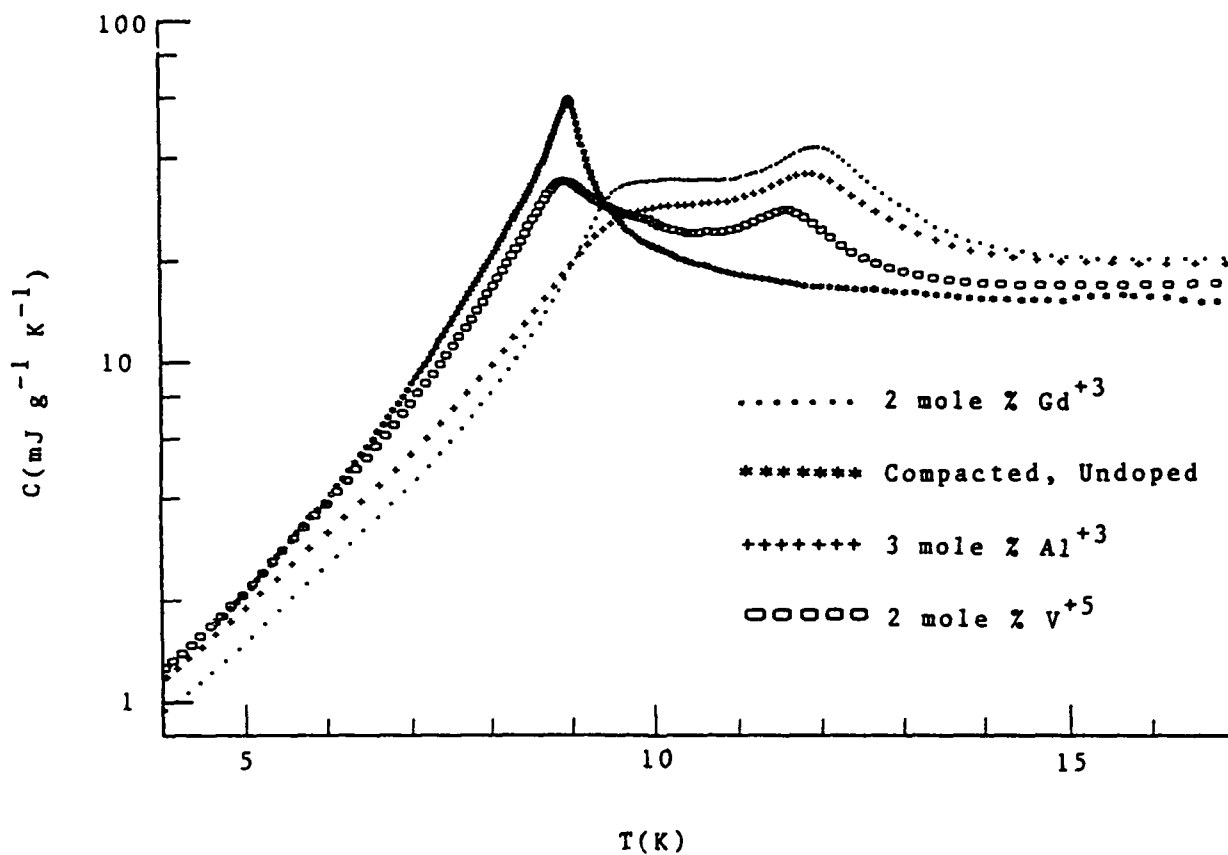


Fig. 1. Experimental specific heat vs. temperature data from Ref. 1 for a number of doped ZnCr_2O_4 ceramics. For the trivalent ionic state, the spin relative to the host Cr^{3+} of Gd, V, and Al are $7/3$, $2/3$, and 0 , respectively.

come out of the Monte Carlo simulations was a splitting of the specific heat peaks. Earlier analysis of this effect suggested to us that the origin of the splitting might arise from local clustering effects. If an impurity spin replaces a host spin in the elementary tetrahedron that makes up the spinel lattice, then the energy levels of that tetrahedron are changed in a characteristic way. Frustration is locally reduced because the impurity spin breaks the symmetry of the tetrahedron. Since we have shown in many ways that frustration is the key property of the spinel materials CdCr_2O_4 and ZnCr_2O_4 , the impurity spin would therefore be expected to have a significant effect.

III. Theoretical Calculations of Cubic and Tetragonal Spin Clusters

In our Monte Carlo calculations, reported previously,^{2,3,4} doped impurity spins were distributed at random in the host lattice. This model is appropriate for a quenched sample in which there is no correlations between the positions of the impurities ions. However, in a sample which is annealed for a period of time, the impurities may develop a regular pattern of distribution. As a result, the sample may then be characterized by the presence of clusters composed of host spins with an impurity spin.

We will consider first the effects of spin clustering on the undistorted cubic spinel lattice. The procedure is to take a finite cluster of N spins, replace one spin with an impurity spin

of different magnitude, and connect the spins on opposite sides of the cluster with periodic boundary conditions. This effectively constructs an infinite crystal with a unit cell composed of the cluster. The properties of this lattice will therefore be dominated by the properties of the cluster. The thermodynamic properties such as the energy, the specific heat, and the susceptibility may be calculated numerically, exploiting the periodicity of the crystal.

The simplest cluster that can form is one impurity spin in a tetrahedron of four spins, which corresponds to a doping fraction of 25%. The result for the specific heat is shown in Fig. 2, for various values of the dopant spin, measured in units of the host spin, as is the temperature. Since the host ion is Cr^{3+} with spin $3/2$, the impurities in Fig. 1, namely, Gd, V, and Al, have a spin relative to Cr of $7/3$, $2/3$, and 0, assuming the trivalent ionic configuration for the dopants. For this cluster a splitting begins to develop for the largest spin $5/3$, consistent with the fact that the largest effect in the data of Fig. 1 is for the largest spin, Gd. However, a splitting does not occur for smaller values of the relative spin S , in particular for the value $S = 2/3$, corresponding to V^{3+} .

The next larger cluster that can form involves an impurity spin bridging two tetrahedral units, with typical configurations illustrated in Fig. 3. This cluster involves seven spins and a doping fraction of 14%. The results for this lattice are shown in Fig. 4. The most striking result for this cluster is the development of splitting for relative spin less than one. Since

the actual experiment sample will contain clusters of all sizes, our cluster results indicate that splitting of the specific heat peak is possible for impurity spins both larger and smaller than the host spin.

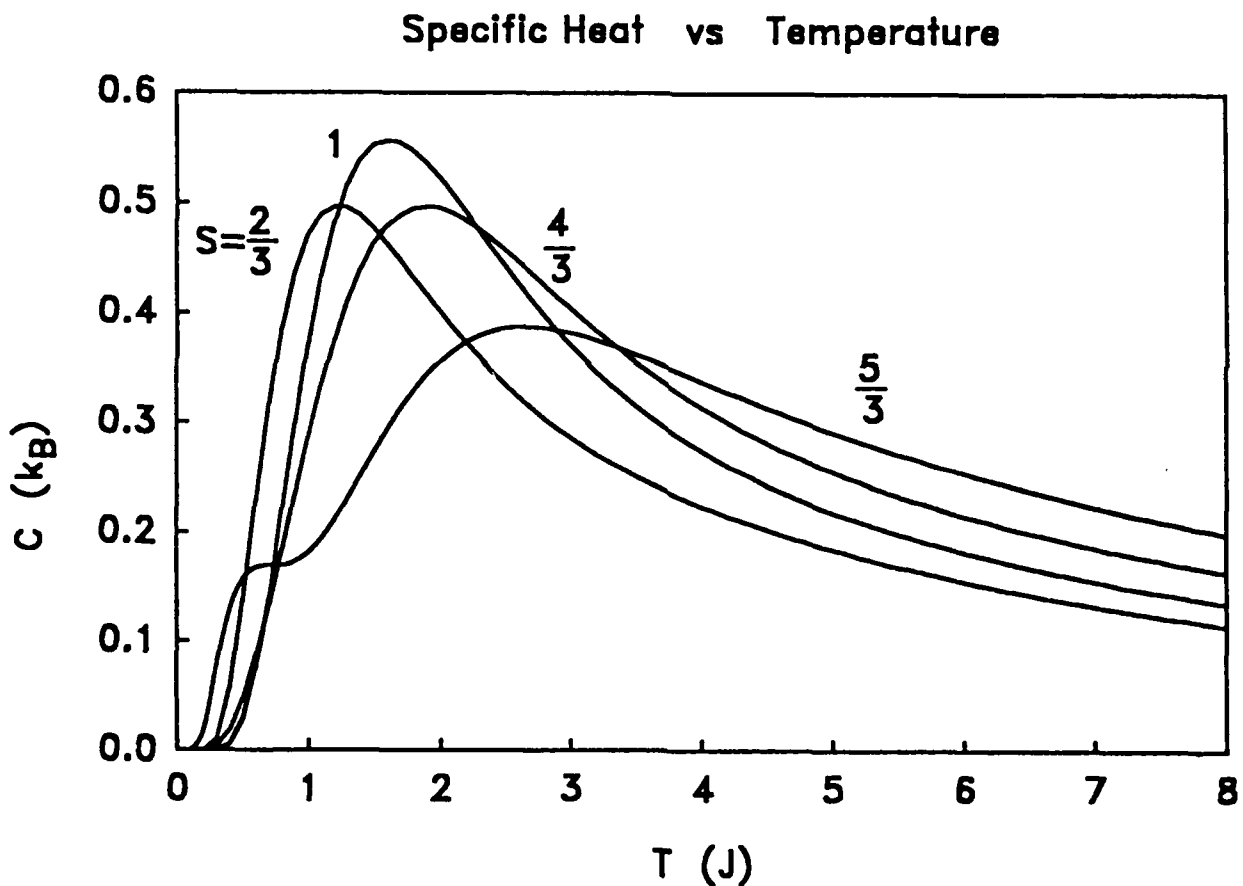


Fig. 2. Specific heat vs. temperature T for cubic lattice composed of four spin clusters with $J_2/J_1 = 1$.

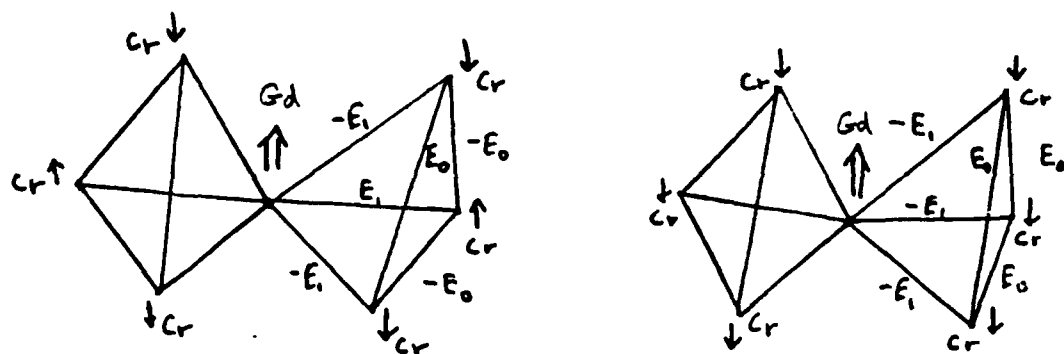


Fig. 3. Impurity spin configurations in double tetrahedra with seven spins: six Cr spins and one impurity spin.

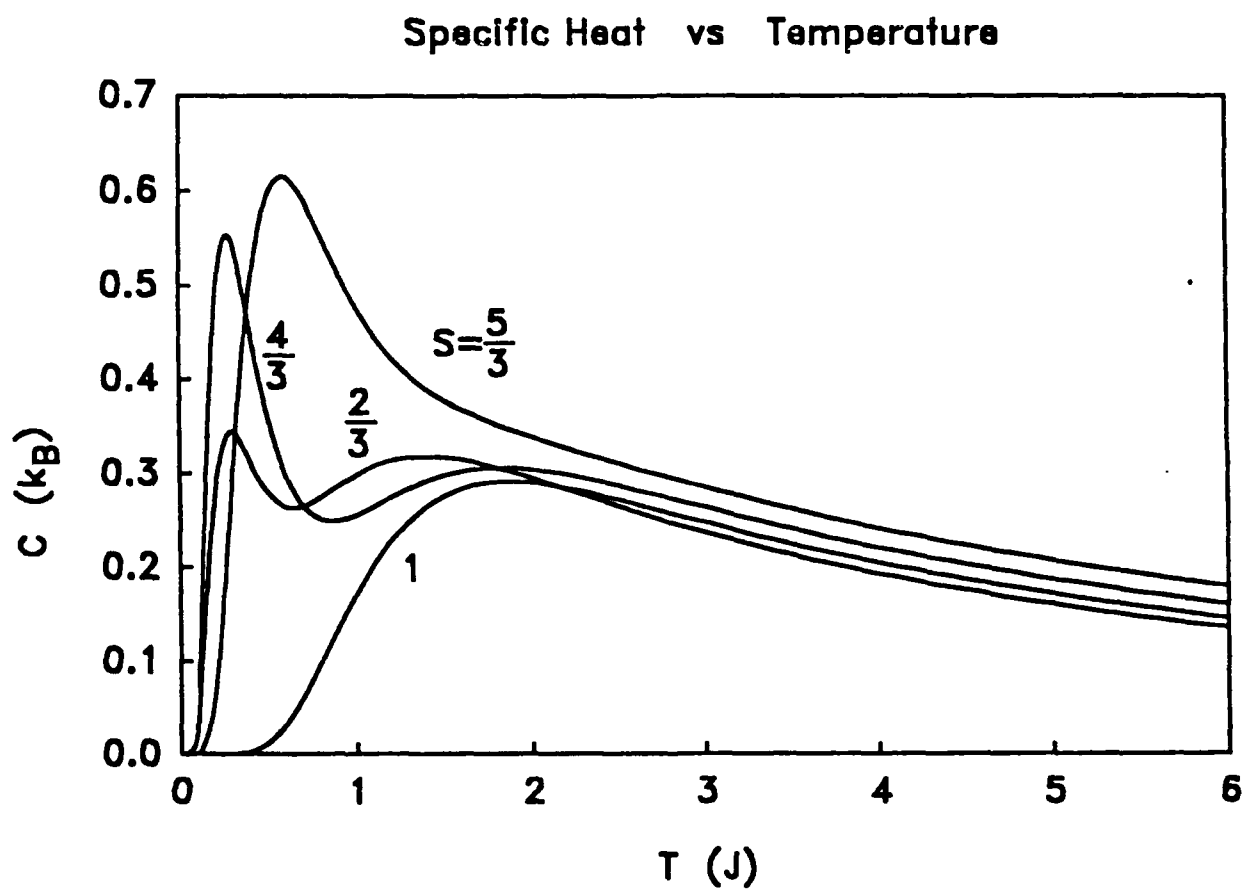


Fig. 4. Specific heat vs. temperature T for cubic lattice composed of seven spin clusters with $J_2/J_1 = 1$.

As a result of these promising indications that the specific heat splitting was associated with the local spin configurations in a cluster, we undertook a study of these clustering effects when the spinel lattice was distorted into the tetragonal state, since our previous work has shown that the tetragonal lattice has a major effect on the phase transition.^{5,6}

In the tetragonal phase, the tetragonal lattice distortion parameter c/a becomes not equal to unity. The difference in the lattice constants a ($= b$) and c implies a difference in the exchange couplings J_{ij} in the x - y plane J_1 and the coupling J_2 in the z direction entering the spin Hamiltonian⁵

$$H = \sum_{\langle ij \rangle} J_{ij} S_i S_j \quad (1)$$

The frustration of the cubic spinel lattice is completely removed by a tetragonal distortion with decreased lattice constant in the z direction, $c < a$, corresponding to $J_2 > J_1$. The frustration of the cubic spinel lattice may also be reduced by a tetragonal distortion with increased lattice constant in the z direction, $c > a$, corresponding to $J_2 < J_1$. In this case, however, unlike the case $c < a$ discussed above, the distortion does not completely remove the frustration.

The calculations were carried out for the seven-spin cluster lattice, since the doping experiments were mostly carried out at lower concentrations.¹ The results for a range of tetragonal lattices corresponding to an exchange coupling ratio J_2/J_1 of 0.5, 0.9, 1.1, and 2.0 are presented in Figs. 5 to 9 as well as additional results for $J_2/J_1 = 1$.

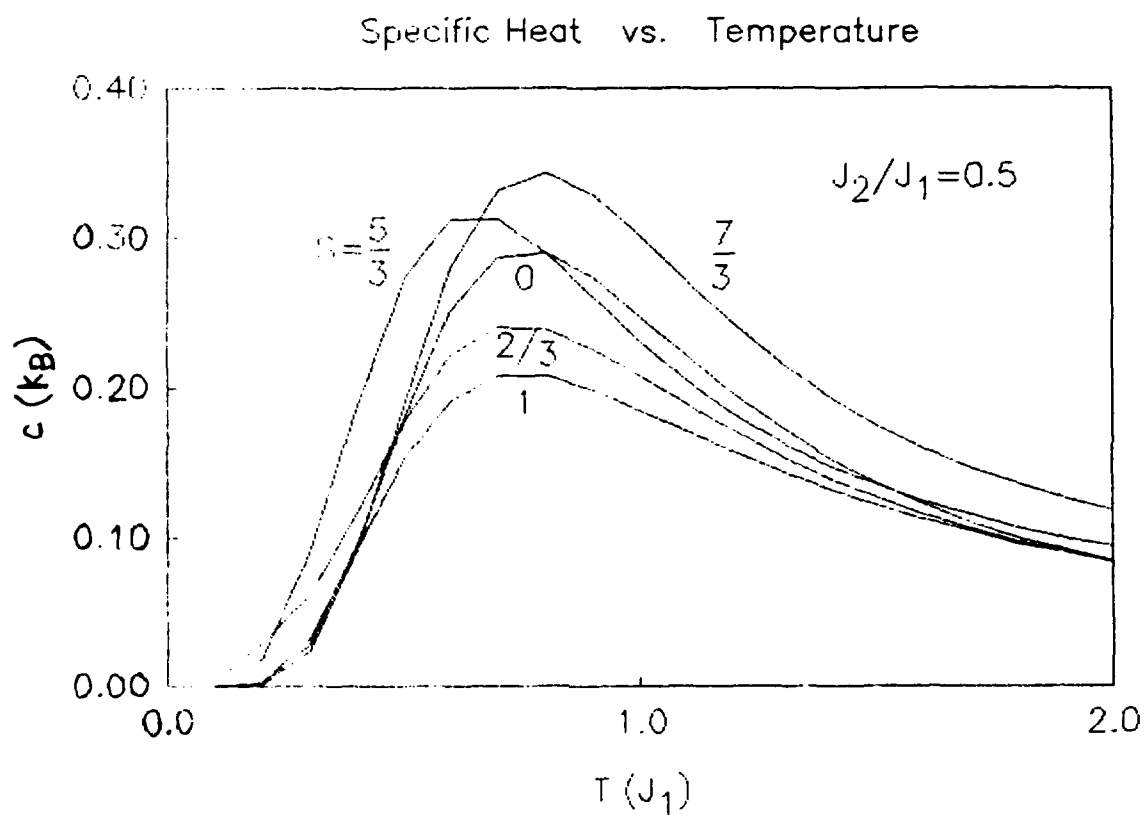


Fig. 5. Specific heat vs. temperature T for $c > a$ tetragonal spinel lattice composed of seven spin clusters with $J_2/J_1 = 0.5$.

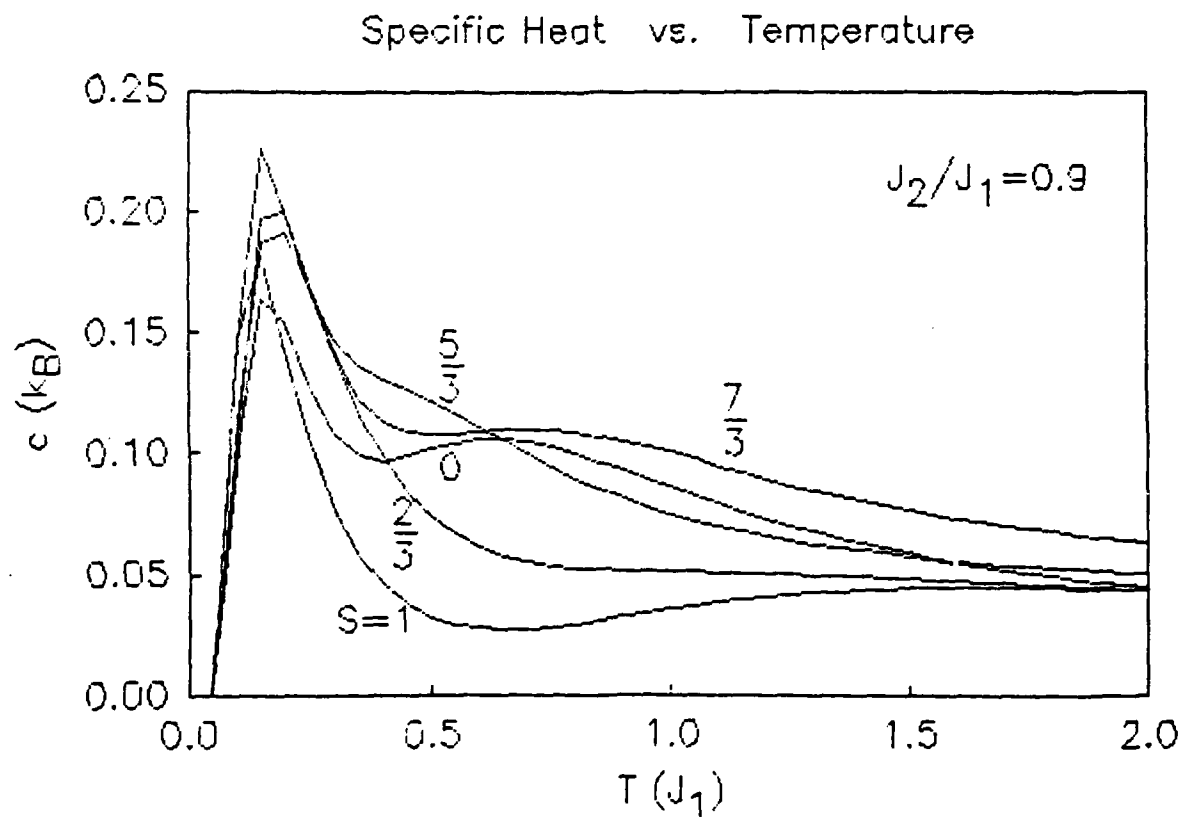


Fig. 6. Specific heat vs. temperature T for $c > a$ tetragonal spinel lattice composed of seven spin clusters with $J_2/J_1 = 0.9$.

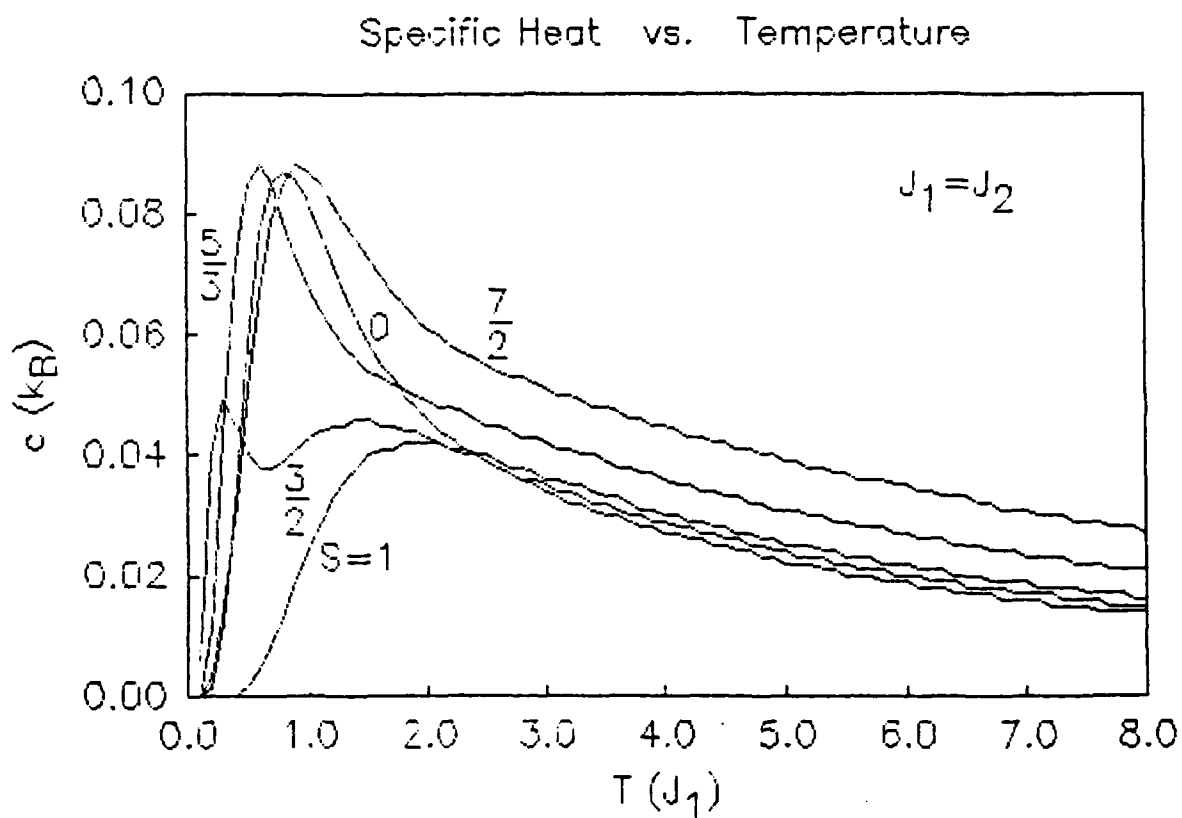


Fig. 7. Specific heat vs. temperature T for $c =$ a cubic spinel lattice composed of seven spin clusters with $J_2/J_1 = 1$.

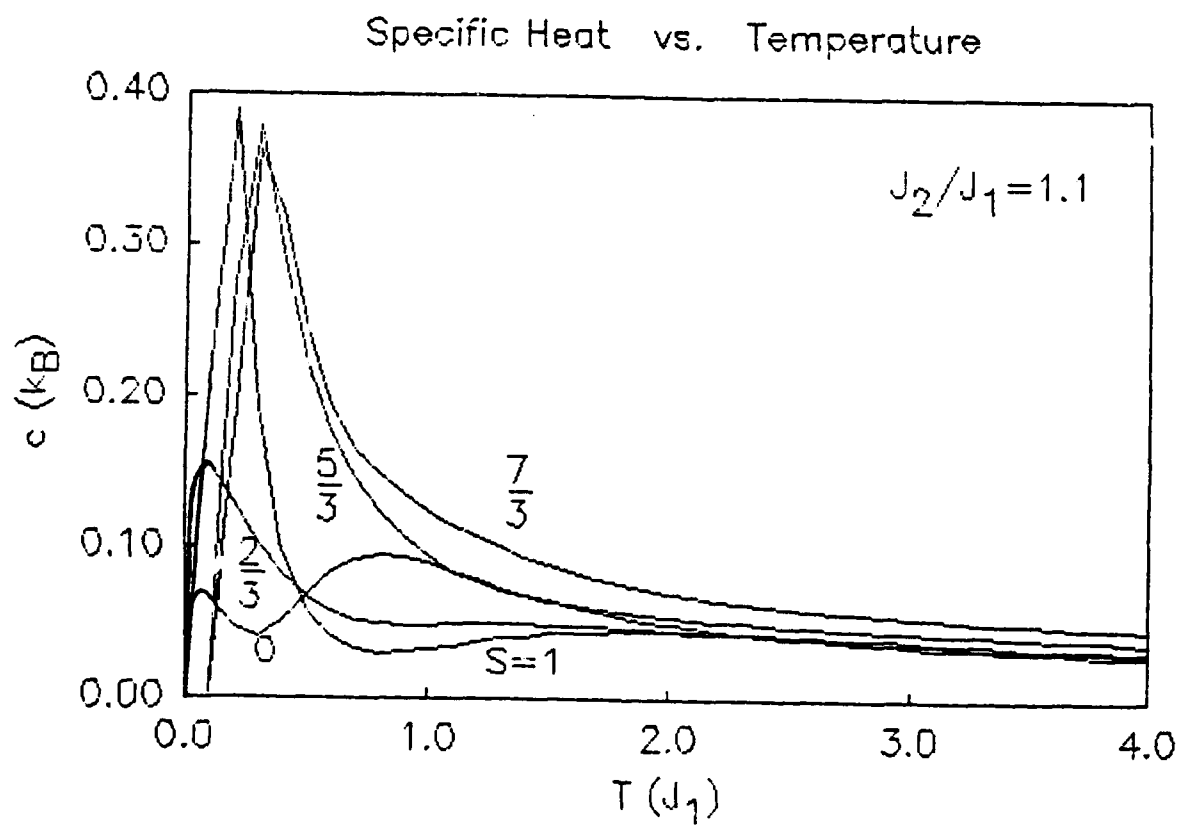


Fig. 8. Specific heat vs. temperature T for $c < a$ tetragonal spinel lattice composed of seven spin clusters with $J_2/J_1 = 1.1$.

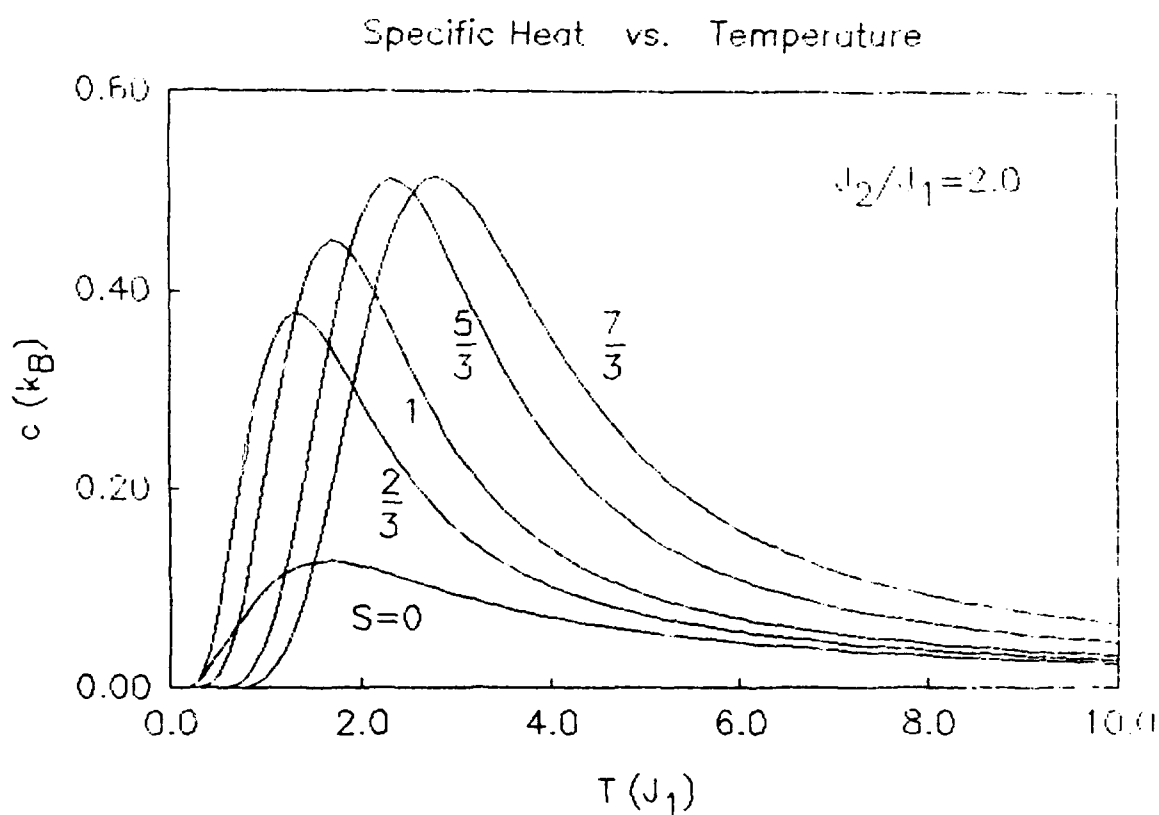


Fig. 9. Specific heat vs. temperature T for $c < a$ tetragonal spinel lattice composed of seven spin clusters with $J_2/J_1 = 2.0$.

The results show that when the lattice is distorted, split peaks occur for both impurity spins larger and smaller than the host spin: $S = 0$ and $S = 7/3$ in Fig. 6 for $J_2/J_1 = 0.9$. These values correspond to Al and Gd, and thus account nicely for the experimental results in Fig. 1 if those samples have c/a slightly greater than one. From our previous report⁵, this is the likely distortion in ZnCr_2O_4 . The split peak in the V case is also explained if that sample is not distorted, i.e., it has the cubic phase, $c = a$. In that case Fig. 4, shows a split peak for $S = 2/3$, corresponding to the relative spin of V.

The additional interesting feature is the disappearance of the split peaks when the lattice distortion becomes large, as shown in Fig. 5 ($c > a$) and Fig. 9 ($c < a$). Thus we may conclude that the experimental samples probably have small tetragonal distortions, and that the tetragonal distortion depends on the particular impurity substituted, due in part to ionic size considerations, for example.

IV. Summary and Conclusions

These results have provided an explanation of some unusual experimental data on doped spinel materials. The splitting in the specific heat arise from the change in the local exchange field produced by the presence of an impurity spin. The features of our results may be summarized as follows:

1. No significant change in the location of the specific heat peak of a cluster is produced by an impurity or a lattice distortion.
2. A splitting into two peaks is a general feature of doping with both larger and smaller spins relative to the host spin, as long as a tetragonal distortion is present.
3. Large values of tetragonal distortion remove the split peaks in the specific heat.

These results on the cluster effects of impurities in both cubic and tetragonal spinel lattice, together with our Monte Carlo calculations reported earlier, provide a rather complete picture of the phase transitions in the ZnCr_2O_4 and CdCr_2O_4 spinel materials. The reason the split peaks are not observed in the CdCr_2O_4 samples is no doubt associated with the much greater sensitivity of that transition to the effects of disorder in general. As indicated in our previous report the CdCr_2O_4 system is not known to distort tetragonally at the magnetic transition, thus frustration is much stronger, and the phase transition correspondingly weaker, in that material.

REFERENCES

1. CeramPhysics, Inc. Progress Report, Research on High-Specific-Heat Dielectrics, AFOSR Contract F49620-86-C-0049, Broad-Range Specific Heat Measurements, August 26, 1988.
2. OSU Progress Report, Research on High-Specific-Heat Dielectrics, Theoretical Studies I: Effects of Impurity Spin Doping on Undistorted Spinel Lattice, AFOSR Contract F49620-86-C-0049, August 31, 1988.
3. OSU Progress Report, Research on High-Specific-Heat Dielectrics, Theoretical Studies II: Effects of Impurity Spin Doping on Tetragonally Distorted Spinel Lattice - $c < a$ Case, AFOSR Contract F49620-86-C-0049, September 30, 1988.
4. OSU Progress Report, Research on High-Specific-Heat Dielectrics, Theoretical Studies III: Effects of Impurity Spin Doping on Tetragonally Distorted Spinel Lattice - $c > a$ Case, AFOSR Contract F49620-86-C-0049, October 30, 1988.
5. OSU Progress Report, Research on High-Specific-Heat Dielectrics, Theoretical Studies VII: Monte Carlo Calculations of Magnetic Phase Diagram of Spinel Chromite Materials, AFOSR Contract F49620-86-C-0049, December 7, 1988.
6. OSU Progress Report, Research on High-Specific-Heat Dielectrics, Theoretical Studies IV: Ginzburg-Landau Analysis of Nature of Magnetic Phase Transitions in Spinel Chromite Materials, AFOSR Contract F49620-86-C-0049, November 30, 1988.

VII.G. SUMMARY OF THEORETICAL STUDIES

Considerable attention has been devoted to the problem of randomly quenched dopants (impurities) on the spinel lattice using the theoretical tool of Monte Carlo calculations. Three lattice conditions have been examined: the cubic lattice ($a=b=c$), and the tetragonal lattice with both $a > c$ and with $a < c$. The dopants considered can have large spin values, or zero spin.

The salient findings can be grouped relative to important, experimentally observable properties, as follows:

1. Specific Heat Peak

- (a) Cubic Case: Large-spin dopants broaden the specific heat peak and increase the peak temperature, whereas spin-zero dopants reduce the magnitude of the peak but do not shift the transition temperature.
- (b) Tetragonal Case: Regardless of the spin, all dopants produce much larger and sharper specific heat peaks, indicating true long-range antiferromagnetic ordering, and large-spin dopants broaden and lower the peak. For spin-zero dopants, there is a sharp drop in the transition temperature if $a < c$.

2. Magnetic Susceptibility

- (a) Cubic Case: Regardless of the spin, all dopants produce free spins that show up as a $1/T$ Curie tail in the susceptibility. However, for large concentrations (above 50%) of large-spin dopants, this curie tail disappears.
- (b) Tetragonal Case: For $a > c$, both large-spin and zero-spin dopants remove the $1/T$ Curie tails in the susceptibility. However, for $a < c$, both these types of spins give rise to cusps in the susceptibility.

Whether the transitions in these spinels are first order or

second order has been studied using both a Ginzburg-Landau microscopic model and Monte Carlo calculations. The G-L model is only valid for the $a > c$ tetragonal distortion. A phase diagram for the transition is derived consisting of Phase I ($a > c$) and Phase II ($a < c$), and both the G-L and Monte Carlo calculations reveal that Phase I transitions are second order in all cases, with potentially higher temperature transitions. The Phase II transitions can be first or second order, and it is suggested that the preparation conditions can determine whether the spinel is in Phase I or Phase II.

The Monte Carlo calculations yield four central results: (1) A spin-glass-like freezing transition in the perfectly frustrated cubic case; (2) A completely unfrustrated antiferromagnetic, second order transition for a Phase I, $a > c$ tetragonal distortion; (3) A partially frustrated, antiferromagnetic transition for a Phase II, $a < c$ tetragonal distortion; and (4) No splitting of the specific heat peak under any conditions.

The splitting of the specific heat does not come out of the Monte Carlo calculations because the effects of spin clustering have been ignored in the assumption that the dopant (impurity) spins are randomly distributed. In fact, spin clustering effects are expected due to correlations between these impurity spins, and spin-clustering reduces the local frustration. A seven-spin cluster is examined for the Phase II, $a < c$ tetragonal-distortion case, and it is found that the specific heat is split into two peaks for spin values between zero and $7/2$ but the temperature of the peak(s) is not shifted significantly (A similar result is found for the cubic case for one bridging impurity between two tetrahedra). A further prediction of this Phase II calculations is that the peak-splitting disappears if the tetragonal distortion is too large.

These results on cluster effects together with the Monte Carlo calculations provide a good preliminary picture of the phase transitions in the ZnCr_2O_4 and CdCr_2O_4 spinels. The evidence strongly suggests that the transition in ZnCr_2O_4 is of the Phase II, $a < c$ case. The tetragonal distortion in CdCr_2O_4 is

less clear, and this spinel may remain essentially cubic and highly frustrated. Split specific-heat peaks may not be observed in CdCr_2O_4 because the transition in this material may be much more sensitive to disorder in general.

VIII. CONCLUSIONS AND DISCUSSION

In this concluding section, two areas will be focused on: In Section VIII.A., comparisons and contrasts between the experiments and theory will be made, and in Section VIII.B. future research directions will be identified.

VIII.A. STATUS OF EXPERIMENTS AND THEORY TO DATE

A large amount of experimentation has been performed on ceramic samples of ZnCr_2O_4 and CdCr_2O_4 prepared under new conditions of doping, stress, purity, and particle size. No structures in the specific heats of these spinels are induced above 15 K by wide variations in one or all of these conditions.

Under various doping conditions, the specific heat peak in CdCr_2O_4 can be sharpened, broadened, or eliminated, but not split. In contrast, the specific heat peak in ZnCr_2O_4 is easily split into two components by all dopants studied. Calorimetric, magnetic susceptibility, and EPR measurements are in basic agreement in characterizing these effects.

Monte Carlo calculations have shown how the perfect frustration of the cubic lattice can be partially or fully removed by tetragonal distortions, and the theoretical suggestions are that ZnCr_2O_4 is characterized by a partially frustrated, $a < c$, second-order, antiferromagnetic transition, whereas CdCr_2O_4 may remain essentially cubic and highly frustrated. Incorporation of spin-clustering successfully explains the double specific heat peaks observed in ZnCr_2O_4 .

The Monte Carlo calculations show the sensitivity of the thermal properties of the chromite spinel lattice to tetragonal distortions. In contrast, however, the specific heat peaks in ZnCr_2O_4 and CdCr_2O_4 are experimentally unaffected by stress types (tensile or compressive) or stress magnitudes. Here also, the thermal, magnetic susceptibility, and EPR measurements are in basic agreement.

In very fine-grain powders ($\sim 100 \text{ \AA}$), broad specific heat

maxima are found in these spinels and correspond to antiferromagnetic transitions. Surprisingly, a 5% Gd doping restores a sharp specific heat peak in ZnCr_2O_4 but not in CdCr_2O_4 . Calorimetric data show that powders have the highest density of free spins below the transition, especially so in the case of Gd doping. The EPR measurements, however, are not in agreement with this finding.

Monte Carlo calculations show that for the $a < c$ tetragonal distortion, the transition is second order; however, for the $a > c$ distortion, the transition can be either first or second order. The slow temperature drifts used in the specific heat measurements are extremely sensitive to first-order latent heats at transitions, and no evidence of a latent heat is observed in all of the samples. Either all transitions are second order, or, if first order, have very small latent heats.

Low temperature thermal contraction measurements on ZCN(9/1) and CCN(9/1) ceramic samples show that there is a distortion in the lattice constants of each material at the respective antiferromagnetic transition temperature.

Dielectric anomalies are observed at the transitions in ZnCr_2O_4 and CdCr_2O_4 , and these findings have been explained theoretically by incorporating a coupling between the polarization and the magnetization in the spin-frustration model.

VIII.B. FUTURE RESEARCH DIRECTIONS

At this point in the research, the effects of doping and stress on the transition have been thoroughly explored experimentally using ceramic samples. Future research areas should embrace three general areas, as follows:

1. Single Crystals. No experiments to date have been performed on single crystals, but the growth furnace and auxiliary equipment have now been completed. Future research should be devoted to growing and measuring single crystals.
2. Free Spin. The density of free spins has now been seen

to vary by a factor of 50 - 60, depending on sample preparation and doping. This area needs further research by measuring specific heats down to 1.8 K of the samples on hand. The EPR and calorimetric measurements have to be brought into agreement here.

3. Theoretical Research. The theoretical research needs to explore further into the nature of the transitions in these spinels in light of the finding that transitions are not affected by stress. The large variation in the density of free spins found below the transition temperature is a new, rich area for theoretical research.